Emergence, Complexity and Computation ECC

Ali Sanayei
Otto E. Rössler
Ivan Zelinka *Editors*

# ISCS 2014: Interdisciplinary Symposium on Complex Systems

Springer

# Emergence, Complexity and Computation

Volume 14

*About this Series*

The Emergence, Complexity and Computation (ECC) series publishes new developments, advancements and selected topics in the fields of complexity, computation and emergence. The series focuses on all aspects of reality-based computation approaches from an interdisciplinary point of view especially from applied sciences, biology, physics, or Chemistry. It presents new ideas and interdisciplinary insight on the mutual intersection of subareas of computation, complexity and emergence and its impact and limits to any computing based on physical limits (thermodynamic and quantum limits, Bremermann's limit, Seth Lloyd limits...) as well as algorithmic limits (Gödel's proof and its impact on calculation, algorithmic complexity, the Chaitin's Omega number and Kolmogorov complexity, non-traditional calculations like Turing machine process and its consequences,...) and limitations arising in artificial intelligence field. The topics are (but not limited to) membrane computing, DNA computing, immune computing, quantum computing, swarm computing, analogic computing, chaos computing and computing on the edge of chaos, computational aspects of dynamics of complex systems (systems with self-organization, multiagent systems, cellular automata, artificial life,...), emergence of complex systems and its computational aspects, and agent based computation. The main aim of this series it to discuss the above mentioned topics from an interdisciplinary point of view and present new ideas coming from mutual intersection of classical as well as modern methods of computation. Within the scope of the series are monographs, lecture notes, selected contributions from specialized conferences and workshops, special contribution from international experts. More information

about this series at http://www.springer.com/series/10624

Ali Sanayei · Otto E. Rössler
Ivan Zelinka
Editors

# ISCS 2014: Interdisciplinary Symposium on Complex Systems

Springer

*Editors*
Ali Sanayei
Institute for Theoretical Physics
Tübingen
Germany

Otto E. Rössler
Institute for Physical and Theoretical
Chemistry
University of Tübingen
Tübingen
Germany

Ivan Zelinka
Department of Computer Science
Faculty of Elect. Eng. and Comp.Sci.
Ostrava-Poruba
Czech Republic

ISSN 2194-7287 ISSN 2194-7295 (electronic)
ISBN 978-3-319-10758-5 ISBN 978-3-319-10759-2 (eBook)
DOI 10.1007/978-3-319-10759-2

Library of Congress Control Number: 2014949171

Springer Cham Heidelberg New York Dordrecht London



Printed on acid-free paper

Springer is part of Springer Science+Business Media (www.springer.com)

# Preface

The present book is the upshot of the "2014 Interdisciplinary Symposium on Complex Systems," held at the "Athens of the Middle Ages" as a continuation of our symposia series. Florence, birthplace of the Italian Renaissance, has a unique genius loci to it. It suffices to point to the eminent physicist who was buried there after playing here his pivotal role in the modern scientific revolution. He was a "Sire" in the word of his faithful daughter Virginia (Sister Maria Celste) and was "the father of modern physics – indeed of modern science altogether" in Einstein's words. When Galileo Galilei was 68 years old he wrote the epoch making book "A Dialogue Concerning the Two Chief World Systems: Ptolemaic and Copernican." Because of this he found himself "vehemently suspected of heresy" and got forced down on his knees to eat his words and was sentenced to permanent house arrest. He can also be seen in the tradition of an earlier more eastern school, Rumi's, which held that "there is no limit to thinking and there is a world of freedom inside every person."

In accordance with Galilei, the main aim of the symposium was to bring together many diverse points of view by scientists working on complex systems in a both divergent and convergent manner. The reader – student or professional scientist – will encounter four general categories of papers: Physical modeling of complex systems, Evolutionary computations, Complex biological systems, and Complex networks. The presentations comprise innovative ideas, philosophical overviews or state-of-the-art applications in miscellaneous fields.

At this point, we would like to express our special gratitude to our participants, our program committee, the keynote speakers (Yuri Manin, Rudolf Kalman, Karoline Wiesner and Antonio Politi), the University of Florence and the Galileo Galilei Institute for Theoretical Physics who helped us a lot to continue our symposium series in an efficient way.

The special event of this year's symposium was a "Galilei-Turing Round-table" held among our keynote speakers, accompanied by John Symons, and chaired by Barry Cooper. The round-table was devoted to diverse open problems in the physics and computation of complex systems. We accordingly dedicate the book to the memory of

Alan Turing who believed that “mathematical reasoning may be regarded rather schematically as the exercise of a combination of two facilities which we may call *intuition* and *ingenuity*.”

July 2014

Ali Sanayei
Ivan Zelinka
Otto E. Rössler

# Contents

## Part II: Evolutionary Computations



## Part III: Complex Biological Systems

## Part IV: Complex Networks

# Part I

# Physical Modeling of Complex Systems

# Physics in the World of Ideas: Complexity as Energy*

Yuri I. Manin

Max–Planck–Institut für Mathematik, Bonn, Germany

## Introduction: Two Faces of Computation

Since the origins of civilisation, computation methods adopted in various cultures could be roughly subdivided into two types.

One relied upon a system of notation, initially only for numbers, and rules of performing arithmetical operations on these notations. I will refer to this type as the *linguistic* one. Gradually it developed into *algebra* where generic or specific names could be ascribed to other mathematical objects, and then to operations on them as well.

The second type of computation methods stressed their *manipulation with objects*, such as arithmetical computations using abacus, Chinese counting sticks, arithmometer, slide rule, geometric measurements etc.

The discovery of the abstract theory of computability in the 1930's followed this pattern as well: Alonzo Church and Andrey Markov used linguistic models whereas Alan Turing introduced his celebrated "machine". In the powerful image of Turing machine a computation is "a physical process performing linguistic tasks". Finally, the opposition *software/hardware* in applied computer science is the contemporary avatar of this duality.

Introduction of entropy in the information theory by C. Shannon in 1948 was probably the key moment in the development of *"physics of the world of ideas"*.

However, at least before 1980's, theory of computability did not really use conceptual richness of theoretical physics: principle of minimal action, conservation laws, basic symmetry groups of fundamental physical models. For example, space–time of a Turing machine is "Galilean" one: space dimension is stretched along the tape whereas time dimension is embodied in the sequence of states and positions of the head.

With advent of the idea of quantum computing, the necessity of bridging world of physics and Platonic world of (un)computable became urgent. There were many attempts to do this: see a lively survey [A1], and [Man4], [Man5] motivated by path integration in quantum field theory.

However, most of these attempts were dedicated to "mental engineering": attempts to devise quantum (or mixed quantum/classical, cf. [Man3]) gadgets capable to solve, say, NP–complete problems in polynomial time. S. Aaronson in

* Keynote talk at the 2014 Interdisciplinary Symposium on Complex Systems (ISCS'14), University of Florence, September 15–18, 2014.



A. Sanayei et al. (eds.), *ISCS 2014: Interdisciplinary Symposium on Complex Systems*, Emergence, Complexity and Computation 14, DOI: 10.1007/978-3-319-10759-2_1

[A1] eloquently puts forward the idea that $P \neq NP$ principle might be elevated to the status of an important law of physics, cf. also [A2].

In my work of the last years, I was trying to develop the beautiful idea of Andrey Kolmogorov who connected the physical idea of "randomness" of, say, a finite sequence of bits ("string") $w$, with the mathematical idea of "incompressibility" of this string. Incompressibility here means impossibility to get $w$ as the output of a Kolmogorov optimal Turing machine taking as input a considerably shorter than $w$ sequence of bits, whereas "randomness" means absence of all nontrivial regularities or correlations. See [ZvLe] for an early development of this idea.

As I will explain in this talk, the Kolmogorov complexity of a combinatorial object (and more generally, of a semicomputable function) has strong similarities to the physical notion of *energy level* of an isolated system. I will show that partition functions and quantum evolution operators involving Kolmogorov complexity throw new light upon such problems as computation of asymptotical bounds of error–correcting codes ([VlaNoTsfa], [ManMar1], [ManMar3]), and origins of Zipf's law ([Zi1], [Zi2], [Mand], [Ma1], [Ma2]).

## 1 Complexity as Energy

### 1.1 Energy, Partition Function and Hamiltonian Evolution

Here I briefly remind two basic contexts in which the notion of energy is used in theoretical physics.

(i) In statistical thermodynamics, we imagine that a system can occupy an enumerable set of states, with energy $E_n$ at the state number $n = 1, 2, 3, \ldots$. Its interaction with environment is described via thermal contact; the temperature of the system is denoted $T$. Put $\beta := -1/kT$ where $k$ is the Boltzman constant. The partition function of the system

$$Z := \sum_n e^{-\beta E_n} \tag{1.1}$$

defines the probability $p_n := e^{-\beta E_n}/Z$ for the system to occupy the $n$–the state. Using this probability distribution, one calculates mean values of various observables as functions of temperature, volume etc. Singularities of such mean values determine phase transitions.

(ii) In quantum mechanics, $(E_n)$ appear as eigenvalues of the Hamiltonian operator $H$ acting upon a Hilbert space with orthonormal basis $(|n\rangle)$ of eigenvectors of $H$. The Hamiltonian defines the time evolution which is given by the operator $e^{iHt}$. Formally replacing in $H$ time $t$ by the imaginary inverse temperature $i/kT$, we get an interpretation of the partition function (1.1) as "trace of of the quantum evolution operator in imaginary time".

In the recent paper [ManMar2], we suggested that this formal substitution may have a physical meaning in the "thermodynamics of the Universe", where one of the versions of global cosmological time is given by the inverse temperature

of the cosmic microwave background (CMB) radiation, and transition of time (or temperature) to the imaginary axis may describe the statistical physics of the Big Bang.

Below we argue that the values of Kolmogorov complexity in the computability theory can be fruitfully interpreted as such "energy levels" $E_n$.

### 1.2 Constructive Worlds

Markov algorithms process finite strings in a given finite alphabet. Turing machines do the same, although usually the respective alphabet consists of bits $\{0, 1\}$. Church's lambda–calculus processes certain *syntactically correct* finite strings. Partial recursive functions are certain "(semi)computable" partial functions $f : D(f) \to \mathbf{Z}_+^n$, with definition domains $D(f) \subset \mathbf{Z}_+^m$. Positive integers $\mathbf{Z}_+$ here are not supposed to be encoded in any specific way.

Proofs that any two of these (and other) methods calculate "the same" class of partial functions can be reduced to the following general scheme.

Define an (infinite) *constructive world* as a countable set $X$ (usually of some finite Bourbaki structures, such as the set of all error–correcting codes in a fixed alphabet) given together with a set of *structural numberings:* bijections $\nu : \mathbf{Z}_+ \to X$. This set must have the following formal property: for any two numberings $\nu_1, \nu_2$ there exists a *total recursive permutation* $\sigma : \mathbf{Z}_+ \to \mathbf{Z}_+$ such that $\nu_2 = \nu_1 \circ \sigma$, and conversely, if $\nu$ is structural numbering, all $\nu \circ \sigma$ are also such numberings.

Informally, structural numberings must be algorithmically computable, together with their inverses.

A finite constructive world is any finite set.

*Categorical Church–Turing thesis, Part I.* Let $X$, $Y$ be two infinite constructive worlds, $\nu_X : \mathbf{Z}_+ \to X$ $\nu_Y : \mathbf{Z}_+ \to X$ their structural numberings, and $F$ an (intuitive) algorithm that takes as input an object $x \in X$ and produces an object $F(x) \in Y$ whenever $x$ lies in the domain of definition of $F$; otherwise it outputs "NO" or works indefinitely.

Conversely, any algorithmically (semi) computable partial map $F : X \to Y$ is induced by a partial recursive function $f$ in this way.

Then $f := \nu_Y^{-1} \circ F \circ \nu_X : \mathbf{Z}_+ \to \mathbf{Z}_+$ is a partial recursive function.

*Categorical Church–Turing thesis, Part II.* Let $\mathcal{C}$ be a category, whose objects are some infinite constructive worlds, and some finite constructive worlds of all finite cardinalities. Define the set of morphisms $\mathcal{C}(X, Y)$ to be the set of all partial maps that can be algorithmically (semi)computed in an intuitive sense.

Then $\mathcal{C}$ is equivalent to the category having one infinite object $\mathbf{Z}$, one finite object $\{1, \ldots, n\}$ of each cardinality, and partial recursive functions as morphisms. If $X$ is finite, then $\mathcal{C}(X, Y)$ consists of all partial maps.

One must keep in mind, that if $X$ is infinite, then $\mathcal{C}(X, Y)$ has *no* natural structure of a constructive world. In particular, various numberings of partial recursive functions discussed in the literature are *not* structural numberings in our sense, they enumerate "programs" rather than functions themselves, and the

binary relations "two programs calculate one and the same partial function" is undecidable.

### 1.3 Kolmogorov Complexity of Constructive Objects

Consider now an infinite a constructive world. For any (semi)–computable function $u : \mathbf{Z}_+ \to X$, the (exponential) complexity of an object $x \in X$ relative to $u$ is

$$K_u(x) := \min \{m \in \mathbf{Z}_+ \mid u(m) = x\}.$$

If such $m$ does not exist, we put $K_u(x) = \infty$.

*Claim:* there exists such $u$ ("an optimal Kolmogorov numbering", or "decompressor") that for each other $v : \mathbf{Z}_+ \to X$, some constant $c_{u,v} > 0$, and all $x \in X$,

$$K_u(x) \leq c_{u,v} K_v(x).$$

This $K_u(x)$ is called *Kolmogorov complexity* of $x$.

*A Kolmogorov order* of a constructive world $X$ is a bijection $\mathbf{K} = \mathbf{K}_u : X \to \mathbf{Z}$ arranging elements of $X$ in the increasing order of their complexities $K_u$.

Notice that any optimal numbering is only partial function, and its definition domain is not decidable. Moreover, the Kolmogorov complexity $K_u$ itself is *not computable*: it is the lower bound of a sequence of computable functions.

The same can be said about the Kolmogorov order. Moreover, on $\mathbf{Z}_+$ it cardinally differs from the natural order in the following sense: it puts in the initial segments very large numbers that can be at the same time Kolmogorov simple. For example, let $a_n := n^{n^{\cdot^{\cdot^{\cdot^{n}}}}}$ ($n$ times). Then $K_u(a_n) \leq cn$ for some $c > 0$.

Finally, the indeterminacy of the complexity related to different choices of optimal functions $u, v$ is multiplicatively $\exp(O(1))$. The same is true for the Kolmogorov order.

For a concise treatment of Kolmogorov complexity, see [Man1], pp. 226–231, and for a thorough one, see [LiVi]. Notice that in the literature one often uses the *logarithmic* Kolmogorov complexity which is defined as the length of the binary presentation of $K_u(x)$. It is interpreted as the length of the *maximally compressed description* of $x$. For our purposes, exponential version is more convenient, in particular, because as soon as an optimal programming method $u$ is chosen, $K_u$ allows us to define an unambiguous Kolmogorov order on $\mathbf{Z}_+$ or on any infinite constructive world given together with its structural numbering.

### 1.4 Fractality and Symmetries of the Kolmogorov Complexity

In [LiVi], pp. 103, 105, 178, one can find a schematic graph of logarithmic complexity of integers. The visible"continuity" of this graph reflects the fact that complexity of $n+1$ in any reasonable encoding is almost the same as complexity of $n$. The graph "most of the time" follows closely the graph of $\log_2 n$: as soon as an optimal family is chosen, the respective complexity differs from $\log_2 K_u(n)$ by a bounded function. However, infinitely often the graph drops down, lower

than any given computable function of $n$. We will sometimes write $K$ in place of $K_u$ when change of optimal $u$ is not essential.

Looking only at such graphs one does not see or suspect any kind of self–similarity. But it is there: if one restricts this graph onto any infinite decidable subset of $\mathbf{Z}_+$ in increasing order, one will get the same complexity relief as for the whole $\mathbf{Z}_+$: in fact, for any recursive bijection $f$ of $\mathbf{Z}_+$ with a subset of $\mathbf{Z}_+$ we have $K(f(x)) = exp(O(1)) \cdot K(x)$.

The natural symmetry group of the logarithmic Kolmogorov complexity is the group $S_\infty^{comp}$ of total recursive permutations of $\mathbf{Z}_+$: for each such permutation $\sigma$, there exists a constant $c(\sigma)$ such that for all $n$ we have

$$|\log_2 K(\sigma(n)) - \log_2 K(n)| < c(\sigma).$$

This symmetry reflects the essential independence of complexity on a chosen initial structural numbering. The group $S_\infty^{comp}$ is pretty mysterious one.

However, an inner conjugation inside the total permutation group of $\mathbf{Z}_+$ allows one to embed it into a less mysterious group of permutations $S_\infty^{lin}$ of $\mathbf{Z}_+$, consisting of all permutations which together with their inverses have no more than linear growth.

To achieve this, it suffices to replace the natural order of $\mathbf{Z}_+$ by its Kolmogorov order. This remark is essentially used in the proof of the Theorem 3.5 of the next section.

## 2 Probability Distributions on Constructive Worlds and Zipf's Law

### 2.1 Zipf's Law

Zipf ([Zi1], [Zi2]) studied statistics of usage of words in natural languages. His main empirical observation was this: if all words $\{w_k\}$ of a language in a representative corpus of texts are ranked according to decreasing frequency of their appearance, and the rank $k$ and the number of the occurrences of $w_k$ are plotted in the logarithmic scale, then the data approximately fit on a line. This means that the frequency of usage of the word of rank $k$ is approximatetely $C/k^\alpha$ where C and $\alpha$ are some constants. Moreover, for natural languages $\alpha$ is close to one: see e. g. Fig. 1 in [Ma1] based upon a corpus containing $4 \cdot 10^7$ Russian words.

This general power law, and its particular $\alpha = 1$ realization turned out to be very universal, see [MurSo], [Pi]. It was observed in the texts of an extinct and not deciphered Meroitic language ([Sm]), and in the frequency of certain patterns in databases of financial reports of businesses: see [HuYeYaHua]. In the latter article, it was suggested that systemtic deviations from Zipf's law might be useful for fraud detection.

Zipf himself ([Zi2], [Zi1]) conjectured that his distribution "minimizes effort". Mandelbrot in [Mand] made this mathematically precise in the following way. If we postulate and denote by $C_k$ a certain "cost" (of producing, using etc.) of the word of rank $k$, then the frequency distribution $p_k \sim 2^{-h^{-1}C_k}$ minimizes

the ratio $h = C/H$, where $C := \sum_k p_k C_k$ is the average cost per word, and $H := -\sum_k p_k \log_2 p_k$ is the average entropy: see a discussion in [Ma2]. This produces a power law, if $C_k \sim \log k$. An additional problem, explanation of $\alpha = -1$, must be addressed separately. For one possibility, see [MurSo], sec. III.

In [Man7], I suggested a similar background but replaced logarithm in $C_k \sim \log k$ by the logarithmic Kolmogorov complexity. This means, in particular, that Zipf's rank corresponds to the ranking in order of growing complexity, and identifies complexity with Zipf's "effort". Underlying this metaphor is the image of brain/society dealing with compressed descriptions of units of information. Intuitively, whenever an individual mind, or a society, finds a compressed description of something, this something becomes usable, and is used more often than other "something" whose description length is longer. In experimental psychology, this corresponds to the *"availability bias"* studied by A. Tversky and D. Kahneman: as they write in [TvKa], this is *"a judgemental heuristic in which a person evaluates the frequency of classes or the probability of events by availability, i. e., by the ease with which relevant instances come to mind."*

For an expanded version of this metaphor applied to the history of science, see [Man6], and for related suggestions see [DeMe], [Del], [Ve].

In the context of [Man7], the $\alpha = -1$ enigma is solved by appealing to another mathematical discovery. Namely, L. Levin has established that the power law with $\alpha = -1$ appears as the *maximal* (up to a multiplicative constant) probability distribution that is *computable from below*: see [Lev1], [Lev2].

In all theoretical discussions, it is more or less implicitly assumed that empirically observed distributions concern fragments of a potential countable infinity of objects. I also postulate this, and work in a "constructive world".

### 2.2 Zipf's Law from Complexity

Here is the summary of my arguments. Zipf's law emerges as the combined effect of two factors:

*(A) Zipf's rank ordering of a constructive world coincides with the ordering with respect to the growing (exponential) Kolmogorov complexity $K(w)$.*

*(B) The probability distribution producing Zipf's law (with exponent $-1$) is (an approximation to) the L. Levin maximal computable from below distribution: see [ZvLe], [Le] and [LiVi].*

The $\alpha = -1$ power law follows from the fact that Levin's distribution assigns to an object $w$ probability $\sim KP(w)^{-1}$ where $KP$ is the exponentiated prefix Kolmogorov complexity, and we have, up to $exp\,(O(1))$–factors,

$$K(w) \preceq KP(w) \preceq K(w) \cdot \log^{1+\varepsilon} K(w)$$

with arbitrary $\varepsilon > 0$.

Discrepancy between the growth orders of $K$ and $KP$ is the reason why a probability distribution on infinity of objects cannot be constructed from $K$: the series $\sum_m K(m)^{-1}$ diverges. However, on finite sets of data this small discrepancy is additionally masked by the dependence of both $K$ and $KP$ on the

choice of an optimal encoding. Therefore, when speaking about Zipf's Law, we will mostly disregard this difference. One could however argue that it is at least partly responsible for *"numerous minima and maxima in the error of [Zipf's] fit"*: see [Pi], Sec. 2.

## 3 Error–Correcting Codes and Their Asymptotic Bounds

### 3.1 Codes and Code Points

Fix an alphabet $A$ which a finite set of cardinality $q \geq 2$. A *code* $C \subset A^n$ is a subset of words of length $n$. *Hamming distance* between two words of the same length is defined as

$$d((a_i),(b_i)) := \mathrm{card}\{i \in (1,\ldots,n) \,|\, a_i \neq b_i\}.$$

*Code parameters* are the cardinality of the alphabet $q$ and the numbers $n(C)$, $k(C), d(C)$ defined by:

$$n(C) := n, \quad k(C) := k := [\log_q \mathrm{card}(C)],$$

where $[x]$ is the maximal integer $\leq x$;

$$d(C) := d = \min\{d(a,b) \,|\, a,b \in C, a \neq b\}.$$

Briefly, $C$ is an $[n,k,d]_q$–code. Its *code point* is the point

$$x(C) := \left(\frac{k(C)}{n(C)}, \frac{d(C)}{n(C)}, \right) \in [0,1]^2$$

Coordinates of $x(C) = (R(C), \delta(C))$ are called *transmission rate* and *relative distance* respectively.

The idealized scheme of using error–correcting codes for information transmission can be described as follows. Some source data are encoded by a sequence of code words. After transmission through a noisy channel at the receiving end we will get a sequence of possibly corrupted words. If we know probability of corruption of a single letter, we can calculate, how many corrupted letters in a word we may allow for safe transmission; pairs of code words must be then separated by a larger Hamming distance. This necessity puts an upper bound on the achievable transmission rate.

*A good code* must maximize minimal relative distance when the transmission rate is chosen.

Our discussion up to now was restricted to *unstructured* codes: arbitrary subsets of words. Arguably, one more property of good codes is the existence of efficient algorithms of encoding and decoding. This can be achieved by introduction of *structured* codes. A typical choice is represented by *linear codes*: for them, $A$ is a finite field of $q$ elements, and $C$ is a linear subspace of $\mathbf{F}_q^n$.

Now, let us call *the multiplicity* of a code point the number of codes that project onto it.

All codes (with fixed $q$), and all rational points in $[0,1]^2$ constitute examples of constructive worlds. The map $C \mapsto x(C)$ is a computable function. The same refers to structured codes considered in the literature, in particular, to linear codes.

**Theorem 1.** (Yu. M., 1981 + 2011). *There exists a continuous function $\alpha_q(\delta)$, $\delta \in [0,1]$, with the following properties:*

*(i) The set of code points of infinite multiplicity is exactly the set of rational points $(R,\delta) \in [0,1]^2$ satisfying $R \leq \alpha_q(\delta)$. The curve $R = \alpha_q(\delta)$ is called the asymptotic bound.*

*(ii) Code points $x$ of finite multiplicity all lie strictly above the asymptotic bound and are called isolated ones: for each such point there is an open neighborhood containing $x$ as the only code point.*

*(iii) The same statements are true for linear codes, with a possibly different asymptotic bound $R = \alpha_q^{lin}(\delta)$.*

In a paper published in 1981, I proved that all limit points of the set of code points ($q$ being fixed) lie under the graph of a monotone function $\alpha_q$ that was later called the asymptotic bound. Its characterisation via multiplicity used here was proved in [Man2].

### 3.2 Can One Compute an Asymptotic Bound?

During the thirty years since the discovery of the asymptotic bounds, many upper and lower estimates were established for them, especially for the linear case: see the monograph [VlaNoTsfa]. Upper bounds helped pinpoint a number of isolated codes.

However, the following most natural problems remain unsolved: – To find an explicit formula for $\alpha_q$ or $\alpha_q^{lin}$.

– To find any single value of $\alpha_q(\delta)$ or $\alpha_q^{lin}(\delta)$ for $0 < \delta < 1 - q^{-1}$ (at the end segment $[1 - q^{-1}, 1]$ these function vanish).

– To find any method of approximate computation of $\alpha_q(\delta)$ or $\alpha_q^{lin}(\delta)$.

– Clearly, $\alpha_q^{lin} \leq \alpha_q$. Is this inequaliy *strict* somewhere?

### 3.3 A Brief Survey of Some Known Results

(i) One can count the number of codes of bounded block length $n$ and plot their code points. The standard probabilistic methods then give the following *Gilbert–Varshamov bounds*.

Most unstructured $q$–ary codes lie lower or only slightly above the Hamming curve

$$R = 1 - H_q(\delta/2),$$

$$H_q(\delta) = \delta \log_q(q-1) - \delta \log_q \delta - (1-\delta)\log_q(1-\delta).$$

Most linear $q$–ary codes lie near or only slightly above the Gilbert–Varshamov bound

$$R = 1 - H_q(\delta).$$

In particular,

$$\alpha_q(R) \geq \alpha_q^{lin}(R) \geq 1 - H_q(\delta)$$

(ii) A useful combinatorial upper estimate is the Singleton bound:

$$R(C) + \delta(C) \leq 1 + \frac{1}{n(C)}.$$

Hence

$$\alpha_q(\delta) \leq 1 - \delta.$$

It follows that code points lying above this bound are isolated. The following Reed–Solomon (linear) codes $C \subset \mathbf{F}_q^n$ belong to this group.

Choose parameters $1 \leq k \leq n \leq q, d = n + 1 - k$. Choose pairwise distinct $x_1, \ldots, x_n \in \mathbf{F}_q$, Embed the space of polynomials $f(x) \in \mathbf{F}_q[x]$ of degree $\leq k-1$ into $\mathbf{F}_q^n$ by

$$f \mapsto (f(x_1), \ldots, f(x_n)) \in \mathbf{F}_q^n.$$

After works of Goppa, this construction was generalized. Points $x_1, \ldots, x_n \in \mathbf{F}_q$ were replaced by rational points of any smooth algebraic curve over $\mathbf{F}_q$, and polynomials by sections of an invertible sheaf. This allowed one to construct non–isolated linear codes lying partly strictly above the Gilbert–Varshamov bound.

This implies that we cannot "see" the asymptotic bound, plotting the set of (linear) code points of bounded size: we will see a cloud of points, whose upper bound concentrates near the Hamming or Varshamov–Gilbert bounds.

The proof of the following theorem given in [ManMar1] again uses reordering codes by their growing Kolmogorov complexity and basic properties of the Levin distribution (in this context the difference between $K$ and $KP$ becomes negligible). Imaginatively, one can say that the asymptotic bound becomes plottable with help of oracle–assisted computation: oracle should produce for us codes in their Kolmogorov order.

In order to state our theorem, notice that the function $\alpha_q(\delta)$ is continuous and strictly decreasing for $\delta \in [1, 1 - q^{-1})$. Hence the limit points domain $R \leq \alpha_q(\delta)$ can be equally well described by the inequality $\delta \leq \beta_q(R)$ where $\beta_q$ is the function inverse to $\alpha_q$.

Fix an $R \in \mathbf{Q} \cap (0, 1)$. For $\Delta \in \mathbf{Q} \cap (0, 1)$, put

$$Z(R, \Delta; \beta) := \sum_{C:\, R(C) = R,\ \Delta \leq \delta(C) \leq 1} K_u(C)^{-\beta + \delta(C) - 1},$$

where $K_u$ is an (exponential) Kolmogorov complexity on the constructive world of all codes in a given alphabet of cardinality $q$.

**Theorem 2.** *(i) If $\Delta > \beta_q(R)$, then $Z(R, \Delta; \beta)$ is a real analytic function of $\beta$.*

*(ii) If $\Delta < \beta_q(R)$, then $Z(R, \Delta; \beta)$ is a real analytic function of $\beta$ for $\beta > \beta_q(R)$ such that its limit for $\beta - \beta_q(R) \to +0$ does not exist.*

The following thermodynamical analogies justify our interpretation of the asymptotic bound as a phase transition curve in the "statistical physics of Platonian world." a) The argument $\beta$ of the partition function corresponds to the inverse temperature.

b) The transmission rate $R$ corresponds to the density $\rho$.

c) Our asymptotic bound transported into $(T = \beta^{-1}, R)$–plane as $T = \beta_q(R)^{-1}$ becomes the phase transition boundary in the *(temperature, density)*–plane.

For other mathematical contexts in which our partition function and other characteristics of codes appear, in particular, for relevant quantum mechanical analogies, see [ManMar3].

## References


[A1] Aaronson, S.: NP–complete problems and physical reality, 23. arXiv:quant–ph/0502072

[A2] Aaronson, S.: Why philosophers should care about computational complexity, 58. arXiv:1108.1791

[DeMe] Dehaene, S., Mehler, J.: Cross–linguistic regularities in the frequency of number words. Cognition 43, 1–29 (1992)

[Del] Delahaye, J.–P.: Les entiers ne naissent pas égaux. Pour la Science (421), 80–85 (2012)

[HuYeYaHua] Huang, S.-M., Yen, D.C., Yang, L.-W., Hua, J.-S.: An investigation of Zipf's Law for fraud detection. Decision Support Systems 46, 70–83 (2008)

[Lev1] Levin, L.A.: Various measures of complexity for finite objects (axiomatic description). Soviet Math. Dokl. 17(2), 522–526 (1976)

[Lev2] Levin, L.A.: Randomness conservation inequalities: information and independence in mathematical theories. Information and Control 61, 15–37 (1984)

[LiVi] Li, M., Vitányi, P.: An introduction to Kolmogorov complexity and its applications. Springer (1993)

[Mand] Mandelbrot, B.: An information theory of the statistical structure of languages. In: Jackson, W. (ed.) Communication Theory, pp. 486–502. Butterworth, Woburn (1953)

[Ma1] Manin, D.Y.: Zipf's Law and Avoidance of Excessive Synonymy. Cognitive Science 32(7), 1075–1078 (2008), arXiv:0710.0105

[Ma2] Manin, D.Y.: Mandelbrot's model for Zipf's Law. Can Mandelbrot's model explain Zipf's Law for language? Journ of Quantitative Linguistics 16(3), 274–285 (2009)

[Man1] Manin, Y.I.: A Course in Mathematical Logic for Mathematicians, 2nd edn. Graduate Texts in Mathematics. Springer (2010)

[Man2] Manin, Y.I.: A computability challenge: Asymptotic bounds and isolated error-correcting codes. In: Dinneen, M.J., Khoussainov, B., Nies, A. (eds.) WTCS 2012 (Calude Festschrift). LNCS, vol. 7160, pp. 174–182. Springer, Heidelberg (2012)

[Man3] Manin, Y.I.: Classical computing, quantum computing, and Shor's factoring algorithm, Séminaire Bourbaki, no. 862, vol. 266, pp. 375–404. Astérisque (June 1999/2000), arXiv: quant-ph/9903008

[Man4] Manin, Y.I.: Renormalization and computation I. Motivation and background. In: Loday, J., Vallette, B. (eds.) Proceedings OPERADS 2009. Séminaires et Congrès, vol. 26, pp. 181–223. Soc. Math. de France (2012), math.QA/0904.492

[Man5] Manin, Y.I.: Renormalization and computation II: Time cut–off and the Halting Problem. Math. Struct. in Comp. Science 22, 729–751 (2012), Special issue, Cambridge UP. math.QA/0908.3430

[Man6] Manin, Y.I.: Kolmogorov complexity as a hidden factor of scientific discourse: From Newton's law to data mining. In: Talk at the Plenary Session of the Pontifical Academy of Sciences on Complexity and Analogy in Science: Theoretical, Methodological and Epistemological Aspects, Vatican, November 5–7 (2012) arXiv:1301.0081

[Man7] Manin, Y.I.: Zipf's law and L. Levin's probability distributions. Functional Analysis and its Applications, Vol. 48(2) (2014), arXiv:1301.0427

[ManMar1] Manin, Y., Marcoll, M.: Kolmogorov complexity and the asymptotic bound for error-correcting codes. Journ. of Diff. Geometry (to appear in 2014), arXiv:1203.0653

[ManMar2] Manin, Y., Marcolli, M.: Big Bang, Blow Up, and Modular Curves: Algebraic Geometry in Cosmology. arXiv:1402.2158

[ManMar3] Manin, Y., Marcolli, M.: Error–correcting codes and phase transitions. Math. in Comp. Science 5, 133–170 (2011), arXiv:mat.QA/0910.5135

[MurSo] Murtra, B.C., Solé, R.: On the Universality of Zipf's Law. Phys. Rev. E 82 (2010)

[Pi] Piantadosi, S.T.: Zipf's word frequency law in natural language: A critical review and future directions, `http://colala.bcs.rochester.edu/papers/piantadosi2014zipfs.pdf`

[Sm] Smith, R.: Investigation of the Zipf–plot of the extinct Meroitic language. Glottometrics 15, 53–61 (2007)

[TvKa] Tversky, A., Kahneman, D.: Availability; A Heuristic for Judging Frequency and Probability. Cognitive Psychology 5, 207–232 (1973)

[Ve] Todd, L.: Veldhuizen. Software Libraries and Their Reuse: Entropy, Kolmogorov Complexity, and Zipf's Law. arXiv:cs/0508023

[VlaNoTsfa] Vladut, S.G., Nogin, D.Y., Tsfasman, M.A.: Algebraic geometric codes: Basic notions. Mathematical Surveys and Monographs. American Mathematical Society, Providence (2007)

[Zi1] Zipf, G.K.: The psycho–biology of language. Routledge, London (1936)

[Zi2] Zipf, G.K.: Human behavior and the principle of least effort. Addison–Wesley (1949)

[ZvLe] Zvonkin, A.K., Levin, L.A.: The complexity of finite objects and the basing of the concepts of information and randomness on the theory of algorithms. Uspehi Mat. Nauk 25(6(156)), 8–127 (1970), (Russian)

# Complexity Measures and Physical Principles

Karoline Wiesner

School of Mathematics, University of Bristol, Bristol, U.K.

**Abstract.** I summarise some recent results on physics of information and discuss their impact on our understanding of complexity. A surprisingly coherent picture of measures of complexity, information theoretic functions, and thermodynamical quantities arises.

## 1 Introduction

Complexity is a concept thoroughly defeating any unique definition. One notion is that a complex system is an open system exchanging matter and / or signals with the environment while being robust in its structure and adapting to environmental circumstances without any internal central control unit [11]. One can take this view into a more quantitative realm by considering a complex system as an information processor. The above description can then be recast as follows: A complex system takes in and puts out information, it has an internal memory, and robust and decentralised information processing capacity. For complex systems this is a very helpful starting point as it allows quantitative statements about systems of which we do not know the Hamiltonian or any other form of energetic characterisation. The idea to put physics – which deals with matter and energy – and information – which deals with bits and memory on the same footing is not new. The most pointed statement in this context is probably Wheeler's "It from bit", implying that every physical quantity derives its function from answers to yes-no questions [20].

In the following I will sketch some recent developments in the area of physics of information and outline parallels to information-theoretic treatments of complex systems.

## 2 Measures of Complexity

One way of measuring the complexity of a system is to quantify the amount of correlation a system exhibits in its temporal behaviour. The temporal behaviour is captured in observations over time and can be formalised as a *stochastic process*. The most generally applicable measure of correlation in a stochastic process is the mutual information which is a function of the joint probability distribution of two random varibles[1]. We will consider the past data to be one random

[1] For definitions of Shannon entropy, conditional entropy, and mutual information, see for example [2].



A. Sanayei et al. (eds.), *ISCS 2014: Interdisciplinary Symposium on Complex Systems*, Emergence, Complexity and Computation 14, DOI: 10.1007/978-3-319-10759-2_2

variable, $\overleftarrow{X}$, and the future data to be another random variable, $\overrightarrow{X}$. In the limit of infinite data the mutual information between these two variables has been taken as a measure of complexity ([13,4]):

$$E = I[\overleftarrow{X}; \overrightarrow{X}] \ . \tag{1}$$

$E$ has been given different names, such as *predictive information*, excess entropy, effective measure complexity, and stored information (see [4] and refs. therein).

We can interpret $E$ as the amount of communication between a system's past and its future. Any positive mutual information means that the system remembers some of its past and its future behaviour is influenced by that memory. In this sense, $E$ is the system's complexity, measured in bits.

I now turn to a second measure of complexity, the *statistical complexity*, as introduced by Crutchfield and Young [5]. It is related to the *true metric complexity* initially discussed by Grassberger [8]. Given a stochastic process, the provably unique minimal (in terms of information stored) and optimal (in terms of prediction) computation-theoretic representation summarising the regularities of the process is the so-called $\epsilon$-machine [5,13]. It consists of an output alphabet $\mathcal{X}$, a set of *states* $\mathcal{S}$ and stochastic transitions between them. For every pair of states $s, s' \in \mathcal{S}$ probabilities $\Pr(S_i = s', X_i = x | S_{i-1} = s)$ are defined for going from state $s$ to state $s'$ while outputting symbol $x \in \mathcal{X}$. The *statistical complexity* of a process is defined as the Shannon entropy over the stationary distribution of its $\epsilon$-machine's states:

$$C_\mu := -\sum_s \Pr(s) \log \Pr(s) \ . \tag{2}$$

$C_\mu$ is the number of bits required to specify a particular state of the $\epsilon$-machine. Since knowing the state means knowing everything there is to know about future observations, $C_\mu$ is the number of bits that need to be stored to optimally predict future data points from the $\epsilon$-machine.

The statistical complexity is bounded from below by the predictive information: $E \leq C_\mu$ [13]. It is intuitive that the amount of memory of a predicting device should be at least as big as the number of bits it is predicting about a system. There have been different approaches to derive the exact difference between $E$ and $C_\mu$ analytically. Crutchfield and co-workers explained it through the asymmetry between prediction and retrodiction [6]. They were able to show that the predictive information is equal to the mutual information between the states predicting the stochastic process forward in time and the states retrodicting the process backward in time. Wiesner et al. took a different approach to explaining the difference between the two complexity measures [19]. They considered the computational irreversibility of the $\epsilon$-machine and showed that it accounts exactly for the difference between the two complexity measures. The extra memory kept by the $\epsilon$-machine which is not predictive incurs an entropic cost to the computation. Computing $E$ (Eq. 1) requires numerical approximation from finite data. Finding an analytic expression for the predictive information from the predictive states is an open problem.

Gu et al. extended the framework of $\epsilon$-machines by allowing the states to have quantum mechanical properties [9]. Once the (classical) states $\mathcal{S}$ are known the quantum mechanical states (here in ket notation) can be easily constructed as

$$|s\rangle = \sum_{s' \in \mathcal{S}} \sum_{x \in \mathcal{X}} \sqrt{\Pr(S_i = s', X_i = x | S_{i-1} = s)} |x\rangle |s'\rangle \ , \tag{3}$$

This is related to an earlier quantum model of a stochastic process [12]. Gu et al. define the quantum complexity of the process as the von Neumann entropy over the resulting density matrix $\rho = \sum_s \Pr(s) |s\rangle\langle s|$:

$$C_q := -\mathrm{Tr} \rho \log \rho \ . \tag{4}$$

It can be easily shown that $C_q$ is bounded above and below by the statistical complexity and the predictive information, respectively:

$$E \leq C_q \leq C_\mu . \tag{5}$$

Equality holds if and only if the upper and lower bound coincide [9,19]. Whenever $C_q$ is strictly less than $C_\mu$ the quantum states $|s\rangle$ are non-orthogonal. This means that there exists no quantum measurement which could perfectly distinguish between them. Since the machines both predict $E$ bits about future observations the additional bits stored in the classical machine are non-predictive. This, again, indicates that the difference between $E$ and $C_\mu$ represents an inefficiency in the model. Explaining the gap between $C_q$ and $E$ remains an open problem.

## 3 Finding an Optimal Model under Constraints

Finding an efficient model is a classical optimisation problem under costraints: One wants to minimise the size of a model while maximising its predictive power. Any model is some form of summary of past observations. A good model retains as much *relevant* information about the past as possible and discards anything beyond that. The so-called *information bottleneck method*, introduced by Tishby, Pereira and Bialek, provides the tools for finding a minimal model under the constraint of maximal predictive power [18]. They formalise this task as finding an optimal compression of data (the "summary") under the constraint of minimal error upon decompression (equivalent to "prediction" of observations). Furthermore, the bottleneck method allows for the case where the data, $X$, are descriptions of another, correlated variable $Y$. The optimisation task they solve is to compress the data $X$ into $\tilde{X}$ as much as possible while retaining as much information about $Y$ as needed. Tishby et al. were able to show that the optimal compression minimises the relative entropy (also known as Kullback-Leibler divergence) between the conditional distributions $\Pr(Y|X)$ and $\Pr(Y|\tilde{X})$, $D_{KL}[\Pr(Y|X) || \Pr(Y|\tilde{X})]$.

Still et al. applied the bottleneck method to the problem of finding a predictive model for a stochastic process as discussed above [16,15], see also [14]. Here the

future behaviour $\overrightarrow{X}$ of the system corresponds to the variable of interest $Y$. Past observations $\overleftarrow{X}$ are analogous to the data $X$ to be compressed. The states $\mathcal{S}$ and associated transition probabilities are the compressed version $\tilde{X}$ of the data. A minimal model under the constraint of maximal predictive power can be found by solving the following optimisation problem:

$$\min_{\Pr(\mathcal{S}|\overleftarrow{X})} \left( I(\overleftarrow{X};\mathcal{S}) + \beta I(\overleftarrow{X};\overrightarrow{X}|\mathcal{S}) \right) , \tag{6}$$

where $\beta$ is the remaining parameter (Lagrange multiplier) representing the trade-off between model complexity and predictive power. It turns out that the solution to this optimisation problem minimises the relative entropy $D_{KL}[\Pr(\overrightarrow{X}|\overleftarrow{X})||\Pr(\overrightarrow{X}|\mathcal{S})]$. In the limit of $\beta \to \infty$ equivalent to unrestricted model complexity, the states of the $\epsilon$-machine are recovered [16].

Still et al. expanded this framework to a more general setting [17]. The view point taken is slightly different from that of optimally modeling observations of a complex system's dynamics. Rather, they consider a complex system as making a model of the world. The system remembers some of the past experiences in the world and tries to predict future experiences. Mathematically this framework is identical to the one discussed above. Still et al. define *predictive power* as the mutual information between the system's state $s_t$ at time $t$ and the environmental signal $x_{t+1}$ at time $t+1$. Similarly, *instantaneous memory* is defined as the mutual information between the system's state $s_t$ at time $t$ and the environmental signal $x_t$ at time $t$:

$$I_{\text{mem}}(t) = I(s_t; x_t) , \tag{7}$$

$$I_{\text{pred}} = I(s_t; x_{t+1}) . \tag{8}$$

Both $I_{\text{mem}}$ and $I_{\text{pred}}$ are instantaneous quantities, i.e. they extend over one time point into the future or the past. The instantaneous nonpredictive information is then defined as the difference between instantaneous memory and predictive power, $I_{\text{mem}} - I_{\text{pred}}$. Given these definitions, Still et al. find that the unnecessary retention of past information is fundamentally equivalent to energetic inefficiency which results in energy dissipation $W_{\text{diss}}$. This dissipation is an upper bound to the difference between memory and predictive information [17]:

$$I_{\text{mem}} - I_{\text{pred}} \leq \beta W_{\text{diss}} \tag{9}$$

The inequality relies on a result by Jarzynski who found a mathematically exact relation between the amount of work put into a system and the resulting average free energy change which holds for systems driven arbitrarily far away from the initial equilibrium: $\langle e^{-\beta W} \rangle = e^{-\beta \Delta F}$ [10]. Here, $W$ is the total work performed on the system, the average is taken over an ensemble of measurements, and $\Delta F$ is the total change in free energy between the initial and final state. Crooks was able to show that the assumptions of Markovian dynamics and microscopic reversibility lead to the same result [3].

## 4 Discussion

We have seen that the complexity of a stochastic process can be measured in various ways. While the predictive information $E$ is the number of bits stored by the process itself, the statistical complexity $C_\mu$ and the quantum statistical complexity $C_q$ quantify the minimum amount of memory necessary to optimally predict the process. In general all three measures differ for any given stochastic process. While the minimum amount of information required for optimal prediction is $E$, the actual information stored to make that prediction is usually higher due to the architecture of the storage device, i.e. the discreteness and physical nature of the states. Hence, the physical architecture of the prediction device matters.

A slight change in perspective shed new light on the physical implications of this information processing inefficiency. Instead of a complex system being predicted by a modeler as best she can, Still et al. considered a complex system which stores information about past environmental signals to predict future environmental signals. The assumption is that the system, just like the modeler before, wants to minimise the amount of information stored while predicting as much about the next environmental state as possible. Based on a direct proportionality between free energy and relative entropy they established an equivalence between the non-predictive information which the system holds and the energy dissipation during state changes of the system.

Whether and how energy dissipation caused by inefficient prediction can be measured experimentally is an open question at this point. The equivalence between complexity measures and physical principles yields lower bounds only. Heat dissipation in real complex systems might be orders of magnitude higher. The basic unit of dissipation in a logical operation is $kT \ln 2$ where $k$ is the Boltzmann constant and $T$ is the temperature. The heat dissipated during a logical operation in a modern processing chip, for example, is an estimated $10^{11} kT \ln 2$ at room temperature[2].

However, there exist experiments in this direction. Energy dissipation has been measured in small molecular machines performing logical operations [1]. The measured values were only a few ten times larger than the basic unit of $kT \ln 2$. Furthermore, a free energy principle has been proposed accounting for perception and learning in the brain [7]. This, again, is based on the proportionality between relative entropy and free energy which suggests that the above discussion on information and energy (dissipation) might be highly relevant in this context.

Much work is still to be done to close the gap between rigorous mathematical results in the physics of information and characterisation of complexity. I hope to have conveyed to the reader that some very promising steps have been taken.

**Acknowledgements.** The Author would like to thank A. Houston for very helpful comments on a draft of this article.

[2] This is an order-of-magnitude estimate based on thermal specifications of an Intel processor.

## References


1. Benenson, Y., Adar, R., Paz-Elizur, T., Livneh, Z., Shapiro, E.: DNA molecule provides a computing machine with both data and fuel. Proceedings of the National Academy of Sciences 100(5), 2191–2196 (2003)
2. Cover, T.M., Thomas, J.A.: Elements of Information Theory. WileyBlackwell (2006)
3. Crooks, G.E.: Entropy production fluctuation theorem and the nonequilibrium work relation for free energy differences. Physical Review E 60(3), 2721–2726 (1999)
4. Crutchfield, J.P., Feldman, D.P.: Regularities unseen, randomness observed: Levels of entropy convergence. Chaos 13(1), 25–54 (2003)
5. Crutchfield, J.P., Young, K.: Inferring statistical complexity. Physical Revue Letters 63(2), 105 (1989)
6. Crutchfield, J.P., Ellison, C.J., Mahoney, J.R.: Time's barbed arrow: Irreversibility, crypticity, and stored information. Physical Review Letters 103(9), 94101–94104 (2009)
7. Friston, K., Kilner, J., Harrison, L.: A free energy principle for the brain. Journal of Physiology-Paris 100(1-3), 70–87 (2006)
8. Grassberger, P.: Toward a quantitative theory of self-generated complexity. International Journal of Theoretical Physics 25(9), 907–938 (1986)
9. Gu, M., Wiesner, K., Rieper, E., Vedral, V.: Quantum mechanics can reduce the complexity of classical models. Nature Communications 3, 762 (2012)
10. Jarzynski, C.: Nonequilibrium equality for free energy differences. Physical Review Letters 78(14), 2690–2693 (1997)
11. Ladyman, J., Lambert, J., Wiesner, K.: What is a complex system? European Journal for Philosophy of Science 3(1), 33–67 (2013)
12. Monras, A., Beige, A., Wiesner, K.: Hidden quantum markov models and non-adaptive read-out of many-body states. Applied Mathematical and Computational Sciences 3, 93 (2011)
13. Shalizi, C.R., Crutchfield, J.P.: Computational mechanics: Pattern and prediction, structure and simplicity. Journal of Statistical Physics 104(3), 817–879 (2001)
14. Still, S.: Information bottleneck approach to predictive inference. Entropy 16(2), 968–989 (2014)
15. Still, S., Crutchfield, J.P.: Structure or noise? arXiv/0708.0654 (2007)
16. Still, S., Crutchfield, J.P., Ellison, C.J.: Optimal causal inference: Estimating stored information and approximating causal architecture. arXiv/0708.1580 (2007)
17. Still, S., Sivak, D.A., Bell, A.J., Crooks, G.E.: Thermodynamics of prediction. Physical Review Letters 109(12), 120604 (2012)
18. Tishby, N., Pereira, F.C., Bialek, W.: The information bottleneck method. arXiv/physics/0004057 (2000)
19. Wiesner, K., Gu, M., Rieper, E., Vedral, V.: Information-theoretic lower bound on energy cost of stochastic computation. Proceedings of the Royal Society A: Mathematical, Physical and Engineering Science 468(2148), 4058–4066 (2012)
20. Zurek, W.H. (ed.): Information, physics, quantum: The search for links. Santa Fe Institute Studies in the Sciences of Complex Systems, vol. 8. Advanced Book Programme (1990)

# Collective Dynamics in Neural Networks

Antonio Politi

Institute for Complex Systems and Mathematical Biology,
University of Aberdeen, UK

## 1 Introduction

A wealth of natural and artificial systems are composed of many coupled subunits: examples are electric, metabolic, and neural networks that are encountered in engineering and biological contexts, but also the granular media and fluids studied in physics. In such cases, it is natural to expect substantial changes induced by the mutual coupling and it is customary to qualify the overall behaviour as *collective*. There exists, however, a deeper notion of the term *collective*, that is related to the concept of thermodynamic phase within equilibrium statistical mechanics. The same set of microscopic equations may generate and sustain different macroscopic states (see, e.g., the gas, liquid, and solid phases), that may be selected by varying a suitable control parameter (e.g., the temperature, or an external field). At equilibrium, the macroscopic phases are necessarily stationary (time-independent) but, out-of-equilibrium, detailed balance is violated, currents are generated and macroscopic oscillations may appear as well. The emergence of collective motion is particularly relevant in the context of neural networks, where its properties are likely to be connected to information processing in a way still to be understood.

As a general theory is still lacking, it is convenient to review a series of various examples, starting from the simple and yet general synchronization transition occurring in the Kuramoto model [1]. It describes an ensemble of sinusoidally coupled phase-oscillators

$$\dot{\phi}_i = \omega_i + \frac{g}{N}\sum_j^N \sin(\phi_j - \phi_i) = \omega_i + gR\sin(\psi - \phi_i)\,,$$

where each oscillator is characterized by a different bare frequency $\omega_i$ and

$$Re^{i\psi} = \frac{1}{N}\sum_j^N e^{i\phi_j}$$

represents the order parameter. Upon increasing the coupling constant $g$ from zero, the system undergoes a phase transition from an asynchronous regime characterized by $R = 0$ (in the $N \to \infty$ limit), to a coherent phase, where $R > 0$, meaning that a finite fraction of the oscillators are mutually locked. This mean-field model can be properly analysed by writing an evolution equation for the



A. Sanayei et al. (eds.), *ISCS 2014: Interdisciplinary Symposium on Complex Systems*,
Emergence, Complexity and Computation 14, DOI: 10.1007/978-3-319-10759-2_3

probability density $P(\phi, \omega, t)d\phi d\omega$ of the oscillator phases at time $t$. Although such a nonlinear equation is a functional and hence infinite-dimensional, the resulting scenario is not qualitatively different from that of a typical equilibrium transition: above transition, $R$ is indeed constant and the only time-dependence is a trivial homogeneous rotation of the phase $\psi$ which can be eliminated by suitably choosing the reference frame.

A by far less trivial scenario arises in models of globally coupled logistic maps [2]

$$x_{n+1}(i) = f\left[(1-g)x_n(i) + g\langle x_n\rangle\right] \quad , \quad f(x) = ax(1-x)$$

where the angular brackets denote an ensemble average over the $N$ dynamical units (the mean field). Here, for some $a$ and $g$ values, the "microscopic" chaotic dynamics induced by the logistic map is accompanied by an irregular behaviour of the collective variable $\langle x_n\rangle$. This observation could be mistaken for a violation of the law of large numbers, if one (incorrectly) assumed that the single maps are statistically independent (because of the chaotic dynamics). In practice, analogously to the Kuramoto case, one should more properly look at the evolution of the probability distribution $P(x, n)$, which is again described by a nonlinear functional equation. At variance with the previous case, however, here $P(x, n)$ does not converge towards a fixed point, but keeps showing irregular oscillations which appear even to be infinite dimensional [2,3].

It is natural to ask whether there are general rules, which can allow predicting the complexity of the macroscopic dynamics, given the microscopic equations of motion. The comparison between the Kuramoto setup and the logistic maps seems to suggest that a more complex microscopic dynamics is necessary to generate a more complex collective motion, but such a conclusion is untimely, as the study of various phase-oscillator networks has revealed. Let us start by briefly reviewing the expected asymptotic regimes in the case of identical oscillators. First of all, there exist two highly symmetric solutions: (i) a fully synchronous state, where all units evolve periodically with the same phase, so that the Kuramoto order parameter is $R = 1$; (ii) the so-called splay state, where the single units follow the same periodic dynamics, but their phases are uniformly distributed, so that $R = 0$. Furthermore, it may happen that the oscillator phases group in clusters, each characterized by a single value [4]. This phenomenon is rather general, but a corresponding theory has not yet been fully elaborated. Finally, there exists the less known phenomenon of *partial synchronization*. In this regime the (identical) oscillators follow a quasiperiodic dynamics, while the overall probability density exhibits periodic oscillations: in practice the macroscopic density rotates with a frequency that happens to be larger than the average frequency of the single oscillators. This regime was first discovered by van Vreeswijk in a network of leaky-integrate-and-fire (LIF) neurons [5]

$$\dot{v}_i = a - v_i + gE(t) \ :$$

when the membrane potential $v_i$ reaches the threshold $v_i = 1$, its value is reset to $v_i = 0$, while a pulse $W(t)$ is sent to all other oscillators with some delay $\tau$. All such pulses contribute to defining the mean field $E = \frac{1}{N}\sum_{n|t_n<t} W(t - t_n - \tau)$.

For many years, it was believed that partial synchronization is a special regime which arises only in the LIF model, until a generalized Kuramoto model with a nonlinear dependence on the order parameter $R$ was shown to give rise to a similar scenario [6]. Partial synchronization is, however, a yet more general regime and its properties can be fully appreciated by discussing the relationship between pulse-coupled oscillators, such as the LIF model, and Kuramoto-like systems.

At a first sight, there are two main differences between the two models: (i) in the LIF case, the membrane potential $v_i$ is not a true phase variable (it does not rotate uniformly); (ii) the mean-field $E$ has its own dynamics (it is indeed necessary to add some equations which account for the pulse shape $W$). The first difference can be eliminated by a suitable change of variables which straighten the phase dynamics [7]. As for the second one, one can eliminate the field dynamics, by transforming the pulse height at time $t$ with a phase-dependence coupling strength. Upon following this strategy, one can transform the LIF dynamics into a Winfree model [8]

$$\dot{\phi}_i = \nu + g\Gamma(\phi_i)\frac{1}{N}\sum_j S(\phi_j).$$

This is perhaps the first model ever proposed to describe the evolution of coupled oscillators: $\Gamma(\phi)$ is the so-called *phase-response* curve, which expresses the effectiveness of a perturbation; $S(\phi)$ is the *coupling* function, which, in this case, encodes the pulse shape. Upon suitably choosing the functions $\Gamma$ and $S$, it is possible to observe the onset of partial synchronization [10]. This confirms a substantial equivalence with the original pulse-coupled model.

The Winfree model is closer to the Kuramoto model in that the coupling is instantaneous. There is still, however, a distinguishing feature: the velocity field depends on the absolute phases of the oscillators. This is due to the weak-coupling limit implicitly assumed while deriving the Kuramoto model. In such a limit, with the help of averaging techniques, it is possible to map Winfree model onto the so-called Kuramoto-Daido structure

$$\dot{\phi}_i = \nu + g\frac{1}{N}\sum_j G(\phi_i - \phi_j)\,.$$

where the interaction structure is fully encoded into the periodic *phase-interaction* function $G$ that is obtained by convolving $\Gamma$ and $S$ [8]. The stadard Kuramoto model would correspond to $G(\phi) = \sin\phi$. The shape of the phase-interaction curve which corresponds to the original LIF model (for some parameter values which support partial synchronization) is reported in Fig. 1.

There, we see that it is not drastically different from the sinusoidal shape of the original Kuramoto model (the presence of additional harmonics make $G$ a bit skewed). In fact, it is possible to prove that the Kuramoto model is rather singular: although it cannot give rise to partial synchronization, the addition of one harmonic suffices to make this possible [10]. As a result, the missed observation of this regime is more to be attributed to the fact most of the studies have

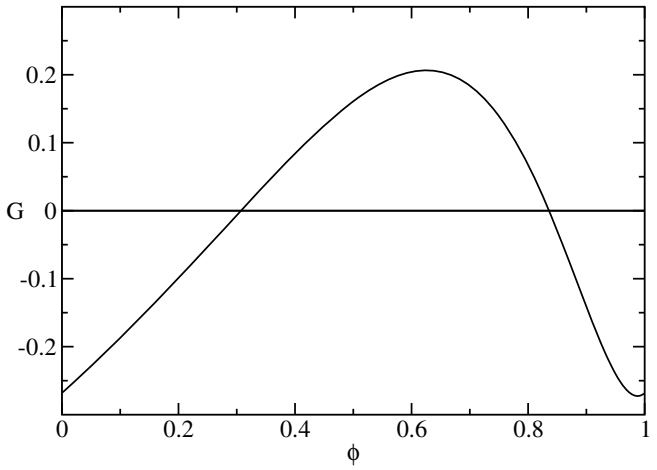


**Fig. 1.** The phase-interaction function which corresponds to the LIF model for $g = 0.1$, $a = 1.3$ and $W(t) = \alpha^2 \exp(-\alpha t)$ with $\alpha = 6$ and with zero delay

been focused on the original Kuramoto model, rather than to the specificity of the phenomenon.

Interestingly enough, numerical studies have revealed that partial synchronization is also rather robust. First of all it surives to the addition of a finite amount of noise [11] (independently on each oscillator). This suggests that it should be observable in experimental setups, that are unavoidably affected by external and internal noise. Furthermore, this phenomenon survives even in sparse networks, when each oscillator is coupled only to $K$ other oscillators. It appears that an average connectivity $K = 10$ is sufficient to sustain stable periodic periodic collective oscillations [12]. In other worlds, the phenomenology goes beyond the simple mean-field setup where it has been originally observed. Moreover, the relatively small connectivity that is required suggests that collective phenomena should play a crucial role in more realistic neural networks.

A last crucial point that is worth considering is the role of disoder. In the original Kuramoto model, the "partial" synchronization signalled by intermediate $R$ values is the result of a distribution of the bare frequencies: those oscillators with either too-large or too-small frequencies cannot lock. In the LIF setup, all oscillators are identical and none of them is locked with the mean field: the onset of partial synchronization is the result of an atypical Hopf bifurcation, which leads to the onset of two frequencies. It is therefore legitimate to ask what happens in pulse-coupled oscillators in the presence of additional disorder. Strange enough, this question has not been thoroughly explored in the literature. The most appropriate setup is that of $\delta$ pulses with a small delay (about 10% of the average interspike interval). Numerical studies have revealed that a standard synchronization transition (similar to that occurring in the Kuramoto model) is accompanied by the emergence of a nontrivial collective motion [13]. This confirms that the LIF

model (and pulse-coupled oscillators, in gneral) is a richer dynamical system than the standard Kuramoto model, where, at most, periodic oscillations of the order parameter $R$ can be observed. Moreover, we see that the complexity of the collective dynamics is not directly linked to the complexity of the single units.

Finally, for the sake of completeness, I wish to briefly recall another collective behaviour that may arise in (identical) phase oscillators. In the presence of a global coupling which, nevertheless depends on the physical distance, the symmetry among all oscillators may break giving birth to the so-called *chimera* states [14] characterized by the spontaneous birth of two sub-populations: those which are synchronous with the mean field and the unlocked ones. Altogether, much progress is still needed to build a general theory of collective dynamics in neural networks, especially in the presence of disordered and/or nontrivial topological structures.

## References

1. Kuramoto, Y.: Chemical Oscillations, Waves, and Turbulence. Springer, Berlin (1984)
2. Shibata, T., Kaneko, K.: Phys. Rev. Lett. 81, 4116 (1998)
3. Takeuchi, K.A., Chaté, H.: J. Phys. A 46, 254007 (2013)
4. Golomb, D., Rinzel, J.: Physica D 72, 259 (1994)
5. van Vreeswijk, C.: Phys. Rev. E 54, 5522 (1996)
6. Rosenblum, M., Pikovsky, A.: Phys. Rev. Lett. 98, 64101 (2007)
7. Abbott, L.F., van Vreeswijk, C.: Phys. Rev. E 48, 1483–1490 (1993)
8. Hansel, D., Mato, G., Meunier, C.: Neural Comput. 7, 307 (1995)
9. Winfree, A.T.: J. Theor. Biol. 16, 15 (1967)
10. Politi, A., Rosenblum, M.: in preparation
11. Mohanty, P.K., Politi, A.: J. Phys. A 39, L415 (2006)
12. Luccioli, S., Olmi, S., Politi, A., Torcini, A.: Phys. Rev. Lett. 109, 138103 (2012)
13. Luccioli, S., Politi, A.: Phys. Rev. Lett. 105, 158104 (2010)
14. Abrams, D.M., Strogatz, S.H.: Phys. Rev. Lett. 93, 174102 (2004)

# Transient Sequences in a Network of Excitatory Coupled Morris-Lecar Neurons

Dmitry V. Kasatkin, Aleksey Dmitrichev, and Vladimir I. Nekorkin

Institute of Applied Physics of the Russian Academy of Sciences,
Ulyanov str. 46, 603950 Nizhny Novgorod, Russia
{kasatkin,admitry,vnekorkin}@neuron.appl.sci-nnov.ru

**Abstract.** We propose a model of neural network demonstrating variety of sequential activity modes. Unlike the previously known models of transient dynamics, in the present model transient sequential modes are formed by means of dynamical bifurcations and not directly related to the existence of heteroclinic channels. It is shown that network being initially at rest generates a sequence of metastable oscillatory states of activity in response to an external stimulus. We study the influence of the parameters characterized the initial times of synaptic activation processes caused by input information signals on the network dynamics. Numerical simulation of the model has shown, that these parameters determine not only the structure of the set of oscillatory metastable states and the sequence of transitions between them, but also the temporal characteristics of the transition sequences such as the time duration of the oscillatory metastable states.

**Keywords:** neural network, transient dynamics, oscillatory metastable states, dynamical bifurcation.

## 1 Introduction

Many neurophysiological experiments [1–4] have indicated that some neural processes related, for example, with performing of different cognitive tasks (memory, attention, psychomotor coordination, and so on) are accompanied only by transient activity at the level of individual neurons or small enough groups of neurons. As a result of such processes a certain sequence of transitional activity phases appears in neural network. It is clear that such activity of neural networks cannot be understood within the framework of classical models of nonlinear dynamics which are based on the concept of attractor because here the main effect is achieved long before the system reaches its neighborhood. Therefore, to adequately describe transient and sequential neural processes a novel class of models should be developed. One of the popular points of view is that such models should be based primarily on the concept of metastable states. Transient dynamics here is formed by sequential switching between these states. Recently several phenomenological models based on the metastable states concept have been proposed [5–9]. These models operate with variables characterizing averaged activity of neural networks. To describe the dynamics of such variables



A. Sanayei et al. (eds.), *ISCS 2014: Interdisciplinary Symposium on Complex Systems*, Emergence, Complexity and Computation 14, DOI: 10.1007/978-3-319-10759-2_4

either a generalized Lotka-Volterra system or a Wilson-Cowan system is used. It has been shown that under appropriate conditions a stable heteroclinic channel appears in the phase space of the models. This channel represents a mathematical image of transient activity. Indeed, the channel is formed by a set of trajectories in the vicinity of a heteroclinic skeleton which consists of saddles and unstable separatrices which connect their surroundings. Each trajectory of the channel sequentially passes the neighborhoods of saddle fixed points "staying" there for some (finite) time. However, the models have significant limitations. First of all, they do not account for dynamical properties of individual neurons. Another limitation consists in significant simplification of architecture and properties of interneuron synaptic couplings.

In this work we propose a model demonstrating various structurally stable transient dynamics and taking into account individual properties of neurons. The model represents a network of Morris-Lecar neurons [10] coupled by means of excitatory chemical synapses. In this model sequential activity modes are formed by means of dynamical bifurcation and not directly related to the existence of heteroclinic channels.

## 2 Model

Consider a neural network consisting of $N$ neurons coupled by excitatory synapses. The dynamics of such a network is described by the following system of ODEs:

$$C\frac{dv_i}{dt} = -g_L(v_i - v_L) - g_{Ca}M_\infty(v_i)(v_i - v_{Ca}) - \tag{1}$$
$$-g_K n_i(v_i - v_K) + I_i^{ext} - g_{syn}s_i(v_i - v_{rev}),$$
$$\frac{dn_i}{dt} = \frac{n_\infty(v_i) - n_i}{\tau_n(v_i)}, \tag{2}$$
$$\frac{dr_i}{dt} = f_1(r_i) - s_i - k_1, \tag{3}$$
$$\frac{ds_i}{dt} = \varepsilon(f_2(r_i) - s_i - k_2 - \mu\sum_{\substack{j=1,\\ j\neq i}}^{N} H(v_j - \theta_{ji})), \tag{4}$$
$$i, j = \overline{1, N}.$$

The neurons dynamics is given by the two-variable Morris-Lecar (ML) neuronal model (1)-(2), equations (3)-(4) describe synaptic couplings between neurons. Here, the variables $v_i$, $n_i$ correspond to the membrane potential and the state of activation of $K^+$ channels of the $i$-th neuron, $C$ is the capacitance of the membrane. The parameters $g_L$, $g_{Ca}$, $g_K$ are the maximal conductances associated with the leak, $Ca^{2+}$ and $K^+$ transmembrane currents, respectively; $v_L$, $v_{Ca}$, $v_K$ are the corresponding reversal potentials; $I_i^{ext}$ are the external currents. The voltage-dependent gating functions $M_\infty(v)$, $n_\infty(v)$ and $\tau_n(v)$ are given by:

$$M_\infty(v) = 0.5\left[1 + \tanh\left(\frac{v - v^{(1)}}{v^{(2)}}\right)\right],$$

$$n_\infty(v) = 0.5\left[1 + \tanh\left(\frac{v - v^{(3)}}{v^{(4)}}\right)\right],$$
$$\tau_n(v) = \left[\phi\cosh\left(\frac{v - v^{(3)}}{2v^{(4)}}\right)\right]^{-1},$$

where $v^{(1)} = -0.01$, $v^{(2)} = 0.15$, $v^{(3)} = 0$, $v^{(4)} = 0.3$, $\phi = 1$. The coupling between neurons is defined by adding the synaptic current term $-g_{syn}s_i(v_i - v_{rev})$ to the right side of equation (1). The parameter $g_{syn}$ is the maximal synaptic conductance and $v_{rev}$ is the synaptic reversal potential. The variable $s_i$ characterizes how the postsynaptic conductance depends on the presynaptic potentials $v_j$, $(j \neq i)$. To describe the dynamics of synaptic interneuron interaction we introduce a phenomenological model in the form of equations (3),(4), where

$$f_1(r) = r - \frac{r^3}{3},$$
$$f_2(r) = \begin{cases} \alpha r, & r < 0 \\ \beta r, & r \geq 0 \end{cases},$$
$$H(x) = (1 + \exp(-\frac{x}{K_p}))^{-1},$$

$K_p = 0.001$, $\alpha = 0.5$, $\beta = 2$, $\varepsilon = 0.005$, $\mu = 0.07$, $k_1 = -0.666$, $k_2 = -0.5$. The parameters $\theta_{ji}$ characterize the initial times of synaptic activation processes caused by input information signals. In the ML neuronal model (equations (1),(2)) values of parameters are fixed as follows: $C = 1$, $g_L = 0.1$, $g_{Ca} = 1.1$, $g_K = 2$, $v_L = -0.5$, $v_{Ca} = 1$, $v_K = -0.7$, $g_{syn} = 0.0409$, $v_{rev} = 0.5$, $I_i^{ext} = 0.13$, $(i = \overline{1, N})$. With these parameter values the uncoupled single neuron is in the rest state.

## 3 Synaptic Coupling Dynamics

The term $-s_i g_{syn}(v_i - v_{rev})$ in the right side of equation (1) models synaptic current that can changes the membrane potential of the $i$-th neuron $v_i$. Activation variable $s_i$ shows the dependence of postsynaptic conductance on presynaptic potential $v_j$. Here, we propose a new phenomenological dynamical model of synapse possessing the threshold features and realistic form of synaptic current as well as synaptic delay.

The FitzHugh-Nagumo system (equations (3),(4) with $\mu = 0$) in the parameters region, where it has three equilibrium states, was used here for describing dynamics of variable $s_i$. Let us consider in detail an activation process of synaptic coupling in our model. If the condition $v_j < \theta_{ji}$ is satisfied for all the neurons membrane potentials, then all the functions $H(v_j - \theta_{ji}) \approx 0$ and equations (3),(4) can be rewritten as follows:

$$\frac{dr_i}{dt} = f_1(r_i) - s_i - k_1, \tag{5}$$
$$\frac{ds_i}{dt} = \varepsilon(f_2(r_i) - s_i - k_2).$$

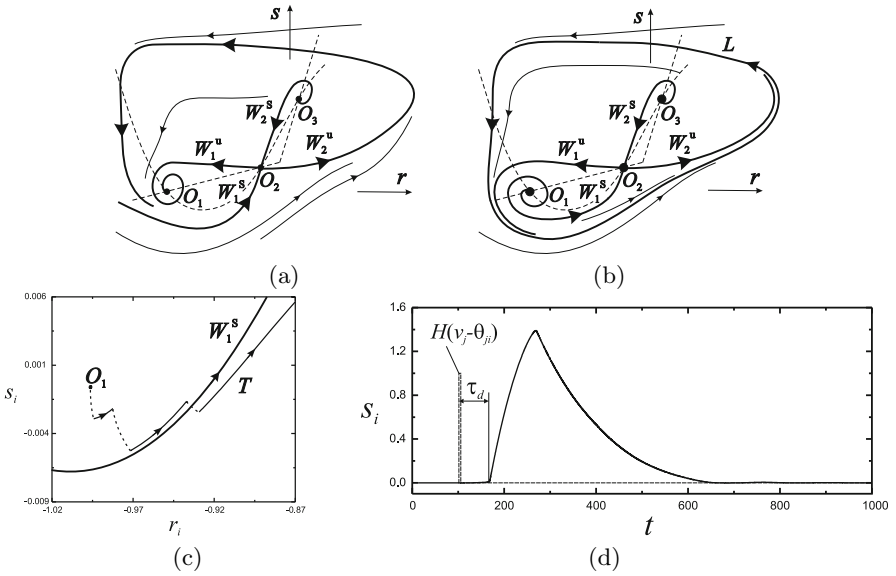


**Fig. 1.** Phase portraits of system (3),(4) for: (a) $v_j < \theta_{ji}$; (b) $v_j > \theta_{ji}$. (c) Fragment of trajectory forming in system (3),(4) as a result of processes of its activation and inactivation; (d) Evolution of variable $s_i(t)$ caused by changing of membrane potential $v_j$.

Under the chosen parameter values, the system (5) has a phase portrait presented in fig. 1a. In this case, for any initial conditions the system comes to the rest state associated with stable equilibrium state $O_1$. Parameters $k_1$ and $k_2$ are chosen such, that the ordinate of this equilibrium state is equal to zero. There is also saddle equilibrium state $O_2$ in phase plane. Stable separatrix of this state defines the activation threshold of the system. Assume that at some moment the potential of the $j$-th neuron exceeds $\theta_{ji}$ value. Then, function $H(v_j - \theta_{ji})$ rapidly takes on the value equal to unity ($H$ is close to Heaviside function) and for throughout the period when $v_j > \theta_{ji}$, equations (3),(4) are written in the form:

$$\begin{aligned} \frac{dr_i}{dt} &= f_1(r_i) - s_i - k_1, \\ \frac{ds_i}{dt} &= \varepsilon(f_2(r_i) - s_i - k_2 - \mu)). \end{aligned} \tag{6}$$

At the same time, the initial conditions for system (3),(4) are defined by dynamics of the previous system (5) and correspond to its equilibrium state $O_1$. In fig. 1b the phase portrait of system (6) is presented. In this case there is only one attractor of the system – stable limit cycle $L$. Note, that transformation of the phase portrait, presented in fig. 1a, into the one, illustrated in fig. 1b is realized through Andronov-Hopf bifurcation, loop of separatrix $W_1^s$ and $W_1^u$ and saddle-

node bifurcation of limit cycle. However, appearing modes have no significant influence on dynamics of system (3),(4), because the function $H(v_j - \theta_{ji})$ takes one of two possible values 0 or 1 rather quickly. The trajectory of system (6), originating from equilibrium state $O_1$ returns to the vicinity of stable limit cycle $L$ in accordance with dynamics of system (6). When the variable $v_j$ becomes less than $\theta_{ji}$, the system dynamics is described by equations (5), i.e. the trajectory returns to the vicinity of equilibrium state $O_1$. Therefore, dynamics of synapse is caused by both systems (5) and (6) in turn. If the excess of potential $v_j$ over $\theta_{ji}$ is multiple, then some trajectory $T$ (fig. 1c) appears in the phase plane of variables $(r_i, s_i)$. This trajectory consists of fragments of trajectories of systems (6) (dot line) and system (5) (solid line) in turn. If the representation point finds itself to the right of separatrix $W_1^s$ after the presynaptic potential ceases to increase, then the system returns to the vicinity of equilibrium state $O_1$ according to system (5) dynamics. This process is followed by "powerful" pulse change of variable $r$, i.e. activation of synaptic coupling. In this case evolution of variable $s$ has a typical form for synaptic current (fig. 1d). Separatrix $W_1^s$ defines activation threshold for synaptic coupling. The time needed for the representation point to find itself to the right of separatrix $W_1^s$ determines synaptic delay in our model. Thus, the parameters $\theta_{ji}$ in system (1)-(4) control the start of synaptic processes and synaptic delay is defined by dynamical properties of two "joining" nonlinear systems.

## 4 Oscillatory Metastable States

Consider dynamics of the model (1)-(4). All the neurons are in the rest state at the initial moment. Suppose one of the neurons (for example, the second one) to be affected by external current (information signal). It causes change of membrane potential $v_2(t)$. When the variable $v_2(t)$ exceeds the value of $\theta_{2i}$ synaptic coupling between the second and the $i$-th neurons may be activated. In the phase plane of system (3),(4) there appears trajectory $T$ which in some time exceeds the threshold corresponding to separatrix $W_1^s$, and causes an increase of variable $s_i$ (fig. 1d). Increasing of variable $s_i$ means appearance of synaptic current coming to the $i$-th neuron. Under the action of the synaptic current, the dynamical system (1),(2), describing the $i$-th neuron, is non-autonomous and is defined in three-dimensional phase space. The system (3),(4) have a small parameter $\varepsilon$ and therefore the evolution of the $s_i$-variable is slow with respect to the evolution of variables $v_i$, $n_i$. Hence, in the first approximation one can suppose variable $s_i(t)$ in system (1),(2) to be a quasistatically varying parameter. The bifurcation diagram of system (1),(2) where $s_i$ is playing a role of parameter is presented in fig. 2a. For $s_i < s_d \approx 0.724$ the only stable equilibrium state $P_1$ exists. For $s_i = s_d$ the saddle-node bifurcation of limit cycle holds, and two limit cycles – stable $C^s$ and unstable $C^u$ appear on the phase plane (fig. 2a). Further increasing of $s_i$ leads to the shrinking of $C^u$ to the equilibrium state $P_1$, and for $s_i = s_h \approx 1.092$, the equilibrium state $P_1$ changes its stability due to the subcritical Andronov-Hopf bifurcation. For $s_i > s_f \approx 1.327$, two

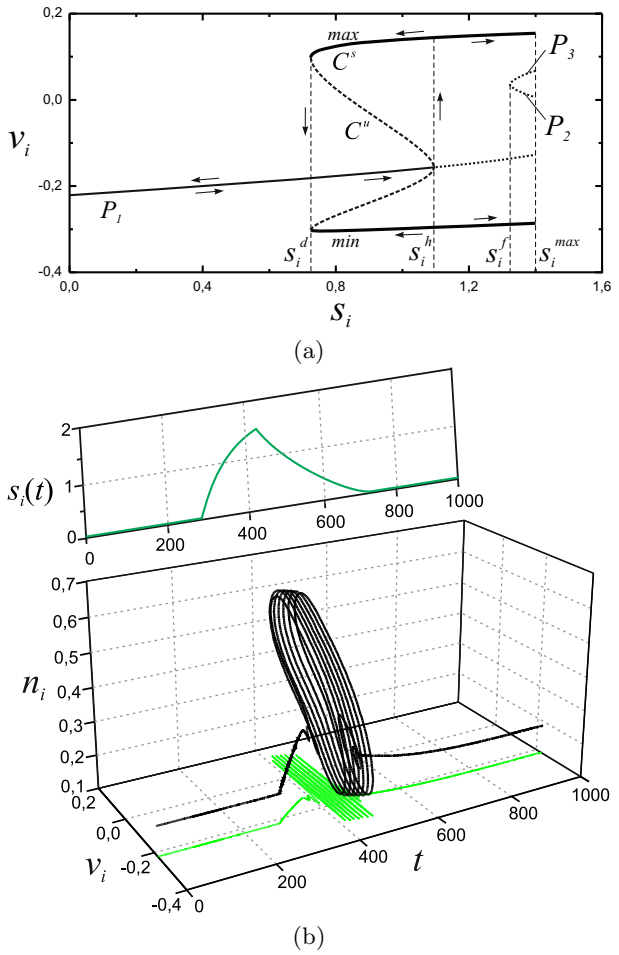


**Fig. 2.** Dynamics of system (1),(2) for changing $s_i$ value. (a) One-parametric bifurcation diagram; (b) The trajectory forming in non-autonomous phase space for changing $s_i(t)$.

more equilibrium states appear - saddle $P_2$ and unstable $P_3$ (fig. 2a). Therefore, if $s_i > s_h$, the only attractor of system (1),(2) is stable limit cycle $C^s$. In non-autonomous phase space, the stable equilibrium states $P_1(s_i)$ form a stable one-dimensional integral manifold $M^s_{st}(0)$ and the stable limit cycles $C^s$ form a stable two-dimensional integral manifold $M^s_c(0)$. According to the theorem of persistence of integral manifolds [11] there are integral manifolds $M^s_{st}(\varepsilon)$ and $M^s_c(\varepsilon)$ close to $M^s_{st}(0)$ and $M^s_c(0)$ correspondingly. Since initially the $i$-th neuron is at the rest, the representative point in the non-autonomous phase space is situated on the manifold $M^s_{st}(\varepsilon)$. Under a synaptic action the representative point starts moving along $M^s_{st}(\varepsilon)$ until it reaches the boundary of $M^s_{st}(\varepsilon)$. After

that the representative point passes rapidly into a vicinity of $M_c^s(\varepsilon)$ forming an oscillatory motion. The oscillating process is over when the representative point reaches the boundary of the manifold $M_c^s(\varepsilon)$. Fig. 2b illustrates a numerically obtained trajectory in non-autonomous phase space laying in manifolds $M_{st}^s(\varepsilon)$ and $M_c^s(\varepsilon)$. The trajectory includes an oscillating part related to the phase of transient oscillating activity of a neuron, and the part corresponding to the phase of rest state of a neuron.

## 5 Transient Sequences

We considered the process of activation of a neuron and described dynamical mechanism of arising of the process. Activation of other neurons of the network occurs analogously. As a result, a sequence of oscillation activity phases of different neurons of the network emerges successively in time. Numerical study of system (1)-(4) has shown, that any set of parameters $\theta_{ij}$ corresponds to some sequence ("path") of transient oscillatory states of neurons of the network. Figure 3 depicts partition of $(\theta_{13}, \theta_{32})$-parameters plane into domains corresponding to different transient dynamical modes of the network (1)-(4) for $N = 3$.

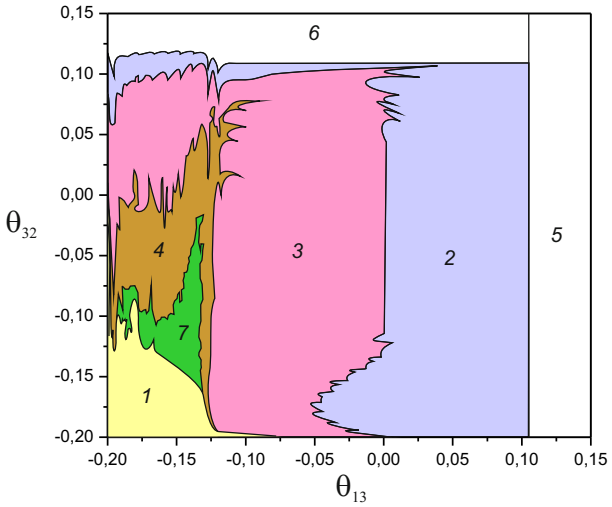


**Fig. 3.** Diagram of transient dynamical modes of system (1)-(4) for $N = 3$ in the plane of parameters $(\theta_{13}, \theta_{32})$, $\theta_{21} = -0.2, \theta_{12} = \theta_{23} = \theta_{31} = 0.2$

In domain 1, sequential excitation of the first, third and second neurons (basic sequence) is observed in the system (fig. 4a). If the parameters $\theta_{13}$ and $\theta_{32}$ belong to the domain 2 there is only the successive excitation of the first and third neuron, but the second neuron remains unexcited. Domain 3 corresponds to the excitation of only the first neuron, while the others remain at the rest.

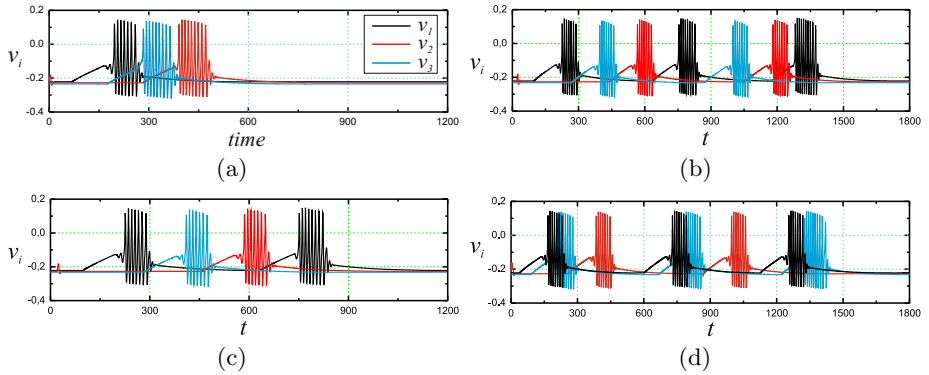


**Fig. 4.** Examples of transient sequences generated by a network of three Morris-Lecar neurons with excitatory synaptic connections for different parameters $\theta_{ij}$: $\theta_{13} = -0.146$, $\theta_{32} = -0.146$ (a); $\theta_{13} = -0.05$, $\theta_{32} = -0.05$ (b); $\theta_{13} = 0.05$, $\theta_{32} = -0.05$ (c); $\theta_{13} = -0.175$, $\theta_{32} = -0.05$ (d). The other parameters $\theta_{ij}$ are chosen as in fig. 3.

Transient sequences realized in such a network represent not only processes of single activation of neurons. It has been found, that the phases of activity of neurons may be not single and may take place irregularly. The examples of such transient sequences are presented in fig. 4b-d. These modes are realized for parameter values from domains 4 and 5 (fig. 3). Domain 6 corresponds to the mode when the basic sequence is repeated three times. Domain 7 has sufficient complex structure and contains a set of subdomains that is not shown here because they are relatively narrow. In general, the dynamics in this domain is characterized by nontrivial transient modes with multiply repetition of basis sequence. Parameters $\theta_{ij}$ determine not only the structure of the set of metastable states and the sequence of transitions between them, but also the temporal characteristics of the transition sequences such as the time duration of the oscillatory metastable state. Furthermore it was established that a set of metastable states and the transient sequence among them are also sensitive to initial conditions (input information signals). Transient sequences may vary depending on amplitude and duration of an external initial action and element of network where external action is applied.

All results presented here for the three coupled neurons will take place in the case of large neural network. Numerical study showed that the more elements are in the network the more different sequential modes the network can form. Also the sequences themselves become more complex. For example, the figure 5 shows one of the sequential modes formed in the network of 100 Morris-Lecar neurons coupled randomly (Erdos-Renyi model with probability 0.2) by means of excitatory synapses with identical activation thresholds.

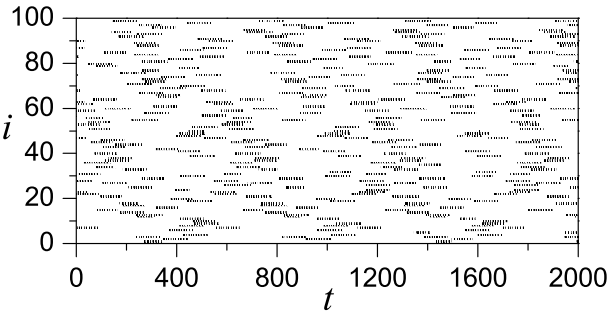


**Fig. 5.** Spatiotemporal pattern of transient activity generated by a network of hundred Morris-Lecar neurons with excitatory synaptic connections. Points indicate the spikes generated by neurons of the network.

## 6 Conclusion

Sequential activity inherent to a wide range of neural systems is associated with cognitive processes like memory, attention, decision making, motor actions. In the present work we develop an approach for describing sequential dynamics. We propose a model of neural network demonstrating variety of sequential activity modes which are formed by means of dynamical bifurcations. Unlike the previously known models [5, 8, 9] of transient dynamics, in the present model transient sequential modes are not directly related to the existence of heteroclinic channels. To simulate excitatory synaptic couplings between neurons we propose two-dimensional dynamical system with nonunique equilibrium state. It is shown that a sequence of metastable oscillatory states of activity occurs in the network initially at rest in response to an external stimulus. We study the influence of the parameters characterized the initial times of synaptic activation processes caused by input information signals on the network dynamics. Numerical simulation of the model has shown, that these parameters determine the structure of the set of oscillatory metastable states, the sequence of transitions between them and temporal characteristics of the transition sequences. It has been established that the transient sequences realized in the network are selective to input information signals and robust against small perturbations of initial conditions. Application of the proposed approach to the problem of modeling sequential activity allow us to describe, explain and predict the possible spatio-temporal activation processes of some neural systems in the brain.

**Acknowledgment.** The authors would like to thank the support of the Russian Foundation for Basic Research (grants Nos. 13-02-00858, 12-02-00526).

## References

1. Stopfer, M., Jayaraman, V., Laurent, G.: Intensity versus Identity Coding in an Olfactory System. Neuron 39, 991–1004 (2003)
2. Mazur, O., Laurent, G.: Transient Dynamics versus Fixed Points in Odor Representations by Locust Antennal Lobe Projection Neurons. Neuron 48, 661–673 (2005)
3. Jones, L.M., Fontanini, A., Sadacca, B.F., Miller, P., Katz, D.B.: Natural Stimuli Evoke Dynamic Sequences of States in Sensory Cortical Ensembles. Proc. Natl. Acad. Sci. USA 104, 18772–18777 (2007)
4. Orlandi, J.G., Soriano, J., Alvarez-Lacalle, E., Teller, S., Casademunt, J.: Noise Focusing and the Emergence of Coherent Activity in Neuronal Cultures. Nature Phys. 9, 582–590 (2013)
5. Afraimovich, V.S., Zhigulin, V.P., Rabinovich, M.I.: On the Origin of Reproducible Sequential Activity in Neural Circuits. Chaos 14, 1123–1129 (2004)
6. Rabinovich, M.I., Huerta, R., Afraimovich, V.S.: Dynamics of Sequential Decision Making. Phys. Rev. Lett. 97, 188103 (2006)
7. Rabinovich, M.I., Huerta, R., Varona, P., Afraimovich, V.S.: Generation and Reshaping of Sequences in Neural Systems. Biol. Cybern. 95, 519–536 (2006)
8. Rabinovich, M.I., Varona, P., Tristan, I., Afraimovich, V.S.: Chunking dynamics: heteroclinics in mind. Front. Comput. Neurosci. 8, 1–10 (2014)
9. Komarov, M.A., Osipov, G.V., Zhou, C.S.: Heteroclinic contours in oscillatory ensembles. Phys. Rev. E. 87, 022909 (2013)
10. Morris, C., Lecar, H.: Voltage Oscillations in the Barnacle Giant Muscle Fiber. Biophys. J. 35, 193–213 (1981)
11. Hirsh, M.V., Pugh, C.C., Shub, M.: Invariant manifolds. In: Dold, A., Eckmann, B. (eds.) LNM, vol. 583, pp. 2–148. Springer, Berlin (1977)

# The Development of Chemical Artificial Intelligence Processing Fuzzy Logic

Pier Luigi Gentili

Department of Chemistry, Biology and Biotechnology, University of Perugia, Italy
pierluigi.gentili@unipg.it

**Abstract.** The Human Nervous System is an outstanding example of natural complex system. Its hierarchical architecture and its basic nonlinear working principles store the secrets of Complexity. Of course, a scrutiny of the Human Nervous System is going to have a profound impact on the challenges to Complexity. In this contribution, we present the first results in our analysis of the human nervous system at the "computational", "algorithmic" and "implementation" levels. Such analysis will probably bring to the development of a new generation of computing machines imitating the human intelligence that computes with words and solves quite easily computational problems like the recognition of variable patterns.

**Keywords:** Complexity, Fuzzy Information, Bayes theory, Chromogenic materials, Bistable reactions, Belousov-Zhabotinsky reaction.

## 1 Introduction

Nowadays, one of the most exciting and compelling goal of science is trying to win the Complexity Challenges. There are two types of Complexity Challenges. The first type regards Natural Complexity and the development of a unifying theory which should describe and predict the behavior of any Natural Complex System. Whatever is the character of the Complex System, that is if it is of either chemical or physical, or biological or geological, or social or economic, etc…, character, science is spurred to unveil the shared working principles. The second type of Complexity Challenges concerns about the Computational Complexity; we need to devise effective ways to find accurate solutions of NP-problems in reasonable time. Moreover, we need to search for universally acceptable solutions of pattern-recognition problems.

Two main strategies are being followed to face the Complexity Challenges. The first strategy consists in developing always more powerful electronic supercomputers [1], because facing both Natural and Computational Complexity means handling a huge number of data. The second strategy is the interdisciplinary endeavor known as Natural Computing [2]. It involves mathematicians, computer scientists, biologists, physicists, chemists, engineers, etc…, and its goals are to propose (1) new models to describe Natural Complex Systems; (2) new algorithms to face the Computational Complexity Challenges; (3) new materials, alternative to the inorganic semiconductors used in current computers, to make easier the implementation of the new



A. Sanayei et al. (eds.), *ISCS 2014: Interdisciplinary Symposium on Complex Systems*,
Emergence, Complexity and Computation 14, DOI: 10.1007/978-3-319-10759-2_5

algorithms. The rationale of this interdisciplinary research line is that every natural process is a kind of computation. It derives that many natural systems become prototypes of new computational machines. For instance, the human nervous system is a wealthy source of inspiration for the development of Artificial Intelligence. The teams working in the field of Artificial Intelligence are driven by the ambitious project of understanding the foundations and running mechanisms of human mind in order to try to reproduce them artificially. Any success in the field of Artificial Intelligence is having positive impact on the challenges to Complexity. In fact, a deeper understating of human brain, being a prototype of Complex System, allows secrets of Natural Complexity to be unveiled. Moreover, a computational machine, mocking human intelligence, will be a new effective tool to tackle at least some of the Computational Complexity challenges.

In a fairly recent book [3], the cognitive scientists Gallistel and King, in agreement with the neuroscientist Marr [4], argue that to understand a complex biological system like our brain, it is necessary to perform an analysis at three distinct levels. The first is the "computational level" and consists in describing the inputs, outputs and the task of the system. The second is the "algorithmic level" and consists in formulating algorithms that might carry out those computations. Finally, the third is the "implementation level" and consists in searching for mechanisms of the kind that would make the algorithm work.

In this contribution, we are presenting the results achieved so far in our group in the development of Chemical Artificial Intelligence [5] by following the methodology proposed by Gallistel, King and Marr. In paragraph 2, we are introducing the first results on the analysis of the Human Nervous System at the "computational" and "algorithmic" level. Specifically, I propose a combination of Fuzzy logic with the theory that describes human inference as Bayesian probabilistic event [6]. In the ensuing paragraphs, we are describing the properties of few chemical systems that are useful in imitating the working mechanism and performances of the elements of the Human Nervous System. Since fuzzy logic is a good model of the human power of "computing" with words and taking decision in Complex situations [7], in paragraphs 3 and 4 we are presenting the ways of implementing fuzzy logic at the molecular level. Any success in this field will push the Chemical Artificial Intelligence towards the human abilities of (i) taking decisions in Complex situations and (ii) recognizing variable patterns.

## 2 Computational and Algorithmic Analysis of Human Nervous System

The human nervous system [8] is a complex network of billions of nerve cells unevenly spread throughout the body. It controls and rules the behavior of the entire body by catching, retrieving, processing, memorizing, sending either accurate or vague information. It allows humans to take decisions as responses to incoming stimuli and signals; it computes by using words or handling at the same time numbers and words. The human nervous system comprises three main elements: (a) the sensory system

(SS), (b) the central nervous system (CNS), and (c) the effectors' system (ES) [6] and it can be structurally and intrinsically compared with a Fuzzy Logic System (FLS). A FLS consists of three main elements (see Figure 1): (a') the Fuzzifier, based on the partition of the input variables in fuzzy sets, and transforming crisp inputs in vectors of degrees of membership to the input fuzzy sets; (b') the Fuzzy Inference Engine that contains IF-THEN rules linking input fuzzy sets with output fuzzy sets; (c') the Defuzzifier, transforming the activated output fuzzy sets in crisp outputs.

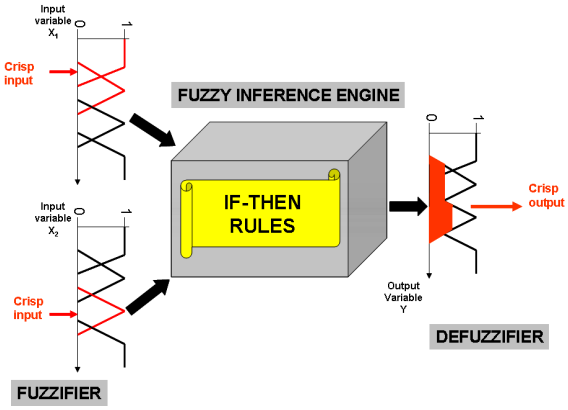


**Fig. 1.** The three elements of a FLS built according to the Mamdani's method (see [9]) are the Fuzzifier, the Fuzzy Inference Engine and the Defuzzifier

The sensory system collects specific physical and chemical stimuli. It codes for four aspects of a stimulus: modality (M), intensity ($I_M$), time-evolution ($I_M(t)$) and spatial distribution ($I_M(t,x,y,z)$). The power to distinguish different modalities is due to the existence of specialized receptor cells. Receptor cells in our SS can be sorted out in photoreceptors collecting visible light; mechanoreceptors sensing mechanical stimuli; thermo-receptors perceiving thermal stimuli; chemo-receptors detecting and distinguishing several chemicals. Each sensory organ has a hierarchical structure. At the smallest level, that is at the molecular level, the fundamental elements are macromolecular switches, i.e. proteins. Then, at an upper level, i.e. at the cellular level, there are the sensory cells containing many replicas of the macromolecular switches that are spatially organized. Finally, at the highest level, i.e. at the organ level, there are many copies of the different cells, properly distributed in space according to the architectures of the organ itself. Each sensory organ plays like a Fuzzifier. The manifold content of information of a stimulus, i.e. its value, intensity, time-evolution and spatial distribution is encoded as fuzzy information. The interaction between a stimulus and each type of molecular switches allows the value of the stimulus to be encoded as degrees of membership of the stimulus to the different molecular switches. Such information is encoded as a vector of degrees of membership $\overline{\mu}_{ML}$ (where ML stands for Molecular Level). The information of the intensity and its temporal evolution are encoded as degrees of membership of the stimulus to the sensory cells, i.e. as

the vector $\overline{\mu}_{CL}$ (where CL stands for Cellular Level). The value of the membership function at the cellular level corresponds to the ratio of molecular switches activated per unit cell and per unit of time. Finally, the information regarding the spatial distribution is encoded as degrees of membership of the stimulus to the properly arranged array of sensory cells, $\overline{\mu}_{OL}$ (where OL stands for Organ Level). The overall fuzzy information $\overline{\mu}_{T}$ (where T stands for Total) is a composition of the three contributions, $\overline{\mu}_{ML}$, $\overline{\mu}_{CL}$, and $\overline{\mu}_{OL}$; it is deterministic and should be, in principle, reproducible and universal. However, there are many factors that contribute to limiting the reliability of sensory information about the world. Structural constraints on neural representations and computations, neural noise introduced in early stages of sensory coding, past experiences, and the temporary physiological state of the fellow receiving the stimuli contribute to limiting the reliability, reproducibility and the universality of sensory information about the world. Close values of $\overline{\mu}_{T}$ become indistinguishable and are grouped together into granules. Every human brain must deal with the resulting uncertainty to generate perceptual representations of the world. Cox's theorem along with the Dutch Book argument tell us that the probability theory constitutes a coherent way of reasoning under uncertainty [10, 11]. This leads to the idea that human brain performs probabilistic reasoning, whether for sensory processing, motor control or cognitive computing. Therefore, perception can be described as a subjective process of Bayesian probabilistic inference [12, 13]. If $I_M$ is the intensity of the stimulus of modality M, and $X_M$ represents the collection of cells sensitive to it, applying the Bayes' rule, it derives that

$$p(I_M|X_M) = \frac{p(I_M)\,p(X_M|I_M)}{p(X_M)} \tag{1}$$

The term $p(I_M|X_M)$ represents the "posterior probability". It is proportional to the product of the "prior probability" $p(I_M)$ and the "likelihood" $p(X_M|I_M)$. $p(I_M)$ is the probability of each perception prior to receiving the stimulus: it represents knowledge of the regularities and it is strongly subjective. In agreement with the theory of Bayesian inference generalized in fuzzy context [14], $p(X_M|I_M)$ can be identified with the fuzzy information $\overline{\mu}_{T}$. The term $p(X_M)$ is the "plausibility" and is merely a normalization factor. Bayes formula implies that human perception is a trade-off between $p(X_M|I_M)$ and $p(I_M)$ [15]. Some perceptions may be more "prior probability" driven, and others more data (that is $\overline{\mu}_{T}$) driven. The more noisy and ambiguous the perception features, the more relevant the role played by $p(I_M)$, and the less reproducible is the sensation. The population of $X_M$ sensory neurons activated by the stimulus, evokes the activity of a population of N' downstream neurons ($R_M$). The terms $I_M$, $X_M$ and $R_M$ form a chain communication system. At each step along the communication chain, the uncertainty does not decrease. It rather increases due to the noise operating in the communication among neurons. Thus, the information that

$R_M$ gives about $I_M$ cannot be greater than the information $X_M$ gives about $I_M$, in agreement with the Law of Diminishing Information [16]:

$$\inf(R_M@I_M) \leq \inf(X_M@I_M) \tag{2}$$

Finally, after one or more of these communication steps, our brain receives an information about a stimulus of a specific modality. Such information is fuzzy granular due to the uncertainty and indistinguishability, and it is properly described by words.

Most often, we receive multimodal stimuli that interact with more than one sensory system. Multisensory processing pieces signals of different modality if stimuli fall on (i) the same or adjacent receptive fields (according to the "spatial rule") and (ii) within close temporal proximity (according to the "temporal rule"). Multisensory processing forms a total picture that differs from the sum of its unimodal contributions, a phenomenon called multisensory enhancement in neuroscience [17] or colligation in the Information theory [16]. The principle of inverse effectiveness states that the multisensory enhancement is stronger for weaker stimuli. Physiological and behavioural experiments have shown that a number of brain areas, such as the Superior Colliculus [17], contain distinct monosensory, as well as multisensory neurons. Neuro-physiological data have revealed also cross-modal influences on unimodal brain areas. All these evidences suggest a role of both feed-forward connections from unimodal to multimodal areas and feedback connections from multimodal to unimodal areas [17]. The human brain results a collection of intertwined Fuzzy Inference Engines, whose working principles still need to be more deeply studied and rationalized. So far, it is evident that since sensory modalities are not equally reliable and their reliability can change with context, multisensory integration may be assumed a Bayesian probabilistic inference. The posterior probabilities of Bayes formula (see equation 1) are actually granules of fuzzy information properly described by the use of words. The computation carried out by our brain triggers a response on the effectors' system. The ES can be assumed to be a collection of mutually interacting Defuzzifiers, whose properties still need to be analyzed.

## 3 Chromogenic Materials as Artificial Sensory Elements to Process Fuzzy Logic

In human sensory systems there are many types of responsive molecules catching physical and chemical stimuli [5], as said before. These natural responsive molecules can be artificially imitated by chromogenic and fluorogenic materials that are switchable molecules sending signals of transmitted and emitted light, respectively. Before receiving any perturbation, chromogenic compounds are in a structural A state that is quite often uncolored. After a perturbation, they acquire a new structure B, and hence a new color. This chemical transformation is reversible: through a suitable stimulus, the system may be transformed back to the initial state. Chromogenic materials are classified according to the kind of external perturbation that promotes the conversion from A to B. There are photochromic species that are sensitive to UV-visible radiation; piezochromic compounds that respond to mechanical forces; thermochromic

molecules sensitive to heat; electrochromic species responding to electric fields; acidichromic and metallochromic compounds that change colors in response to protons and metal cations, respectively; and so on [5]. To quantify the information a chromogenic species may send, it is useful to define its Colorability (C) through the equation below [19]:

$$C = I_B - I_A = x_B \log_2(x_B) - x_A \log_2(x_A) + y_B \log_2(y_B) - y_A \log_2(y_A) + z_B \log_2(z_B) - z_A \log_2(z_A) \quad (3)$$

where $x_i$, $y_i$, $z_i$ are the chromaticity's coordinates of the i-th state, and $I_i$ is the information sent by the i-th state. From equation (3), it is easy to infer that the Colourability of a chromogenic compound is large when there is a sharp color contrast between A and B; for example, when A is transparent in the visible region and B transmits radiations belonging only to a narrow band of visible wavelengths.

The spectral features of chromogenic materials and hence the values of the chromaticity coordinates can be changed in continuous way by proper selection of the type of stimulus and by modulating its intensity. This property makes chromogenic compounds the right candidates for processing the infinite-valued Fuzzy logic. Two strategies may be followed [19, 20], herein described by using the same spirooxazine SpO (whose structure is shown in the upper left part of Figure 2).

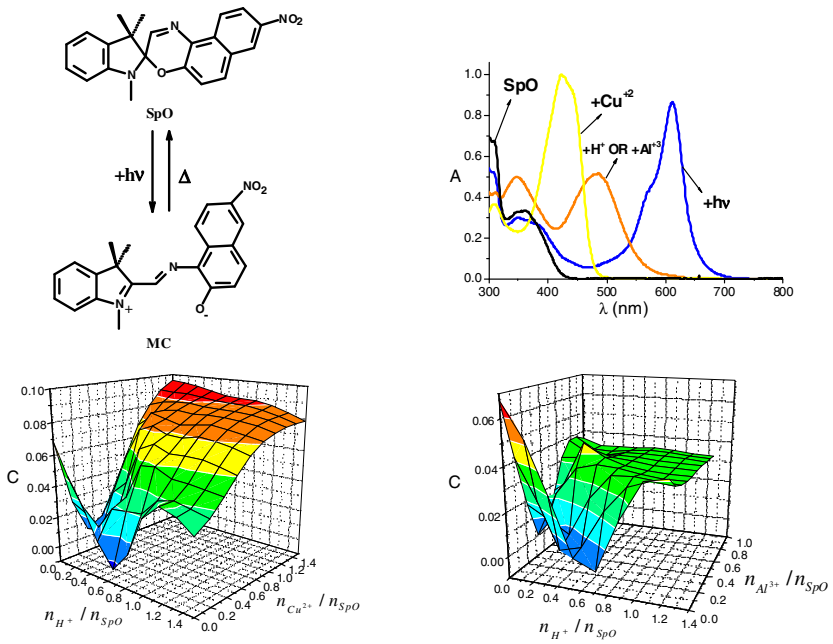


**Fig. 2.** Chromogenic properties of the spirooxazine SpO that under UV irradiation produces the merocyanine MC depicted in the upper left part. The absorption spectra recorded before any perturbation (black), after UV (blue), after UV and addition of $H^+$ or $Al^{3+}$ (orange), and after UV and addition of $Cu^{2+}$ (yellow) are shown in the upper right plot. The lower plots show the trend of C as function of the molar ratios $n_{H^+}/n_{SpO}$, $n_{Cu^{2+}}/n_{SpO}$ (on the left), and $n_{H^+}/n_{SpO}$, $n_{Al^{3+}}/n_{SpO}$ (on the right).

SpO is photochromic: under UV irradiation, it produces MC which is blue colored. It is also acidichromic: if it is UV irradiated in the presence of $H^+$ it gives rise to $MCH^+$ which is orange. The same orange is obtained in the presence of $Al^{3+}$, when the complex $Al^{3+}MC$ is produced. On the other hand, in the presence of $Cu^{2+}$, the solution becomes yellow when $Cu^{2+}MC$ is formed. The plot of C versus the molar ratios $n_{H^+}/n_{SpO}$, $n_{Cu^{2+}}/n_{SpO}$, and that of C versus $n_{H^+}/n_{SpO}$ and $n_{Al^{3+}}/n_{SpO}$ are shown in the lower part of Figure 2. They are nonlinear smooth functions [21] that can be exploited to build two Fuzzy Logic Systems. The shapes of the functions along with the partitions of the variables in fuzzy sets impose what fuzzy rules can be formulated. In particular, the asymmetric shape of C as function of $n_{H^+}/n_{SpO}$, $n_{Cu^{2+}}/n_{SpO}$ allows rules with the AND operator to be defined. On the other hand, the symmetric trend of C as function of $n_{H^+}/n_{SpO}$ and $n_{Al^{3+}}/n_{SpO}$ allows also rules with the OR operator to be formulated.

The second strategy to process Fuzzy logic at the molecular level may be explained by exploiting further chromogenic and computational properties of SpO. These may be unfolded using physical and chemical inputs different from UV radiation, $H^+$, $Al^{3+}$ and $Cu^{2+}$ ions. For instance, SpO has a Colorability that increases by reducing temperature [19]. In fact, the kinetic constant of the MC→SpO process ($k_\Delta$) decreases by cooling. Therefore, the photostationary concentration of MC may be higher at lower temperature (T). SpO has also the ability to distinguish an α-aminoacid $RCHNH_3^+COO^-$ with a small R group from one with a bulky R. The photomerocyanine MC interplays appreciably with glycine (where R is the tiny hydrogen atom), but not with tryptophan (where R is the large indole) [22, 19]. The supramolecular adduct between MC and glycine does not produce any spectral shift of the color band, but it exerts a "braking effect" on the bleaching kinetic constant of merocyanine and an increase in its Colorability [19]. Moreover, the analysis of the bleaching kinetics through the Maximum Entropy method [19] proves that merocyanine exists as a collection of many conformers. The properties of the conformational distribution, i.e. its broadness and shape, may be influenced by T and glycine. A high T produces a broad distribution of MC conformational substates. On the other hand, a high concentration of glycine shrinks the number of MC conformers because aminoacidic molecules duck only to few substates [19]. The set of conformers under which MC exists is actually fuzzy. Its characteristics are context dependent. The fuzziness or vagueness of the set of conformers may be featured by the measure of its fuzzy entropy, through equation (4):

$$H = -K\sum_{i=1}^{n}(\mu_i \log_{10}(\mu_i) + (1-\mu_i)\log_{10}(1-\mu_i)) \tag{4}$$

where K is a constant equal to 1/n [23] with n being the number of conformers, and $\mu_i$ is the relative weight of the i-th substate. Therefore, a compound such as MC does exist as a context-dependent ensemble of substates, each one reacting with its own kinetic constant. If we represent the absorption spectra of the chromogenic species as vectors in the space of the La*b* color coordinates, a cycle of coloration and bleaching for the photochromic SpO becomes a reversible rotation, shrinking and stretching of the vector accompanied by the production and erasure of fuzzy information [19].

This latter case shows that molecules actually process Fuzzy logic. A compound does not react with only one kinetic constant, but with as many $k_i$ as are the different conformers. The set of conformers is a fuzzy set whose characteristics are context dependent. A chemical reaction will correspond to an event of fuzzy information processing, which is ruled by the inter- and intramolecular forces. The Fuzziness of a chemical compound becomes particularly important when we consider macromolecules, like those we have in our cells, where we can have a huge number of conformational substates. The cellular processes should now be analyzed under this new point of view to appreciate the molecular language of living cells.

## 4 Excitable and Oscillatory Reactions as Prototypes of Artificial Neurons

The nonlinear dynamical properties of neurons in the brain can be imitated through particular chemical transformations such as the Belousov-Zhabotinsky (BZ) reaction, which, in the whole, is a catalytic oxidative bromination of malonic acid by bromate in acidic medium [5]:

$$2H^+ + 2BrO_3^- + 3CH_2(COOH)_2 \xrightarrow{cat.} 2BrCH(COOH)_2 + 4H_2O + 3CO_2 \qquad (5)$$

Various metal ions or metallo-complexes, for example cerious ions or ferroin (i.e. tris-(1,10-phenantroline)-iron(II)), can serve as the catalyst. Although the chemistry of the BZ reaction does not share anything with the chemistry involved in the workings of a neuron, the BZ reaction can reproduce the main neural dynamical behaviours. A neuron is an example of a very far-from-equilibrium system, which, in its phase space, can trace a limit cycle or stand on a stable stationary state. In the former case, the neuron will show periodic spiking, whereas in the latter, it will be resting unless a strong perturbation will promote a provisional shift away from the initial condition, corresponding to the release of an action potential. The same holds for the BZ reaction. When the BZ reaction is in oscillatory regime, it can be formally compared to the dynamical behaviour of pacemaker cells, i.e. neurons which spontaneously depolarize their axon hillock and fire action potentials, often at a regular rate. Although such natural oscillators have their own internal rhythm, external stimuli can alter their timing. In pacemaker cells, information about a stimulus is encoded by changes in the timing of individual action potentials, and it is used to rule proprioception and motor coordination for running, swimming, and flying. Similarly to neurons, the BZ reaction in oscillatory regime can be perturbed in its timing by both inhibitors and activators. The response of the system is phase dependent, where for phase of addition we mean the ratio $\varphi = \tau/T_0$: $\tau$ is the "time delay", i.e. the time since the most recent spike occurred, and $T_0$ is the period of the previous oscillations. The addition of $Br^-$ leads always to a delay in the appearance of a spike. In other words, $\Delta T = T_{pert} - T_0$ ($T_{pert}$ is the period of the perturbed oscillation) is always positive. The higher the phase of addition of $Br^-$, the larger the $\Delta T$. The addition of silver ions decreases the period because $Ag^+$ removes bromide, forming a AgBr precipitate. In other words, $Ag^+$ is an activator

unless it is injected in small quantities and at low phase, inducing a slight lengthening of the period of oscillations [24]. An analytic investigation of the dependences of $\Delta T$ on the volumes of the KBr and $AgNO_3$ solutions and their phase of addition, reveals that such relations are smooth and almost linear. Therefore, these relations are suitable to process fuzzy logic according to the first strategy described in the previous paragraph. Such possibility suggests that a real pacemaker cell could process fuzzy logic in much the same fashion as the BZ reaction does.

Since the amazing computational performances of our brain relies mainly on the emergent properties of neural networks, it is important to study the coupling between artificial neurons. In real neurons, signal transmission is typically unidirectional and takes place by discrete pulses of neurotransmitters at synapses. Therefore, the attention must be focused on pulse-coupled oscillators. When two ferroin-catalyzed BZ oscillators, operating in continuously fed stirred tank reactors (CSTRs), are pulse-coupled through symmetric, reciprocal release of either inhibitor or activator or mixed, and at variable time delay, many dynamical regimes can be obtained [25]. Such dynamical regimes are examples of temporal patterns. They are achievable for different combinations of effectors and different delay times of their release. These temporal patterns constitute the reasoning code for neurons and their nets, according to the neuroscience axiom that "neurons that fire together, wire together" [26]. The next step along this research path is to increase the number of coupled artificial neurons, study the emerging temporal patterns and see if fuzzy logic can ground on them.

## 5 Conclusion

The computational and algorithmic investigation of the human nervous system is unveiling important properties of Complexity that is rooted on hierarchical processing of Information. The analysis of the human nervous system at the implementation level is spurring the design of a new generation of computing machines imitating the performances of human intelligence. The new computing machines will be probably three-dimensional wetware containing encapsulated bistable reactions [5] playing like neurons. They will be encompassed by chromogenic and fluorogenic compounds [5] playing like sensory elements. The chromogenic and fluorogenic compounds will collect the external stimuli and they will encode them as fuzzy information. The communication inside the 3-D wetware will be based on light and photo/chemical waves. An intertwined system of fuzzy inference engine will allow to integrate granules of information and to compute with words and numbers. A success in the project of reverse engineering the nervous system will provide great benefits to solve the computational problems of variable patterns recognition.

## References

1. TOP500 Project, `http://www.top500.org`
2. de Castro, L.N.: Fundamentals of natural computing: an overview. Phys. of Life Rev. 4, 1–36 (2007)

3. Gallistel, C.R., King, A.: Memory and the computational brain: Why cognitive science will transform neuroscience. Blackwell/Wiley, New York (2009)
4. Marr, D.: Vision. A Computational Investigation into the Human Representation and Processing of Visual Information. The MIT Press (2010)
5. Gentili, P.L.: Small Steps towards the Development of Chemical Artificial Intelligent Systems. RSC Adv. 3, 25523–25549 (2013)
6. Gentili, P.L.: The Human Sensory System as a collection of specialized Fuzzifiers: a conceptual framework to inspire new Artificial Intelligent Systems computing with words. J. Intel. & Fuzzy Sys. (2014), doi:10.3233/IFS-141179
7. Zadeh, L.A.: A New Direction in AI. AI Magazine 22, 73–84 (2001)
8. Paxinos, G., Mai, J.K.: The Human Nervous System, 2nd edn. Elsevier (2004)
9. Mendel, J.M.: Fuzzy logic systems for engineering: a tutorial. Proc. IEEE 83(3), 345–377 (1995)
10. Van Horn, K.S.: Constructing a logic of plausible inference: a guide to Cox's theorem. Int. J. Approx. Reason. 34, 3–24 (2003)
11. De Finetti, B., Machi, A., Smith, A.: Theory of Probability: a Critical Introductory Treatment. Wiley, New York (1993)
12. Mach, E.: Contributions to the Analysis of the Sensations (C. M. Williams, Trans.). Open Court Publishing Co., Chicago (1980)
13. Knill, D.C., Pouget, A.: The Bayesian brain: the role of uncertainty in neural coding and computation. Trends Neur. 27(12), 712–719 (2004)
14. Coletti, G., Scozzafava, R.: Conditional probability, fuzzy sets, and possibility: a unifying view. Fuzzy Sets and Systems 144(1), 227–249 (2004)
15. Kersten, D., Mamassian, P., Yuille, A.: Object Perception as Bayesian Inference. Annu. Rev. Psychol. 55, 271–304 (2004)
16. Kåhre, J.: The Mathematical Theory of Information. Kluwer Academic Publishers, Norwell (2002)
17. Stein, B.E., Meredith, M.A.: The merging of the senses. MIT Press, Cambridge (1993)
18. Driver, J., Spense, C.: Multisensory perception: beyond modularity and convergence. Curr. Biol. 10, R731–R735 (2000)
19. Gentili, P.L.: The fuzziness of a chromogenic spirooxazine. Dyes and Pigments 110, 235–248 (2014)
20. Gentili, P.L.: The fundamental Fuzzy logic operators and some complex Boolean logic circuits implemented by the chromogenism of a spirooxazine. Phys. Chem. Chem. Phys. 13, 20335–20344 (2011)
21. Gentili, P.L.: Molecular Processors: From Qubits to Fuzzy Logic. ChemPhysChem. 12, 739–745 (2011)
22. Gentili, P.L., Ortica, F., Favaro, G.: Supramolecular interaction of a spirooxazine with amino acids. Chem. Phys. Lett. 444, 135–139 (2007)
23. Al-sharhan, S., Karray, F., Gueaieb, W., Basir, O.: Fuzzy entropy: a brief survey. In: IEEE International Fuzzy Systems Conference, pp. 1135–1139 (2001)
24. Gentili, P.L., Horvath, V., Vanag, V.K., Epstein, I.R.: Belousov-Zhabotinsky "chemical neuron" as a binary and fuzzy logic processor. Int. Journ. of Unconventional Computing 8, 177–192 (2012)
25. Horvath, V., Gentili, P.L., Vanag, V.K., Epstein, I.R.: Pulse-Coupled Chemical Oscillators with Time Delay. Angew. Chem. Int. Ed. 51, 6878–6881 (2012)
26. Rabinovich, M.I., Varona, P., Selverston, A.I., Abardanel, H.D.I.: Dynamical Principles in Neuroscience. Rev. Mod. Phys. 78, 1213–1265 (2006)

# Weak Sensitivity to Initial Conditions for Generating Temporal Patterns in Recurrent Neural Networks: A Reservoir Computing Approach

Hiromichi Suetani

Department of Physics and Astronomy, Kagoshima University,
Kagoshima 890-0065, Japan

**Abstract.** A function for generating temporal patterns such as melody of the music and motor commands for body movements is one of major roles in the brain. In this paper, we study how such temporal patterns can be generated from nonlinear dynamics of recurrent neural networks (RNNs) and clarify the hidden mechanism that supports the functional ability of RNNs from reservoir computing (RC) approach. We show that when the reservoir (random recurrent neural network) shows weak instability to initial conditions, the error of the output from the reservoir and the target pattern is sufficiently small and robust to noise. It is also shown that the output from the spontaneous activity of the trained system intermittently exhibits response-like activity to the trigger input, which may be related to recent experimental findings in the neuroscience.

## 1 Introduction

A function for generating temporal patterns is one of major roles in the central nervous system (CNS) ranging from melodies of music to sequences of commands for the body movements such speech and hand-writing of letters. On the other hand, it has been identified that there is a rich variety of nonlinear dynamics ubiquitously in the brain from the single neural cell to the cortex[1]. Therefore, a question how generations of functional patterns can be understood in terms of nonlinear dynamics is very important from the viewpoint of neuroscience.

In real biological brains, asymmetry is more plausible than symmetry as a way of connectivity among neurons in networks, and it has been also known that asymmetrical recurrent neural networks exhibit chaotic dynamics[2] whereas symmetrical networks such as Hopfield network only yielding fixed point attractors.

Recently, random recurrent neural networks (RNNs) have attracted considerable attentions under the name of "reservoir computing" (RC) paradigm[3,4]. In the framework of RC, connectivity matrices within a RNN and from the input to the RNN are given at first and they do not change with time, only the connectivity from the RNN to readout neurons is updated so as to minimize, for example, the root-mean-squared error between the output from the neural network and a given target (supervised) signal. Here, RC basically learns the input-ouput relationship, i.e., a static nonlinear function from the input to the output, so it is required that the dynamics in the RNN is "echo state", i.e., the state of the RNN is activated by the injection of the input first (echo of the



A. Sanayei et al. (eds.), *ISCS 2014: Interdisciplinary Symposium on Complex Systems*,
Emergence, Complexity and Computation 14, DOI: 10.1007/978-3-319-10759-2_6

input in the RNN), then going to the static state, so that there is a deterministic function between the shape of the wave in the RNN and that of the input signal. Furthermore, a significant progress has been done by Sussillo and Abbott. In their paper[5], they proposed an online learning extension RCs, called FORCE learning, and they explores that not relaxation dynamics but sustained chaotic activity in RNNs plays a constructive role for generating temporal patterns.

In this paper, we study how the performance of temporal pattern generations depends on parameters that determine the dynamical properties of RNNs and clarify the hidden mechanism supporting the functional ability of RNNs based on the RC paradigm. We show that when the reservoir shows "weak" instability to initial conditions, the error of the output from the reservoir and the target pattern is sufficiently small and robust to noise. It is also shown that the output from the spontaneous activity of the trained system intermittently exhibits response-like activity to the trigger input, which may be related to recent experimental findings in the neuroscience.

## 2 Model and Method

First, we introduce the architecture of a model used in this study. We consider the following system consisting of a continuous-time RNN (called a "reservoir") with $M$ input units, $N$ internal units, and $L$ readout units defined as

$$\tau \dot{x}_n(t) = -x_n(t) + g \sum_{n'=1}^{N} w^{\mathrm{rec}}_{nn'} \tanh(x_{n'}(t)) + \sum_{m=1}^{M} w^{\mathrm{in}}_{nm} u_m(t) + \sum_{l=1}^{L} w^{\mathrm{fb}}_{nl} z_l(t) + b_n, \ n = 1, ..., N, \tag{1}$$

(see Fig. 1) . Here, $x_n$ is the state variable of the $n$-th internal unit, $u_m$ is that of the $m$-th input unit, $g$ is the parameter of gain control from other units, and $\gamma$ is the parameter determining the characteristic time-scale of dynamics. Also, as readout units, we consider the following linear projection defined as

$$z_l(t) = \sum_{n=1}^{N} w^{\mathrm{out}}_{ln} \tanh(x_n(t)), \ l = 1, ..., L, \tag{2}$$

where $z_l$ is the state variable of the $l$-th readout unit. The connection weights are given in a $N \times N$ matrix $\boldsymbol{W}^{\mathrm{rec}} = (w^{\mathrm{rec}}_{nn'})$ for connections between the internal units, a $N \times M$ matrix $\boldsymbol{W}^{\mathrm{in}} = (w^{\mathrm{in}}_{nm})$ for those between the input and the internal units, a $N \times L$ matrix $\boldsymbol{W}^{\mathrm{fb}} = (w^{\mathrm{fb}}_{nl})$ for a feedback from the readout to the internal units, and a $L \times N$ matrix $\boldsymbol{W}^{\mathrm{out}} = (w^{\mathrm{out}}_{ln})$ for those between the internal and the readout units. The term $b_n$ denotes bias of the $n$-th internal unit and is given by a Gaussian random number obeying $\mathcal{N}(0, 10^{-3})$

In the framework of RC, the matrices $\boldsymbol{W}^{\mathrm{rec}}$, $\boldsymbol{W}^{\mathrm{in}}$, and $\boldsymbol{W}^{\mathrm{fb}}$ are given at first and do not change with time, only the readout matrix $\boldsymbol{W}^{\mathrm{out}}$ is updated so as to minimize, for example, the root-mean-squared error between the output $\boldsymbol{z}(t)$ from the neural network

and the target (supervised) signal $z^{\text{target}}(t)$. In FORCE learning[5], synaptic weights in $\boldsymbol{W}^{\text{out}}$ are updated in an online way using, e.g., the recursive least squares (RLS) method. We also use RLS in this paper. It is supposed here that the matrix $\boldsymbol{W}^{\text{rec}}$ is a sparse one, i.e., the probability of the existence of connection between two units is $p = 0.1$, and its intensity obeys Gaussian distribution as $w^{\text{rec}}_{nn'} \sim (g/\sqrt{N})\mathcal{N}(0,1)$ if there is a connection between the $n$ and the $n'$-th units. Also, elements in $\boldsymbol{W}^{\text{in}}$ and $\boldsymbol{W}^{\text{fb}}$ are supposed to obey the uniform distribution as $w^{\text{in}}_{nm} \sim \mathcal{U}(-0.75, 0.75)$ and $w^{\text{fb}}_{nl} \sim \mathcal{U}(-0.5a^{\text{fb}}, 0.5a^{\text{fb}})$, respectively. The values of $g$ and $a^{\text{fb}}$ are varied in the following as the control parameters, and other parameters are set to $\tau = 10$ [msec] of the characteristic time scale of the reservoir, $N = 10^3$ units in the reservoir, and $M = 1$ input channel.

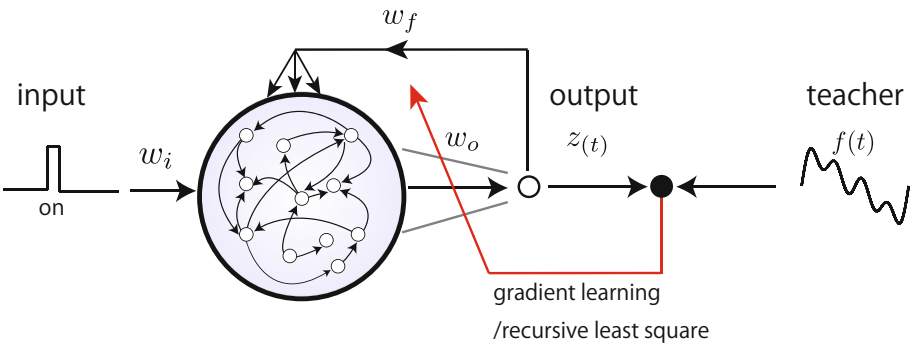


**Fig. 1.** Schematic plot of the reservoir network employed in this paper

The purpose of this network system now is to generate an output signal $z(t)$ close to a target signal $f(t)$ as possible as one can with precise timing. Here, the system is stimulated by a pulse with the duration $\Delta T = 50$[msec] as the input trigger in order to train the network to generate the desired output at this timing. And, this network system is trained from the beginning of the trigger stimulus followed by the presentation of the target signal $f(t)$. We repeat this process(called an "episode") up to $10^2$ times, then we check whether the desired temporal pattern can be generated by giving a trigger pulse to the trained network. In particular, we focus on how the performance of learning depends on the parameters of the system such as the nonlinear gain $g$ and the feedback strength $a^{\text{fb}}$, and what kinds of dynamical properties supporting the performance.

## 3 Numerical Simulations and Results

As a demonstration, we consider a linear combination of sinusoidal signals (i.e., $L = 1$ in Eqs. (1) and (2) ) $f(t)$, shown in Fig. 2(a), as the target pattern. Figure 2(b) shows the outputs $z(t)$ of the system after training for the parameters $g = 1.3$ and $a^{\text{fb}} = 0.5$. In training process, we add small Gaussian white noise with the standard deviation $\sigma_1 = 10^{-4}$, as well as noise with $\sigma_2 = 10^{-2}$ in generating process. Here, time series depicted in different colors indicate different trials (trajectories starting from different

initial conditions) and a short trigger pulse is given at $t = 10^3$ [msec] for each trial. We can see that the RNN can generate the temporal patterns which are very similar to the target $f(t)$ over trials starting from different initial conditions. Then, after generating the desired pattern, the system goes back to chaotic state again.

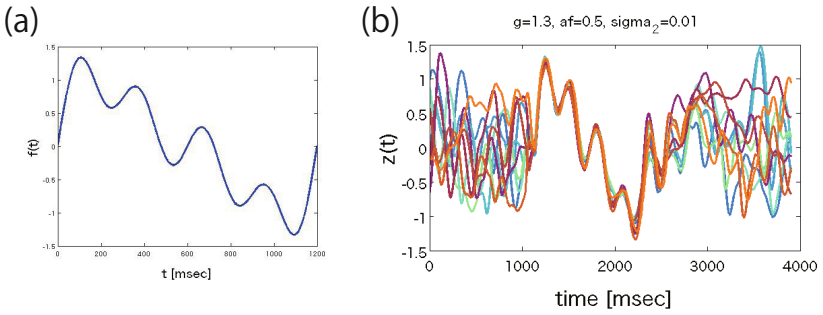


**Fig. 2.** (a) Target signal $f(t)$ and (b) outputs $z(t)$ from the trained network for several different trials (initial conditions). Time series in different colors indicate different trials. Gaussian white noise with the standard deviation $\sigma = 10^{-2}$ is injected to the system.

A success of learning is shown in Fig. 2 (b), but the performance depends on the choice of parameters of the system. Figure 3(a) shows the outputs $z(t)$ of the system after training for three different values of $g$ ($a^{\mathrm{fb}}$ is set to 0.5). In Ref.[2], it is said that a reservoir recurrent network in Eq. (1) exhibits chaos for $g > 1$, so the results in Fig. 3(a) indicate that neither "no"-chaos and "strong"-chaos in the inside RNN can generate the desired pattern nor even have reproducibility over different trials. We note here that the existence of noise and the feedback term yields sustained oscillatory behaviors in the case of $g < 1$ after training. Figure 3(b) also shows the outputs $z(t)$ of the system after training for three different values of $a^{\mathrm{fb}}$ ($g$ is set to 1.3). We can see that the feedback term induces the reproducibility of the output.

Figure 4 shows the performance of the system as a function of $g$ for three different noise strength $\sigma_2$ in generation process. Here the "performance" means the average of the root-mean-squared error between the output $z(t)$ from the RNN and the target $f(t)$ over different trials, defined as

$$E(z, f) = \langle \sqrt{\frac{1}{T}\int_0^T (z(t) - f(t))^2 \mathrm{d}t} \rangle, \tag{3}$$

where $T = 1.2$ [sec] (the length of the target signal) and the average $\langle \cdots \rangle$ is taken over $10^2$ different trials. In the noiseless case ($\sigma_2 = 0$), the reservoir can generate the desired pattern successfully even for $g \sim 1$. It is, however, seen that the error becomes quite large for the larger noise ($\sigma_2 = 10^{-2}$) for $g \sim 1$, i.e., susceptible to noise for coherent generation of the pattern. On the other hand, the error grows rapidly for $g > 1.4$ for all noise cases. There is an optimal value of $g$ around at $g = 1.2$ which keeps the error sufficiently small and robust to noise.

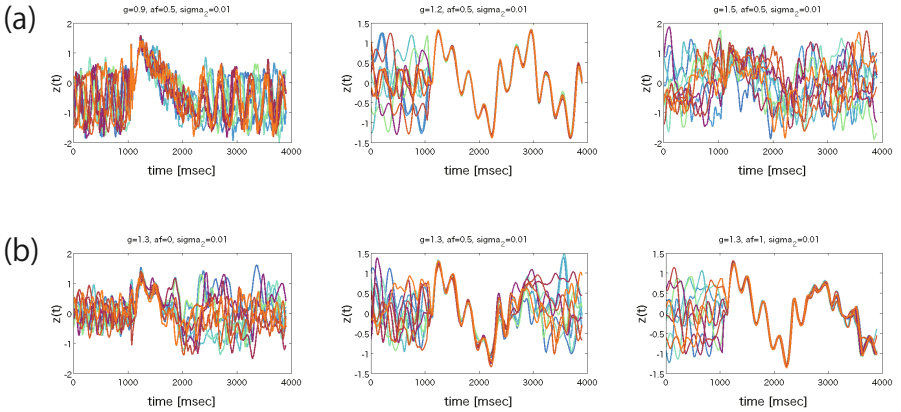


**Fig. 3.** (a) Outputs $z(t)$ from the trained network for several different trials and for three different values of $g = 0.9, 1.2$ and $1.5$ ($a^{\mathrm{fb}}$ is set to 0.5). (a) Outputs $z(t)$ from the trained network for several different trials and for three different values of $a^{\mathrm{fb}} = 0, 0.5$ and $1.0$ ($g$ is set to 1.3).

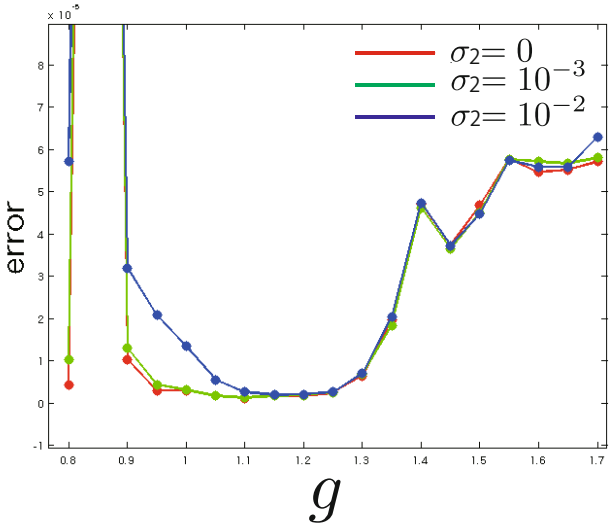


**Fig. 4.** The averaged error $E(z, f)$ vs. the nonlinear gain $g$ for three different noise cases. $a^{\mathrm{fb}} = 0.5$. The number of $10^2$ trials is used for taking the average for each parameter case.

Furthermore, we investigate how the performance depends on the feedback term. Figure 5(a) shows that the norm of the readout matrix (or vector if the target signal is scalar) $\|\boldsymbol{W}^{\mathrm{out}}\|$ as a function of the number of episodes in training process for three different values of $a^{\mathrm{fb}}$. The norm $\|\boldsymbol{W}^{\mathrm{out}}\|$ converges to stationary state after sufficient trainings, and the value for the no-feedback case ($a^{\mathrm{fb}} = 0$) is quite large compared to other cases ($a^{\mathrm{fb}} = 0.5$ and $1.0$). This result indicates that the frequency that coefficients

in $\boldsymbol{W}^{\text{out}}$ for $a^{\text{fb}} = 0$ take both large positive and negative values is high compared to those for the cases of $a^{\text{fb}} = 0.5$ and 1.0 because the amplitude of the output $z(t)$ is same order for all three cases, which causes a susceptibility to noise. Figure 5(b) shows the error averaged over $10^2$ trials against the strength $a^{\text{fb}}$ t of the feedback term. We see that the existence of the feedback actually reduces the error. But, we also note that too strong feedback may also induce the instability to the system so the performance decreases in such a case.

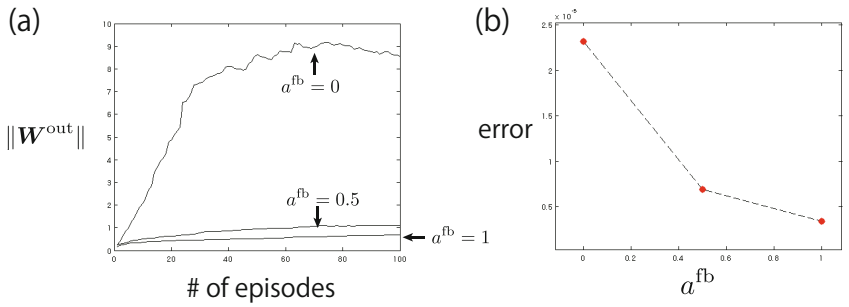


**Fig. 5.** Effects of the feedback term. (a) the norm $\|\boldsymbol{W}^{\text{out}}\|$ vs. the number of episodes for three different values of $a^{\text{fb}}$ and (b) the averaged error vs. $a^{\text{fb}}$.

Now, we turn our interests to a problem what kinds of dynamical properties determine the "optimality" of the performance ($g \sim 1.2$ in the current case). In order to explore this problem, we first investigate how a cloud of points (each point corresponds to a single trial) on the attractor of the reservoir is condensed by the trigger pulse input. Figure 6 shows the time evolution of the "volume" $\rho$ of the cloud of points after

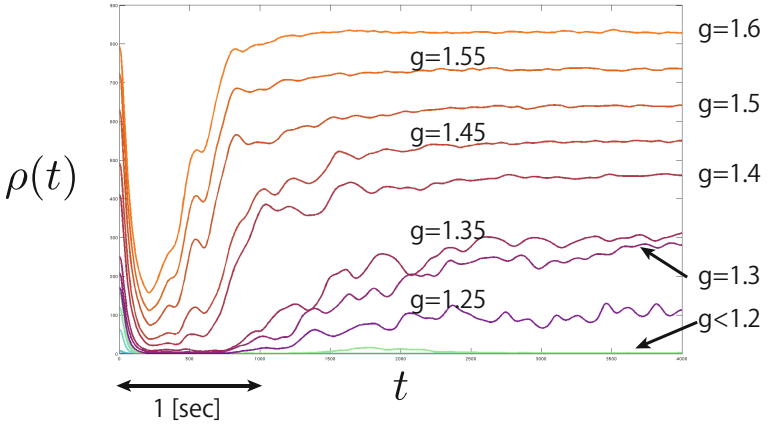


**Fig. 6.** Time evolution of the volume $\rho$ of the reservoir for several different values of $g$

injecting the trigger pulse input at time $t = 0$ for several different values of $g$. Here, the volume $\rho(t)$ at time $t$ is determined as

$$\rho(t) = \sum_{j=1}^{N} \lambda_j(t), \tag{4}$$

where $\lambda_j(t)$ is the $j$-th eigenvalue of principle component analysis (PCA) at time $t$. We prepare $J = 10^3$ different initial points and evolve these points under the time evolution law Eq. (1) for $\boldsymbol{W}^{\text{out}} = 0$ (i.e., there is no feedback) to perform PCA and calculate $\rho(t)$ at each time step. In Fig. 6, first the volume $\rho(t)$ decreases rapidly for all cases, which indicates that the reduction of the sensitivity to initial conditions is induced by the trigger pulse input. After such process, the volume $\rho(t)$ increases rapidly again and converges to the initial volumes $\rho(0)$ with time for $g > 1.4$ due to the existence of chaotic nature of the reservoir. Remarkably, however, $\rho(t)$ does not recover to $\rho(0)$ for $g < 1.2$, this fact means that the reservoir "remembers" the trigger input for long time. For $1.25 \leq g \leq 1.35$, $\rho(t)$ seems recover to $\rho(0)$, but their relaxations are slow.

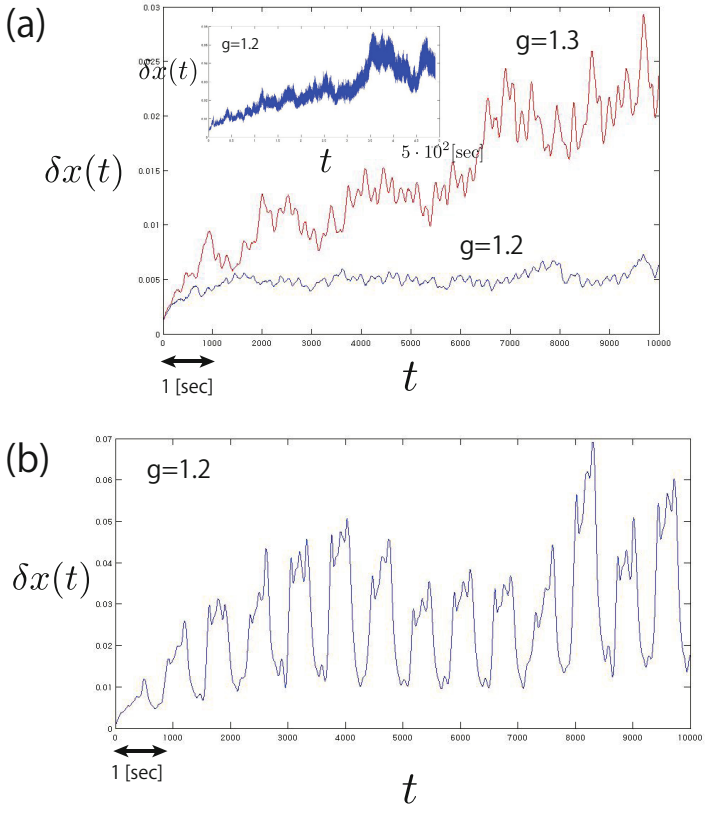


**Fig. 7.** Growth of the error of initial conditions (a) before training and (b) after training

Therefore, we also investigate temporal change of the initial error $\delta x(t)$ of the reservoir for longer time periods. Figure 7(a) shows the error growth $\delta x(t)$ of the initial conditions for the reservoir, which is averaged over $J = 10^2$ trials up to 10 seconds. The value of $\delta x(t)$ seems fluctuate around some constant for $g = 1.2$ whereas the error increases with time for $g = 1.3$. But, for more longer time scale, up to $5 \times 10^2$ seconds, the error $\delta x(t)$ grows with fluctuation even for $g = 1.2$ as shown in the inside figure of Fig. 7 (a). Although we have not clarified whether this sensitivity initial conditions exhibits power-law behavior[6] or not, this result suggests that there is "weak" sensitivity to initial conditions for $g = 1.2$ yielding optimal performance for generating temporal patterns. Figure 7(b) also shows the error growth $\delta x(t)$ of the initial conditions for the system after training, i.e., the system also includes the feedback term that reflects the effect of training. Here, we can see that there are large fluctuations, divergence or convergence of the error growth, which reflects the existence of a coherent object associated with the target pattern $f(t)$ is embedded in the state space.

Finally, we compare between responses to the trigger input and "spontaneous activity" (no input signal) of the trained system. Figure 8 shows such a comparison. There is a remarkable finding that a time-delay embedding of the spontaneous activity (Fig. 8(b)) is very similar to that of responses to the trigger input (Fig. 8(a), here different colors indicates different trials). This result suggests that the system sometimes "recalls" the target pattern even if there is no trigger input to the system. Figure 8(c) shows the time series of $z(t)$ in the case the spontaneous activity. Actually, there is a resonant-like behavior, i.e., there is intermittent traces of the target pattern with a few cycles.

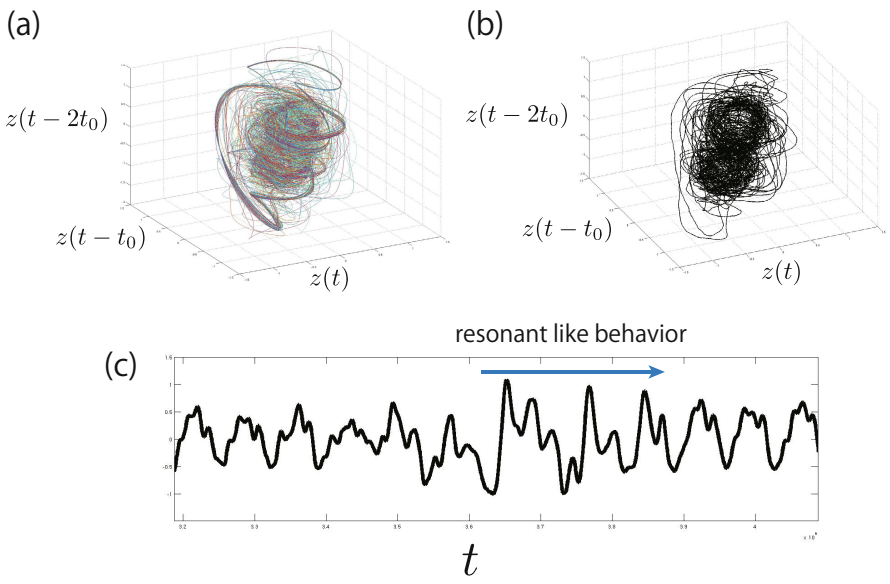


**Fig. 8.** Comparison between (a) response to the trigger pulse (different colors indicate different trials) and (b) spontaneous activity of the output $z(t)$ in the time-delay embedding space. (c) Time series of the output $z(t)$ in the case of spontaneous activity.

## 4 Conclusion

In conclusion, we have investigated a problem about generation of coherent temporal patterns using nonlinear dynamics of recurrent neural networks based on the reservoir computing approach. In this study, we considered a situation that a short pulse is employed to reset trajectories to a "pseudo" stable fixed point and the transient dynamics starting from this fixed point-like state is harnessed so that the corresponding readout pattern $z(t)$ trace the target pattern $f(t)$ by FORCE learning. For an example of the target pattern, we found that there is an optimal value of $g$ where the error of the output from the reservoir and the target pattern is sufficiently small and robust to noise. Here, weak instability to initial conditions of the reservoir is important. We do not show results against other examples of the target pattern, but similar optimality is obtained if the length and characteristic time-scale of the target patterns are same as those used in this paper. We also showed that the output from the spontaneous activity of the trained system intermittently exhibits response-like activity to the trigger input. This finding may relate to experimental observations by Arieli et al.[7] and Kenet et al.[8]

**Acknowledgements.** This study is supported by "Decoding and Controlling Brain Information", PRESTO, JST, Japan. We thank M. Kawato (Supervisor of the project) for supporting. MATLAB codes for numerical simulations in this paper are based on preliminary ones prepared by D. Rodriguez. We thank him for preparations to start this study. We also thank I. Tsuda, Y. Yamaguchi, S. Kuroda, Y. Katori, T. Leleu, and K. Aihara for fruitful discussions and comments.

## References

1. Tsuda, I.: Behavioral and Brain Sciences 24, 793–810 (2001)
2. Sompolinsky, H., Crisanti, A., Sommers, H.J.: Phys. Rev. Lett. 61, 259 (1988)
3. Maas, W., Natschläger, T., Markam, H.: Neural Comp. 14, 2351 (2002)
4. Jaeger, H., Haas, H.: Science 304, 78 (2004)
5. Sussillo, D., Abbott, L.F.: Neuron 63, 544 (2009)
6. Costa, U.M.S., Lyra, M.L., Plastino, A.R., Tsallis, C.: Phys. Rev. E 56, 245 (1997)
7. Arieli, A., Sterkin, A., Grinvald, A., Aertsen, A.: Science 273, 1868 (1996)
8. Kenet, T., Bibitchko, D., Tsodyks, M., Grinvald, A., Arieli, A.: Nature 425, 954 (2003)

# Synchronization and Control in Modular Networks of Spiking Neurons

Oleg V. Maslennikov*, Dmitry V. Kasatkin, and Vladimir I. Nekorkin

Institute of Applied Physics of the Russian Academy of Sciences,
Nizhny Novgorod, Russia
{olmaov,kasatkin,vnekorkin}@neuron.appl.sci-nnov.ru

**Abstract.** In this paper, we consider the dynamics of two types of modular neural networks. The first network consists of two modules of non-interacting neurons while each neuron inhibits all the neurons of an opposite module. We explain the mechanism for emergence of anti-phase group bursts in the network and showed that the collective behavior underlies a regular response of the system to external pulse stimulation. The networks of the second type contain modules with complex topology which are connected by relatively sparse excitatory delayed coupling. We found a dual role of the inter-module coupling delay in the collective network dynamics. First, with increasing time delay, in-phase and anti-phase regimes, where individual spikes form rhythmic modular burst-like oscillations, alternate with each other. Second, the average frequency of the collective oscillations in each of these regimes decreases with increasing inter-module coupling delay.

**Keywords:** Complex networks, nonlinear dynamics, neurodynamics, synchronization, delayed coupling, maps.

## 1 Introduction

Many natural systems, including biological ones, are generally organized as complex networks consisting of several modules (or groups, populations)—sets of somehow grouped elements [1–3]. There are several features characterizing such modular networks. First, each module can often be considered as a unit which operates and functions as a whole. Second, the distance between modules sometimes results in a coupling delay which in turn influences the network dynamics. Third, the connectivity in modular networks is frequently organized in such a way that inter-module connections are sparser than intra-module ones. In this paper, we consider two types of modular networks representing important neural systems. In the first case the network consists of two modules coupled by inhibitory connections while the neurons within the modules are not connected. Such network models an essential part of so-called half-center oscillators—common circuits of central pattern generators responsible for production and control of rhythmic

* Corresponding author.



A. Sanayei et al. (eds.), *ISCS 2014: Interdisciplinary Symposium on Complex Systems*,
Emergence, Complexity and Computation 14, DOI: 10.1007/978-3-319-10759-2_7

motor activity in animals. The second network consists of two modules connected by excitatory links with delay and each module is a subnetwork with complex topology. Such a configuration reproduces main properties of local cortical structures or in vitro neuronal cultures. In all cases a neuron is modeled by a discrete-time two-dimensional system which generates irregular spiking activity, and a coherent collective behavior emerges in the network due to the interplay between connectivity and the individual oscillations.

## 2 Map-Based Model of Neural Activity

In the study we use a dynamical map model with stochastic perturbations in which an isolated neuron exhibits occasional spikes at random moments of time. The dynamics of a neuron is described by the following two-dimensional discrete-time model [4–6]:

$$\begin{cases} x_{n+1} = x_n + F(x_n) - \beta H(x_n - d) - y_n + I_n^{syn}, \\ y_{n+1} = y_n + \varepsilon(x_n - J). \end{cases} \tag{1}$$

where $x$ mimics the qualitative behavior of the neural membrane potential and $y$ models the effects of relatively slow ionic currents governing the transient behavior of the neuron. The nonlinear functions $F(x)$ and $H(x)$ are written

$$F(x) = x(x-a)(1-x), \tag{2}$$

$$H(x) = \begin{cases} 1, & x \geq 0, \\ 0, & x < 0. \end{cases} \tag{3}$$

where $0 < a < 1$. The parameters $\beta$ and $d$ control the shape of bursting oscillations, $\varepsilon$ is a time scale for $y$, and $J$ defines neural excitability. For $J < J_{min}$, where $J_{min} = (1 + a - (1 - a + a^2)^{1/2})/3$ and the function $F(x)$ has a minimum at $x = J_{min}$ [Fig. 1a], the neuron is in a resting state (excitable regime). In contrast, for $J > J_{min}$ the neuron generates spike sequences and the larger $J$ is, the more spikes in a sequence. The phase portrait of the typical dynamics generated by the model is shown in Fig. 1a. Note that the neurons within the networks differ by the value of $J$ so they have different average spiking frequencies. Waveforms with two different excitation levels are shown in Fig. 1b and 1c. Coupling between the neurons is modeled using the input synaptic current as defined by

$$I_n^{syn} = -g_n(x_n^{post} - \nu), \tag{4}$$

where $g$ is the synaptic conductance, $x^{post}$ is the membrane potential of the post-synaptic neuron, and $\nu$ is the reversal potential. The dynamics of the synaptic conductance $g$ is triggered by a presynaptic spike and relaxes in accordance with the dynamics of the following one-dimensional map:

$$g_{n+1} = \gamma g_n + (1 - \gamma) g_{max} H(x_n^{pre} - \theta). \tag{5}$$

Here $\gamma$ $(0 < \gamma < 1)$ defines a relaxation rate for the conductance, $g_{max}$ is a maximum synaptic conductance, $\theta$ is a threshold parameter.

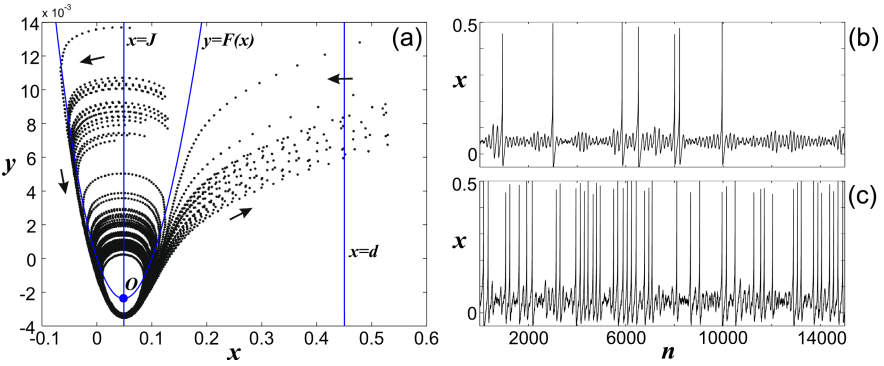


**Fig. 1.** Phase portrait of the map (1) for $a = 0.1$, $\varepsilon = 10^{-4}$, $\beta = 0.5$, $d = 0.4$, $J = 0.04$, with small additive Gaussian noise. (b,c) Waveforms of the map (1) for different excitation levels (b) $J = 0.04$ and (c) $J = 0.044$.

## 3 Modular Network with Inhibitory Coupling

The onset of switching activity in groups of reciprocally coupled populations of neurons is a typical element of many central pattern generators responsible for production and control of rhythmic motor activity in animals. A rather common circuit found in many central pattern generators networks is a half-center oscillator that acts as a core of rhythm generation and control. Many half-center oscillators are formed by two neurons or two groups of neurons linked together by a reciprocal inhibition. Such simple networks play an important role in the control of motor activity patterns such as walking, flying, and swimming. In this section we study the dynamical properties of half-center oscillators in the populations of reciprocally inhibiting neurons. We focus on the case of intrinsically not bursting neurons in which the onset of switching anti-phase oscillations is supported by the effect of post-inhibitory rebound. The neurons within each group do not interact with each other; however, each neuron in one group inhibits all neurons in the other group. Consider the network of two neuron populations schematically shown in Fig. 2. In our example each group contains 100 uncoupled

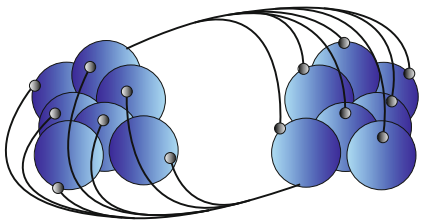

**Fig. 2.** Modular network in the form of two groups of neurons inhibiting each other. For simplicity, synaptic links from only one presynaptic neuron in each module is shown.

neurons and each neuron inhibits all the elements from the other group [7]. First we consider the collective dynamics of the network operating autonomously. Due to the intergroup coupling, irregular action potentials of one group arise in time intervals that do not overlap with those of another group, causing the alternation of group activities. Therefore, the waveforms of the average activities of the two groups are anti-phase bursts. It should be noted that an increase of the value of $J_{mean}$ leads to an increase of the bursting period. To study how the excitability level of the network and the strength of inhibitory coupling affect the parameters of collective activity, we have calculated spectrograms of group bursting oscillations for different $J_{mean}$ and $g_{max}$. We set the sampling frequency equal to 500. Some results are illustrated in Figs. 3a and 3b, which correspond to two different values of the coupling strength $g_{max}$. One can clearly see that there is a threshold value of $J_{mean}$ corresponding to the emergence of bursting activity. This threshold level decreases as the value of $g_{max}$ increases. Another property of these oscillations is that the average bursting frequency decreases with an increase of the excitation level of the network, $J_{mean}$. One of the most important elements in capturing the behavior of central pattern generators is the dynamics of its response to the external sensory or control stimulus. In the case of the half-center oscillator, this dynamics is related to the phase reset properties. Considering the effects of phase reset in the network, we apply a short stimulus with $A = -0.01$ and $\triangle T = 20ms$ to all the elements in one group and examine the phase of new bursting oscillations after the transient is complete. Figure 4a shows that the network responds differently depending on the network state when it receives a stimulus. There are some moments (during the active phase of bursts) when the stimulus hardly disturbs the network oscillations; however, there are moments (during the passive phase of bursts) when the stimulus can lead to a significant phase shift. To quantify this property we plotted the phase resetting curve shown in Fig. 4b. An interesting question that we address in this study is how the model of such a large network of reciprocally inhibiting groups of neurons can be replaced with a pair of reciprocally inhibiting units. Further, we ask whether the units in the pair have parameters similar to the neurons in

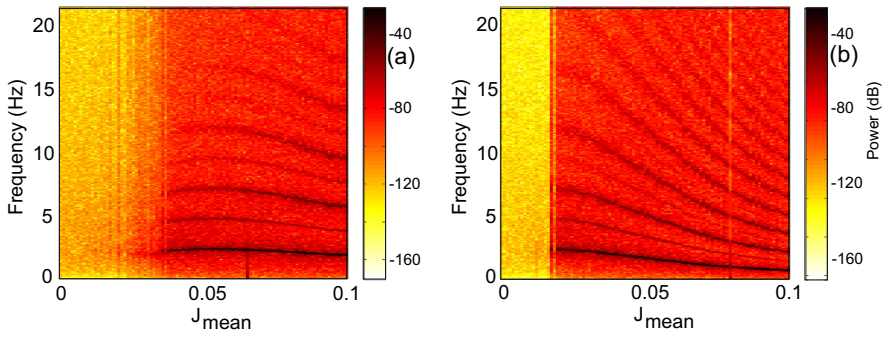


**Fig. 3.** Spectrograms of group bursting for (a) $g_{max} = 10^{-3}$, (b) $g_{max} = 5 \times 10^{-3}$, $\sigma_J = 10^{-2}$

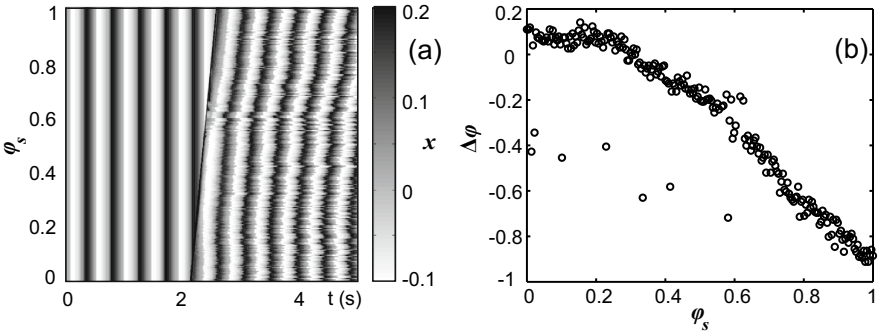


**Fig. 4.** (a) Phase reset in two reciprocally inhibiting groups. Average activity of one group is shown for different moments of stimulation. (b) Corresponding phase resetting curve.

the group. The simulations show that there are no such pronounced oscillatory properties in a pair of spiking neurons mutually inhibiting each other as in the network of two groups. The neurons that produce a robust rhythm of bursting operating in networks generate irregular bursts with fluctuating duration operating in the case of a reduced network model. We argue that it is reasonable to consider two mutually inhibiting units with spike-bursting behavior that is observed in the group average activity. To replicate this regime, we choose values of $\beta$ and $d$ in such a way that each unit generates a sequence of spikes. By tuning other parameters one can obtain the similar dynamical properties in the reduced model as in the network model. This allows us to reveal the dynamical mechanisms of emergence of anti-phase bursting and the phase reset in the interacting groups.

## 4 Modular Networks with Excitatory Delayed Coupling

In this section we consider a modular network where intra-module coupling is instantaneous while the elements of different modules interact with time delay [8]. Schematically the examples of modular networks are shown in Fig. 5. Such models reflect the property of cortical networks that are spatially remote from each other and thus they interact with time delay. As a module, we use complex networks with three different topologies—a random Erdös-Rényi network (Fig. 5a), a small-world Watts-Strogatz network (Fig. 5b), and a scale-free Barabási-Albert network (Fig. 5c)—each of them more or less reproduces structure properties of real neural networks. The interaction between the modules is performed by relatively sparse connections with time delay. For the intra-module topologies indicated we show that with increasing time delay, in-phase and anti-phase regimes of modular synchronization alternate with each other. Moreover, with increasing time delay the network oscillations change their frequency, namely, within every delay interval corresponding to a certain synchronization regime the frequency decreases on the average. Also we study how the collective activity is

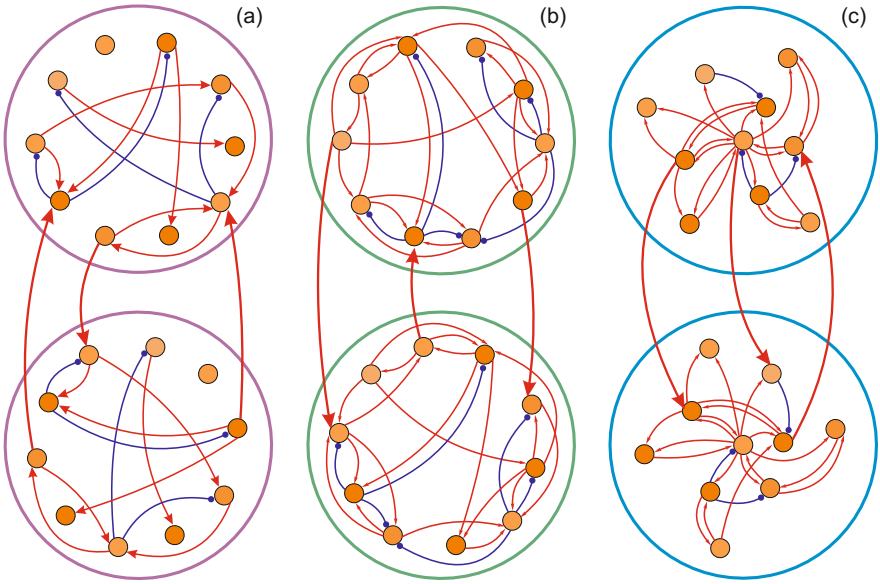


**Fig. 5.** Schematic structure of a modular network consisting of two interacting subnetworks. The nodes within each module are coupled by directed links into a network with a certain topology: (a) a random Erdös–Rényi network, (b) a small-world Watts–Strogatz network, and (c) a scalefree Barabási–Albert network. Intermodule interaction is organized by a relatively small number of random excitatory connections.

influenced by the inter-module coupling strength and the average spike rate of individual neurons. Consider a network which is constituted by two interacting subnetworks-modules schematically shown in Fig. 5. Each module consists of $N = 100$ active nodes coupled with each other by directed links which model the chemical synapses. Following the experimental observations, we set 80% of the total number of neurons sending excitatory connections while the rest 20% neurons—inhibitory. We consider three different algorithms for generating an intra-module connection topology: a random Erdös-Rényi network, a small-world Watts-Strogatz network and a scale-free Barabási-Albert network, in every case with directed links. The connections between the modules are random and relatively sparse: 5% of nodes in one module send directed excitatory links to random nodes of another module (note that the nodes are chosen from those 80% which send excitatory connections inside their module they belong to). We analyze the influence of network modularity on the collective dynamics so we are mainly interested in a role of the parameters of inter-module interaction: the coupling strength and delay. The parameters of intra-module coupling and individual dynamics are chosen in such a way that each module separately displays incoherent activity [see collective dynamics of non-interacting small-world modules in Fig. 6a,b] which is achieved by relatively weak intra-module connections and different $J$-values for network nodes.

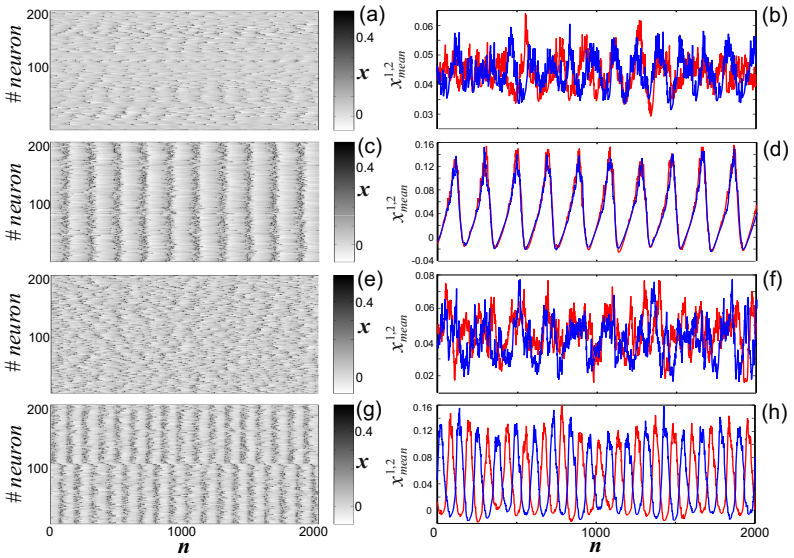


**Fig. 6.** Spike rastrograms (left) and the average module activity (right). (a,b) Two uncoupled modules; (c,d) coupled modules for $g_o = 0.02$ and in the absence of time delay; (e,f) the same coupling strength, the delay is $\tau = 10$; (g,h) the same coupling strength, the delay is $\tau = 50$.

Adding intermodule connections (so far without delay), as it was described above, leads to that the average module activity becomes synchronous rhythmic oscillations when the coupling strength go exceeds some critical value [Fig. 6c,d]. In what follows these oscillations are called bursts of average activity, or group bursts, and we distinguish in them active phases—time intervals during which the averaged module activity is above $x = J_0$, and passive phases in between the active ones. At the nodal level, spike events mainly happen during the active phases of group bursts, however irregularity of the individual dynamics remains and there is no strict periodicity of the individual oscillations.

If a small time delay is introduced into the intermodule coupling then the regime of synchronous group bursts remains almost unchanged. For some critical value of the time delay, the neuronal dynamics becomes incoherent [see Fig. 6e,f] as it was in the case of uncoupled modules but in long enough time series one can find short intervals during which synchronous group bursts appear. Further increasing of the time delay leads to a regime of rhythmic oscillations [Fig. 6g,h], however, in the form of anti-phase group bursts whose average frequency is markedly higher than that of the in-phase bursts at small delays [Fig. 6c,d]. Thus, with increasing time delay in the inter-module coupling, the in-phase group activity is replaced by the anti-phase one as well as one observes the change in the frequency of group oscillations. We have analyzed the spectra of group activity and the regimes of modular synchronization depending on the time delay for three intra-module topologies considered, the results are shown in

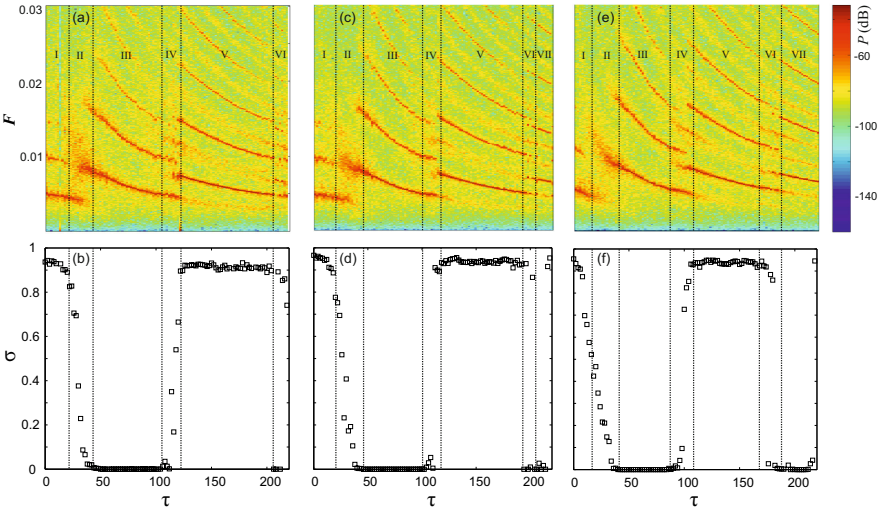


**Fig. 7.** (a),(c),(e) Spectrogram of the average module activity depending on the inter-module coupling delay $\tau$; (b),(d),(f) module synchronization degree $\sigma(\tau)$ for $J_0 = 0.045$ and $g_o = 0.02$. The intra-module connection topology is: (a),(b) random Erdös–Rényi, (c),(d) small-world Watts–Strogatz and(e),(f) scale-free Barabási–Albert.

Fig. 7. Despite the difference in the intra-module connectivity, the impact of the delayed coupling is qualitatively similar for all three cases. One can distinguish in Fig. 7 the delay intervals labeled by the Roman numerals corresponding to different types of collective dynamics. In the intervals I and V where the values of the synchronization parameter $\sigma$ are close to one, there is the in-phase regime of modular synchronization. In the intervals III and VI where $\sigma$ is close to zero, there is the anti-phase regime. The intervals II, IV, and VI correspond to transient regimes where the modules display incoherent activity without any pronounced rhythm. Note that in the intervals of the in-phase and anti-phase regimes, the frequency of lower harmonic as well as its multiples decreases with increasing delay. At the transition from one regime (e.g., anti-phase in the interval III) to another (in-phase in the interval V), the frequency abruptly rises, and the magnitude of the jump is higher for smaller time delays. It is interesting to note that the width of the interval I corresponding to the in-phase group bursts at a small delay, is always less than that of other intervals, in particular, the interval V where there is also the in-phase regime. The impact of the inter-module coupling delay and strength on a synchronization regime and the frequency of bursts generated is summarized in Fig. 8. The two-parameter diagrams show the alternation of the in-phase and anti-phase regimes [Fig. 8a], as well as the decrease in the frequency of the first harmonic of group bursts within each of these regimes with increasing $\tau$ [Fig. 8b]. Note that an unobvious result follows

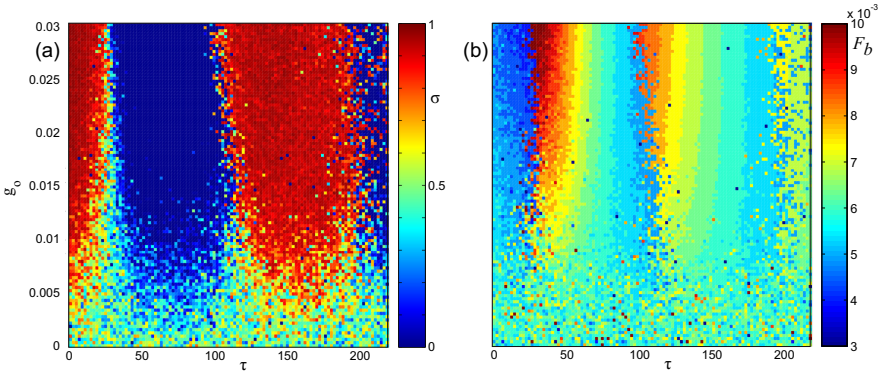


**Fig. 8.** (a) Dependence of the synchronization degree $\sigma$ and (b) the frequency of the first harmonic of group bursts $F_b$ on $\tau = 10$ and $g_o$

from Fig. 8b: with increasing inter-module coupling strength $g_o$, the frequency of group bursts increases for a fixed delay, while in the first zone of in-phase regime the opposite case takes place—a decrease in the frequency with increasing $g_o$.

## 5 Conclusions

In this paper, we considered modular networks of interacting neuron-like elements which generate irregular spike sequences. In the first example the modules are groups of non-interacting neurons which inhibit all the neuron of another module. We explained the mechanism for emergence of anti-phase group bursts in the network and showed that the collective behavior underlies a regular response of the system to external pulse stimulation. In the second example the modules are subnetworks with complex topology which are connected by sparse excitatory delayed coupling. We found a dual role of the inter-module coupling delay in the collective network dynamics. First, with increasing time delay, in-phase and anti-phase regimes, where individual spikes form rhythmic modular burst-like oscillations, alternate with each other. Second, the average frequency of the collective oscillations in each of these regimes decreases with increasing inter-module coupling delay. An increase in the inter-module coupling strength and the network excitation level leads to an enhancement of synchronization in the in-phase as well as anti-phase regimes. The frequency of group bursts rises with increasing inter-module coupling strength for all delay intervals except the first one: for a small time delay in the in-phase regime the frequency decreases with increasing coupling strength.

**Acknowledgments.** This work was supported by the Russian Science Foundation (Project No. 14-12-01358).

## References

1. Arenas, A., Diaz-Guilera, A., Kurths, J., Moreno, Y., Zhou, C.: Synchronization in complex networks. Phys. Rep. 469, 93–153 (2008)
2. Bullmore, E., Sporns, O.: Complex brain networks: graph theoretical analysis of structural and functional systems. Nat. Rev. Neurosci. 10, 186–198 (2009)
3. Girvan, M., Newman, M.E.J.: Community structure in social and biological networks. Proc. Natl. Acad. Sci. USA 99(12), 7821–7826 (2002)
4. Nekorkin, V.I., Vdovin, L.V.: Diskretnaya model neironnoy aktivnosti. Izvest. vys. ucheb. zaved. Prikladnaya Nelineinaya Dinamika 15, 36–60 (2007) (in Russian)
5. Courbage, M., Nekorkin, V.I., Vdovin, L.V.: Chaotic oscillations in a map-based model of neural activity. Chaos 17, 043109 (2007)
6. Courbage, M., Nekorkin, V.I.: Map-based models in neurodynamics. Int. J. Bifurcation and Chaos 20, 1631–1651 (2010)
7. Maslennikov, O.V., Kasatkin, D.V., Rulkov, N.F., Nekorkin, V.I.: Emergence of antiphase bursting in two populations of randomly spiking elements. Phys. Rev. E. 88, 042907 (2013)
8. Maslennikov, O.V., Nekorkin, V.I.: Modular networks with delayed coupling: Synchronization and frequency control. Phys. Rev. E. 90, 012901 (2014)

# Birth-Death Models of Information Spread in Structured Populations

Burton Voorhees

Center for Science, Athabasca University,
1 University Drive Athabasca, AB Canada T9S 3A3
burt@athabascau.ca

## 1 Introduction

Following on the seminal work of Lieberman, et al [1], analysis of information spread in structured populations has become a major area of research interest. This work, together with research on general networks [e.g., 2 – 8], has inspired a number of graph based evolutionary models [e.g. 9 – 21]. The generality of such models can be seen through a partial listing of questions to which they have been applied: the spread of information, gossip, and rumors [22 – 25]; the spread of ideas and innovations [26 – 30]; the probability of a mutant gene becoming fixed in a population [31 – 34]; models of defenses against cancer and epidemics [35, 36]; models of the evolution of cooperation [37 – 39]; and, tracking rumor sources and terrorists [40 - 42].

## 2 Birth-Death Models and the Moran Process

Four of the more popular modeling assumptions are birth-death, death-birth, voter models, and probabilistic voter models, together with game theoretic versions. The focus here is on birth-death models. Members of a population, who either do or do not possess a particular characteristic (e.g., a mutant gene, a particular belief or opinion, an innovative practice, or a disease) occupies each vertex of a graph. Vertices occupied by population members with the characteristic are labeled 1 and those occupied by members not possessing it are labeled 0. The distinguishing characteristic is assigned fitness $r \geq 0$ as compared to fitness 1 of the normal population.

The birth-death process is a discrete time process in which, at each iterate, a vertex is chosen, biased by fitness, to "reproduce." Following on this choice, an adjacent vertex is chosen to die and be replaced by a copy of the reproducing vertex. The edge from vertex i to vertex j is labeled with the probability that if vertex i is chosen for reproduction then vertex j is chosen for death.

This process was introduced by Moran [43] to find the fixation probability of a single mutant gene introduced into an otherwise homogeneous population. It is a biased random drift Markov process on the state space $\{0,1,\ldots,N\}$, where the state m indicates a population state with m mutants and N – m normals. States 0 and N are



A. Sanayei et al. (eds.), *ISCS 2014: Interdisciplinary Symposium on Complex Systems*,
Emergence, Complexity and Computation 14, DOI: 10.1007/978-3-319-10759-2_8

absorbing states and, following Nowak [44], if $p_{m,m-1}$ and $p_{m,m+1}$ are the respective probabilities of the state transitions m → m – 1 and m → m + 1 and if $x_k$ is the probability of reaching fixation (state N) from state k then

$$\begin{aligned} x_0 &= 0 \\ x_k &= p_{k,k-1}x_{k-1} + p_{k,k}x_k + p_{k,k+1}x_{k+1} \\ x_N &= 1 \end{aligned} \tag{1}$$

and the single vertex fixation probability ρ is $x_1$, which is given by

$$\rho = \frac{1}{1+\sum_{j=1}^{N-1}\prod_{k=1}^{j}\frac{p_{k,k+1}}{p_{k,k-1}}} \tag{2}$$

For the Moran process,

$$p_{m,m-1} = \left(\frac{m}{N}\right)\frac{1}{N-m+rm}, \quad p_{m,m+1} = \left(\frac{N-m}{N}\right)\frac{rm}{N-m+rm} \tag{3}$$

and

$$\rho = \frac{1-\frac{1}{r}}{1-\frac{1}{r^N}} \tag{4}$$

Any graph with fixation probability given by equation (5) is fixation equivalent to a Moran process – the population structure it describes has no effect on single mutant fixation probability, although it may influence time to fixation [45 – 47].

The Effect of Population Structure

The obvious next question is whether or not population structure can influence fixation probability. Initial work seemed to indicate there was no influence [48, 49]. Recent results, however, have demonstrated that this is not the general case. In their seminal paper, Lieberman, et al [1] give examples of graphs that suppress or enhance fixation probabilities relative to the Moran probability of equation (4).

Other questions relating to information spread in populations have also been seriously investigated. Two questions of particular interest are:

1. What initial node (or set of nodes) leads to the greatest fixation probability?
2. Given an observed distribution of mutants, what is the most likely starting node (or set of nodes) producing this distribution?

The first of these questions becomes significant for inhomogeneous population structures since the fixation probability itself is defined as the average of the fixation probabilities over all nodes, and the fixation probability at different nodes may differ. The following theorem makes this specific.

Theorem 1 [1, 20, 32]
A graph is fixation equivalent to a Moran process if and only if all single vertex fixation probabilities are equal.

A State Space Approach
In [50, 51], computation of birth-death fixation probabilities is developed using a state space approach: vectors $\vec{a}(\vec{v}), \vec{b}(\vec{v})$ are defined by $\vec{a}(\vec{v}) = \vec{v} \cdot W, \vec{b}(\vec{v}) = \vec{v}' \cdot W$ where $v_i' = 1 - v_i$. For state vector $\vec{v}$, $a_j(\vec{v})$ is the probability that an edge originating at a mutant vertex terminates at vertex j and $b_j(\vec{v})$ is the probability that an edge originating at a normal vertex terminates at vertex j.

Theorem 2 [50]
Let a birth-death process be defined on a graph G with probabilistic edge weight matrix W. Then for all j, $1 \le j \le N$ and for all states $\vec{v}$ with $m = \sum_{i=1}^{N} v_i$:

1. The probability of a transition from the state $(v_1,\ldots,v_{j-1},0,v_{j+1},\ldots,v_N)$ to the state $(v_1,\ldots,v_{j-1},1,v_{j+1},\ldots,v_N)$ is given by

$$\frac{r a_j(\vec{v})}{N - m + rm}. \tag{5}$$

2. The probability of transition from the state $(v_1,\ldots,v_{j-1},1,v_{j+1},\ldots,v_N)$ to the state $(v_1,\ldots,v_{j-1},0,v_{j+1},\ldots,v_N)$ is given by

$$\frac{b_j(\vec{v})}{N - M + rm}. \tag{6}$$

3. The probability that $\vec{v}$ remains unchanged is

$$\frac{r\vec{a}(\vec{v}) \cdot \vec{v} + \vec{b}(\vec{v}) \cdot \vec{v}'}{N - m + rm}. \tag{7}$$

Based on this theorem a state transition matrix $T = (T_{uv})$ can be constructed. Elements on the state space are indexed with letters chosen from the latter part of the alphabet (e.g., u,v) while labels of vertices of the graph are indexed with letters i, j.

Any set of mutants less than the full state space will goes to extinction or fixation, hence the Markov process has only two steady states: extinction, represented by the vector $\underline{0}$ of all zeros; and, fixation, represented by the vector $\underline{1}$ of all ones. Writing $v = \sum_{i=1}^{N} v_i 2^{N-i}$ with $x_v$ the probability that the state $\vec{v}$ goes to fixation, the equation for the Markov steady state, with boundary conditions $x_0 = 0$ and $x_{2^N-1} = 1$, yields

$$\left[N + (r-1)m - r\vec{a}(\vec{v}) \cdot \vec{v} - \vec{b}(\vec{v}) \cdot \vec{v}'\right] x_v - r \sum_{i=1}^{N} a_i(\vec{v}) v_i' x_{v+2^{N-i}} - \sum_{i=1}^{N} b_i(\vec{v}) v_i x_{v-2^{N-i}} = 0. \tag{8}$$

These are linear equations, which can be solved by standard packages in Maple, Mathematica, and Matlab. Solution, however, is only possible for small values of N (say N < 20), and even in these cases, exact solutions are cumbersome. For example, the graph of Figure 1 represents a cycle with a constriction.

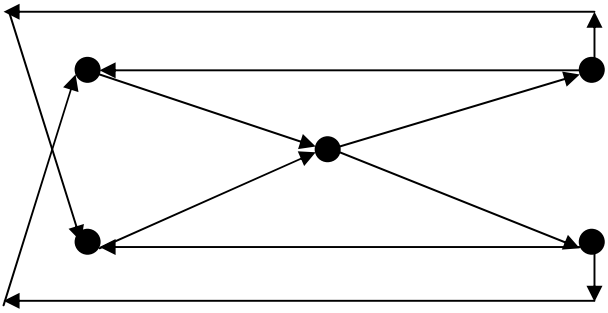

**Fig. 1.** N = 5 Cycle of Width 2 With Constriction

Symmetry conditions reduce the 30 equations arising from equation (8) to 16 equations in 16 unknowns. The fixation probability is given by the ratio of two degree 16 polynomials in the fitness r, with coefficients of up to seven digits. It is best represented graphically in terms of the difference between this probability and the corre sponding Moran probability on five vertices, as indicated in Figure 2:

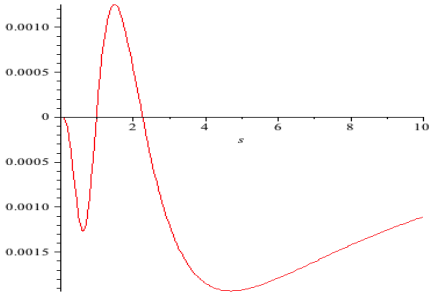


**Fig. 2.** Difference between Fixation Probability for Graphs of Figure 1 and the Equivalent Moran Probability

The fixation probability for the graph of Figure 1 is greater than that of a Moran process for 1< r < 2.267235117. This suggests that the introduction of funnel or star-like constrictions in cycles of width n may lead to enhancement of selection for only particular ranges of fitness, and similar results show up for other graphs.

Circular Flows

In [50, 51] a class of graphs called circular flows is defined. This class contains many of the graphs that have been studied in the literature, including cycles, funnels, cascades, and layered networks [3]. Figure 3 shows an example such a graph.

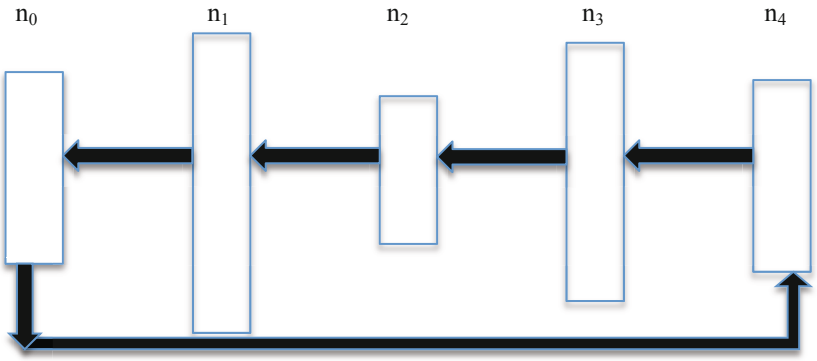


**Fig. 3.** Illustration of a 5-Level Circular Flow

In this figure, the numbers $n_k$ indicate the number of vertices in equivalence classes of vertices while the arrows indicate that every node in class $n_{k+1}$ is connected to every node in class $n_k$ with probability $1/n_k$ (with indices taken mod s+1 where s is the maximum number of classes). If there are k+1 equivalence classes in a circular flow with $n_i$ vertices in the i-th class then this is indicated by the k+1 tuple $(n_0,n_1,\ldots,n_k)$. All vertices in each class are equivalent and this symmetry condition reduces the number of equations and unknowns involved to the product

$$\prod_{i=0}^{k}(n_i+1)$$

Given a class label $(m_0,\ldots,m_{s-1},m_s,m_{s+1},\ldots,m_k)$ where $m_k$ denotes the number of mutants at level k, define

$$\iota(\vec{m}) = m_k + \sum_{s=0}^{k-1} m_s \prod_{j=1}^{k-s}\left(n_{s+j}+1\right). \tag{9}$$

Using the notation $(m_0,\ldots,m_{s-1},m_s\pm 1,m_{s+1},\ldots,m_k)\to \iota(\overrightarrow{m},m_s\pm 1)$ equation (8) becomes

$$\left[\sum_{s=0}^{k}\frac{m_s(n_{s+1}-m_{s+1})+rm_{s+1}(n_s-m_s)}{n_s}\right]x_{\iota(m)} - \left[\sum_{s=0}^{k}\frac{m_s(n_{s+1}-m_{s+1})}{n_s}\right]x_{\iota(m,m_s-1)} - r\left[\sum_{s=0}^{k}\frac{m_{s+1}(n_s-m_s)}{n_s}\right]x_{\iota(m,m_s+1)} = 0 \tag{10}$$

and the single vertex fixation probability is

$$\rho = \frac{1}{N}\left[n_k x_1 + \sum_{s=1}^{k} n_{k-s}x_{\iota(s)}\right], \quad \iota(s) = \prod_{j=k-s}^{k-1}(n_{j+1}+1) \tag{11}$$

with summation indices taken mod(k+1).

The question of the significance of the initial site has been studied in [12], and can be explicitly illustrated with solutions to equations (8). Figure 4 shows examples of three level funnel graphs $(n_0,n_1,n_2) = (1,2,n)$. For the (1,2,n) graphs with $n < 6$ the average fixation probability is enhanced with respect to a Moran process only for limited values of $r > 1$ (for $n \geq 6$ it appears to be enhanced for all $r > 1$), as indicated in Figure 4a. Figure 4b, however, shows the corresponding fixation probabilities for initial mutant placement in the $n_0$, $n_1$, and $n_2$ equivalence classes of vertices. Fixation probability is enhanced relative to a Moran process only if the initial mutant is placed in the $n_2$ equivalence class (upper curves).

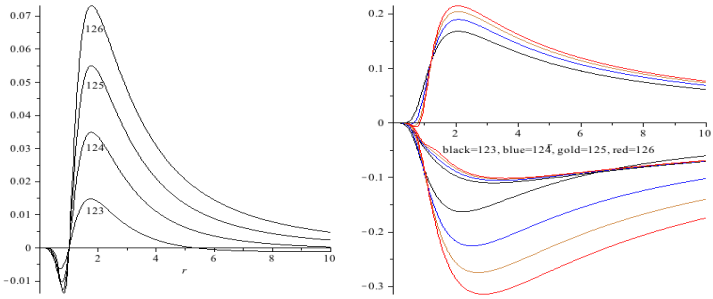


a b

**Fig. 4.** (a) $\rho_G - \rho_M$, (b) single vertex probabilities minus $\rho_M$ for G(1,2,n)

The State Transition Matrix

Useful results can be obtained by consideration of the state transition matrix T. A state $\vec{u} = (u_1, u_2, ..., u_N)$ defines the binary number $u_1u_2\ldots u_N$ with corresponding denary form given by $u = \sum_{i=1}^{N} u_i 2^{N-i}$. The $2^N$ population states are listed from the top down in numerical order to define a $2^N \times N$ matrix S with $S_{ui} = u_i$. As a direct consequence we have:

Lemma 1:

The probability that vertex i will contain a mutant after k iterations, starting from initial state $\vec{u}$, is given by $[T^kS]_{ui}$.

Theorem 6:

Given initial state $\vec{u}$, the probability of fixation is $x_u = \lim_{k\to\infty}\left[T^k \cdot S\right]_{ui}$.

Proof:

Since the Markov process with transition matrix T converges to either extinction or fixation, for large k, $[T^k]_{uv} \sim 0$ unless $\vec{v}$ is $\underline{0}$ or $\underline{1}$, and

$$\lim_{k\to\infty}\left[T^k \cdot S\right]_{ui} = T^*_{u\underline{0}}\underline{0}_0 + T^*_{u\underline{1}}\underline{1}_{2^N-1} = T^*_{u\underline{1}} = x_u, \tag{12}$$

where $T^* = \lim_{k\to\infty} T^k$.

This also provides a determination of upper and lower bounds for the fixation probability of any state $\vec{u}$.

Theorem 7:
Given an initial state $\vec{u}$ and a number of birth-death iterations k,

$$\left[T^k\right]_{u\underline{1}} \le x_u \le 1-\left[T^k\right]_{u\underline{0}}. \tag{13}$$

Lemma 1 and Theorem 7 are reported in [20, 21] in different language.

Interpolation of equation (20) yields an estimate for the fixation probability of $\vec{u}$: set $\Delta_u(k) = 1 - [T^k]_{u\underline{0}} - [T^k]_{u\underline{1}}$ and write the linear interpolation estimate for the fixation probability as:

$$est_k(x_u) = \left[T^k\right]_{u\underline{1}} + \frac{\Delta_u(k)}{\left[T^k\right]_{u\underline{0}} + \left[T^k\right]_{u\underline{1}}} \tag{14}$$

This makes it possible to at least tentatively answer our question (1): given that the observed state after k iterations is $\vec{v}$, what are the most likely initial states to produce this observed configuration? The answer is obtained by finding $\max\left\{T_{uv}^k \middle| \vec{u} \in V\right\}$ for sufficiently large values of k

The Graph Laplacian
Our question (2) can be approached by making use of a suitably defined graph Laplacian [52, 53]. If the eigenvalues of this matrix are ordered from smallest to largest, the first is always 0 and the remaining eigenvalues satisfy $0 \le \lambda_1 \le \lambda_2 \le \ldots \le \lambda_{N-1} \le 2$ for an N vertex graph. The number of 0 eigenvalues equal the number of connected components of the graph, hence $\lambda_1 > 0$ if and only if the graph is connected and the value of $\lambda_1$ provides information about the difficulty of cutting the graph into disconnected parts. If $\lambda_1$ is found to be decreasing in time, for example, it may suggest increasing polarization or conflict in the represented population. Figure 5 shows a simple example.

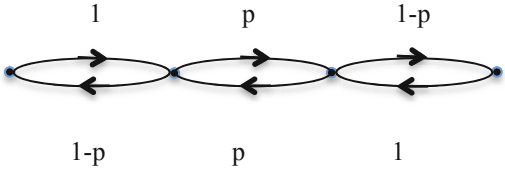


**Fig. 5.** Example of Graph with Disconnect Parameter p

In this graph, the parameter p ranges between zero and one. If p = 0 the graph has been severed into two disconnected components. The edge weight matrix and graph Laplacian for this graph are

$$W = \begin{pmatrix} 0 & 1 & 0 & 0 \\ 1-p & 0 & p & 0 \\ 0 & p & 0 & 1-p \\ 0 & 0 & 1 & 0 \end{pmatrix}, \quad \Delta = \begin{pmatrix} 1 & -\sqrt{1-p} & 0 & 0 \\ -\sqrt{1-p} & 1 & -p & 0 \\ 0 & -p & 1 & -\sqrt{1-p} \\ 0 & 0 & -\sqrt{1-p} & 1 \end{pmatrix} \tag{22}$$

The eigenvalues of $\Delta$ are 0, p, 2-p, and 2. Thus p measures the degree of contact between the first two and final two vertices.

Discussion

The study of information spread in finite populations is a broad and rapidly developing field, subsuming a wide variety of topics and directions of research. The use of edge-weighted graphs to model interaction patterns in heterogeneous populations is a significant tool in this research. One of the questions this tool has been used to study is the fixation probability, that is, the probability that an innovation introduced into a population will eventually take over the entire population. Intuitively, the expectation is that non-homogeneous structure in a population can influence fixation probability and it is now clear that there are indeed population structures that can exert a strong influence, either suppressing or enhancing the effects of selection relative to drift in a homogeneous population. Further, there are sound biological and social reasons to explore these heterogeneous population structures.

A point of interest is the existence of structures that provide suppression or enhancement of selection for limited ranges of a fitness parameter. This places fitness (or any measure of constraint matching) in the role of control parameter.

From a graph theoretic perspective, the graph Laplacian for the population matrix provides a link to research in spectral graph theory [52, 53]. Thus, $\lambda_1$, called the algebraic connectivity of the graph, is non-zero if and only if the graph is connected. Its value provides information about the difficulty of cutting the graph into disconnected parts, giving a measure of the degree of connectivity within a population.

## References

[1] Lieberman, E., Hauert, C., Nowak, M.A.: Evolutionary dynamics on graphs. Nature 433(7023), 312–316 (2005)

[2] Kauffman, S.A.: Origins of Order: Self-Organization and Selection in Evolution. Oxford University Press, Oxford (1993)

[3] Barbosa, V.C., Donangelo, R., Sousa, S.R.: Network growth for enhanced natural selection. Physical Review E 80(2), 026115 (2009)

[4] Birkholz, J.M., Bakhshi, R., Harige, R., van Steen, M., Groenewegen, P. (2012) Scalable analysis of socially informed network models. arXiv:1209.6615v1 (cs.SI) (September 28, 2012)

[5] Chazelle, B. (2012) The dynamics of influence systems. arXiv:1204.3946 (nlin.AO) (April 17, 2012)

[6] Díaz, J., Goldberg, L., Mertzios, G., Richerby, D., Serna, M., Spirakis, P.: Approximating fixation probabilities in the generalized Moran process. In: Proceedings of the ACM-SIAM Symposium on Discrete Algorithms (SODA), Kyoto, Japan. ACM (2012), http://arxiv.org/abs/1111.3321
[7] Ghanbarnejad, F., Klemm, K.: Impact of individual nodes in Boolean network dynamics. arXiv:1111/5334v1 (q-bio.MN) (November 22, 2011)
[8] Mossel, E., Sly, A., Tamuz, O.: Strategic learning and the topology of social networks. arXiv:1209.5527 (cs.GT) (September 25, 2012)
[9] Antal, T., Redner, S., Sood, V.: Evolutionary dynamics on degree-heterogeneous graphs. Physical Review Letters 96(18), 188104 (2006)
[10] Broom, M., Hadjichrysanthou, C., Rychtár, J., Stadler, B.T.: Two results on evolutionary processes on general non-directed graphs. Proceedings of the Royal Society A: Mathematical, Physical and Engineering Sciences 466, 2795–2798 (2010)
[11] Broom, M., Rychtár, J., Stadler, B.T.: Evolutionary dynamics on small-order graphs. Journal of Interdisciplinary Mathematic 12(2), 129–140 (2009)
[12] Broom, M., Rychtár, J., Stadler, B.T.: Evolutionary dynamics on graphs – the effect of graph structure and initial placement on mutant spread. Journal of Statistical Theory and Practice 5(3), 369–381 (2011)
[13] Champagnat, N., Lambert, A., Richard, M.: Birth and death processes with neutral mutations. arXiv:1209.6205.v1 (math.PR) (September 27, 2012)
[14] Fu, F., Wang, L., Nowak, M.A., Hauert, C.: Evolutionary dynamics on graphs: Efficient methods for weak selection. Physical Review E 79(4), 046707 (2009)
[15] Hauert, C.: Evolutionary dynamics. In: Skjeltorp, A.T., Belushkin, A.V. (eds.) Proceedings of the NATO Advanced Study Institute on Evolution From Cellular to Social Scales, pp. 11–44. Springer, Dordrecht (2008)
[16] Masuda, N., Ohtsuki, H.: Evolutionary dynamics and fixation probabilities in directed networks. New Journal of Physics 11, 033012 (2009)
[17] Masuda, N.: Directionality of contact networks suppresses selection pressure in evolutionary dynamics. Journal of Theoretical Biology 258(2), 323–334 (2009)
[18] Nowak, M.A., Tarnita, C.E., Antal, T.: Evolutionary dynamics in structured populations. Philosophical Transactions of the Royal Society B 365, 19–30 (2010)
[19] Santos, F.C., Pacheco, J.M., Lenaerts, T.: Evolutionary dynamics of social dilemmas in structured heterogeneous populations. PNAS 103(9), 3490–3494 (2006)
[20] Shakarian, P., Roos, P., Johnson, A.: A review of evolutionary graph theory with applications to game theory. Biosystems 107(2), 66–80 (2012)
[21] Sharkarian, P., Roos, P., Moores, G.: A novel analytical method for evolutionary graph theory problems. Biosystems (2012) (to appear)
[22] Barbour, A.D., Reinert, G.: Asymptotic behavior of gossip processes and small world networks. arXiv:1202.5895v2 (math.PR) (February 28, 2012)
[23] Coletti, C.F., Rodriguez, P.M., Schinazi, R.B.: A spatial stochastic model for rumor transmission. arXiv:1202.1491v1 (math.PR) (February 17, 2012)
[24] Haeupler, B.: Simple, fast and deterministic gossip and rumor spreading. arXiv:1210.1193v1 (cs.DS) (October 3, 2012)
[25] Shi, G., Johansson, M., Johansson, K.H.: How agreement and disagreement evolve over random dynamic networks. arXiv:1208.3398v1 (cs.SI) (August 16, 2012)
[26] Banos, R.A., Borge-Holthoefer, J., Moreno, Y.: The role of hidden influentials in the diffusion of online information cascades. EJP Data Science 2(6) (2013)
[27] Montanari, A., Saberi, A.: The spread of innovation in social networks. PNAS 107(47), 20196–20201 (2010)
[28] Tu, S.-Y., Sayed, A.H.: On the influence of informed agents on learning and adaptation over networks. arXiv:1203.1524 (cs.IT) (March 7, 2012)

[29] Wang, Y., Xiao, G., Liu, J.: Dynamics of competing ideas in complex social networks. arXiv: 1112.5534v1 (2011)
[30] Lang, J., De Sterck, H.: The Arab Spring: A simple compartmental model for the dynamics of a revolution. ArXiv:1210.1841v1 (math.DS) (October 5, 2012)
[31] Barbosa, V.C., Donangelo, R., Souza, S.R.: Early appraisal of the fixation probability in directed networks. Physical Review E8 2(4), 046114 (2010)
[32] Broom, M., Rychtár, J.: An analysis of the fixation probability of a mutant on special classes of non-directed graphs. Proceedings of the Royal Society A 464, 2609–2627 (2008)
[33] Taylor, P.D., Day, T., Wild, G.: From inclusive fitness to fixation probability in homogeneous structured populations. Journal of Theoretical Biology 249, 101–110 (2007)
[34] Zhang, C., Wu, Y., Liu, W., Yang, X.: Fixation probabilities on complete star and bipartite digraphs. Discrete Dynamics in Nature and Society 940465 (2012)
[35] Nowak, M.A., Michor, F., Iwasa, Y.: The linear process of somatic evolution. Proceedings of the National Academy of Science USA 100, 14966–14969 (2003)
[36] Simon, P.L., Taylor, M., Kiss, I.Z.: Exact epidemic models on graphs using graph automorphism driven lumping. Journal of Mathematical Biology 62(4), 479–508 (2011)
[37] Chen, Y.-T.: Robustness of two simple rules for the evolution of cooperation on regular graphs. arXiv:1107.1513v1 (math.PR) (July 7, 2011)
[38] Dong-Ping, Y., Hai, L., Chen-Xu, W., Jian-Wei, S.: Modeling Moran process with network dynamics for the evolution of cooperation. Chinese Physics Letters 26(6) (2009)
[39] Taylor, P.D., Day, T., Wild, G.: Evolution of cooperation in a finite homogeneous graph. Nature 447, 469–472 (2007)
[40] Dong, W., Zhang, W., Tan, C.W.: Rooting out the rumor culprit from suspects. arXiv:1301.6312v1 (cs.SI) (January 27, 2013)
[41] Shah, D., Zaman, T.R.: Rumors in a network: Who's the culprit? IEEE Transactions on Information Theory 57, 5163–5181 (2011)
[42] Shah, D., Zaman, T.R.: Finding rumor sources on random graphs. arXvi:1110.6230v2 (math.PR) (November 3, 2011)
[43] Moran, P.: Random processes in genetics. Mathematical Proceedings of the Cambridge Philosophical Society 54, 60–71 (1958)
[44] Nowak, M.A.: Evolutionary Dynamics. Harvard University Press, Cambridge (2006)
[45] Broom, M., Hadjichrysanthou, C., Rychtár, J., Stadler, B.T.: Evolutionary games on graphs and the speed of the evolutionary process. Proceedings of the Royal Society A: Mathematical, Physical and Engineering Sciences 466, 1327–1346 (2009)
[46] Altrock, P.M., Traulsen, A.: Fixation times in evolutionary games under weak selection. New Journal of Physics 11, 013012 (2009)
[47] Taylor, C., Iwasa, Y., Nowak, M.A.: A symmetry of fixation times in evolutionary dynamics. Journal of Theoretical Biology 243, 245–251 (2006)
[48] Maruyama, T.: A simple proof that certain quantities are independent of the geographical structure of populations. Theoretical Population Biology 5(2), 148–154 (1974)
[49] Slatkin, M.: Fixation probabilities and fixation times in a subdivided population. Evolution 35, 477–488 (1981)
[50] Voorhees, B.: Birth-death fixation probabilities for structured populations. Proceedings of the Royal Society A 469, 2153 (2013)
[51] Voorhees, B., Murray, A.: Fixation probabilities for simple digraphs. Proceedings of the Royal Society A 469, 2154 (2013)
[52] Banerjee, A.: The Spectrum of the Graph Laplacian as a Tool for Analyzing Structure and Evolution of Networks. Dissertation (Dr. rer. nat.), University of Leipzig (2008)
[53] Li, Y., Zhang, Z.: Digraph Laplacian and the degree of asymmetry. Internet Mathematics 8(4), 381–401 (2012)

# Coexistence of Deterministic and Stochastic Bistability in a 1-D Birth-Death Process with Hill Type Nonlinear Birth Rates

Neslihan Avcu[1,⋆], Nihal Pekergin[2], Ferhan Pekergin[3], Güleser Kalaycı Demir[1], and Cüneyt Güzeliş[4]

[1] Dokuz Eylül University, Faculty of Engineering, Department of Electrical and Electronics Engineering, İzmir, Turkey
{neslihan.avcu,guleser.kalayci}@deu.edu.tr
[2] Université Paris-Est Créteil, LACL, Créteil, France
nihal.pekergin@u-pec.fr
[3] Université Paris 13, Sorbonne Paris Cité, LIPN, CNRS, Paris, France
ferhan.pekergin@lipn.univ-paris13.fr
[4] Izmir University of Economics, Faculty of Engineering and Computer Sciences, Department of Electrical and Electronics Engineering, İzmir, Turkey
cuneyt.guzelis@ieu.edu.tr

**Abstract.** The paper shows that, for a specific $1-D$ birth-death process, the parameter ranges for the existence of the deterministic bistability exactly coincide with the parameter ranges for the existence of the stochastic bistability, namely bimodality. The considered $1-D$ birth-death process is a reduced model of TMG induced lactose operon of *Escherichia coli* in which the birth rate for intra cellular TMG molecules is of Hill type. As opposed to the results reported by some works for other $1-D$ birth-death processes in the literature, such as the observation called Keizer paradox, no bistability without bimodality and also no bimodality without bistability are obtained for any set of model parameters. Bistability without bimodality is observed to occur only when invalid calculations of steady-state probabilities due to i) big number problems related to very small probabilities corresponding to troughs between two peaks and/or ii) inappropriately low choice of molecule numbers are not prevented.

## 1 Introduction

Bistability is a nonlinear dynamical behavior observed in diverse areas of biological systems including gene regulatory networks [5]. For a deterministic system model, the bistability appears with having two stable and one unstable equilibrium points such that the unstable one actually separates the domain of attractions of the stable ones [1]. The deterministic models are usually defined in

⋆ This work was supported in part by the Turkish Scientific and Technological Research Council and Centre National de la Recherche Scientifique in the framework of Bosphorus PIA Program.



A. Sanayei et al. (eds.), *ISCS 2014: Interdisciplinary Symposium on Complex Systems*, Emergence, Complexity and Computation 14, DOI: 10.1007/978-3-319-10759-2_9

terms of Ordinary Differential Equations (ODEs) which are derived by the law of mass action for the case of Gene Regulatory Networks (GRNs) [9], [10], [11], [16]. These ODE models of GRNs represent the change of concentrations of molecules which are the enzyme products, in general, as the sum of a nonlinear birth term and a linear death term; both are functions of molecule concentrations. It is well known [1], [3], [9], [16] that the bistability occurs for some values of model parameters when the birth rates are modeled with Hill type nonlinearity.

It is argued by many researchers [1], [3], [9], [16] that ODE models predict well the average behavior of a population or the behavior of a single cell or a gene regulatory network for high molecule numbers, but their predictions may not be valid for the cases of small molecule numbers. It is further argued [2] that stochastic models such as Chemical Master Equations (CMEs) describing the continuous-time evaluations of probabilities of model's discrete states, i.e. molecule numbers, provide better predictions for small numbers of molecules. It is shown that, for the cases of linear propensities, i.e. birth and death rates, the prediction by a CME model provides a mean value of the steady-state probability distribution identical to the stable state of the corresponding ODE Model. It is further shown in many works [4], [14] for some bistable ODE models such as Schlögl model with a third order polynomial reaction rate that the peaks, i.e. local maxima, of the steady-state probability distribution which is the steady-state solution to the corresponding CME take place at the stable equilibria of the bistable ODE model and there is a trough, i.e. a local minimum, of the steady-state probability distribution at the unstable equilibrium of ODE model.

On the other hand, some works [12] considering ODE models with second order polynomial reaction rates show that the CME counterpart shows bimodality with having a peak at zero molecule number whereas the ODE model has no capacity for possessing a bistable behavior since the quadratic nonlinearity defining the right hand side of the ODE model can provide a positive stable equilibrium and an unstable equilibrium point at zero, only. These observations lead many researchers to investigate the similarities and differences between the ODE and corresponding CME birth-death models. This paper presents a work in this direction for 1-D birth-death processes defined with a Hill type nonlinear birth rate and a linear death rate. The importance of the considered birth death process is that Hill type interaction rates are commonly used for describing the bistable behavior of gene regulatory networks, e.g. lac operon of Escherichia coli.

The main contributions of this paper are given as follows.

- As in accordance with the results obtained in the literature for Schlögl model, the considered 1-D birth death process with Hill type birth rate are shown to demonstrate the bistability and bimodality for the same ranges of the model parameters, i.e. no bistability without bimodality and no bimodality without bistability are shown to occur, if biologically valid values of model parameters are used.
- It is shown that, for a bistable ODE model, bimodality may disappear in the corresponding CME model for some parameter values when the volume of a cell and thus the number of molecules are chosen biologically

unrealistically low or the big number problems due to low probabilities occurring at the trough of steady-state probability distribution are not overcome in calculating the steady-state probabilities.

- In addition to the 1-D birth death lac operon model analyzed in the paper, a similar 1-D birth death model with Hill type birth rate is also considered and it is shown that, as opposed to the conclusions made in the literature [8] that a second peak whose disappearance removes bimodality is observable for the parameter values yielding bistability if the steady-state probabilities are calculated by supposing sufficiently large numbers of molecules and by avoiding numerical problems, in precisely, the bottleneck caused by very low probability at the molecule number corresponding to unstable equilibrium.
- Bimodality without bistability which is observed in some quadratic 1-D birth death process [12] is numerically studied for the considered 1-D birth death lac operon model and such a phenomenon is reported to never occur for the considered model. It is argued in the paper that bimodality without bistability may occur when unstable equilibrium of ODE model with one stable and one unstable equilibria is transformed to an absorbent in the CME counterpart as in the models in which Keizer paradox is observed [12].
- The considered 1-D birth death model is also studied in slow time scale by calculating absorption times. So, transition times from uninduced state, i.e. the small stable equilibrium point to induced state, i.e. the large equilibrium point are calculated and it is concluded that the CME counterpart of the ODE model behaves similar to ODE model for fast time scales such that the trajectories originated from the basin of stable equilibrium tends to this stable equilibrium and any trajectory around or at a stable state switches to the other stable state for fast time scales.

The paper is structured as follows. In Section 2, a reduced lac operon model is presented as a 1-D birth death ODE model and the bistability ranges of the model parameters are given based on a discriminant based analysis [1]. CME counterpart of the reduced lac operon model is derived in Section 3. The calculation of steady-state probabilities based on closed form solution and then the bimodality ranges of the model parameters are described in Section 3. Section 4 is devoted to discuss the results obtained for ODE and CME models and also provides a comparison on bistability versus bimodality for a similar 1-D birth death model which is studied in the literature [8] for the sake of emphasizing the importance of choosing an appropriate number of molecules in solving CME and also avoiding numerical problems involved with very small probabilities at some molecule numbers when calculating steady-state probability distribution. Conclusions are made in Section 5.

## 2 Reduced ODE lac Operon Model

The lac operon is a paradigm for genetic regulation due to the positive feedback resulting bistable behavior [5]. There are lots of experimental and theoretical studies about the bistable behavior of lac operon in the literature for nearly half

a century. Different types of mathematical models and analysis methods have been developed to explain the genetic switching mechanism of lac operon [6], [7], [8], [9], [16].

The lac operon includes three structural genes lacZ, lacY and lacA which respectively encode $\beta$-galactosidase, galactoside permease and thiogalactoside transacetylase enzymes. The permease enzyme transports lactose or its non-metabolizable analogs methyl-1-thio-$\beta$-D-galactoside (TMG) or isopropyl-$\beta$-D-thio-galactoside (IPTG) into the cell. $\beta$-galactosidase hydrolyzes the transported lactose into galactose and glucose to be metabolized, and also catalyzes the conversion of internal lactose to allolactose to induce the transcription of lac operon by binding to lac repressor. Thiogalactoside transacetylase is thought to have roles in the sugar metabolism and detoxification [1]. This study includes a reduced model of TMG induced lac operon with one ordinary differential equation whose state variable denoted by $T$. This model is obtained from the lac operon model with three state variables in [1] by assuming that mRNA transcription and permease translation occur more rapidly according to the transient response of TMG. In quasi steady-state, the rate of the change of molar concentration of TMG is written as in (1) by eliminating mRNA and permease concentrations in terms of TMG concentrations. The reduced TMG model involves the catabolite repression and inducer exclusion effects of the extracellular glucose and the positive effect of TMG on the transcription of mRNA. The translational and transcriptional delays are ignored in the lac operon mechanism.

$$\frac{1}{\widetilde{\gamma}_T}\frac{dT}{dt} = pf_{M,T}(T) - T \tag{1}$$

where $p$ is defined as the combination of the model parameters such as degradation and production constants, the effects of external glucose and TMG in [1] to simplify the analysis of the model and $f_{M,T}(T) = (1 + K_1T^n)/(K + K_1T^n)$ is the Hill type production function of mRNA under TMG concentration. It is an allosteric interaction [15] and $n$ is the required number of TMG for inactivating a repressor protein, $K_1$ is the equilibrium constant of TMG-repressor protein interaction, and $K^{-1}$ is the basal level of mRNA transcription in E.coli [9], [15]. To inactivate the repressor protein, at least two TMG molecules have to bind the repressor, thus $n$ is taken as 2. The Equation (1) can be rearranged and the characteristic equation can be derived for the steady-state case as in (2).

$$K_1T^3 - pK_1T^2 + KT - p = 0 \tag{2}$$

It has been shown that the considered model has either one or three equilibrium points depending on the model parameters [1], [9]. The model always has a real root irrespective of the parameter values. The remaining two roots of (2) are either real or a pair of complex conjugates. In three real roots case, there are three different possibilities: A triple root, two roots such that one of them is double, and three different roots. The bistable behaviour occurs when there exist three equilibria corresponding to the three different real roots of (2). In the previous work [1], to determine the ranges of the parameters ensuring the

existence of three real roots, the discriminant based bistability analysis is applied to the characteristic equation in (2). The bistability condition with three real roots is satisfied by the parameter values that make the discriminant of (2) in (3) is positive, $\Delta > 0$.

$$\Delta = -4K_1^3 p^4 + (18K_1^2 K - 27K_1^2 + K_1^2 K^2)p^2 - 4K_1 K^3 \tag{3}$$

The bistability parameter ranges are calculated for each parameter by substituting the nominal values of other two parameters. To define the bistability range for $p$ parameter, the nominal values of $K = 167.1$ and $K_1 = 1(\mu M)^{-2}$ are chosen from [9] and it is obtained as $p \in (25.7\mu M, 84.1\mu M)$. In the calculations of the other parameter ranges, $p$ is taken as $74.59\mu M$ which is calculated from the formula of $p$ in [1] for the input values $20\mu M$ external TMG, $T_e = 20\mu M$, and $0\mu M$ external glucose, $G_e = 0\mu M$, which the bistability is observed experimentally in [9]. The bistability range for $K$ parameter is determined as $K \in (148, 1390)$ by assuming $K_1 = 1(\mu M)^{-2}$ and $p = 74.59\mu M$. By taking $K = 167.1$ and $p = 74.59\mu M$ in similar calculation, the bistability range is obtained as $K_1 \in (0.119(\mu M)^{-2}, 1.27(\mu M)^{-2})$ for $K_1$ parameter. It is seen that, the nominal values are in the bistability ranges of each parameter defined from reduced ODE model.

## 3 Reduced CME lac Operon Model

The quasi steady-state model in (1) is indeed a one-dimensional birth-death process. The change rate of the TMG concentration depends on two terms. The first one is the birth term, $f(T) = \widetilde{\gamma}_T p \frac{1+K_1 T^2}{K+K_1 T^2}$, explaining the rate of going to the next state and the second one is the death term, $g(T) = \widetilde{\gamma}_T T$, expressing the rate of going to the previous state. The loss constant, $\widetilde{\gamma}_T$, only affects the transient behavior of the system and has no effect on the steady-state (see Equation (1)). So, the loss constant can be ignored in the steady-state analysis. In the stochastic model derived from deterministic quasi steady-state model, the birth and death rates can be defined as state-dependent and time-homogenous. The stochastic 1-D birth death lac operon model can be written in *Chemical Master Equation* form as in (4).

$$\frac{dPr(T,t)}{dt} = f(T-1)Pr(T-1,t) - f(T)Pr(T,t) + g(T+1)Pr(T+1,t) - g(T)Pr(T,t) \tag{4}$$

where, $T$ represent the number of TMG molecule and is a discrete random variable taking values in $\{0 \cdots N\}$. $N$ is the maximum number of $T$ molecules. $\frac{dPr(T,t)}{dt}$ is the rate of change of the probability of TMG molecule in time. In the matrix form, this can be written as follows.

$$\frac{d}{dt}\begin{bmatrix} Pr(0,t) \\ Pr(1,t) \\ \vdots \\ Pr(N,t) \end{bmatrix} = \begin{bmatrix} -f(0) & g(1) & 0 & \cdots & 0 \\ f(0) & -f(1)-g(1) & g(2) & \cdots & 0 \\ 0 & f(1) & -f(2)-g(2) & \cdots & 0 \\ \vdots & \vdots & \vdots & \vdots & \vdots \\ 0 & 0 & 0 & \cdots & g(N) \\ 0 & 0 & 0 & \cdots & -g(N) \end{bmatrix} \begin{bmatrix} Pr(0,t) \\ Pr(1,t) \\ \vdots \\ Pr(N,t) \end{bmatrix}$$

A steady-state probability distribution, $\pi$, exists for this time homogeneous, finite, irreducible Continuous Time Markov Chain (CTMC) [13]. The unique steady-state distribution $\pi^T = [\pi_0\, \pi_1 \cdots \pi_N]$ where $\pi_i = \lim_{t\to\infty} Pr(i,t) \forall i \in \{0, 1, 2, \cdots, N\}$ can be found by taking the derivatives equal to 0 as $0 = Q^T\pi$ or $0 = \pi^T Q$. In steady-state, a detailed balance equation between each connected state couple is obtained by assuming that there is no transition between states, $\pi_{i-1} f(i-1) = \pi_i g(i)$. According to these balance equations, all state probabilities can be written iteratively in terms of the probability of the first state as in (5).

$$\pi_i = \pi_0 \prod_{j=0}^{i-1} \frac{f(j)}{g(j+1)} \tag{5}$$

The steady-state probability distribution, $\pi$, is a probability mass function and the sum of all state probabilities must be equal to 1, $\sum_{i=0}^{N} \pi_i = 1$. By using this property, the probability of the first state, $\pi_0$, can be obtained as in (6). Then, all the steady-state probabilities are calculated according to (5).

$$\pi_0 = \frac{1}{1 + \sum_{i=1}^{N} \prod_{j=0}^{i-1} \frac{f(j)}{g(j+1)}} \tag{6}$$

The closed form steady-state solution of 1-D birth death lac operon model with the nominal parameter values, $K = 167.1$ and $K_1 = 1(\mu M)^2$, are calculated in MATLAB. In these calculations, the range of $T$ values are chosen in molar concentration, $T \in [0M, 150M]$, to compare the results of two models [17]. The $p$ parameter value is chosen as $74.59(\mu M)^2$, this value is obtained under the absence of external glucose and for $T_e = 20\mu M$ external TMG used as a mid-value of bistable interval in the experiments by [9]. Even though the lac operon has a bistable behavior with these parameter values in experimental studies, the closed-form steady-state solution has a unimodal probability distribution for stochastic model in Figure.1. When the closed form steady-state solutions are calculated with the $p$ values in the bistability range determined from the deterministic model and consistent with the experimental studies, it is observed that there is a narrower range for $p$ parameter to satisfy the bistable behavior with bimodal probability distribution. The bistability range for $p$ parameter is found as respectively $p \in (25.7\mu M, 84.1\mu M)$ and $p \in (30\mu M, 40\mu M)$ in the deterministic and stochastic mathematical models. The analyses in $K$ and $K_1$ parameter spaces give a similar contraction in the ranges with respect to the results of the deterministic model. The bistability range for $K$ parameter is obtained $K \in (80, 250)$ from the analysis of stochastic model when $p = 35\mu M$, the middle point of the stochastic bistability ranges for $p$ and $K \in (148, 1390)$ from the deterministic one for $p = 74.59\mu M$. In $K_1$ parameter space, the range for bistable behaviour of lac operon is identified as $K_1 \in (0.6(\mu M)^{-2}, 2.4(\mu M)^{-2})$ with $p = 35\mu M$ and $K_1 \in (0.119(\mu M)^{-2}, 1.27(\mu M)^{-2})$ with $p = 74.59\mu M$ from the stochastic and deterministic models, respectively. The reason of these contractions in the parameter ranges is related to the granularity of the state space of $T$. Recall that in a CTMC, while the time is continuous, the states are

discrete valued. When the state representation is in molar concentration, it is not possible to capture the bistability behavior for some parameter values. It is given in the following figure that the steady-state distribution for $K = 167.1$, $K_1 = 1(\mu M)^{-2}$, and $p = 74.59\mu M$ is unimodal. The roots of the characteristic equation, equilibrium points, are $T_{1,2,3} = \{72.162\mu M, 1.6639\mu M, 0.6199\mu M\}$. The first and last ones of roots are stable equilibrium points and the middle one is unstable. The domain of attraction point between the smaller stable and unstable points does not include any states. So it is not possible to capture the first trough of bimodal distribution. The peak states of unimodal distribution in Figure.1 corresponds to induced states. If we consider the first mean passage time (computed as given in [13]) from other states to induced states made absorbing, it is observed that the mean number of steps to reach induced states from states in the domain of smaller stable equilibrium point are bigger (ten times more than the other states). The situation shows that there must be an other probability accumulation in this region. This is not only parameter set to observe unimodal steady-state probability distribution in stochastic model but bistable behaviour in deterministic model. When two roots become closer to each other, the second trough does not appear and a unimodal distribution observed in steady-state. Thus, it is not obtained the same bistability parameter range in stochastic model. The model parameters in molar concentration are transformed in number of molecules.

| Deterministic Model | | Stochastic Model | |
|---|---|---|---|
| Parameters | Units | Parameters | Units |
| $p^*$ | Molar concentration | $p$ | Number of molecule |
| $K^*$ | Unitless | $K$ | Unitless |
| $K_1^*$ | (Molar concentration)$^{-2}$ | $K_1$ | (Number of molecule)$^{-2}$ |

To convert the parameter to the number of molecule from molar concentration, each parameter value is multiplied by Avogadro constant and the average volume of E. coli. The minimum and maximum volume values are calculated by taking two different diameters of cylindrical shape of *E. coli* given similar in [8] and the average of these two volumes is found as $1 \times 10^{-18} m^3$. The unitless parameter in deterministic model, $K$, is taken as the same in stochastic model and the parameter with $(\mu M)^{-2}$ unit, $K_1$, is multiplied by two times by Avogadro constant and volume in stochastic model. The parameters in deterministic model are noted with asterix and the stochastic model parameters are noted without asterix.

The steady-state probability distribution of 1-D birth death model with transformed parameter values can not be calculated in terms of number of molecule by MATLAB due to the numerical problems. The representation limit of MATLAB is reached: some probability values become smaller or greater than the extreme values represented by MATLAB. To overcome this numerical problem, the steady-state probabilities of the stochastic model are calculated in C by using the GNU Multiple Precision Arithmetic Library. The bistability regions for each parameter are obtained by the nominal parameters values as in deterministic model. For

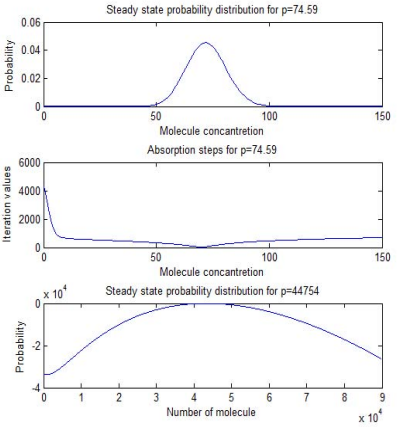


**Fig. 1.** Simulation for molar concentration, absorption time, simulation for number of molecule

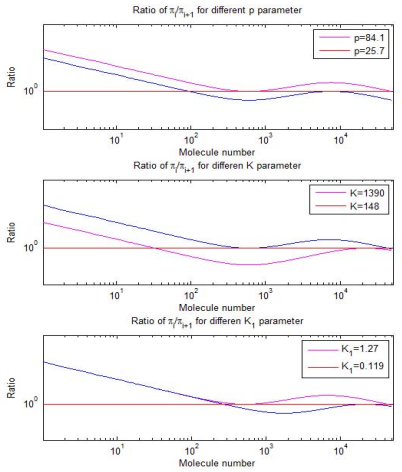


**Fig. 2.** Bistability ranges for each parameter

a better graphical representation of the probability distribution, the ratio of the successive state probabilities are drawn in logarithmic scale in Figure.2. As similar in deterministic reduced lac operon model, the bistability ranges for $p$, $K$ and $K_1$ parameters in 1-D birth death model are obtained as $p \in (25.7\mu M, 84.1\mu M)$, $K \in (148, 1390)$ and $K_1 \in (0.119(\mu M)^{-2}, 1.27(\mu M)^{-2})$, respectively.

## 4 A Comparative Study on a Benchmark 1-D Birth Death Model

A similar 1-D birth death model is studied in [8] with a Hill type nonlinear birth rate, $f(x) = v(\alpha + kx^n)/(1 + kx^n)$, and linear death rate, $g(x) = \beta x$. The Hill coefficient $n$ is chosen as 3. The ODE model for this 1-D birth death process is defined as $\dot{x} = f(x) - g(x)$ where the model parameters are given as $v = 40$, $\alpha = 0.125$, and $k = 0.093750x10^{-3}$ in [8]. In this study, it is reported that the deterministic and stochastic model give different results for the same parameter sets. It is stated in [8] that the bimodal distribution could not be obtained in the stochastic model for some parameter values ensuring bistability for the ODE model, and further that bimodality occurs without having bistability for some parameter values. However, the results derived by choosing the convenient transformation to the number of molecule shows that the bistability and bimodality respectively in deterministic and stochastic models can be obtained for the same parameter sets even with doubling the volume. The difference between the results reported in [8] and the one presented in this paper is due to the followings: The ODE model and the corresponding stochastic model are solved in [8] for the

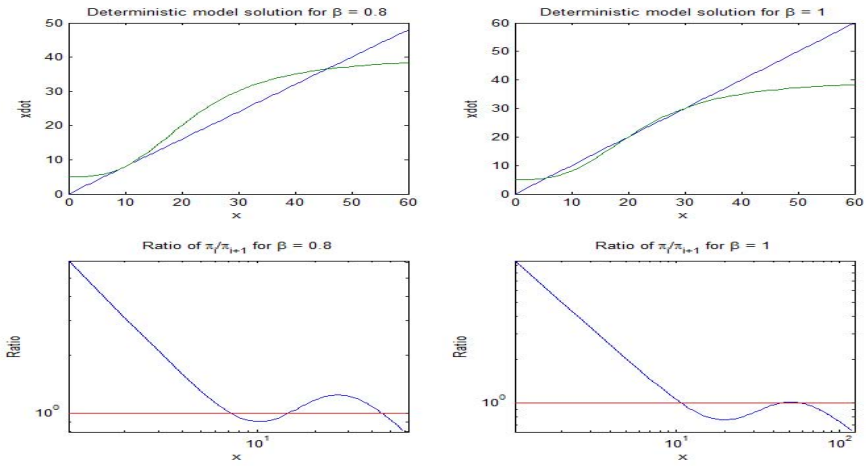


**Fig. 3.** Simulation results of $1-D$ birth death model

same $x$ variable without applying any transformation from molecular concentration into molecular number, however, this paper uses the scaled versions of $x$ variable in the stocastic model as a kind of transformation from concentration into molecular numbers with choosing the volume as a scaled parameter. On the other hand, in [8], the steady-state solution to the master equation is probably calculated without running the solution algorithm for a sufficiently long time period allowing the transitions from one stable state to the other, so making the visible both of the peaks in the steady-state distributions.

## 5 Conclusion

The work presented in the paper shows that, for two specific $1-D$ birth death models with Hill type birth and linear death rates, the bistability and bimodality exist for the same parameter ranges. The work may be extended to general classes of $1-D$ and also $n-D$ with $n>1$ birth death models with Hill type and also other type nonlinearities such as Michealies-Menten and polynomial types. It is worth to study the effect of the existence of unstable equilibrium of ODE models, on the occurrence of bimodality without bistability and also the qualitative properties of the ODE models causing the disappearance of bimodality under the existence of bistability.

## References

1. Avcu, N., Demir, G.K., Pekergin, F., Alyürük, H., Çavaş, L., Güzeliş, C.: Discriminant based bistability analysis of a TMG induced lac operon model supported with boundedness and local stability results. Turkish Jour. of Elec. Eng.and Comp. Sciences, 1–11 (2013), doi:10.3906/elk-1305-264

2. Baras, F., Mansour, M.M., Pearson, J.E.: Microscopic simulation of chemical bistability in homogeneous systems. J. Chem. Phys. 105, 8257–8261 (1996)
3. van Hoek, M., Hogeweg, P.: The Effect of Stochasticity on the Lac Operon: An Evolutionary Perspective. Plos Comp. Biology 3, 1071–1082 (2007)
4. Gillespie, D.T.: Stochastic Simulation of Chemical Kinetics. Annu. Rev. Phys. Chem. 58, 35–55 (2007)
5. Jacob, F., Perrin, D., Sanchez, C., Monod, J.: Operon: a group of genes with the expression coordinated by an operator. C. R. Acad. Sci. 250, 1727–1729 (1960)
6. Julius, A., Halasz, A., Sakar, S., Harvey, R., Pappas, G.J.: Stochastic modeling and control of biological systems: the lactose regulation system of E. coli. IEEE Trans. Auto. Cont. 53, 51–65 (2008)
7. Kim, H., Gelenbe, E.: Stochastic Gene Expression Modeling with Hill Function for Switch-like Gene Responses. IEEE/ACM Transactions on Computational Biology and Bioinformatics 9, 973–9979 (2012)
8. Lestas, I., Paulsson, J., Ross, N.E., Vinnicombe, G.: Noise in gene regulatory networks. IEEE Trans. Automatic Control 53, 189–200 (2008)
9. Özbudak, E.M., Thattai, M., Lim, H.N., Shraiman, B.I., van Oudenaarden, A.: Multistability in the lactose utilization network of Escherichia coli. Nature 427, 737–740 (2004)
10. Stamatakis, M., Mantzaris, N.V.: Comparison of deterministic and stochastic models of the lac operon genetic network. Biophys. J. 96, 887–906 (2009)
11. Stamatakis, M., Zygourakis, K.: Deterministic and stochastic population-level simulations of an artificial lac operon genetic network. BMC Bioinformatics 12, 301–317 (2011)
12. Qian, H., Bishop, L.M.: The Chemical Master Equation Approach to Nonequilibrium Steady-State of Open Biochemical Systems: Linear Single-Molecule Enzyme Kinetics and Nonlinear Biochemical Reaction Networks. International Journal of Molecular Sciences 11, 3472–3500 (2010), doi:10.3390/ijms11093472
13. Trivedi, K.S.: Probability and statistics with reliability, queuing and computer science applications. John Wiley and Sons Ltd., Chichester (2001)
14. Vellela, M., Qian, H.: Stochastic dynamics and non-equilibrium thermodynamics of a bistable chemical system: the Schlögl model revisited. J. R. Soc. Interface 6, 925–940 (2008)
15. Yagil, G., Yagil, E.: On the relation between effector concentration and the rate of induced enzyme synthesis. Biophys. J. 11, 11–27 (1971)
16. Yıldırım, N., Santillàn, M., Horike, D., Mackey, M.C.: Dynamics and bistability in a reduced model of the lac operon. Chaos 14, 279–292 (2004)
17. Yıldırım, N., Kazancı, C.: Deterministic and stochastic simulation and analysis of biochemical reaction networks: The lactose operon example. Methods Enz. 487, 371–395 (2011)

# Intellectualized Home Environment as a Complex System

Raimundas Jasinevicius, Egidijus Kazanavicius, and Vytautas Petrauskas

Real Time Computer Systems Centre, Kaunas University of Technology,
Studentu 50-204a, Kaunas, LT-51368, Lithuania
{raimundas.jasinevicius,egidijus.kazanavicius,
vytautas.petrauskas}@ktu.lt

**Abstract.** In the analytical part of this report several EC projects, developing an idea to create the intellectualized home environment (IHE) serving for peoples' comfort on the base of multiple internet things and services (IoT&S), are discussed, and the EC HORIZON 2020 program perspectives in this field are presented.

The IHE itself is presented as a complex sociotechnical fabric with the inherited mixture of real human and elements of artificial intellect as well. Multi-agent-system-based intellectics is used for the IHE's training, retraining, self-training, and functional behavior. Three aspects of human being's behavioral features, usually considered as intellectual actions, were practically realized, and they introduced new additional dimension to the systems complexity.

The IHE's complex systems model implementation was simulated to demonstrate the practical vitality and efficiency of the theoretical approach to the realization of intelligent environment of IoT&S for usre's comfort in two projects: „Research and Development of Internet Infrastructure for IoT&S in the Smart Environment (IDAPI)", and "Research on Smart Home Environment and Development of Intelligent Technologies (BIATech)".

**Keywords:** Complex systems science, Intellectualized home environment, Internet of things and services, Human being's intellectics, Multi agent system, Systems training, retraining, self-training.

## 1 Introduction: State-of-the-Art

In spite of the fact that the idea of an Internet of Things (IoT) has born many years ago, after Nikola Tesla's interview with Colliers magazine (1926 [1]) where was stated: "When wireless is perfectly applied the whole earth will be converted into a huge brain, which in fact it is, all things being particles of a real and rhythmic whole ... and the instruments through which we shall be able to do this will be amazingly simple compared with our present telephone," we were forced to wait approximately a hundred years to be able to start the full-fledged implementation of the idea in our home ambience. Huge amounts of research publications devoted to the IoT problems solutions can be find today; for example, Google presents 39 600 000 citations in the year



A. Sanayei et al. (eds.), *ISCS 2014: Interdisciplinary Symposium on Complex Systems*,
Emergence, Complexity and Computation 14, DOI: 10.1007/978-3-319-10759-2_10

2008, and 130 000 000 - in the year 2013. Five commonly agreed areas of human life are considered as ready for IoT involvement: Smart transport, Smart health, Smart shopping, Smart city and Smart home/office are on the top of the list of broad applications of different IoT computerized gadgets, artefacts and services ([2], [3]). Worldwidely recognized significance of the problem under consideration is witnessed not only by the yearly organized IoT forums under hospice of the IEEE (The IEEE Standards Association; an Internet of Things (IoT); 5-6 November 2013 in Silicon Valley, Calif. [4] , and IEEE World Forum on Internet of Things (WF-IoT); 6-8 March 2014, Seoul, Korea [5]), but by a very serious attitude of the European Commission (EC) to the problem expressed by organizing the IERC - European Research cluster on the IoT&S consisting of 33 research and development projects [6] as well. In general, an European road map for the future research and innovations in the field of Internet of things and services for smart home environment is discussed and delivered in the Horizon 2020 programs and documents (see, for example, [7], [8], and [9])

Such an approach to various engineering applications, especially to those which involve IT – enabled technologies, is very popular nowadays for two reasons. The first one – the term "agent" itself is very attractive, as mysterious and suitable for a purpose of advertising new products, and sounds scientifically enough in the research people circles. The second reason – a fuzziness of agent's definitions. [10] – [18] and many others have produced a lot of agents' definitions, some of which are cited here. According to these an agent is:

"an entity that senses its environment and acts upon it";

"an entity that functions continuously and autonomously in an environment in which other processes take place and other agents exist";

"a computer system that is situated in some environment, and that is capable of autonomous action in this environment in order to meet its design objectives".

"Intelligent agent is a computer system capable of flexible autonomous actions in order to meet its design objectives".

"Intelligent agents are software entities that carry out some set of operations on behalf of a user or another program, with some degree of independence and autonomy, and in so doing, employ some knowledge or representation of the user's goals or desires".

So, according to those popular definitions an agent is – an entity, a piece of software or a computer system, which functions in environment in order to meet its design objectives. And if this behavior is autonomous, the agent is called intelligent.

In this paper we consider such a definition too fuzzy, and the agent's intelligence definition even too poor. We understand the danger of even the authors' attempt to precisiate any term, but we take a risk to start to disclose the meaning of agents' intellectics or at least to put in it very clearly understandable content and to demonstrate its practicability in case of the intellectualized home environment (IHE). In case of presence of several interacting agents we have a multi agent system. IHE multi agent system's intellectics is hidden in those two terms: "autonomous" and "design objectives". We pretend to cover those terms by putting some contemporary mathematics and soft computing modeling three most simple human beings' features widely considered as his/her intellectual activity: 1) the recognition and classification (of

patterns, processes, situations); 2) the behavior according to the set of fuzzy rules and 3) the functioning according to some prescribed tendency. Those three activities mentioned above from a mathematical point of view are covered by mathematical programming, fuzzy logic and soft computing, and stochastic approximation correspondingly.

We claim that our approach to the IHE intellectics is different than those proposed, for example, in [10] – [19] and others. And the purpose of this paper is to demonstrate on the model the practical vitality and efficiency of this approach to the realization of intelligent home environment of IoT&S for usre‘s comfort.

The reminder of this paper is organized as follows: Sections 2 is devoted to the description of the IHE; in Section 3 the complex systems model’s implementation is presented; in the Section 4; in Section 5 the experimental simulation results are discussed. Concluding remarks are given in Section 5.

## 2 IHE: The Descriptive Approach

In a modern world it is increasingly realized that complex systems are messy combination of many physical, technical and social systems as it is symbolically shown in Figure 1.

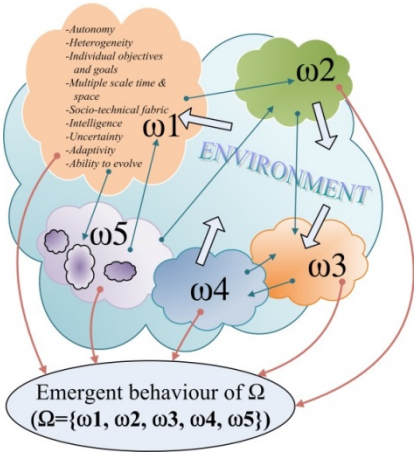


**Fig. 1.** IHE as a system of control systems

Here we see several evolving interacting entities each of which has a certain level of autonomy, heterogeneity, intelligence, uncertainty and so on, as it is written in the ω1. Dynamic coexistence of all those entities (for example: ω1- ω5) creates an emergent behavior Ω – a “life” of the complex system [20]. As a matter of fact each home environment to be intellectualized is such a complex system: it is a system of control systems consisting not only of a certain set of sensors, actuators and means of inter

and intra communication and smart things, but also a complex of sociotechnical fabrics with the inherited mixture of real human and elements of artificial intelligence as well. Such a model emphasizes the significance of its structural and uncertainty-based complexity and the behavioral complexity as well ([21]).

An elaborated structure of the typical smart home environment and its functional organization is presented in Figure 2. On the level of a real smart home environment a lot of internet things and services (IoT&S) are presented under agents' control. System of agents is shown on a real multi agent environment level (R_MAS). This MAS communicates with the IoT&Ss through the data normalization and conversion level. On this level available real data ({X}, {Y}, {K}) are converted into computerized format ([X], [Y], [K]) and vice versa. It must be emphasized that X, Y, and K mean input, output and internal state variables of each element under consideration. Real implementation of the R_MAS depends on concrete type of the IHS itself, and must be concentrated in one server, or distributed over a certain specialized network, Internet or cloud, or even in a network of smart things on the real smart home environment level. It is naturally to predict that in a case of complex IHE this R_MAS implementation will have a combined functional organization of solutions mentioned above.

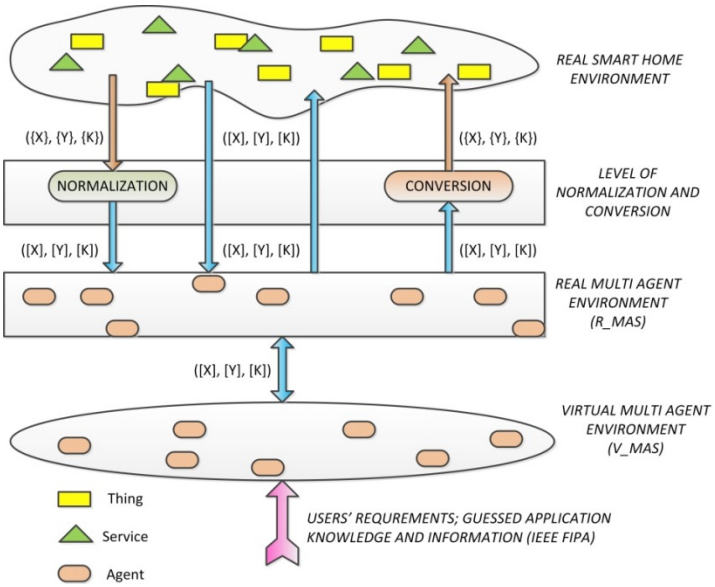


**Fig. 2.** Structure of the typical smart home environment and its functional organization

Whatever the R_MAS implementation is, its intellectics must be designed and tested on a certain virtual multi agent environment level (V_MAS, as it is shown in Figure 2.) according to users' requirements, guessed application knowledge and available information using one of the most popular standards, for example, the IEEE FIPA [4], [22].

Considering the IHE as a complex system, and keeping in mind that a number of the IoT&Ss is very high (in general case - thousands and thousands), and such must be the number of controlling agents, it is worth to use a unified description for every element of the system: for things, services, agents, and even for their subsystems. Such an approach permits us to create IHE model from those unified elements as it is commonly appropriate using Lego bricks.

The best attempt to create such "Lego bricks" for complex systems description in space – time coordinate system was proposed by prof. Gerhard Wunch from Dresden University in 1975 [23]. According to him, each "brick" is presented by a raw consisting of five sets of variables *X, K, Y, R, T* and two functional transformations Φ, Ψ:

$$A = \{X, K, Y, R, T, \Phi, \Psi\}; \quad (1)$$

here X – a set of inputs I, K – a set of "brick's" internal states S, Y – a set of its outputs O, R – an independent space variable, and T – an independent time variable.

$$\Phi: X \times K \times R \times T \rightarrow K \quad (2)$$

and

$$\Psi: K \times R \times T \rightarrow Y \quad (3)$$

are the transformations of "brick's" internal states and the transformation of its outputs correspondingly (see figure 3). Here we mean that all dependent variables are functions of space and time coordinates: $X(\rho, t)$, $Y(\rho, t)$ and $K(\rho, t)$.

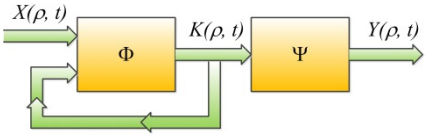


**Fig. 3.** Functional organization of the unified IHE element ("Lego brick")

Parameters ($X=\vec{\alpha}$) emitted by each element of the home environment (and by persons/IHE users as well), create conditions for a certain actions $Y = \vec{V}$ according to those Φ and Ψ. Any reasonable sequence of actions and their durations create one or several services $Y = \vec{V}$ . On the other hand a reasonable sequence of separate actions together with a set of services may be considered as IHE user's life scenario. A vector type symbolic structure producing $\vec{V}$ and $\vec{\Pi}$ is delivered in Figure 4.

Set of evolving and changing at a time scenarios actually is a "real life" in this IoT&S based IHE under MAS intellectics control. The intellectics itself for actions as well as for services are usually transferred from virtual "V and Π agencies" into corresponding Φ and Ψ software/hardware based entities as it is shown in Figure 4.

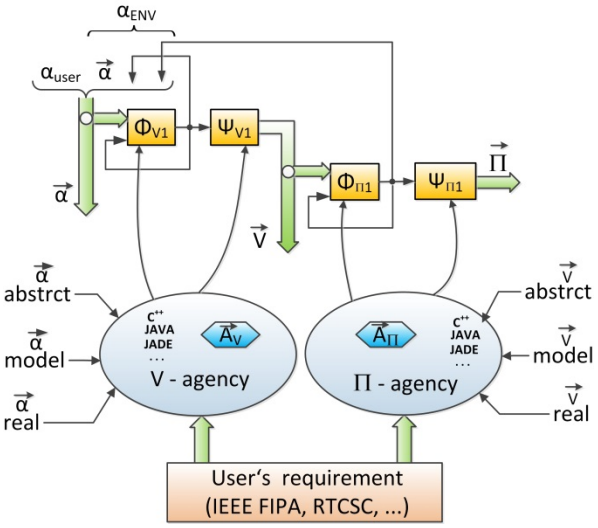


**Fig. 4.** A vector type symbolic structure producing V and Π

It must be emphasized that real agents' algorithms and machine codes are created and tested in corresponding "agencies" using abstract, model and/or real situations' descriptions (X) for the V-agents, and using abstract, model and/or real actions' descriptions (V) for the Π-agents. The activities of "V and Π agencies' " usually are organized according to the users' requirements and IEEE FIPA standards.

## 3 Intellectual Complex Systems Model Implementation

The generalized description of the whole IHE development process is presented in Figure 5. Usually the team (a), consisting of users, professional experts and IT people accumulate, discuss and prepare a set or requirements (b) to be formalized (c) in the design computer BIAcomp and presented in the form of a special type of user cases (UC) and systems functional requirements (FR) matrix (d) [2], [6], [8]. At the same time an analogous FRxUC matrix must be created, which serves as an information necessary to produce a virtual home environment (f) in the BIAsim where the user and IT people are able to model, visualize and simulate in 3D-coordinate system all effects and consequences of requirements' changes. The "tailor made, on a shelf ready" approach based software and hardware artefacts' prototypes for the smart home environment's intellectualization are selected from the data base (DB) and are transferred to the virtual multi agent system (MAS) (g) to be implemented in the real MAS (h) serving for the direct intellectualized smart home environment's control.

The approach based on the considerations that the IHE's practical development is similar to the hierarchical complex system's implementation leads to the following future steps: 1) top-down elaboration of the FRxUC matrix until we get the smallest

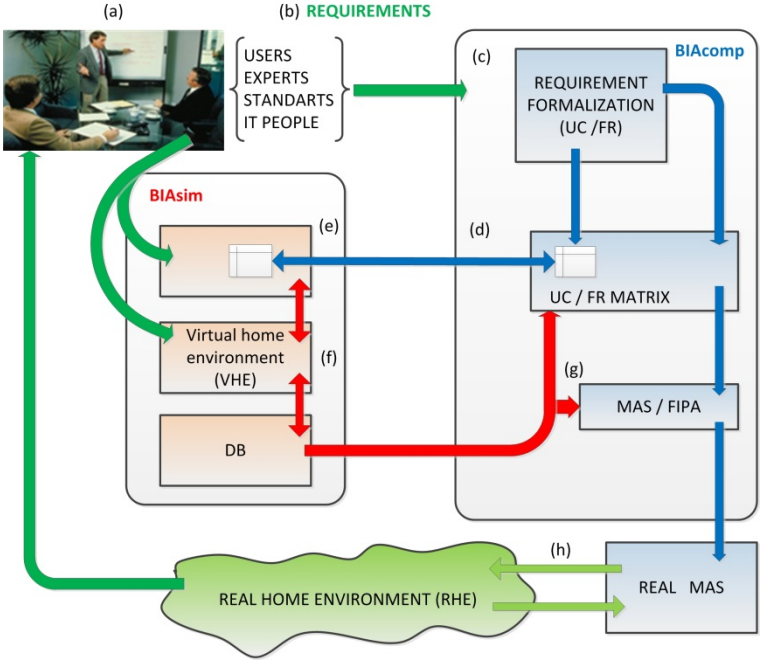


**Fig. 5.** IHE development process' block- diagram

"tailor made" software/hardware artefacts as "on a shelf ready" items to be transferred into corresponding agents; 2) the "agents community's" control actions, caused by the real life situations observed in the RHE, and the possible consequences of those actions, must be tested on-line in the VHE before they are supplied for the real activity.

Must be outlined that the information and knowledge obtained during the concrete real IHE design and implementation serves as a background for systems' multiplication and industrial producing of systems' components in a certain IT products' supply chain.

## 4 Experimental Simulation Results

Modeling and simulation of the simplified IHE under MAS control was performed at the Real Time Computer Systems Center of the Kaunas University of Technology. Four different intellectics technologies were used in systems' agents for situation analysis and decision making: NN (artificial neural network based), FL (fuzzy reasoning and fuzzy control based), LP (linear programming based) and BA (Bayes methodology based) technologies. They were used for a virtual IHE training, retraining (when suddenly any user changes his/her wishes or habits), and self training (when the system has no a priori information and learns from the observations of user's activity in the HE to be intellectualized). Block diagrams of a functional organization for all four cases are presented in Figure 6 (a, b, c, and d).

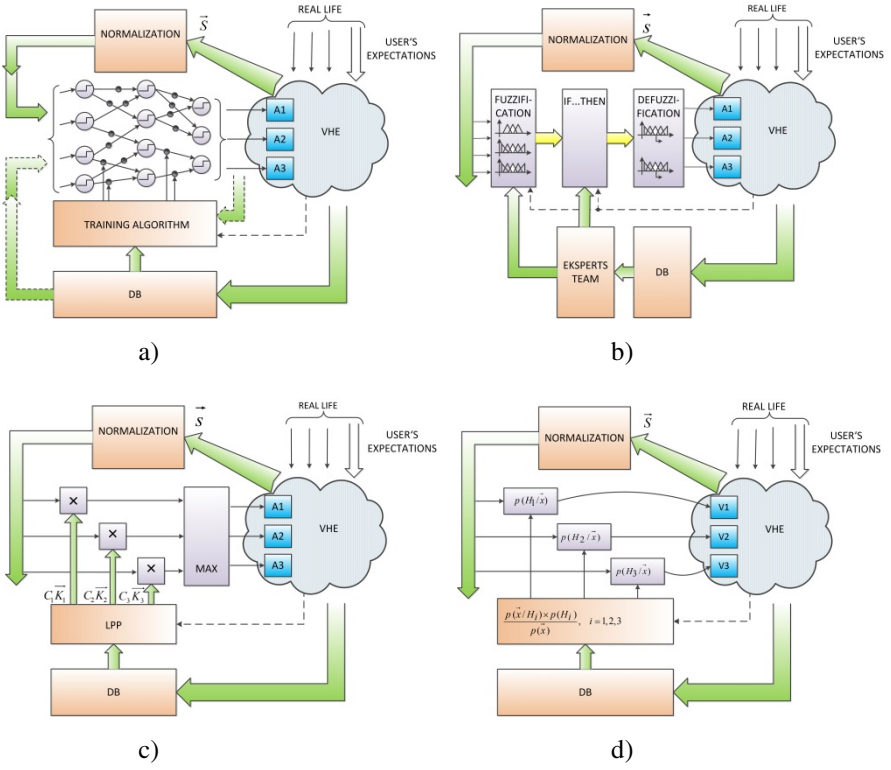


**Fig. 6.** IHE model's functional organization for NN, FL, LP and BA cases: a) NN_technology; b) FL_technology; c) LP_technology; d) BA_technology

Worth of mentioning that agents were able to increase, decrease and keep themselves out of any actions concerning certain parameters and characteristics under control according to the learned user's wishes and expectations.

All four technologies were tested according to the speed and data amount used for the action performance when:1) the training process takes place; 2) decision is made for action; 3) the retraining process takes place in two different regimes – when user's wishes change momentarily and when those changes are accumulated gradually; 4) when the intellectualized smart environment is under permanent observation starting "from zero information" (the self training regime) and obtains possibility to react adequately to the implicit user's wishes. The received simulation results were evaluated by eight independent decision making experts according to the 10 degree system. Their average evaluations are presented in the Table 1- before and Table 2 after the round up procedure.

**Table 1.** Expert evaluations before round up procedure

| | | NN | FL | LP | BA |
|---|---|---|---|---|---|
| Training process | | | | | |
| | Speed | 5,88 | 8 | 7,13 | 8,88 |
| | Space | 6,25 | 6,75 | 6,88 | 7,63 |
| | Σ | 6,06 | 7,38 | 7 | 8,25 |
| Decission making | | | | | |
| | Speed | 9 | 8,75 | 7,88 | 8,63 |
| | Space | 8,38 | 8,25 | 7,75 | 8,5 |
| | Σ | 8,69 | 8,5 | 7,81 | 8,56 |
| Retraining process | | | | | |
| (momentary wish) | | | | | |
| | Speed | 4,88 | 9,13 | 7,38 | 8,25 |
| | Space | 6,25 | 6,63 | 6 | 7,5 |
| | Σ | 5,56 | 7,88 | 6,69 | 7,88 |
| (weighted average wish) | | | | | |
| | Speed | 8 | 5,25 | 6,13 | 9 |
| | Space | 6,5 | 5,5 | 5,5 | 8,25 |
| | Σ | 7,25 | 5,38 | 5,81 | 8,63 |
| Self training process | | | | | |
| | Speed | 5,38 | 8,13 | 6,88 | 8,63 |
| | Space | 6,5 | 7,5 | 6,75 | 8 |
| | Σ | 5,94 | 7,81 | 6,81 | 8,31 |
| **Σ (speed)** | | **6,63** | **7,85** | **7,08** | **8,68** |
| **ΣΣ** | | **6,7** | **7,39** | **6,83** | **8,33** |

**Table 2.** Expert evaluations after round up procedure

| No. | Feature / characteristics | Evaluation | | | |
|---|---|---|---|---|---|
| | | **Type of DM- technology** | | | |
| | | **NN** | **FL** | **LP** | **BA** |
| 1 | Training process | | | | |
| | Speed | 6 | 8 | 7 | 9 |
| | Space | 6 | 7 | 7 | 8 |
| | Σ | 6 | 7 | 7 | 8 |
| 2 | Decission making | | | | |
| | Speed | 9 | 9 | 8 | 9 |
| | Space | 8 | 8 | 8 | 9 |
| | Σ | 9 | 9 | 8 | 9 |
| 3 | Retraining process | | | | |
| 3.1 | (momentary wish) | | | | |
| | Speed | 5 | 9 | 7 | 8 |
| | Space | 6 | 7 | 6 | 8 |
| | Σ | 6 | 8 | 7 | 8 |
| 3.2 | (weighted average wish) | | | | |
| | Speed | 8 | 5 | 6 | 9 |
| | Space | 7 | 6 | 6 | 8 |
| | Σ | 7 | 5 | 6 | 9 |
| 4 | Self training process | | | | |
| | Speed | 5 | 8 | 7 | 9 |
| | Space | 7 | 8 | 7 | 8 |
| | Σ | 6 | 8 | 7 | 8 |
| | **Σ (speed)** | **7** | **8** | **7** | **9** |
| | **ΣΣΣ** | **7** | **7** | **7** | **8** |

The Table 1 clearly shows that according to the average performance speed the preference must be given to the BA technology, but the total average summary (Table 2) confirms the opinion that all for technologies are approximately equal for the purpose under investigation.

The modeling and simulation confirmed a vitality of this approach and efficiency of the investigated MAS intellectics algorithms and technology.

The main research ideology was developed and implemented under guidance of the COST Action IC0702 „Combining Soft Computing Techniques and Statistical Methods to Improve Data Analysis Solutions (SOFTSTAT)“. The research itself was performed under support of two EU Structural Funds projects: a) VP1 - 3.1-ŠMM-08-K-01-018 “Research and Development of Internet Infrastructure for IoT& S in the Smart Environment (IDAPI)“, and b) VP1-3.1-ŠMM-10-V-02-020 "Research on Smart Home Environment and Development of Intelligent Technologies (BIATech)".

## 5 Concluding Remarks

As a matter of fact, we expect about 50 bn things and social services (IoT&SS) to be connected by 2030. We count on multi agent systems (MAS) as a sort of complex systems or „soft infrastructure“ for such systems. And in such a situation we face at least three approaching challenges.

*The first challenge*: we need standardized and documented procedures and recommendations how to create agent’s intellectics and how to implement it in a computerized environment. Shortly, we need world-wide standards.

*The second challenge*: we must decide, how we can cope with the three main problems accompanying the globalized approach of the IoT&SS complex systems such as:

1. Total emission of electromagnetic signals (RFID; EPC; ...) and peoples’ safety.
2. Who intends to control the centralized/decentralized assignment of names, IDs, tags and labels for things and services.
3. What sort of social and cultural values remain stable, or will be harmed, or intend to be newly developed, delivered and accepted.

*The third challenge*: we must discuss and decide, what sort of researchers (and what sort of people in general) does the EU (and our world in general) need to cope with the IoT&SS complex systems problems (the task for our universities).

And the answer is like this: THE COMPLEX SYSTEM SCIENCE is the essential 21st Century science. This new science is providing radical new way of understanding, modeling, predicting, managing the physical, biological, ecological, and social universe of the IoT&SS.

## References

1. History of the Internet of Things (postscapes.com/internet-of-things-history)
2. D1.1 - Requirements and Exploitation Strategy/BUTLER, ALBLF, No 287901, p. 178 (2012), http://www.iot-butler.eu
3. D3.2 Integrated System Architecture and Initial Pervasive BUTLER proof of concept/ BUTLER, ERC, No 287901, p. 191 (2013), http://www.iot-butler.eu
4. The IEEE Standards Association (IEEE-SA); Internet of Things (IoT) Workshop, November 5-6, Silicon Valley, Calif. (2013), http://sites.ieee.org/wf-iot/
5. IEEE World Forum on Internet of Things (WF-IoT); March 6-8, Seoul, Korea (2014), http://sites.ieee.org/wf-iot/

6. IERC - European Research Cluster on the Internet of Things, Future Network Technologies Research and Innovation in HORIZON2020, Consultation Workshop, June 29 2012, Brussels, Avenue de Beaulieu 25; Dr. Ovidiu Vermesan, Coordinator of IERC, Chief Scientist, SINTEF, Norway; Seventh Framework Programme, p. 54 (2012)
7. Internet of Things in 2020. A Roadmap For The Future Infso D.4Networked Enterprise & Rfid Infso G.2Micro &Nanosystem. In: Co-Operation With The Rfidworking Group Of The European Technology Platform On Smart Systems Integration (Eposs); 05, European Commission; Information Society and Media, p. 32 (September 2008)
8. Smith, I.G.: The Internet of Things 2012, New Horizons, Technical Editors: Ovidiu Vermesan Peter Friess Anthony Furness, p. 360. Platinum, Halifax (2012)
9. Future Network Technologies Research and Innovation in HORIZON2020, Consultation Workshop, June 29, Brussels, Avenue de Beaulieu 25 Dr. Ovidiu Vermesan, Coordinator of IERC Chief Scientist, SINTEF, Norway (2012), http://www.internet-of-things-research.eu
10. Wooldridge, M.: An Introduction to Multi-Agent Systems, p. 366. John Willey & Sons, ltd. (2008)
11. Shoham, Y., Tennenholtz, M.: On the emergence of social conversions: modeling, analysis, and simulations. Artificial Intelligence, 165–200 (1997)
12. Jennings, N.R., Sierra, C., Sonenberg, L., Tambe, M.: Proceedings of the Third International Joint Conference on Autonomous Agents and Multi Agent Systems. ACM Press, NY (2004)
13. Russel, S., Norvig, P.: Artificial Intelligence: A Modern Approach. Prentice Hall (2003)
14. Weiss, G., Sen, S.: Adaptation and Learning in Multiagent Systems. Springer, Berlin (1996)
15. Shoham, Y., Leyton-Brown, K.: Multiagent Systems: Algorithmic, Game-Theoretic, and Logical Foundations, p. 504. Cambridge University Press (2009)
16. Ferber, J.: Multi-agent systems; an introduction to distributed artificial intelligence, p. 509. Addison Wesley (1999)
17. Hayes-Roth, B., Brownston, L., van Gent, R.: Multiagent collaboration in direct improvisation. In: Proceedings of the First International Conference on Multi-Agent Systems, pp. 148–154. AAAI Press, Menlo Park (1995)
18. Dickinson, I.J.: Agent Standards. Living of the Vision HP Laboratories, Bristol, HPL-97-156, p. 8 (1997)
19. Vasseur, J.-P., Dunkels, A.: Interconnecting Smart Objects with IP - The Next Internet, p. 432. Morgan Kaufmann (2010)
20. Jasinevicius, R., Petrauskas, V.: On Fundamentals of Global Systems Control Science (GSCS). In: ISCS 2013: Interdisciplainary Symposium on Complex Systems, pp. 77–88. Springer (2014)
21. Sanayei, A.: Complexity as a Linguistic Variable. Complex Systems 20(3), 253–263 (2012)
22. Foundation For Intelligent Physical Agents, FIPA Ontology Service Specification, Geneva, Switzerland, p. 58. Foundation for Intelligent Physical Agents (2001), http://www.fipa.org/
23. Wunch, G.: Systemtheorie. Akademische Verlag-sgesellschaft Geest& Porting K.- G. Leipcig, p. 286 (1975)

# Desertification Transition in Semi-arid Ecosystems and Directed Percolation

Raffaele Corrado[1], Anna Maria Cherubini[2], and Cecilia Pennetta[2,3,⋆]

[1] PhD School on Climate Change Sciences, Università del Salento, I-73100 Lecce and Istituto di Scienze dell'Atmosfera e del Clima, CNR, I-73100 Lecce, Italy
[2] Dipartimento di Matematica e Fisica "Ennio De Giorgi", Università del Salento, I-73100 Lecce, Italy
[3] Istituto Nazionale di Fisica Nucleare (INFN), Italy
cecilia.pennetta@unisalento.it

**Abstract.** Regime shifts in ecosystems caused by climatic or anthropogenic factors can happen on a relatively short timescale with relevant economic and social effects, a consideration which motivates the large interest in the literature to this topic. A special case of regime shift is given by desertification transitions in semi-arid ecosystems. One desertification model, recently proposed, seems particularly effective in describing several ecological landscapes, taking into account different ecological mechanisms. This model simulates an ecosystem undergoing a desertification transition in term of a stochastic cellular automaton (SCA) subjected to a damage spreading (DS) transition. On the other hand, it is well known that many DS transitions belong to the directed percolation (DP) universality class under certain rather general conditions. Here we investigate the universality class of the SCA model and we identify the region of parameters space inside which it belongs to the DP class.

**Keywords:** Desertification, Percolation in phase transitions, Critical transitions, Complex biological systems.

## 1 Introduction

Climatic or anthropogenic factors can induce or accelerate the regime shift of an ecosystem [1, 2]. This kind of transitions often implies relevant economic and social effects, in particular when they occur on a relatively short timescale, a consideration which motivates the large interest in the literature to this topic [1–16]. An important case of regime shift is given by the desertification transition in arid or semi-arid ecosystems [1]. Concerning this transition, many efforts are devoted to the identification of early warning signals and early transition indicators [10–18]. Among the different approaches that have been proposed to study desertification processes [10–16], the model introduced by Kéfi et al. [15] seems particularly effective in describing several ecological landscapes, taking into account different ecological mechanisms [14, 15] and providing a good

⋆ Corresponding author.



A. Sanayei et al. (eds.), *ISCS 2014: Interdisciplinary Symposium on Complex Systems*, Emergence, Complexity and Computation 14, DOI: 10.1007/978-3-319-10759-2_11

starting point for the identification of early warning signals [10, 17, 18]. This model simulates an ecosystem undergoing a desertification transition in term of a stochastic cellular automaton (SCA) subjected to a damage spreading (DS) transition [19–24]. On the other hand, it is well known that many DS transitions belong to the directed percolation (DP) universality class under certain rather general conditions [20–23]. In fact, according to the so called Grassberger conjecture [23], short-range interacting systems undergoing continuous phase transition into an absorbing state, in absence of frozen disorder and without additional symmetries, belong to the DP class [20–23].

Actually for a wide region of the parameters space the SCA model of Kéfi et al. predicts continuous transitions into a state characterized by the complete extinction of vegetation (full desertification transition) [17, 25]. The model does not contain explicitly long-range interactions, frozen disorder or additional symmetries. However the critical exponents, $\beta$ and $\gamma'$, characterizing the approach to the extinction threshold respectively of the vegetation density and its variance, are found different from the DP values [17, 26] and strongly dependent on the model parameters [25]. So here we investigate the universality class of the SCA model and we identify the region of parameter space inside which it belongs to the DP class.

## 2 Model and Discussion

The desertification model of Kéfi et al. is a two-dimensional SCA [14, 15]. The ecosystem is modeled as a $L \times L$ square lattice, where the linear size of the lattice $L$ is multiple of the size of the elementary cell. Each cell can be found in three states: $\{+\}$ (cell covered by vegetation or living cell); $\{0\}$ (cell empty but colonizable or dead cell); $\{-\}$ (cell empty and degraded). A degraded cell cannot be colonized before recovering, i.e. moving first to the $\{0\}$ state. Similarly, also the reverse transition $\{+\} \to \{-\}$ is forbidden. The rates of the allowed transitions are:

$$W_{+0} = m \; . \tag{1}$$

$$W_{0+} = \left[\delta\rho_+ + (1-\delta)\, q_{+|0}\right](b - c\rho_+) \; . \tag{2}$$

$$W_{0-} = d \; . \tag{3}$$

$$W_{-0} = r + f q_{+|-} \; . \tag{4}$$

Equations (1), (2),(3) and (4) define respectively the rates of the *mortality, colonization, degradation* and *recovery* processes. The mortality parameter $m$ measures the strength of external stresses and is taken here as the control parameter of the transition. $\rho_+$ is the global vegetation mass fraction or living cells density (i.e. total number of living cells normalized to the total number of

lattice cells) and it plays the role of order parameter of the transition. $\rho_0$ and $\rho_-$ are the densities of $\{0\}$ and $\{-\}$ cells respectively ($\rho_+ + \rho_0 + \rho_- = 1$). $q_{i|j}$ is the fraction of first neighbors in the state $i$ around a cell in the state $j$ (the average of $q_{i|j}$ over all the pairs of cells gives the joint probability of finding a $\{i\}$-cell as a first neighbor of a $\{j\}$-cell). $\delta$ gives the fraction of seeds globally dispersed by wind, animals etc. $b$ is the colonization parameter, controlling several intrinsic properties of a vegetated cell, such as seed production rate, seed survival, germination and survival probabilities (intrinsic properties because $b$ accounts for these features without considering global competition effects among plants). The strength of competition effects is instead controlled by the parameter $c$. The parameter $d$, representing the rate of soil degradation, depends on the intrinsic soil characteristics, on climatics and/or anthropogenic factors. $f$ is the local facilitation parameter which describes positive local interactions among plants and between soil and plants. Finally, $r$ is the spontaneous regenerative rate of a degraded cell in absence of vegetation covering first neighbor cells.

The evolutions of the CA are obtained by numerical simulations with syncronous update of the states of all the lattice cells and by associating each iteration step with an elementary time step in an appropriate time-scale. Consequently, transition rates are expressed in arbitrary units. Periodic boundary conditions are used for the calculation of the transition rates at the boundaries. The initial configurations of the CA are taken corresponding to $\rho_+(t_0) = 0.5$, $\rho_0(t_0) = 0.2$, with random distribution of $\{+\}$ and $\{0\}$ cells. In the region of parameter space explored, the initial configuration do not affect the statistical properties of the stationary regime discussed here. The results reported below for $\langle \rho_+ \rangle$ and $\langle \Delta\rho_+^2 \rangle$ are obtained by averaging over the stationary portion of the time series, after the relaxation of the initial transient. The typical length of the time series was $1 \div 5 \times 10^4$ records. In the following we consider lattices of linear size $L = 100$. More details on the model can be found in [14, 15] and in [17]).

To clarify the relation of the SCA model with the DP universality class, we first have considered the question of the effective range of the interactions among the different cells. Differently from Eq. (4), which concerns the recovery process and allows only first-neighbor interactions, Eq. (2) which describes the colonization process includes two contributions dependent on the global density $\rho_+$. These contributions account for two different ecological mechanisms: seed dispersion (when $\delta \neq 0$) and competition among plants for global resources (when $c \neq 0$). Both these mechanisms are expected to act on a long or at least on an intermediate range of distances, even if they are described in Eq. (2) by the average quantity $\rho_+$, thus by adopting a sort of mean field approximation. To suppress these effects, keeping only strictly short-range interactions, we performed numerical simulations of the CA by taking $\delta = 0$ and $c = 0$. Figure 1 compares the two plots of $\langle \rho_+ \rangle$ as a function of $m$ obtained for $\delta = 0$ and $c = 0$ (blue circles) and $\delta = 0.1$ and $c = 0.3$ (green trianges). The values of the other parameters are: $b = 0.6$, $f = 0.9$, $d = 0.2$, $r = 0.0004$ in both cases. These values of the parameters have been chosen as reasonable values to simulate "real world" field data [14, 10]. Similarly, Fig. 2 compares the behavior of the variance $\langle \Delta\rho_+^2 \rangle$ vs.

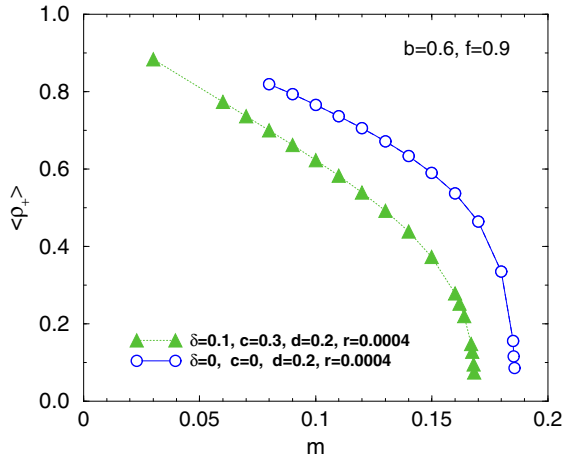


**Fig. 1.** Average density of the living cells $\langle \rho_+ \rangle$ vs. mortality rate $m$. The values of the other parameters are reported in the figure. Triangles and circles show the numerical data obtained respectively by including ($\delta \neq 0$ and $c \neq 0$) or not ($\delta = 0$ and $c = 0$) the effect of the living cell density on the colonization rate.

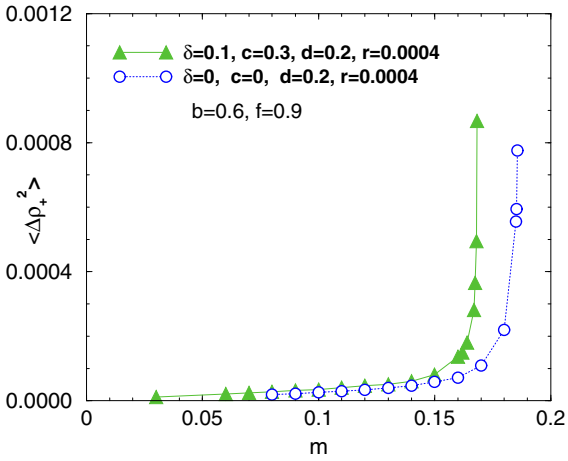


**Fig. 2.** Variance of the living cells density $\langle \Delta\rho_+^2 \rangle$ vs. mortality rate $m$. The values of the other parameters are reported in the figure. Triangles and circles show the data obtained respectively by including ($\delta \neq 0$ and $c \neq 0$) or not ($\delta = 0$ and $c = 0$) the effect of the living cell density on the colonization rate.

$m$ for the two sets of data. It must be noted that the variance sharply increases in both cases, approaching the critical value of mortality rate $m_c$ associated with the full extinction of the vegetation, i.e. the threshold value of $m$ above which $\langle \rho_+ \rangle = 0$ [17]. Actually, the rise in the variance of the vegetation density provides a well recognized indicator of the desertification transition [3, 10, 17]. It must also be remarked that competitive effects, which limit the colonization process, accelerate the vegetation extinction, lowering the critical threshold $m_c$ from $0.1860 \pm 0.0001$ to $0.1685 \pm 0.0001$ (Figs. 1 and 2).

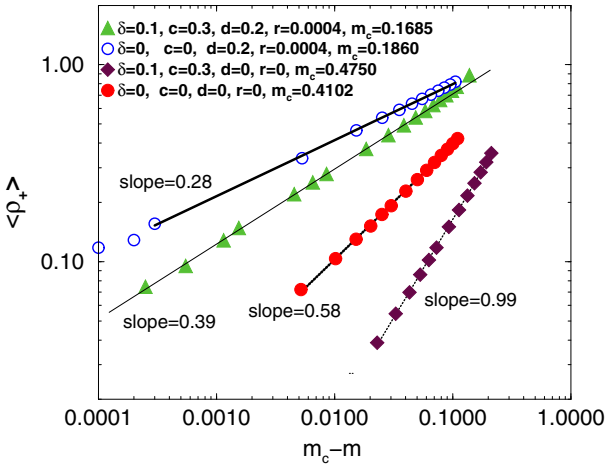


**Fig. 3.** Log-Log plot of the average density of living cells $\langle \rho_+ \rangle$ vs. $|m - m_c|$. The values of the parameters are reported in the figure together with the corresponding values of the critical mortality $m_c$. The two upper curves correspond to $d \neq 0$: triangles and open circles are obtained respectively by including ($\delta \neq 0$ and $c \neq 0$) or not ($\delta = 0$ and $c = 0$) the effect of the living cell density on the colonization rate. The two lower curves show the behavior for $d = 0$: diamonds are obtained for $\delta \neq 0$ and $c \neq 0$ and full circles for $\delta = 0$ and $c = 0$. The straight lines are the best-fit with power laws.

Figure 3 displays on a double logarithmic scale the same $\langle \rho_+ \rangle$ data sets of Fig. 1 as a function of $|m - m_c|$. The straight lines are the best-fit with power laws of exponent $\beta = 0.28 \pm 0.01$ (for $\delta = 0$ and $c = 0$) and $\beta = 0.39 \pm 0.01$ (for $\delta = 0.1$ and $c = 0.3$), where $\beta$ is the critical exponent characterizing the scaling of the average living cell density when the system approaches the mortality threshold:

$$\langle \rho_+ \rangle = C_\rho |m - m_c|^\beta \ . \tag{5}$$

The double logarithmic plot of the variance (same data of Fig. 2) as a function of $|1 - m_c/m|$ is shown in Fig. 4. The straight lines are the best-fit with power laws of slope $-0.59 \pm 0.01$ (for $\delta = 0$ and $c = 0$) and $-0.50 \pm 0.01$ (for $\delta = 0.1$ and $c = 0.3$). Thus the variance can be written as:

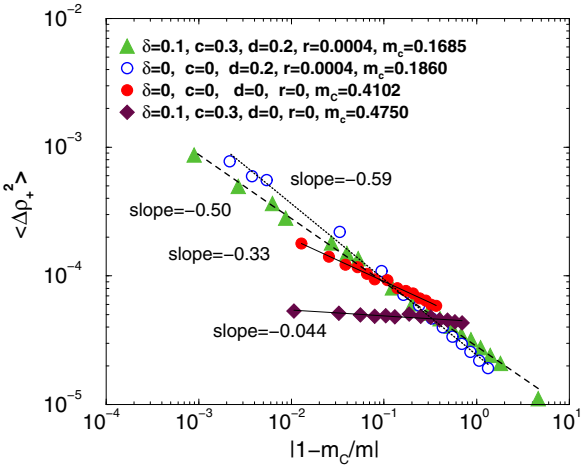


**Fig. 4.** Log-Log plot of the variance $\langle \Delta\rho_+^2 \rangle$ vs. $|1 - m_c/m|$. The values of the parameters are reported in the figure together with the corresponding values of the critical mortality $m_c$. Triangles and open circles show the data obtained for $d \neq 0$. Precisely: triangles correspond to $\delta \neq 0$ and $c \neq 0$ and open circles to $\delta = 0$ and $c = 0$. Diamonds and full circles show the behavior for $d = 0$. Diamonds: $\delta \neq 0$ and $c \neq 0$; full circles: $\delta = 0$ and $c = 0$. The straight lines are the best-fit with power laws.

$$\langle \Delta\rho_+^2 \rangle = C_\Delta \left| 1 - \frac{m_c}{m} \right|^{-\gamma'} . \tag{6}$$

where $\gamma'$ is the critical exponent of the variance. Therefore, the values of $\beta$ and $\gamma'$ obtained for $\delta = 0$ and $c = 0$, strongly differ from the values reported in the literature [20–22, 26] for the corresponding critical exponents of the DP class in 2D systems: $\beta_{DP} = 0.583 \div 0.584$ and $\gamma'_{DP} = 0.30 \div 0.35$. In spite of the suppression of the $\rho_+$ dependent terms in the expression of the colonization rate, Eq. (2), which explicitely limits the range of interactions to first neighbors only, the SCA desertification model does not belong to the DP class.

On the other hand, it should be noted that numerical simulations [25] have proved the independence of both $\beta$ and $\gamma'$ from the value of the facilitation parameter $f$ associated with short-range interactions. Similarly, we expect that when $\delta = 0$ and $c = 0$, the exponents $\beta$ and $\gamma'$ would be independent also of $b$, intrinsic colonization parameter. In other terms, we expect that when the evolution of the CA is controlled uniquely by short-range interactions, the only parameters controlling the universality class of the model are $d$ and $r$, as we discuss below. For contrast, when $\delta \neq 0$ and $c \neq 0$, the model provides non universal exponents, depending not only on $d$ and $r$ but also on $\delta$, $c$, $b$ (which determine the interplay between short and long-range interactions).

Actually, the model under consideration is a three states CA. However dead cells are mainly confined to the interface between living and degraded cells [17]. Therefore, approaching the desertification transition, dead cells essentially represent the

perimeter of the living cell clusters embedded in the "sea" of degraded cells. As a consequence, close to the transition, when living cell clusters are few and small, degraded cells dominate. The absorbing state, over the threshold $m_c$, is characterized by: $\rho_+ = 0$ and $\langle \rho_- \rangle >> \langle \rho_0 \rangle$. However, in general $\langle \rho_0 \rangle \neq 0$. In fact, according to Eq. (4), even when $\rho_+ = 0$ and $q_{+|-} = 0$, there is a spontaneous recovery probability if $r \neq 0$. After the complete vegetation extinction, the system reaches an absorbing state which is not completely frozen but which corresponds to a two state CA, characterized by purely random (white noise) fluctuations of the number of degraded cells: $\{0\} \leftrightarrow \{-\}$. In particular, over the vegetation extinction threshold, $\langle \rho_- \rangle$ and $\langle \rho_0 \rangle$ depend only on the degradation and recovery rates:

$$\langle \rho_0 \rangle = \frac{r}{r+d} \quad ; \quad \langle \rho_- \rangle = \frac{d}{r+d} \tag{7}$$

Thus a single frozen absorbing state exists only when: i) $r = 0$ and $d \neq 0$ (the absorbing state is a completely degraded lattice); ii) $d = 0$ and $r \neq 0$ (the absorbing state is an empty lattice); iii) $r = 0$ and $d = 0$. The last two conditions actually define a *two* states CA with only $\{+\}$ and $\{0\}$ cells (it should be noted that when $d = 0$ and $\rho_+(t_0) \neq 0$, even if there is an initial non zero concentration of degraded cells, the stationary state of the lattice contains only $\{+\}$ and $\{0\}$ cells, as a consequence of Eq. (4)). In all the three cases, the critical exponents are expected to be the same of the directed percolation in 2D, at least when only short-range interactions are present. Figures 3 and 4 respectively display $\langle \rho_+ \rangle$ and its variance $\langle \Delta \rho_+^2 \rangle$ calculated by taking: $\delta = 0$, $c = 0$, $d = 0$, $r = 0$ and $\delta = 0.1$, $c = 0.3$, $d = 0$, $r = 0$. Both curves are obtained by considering $b = 0.6$ and $f = 0.9$ (when $c = 0$ and $d = 0$, $f$ only determines the relaxation time to achieve the stationary state of the two states CA). The first set of parameter values actually provides $\beta = 0.58 \pm 0.01$ and $\gamma' = 0.33 \pm 0.01$, in good agreement with the values reported in the literature for the DP universality class. On the contrary, the second set of parameters gives $\beta = 0.99 \pm 0.01$ and $\gamma' = 0.044 \pm 0.001$.

## 3 Conclusions

Among the different approaches that have been proposed to study desertification processes, the model introduced by Kéfi et al. [15] seems particularly effective in describing several ecological landscapes, taking into account different ecological mechanisms [14, 15] and providing a good starting point for the identification of early warning signals [10, 17, 18]. This model simulates an ecosystem undergoing a desertification transition in term of a SCA subjected to a damage spreading transition [19–24]. Here we have investigated the universality class of the SCA model, looking for its relation with the directed percolation [20–23]. The results of our numerical simulations show that two features of the SCA desertification model are responsible of its non universal critical behavior and deviation from the DP class: the presence of the $\rho_+$ dependent terms in the colonization rate, which destroy the requirement of short-range interactions, and the existence of a not frozen absorbing state when $d \neq 0$ and $r \neq 0$.

Our results, clarifying some features of the SCA model and in particular the behavior of its critical exponents can help the research of early indicators of the desertification transition. In particular, since the rise in the variance of the vegetation density is a well recognized indicator of the desertification transition [3, 10, 17] and the steepness of this rise is determined by $\gamma'$, the study of the relative impact of the different ecological factors (rates of colonization, facilitation, degradation, etc.) on the critical exponent of the variance is of help to identify the most relevant actions which can contrast desertification phenomena.

**Acknowledgments.** A.M.C. thanks the members of the Dynamical Systems Group (DynamIC) at the Department of Mathematics of Imperical College London for friendly collaboration during her academic visit, R.C. acknowledges the support from the Euro-Mediterranean Center on Climate Change (CMCC). The authors thank Profs. Nadav Shenrb and Haim Weissmann (Department of Physics, Bar-Ilan University) for stimulating comments.

## References

1. Reynolds, J.F., Stafford Smith, D.M., Lambin, E.F., Turner II, B.L., Mortimore, M., Batterbury, S.P.J., Downing, T.E., Dowlatabadi, H., Fernández, R.J., Herrick, J.E., Huber-Sannwald, E., Jiang, H., Leemans, R., Lynam, T., Maestre, F.T., Ayarza, M., Walker, B.: Global desertification: building a science for dryland development. Science 316, 847–851 (2007)
2. Rietkerk, M., Dekeer, S.C., de. Ruiter, P.C., van de Koppel, J.: Self-organized patchiness and catastrophic shifts in ecosystems. Science 305, 1926–1929 (2004)
3. Carpenter, S.R., Brock, W.A.: Rising variance: a leading indicator of ecological transition. Ecology Lett. 9, 311–318 (2006)
4. Dakos, V., Scheffer, M., van Nes, E.H., Brovkin, V., Petoukhov, V., Held, H.: Slowing down as an early warning signal for abroupt climate change. PNAS 105, 14308–14312 (2008)
5. Scheffer, M., Bascompte, J., Brock, W.A., Brovkin, V., Carpenter, S.R., Dakos, V., Held, H., van Nes, E.H., Rietkerk, M., Sugihara, G.: Early-warning signals for critical transitions. Nature 461, 53–59 (2009)
6. Asner, G.P., Knapp, D.E., Balaji, A., Páez-Acosta, G.: Automated mapping of tropical deforestation and forest degration: CLASlite. J. of Appl. Remote Sensing 3, 033543-1–13 (2009)
7. Donangelo, R., Fort, H., Dakos, V., Scheffer, M., van Nes, E.H.: Early warnings for catastrophic shifts in ecosystems: comparison between spatial and temporal indicators. Int. J. of Bifurcation and Chaos 20, 315–321 (2010)
8. Dakos, V., van Nes, E.H., Donangelo, R., Fort, H., Scheffer, M.: Spatial correlation as leading indicator of catastrophic shifts. Theor. Ecol. 3, 163–174 (2010)
9. Dahlin, K.M., Asner, G.P., Field, C.B.: Environmental and community controls on plant canopy chemistry in a Mediterranean-type ecosystem. Procs. Nat. Ac. of Science 110, 6895–6900 (2013)
10. Kéfi, S., Guttal, V., Brock, W.A., Carpenter, S.R., Ellison, A.M., Livina, V.N., Seekell, D.A., Scheffer, M., van Nes, E.H., Dakos, V.: Early warnings signals of ecological transitions: methods for spatial patterns. PLoS One 9, e41010 (2012)

11. von Hardenberg, J., Meron, E., Shachak, M., Zarmi, Y.: Diversity of vegetation patterns and desertification. Phys. Rev. Lett. 87, 198101–198104 (2001)
12. Rietkerk, M., Boerlijst, M.C., van Langvelde, F., HilleRis Lambers, R., van de Koppel, J., et al.: Self-organization of vegetation in arid ecosystems. American Naturalist 160, 524–530 (2002)
13. Shnerb, N.M., Sarah, P., Lavee, H., Solomon, S.: Reactive glass and vegetation patterns. Phys. Rev. Lett. 90, 038101–1–4 (2003)
14. Kéfi, S., Rietkerk, M., Alados, C.L., Pueyo, Y., Papanastasis, V.P., ElAich, A., de Ruiter, P.C.: Spatial vegetation patterns and imminent desertification in Mediterranean arid ecosystems. Nature 449, 213–217 (2007)
15. Kéfi, S., Rietkerk, M., van Baalen, M., Loreau, M.: Local facilitation, bistability and transitions in arid ecosystems. Theor. Popul. Biolog 71, 367–379 (2007)
16. Scanlon, T.M., Caylor, K.K., Levin, S.A., Rodriguez-Iturbe, I.: Positive feedbacks promote power-law clustering of Kalahari vegetation. Nature 449, 209–212 (2007)
17. Corrado, R., Cherubini, A.M., Pennetta, C.: Early warning signals of desertification transitions in semi-arid ecosystems (submitted for publication)
18. Corrado, R., Cherubini, A.M., Pennetta, C.: Signals of Critical Transitions in Ecosystems Associated with Fluctuations of Spatial Patterns. In: 22nd Int. Conf. Noise and Fluctuations (ICNF), pp. 1–4. IEEE Press, New York (2013)
19. Ilachinski, A.: Cellular Automata, a Discrete Universe. World Scientific, Singapore (2002)
20. Henkel, M., Hinrichsen, H., Lũbeck, S.: Non-Equilibrium Phase Transitions. Springer, Berlin (2008)
21. Ódor, G.: Universality classes in nonequilibrium lattice systems. Review of Modern Physics 76, 663–724 (2004)
22. Hinrichsen, H.: Non-equilibrium critical phenomena and phase transitions into absorbing states. Advances in Phys. 49, 815–958 (2000)
23. Grassberger, P.: Are damage spreading transitions generically in the universality class of directed percolation. Journ. Stat. Phys. 79, 13–23 (1995)
24. Bagnoli, F.: On damage spreading transitions. Journal Stat. Phys. 85, 151–164 (1996)
25. Corrado, R., Cherubini, A.M., Pennetta, C.: Critical Desertification Transition in Semi-Arid Ecosystems: The Role of Local Facilitation and Colonization Rate (submitted for publication)
26. Munoz, M.A., Dickman, R., Vespignani, A., Zapperi, S.: Avalanche and spreading exponents in systems with absorbing states. Phys. Review E 59, 6175–6179 (1999)

# Lognormality Observed for Additive Processes: Application to Turbulence

Hideaki Mouri

Meteorological Research Institute, Nagamine, Tsukuba 305-0052, Japan

**Abstract.** The lognormal distribution has been observed across the natural and social sciences. It is always ascribed to a multiplicative process, i.e., a product of random variables, or equivalently to nonlinearity of the system, which always appears to be complex. However, we find that the lognormal distribution is also observable for a sum of random variables, i.e., an additive process in a linear system. The application is shown for large-scale fluctuations of fluid turbulence.

**Keywords:** statistical description of complex systems.

## 1 Introduction

If the logarithm of a positive random variable $z > 0$ is Gaussian, $z$ is said to obey a lognormal distribution, which has been observed across the natural and social sciences [1]. The current paradigm is that any lognormality is caused by a multiplicative process [2], i.e., a product of random variables $\prod_{n=1}^{N} z_n$. Its logarithm is a sum of random variables $\sum_{n=1}^{N} \ln z_n$. This tends to a Gaussian distribution as $N \to \infty$, according to the central limit theorem [3], if the summands have finite variances, if none of them dominates the others, and also if they do not so depend on one another. As a result, $\prod_{n=1}^{N} z_n$ tends to a lognormal distribution. The multiplicative process is in turn ascribed to some nonlinearity of the system, which always appears to be complex.

However, for a class of positive random variables, we find that the sum tends faster to a lognormal distribution [4]. While the sum tends eventually to a Gaussian distribution, the distribution of the sum is close to a lognormal distribution rather than to any Gaussian distribution so far as the number of the summands is large enough. Thus, the lognormal distribution is also observable for a sum, i.e., an additive process in a linear system that consists of independent subsystems. We discuss the condition for such a sum [4], an analytical example [4], and the application to large-scale fluctuations of fluid turbulence [5].

## 2 Condition for Additive Processes

To study an additive process, we consider an average of positive random variables $z_n > 0$,

$$\bar{z}_N = \frac{1}{N} \sum_{n=1}^{N} z_n \ . \tag{1a}$$



A. Sanayei et al. (eds.), *ISCS 2014: Interdisciplinary Symposium on Complex Systems*, Emergence, Complexity and Computation 14, DOI: 10.1007/978-3-319-10759-2_12

Instead of moments $\langle z^m \rangle$, we use cumulants $\langle z^m \rangle_\kappa$. They are $\langle z^2 \rangle_\kappa = \langle (z - \langle z \rangle)^2 \rangle$, $\langle z^3 \rangle_\kappa = \langle (z - \langle z \rangle)^3 \rangle$, $\langle z^4 \rangle_\kappa = \langle (z - \langle z \rangle)^4 \rangle - 3 \langle (z - \langle z \rangle)^2 \rangle^2$, and so on [3]. The cumulant for $m = 2$ is the variance.

We explain the central limit theorem in a simple form, by assuming that the variables $z_n$ are independent and identically distributed with the distribution of some variable $z_*$. Its cumulants are all assumed to be finite. These assumptions lead to $\langle \bar{z}_N^m \rangle_\kappa = \sum_{n=1}^N \langle z_n^m \rangle_\kappa / N^m = \langle z_*^m \rangle_\kappa / N^{m-1}$. The skewness and kurtosis of $\bar{z}_N$ are obtained as

$$\frac{\langle \bar{z}_N^3 \rangle_\kappa}{\langle \bar{z}_N^2 \rangle_\kappa^{1.5}} = \frac{1}{N^{0.5}} \frac{\langle z_*^3 \rangle_\kappa}{\langle z_*^2 \rangle_\kappa^{1.5}} \quad \text{and} \quad \frac{\langle \bar{z}_N^4 \rangle_\kappa}{\langle \bar{z}_N^2 \rangle_\kappa^2} = \frac{1}{N} \frac{\langle z_*^4 \rangle_\kappa}{\langle z_*^2 \rangle_\kappa^2} \ . \tag{1b}$$

With an increase in $N$, they decay to the Gaussian value of 0. A faster decay to this value is found for $\langle \bar{z}_N^m \rangle_\kappa / \langle \bar{z}_N^2 \rangle_\kappa^{m/2} \propto 1/N^{m/2-1}$ at $m \geq 5$. Thus, $\bar{z}_N$ tends to a Gaussian distribution.

The central limit theorem is approximate in that it ignores the tails of the distribution at deviations of $\bar{z}_N$ from $\langle \bar{z}_N \rangle$ that are larger than several of $\langle \bar{z}_N^2 \rangle_\kappa^{0.5}$. It is still a practical approximation because those tails are not exactly determined in any actual observation. Also, in any actual system, $N$ is not infinite. We define that $\bar{z}_N$ is observed to be Gaussian, irrespective of its exact distribution, if its skewness and kurtosis are close enough to 0.

We regard the additive process (1a) as if it were multiplicative. By ignoring large deviations of $z_n$ from $\langle z_n \rangle$, the arithmetic average of $z_n$ is approximated as a geometric average, $\sum_{n=1}^N z_n / N \simeq (\prod_{n=1}^N z_n)^{1/N}$. Then,

$$\bar{z}_N \simeq \left( \prod_{n=1}^N z_n \right)^{1/N} \quad \text{and} \quad \ln \bar{z}_N \simeq \frac{1}{N} \sum_{n=1}^N \ln z_n \ . \tag{2a}$$

The above approximation is used at large $N$ as an exact relation. We do expect the exactness in the limit $N \to \infty$ if $z_n$ is distributed within a finite range. The skewness and kurtosis of $\ln \bar{z}_N$ are

$$\frac{\langle (\ln \bar{z}_N)^3 \rangle_\kappa}{\langle (\ln \bar{z}_N)^2 \rangle_\kappa^{1.5}} = \frac{1}{N^{0.5}} \frac{\langle (\ln z_*)^3 \rangle_\kappa}{\langle (\ln z_*)^2 \rangle_\kappa^{1.5}} \quad \text{and} \quad \frac{\langle (\ln \bar{z}_N)^4 \rangle_\kappa}{\langle (\ln \bar{z}_N)^2 \rangle_\kappa^2} = \frac{1}{N} \frac{\langle (\ln z_*)^4 \rangle_\kappa}{\langle (\ln z_*)^2 \rangle_\kappa^2} \ . \tag{2b}$$

With an increase in $N$, they decay to the Gaussian value of 0. Thus, although $\bar{z}_N$ is observed to become Gaussian, $\bar{z}_N$ is also observed to become lognormal. The large deviations ignored to observe the lognormal distribution are not always the same as those ignored to observe the Gaussian distribution.

For $\bar{z}_N$ to tend to a lognormal distribution faster than to any Gaussian distribution, a necessary condition is obtained as

$$\left| \frac{\langle (\ln z_*)^3 \rangle_\kappa}{\langle (\ln z_*)^2 \rangle_\kappa^{1.5}} \right| < \left| \frac{\langle z_*^3 \rangle_\kappa}{\langle z_*^2 \rangle_\kappa^{1.5}} \right| \quad \text{and} \quad \left| \frac{\langle (\ln z_*)^4 \rangle_\kappa}{\langle (\ln z_*)^2 \rangle_\kappa^2} \right| < \left| \frac{\langle z_*^4 \rangle_\kappa}{\langle z_*^2 \rangle_\kappa^2} \right| \ . \tag{3}$$

This is also a practically sufficient condition, which implies that $\bar{z}_N$ at large $N$ is observed to be lognormal rather than to be Gaussian so far as the observation is based on the skewness and kurtosis as defined above. Since the condition (3) is not strict, it would hold for a wide class of positive random variables.

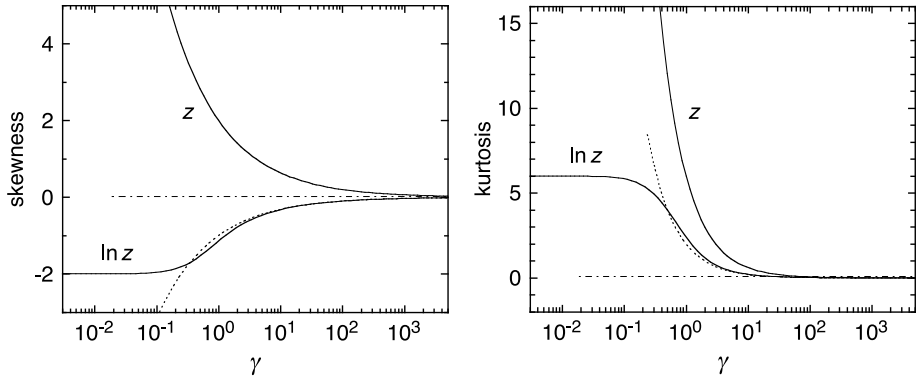


**Fig. 1.** Skewness and kurtosis of $z$ and of $\ln z$ as a function of $\gamma$ for the gamma distribution (4a). The dotted curves are the asymptotes (4c). The dot-dashed lines stand for the Gaussian value of 0.

## 3 Example: Gamma Distribution

We discuss the gamma distribution of a positive random variable $z > 0$ [3] as an example to observe the lognormality for an additive process. Its probability density is

$$f(z) = \frac{1}{\Gamma(\gamma)} z^{\gamma-1} \exp(-z) \ . \tag{4a}$$

Here $\Gamma$ is the gamma function. The parameter $\gamma > 0$ determines the shape of the distribution. While $\gamma = 1/2$ is for the distribution of the square of a zero-mean Gaussian random variable, $\gamma = 1$ is for an exponential distribution.

Since the cumulant of $z$ is $\langle z^m \rangle_\kappa = \gamma(m-1)!$, its skewness and kurtosis are obtained as

$$\frac{\langle z^3 \rangle_\kappa}{\langle z^2 \rangle_\kappa^{1.5}} = \frac{2}{\gamma^{0.5}} \quad \text{and} \quad \frac{\langle z^4 \rangle_\kappa}{\langle z^2 \rangle_\kappa^2} = \frac{6}{\gamma} \ . \tag{4b}$$

The cumulant of $\ln z$ is written as $\langle (\ln z)^m \rangle_\kappa = d^m \ln \langle \exp(i\xi \ln z) \rangle / d(i\xi)^m |_{\xi=0} = d^m \ln \Gamma(\gamma) / d\gamma^m$ [3]. This is a poly-gamma function. From its asymptote for $\gamma \to \infty$ [6], we find $\langle (\ln z)^m \rangle_\kappa \to (-1)^m (m-2)! / \gamma^{m-1}$ at $m \geq 2$. The skewness and kurtosis of $\ln z$ are

$$\frac{\langle (\ln z)^3 \rangle_\kappa}{\langle (\ln z)^2 \rangle_\kappa^{1.5}} \to -\frac{1}{\gamma^{0.5}} \quad \text{and} \quad \frac{\langle (\ln z)^4 \rangle_\kappa}{\langle (\ln z)^2 \rangle_\kappa^2} \to \frac{2}{\gamma} \quad \text{as} \quad \gamma \to \infty \ . \tag{4c}$$

These are good approximations for $\gamma \gtrsim 10^0$ as shown by dotted and solid curves in Fig. 1.

The gamma distribution is reproductive [3]. Recall the additive process (1a) for independent random variables $z_n$. If each of them obeys a gamma distribution for $\gamma = \gamma_*$, the sum $\sum_{n=1}^N z_n$ obeys a gamma distribution for $\gamma = N\gamma_*$. The distribution of the average $\bar{z}_N = \sum_{n=1}^N z_n / N$ has the same shape.

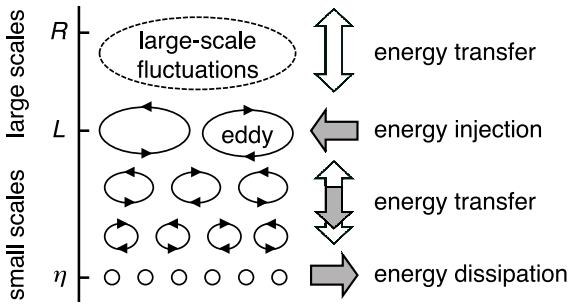


**Fig. 2.** Energy budget in three-dimensional turbulence. The open arrows are the local and instantaneous energy transfer. The filled arrows are the mean energy transfer along with the energy injection and dissipation.

With an increase in $N = \gamma/\gamma_*$, we find that $\langle(\ln \bar{z}_N)^m\rangle_\kappa / \langle(\ln \bar{z}_N)^2\rangle_\kappa^{m/2}$ at $m \geq 3$ decays to the Gaussian value of 0 faster than $\langle \bar{z}_N^m\rangle_\kappa / \langle \bar{z}_N^2\rangle_\kappa^{m/2}$ by a factor of $m-1$ in units of $N^{m/2-1}$. In particular, the skewness and kurtosis of $\ln \bar{z}_N$ decay faster than those of $\bar{z}_N$ by factors of 2 and 3. Thus, $\bar{z}_N$ tends to a lognormal distribution faster than to any Gaussian distribution. If $N$ is large, $\bar{z}_N$ is observed to be lognormal on the basis of our definition. The condition (3) actually holds for any value of $\gamma_* > 0$ in Fig. 1.

The gamma distribution is caused by many processes. We accordingly expect that it explains at least some of the observations of the lognormality in terms of the additive process. For example, the duration $\tau$ of an event of a complex system is often observed to be lognormal [1], which could be reproduced by a series of subevents, $\sum_{n=1}^{N} \tau_n$, if each of them is exponential, $f(\tau_n) \propto \exp(-\tau_n/\tau_*)$, or equivalently obeys the gamma distribution for $\gamma_* = 1$.

## 4 Application: Fluid Turbulence

The kinetic energy of turbulence is injected at some length scale $L$. As sketched in Fig. 2, if the turbulence is three dimensional, the energy is on average transferred to smaller and smaller scales because it is eventually dissipated into heat at the smallest scale of the Kolmogorov length $\eta$. This is known as the energy cascade [7]. However, locally and instantaneously, the energy is transferred to the larger scales as well as to the smaller scales. As a result, it is transferred to scales much larger than $L$ and cause fluctuations there [8]. The presence of such large-scale fluctuations was pointed out for the first time by L.D. Landau [9].

If the turbulence is homogeneous, any spatial correlation is negligible at the large scales. The kinetic energy there is additive. Its value for a large-scale region is the sum of its values for the yet large-scale subregions that are not correlated at all. This situation is in contrast to the situation of small-scale motions, which are correlated, multiplicative, and thus typical of complex systems [7]. We are to

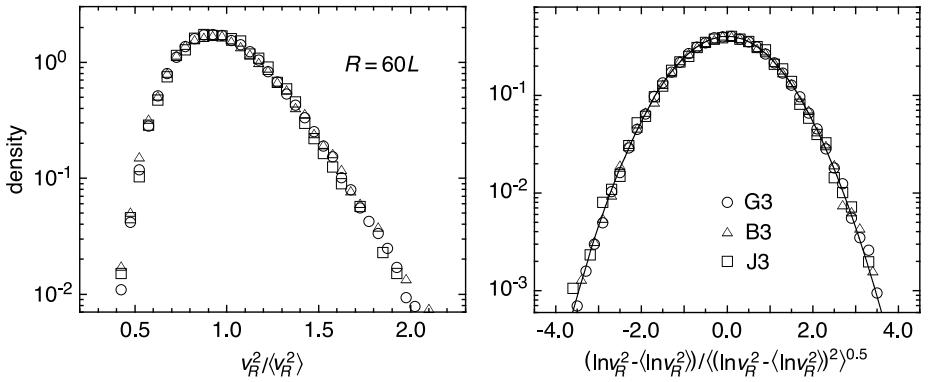


**Fig. 3.** Probability densities of $\bar{v}_R^2/\langle \bar{v}_R^2 \rangle$ and of $(\ln \bar{v}_R^2 - \langle \ln \bar{v}_R^2 \rangle)/\langle (\ln \bar{v}_R^2 - \langle \ln \bar{v}_R^2 \rangle)^2 \rangle^{0.5}$ at $R = 60L$ for the data of a flow of grid turbulence G3 (*circles*), a turbulent boundary layer B3 (*triangles*), and a turbulent jet J3 (*squares*) taken from our past experiments [8]. The solid curve stands for the Gaussian distribution.

demonstrate that the energy is fluctuating at those large scales in a lognormal distribution.

Consider that a velocity component $v(x)$ is obtained along a one-dimensional section $x$ of the three-dimensional space, as is usual in experiments of turbulent flows. The average $\langle v \rangle$ is subtracted to have $\langle v \rangle = 0$. As an estimate of the scale $L$ of the energy injection, we use the correlation length of the energy $v^2$ [8]:

$$L = \frac{\int_0^\infty \langle [v^2(x+r) - \langle v^2 \rangle][v^2(x) - \langle v^2 \rangle] \rangle \, dr}{2\langle v^2 \rangle^2} \quad . \tag{5a}$$

The one-dimensional section is divided into segments with length $R$. For each segment, the energy $v^2$ is coarse-grained as

$$\bar{v}_R^2(x_*) = \frac{1}{R} \int_{-R/2}^{+R/2} v^2(x_* + x) \, dx \quad . \tag{5b}$$

This corresponds to the additive process (1a) in case of $R \gg L$, where the correlations of $v^2$ are negligible. The segment serves as a linear system that consists of independent subsegments. In each of them, we regard $v^2$ as a constant. Since $v$ is closely Gaussian, the distribution of $v^2$ is close to the gamma distribution (4a) for $\gamma = 1/2$. It satisfies the condition (3) for a lognormal distribution of $\bar{v}_R^2$ to be observable among the segments.

Figure 3 shows the distributions of $\bar{v}_R^2$ and of $\ln \bar{v}_R^2$ at large $R$ for the data of some different flows of turbulence taken from our past experiments in a wind tunnel [8]. They are consistent with the lognormal distribution of $\bar{v}_R^2$. Since the data points for the different flows collapse into single curves, it would be possible to formulate a theory of large-scale fluctuations that is also applicable to random fields other than those of turbulence [4,8].

## 5 Conclusion and Prospects

The central limit theorem says that a sum of random variables is observed to become Gaussian with an increase in the number of the variables, if we ignore too large deviations of the sum from its average [3]. However, also if the variables satisfy the condition (3), the sum is observed to become lognormal before it is observed to become Gaussian [4]. The large-scale fluctuations of kinetic energy of fluid turbulence is just the case [5].

It is known that the lognormal distribution is infinitely divisible [10], i.e., written as the distribution of a sum of an arbitrary number of independent and identically distributed random variables. It is also known that the sum of exactly lognormal variables is approximately lognormal [11]. These are features of special sums and are consistent with those found in our study.

The present result contradicts the current paradigm that any lognormal distribution is due to a multiplicative process, i.e., a product of random variables, or equivalently to nonlinearity of the system [2]. In fact, some are due to additive processes in linear systems. It is desirable to explore such an additive process among the observations of the lognormal distribution [1]. The exploration would be to study the distribution outside the range of the central limit theorem, i.e., the large deviations. Although complexity and hence the nonlinearity appear to exist in any system that exhibits the lognormality, we would have to reconsider whether the system is effectively linear or not.

**Acknowledgments.** This work was supported in part by KAKENHI 25340018.

## References

1. Limpert, E., Stahel, W.A., Abbt, M.: Log-Normal Distributions across the Sciences: Keys and Clues. BioScience 51, 341–352 (2001)
2. Mitzenmacher, M.: A Brief History of Generative Models for Power Law and Lognormal Distributions. Internet Math. 1, 226–251 (2004)
3. Kendall, M., Stuart, A.: The Advanced Theory of Statistics, 4th edn., vol. 1. Griffin, London (1977)
4. Mouri, H.: Log-Normal Distribution from a Process that is not Multiplicative but is Additive. Phys. Rev. E 88, 042124 (2013)
5. Mouri, H., Hori, A., Takaoka, M.: Large-Scale Lognormal Fluctuations in Turbulence Velocity Fields. Phys. Fluids 21, 065107 (2009)
6. Abramowitz, M., Stegun, I.A.: Handbook of Mathematical Functions with Formulas, Graphs, and Mathematical Tables. Dover, New York (1965)
7. Monin, A.S., Yaglom, A.M.: Statistical Fluid Mechanics: Mechanics of Turbulence, vol. 2. MIT Press, Cambridge (1975)
8. Mouri, H., Hori, A., Kawashima, Y., Hashimoto, K.: Statistical Mechanics and Large-Scale Velocity Fluctuations of Turbulence. Phys. Fluids 23, 125110 (2011)
9. Landau, L.D., Lifshitz, E.M.: Fluid Mechanics. Pergamon, London (1959)
10. Thorin, O.: On the Infinite Divisibility of the Lognormal Distribution. Scand. Actuarial J. 1977, 121–148 (1977)
11. Fenton, L.F.: The Sum of Log-Normal Probability Distributions in Scatter Transmission Systems. IRE Trans. Commun. Syst. 8, 57–67 (1960)

# The Prediction of Tropospheric Ozone Using a Radial Basis Function Network

Kříž Radko[1] and Šedek Pavel[2]

[1] University of Pardubice, Faculty of Economics and Administration, Institute of Administrative and Social Sciences, Studentská 84, 532 10 Pardubice Czech Republic
[2] Czech Technical University, Faculty of Electrical Engineering, Dept. of Economics, Management and Humanities, Technická 2, 166 27 Praha, Czech Republic
Radko.Kriz@upce.cz, sedekpav@fel.cvut.cz

**Abstract.** The goal of this paper is to analyze the tropospheric ozone ($O_3$) concentration time series and its prediction using artificial neural networks (ANNs). Tropospheric ozone has harmful effects on human health and on the environment. This study was based on daily averaged tropospheric ozone ($O_3$) data from Pardubice in the Czech Republic. In this study, daily averaged ozone concentrations in Pardubice were predicted using a radial basis function network (RBFN) with three pollutant parameters and three meteorological factors in selected areas. We used a three-layer ANN, which consists of input, hidden, and output layers.

**Keywords:** Tropospheric ozone, Time series analysis, Artificial neural network, Prediction, Radial basis function network.

## 1 Introduction

Tropospheric ozone ($O_3$) is one of the major air pollutants. $O_3$ is one of the secondary pollutants. Secondary pollutants are not emitted directly to the air, water, or soil. Secondary pollutants are synthesized in the environment by chemical reactions involving primary or emitted chemicals. The formation of ozone in the troposphere is a complex system involving the reactions of hundreds of precursors depending on the physical conditions. To predict ozone you must understand not only the ozone itself, but also the conditions that contribute to its creation. In addition, ozone concentrations are strongly associated with meteorological conditions. To predict the concentration of ozone, it is necessary to use a model that contains complex relationships between ozone and other variables [1]. Photochemical pollution is formed from emissions of nitrogen oxides ($NO_x$, where $NO_x = NO + NO_2$), volatile organic compounds (VOCs) and carbon monoxide (CO) in the presence of sunlight [2]. The most prominent sources of $NO_2$ are internal combustion engines, thermal power stations and, to a lesser extent, pulp mills. The burning of biomass also creates additional pollutants including $NO_x$ [3]. More information analysis of Nitrogen Dioxide ($NO_2$) concentration time series is in [4].



A. Sanayei et al. (eds.), *ISCS 2014: Interdisciplinary Symposium on Complex Systems*, Emergence, Complexity and Computation 14, DOI: 10.1007/978-3-319-10759-2_13

Ozone has strong oxidant properties. Exposure to $O_3$ induces effects on health and the environment, causing respiratory difficulties in sensitive people and possible damage to vegetation and ecosystems. There is evidence from controlled human and animal exposure studies of the potential for $O_3$ to cause harmful health effects. There is a great deal of evidence to show that $O_3$ can harm lung function and irritate the respiratory system. Exposure to ozone and the pollutants that produce it is linked to premature death, asthma, bronchitis, heart attack, and other cardiopulmonary problems. [5] Public announcements, or forecasts, of potential unhealthy $O_3$ air quality for the next day can be of great benefit to those at risk of respiratory distress. In addition, some cities have voluntary episodic emission control programs, typically called "ozone action" programs, which are initiated on days of forecasted high $O_3$. Accurate forecasts of $O_3$ are an essential component of such programs, particularly on the high $O_3$ days when the health effects are most acute. [6]

ANNs have become a frequently used tool among various industries during the past decades, especially because the computational performance is easily available. Their absolutely unique ability to learn from collected data and then to apply the acquired knowledge enables us to solve complicated computational tasks, where other convenience methods would fail. The modeling of $O_3$ concentration has been studied in several works based on ANN [1, 4, 6, 7, 8, 9, 10, 11, 12].

## 2 Artificial Neural Networks

There exist several similar definitions of what an artificial neural network (ANN) is. For example Gurney [13] states that an ANN is an interconnected assembly of simple processing elements, units or nodes, whose functionality is loosely based on the animal neuron. The processing ability of the network is stored in the interunit connection strengths, or weights, obtained by a process of adaptation to, or learning from, a set of training patterns. In the Encyclopedia of Machine Learning [14] an ANN term is defined as a computational model based on biological neural networks. It consists of an interconnected group of artificial neurons and processes information using a connectionist approach to computation. In most cases an ANN is an adaptive system that changes its structure based on external or internal information that flows through the network during the learning phase. Generally, an ANN is a computational model inspired by the biological structure of neuron.

The ANN consists of neurons, connected by edges. These neurons are organized into layers. The first layer processes input data and passes it to the next layer. This process is repeated until the last layer in the network is reached and the calculated output is returned. Each neuron may recieve input data from more edges, which has different weights, sums them and applies an activation function to calculate it's output value, which may be an input to the other layer, or the network output. Thus the neuron output value could be described by the following formula:

$$o = f\left(\sum_{j=1}^{N} w_j y_j + b\right) \tag{1}$$

The structure of ANN is shown on Fig. 1. During the learning process, the network modifies the connection weights to achieve a target. Obviously, the performance is measured by an error function and the target is to minimize the error.

Unlike other statistical methods, an ANN makes no prior assumption concerning the data distribution.

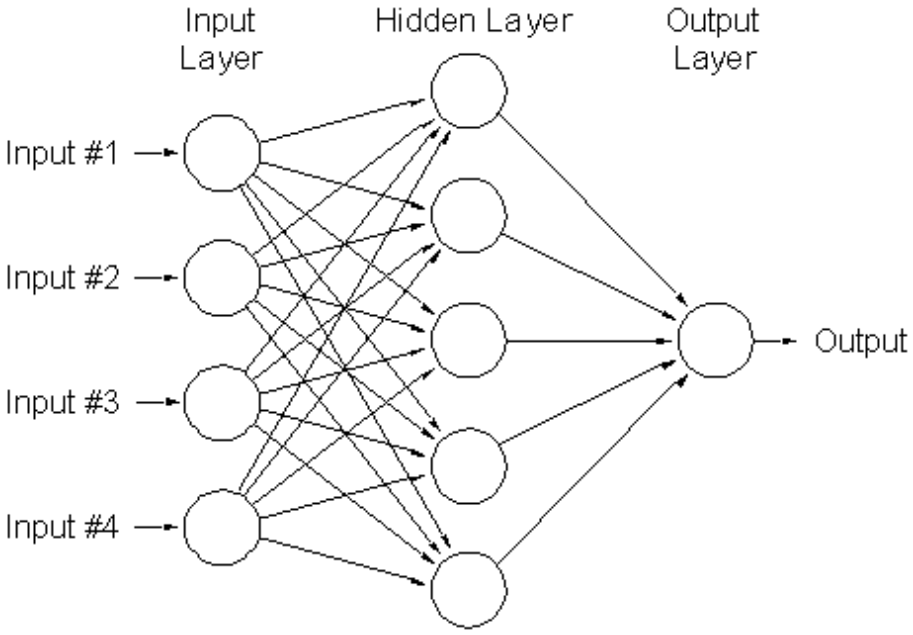


**Fig. 1.** Structure of artificial neural network [15]

### 2.1 Radial Basis Function Network

Generally, a radial basis function network (RBFN) is an ANN that uses radial basis functions (RBF) as activation functions. They were first formulated by Broomhead and Lowe [16]. The output of the network is a linear combination of radial basis functions (RBF) of the inputs and neuron parameters. The RBFN model is an ANN model with the multilayer feed-forward network topology. As stated in [17, p. 2], despite of the identical model, the node activation function and the training algorithms are very different. In the RBFN model, the RBF is used as the activation function instead of the sigmoidal functions obviously used in multilayer feed-forward network.

A RBF is a real-valued function whose value depends only on the distance from the origin, or alternatively on the distance from some other point $x_i$, called a center, so that

$$\Phi(x, x_i) = \Phi(\|x - x_i\|) . \tag{2}$$

Gaussian kernel is used in this analysis.

$$\Phi(x, x_i) = e^{-c^2 \|x - x_i\|^2} . \tag{3}$$

Thus the network output is calculated using formula [13, p. 171]:

$$\hat{y}_j = \sum_{i=1}^{M} w_{ij} \Phi_i(x) = \sum_{i=1}^{M} w_{ij} e^{-\frac{|x - c_i|^2}{2\sigma_i^2}} \tag{4}$$

where $M$ is number of neurons in hidden layer, $c_i$ is the center vector for neuron $i$ and $w_{ij}$ is the weight of neuron $i$ in the linear output neuron.

## 2.2 Training Algorithm

Literature states many different approaches of training RBFN as Orthogonal forward regression, Hierarchically Self-Organizin Learning, Resource Allocating Network or Heuristic Called Forward Selection [17]. Construction and training of the ANN is an iterative rather than a deterministic process, requiring a certain amount of expertise. In this case, the reduction in the number of input nodes greatly reduced the training time and improved the model fit. [6] The MathWorks Matlab software implementation of RBFN was used. Brief schema of the network topology is shown on Fig. 2.

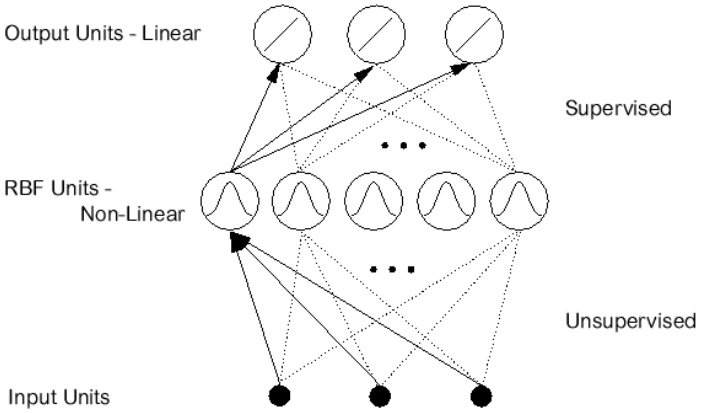


**Fig. 2.** Schema of the network topology [18]

The training algorithm used with this implementation is shown on Fig. 3 and described in the software documentation [19] as follows:

Initially the hidden layer has no neurons. The following steps are repeated until the network's mean squared error falls below goal.

- The network is simulated.
- The input vector with the greatest error is found.
- A new neuron is added to the hidden layer with weights equal to that vector.

- The weights are redesigned to minimize error.

The network performance function used for training is mean square error described by following formula [20, p. 171]:

$$E = \sum_{j=1}^{P} \left( y_j - \hat{y}_j \right)^2 = \sum_{j=1}^{M} \left( y_j - \sum_{i=1}^{M} w_{ij} \Phi_i(x) \right)^2 \tag{5}$$

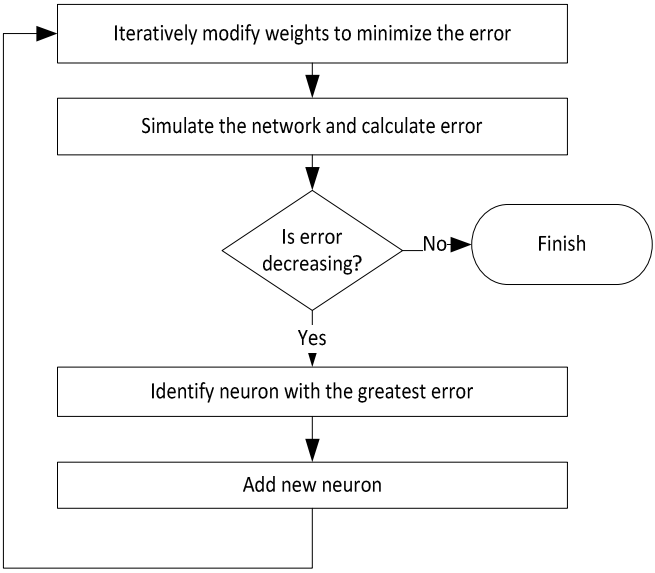


**Fig. 3.** Training algorithm used with the implementation

## 3 Case Study

### 3.1 Input Data

This study was based on daily averaged tropospheric ozone (O3) data from Pardubice-Rosice from 1.1.2005 to 31.12.2011. Dates, which have missing data, are removed. The data were provided by the Czech Hydrometeorological Institute for a related diploma thesis that is aimed at nonlinear and chaotic behavior of air pollutants time series. Pardubice is the capital of the Pardubice Region and lies on the river Elbe, 100 km east of Prague.

### 3.2 Description of Model

In the prediction of the concentrations, input variables of the model are arranged on time t and outputs on time t +1. Here, t defines the average daily concentration. The

neural network model program is trained and tested using MATLAB 2014, a three-layer neural network that consists of an input, hidden, and output layer.

**Table 1.** Model parameters

| Parameter | Unit |
|---|---|
| $O_3$ | $\mu g.m^{-3}$ |
| $NO_2$ | $\mu g.m^{-3}$ |
| NOx | $\mu g.m^{-3}$ |
| Temperature (in 2 m high) | K |
| Global radiation | $W.m^{-2}$ |
| Wind spead | $m.s^{-1}$ |

### 3.3 Network Training

As the experimental data for the network, the 3 days of all parameters were used, adding one input representing the day of year. That means, the network has 22 inputs. The predicted value should be the concentration of $O_3$ one day forever. For the training purpose, 90% of the time series were employed as the training data and the rest 10% as the testing data.

During the training process the mean square error steadily decreases (Fig. 4) when a neuron is added to the hidden layer. However adding unlimited number of neurons causes the network to learn exact patterns instead of the generalization ability. Because the training set had approximately 2000 samples, the training process was constrained by adding at most 100 neurons to the hidden layer.

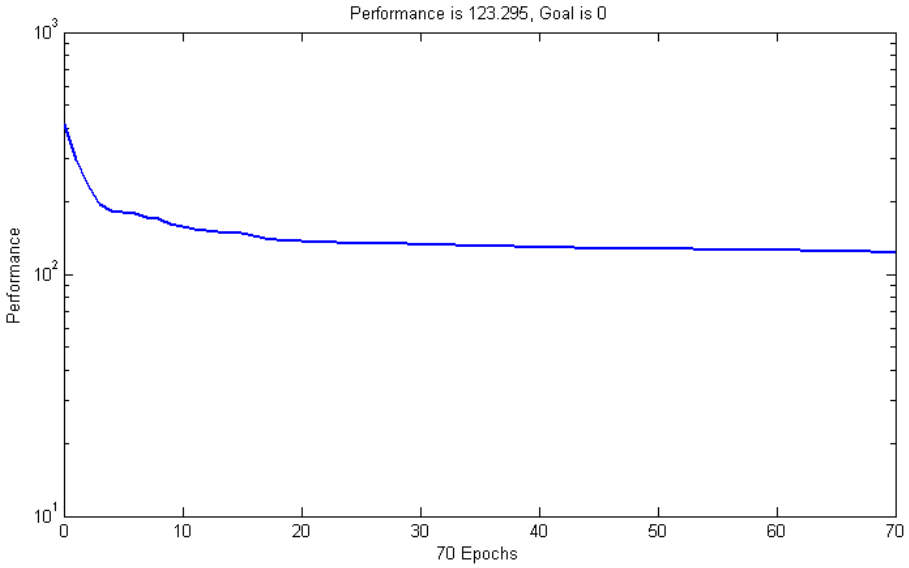


**Fig. 4.** Root mean square error (RMSE) during training process

### 3.4 Testing Results

The rest 10% of input data were simulated using the trained network and the result was compared to the inputs. On the Fig. 5 and Fig. 6 showing prediction it could be seen, that the predicted values are merely the same as the target. Root mean square error is 13,7648.

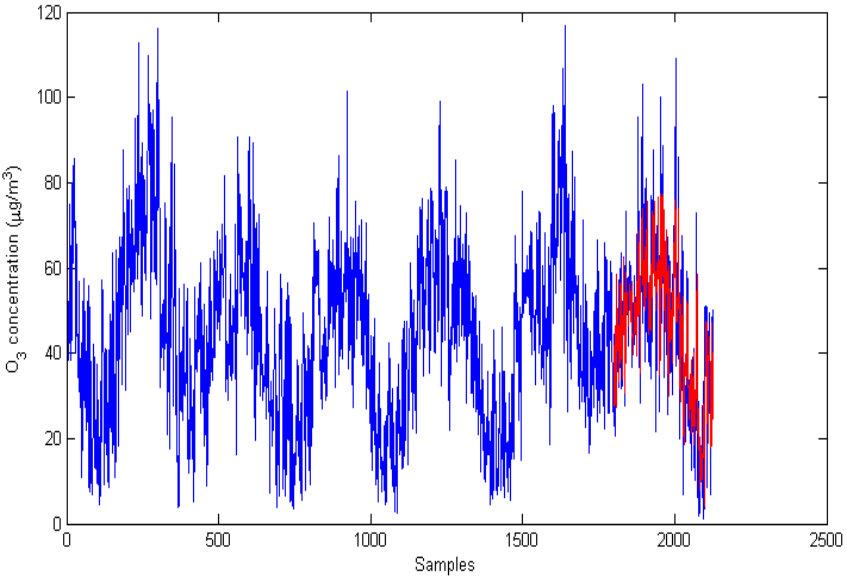


**Fig. 5.** Prediction (red line) of $O_3$ concentration time series using RBFN

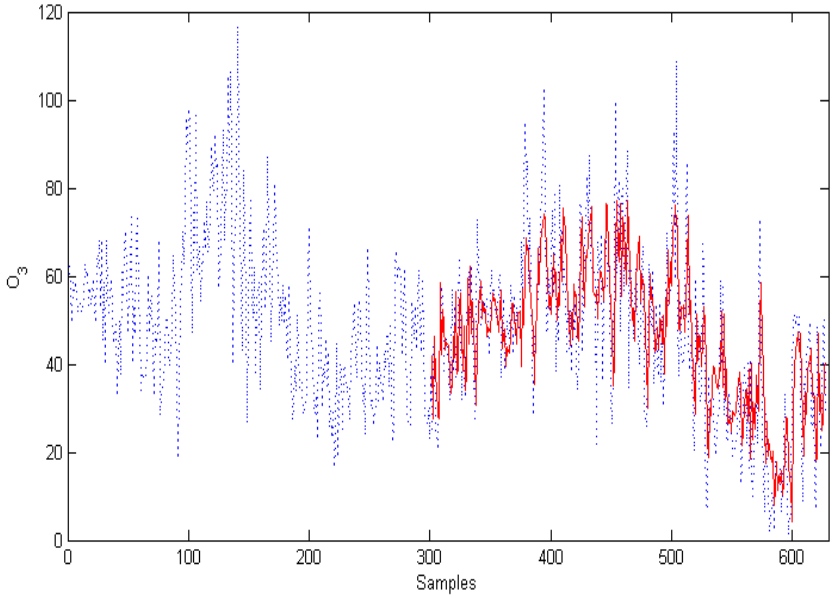


**Fig. 6.** Prediction (red line) of $O_3$ concentration time series using RBFN

Performance of the model is determined by comparing the produced model predictions and observed results c.f. Fig. 7.

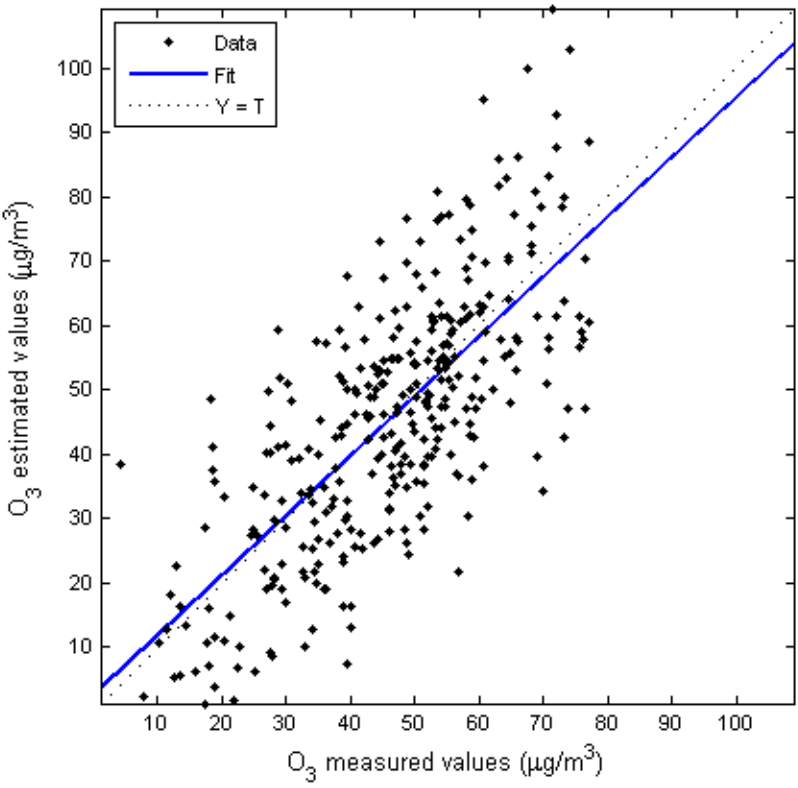


**Fig. 7.** Comparison between the measured (x-axis) and the estimated (y-axis) $O_3$ concentration values

## 4 Conclusion

Obtained results revealed that although the prediction of ozone is a highly complex and nonlinear problem, the ANN produces a quite good estimation of the ozone concentration level. Considering all these findings, we would recommend the RBF network as one of the methods used for prediction. As it may not be reliable under certain circumstances, it should be used in combination with other prediction methods.

## References

[1] Abdul-Wahab, S.A., Al-Alawi, S.M.: Assessment and prediction of tropospheric ozone concentration levels using artificial neural networks. Environmental Modelling & Software 17(3), 219–228 (2002)

[2] Tropospheric ozone in the European Union, The consolidated Report, Luxembourg (1999)
[3] Baťa, R., Půlkrábková, P.: The importance of Modelling the Environmental Impacts of a Biomass Based Electric Power Generation for public safety. WSEAS Transactions on Environment & Development 9(4) (2013)
[4] Kříž, R.: Chaos in Nitrogen Dioxide Concentration Time Series and Its Prediction. In: Nostradamus 2014: Prediction, Modeling and Analysis of Complex Systems, pp. 365–376. Springer International Publishing (2014)
[5] Health Aspects of Air Pollution with Particulate Matter, Ozone and Nitrogen Dioxide. WHO-Europe report, Bonn (2003)
[6] Cobourn, W.G., Dolcine, L., French, M., Hubbard, M.C.: A comparison of nonlinear regression and neural network models for ground-level ozone forecasting. Journal of the Air & Waste Management Association 50(11), 1999–2009 (2000)
[7] Sousa, S.I.V., Martins, F.G., Alvim-Ferraz, M.C.M., Pereira, M.C.: Multiple linear regression and artificial neural networks based on principal components to predict ozone concentrations. Environmental Modelling & Software 22(1), 97–103 (2007)
[8] Bandyopadhyay, G., Chattopadhyay, S.: Single hidden layer artificial neural network models versus multiple linear regression model in forecasting the time series of total ozone. International Journal of Environmental Science & Technology 4, 141–149 (2007)
[9] Ozdemir, H., et al.: Prediction of tropospheric ozone concentration by employing artificial neural networks. Environmental Engineering Science 25(9), 1249–1254 (2008)
[10] Al-Alawi, S.M., Abdul-Wahab, S.A., Bakheit, C.S.: Combining principal component regression and artificial neural networks for more accurate predictions of ground-level ozone. Environmental Modelling & Software 23(4), 396–403 (2008)
[11] Yi, J., Prybutok, V.R.: A neural network model forecasting for prediction of daily maximum ozone concentration in an industrialized urban area. Environmental Pollution 92(3), 349–357 (1996)
[12] Yi, J., Prybutok, R.: A Neural Network Model Forecasting for Prediction of Daily Maximum Ozone Concentration in an Industrialized Urban Area. Environ. Pollut. 92, 349–357 (1996)
[13] Gurney, K.: An introduction to neural networks. CRC Press (1997)
[14] Artificial Neural Networks. In: Sammut, C., Webb, G.I. (eds.) Encyclopedia of Machine Learning SE - 35, p. 44. Springer, US (2010), http://dx.doi.org/10.1007/978-0-387-30164-8_35, doi:10.1007/978-0-387-30164-8_35, ISBN: 978-0-387-30768-8
[15] http://www.cs.bgu.ac.il/~ben-shahar/Teaching/Computational-Vision/StudentProjects/ICBV061/ICBV-2006-1-TorIvry-ShaharMichal/index.php
[16] Broomhead, D.S., Lowe, D.: Radial basis functions, multi-variable functional interpolation and adaptive networks. No. RSRE-MEMO-4148. Royal Signals And Radar Establishment Malvern, United Kingdom (1988)
[17] Sundararajan, N., Saratchandran, P., Lu, Y.W.: Radial Basis Function Neural Networks with Sequential Learning: MRAN and Its Applications. Progress in neural processing. World Scientific (1999)
[18] http://www.cs.hmc.edu/~bfeinste/rbf/
[19] Mathworks Inc.: MATLAB Functions in Neural Network Toolbox
[20] Mathworks Inc.: Radial Basis Neural Networks – MATLAB & Simulink

# Physical Experiments and Stochastic Modeling to Clarify the System Containing the Seismic Source and the Ground

Alexander V. Smaglichenko[1], Maria K. Sayankina[2], Tatyana A. Smaglichenko[2], and Igor A. Volodin[2]

[1] RTSoft Company "Tools and Automation Systems", Moscow, Russia
asmaglichenko@dev.rtsoft.ru
[2] Research Oil and Gas Institute of Russian Academy of Sciences, Moscow, Russia
{t.a.smaglichenko,msayankina}@gmail.com, volodin@ipng.ru

**Abstract.** The nonlinearity of the system containing the source of seismic energy and the ground creates a difficulty for application of geophysical methods. The initial reason is in a distortion of signals radiated by the source. In this article the results of physical experiments using of an impulse source have been investigated. It has been demonstrated that in order to get a reliable Earth's images is necessary to process signal series records from repeated experiments instead of traditional using of the record of one selected signal. The proposed technique is based on an application of the method of microseismic sounding, stochastic modeling and calculation of arithmetic mean values. The technique can be extended for other sources of seismic energy, where the radiated signal can be transformed to series of impulses.

**Keywords:** Rayleigh surface waves, recording of seismic signals, inhomogeneous structure, stochastic seismic process.

## 1 Introduction

Exploration of Earth's structure can be made by using controlled seismic sources. There are two popular types of devices that produce vibrations into the ground and generate the seismic waves: a seismic vibrator and an impulse hammer. The generated waves from a source travel down into a soil until change its characteristics depending on properties of earth materials. Seismic records are collected by using receivers (seismometers or accelerometers) located at known distances from the source. The exploration techniques are applied by processing the registration data to determine Earth's structure, which can contain deposits, karsts cavities, karsts related to water resources or other heterogeneities.

However it often happens that it is very difficult to do the interpretation of the exploration method results. The reason can be in the nonlinearity of the system that involves the source of seismic energy and the ground. Namely, the record of receiver (outgoing signal) does not equal to the linear sum of the record of source (radiated signal) and the record that corresponds to the existing heterogeneity. The initial



A. Sanayei et al. (eds.), *ISCS 2014: Interdisciplinary Symposium on Complex Systems*,
Emergence, Complexity and Computation 14, DOI: 10.1007/978-3-319-10759-2_14

reason may be in the distortion of the radiated signal. When using a seismic vibrator the nonlinear distortion of outgoing waves has been observed and investigated by many authors [1, 2, 3, 4]. However fundamental investigation of signals radiated by an impulse hammer is not available. In the work [5] it was pointed that repetition of a number of hammer blows at the same location allows us to find an appropriate signal and improve the signal-to-noise ratio. In this article it has been illustrated that using of the average value of the stochastic parameter that was obtained by processing series of seismic signals from the increasing number of hammer blows can provide more reliable result of the exploration method than in the case of one selected signal. Thus the processing of seismic records of many repeating experiments, their stochastic analysis are needed to overcome practical issues connected with the nonlinearity of the system containing the impulse source of seismic energy and the ground.

The exploration method that is applied to seismic records is the method of microseismic sounding [6]. This method uses Rayleigh waves. In order to estimate the effectiveness of the method we use the next physical model. The plastic water bottle (heterogeneity) is located to soil sand at known depth. Rayleigh waves are created by an impulse hammer, which is needed for shallow investigation. In the following section, we briefly describe the measuring equipment, which was made to get high frequency signals radiated by the hammer. Next, on the base of the method of microseismic sounding we propose the stochastic parameter, numerical values of which characterize the presence of heterogeneity in a soil. We compare outcomes of the stochastic parameter for the two cases: 1) when one signal was selected from a set of records; 2) when series of signals from repeating of the number of hammer blows are simultaneously processed.

## 2 The Measuring Equipment

The review of publications about spectrum analysis (see for example [7]) shows that it is difficult to generate and record high-frequency elastic vibrations. However high frequency data should be analyzed if we place the physical object at a depth of a half of the meter. The deeper the penetration of the Rayleigh surface wave, the lower the frequency of this wave. Therefore it is necessary to measure high frequency waves and apply the exploration method to "catch" the process of interaction of these waves with heterogeneity. Figure 1 illustrates the measuring equipment that was made by the first author of this article [8].

The measuring equipment consist of four receivers (accelerometers), which have universal design to remove the possibility of noise and to connect with Analog-to-Digital Converter (ADC), debug stabilization board, battery, glass textolite base having slots for each accelerometer. The upper boundary of a bandwidth for the measurement system is equal to 20000 Hz. The software developed by company "L-Card" is used when processing the ADC data. It permits to create the unlimited size of record, multi-module regime of work, any frequency of interrogation when recording. All parts of the equipment are detachable that provides its small-size and versatility in land exploration.

**Fig. 1.** Measuring equipment for recording high-frequency elastic vibrations

Measuring channels have been checked by using records of elastic vibrations produced by musical tuning fork. The musical fork makes a sound A 1st octave 440 Hz (Fig. 2). This original method for metrological verification has also been proposed by the first author of this work. Frequency was measured several ten of times. The arithmetic mean value of deviation of the frequency from 440 Hz was 1.2 Hz.

**Fig. 2.** Musical tuning fork used to test measuring channels of the equipment

## 3 Physical Experiments

Physical science experiments were conducted in sand quarry located near by the village Aniskino, Shelkovo's district, Moscow's province. A geological medium was homogeneous and it consists of sand. The investigated area had a size of 10 x 10 meters. The physical model was presented by the plastic water bottle. The size of the bottle is 0.4 x 0.2 x 0.2 meters (Fig.3).

**Fig. 3.** Heterogeneity is imitated by the plastic water bottle. Measurements were performed along the profiles denoted by blue lines (shown on the left). The water bottle has placed at the depth of a half of the meter (shown on the right).

A small seismic energy source that is the impulse hummer was used to generate the seismic waves. Two pairs of accelerometers were utilized to record signals radiated by hammer strikes. The pair includes the base accelerometer located at some place and the other accelerometer, which moves along a profile with some step. Fig. 4 illustrates a schematic diagram of the experiment and its performing in real conditions. The heterogeneity and the source are shown by blue and black colors on the diagram. Four accelerometers register seismic signals, which are going to the ADC and then to the debug stabilization board connected with a notebook.

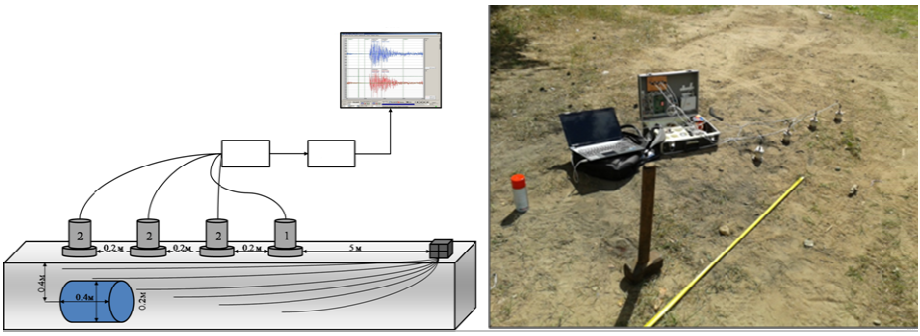


**Fig. 4.** Schematic diagram of experiments (shown on the left) and its preparing in field conditions (shown on the right)

## 4 Automatic Processing of Experimental Data

The recording of signals requires the storing of huge digital data sets. In order to store the information in compact form the software has been developed by the first author of the article. Figure 5 illustrates the program outcome, which detects “the breaks” in digital records and selects the seismic signal record. All records are kept in separated files. Each experiment has their “tree of files”.

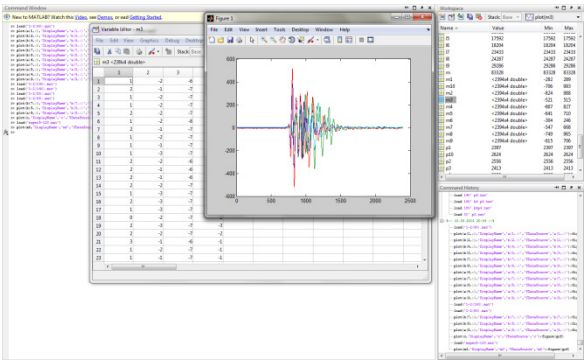

**Fig. 5.** Selection of different seismic signals as the result of software application

Note that there are other works that also simplify the signal records (see for example [9]). Nevertheless in practice the data corresponding to seismic signals are often manually chosen.

## 5 A Proposed Stochastic Analysis

In the work [10] authors Lim and Harris introduced a new spectrum presentation for stochastic signals. They called it "the ratio spectrum". The ratio spectrum *R(m)* is determined as the ratio of the output power that was filtered for some frequencies to the input power having all frequencies range. In the work [11] authors Skowronski and Harris determined the analytical expression of this parameter for a white noise model. It has been shown that the ratio spectrum can be used "to extract features from regions of high energy". It is known that a white noise describes the stochastic process having uniform probability distribution. Models of a white noise correspond to an appearance of distortions of the uniform stochastic process.

If we study the stochastic seismic process we can consider the appearance of inhomogeneous structure having contrast properties for some medium as the appearance of a real distortion for this medium. In our assumption, the interaction of the Rayleigh waves with the heterogeneity can be detected by studying the ratio spectrum of seismic signals. By analogy with the ratio spectrum, which was defined in [10, 11], we propose to introduce a parameter that is formed by taking the ratio of the power of a signal from the moving accelerometer to the power of a signal from the base accelerometer. Thus in the case of the microseismic sounding method the parameter can be described in the following form:

$$r(f)^j = \frac{the\ power\ from\ the\ moving\ accelerometer}{the\ power\ from\ the\ base\ accelerometer} = \frac{\sum_{k=0}^{N-1}\left|A_f^2(k)\right|^2}{\sum_{k=0}^{N-1}\left|A_f^1(k)\right|^2} \quad (1)$$

where $j$ is the registration point of the pair "the moving accelerometer – the base accelerometer", $A_f^1$ и $A_f^2$ are values in the domain of Rayleigh wave frequencies $f$ that were found due to the Fourier transformation of signal records registered by using the pair of accelerometers in the j-th point, N is the length of the discrete time series.

In accordance with the base of the method of microseismic sounding we will study the variations of the power spectrum in each registration points from the arithmetical

mean value of the power spectrum for all registration points. For each frequency $f$ the arithmetical mean value $\overline{r(f)}$ is equal to:

$$\overline{r(f)} = \sum_{j=1}^{K} r_j(f) \quad , \tag{2}$$

where j is the registration point number. Then the parameter that characterizes a presence of the heterogeneity having contrast property is determined as following:

$$S(f)^j = r(f)^j - \overline{r(f)} \tag{3}$$

We will call the parameter $S(f)^j$ by the stochastic parameter.

## 6 A Comparison of Results for One Selected Signal and for Series of Repeating Signals

Let us analyze outcomes of the method based on using of the stochastic parameter. The first image of heterogeneity has been obtained processing the record of one seismic signal. This signal was selected from a set of signals that were obtained due to repeating of a number of hammer blows at the same location (Fig.6-a). The next image was restored using data of 10 seismic signals (Fig 6-b). One can see that the shape of the original heterogeneity that is denoted by a rectangle is better manifested in the given case. Numerical values of the stochastic parameter in the domain of a rectangle are in the range from 0.3 to 1.0. These values are maximal absolute values among values of the parameter that were determined for all points of the investigated area. At the same time it should be noted the presence of values in the range from -0.8 to -0.3, absolute values of which close to the maximum values (Table 1). These values can point a false position of the heterogeneity if researcher does not know where it is.

**Table 1.** Values of the stochastic parameter. Data of 10 seismic signals.

| | | | | | | | | |
|---|---|---|---|---|---|---|---|---|
| -0.3 | -0.2 | -0.3 | -0.2 | -0.2 | 0.3 | 0.4 | 0.3 | -- |
| -0.1 | -- | 0.1 | 0.3 | 0.4 | 0.3 | -- | -0.1 | -0.3 |
| -- | -- | 0.2 | 0.5 | 1.0 | 0.1 | -0.1 | -0.4 | -0.6 |
| -- | -- | 0.1 | 0.3 | 0.6 | 0.1 | -0.1 | -0.3 | -0.8 |
| -- | -- | -- | 0.2 | 0.2 | -- | -- | -0.3 | -0.4 |
| -- | -- | -- | 0.1 | 0.1 | -- | -- | -0.2 | -0.3 |
| -- | -- | -- | -- | -- | -- | -- | -- | -0.2 |
| -- | -- | -- | -- | -- | -- | -- | -- | -0.2 |
| -- | -- | -- | -- | -- | -- | -- | -- | -0.2 |
| -- | -- | -- | -- | -- | -- | -- | -- | -- |
| -- | -- | -- | -- | -- | -- | -- | -- | -- |
| -- | -- | -- | -- | -- | -- | -- | -- | -- |
| -- | -- | -- | -- | -- | -- | -- | -- | -- |
| -- | -- | -- | -- | -- | -- | -- | -- | -- |
| -- | -- | -- | -- | -- | -- | -- | -- | -- |
| -- | -- | -- | -- | -- | -- | -- | -- | -- |
| -- | -- | -- | -- | -- | -- | -- | -- | -- |
| -- | -- | -- | -- | -- | -- | -0.1 | -0.2 | -0.2 |

In order to understand how the number of outgoing seismic signals and a distance between accelerometers affects on reconstruction image quality we conducted additional experiments. The distance between accelerometers has been reduced from 20 cm to 12.5 cm. 20 seismic signals were generated by the impulse hammer. Thus the amount of signals exceeds the previous amount in 2 times. Fig. 6-c demonstrates the improvement of the heterogeneity shape quality. Numerical values of the stochastic parameter in the domain of a rectangle are in the range from 0.7 to 1.0 (Table 2).

**Table 2.** Values of the stochastic parameter. Data of 20 seismic signals.

| | | | | | | | | | | | | |
|---|---|---|---|---|---|---|---|---|---|---|---|---|
| 0.7 | 0.6 | 0.5 | 0.5 | 0.3 | -0.4 | -0.4 | 0.2 | 0.1 | -0.1 | -0.7 | -0.7 | -0.4 |
| 0.9 | 0.8 | 0.8 | 0.6 | 0.4 | -0.5 | -0.4 | 0.4 | 0.1 | -0.2 | -0.7 | -0.7 | 0.1 |
| 0.8 | 0.8 | 0.8 | 0.7 | 0.5 | -- | -- | 0.6 | -- | -0.3 | -0.7 | -0.3 | 0.3 |
| 0.5 | 0.5 | 0.6 | 0.8 | 0.6 | 1.0 | 0.9 | 0.4 | -0.1 | -0.3 | -0.3 | -0.1 | 0.3 |
| -- | 0.2 | 0.1 | 0.7 | 0.6 | 1.0 | 1.0 | -0.1 | -0.1 | -0.5 | -0.3 | -0.1 | -0.3 |
| 0.2 | 0.2 | 0.1 | 0.5 | 0.5 | 0.9 | 0.7 | -0.1 | -0.2 | -0.5 | -0.5 | -0.3 | -0.5 |
| 0.3 | 0.1 | 0.2 | 0.4 | 0.4 | 0.6 | 0.3 | -0.1 | -0.3 | -0.5 | -0.5 | -0.5 | -0.5 |
| 0.3 | 0.1 | 0.2 | 0.3 | 0.3 | 0.5 | 0.2 | -- | -0.2 | -0.4 | -0.5 | -0.5 | -0.5 |
| 0.3 | 0.1 | 0.2 | 0.3 | 0.3 | 0.4 | 0.1 | -- | -0.2 | -0.4 | -0.4 | -0.5 | -0.5 |
| 0.2 | 0.1 | 0.2 | 0.2 | 0.2 | 0.3 | -- | -- | -0.2 | -0.4 | -0.4 | -0.4 | -0.5 |
| 0.1 | -- | 0.2 | 0.1 | 0.1 | 0.2 | -- | -- | -0.2 | -0.4 | -0.4 | -0.4 | -0.4 |
| -- | 0.1 | 0.1 | -- | -- | 0.1 | -- | -0.1 | -0.2 | -0.3 | -0.4 | -0.4 | -0.4 |
| -- | 0.1 | -- | -- | 0.1 | 0.1 | -- | -0.2 | -0.2 | -0.2 | -0.3 | -0.3 | -0.3 |
| -- | 0.1 | 0.1 | 0.1 | 0.1 | 0.1 | -- | -0.1 | -0.1 | -0.2 | -0.3 | -0.5 | -0.2 |
| -- | 0.1 | 0.1 | 0.1 | 0.1 | 0.1 | -- | -- | -0.1 | -0.2 | -0.2 | -0.2 | -0.2 |
| 0.1 | 0.1 | 0.1 | 0.1 | 0.1 | 0.1 | -- | -- | -0.1 | -0.2 | -0.2 | -0.2 | -0.2 |
| -- | 0.1 | -- | -- | -- | -- | -- | -- | -0.1 | -0.2 | -0.2 | -0.2 | -0.1 |
| -- | -- | -- | -- | -- | -- | -- | -- | -0.1 | -0.1 | -0.1 | -0.1 | -0.1 |
| -- | -- | -- | -0.1 | -- | -0.1 | -- | -- | -- | -0.1 | -- | -- | -- |
| 0.2 | -0.1 | -- | -0.3 | -0.1 | -0.3 | -- | -- | -- | -- | 0.1 | 0.1 | 0.1 |
| 0.2 | -- | -- | -0.3 | -0.1 | -0.3 | -- | -- | -- | -- | 0.3 | 0.3 | 0.3 |
| -- | -- | -- | -0.1 | -- | -0.1 | -- | -- | -- | -- | -- | -- | -- |
| -- | -- | -- | -- | -- | -- | -- | -- | -- | -- | -- | -- | -- |
| -- | -- | -- | -- | -- | -- | -- | -- | -- | -- | -- | -- | -- |
| -- | -- | -- | -- | -- | -- | -- | -- | -- | -- | -- | -- | -- |
| -- | -- | -- | -- | -- | -- | -- | -- | -- | -- | -- | -- | -- |
| 0.1 | 0.1 | 0.1 | -- | -- | -- | -- | -- | -- | -- | -- | -- | -- |
| 0.2 | 0.1 | 0.1 | -- | -- | -- | -- | -- | -0.1 | -0.1 | -0.1 | -0.1 | -0.1 |
| 0.2 | 0.1 | 0.1 | -- | -- | -- | -- | -- | -0.1 | -0.1 | -0.1 | -0.1 | -0.1 |
| -- | -- | -- | -- | -- | -- | -- | -- | -- | -- | -- | -- | -- |

However the problem of fuzzy boundaries remains. In order to overcome this problem we applied the data emulation. Namely, data obtained from a real experiment were duplicated from the other side of the profile. The final result was reliable (Fig. 6-d). Values of the stochastic parameter are equal to 1.0 in the heterogeneity domain. There are no artifacts.

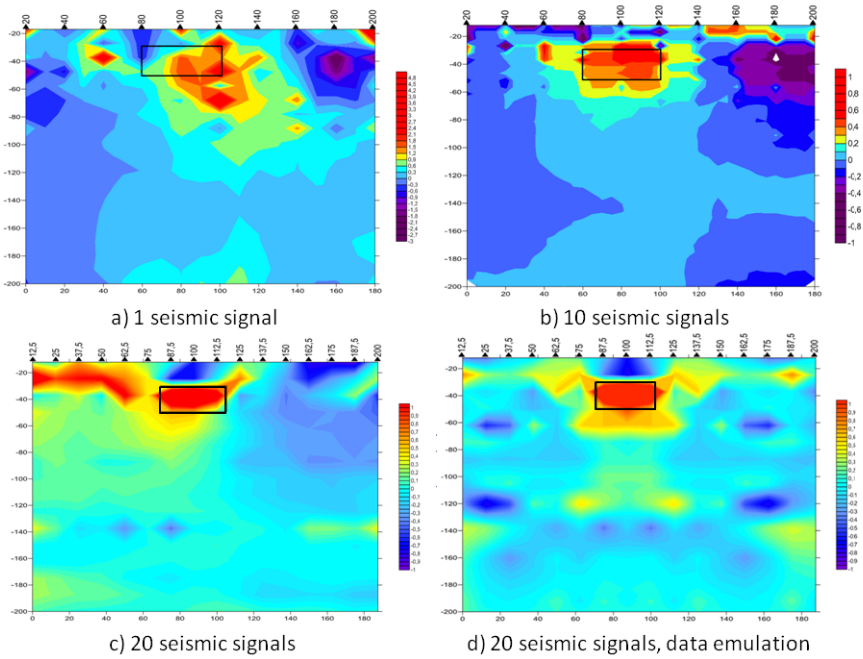


**Fig. 6.** Images of interaction of the Rayleigh surface waves with the heterogeneity under the following conditions: a) data of one signal have been processed; the distance between accelerometers is 20 cm; b) data of 10 signals have been processed; the distance is 20 cm; c) data of 20 signals have been processed; the distance is 12.5 cm; d) data of 40 signals have been used due to the data emulation; the distance is 12.5 cm.

## 7 Conclusion

In this article we briefly described the measuring equipment for recording of high frequency signals radiated by the impulse hammer, the physical model imitating Earth's heterogeneity, physical experiments, in which the inhomogeneous medium has been sounded by seismic impulses. Processing of experimental data has been illustrated.

On the base of microseismic method we proposed the technique, which presents seismic process as a stochastic process. This permits us to apply the novel parameter that was developed in works [10, 11] for a white noise model. The next results have been obtained using the stochastic technique. The shape of heterogeneity is not reconstructed when processing one selected signal. The image of heterogeneity is partly reconstructed when using of series of 10 signals. However significant artifact exists. If we use records of 20 signals from repeating number of hammer strikes then the shape of heterogeneity can be restored having a small artifact. The heterogeneity image well reconstructed if records of signals are added from an opposite side of the profile.

Thus we conclude that the processing of numerous records of seismic signals radiated by the impulse source from different sides of the seismic profile leads to reliable results of the exploration method. This reduces the influence of the nonlinear system containing the source of seismic energy and the ground on the exploration method application.

We assume that the technique can be used for other seismic sources, for instance for the vibrator, if its extended signal will be converted to separated impulses.

**Acknowledgments.** We are very grateful to Marina Stepanova (Institute of Physics of the Earth, RAS) for her help in using of the microseismic sounding method. We sincerely thank to an anonymous reviewer and an editor for their comments that helped to clarify the basic purpose of the manuscript.

## References

1. Martin, J.E., Jack, I.G.: The behavior of a seismic vibrator using different phase control methods and drive level. First Break 8, 404–414 (1990)
2. Walker, D.: Harmonic resonance structure and chaotic dynamics in the earth-vibrator system. Geophysical Prospecting 43, 487–507 (1995)
3. Jeffryes, B.P.: Far-field harmonic measurement for seismic vibrators. In: 66th Annual International Meeting, SEG, Expanded Abstracts, pp. 60–63 (1996)
4. Lebedev, A., Beresnev, I.: Nonlinear distortion of signals radiated by vibroseis sources. Geophysics 69(4), 968–977 (2004)
5. Wightman, W., Jalinoos, F., Sirles, P., Hanna, K.: Application of geophysical methods to high way related problems. Technical report, DTFH 68-02-P-00083 (2003)
6. Gorbatikov, A.V., Montesinos, F.G., Arnoso, J., Stepanova, M.Y., Benavent, M., Tsukanov, A.A.: New Features in the Subsurface Structure Model of El Hierro Island (Canaries) from Low-Frequency Microseismic Sounding: An Insight into the 2011 Seismo-Volcanic Crisis. Surveys in Geophysics 34(3), 463–489 (2013)
7. Milsom, J.A., Eriksen, A.: Field Geophysics. Geological Field Guide. Book 28, 304 p. Willey (2011)
8. Smaglichenko, A.V.: The complex of measuring equipment and software to estimate the location of inhomogeneity using a seismic data. Seismic Instruments 50(2), 20–38 (2014) (in Russian)
9. Abancó, C., Hürlimann, M., Fritschi, B., Graf, C., Moya, J.: Transformation of Ground Vibration Signal for Debris-Flow Monitoring and Detection in Alarm Systems. Sensors (Basel) 12(4), 4870–4891 (2012)
10. Lim, S., Harris, J.G.: Analog implementation of ratio spectrum. In: Proc. of the IEEE International Symposium on Circuits and Systems, Monterey, pp. 277–280 (1998)
11. Skowronski, M.D., Harris, J.A.: Probabilistic Analysis of the Ratio Spectrum. In: Proc. of the IEEE Adaptive Systems for Signal Processing, Communications, and Control Symposium, Lake Louise, Alta, pp. 333–336 (2000)

# *Cosmology 2.0:* Convergent Implication of Cryodynamics and Global-*c* General Relativity

Otto E. Rossler

Faculty of Science, University of Tübingen, Auf der Morgenstelle 8
D-72076 Tübingen, Germany
oeross00@yahoo.com

**Abstract.** Two building blocks valid in two unrelated physical disciplines, statistical mechanics and general relativity, respectively, have convergent implications for cosmology. *Firstly*, cryodynamics – the recent new sister discipline to thermodynamics which applies to gases that are made up from mutually attractive rather than repulsive particles – is anti-entropic. Its statistical equilibrium is unstable rather than stable. This fact confirms Fritz Zwicky's 1929 intuitive explanation of cosmological redshift as generated by the randomly distributed moving galaxies. *Secondly*, global-c general relativity – the unfinished global-*c* version of general relativity – implies that gravitational redshift is no longer accompanied by a proportional reduction in the speed of light *c*. Rather, the constant recession speed of the bottom of the Einstein rocketship relative to the tip implies a proportional local size increase that is optically masked from above. The new *global c* excludes cosmic expansion directly, since the global space expansion of the Big Bang involves superluminal speeds by definition. Thus the cosmological standard model is refuted regarding its main assumption of space expansion in two independent ways. The second pillar of the cosmological standard model besides expansion, the "cosmological background radiation," now necessarily comes from a close-by source, the Milky Way galaxy's halo. A Clifford-Einstein-Mandelbrot cosmos comes in sight along with an eternal cosmological metabolism (Heraclitus). Thus the non-experimental (observational) physical discipline – cosmology – presents itself in a new light.

**Keywords:** Cosmological Standard model, superluminality, tired light, deterministic statistical mechanics, cryodynamics, global-*c*, Clifford, Mandelbrot, Heraclitus.

## 1 Introduction

Statistical mechanics and general relativity currently undergo an update: In Stat Mech, on one hand, the existence of a second fundamental paradigm based on mutually attractive rather than repulsive particles was discovered: cryodynamics, sister discipline to thermodynamics [1] (crýos means cold, thermós means hot in Greek). In general relativity, on the other hand, the existence of a new global-c



A. Sanayei et al. (eds.), *ISCS 2014: Interdisciplinary Symposium on Complex Systems*,
Emergence, Complexity and Computation 14, DOI: 10.1007/978-3-319-10759-2_15

transform of the Einstein equation follows from the discovery of a global-c version of the Schwarzschild metric [2,3] and the equivalence principle [4]. The two independent results converge in ruling out the cosmological standard model founded on the assumption of cosmic expansion. “Cosmology 2.0” is an active construction site.

## 2 Cryodynamics

Thermodynamics is applicable at all temperatures despite its hot name as is well-known. So is cryodynamics in spite of its cold name. The difference lies only in the numerical sign of the inter-particle potential. While thermodynamics is based on (short-range) repulsion between the gas particles, cryodynamics is based on (long-range) attraction. Since thermodynamics still works when the repulsive inter-particle potential is made long-range (anti-Newtonian) [5], cryodynamics with its long-range attractive Newtonian (or post-Newtonian) potentials is a genuine dual to thermodynamics, arrived at after a 150 years long delay.

Cryodynamics, like thermodynamics, admits an entropy-like macroscopic observable which differs from the latter’s Sackur-Tetrode deterministic entropy formula (see [6]) only by a sign flip. This new macro observable can be called “ectropy.” While *entropy* is spontaneously increasing or constant in deterministic statistical thermodynamics, *ectropy* is spontaneously increasing or constant in deterministic statistical cryodynamics. Time’s arrow is inverted. Apart from the sky, cryodynamics possesses also an applied domain down on earth: Hotter electrons can be used in principle to locally cool-down a run-away plasma instability in a hot-fusion reactor [7].

The main implication of cryodynamics, however, concerns cosmology. In retrospect it is not surprising that when cryodynamics was first intuitively envisioned by Zwicky in 1929 [8] it was met with ridicule as “tired light theory.” This response from the part of the community prevented Zwicky from making his intuition formally consistent. The at first similarly naïve re-discovery of the idea of an intergalactic cooling of photons 74 years later [9] was initially met with silence.

At this point, the reader no doubt asks for numerical evidence. After all, a huge number of numerical simulations of multi-particle celestial mechanical systems have been performed during the last two thirds of a century. If Zwicky’s brainchild were for real, the phenomenon ought to be well-known empirically. No “anti-entropic” effects were observed. Only in 2010 quite recently, positive numerical evidence was found in a high-accuracy symplectic two-particle simulation in a formally one-dimensional T-tube configuration [10]. An independent analytical confirmation also exists [11]. The evidence so far points to the interpretation that, unlike statistical thermodynamics, statistical cryodynamics is numerically unstable.

Recently a mathematical proof of cryodynamics (smoothed inverted Sinai paradigm, cf. Sinai [12]) was offered: the “breathing plane-tree alley paradigm” [13]. A first textbook on cryodynamics in the footsteps of Richard Becker’s classic introductory treatise on deterministic thermodynamics [14] waits to be written.

## 3 Global-*c* General Relativity

The very existence of general relativity is a miracle of scientific tenacity; the time gap of four years between the discovery of the equivalence principle by Einstein in 1907 [15] (marred by the loss of c-global) and the first follow-up paper on the way towards general relativity [16] could as well have lasted indefinitely. The finished theory five more years later had to be built carefully around the obstacle that $c$ was assumed reduced in proportion to the local gravitational potential – the very drawback which had crept-in in 1907 (a fact which is not widely known).

The full Einstein equation of 1916 [17] still waits to be written down in its global-$c$ transform. The global-$c$ transform of the Schwarzschild metric was the first evidence found in 2007 as mentioned [2, 3]. Eventually, the Noether theorem (see [18]) and quantum electrodynamics (see [19]) confirmed the generality of the finding. The plain special-relativistic fact that a constantly receding light clock mimics the presence of a reduced speed of light $c$ inside when watched from behind, offers the best explanation for the analogous shrinking of the speed of light $c$ seen by Einstein at the bottom of his extended long rocketship in outer space in 1907 [15]. However, without the aid of quantum electrodynamics [19], the error may have remained as unrecognizable as it was in 1907.

The new convergence between quantum mechanics [19] and general relativity, valid in the wake of $c$-global, is most encouraging for fundamental particle physics. Big theoretical progress can be expected. At the present moment in time, black hole theory is particularly affected by $c$-global. Black holes cease to "Hawking evaporate [20]", see [3], and cease to be finished in finite outer time in accordance with Oppenheimer and Snyder's original prediction of 1939 [21]. $c$-global makes the distance to the horizon infinite, not only in time as is well known [21], but also in space (while the short proper times of in-falling observers lose their erroneously assumed equivalent status). The altered features of black holes due to $c$-global make any attempt at producing them down on earth counter advisable [3].

$c$-global has many further implications, see [4]. The main point in our context is that it pays to return to the young Einstein. Near the beginnings of a new gold vein in science, one always finds further gold when digging there, Maxwell advised. In this way a seemingly "undergraduate" type of approach (like the present one) can prove superior to formally advanced later work, no matter how paradoxical this looks at first sight.

## 4 Convergent Implications for Cosmology

Each of the two mathematically unrelated approaches discussed above (cryodynamics; $c$-global) implies absence of cosmological expansion. The Big Bang has become a redundant hypothesis in light of cryodynamics just as Zwicky had conjectured; and the Big Bang has become an inadmissible hypothesis in light of the repaired constant-$c$ element of general relativity (Schwarzschild metric [3], equivalence principle [4]).

The lack of expansion is the main new feature of *Cosmology 2.0*. It allows the prediction that an unbounded "Clifford-Einstein cosmos" can be formulated eventually. Many new and novel questions will need to be answered along the way. Since black holes are no longer finished in finite outer time: can it be that the bigger partner in a merger of two black holes "recycles" the likewise unfinished smaller one? This is the hypothesis of a "blue-sky catastrophe" in the sense of differential topology (see Ralph Abraham [22]) leading to black hole recycling [23]. Alternatively, the quasar ejection mechanism [24] will need to be shown to be more efficient than is currently known.

In the absence of some efficient recycling mechanism like the one just mentioned, the cosmos would have long ceased to be an active ballpark. Thus a major new open problem – the nature of the recycling mechanism – deserves urgent attention.

The second major point to be answered is the origin of the so-called cosmic background radiation (CBR) in a non-expanding cosmos. It cannot come from very far away any more. The radiation of the CBR was long before its empirical discovery by Wilson and Penzias [25] predicted by Guillaume in 1896 [26], and later Nernst [27] and Born [28], as Assis and Neves [29,30] showed. It reflects the presence of a virtually constant-temperature shell around our galaxy – the galactic halo. The "anomalies" recently discovered in the Planck mission [31] can now be faced squarely.

The amazing linearity of the Hubble line over orders of magnitude also remains to be explained. The famous "wiggle" at its end [32] follows predictably from the huge voids in the cosmos whose size becomes bigger with distance statistically in a fractal Fournier-Mandelbrot [33] sponge.

## 5 Discussion

Two recent classical-in-spirit physical discoveries, cryodynamics and global-*c* general relativity (the latter still unfinished), were reported on with an eye to their cosmological implications. A whole "bouleversement" of 20th century cosmology followed. Such "swerves" are rare in science.

In a sense, cryodynamics and *c*-global each rest on a naïve question: (a) How about inverting the sign of the interaction-generating forces in classical statistical mechanics?; and (b) How about reconciling constant-*c* special relativity with the apparent non-constant-*c* implication so reluctantly accepted in the equivalence principle and hence in gravitation by Einstein in 1907 [15]? The two questions prove to be far-reaching. Both moreover lead to convergent implications regarding the scientific picture of the cosmos. A potentially infinite and eternal fractal Clifford-Einstein-Fournier-Mandelbrot cosmos appears to take shape in their wake [23].

This conclusion is very baffling since it is a long time that a consensus held by virtually the whole scientific community over many decades, had to be given up. The *phlogiston* theory is the last example that comes to mind. An excuse why such could occur in our own time with the Big Bang theory will be needed. Here chaos theory comes to mind. Its overwhelming, transfinitely exact features go back to Poincaré – the same Poincaré who first wrote down the Lorentz transformation and who had

named and in parallel to Einstein invented the theory of relativity. His deterministic spirit got underestimated in the following decades, cf. [34]. If Poincaré had not died prematurely in 1912, the development sketched above would most likely have taken place a century earlier. It goes without saying that all of the above is mathematically trivial compared to QED and modern field theories.

To conclude, a synopsis of two recent developments in classical fundamental physics was offered. It comes as a surprise that thereby a return to an earlier stage of physics became necessary. On the one hand, the deterministic Boltzmann-Sinai model of classical statistical mechanics admits a generalization towards attractive Newtonian (and post-Newtonian) potentials. On the other, a return to the special-relativistic roots of general relativity enables a revival of the global constancy of the speed of light *c* in the vacuum. Both recent findings independently enforce the same radically new picture of the cosmos. The new picture is maximally old at the same time in light of Heraclitus' now no longer cryptic phrase *metabállon anapaúetai* – "metabolizing it rests."

**Acknowledgements.** I thank the organizer for the kind invitation and advice. For J.O.R.

## References

1. Rössler, O.E.: The new science of cryodynamics and its connection to cosmology. Complex Systems 20, 105–113 (2011); Open access
2. Rössler, O.E.: Abraham-solution to Schwarzschild metric implies that CERN miniblack holes pose a planetary risk. In: Plath, P.J., Hass, E.C. (eds.) Vernetzte Wissenschaften: Crosslinks in Natural and Social Sciences, pp. 263–270. Logos Verlag, Berlin (2008), http://www.wissensnavigator.ch/documents/OTTOROESSLERMINIBLACKHOLE.pdf
3. Rossler, O.E.: Abraham-like return to constant c in general relativity: "ℜ-theorem" demonstrated in Schwarzschild metric. Fractal Spacetime and Noncommutative Geometry in Quantum and High Energy Physics 2, 1–14 (2012), Preprint 2008: http://www.wissensnavigator.com/documents/chaos.pdf
4. Rossler, O.E.: Einstein's equivalence principle has three further implications besides affecting time: T-L-M-Ch theorem ("Telemach"). African Journal of Mathematics and Computer Science Research 5, 44–47 (2012); Open access
5. Diebner, H.H.: Time-dependent Deterministic Entropies and Dissipative Structures in exactly reversible Newtonian Molecular-dynamical Universes. Doctoral thesis. Verlag Ulrich Grauer, Stuttgart (1999) (in German)
6. Diebner, H.H., Rössler, O.E.: A deterministic entropy based on the instantaneous phase space volume. Z. Naturforsch. 53, 51–60 (1998); Open access
7. Rössler, O.E., Sanayei, A., Zelinka, I.: Is hot fusion made feasible by the discovery of cryodynamics? In: Zelinka, I., Snasel, V., Rössler, O.E., Abraham, A., Corchado, E.S. (eds.) Nostradamus: Mod. Meth. of Prediction, Modeling. AISC, vol. 192, pp. 1–4. Springer, Heidelberg (2013), http://link.springer.com/chapter/10.1007/978-3-642-3...ccess=true
8. Zwicky, F.: On the red shift of spectral lines through interstellar space. Proc. Nat. Acad. Sci. 15, 773–779 (1929)

9. Rössler, O.E., Fröhlich, D., Kleiner, N.: A time-symmetric Hubble-like law: light rays grazing randomly moving galaxies show distance proportional redshift. Z. Naturforsch. 58a, 807–809 (2003)
10. Sonnleitner, K.: StV4: A symplectic 4th order Störmer-Verlet Algorithm for Hamiltonian multi-particle Systems with two applied Examples (Gas, T-tube Configuration). PhD dissertation, University of Tubingen (2010), http://www.wissensnavigator.com/documents/StV4-universell.pdf (in German)
11. Movassagh, R.: A time-asymmetric process in central force scatterings. arxiv.org 2010 (2013)
12. Sinai, Y.G.: Dynamical systems with elastic reflections. Russ. Math. Surv. 25, 137–189 (1970)
13. Rossler, O.E.: Rolling ball in breathing plane-tree alley paradigm. European Scientific Journal 9(27), 1–7 (2013); Open access
14. Becker, R.: Theory of Heat. Springer, New York (1967)
15. Einstein, A.: On the relativity principle and the conclusions drawn from it. Jahrbuch der Radioaktivität 4, 411–462, 458 (1907), English translation: http://www.pitt.edu/~jdnorton/teaching/GR&Grav_2007/pdf/Einstein_1907.pdf (second-but-last page)
16. Einstein, A.: On the influence of gravity on the dispersion of light (Über den Einfluss der Schwerkraft auf die Ausbreitung des Lichtes). Annalen der Physik 35, 898–908 (1911)
17. Einstein, A.: The foundation of the general theory of relativity (Die Grundlage der allgemeinen Relativitätstheorie). Annalen der Physik 49, 769–822 (1916)
18. Rossler, O.E.: Olemach theorem: angular-momentum conservation implies gravitational-redshift proportional change of length, mass and charge. European Scientific Journal 9(6), 38–45 (2013); Open access
19. Rossler, O.E.: "Schwinger theorem": ascending photons in equivalence principle imply globally constant *c* in general relativity. European Scientific Journal 10(3), 26–30 (2014); Open access
20. Hawking, S.W.: Black hole explosions. Nature 248, 30–31 (1974)
21. Oppenheimer, J.R., Snyder, H.: On continued gravitational attraction. Phys. Rev. 56, 455–459 (1939)
22. Abraham, R.: Chaostrophes, intermittency, and noise. In: Fischer, P., Smith, W.R. (eds.) Chaos, Fractals and Dynamics, pp. 3–22. Marcel Decker, New York (1985)
23. Rossler, O.E.: Complexity decomplexified: a list of 200+ new results encountered over 55 years. In: Zelinka, I., Sanayei, A., Zenil, H., Rössler, O.E. (eds.) How Nature Works, pp. 1–18. Springer, Heidelberg (2014), see # CXCI, CLXXVII, CLXXXVI
24. Blandford, R.D.: Active Galactic Nuclei. Springer, Heidelberg (2006)
25. Penzias, A.A., Wilson, R.W.: A measurement of excess antenna temperature at 4080 Mc/s. Astrophysical Journal Letters 142, 419–421 (1965)
26. Guillaume, C.E.: La température de l'espace (The temperature of space). La Nature 24(2), 210–234 (1896); Quote: We conclude that the radiation of the stars alone would maintain the test particle, that we suppose might have been placed at different points in the sky, at a temperature of 338/60 = 5.6 abs.
27. Nernst, W.: Further examination of the assumption of a stationary state of the universe. Zeits. Phys. 106, 633–661 (1937); 2.8 K predicted (in German)
28. Born, M.: On the interpretation of Freundlich's red-shift formula. Proc. Phys. Soc. A 67, 193–194 (1954)

29. Assis, A.K.T., Neves, M.C.D.: The redshift revisited. Astrophysics and Space Science 227, 13–24 (1995)
30. Assis, A.K.T., Neves, M.C.D.: History of the 2.7 K temperature prior to Penzias and Wilson. Apeiron 2, 79–84 (1995)
31. ESA, Planck reveals an almost perfect universe (select page 2 there, which contains the decisive figure titled, Asymmetry and cold spot) (2013), http://www.esa.int/Our_Activities/Space_Science/Planck/Planck_reveals_an_almost_perfect_Universe
32. Interview with Saul Perlmutter, Brian P. Schmidt and Adam G. Riess (37 minutes), http://www.nobelprize.org/mediaplayer/index.php?id=1745
33. Mandelbrot, B.B.: Fractal Geometry of Nature. Freeman, San Francisco (1977)
34. Sanayei, A., Rössler, O.E.: Chaotic Harmony – A Dialog about Physics, Complexity and Life. Springer, Heidelberg (2014), http://link.springer.com/book/10.1007/978-3-319-06781-0/page/1

# Hidden Quantum Markov Models and Open Quantum Systems with Instantaneous Feedback

Lewis A. Clark[1], Wei Huang[2], Thomas M. Barlow[1], and Almut Beige[1]

[1] The School of Physics and Astronomy, University of Leeds, Leeds, LS2 9JT, United Kingdom
[2] 20 Dover Drive Singapore, Singapore University of Technology & Design, Singapore, 138682, Singapore

**Abstract.** Hidden Markov Models are widely used in classical computer science to model stochastic processes with a wide range of applications. This paper concerns the quantum analogues of these machines — so-called Hidden Quantum Markov Models (HQMMs). Using the properties of Quantum Physics, HQMMs are able to generate more complex random output sequences than their classical counterparts, even when using the same number of internal states. They are therefore expected to find applications as quantum simulators of stochastic processes. Here, we emphasise that open quantum systems with instantaneous feedback are examples of HQMMs, thereby identifying a novel application of quantum feedback control.

**Keywords:** Stochastic Processes, Hidden Markov Models, Quantum Simulations, Quantum Feedback.

## 1 Introduction

In classical computer science, a Markov chain is a memoryless stochastic machine, which progresses from one state to another on a discrete time scale. Since their introduction in 1906 by Andrey Markov, the properties of Markov chains have been studied in great detail by mathematicians, computer scientists, and physicists alike [1]. In the meantime, more complex versions of stochastic machines, like *Hidden Markov Models* (HMMs), have been introduced. These progress randomly from one internal state to another, which remains unobserved (hidden), while producing a stochastic output sequence. HMMs are widely used for the simulation of stochastic processes [2–4]. Applications include speech recognition, image analysis and the modelling of biological systems.

Over recent years, several attempts have been made to extend the definition of HMMs into the quantum world and to utilise the properties of quantum systems to generate more complex stochastic output sequences [5–9]. For example, in 2011, Monras *et al.* [6] introduced so-called *Hidden Quantum Markov Models* (HQMMs). These are machines that progress from one quantum state to another,



A. Sanayei et al. (eds.), *ISCS 2014: Interdisciplinary Symposium on Complex Systems*, Emergence, Complexity and Computation 14, DOI: 10.1007/978-3-319-10759-2_16

while generating classical output symbols. To produce an output symbol, a so-called generalised measurement or Kraus operation [10] is performed on the internal state of the machine. One way of implementing a Kraus operation is to use an auxiliary quantum system — a so-called ancilla. In every time step, the internal state of the HQMM interacts with its ancilla, which is then read out by a projective measurement. After every measurement, the ancilla is reset into its initial state, while the internal state of the HQMM remains hidden.

A Kraus operation is the most general operation that a quantum system can experience, which is why Kraus operations are a vital part of the definition of a HQMM given by Monras *et al.* [6]. In a previous attempt to introduce quantum analogues of HMMs, Wiesner and Crutchfield [5] defined so-called quantum finite-state generators, which only involved unitary operations and projective measurements. This is the most basic way in which a quantum system may be evolved and measured. The state evolves according to the given unitary operator and is then measured, collapsing the state onto the measurement outcome. In this way, they only obtained a subset of HQMMs, which are less powerful than their classical analogues. Different from quantum finite-state generators, HQMMs are able to produce more complex output sequences than HMMs with the same number of internal states.

Several ways of implementing HQMMs have already been identified:

1. As pointed out in Ref. [6], one way of implementing HQMMs is the successive, non-adaptive read-out of entangled many-body states.
2. Another example of a HQMM is the time evolution of an open quantum system on a coarse grained time scale, $\Delta t$, which produces a random sequence of classical output symbols. Indeed, in Ref. [9], Sweke, Sinayskiy, and Petruccione use the language of HMMs to model open quantum systems.
3. The purpose of this paper is to highlight the connection between HQMMs and open quantum systems with *instantaneous feedback* [11]. In this way, we identify a way of implementing an even wider set of HQMMs.

Like HQMMs, open quantum systems evolve randomly in time. Taking this perspective, the open quantum system itself provides the internal states of a HQMM, while its surrounding bath plays the role of the ancilla, which is constantly reset into an environmentally preferred, or *einselected*, state [12]. By this, we mean the state that the environment would naturally evolve into if left alone. The continuous interaction between the internal states and the bath moves the bath away from its einselected state, thereby usually producing a measurable response that manifests itself as a random classical symbol. The effective dynamics of such a machine, when averaged over all possible trajectories, can be described by a Markovian master equation [13–15]. When describing an open quantum system in this way, its accompanying output sequence is ignored. Here we suggest not to do so and to use the output sequences of open quantum systems to simulate stochastic processes. Like HMMs, we expect HQMMs to find a wide range of applications [6, 16, 17].

Quantum feedback is a process in which the classical output symbols produced by an open quantum system are used to change its internal dynamics.

Applications of quantum feedback control can be found, for example, in Quantum Information Processing [11], where it is especially used to control state preparation [18] and quantum transport [19]. In these applications, the feedback is used to guide the internal dynamics of a quantum system. In contrast to this, this paper proposes to use quantum feedback to manipulate the classical output sequences of open quantum systems.

There are five sections in this paper. Sect. 2 shortly reviews HQMMs. Afterwards, in Sect. 3, we review the master equations of Markovian open quantum systems with and without instantaneous feedback. Sect. 4 shows that open quantum systems with instantaneous feedback are examples of HQMMs. Finally, we summarise our findings in Sect. 5.

## 2 Hidden Quantum Markov Models

Hidden Markov Models (HMMs) are machines that evolve randomly from one internal state to another. In every time step, an output symbol is produced. Only the output symbol is detected externally, while the internal state of the machine remains hidden. Consequently, the time evolution of a HMM is characterised through a set of transition matrices $T_m$, where $m$ denotes the output symbol generated during the respective time step. For example, if the initial probability distribution of the internal states of the HMM is given by a vector $\boldsymbol{p}_0$, then the probability to obtain the outputs $abc\ldots def$, where $a$ is the first symbol produced and $f$ is the last, is given by (see eg. Ref. [6])

$$p(abc\ldots def) = \boldsymbol{\eta}\, T_f T_e T_d \ldots T_c T_b T_a\, \boldsymbol{p}_0\,. \tag{1}$$

Here, $\boldsymbol{\eta}$ is a vector with all of its coefficients equal to 1.

Analogously, a Hidden Quantum Markov Model (HQMM) with a certain probability distribution of its internal state populations can be described by a density matrix, $\rho_{\mathrm{S}}$. In every time step, the system evolves and produces an output symbol. Again, only the output symbol is detected externally, while the internal state of the machine remains hidden. In contrast to HMMs, the time evolution of a HQMM is governed by a set of Kraus operators $K_m$, where the subscripts $m$ coincide again with the output symbols of the machine. Using the same example as above, the probability of the output $abc\ldots def$ occurring is now given by

$$p(abc\ldots def) = \mathrm{Tr}\left(K_f K_e K_d \ldots K_c K_b K_a\, \rho_{\mathrm{S}}\, K_a^\dagger K_b^\dagger K_c^\dagger \ldots K_d^\dagger K_e^\dagger K_f^\dagger\right)\,. \tag{2}$$

If the output symbol is ignored, then the density matrix $\rho_{\mathrm{S}}(t)$ of a HQMM evolves within a time step $(t, t+\Delta t)$ such that

$$\rho_{\mathrm{S}}(t+\Delta t) = \sum_{m=0}^{\infty} K_m\, \rho_{\mathrm{S}}(t)\, K_m^\dagger\,. \tag{3}$$

The above Kraus operators $K_m$ should form a complete set. This means they need to obey the condition

$$\sum_{m=0}^{\infty} K_m^\dagger K_m = 1 \tag{4}$$

for the density matrix $\rho_{\mathrm{S}}(t+\Delta t)$ to be normalised. More details can be found in Ref. [6].

## 3 Open Quantum Systems

In the following, we describe how master equations can be used to model the time evolution of open quantum systems with linear couplings between the quantum system and its surrounding bath. Adopting the ideas of Zurek and others [12, 20], we assume that the bath possesses an environmentally preferred state, a so-called einselected or pointer state. While the internal states of the open quantum system evolve on a relatively slow time scale, the bath relaxes rapidly back into its preferred state whenever its state is perturbed by the system-bath interaction. The more microscopic approach to the derivation of master equations, which we review here, makes it easy to incorporate instantaneous feedback into the dynamics of the open quantum system.

Our starting point is the Hamiltonian, $H$, for system and bath, which can be split into four parts,

$$H = H_{\mathrm{S}} + H_{\mathrm{int}} + H_{\mathrm{B}} + H_{\mathrm{SB}}\,. \tag{5}$$

Here, $H_{\mathrm{S}}$ describes the free energy of the system and $H_{\mathrm{int}}$ allows for some internal system dynamics. Moreover, $H_{\mathrm{B}}$ represents the free energy of the bath and $H_{\mathrm{SB}}$ accounts for the system-bath interaction. When denoting the energy eigenstates of system and bath by $|n\rangle_{\mathrm{S}}$ and $|m\rangle_{\mathrm{B}}$, respectively, and assuming a linear coupling between system and bath, $H_{\mathrm{S}}$, $H_{\mathrm{B}}$, and $H_{\mathrm{SB}}$ can be written as

$$\begin{aligned} H_{\mathrm{S}} &= \sum_{n=1}^{N} \hbar\omega_n |n\rangle_{\mathrm{SS}}\langle n|\,, \\ H_{\mathrm{B}} &= \sum_{m=0}^{\infty} \hbar\omega_m |m\rangle_{\mathrm{BB}}\langle m|\,, \\ H_{\mathrm{SB}} &= \sum_{m,m'=0}^{\infty}\sum_{n,n'=1}^{N} \hbar g_{nm,n'm'} |n'm'\rangle_{\mathrm{SB\,SB}}\langle nm| + \mathrm{H.c.} \end{aligned} \tag{6}$$

without loss of generality. Because of being a bath, an infinite number of highly degenerate energy levels $\hbar\omega_m$ may occur. Finally, the $g$'s are system-bath coupling constants. Here, we assume for simplicity that these are time independent, though this is not always the case.

Since we are interested in identifying the relatively slow, effective internal dynamics of the open quantum system, we now move into the interaction picture with respect to the free system $H_0 = H_{\mathrm{B}} + H_{\mathrm{S}}$, giving the interaction Hamiltonian

$$\begin{aligned} H_{\mathrm{I}}(t) = &\sum_{m,m'=0}^{\infty}\sum_{n,n'=1}^{N} \hbar g_{nm,n'm'} |n'm'\rangle_{\mathrm{SB\,SB}}\langle nm|\, \mathrm{e}^{-\mathrm{i}(\omega_m-\omega_{m'}+\omega_n-\omega_{n'})t} \\ &+\mathrm{H.c.} + H_{\mathrm{int\,I}}(t) \end{aligned} \tag{7}$$

with $H_{\mathrm{int\,I}}(t)$ describing the internal dynamics of the system in the interaction picture. The Hamiltonian $H_{\mathrm{I}}$ no longer contains free energy terms. The time evolution of system and environment in the interaction picture is hence much slower than in the Schrödinger picture.

Suppose the environment, which the bath couples to, thermalises very rapidly, thereby relaxing the bath into an environmentally preferred state — a so-called pointer state. This state minimises the entropy of the bath and does not evolve in time unless there is a very strong system-bath interaction. In the following, we denote the corresponding bath state by $|0\rangle_{\mathrm{B}}$. Without restrictions, the above introduced notation can indeed be chosen such that the pointer state corresponds to $m = 0$. Moreover, we can choose the free energy of the pointer state such that $\omega_0 = 0$, again without loss of generality.

Next we assume that the initial state of the open quantum system at a time $t$ is given by the density matrix $\rho_{\mathrm{S}}(t)$, while the bath is in $|0\rangle_{\mathrm{B}}$. Over a short time $\Delta t$, the system and bath then evolve in the interaction picture into the density matrix $\rho_{\mathrm{SB}}(t + \Delta t)$ with

$$\rho_{\mathrm{SB}}(t + \Delta t) = U_I(t + \Delta t, t)\,|0\rangle_{\mathrm{B}}\,\rho_{\mathrm{S}}(t)\,{}_{\mathrm{B}}\langle 0|U_I^{\dagger}(t + \Delta t, t)\ . \tag{8}$$

Subsequently, on a time scale that is fast compared to $\Delta t$, the surrounding bath thermalises again, which transforms it back into its pointer state. Due to locality, this process should only affect the bath and not the quantum system itself. All the expectation values of the system should remain the same during the relaxation process. Consequently, the time evolution of system and bath within $\Delta t$ can be summarised as

$$\rho_{\mathrm{SB}}(t + \Delta t) \longrightarrow |0\rangle_{\mathrm{B}}\rho_{\mathrm{S}}(t + \Delta t)_{\mathrm{B}}\langle 0| \tag{9}$$

with

$$\rho_{\mathrm{S}}(t + \Delta t) = \mathrm{Tr}_{\mathrm{B}}\left(\rho_{\mathrm{SB}}(t + \Delta t)\right)\ . \tag{10}$$

This equation describes an effective Markovian system dynamics within the time interval $(t, t+\Delta t)$. To summarise the effective time evolution of the open quantum system in a more compact form, i.e. in form of a master equation, we now calculate the time derivative of $\rho_{\mathrm{S}}(t)$,

$$\dot{\rho}_{\mathrm{S}} = \lim_{\Delta t \to 0} \frac{1}{\Delta t}\left(\rho_{\mathrm{S}}(t + \Delta t) - \rho_{\mathrm{S}}(t)\right)\ . \tag{11}$$

Using the above mentioned time scale separation between the internal and external dynamics of the open quantum system allows us to evaluate equation (10) using second order perturbation theory, which implies

$$U_{\mathrm{I}}(\Delta t, 0) = 1 - \frac{i}{\hbar}\int_0^{\Delta t} \mathrm{d}t\, H_{\mathrm{I}}(t) - \frac{1}{\hbar^2}\int_0^{\Delta t}\mathrm{d}t \int_0^{t} \mathrm{d}t'\, H_{\mathrm{I}}(t)\, H_{\mathrm{I}}(t')\ . \tag{12}$$

Substituting Eqs. (7), (10) and (12) into equation (11) eventually yields a master equation of the general form (see e.g. Refs. [13–15, 20] for more details)

$$\dot{\rho}_{\mathrm{S}} = -\frac{i}{\hbar}\left[H_{\mathrm{int\,I}}, \rho_{\mathrm{S}}\right] - \frac{1}{2}\sum_{n,n',n'',n'''=1}^{N} \xi_{nn'}\xi^{*}_{n''n'''}\ \left[L^{\dagger}_{n''n'''}L_{nn'}, \rho_{\mathrm{S}}\right]_{+}$$

$$+ \sum_{n,n',n'',n'''=1}^{N} \xi_{nn'} \xi^*_{n''n'''} \, L_{nn'} \, \rho_{\mathrm{S}} \, L^\dagger_{n''n'''} \, . \tag{13}$$

The $L$'s in this equation are operators that act on the internal states of the open quantum system and the $\xi$'s are constants. In addition, one can show that the above equation is of Lindblad form [21], which is the most general way of expressing the master equation for a Markovian quantum system.

Equation (13) describes open quantum systems without feedback. These are quantum systems, where the environment does nothing else but constantly resets the bath that surrounds the system back into its pointer state. However, this is not necessarily the case. Open quantum systems can be designed such that the population of a state $|m\rangle_{\mathrm{B}}$ that is *not* environmentally preferred, triggers a back action, which changes the density matrix $\rho_{\mathrm{S}}(t)$ by a certain unitary operation $R_m$. Such a back action is known as *feedback*. If the feedback is so fast such that its time scale is short compared to the time scale on which $\rho_{\mathrm{S}}(t)$ evolves, then we talk about instantaneous feedback. Using the same arguments as above, one can show that the open quantum system evolves in this case according to a master equation of the general form

$$\begin{aligned} \dot{\rho}_{\mathrm{S}} = & -\frac{i}{\hbar} \left[ H_{\mathrm{int\,I}}, \rho_{\mathrm{S}} \right] \\ & -\frac{1}{2} \sum_{m=1}^{\infty} \sum_{n,n',n'',n'''=1}^{N} \xi_{nn',m} \xi^*_{n''n''',m} \, \left[ L^\dagger_{n''n''',m} L_{nn',m}, \rho_{\mathrm{S}} \right]_+ \\ & + \sum_{m=1}^{\infty} \sum_{n,n',n'',n'''=1}^{N} \xi_{nn',m} \xi^*_{n''n''',m} \, L_{nn',m} \, \rho_{\mathrm{S}} \, L^\dagger_{n''n''',m} \end{aligned} \tag{14}$$

with the $L_{nn',m}$ operators defined such that

$$L_{nn',m} = R_m \, L_{nn'} \, . \tag{15}$$

This equation is of exactly the same form as the master equation for open quantum systems with instantaneous feedback in Ref. [11].

## 4 Open Quantum Systems as HQMMs

Comparing the above description of open quantum systems with the definition of the HQMM in Sect. 2, it becomes relatively straightforward to see that open quantum systems with instantaneous feedback are concrete examples of HQMMs. To illustrate this in more detail, we notice that $\rho_{\mathrm{S}}(t + \Delta t)$ in equation (10) is a statistical mixture of different subensembles and distinguish two cases.

### 4.1 Energy Exchange with Bath and Environment

The first case is the one, where the bath has been reset into its pointer state, $|0\rangle_{\mathrm{B}}$, within $(t, t + \Delta t)$ after having evolved into $|m\rangle_{\mathrm{B}}$ and experiencing the feedback

operation $R_m$. The above equations and their given interpretation tell us that the density matrix of the corresponding subensemble equals

$$\rho_{\mathrm{S}}(t+\Delta t|m\geq 1)=K_m\,\rho_{\mathrm{S}}(t)\,K_m^{\dagger} \tag{16}$$

in this case, with the operator $K_m$ given by

$$K_m=\sum_{n,n'=1}^{N}\xi_{nn',m}\,L_{nn'm}\sqrt{\Delta t} \tag{17}$$

for $m\geq 1$. As we shall see below, $K_m$ is a Kraus operator, which acts on the internal state of the open quantum system.

### 4.2 No Energy Exchange between Bath and Environment

The remaining terms in the above master equation correspond to $m=0$ and describe the time evolution of the open quantum system under the condition that the surrounding bath remains in its environmentally preferred state $|0\rangle_{\mathrm{B}}$. In this case, $\rho_{\mathrm{S}}(t)$ evolves within $\Delta t$ into

$$\rho_{\mathrm{S}}(t+\Delta t|m=0)=K_0\,\rho_{\mathrm{S}}(t)\,K_0^{\dagger}\,. \tag{18}$$

Up to first order in $\Delta t$, the corresponding operator $K_0$ can be written as

$$K_0=\exp\left(-\frac{\mathrm{i}}{\hbar}H_{\mathrm{cond}}\Delta t\right) \tag{19}$$

with the non-Hermitian Hamiltonian $H_{\mathrm{cond}}$ given by

$$H_{\mathrm{cond}}=H_{\mathrm{int\,I}}-\frac{\mathrm{i}}{2}\hbar\sum_{m=1}^{\infty}\sum_{n,n',n'',n'''=1}^{N}\xi_{nn',m}\xi^{*}_{n''n''',m}\,L^{\dagger}_{n''n''',m}L_{nn',m}\,. \tag{20}$$

The last term in this equation is crucial for the density matrix $\rho_{\mathrm{S}}(t+\Delta t)$ in equation (14) to remain normalised.

### 4.3 Comparison of Kraus Operators

To show that open quantum systems with instantaneous feedback are examples of HQMMs, we now only need to identify the operators $K_m$ in Eqs. (17) and (19) with the Kraus operators in equation (3). Summing over all of the above described subensembles with their respective output symbols given by $m=0,1,...$, we immediately see that equation (3) applies. Since a density matrix $\rho_{\mathrm{S}}(t)$, which evolves according to the master equation of an open quantum system in Lindblad form remains normalised, we moreover have

$$\mathrm{Tr}_{\mathrm{S}}\left(\sum_{m=0}^{\infty}K_m\,\rho_{\mathrm{S}}\,K_m^{\dagger}\right)=\mathrm{Tr}_{\mathrm{S}}\left(\sum_{m=0}^{\infty}K_m^{\dagger}K_m\,\rho_{\mathrm{S}}\right)=1\,. \tag{21}$$

This means, equation (4) too is satisfied. Open quantum systems with instantaneous feedback are indeed examples of HQMMs.

## 5 Conclusions

Motivated by the popularity of Hidden Markov Models (HMMs) in classical computer science, this paper has a closer look at the quantum analogues of these machines — so-called Hidden Quantum Markov Models (HQMMs) [6]. Sect. 2 defines HQMMs in terms of Kraus operators. Sect. 3 gives an overview of how to model open quantum systems with and without instantaneous feedback with the help of master equations in Lindblad form [11, 13–15, 21]. When comparing Sects. 2 and 3 in Sect. 4, it becomes obvious open quantum systems with random classical output sequences are examples of HQMMs. This paper proposes not to ignore the random classical output sequences of open quantum systems, since they could find interesting applications as quantum simulators of stochastic processes.

Finally, it might be worth noting that the above analysis of open quantum systems with instantaneous feedback only allows for an environmental back action when the system-bath interaction changes the bath into a state that is different from its environmentally preferred state, $|0\rangle_{\mathrm{B}}$. This need not be the case. Physically, it is possible to design open quantum systems, which experience feedback also, when no exchange of energy occurs between system and bath. In this case, the open quantum system can no longer be modelled by a master equation. However, the effective system dynamics would remain Markovian and could be described using the language of HQMMs.

**Acknowledgement.** T. B. acknowledges financial support from a White Rose Studentship Network on Optimising Quantum Processes and Quantum Devices for future Digital Economy.

## References

1. Norris, J.R.: Markov chains, Cambridge University Press (1998)
2. Rabiner, L.R.: A tutorial on hidden Markov models and selected applications in speech recognition. Proc. IEEE 77, 257 (1989)
3. Xue, H.: Hidden Markov Models Combining Discrete Symbols and Continuous Attributes in Handwriting Recognition. IEEE Transactions on Pattern Analysis and Machine Intelligence 28, 458 (2006)
4. Vanluyten, B., Willems, J.C., Moor, B.D.: Equivalence of State Representations for Hidden Markov Models. Systems and Control Letters 57, 410 (2008)
5. Wiesner, K., Crutchfield, C.P.: Computation in finitary stochastic and quantum processes. Physica D 237, 1173 (2008)
6. Monras, A., Beige, A., Wiesner, K.: Hidden Quantum Markov Models and non-adaptive read-out of many-body states. App. Math. and Comp. Sciences 3, 93 (2011)
7. Gmeiner, P.: Equality conditions for internal entropies of certain classical and quantum models, arXiv:1108.5303 (2011)
8. O'Neill, B., Barlow, T.M., Safranek, D., Beige, A.: Hidden Quantum Markov Models with one qubit. In: AIP Conf. Proc., vol. 1479, p. 667 (2012)

9. Sweke, R., Sinayskiy, I., Petruccione, F.: Simulation of Single-Qubit Open Quantum Systems, arXiv:1405.6049 (2014)
10. Kraus, K.: States, Effects and Operations. Lecture Notes in Physics, vol. 190. Springer, Berlin (1983)
11. Wiseman, H.M., Milburn, G.J.: Quantum Measurement and Control. Cambridge University Press (2010)
12. Zurek, W.H.: Decoherence, einselection, and the quantum origins of the classical. Rev. Mod. Phys. 75, 715 (2003)
13. Dalibard, J., Castin, Y., Molmer, K.: Wave-function approach to dissipative processes in quantum optics. Phys. Rev. Lett. 68, 580 (1992)
14. Hegerfeldt, G.C.: How to reset an atom after a photon detection. Applications to photon counting processes. Phys. Rev. A 47, 449 (1993)
15. Carmichael, H.: An Open Systems Approach to Quantum Optics. Lecture Notes in Physics, vol. 18. Springer, Berlin (1993)
16. Goldenfeld, N., Woese, C.: Life is Physics: evolution as a collective phenomenon far from equilibrium. Ann. Rev. Cond. Matt. Phys. 2, 375 (2011)
17. Schuld, M., Sinayskiy, I., Petruccione, F.: Quantum walks on graphs representing the firing patterns of a quantum neural network, arXiv:1404.0159 (2014)
18. Kiesslich, G., Emary, C., Schaller, G., Brandes, T.: Reverse quantum state engineering using electronic feedback loops. New. J. Phys. 14, 123036 (2012)
19. Emary, C.: Delayed feedback control in quantum transport. Phil. Trans. R. Soc. A 371, 1999 (2013)
20. Stokes, A., Kurcz, A., Spiller, T.P., Beige, A.: Extending the validity range of quantum optical master equations. Phys. Rev. A 85, 053805 (2012)
21. Lindblad, G.: On the generators of quantum dynamical semigroups. Comm. Math. Phys. 48, 119 (1976)

# An Efficient Strategy to Handle Complex Datasets Having Multimodal Distribution

Samira Ghodratnama and Reza Boostani

School of Electrical and Computer Engineering, Shiraz University, Shiraz, Iran
sghodratnama@cse.shirazu.ac.ir, boostani@shirazu.ac.ir

**Abstract.** One of the main shortcomings of the conventional classifiers is appeared when facing with datasets having multimodal distribution. To overcome this drawback, here, an efficient strategy is proposed in which a clustering phase is firstly executed over all class samples to partition the feature space into separate subspaces (clusters). Since in clustering label of samples are not considered, each cluster contains impure samples belonging to different classes. The next phase is to apply a classifier to each of the created clusters. The main advantage of this proposed distributed approach is to simplify a complex pattern recognition problem by training a specific classifier for each subspace. It is expected applying an efficient classifier to a local cluster leads to better results compared to apply it to several scattered clusters. In the validation and test phases, before make a decision about which classifier should be applied, we should find the nearest cluster to the input sample and then utilize the corresponding trained classifier. Experimental results over different UCI datasets demonstrate a significant supremacy of the proposed distributed classifier system in comparison with single classifier approaches.

**Keywords:** Distributed classifiers, classifier ensembles, subspace classification, distributed learning, complex systems.

## 1 Introduction

Classification is the most popular machine learning task in different applications. Although there are a number of different models on this major, it is still a challenge for experts to discover a model that can efficiently work on data with unknown distribution. Recently, researchers come to this agreement that a single classifier does not have enough ability, in terms of capacity and generalization, to classify a complex dataset. Among different models of classification, ensemble structures have recently attracted much attention because in many real applications they provide suitable results. As far as ensemble learners (e.g. boosting) are highly sensitive to noisy samples, this paper is aimed at proposing a completely new idea to handle datasets having multimodal density distribution. The main idea of this paper is to convert a big complex problem into some small problems with lower complexity and apply a learner to each subspace. It is obvious that the probability of getting good result by applying a classifier to a certain partition is more than expecting good results by applying just one learner for some scattered cluster of samples.



A. Sanayei et al. (eds.), *ISCS 2014: Interdisciplinary Symposium on Complex Systems*,
Emergence, Complexity and Computation 14, DOI: 10.1007/978-3-319-10759-2_17

## 2 Related Work

There are different approaches to combine several methods to achieve a more comprehensive model. Different methods for combining classifiers have been proposed in terms of Bagging [1], Boosting [2] and Stacking [3]. In the most ensemble methods like Boosting, a series of learners are sequentially trained that each tries to cover the former's shortcoming. Nevertheless, boosting use the benefit of parallel decision making via combining its learner's vote [2]. It can be said that each learner of Boosting is more focused on the former misclassified samples but consider the other samples with lower attention. Nevertheless, each learner of Boosting is biased to some samples which are not necessarily localized in a certain subspace.

Therefore, we can say that the idea of partitioning the feature space into non-overlapping regions and make a distributed classifier system is not fully employed in the Boosting framework. Moreover, Bagging employs several classifiers but there is no guarantee that each learner works on a certain subspace because the selected samples (63% from all samples) for each learner are randomly chosen with replacement. Stacking also uses a parallel structure for decision making and has no constraint on using just one type of learner. Stacking yields better performance than any single classifier and has been successfully used to both supervised [4] and unsupervised learning [5] tasks; however, the difficulty of finding a good approach for meta-level makes it difficult to apply this approach in practice. In distributed classification methods which had been proposed, the common ways for partitioning the feature space are r-sampling and d-sampling [6] that suffer from some weaknesses, one of the most obvious limitations is its need of a complete list of all the members of the population, this list is usually not available for large populations. The other is that there may be practical constraints in terms of time available and access to certain parts of the study area .In this paper, we suggest using a clustering algorithm to partition the feature space into local areas and apply a suitable classifier to each of them.

## 3 Methodology

This paper presents a new strategy to handle datasets with multimodal distributions. In this method we first partition the feature space by a clustering method and then train proper classifiers on each subspace based on some statistical features of subspaces.

Using a proper clustering method to partition the feature space can play an important role in the final result. Among variety of clustering methods, density based clustering methods are of interest due to their properties such as interpretability, creating clusters with arbitrarily shapes, insensitivity to the order of the data points and noise [7, 8]. Some of the state of the art density based clustering methods are DBSCAN [9], OPTICS [10], DBCLASD [11] and DENCLUE [12]. It should be mentioned that in this paper DENCLUE is selected because it is not sensitive to the input dimension while the other mentioned density based clustering methods have serious problem with high dimensional data. To improve the performance of clustering, as many researchers do, a feature selection method is applied to achieve more separable clusters.

After partitioning the feature space by applying a good clustering method, a proper classifier based on statistical properties of each cluster should be chosen (similar to Stacking which employs different types of classifiers). The situation of samples in different subspaces (clusters) are not equal, for instance, some of them contain noisy samples, the population samples belonging to different classes in the created clusters is not the same. In the test phase, each sample has to find its nearest cluster based on the Mahalanobis distance and then the corresponding classifier is used to assign the label to that sample. To evaluate the proposed method, state of the art methods are implemented and all applied to some selected datasets driven form UCI database repository [13]. An overview of our method in the train and test phases is demonstrated in Fig. 1.

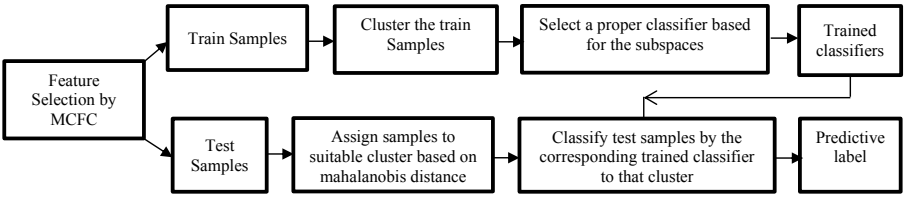


**Fig. 1.** An overview of proposed method

### 3.1 Feature Selection

Reducing the number of features to find the relevant feature subset of the original feature set is important in statistical learning. For many data sets with a large number of features and a limited number of observations, some of the features may usually considered as redundant ones when they do not carry any discriminative information for classifying the samples belong to different classes. Feature selection can also help to avoid the risk of over-fitting and sensitivity to the noisy features. Reducing features can also save storage and computation time and increase the comprehensibility. In this paper, MCFS [14] is used to select the discriminative and informative features. The result of performing this method is illustrated in Table 2.

### 3.2 Clustering Phase

Detecting clusters of points is a challenging issue, especially when the clusters are of different size, density and shape. Many of these issues become even more significant when facing with high dimensional samples when the dataset contains noisy and outlier samples. Density based clustering algorithm is one of the primary methods for clustering. Among the density based algorithms two popular methods are DENCLUE and DBSCAN.

In this paper, DENCLUE algorithm is used as preprocess approach to make subspaces. The advantages of this approach are: (a) it has a firm mathematical basis, (b) it has good clustering properties in data sets with large amounts of noise, (c) it allows a compact mathematical description of arbitrarily shaped clusters in high-dimensional datasets and (d) it is significantly faster than the existing algorithms [12].

Although DENCLUE has some advantages, its problem is the high number of input parameters. We handle this problem by determining the validity of the clusters as it is discussed in next section.

#### 3.2.1 Validation of the Created Clusters

A major challenge in cluster analysis is estimating the optimal number of clusters. There are various methods to determine the validity of the clusters including: Gap statistic [15], Elbows [16], silhouette [17] and prediction strength [18] methods.

We first perform the Gap statistic method to determine optimal number of clusters. When we find out this number, we select the input parameters of DENCLUE method such that the number of clusters become close to the optimal number of clusters achieved by the Gap statistic method. Then we perform Silhouette method to measure how well the samples are clustered.

### 3.3 Classification Phase

The state of the art classifiers are Decision Trees (DT), Random Forest (RF), Support Vector Machine (SVM), k-Nearest Neighbor (KNN), Artificial Neural Networks (ANN), AdaBoost, Bagging and Stacking, and so on. Each of the classification methods shows different efficacy and accuracy based on the statistical characteristics of datasets [19]. Among the mentioned classifiers, SVM, KNN, Neural Network, Decision Tree, Random Forest and AdaBoost are chosen in this study. These selected classifiers can help us having different shape of classes' boundary based on shapes of the data distribution.

Stages of the proposed method are described below in terms of pseudo code.

1. *Perform MCFC algorithm to select the discriminative features*
2. *Run Gap statistic method to find optimal number of clusters*
3. *Perform DENCLUE Algorithm for clustering and adjust its parameter such that the result of clustering become close to the result of Gap statistic method*
4. *The silhouette algorithm is run to determine how valid each of the clusters find out validation of clustering*
5. *Train different classifiers on each cluster*
6. *Use Mahalanobis distance to find the proper cluster of each test data*
7. *Predict the label of test data by classifying the input sample using the trained classifier of the corresponding cluster.*
8. *Use Freidman Test to evaluate the proposed method.*

## 4 Experimental Results

In order to evaluate the proposed method, a set of experiments are run using 12 well-known machine learning datasets driven from the UCI Machine Learning Repository. The details of these data sets are described in Table 1. In selecting the datasets, we tried to cover the following states: low and high dimensional samples, two and multiclass problems, containing noisy and outlier samples, balance and imbalance datasets.

**Table 1.** Selected datasets from UCI database [13]

| Data Set | Number of Features | Number of Samples | Number of classes |
|---|---|---|---|
| Iris | 4 | 150 | 3 |
| Glass | 9 | 214 | 6 |
| Diabetes | 8 | 768 | 2 |
| Bupa | 6 | 345 | 2 |
| Tic_Tac_Toe | 9 | 958 | 2 |
| Heart | 13 | 270 | 2 |
| Wine | 13 | 178 | 3 |
| Seed | 7 | 210 | 3 |
| Satellite | 36 | 6435 | 6 |
| Sonar | 60 | 208 | 2 |
| Blood | 4 | 748 | 2 |
| Letter Recognition | 16 | 20000 | 26 |

**Table 2.** Result of Feature Selection Method

| Data Set | Number of Original Features | Number of Features Selected by MFCF |
|---|---|---|
| Iris | 4 | 4 |
| Glass | 9 | 9 |
| Diabetes | 8 | 8 |
| Bupa | 6 | 6 |
| Tic_Tac_Toe | 9 | 9 |
| Heart | 13 | 5 |
| Wine | 13 | 9 |
| Seed | 7 | 7 |
| Satellite | 36 | 22 |
| Sonar | 60 | 42 |
| Blood | 4 | 4 |
| Letter Recognition | 16 | 16 |

First we applied Gap statistic method to find the suitable number of clusters. The result of Gap statistic, showed in the Table 3, is the median over 10 times running. Then, we execute DENCLUE to cluster the datasets. The number of clusters achieved by this method is also shown in Table 3. After clustering the data points, we perform silhouette method to evaluate the clustering method. The results are illustrated in Table 3.

**Table 3.** The Estimated number of clusters by Gap-Statistics, DENCLUE and the Silhouette value belong to the all samples of DENCLUE clusters

| Data Set | Gap-Statistic Results | Number of Clusters by DENCLUE | Silhouette Results |
|---|---|---|---|
| Iris | 3 | 3 | 0.6992 |
| Glass | 2 | 3 | 0.6178 |
| Diabetes | 3 | 5 | 0.5809 |
| Bupa | 2 | 4 | 0.6513 |
| Tic_Tac_Toe | 3 | 6 | 0.7139 |
| Heart | 3 | 4 | 0.6073 |
| Wine | 3 | 3 | 0.7051 |
| Satellite | 2 | 5 | 0.6647 |
| Sonar | 3 | 2 | 0.7015 |
| Seed | 2 | 3 | 0.6814 |
| Blood | 3 | 4 | 0.7080 |
| Letter Recognition | 3 | 5 | 0.6450 |

After achieving the clusters, we want to classify each cluster to evaluate the proposed method. We first run single classifiers on the selected features of datasets, the results of train and test phases are demonstrated in Tables 3 and 4. In all experiments to validate the results, 10-times 10-fold cross validation is used.

**Table 4.** Result of single classifiers in the train phase (in %)

| Data Set | SVM | AdaBoost | Decision Tree | Random Forest | Neural Network |
|---|---|---|---|---|---|
| Iris | 97.4962± 0.6569 | 97.0666± 0.0063 | 93.8962± 0.0136 | 99.9770± 0.0012 | 97.7472± 1.0404 |
| Glass | 60.5499± 0.6569 | 50.2610± 0.2793 | 70.31855± 1.1931 | 81.7359± 0.0006 | 60.9025± 1.9111 |
| Diabetes | 83.0541± 0.0100 | 80.1373± 0.0224 | 76.4018± 0.3696 | 99.9594± 0.0009 | 77.7748± 0.2660 |

**Table 5.** (*continued*)

| | | | | | |
|---|---|---|---|---|---|
| Bupa | 83.9002± 0.0457 | 82.3961± 0.1302 | 66.8894± 1.7618 | 99.9742± 0.0008 | 71.1108± 1.2184 |
| Tic_Tac_Toe | 99.1336± 0.0006 | 78.6882± 0.0738 | 80.2866± 0.3596 | 99.9976± 0.0002 | 74.8288± 1.5964 |
| heart | 84.0123± 0.0569 | 84.4526± 0.0631 | 67.1563± 1.2886 | 99.8847± 0.0063 | 80.7637± 1.2052 |
| wine | 97.2223± 0.0123 | 99.1260± 0.0129 | 98.7655± 1.1827 | 100.0000± 0.0000 | 97.7037± 0.1522 |
| seed | 92.7566± 0.0363 | 93.6031± 0.0257 | 92.1957± 0.7081 | 99.9894± 0.0004 | 92.5192± 0.3394 |
| Satellite | 80.0800± 0.0010 | 81.1048± 0.0300 | 87.1025± 0.0011 | 100.0000± 0.0000 | 77.6099± 0.0000 |
| Sonar | 99.9821± 0.0430 | 99.9700± 0.045 | 89.5176± 1.3840 | 100.0000± 0.0000 | 85.9441± 1.5579 |
| Blood | 72.7109± 0.0531 | 81.0975± 0.0082 | 60.2559± 0.1475 | 91.8375± 0.0016 | 78.7553± 0.0414 |
| Letter Recognition | 89.0918± 0.0008 | 97.0283± 0.0819 | 79.7195± 0.0198 | 99.3471± 0.00001 | 78.9804± 0.0710 |

**Table 6.** Result of single classifiers in the test phase (in %)

| Data Set | SVM | 1NN | AdaBoost | Decision Tree | Random Forest | Neural Network(MLP) |
|---|---|---|---|---|---|---|
| Iris | 95.4000± 1.3407 | 95.8666± 0.0790 | 95.2000± 0.2765 | 91.7346± 1.0977 | 94.7333± 0.4395 | 93.6571± 1.4427 |
| Glass | 59.5648± 0.1455 | 72.4896± 0.6218 | 48.4976± 0.6600 | 53.2963± 2.317 | 79.1295± 0.8609 | 52.0831± 2.2531 |
| Diabetes | 81.9648± 0.0121 | 67.5622± 0.6604 | 75.4564± 0.3907 | 68.3848± 1.1385 | 76.5085± 0.3660 | 75.9161± 0.7625 |
| Bupa | 82.2405± 0.0392 | 61.8470± 0.6851 | 74.5747± 1.6581 | 51.4974± 2.0210 | 72.3739± 1.7591 | 67.6941± 2.0331 |
| Tic_Tac_Toe | 97.5876± 0.0011 | 69.8941± 0.1024 | 77.1872± 0.2511 | 71.2274± 1.2520 | 94.9783± 0.4466 | 71.0396± 2.1951 |
| heart | 83.1888± 0.0446 | 61.1851± 0.7559 | 76.8888± 0.4328 | 60.1111± 1.2174 | 75.1851± 1.1315 | 77.5389± 1.5282 |
| wine | 95.5134± 0.3623 | 93.2062± 0.1843 | 94.9830± 0.4030 | 92.6662± 1.1959 | 96.8383± 0.6869 | 92.4379± 1.6759 |
| seed | 91.3809± 0.4258 | 90.6190± 0.1033 | 92.1904± 0.4132 | 84.6190± 1.3707 | 93.4761± 0.5568 | 85.7228± 1.2500 |
| Satellite | 78.6500± 0.0000 | 89.8000± 0.0000 | 78.7000± 0.0000 | 75.9500± 0.0000 | 90.8500± 0.0000 | 74.7500± 0.0000 |
| Sonar | 96.0480± 0.0009 | 86.8798± 0.6868 | 82.2930± 1.4187 | 67.6783± 1.4597 | 80.6517± 1.9204 | 72.9322± 2.9881 |
| Blood | 72.4639± 0.0544 | 68.7176± 0.6703 | 79.3063± 0.3253 | 55.0266± 0.9982 | 75.1318± 0.8841 | 77.6245± 0.1308 |
| Letter Recognition | 87.2308± 0.0190 | 96.0129± 0.0026 | 95.2000± 0.2765 | 70.8276± 0.0499 | 92.9871± 0.0054 | 78.5000± 0.4213 |

**Table 7.** Result of the proposed method in the train phase (in %)

| Data Set | SVM | AdaBoost | Decision Tree | Random Forest | Neural Network(MLP) |
|---|---|---|---|---|---|
| Iris | 97.5980± 0.1022 | 99.8460± 0.0634 | 97.5944± 0.1319 | 99.9760± 0.0252 | 88.0865± 1.0405 |
| Glass | 65.4055± 0.2130 | 68.8846± 0.6423 | 71.9866± 1.4389 | 85.9819± 0.0255 | 67.3290± 1.0151 |
| Diabetes | 97.1680± 0.0580 | 95.1057± 0.1391 | 73.2398± 1.1360 | 99.9740± 0.0240 | 83.1820± 1.0012 |
| Bupa | 92.1111± 0.2772 | 97.4543± 0.1108 | 60.1328± 1.0227 | 99.9609± 0.0577 | 66.8888± 1.0902 |
| Tic_Tac_Toe | 99.9388± 0.0080 | 87.4204± 0.1628 | 76.6748± 0.9267 | 99.9596± 0.0268 | 67.0606± 1.0132 |
| Heart | 92.4563± 0.1586 | 91.4914± 0.2394 | 85.4047± 0.5509 | 99.9441± 0.0577 | 71.7695± 1.0335 |
| Wine | 100.000± 0.0000 | 99.9085± 0.0574 | 96.3697± 0.21059 | 100.0000± 0.0000 | 75.6064± 1.0002 |
| Seed | 98.4510± 0.0957 | 98.4873± 0.1518 | 82.2980± 1.2573 | 99.9829± 0.0289 | 66.6320± 1.0122 |
| Satellite | 74.7766± 0.0038 | 79.8715± 0.1002 | 77.5391± 0.5245 | 99.9689± 0.0388 | 72.5204± 1.0295 |
| Sonar | 100.000± 0.0000 | 100.0000± 0.0000 | 82.5325± 1.3477 | 99.9947± 0.0166 | 61.0849± 1.0015 |
| Blood | 76.4389± 0.3329 | 90.0878± 0.0824 | 61.7175± 0.8544 | 96.5688± 0.1884 | 81.1207± 1.0661 |
| Letter Recognition | 90.0412± 0.0320 | 97.9805± 0.0058 | 90.0753± 0.0011 | 99.0810± 0.0000 | 79.9901± 1.0031 |

**Table 8.** Results of the proposed method in the test phase (in %)

| Data Set | SVM | 1NN | AdaBoost | Decision Tree | Random Forest | Neural Network |
|---|---|---|---|---|---|---|
| Iris | 97.6703± 0.1395 | 95.3303± 0.8905 | 93.5122± 0.8060 | 92.1648± 0.2852 | 95.2504± 0.4867 | 85.8000± 1.0094 |
| Glass | 60.9208± 0.4279 | 73.1790± 0.4487 | 60.9159± 0.7094 | 59.0869± 0.0460 | 81.4069± 0.8499 | 56.0029± 2.0901 |
| Diabetes | 87.8929± 0.9643 | 68.3357± 0.6509 | 83.7097± 0.9545 | 70.3452± 0.4882 | 78.1142± 0.7783 | 75.0981± 0.0021 |
| Bupa | 88.2606± 0.6160 | 64.0374± 0.0209 | 80.6944± 0.6032 | 58.3839± 0.2683 | 82.1417± 1.4208 | 61.9761± 1.2387 |
| Tic_Tac_Toe | 98.8454± 0.4492 | 72.0063± 0.5805 | 83.6441± 0.8285 | 74.7350± 0.8476 | 95.7643± 0.6645 | 65.0971± 0.0461 |
| heart | 85.2965± 0.2371 | 66.3667± 0.9837 | 79.0835± 0.1559 | 73.2512± 1.7372 | 88.0271± 0.0906 | 68.6043± 1.0790 |
| wine | 95.4987± 1.4510 | 94.1081± 0.3755 | 94.8566± 0.8298 | 93.4226± 0.7543 | 96.5191± 0.3363 | 71.0512± 1.0816 |
| Seed | 93.6824± 0.6576 | 90.3891± 0.0876 | 92.9188± 0.5909 | 80.0596± 1.5077 | 94.2951± 0.1912 | 62.3809± 1.0300 |
| Satellite | 71.4349± 0.1326 | 90.7558± 0.3425 | 78.3063± 0.0612 | 75.0782± 0.4934 | 91.0341± 0.2092 | 70.0028± 0.1200 |
| Sonar | 97.9587± 0.5514 | 89.1825± 0.3919 | 81.3501± 0.1334 | 62.7111± 0.7949 | 78.1362± 0.4637 | 59.3451± 0.5419 |
| Blood | 75.3054± 0.5344 | 70.6725± 0.8280 | 83.0599± 0.4114 | 58.0657± 0.4191 | 77.2757± 0.8171 | 73.2415± 0.0002 |
| Letter Recognition | 88.9871± 0.0001 | 98.8466± 0.1854 | 95.9099± 0.0065 | 73.1114± 0.0098 | 93.9104± 0.0041 | 75.0817± 0.0361 |

Results of executing classifiers on each cluster of a dataset are shown in Table 5 and Table 6. The final result is the mean over the performance of each cluster.

Our results indicate that ensemble of individual partitions can yield better results than learning one classifier over the entire dataset.

## 5 Evaluation

To measure the performance of the proposed method, especially for multiclass problems, we execute the Friedman test [20]. We compare the result of each single classifier to considering that classifier in the proposed framework in both test and train phase. The results illustrate that 1NN, AdaBoost and Random Forest have remarkable improvement in almost datasets in both train and test phases but Neural Network and SVM do not perform that well.

To demonstrate the supremacy of the proposed distributed method, we plot the performance of each single classifier versus corresponding distributed classifier over mean of all datasets in Fig. 2 As we see in most classifiers, the proposed distributed method (DMethod) is performed better, although the rate of improvements are different depending on the structure of classifiers. As an example the KNN method is locally acted, it is clear that in the distributed KNN method (DKNN) which locality is considered, the rate of the improvement would be much more significant compare to methods like decision tree that locality is not that important. In Fig. 2, it is showed that MLP performs not well, it is not surprising since MLP is a classifier that learns from samples, reducing sample size leads to information loss and therefore do not provide a remarkable result. The other method which is not performed well is SVM; since using nonlinear kernel is somehow a blind process, we cannot exactly figure out how the input distribution is changed in the higher dimensional space (kernel space). Based on cover's theorem [21], mapping the original data by a suitable kernel leads to re-distribute the transformed samples such that they are more likely to be linearly separable in transformed space. Nevertheless, there is no guaranty that a proper kernel can act well on all existing datasets. Thus, as we can see from Fig. 3, the results for some datasets are improved and for some others are diminished.

In Fig. 2, we plot for each point a square which illustrates the standard deviation (mean+SD and mean-SD). As it is showed, the standard deviation in the proposed method is a very small value such that in the figure it cannot be seen but in single classifier is noticeable. This result presents that the proposed distributed method is more stable than the single classifiers.

The other strength of our method is that by reducing the sample size and also features size, it is clear that the complexity of each classifier for each local cluster is reduced and therefore the overall complexity is reduced.

To analysis the results based on the selected features of datasets, we choose the best classifier (from Fig. 2) and compare the result of this classifier in the single mode (KNN) and distributed (DKNN) mode for all 12 datasets, separately. Although the rate of improvement is different over datasets, in all datasets, the distributed method mode has perform better except for the Glass dataset that the results get worse and in

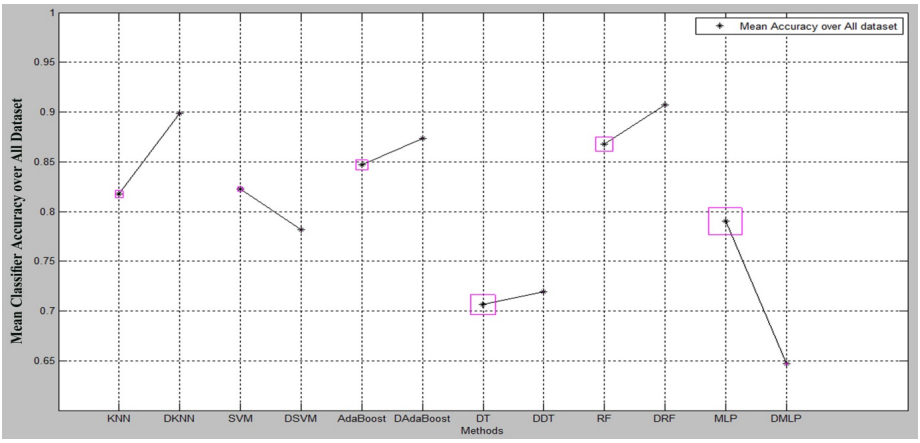


**Fig. 2.** Compare the results of single classifier and the proposed method over all datasets

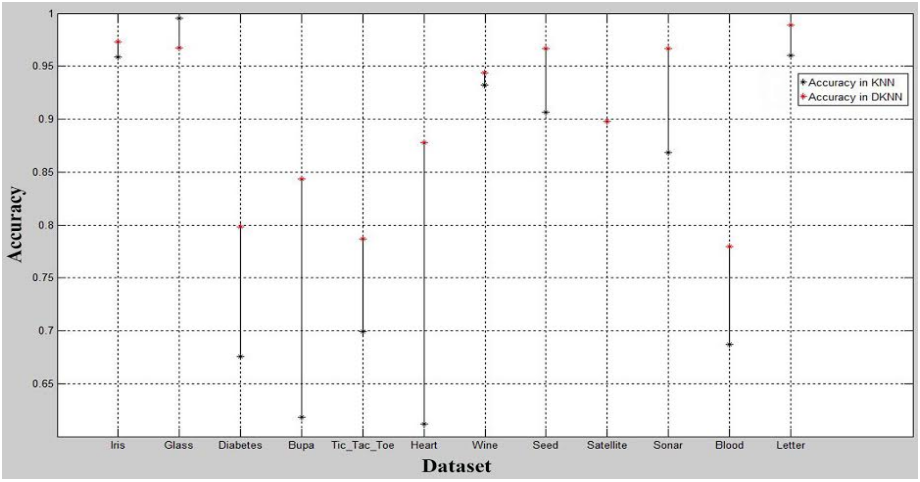


**Fig. 3.** Compare the results of KNN and DKNN for each dataset separately

Satimage (Satellite) which the results are near the same. Since we remove the noise in the clustering phase, in datasets contains noisy samples and also in datasets where data points are not well-separated (highly overlapped), the results show significant improvement but in datasets which points are well-separated, the improvement is not that significant.

## 6 Conclusions

In this paper, we present a novel approach to improve the performance of distributed classifier systems based on local learning. The idea of this approach is to simplify a complex problem into some simpler problems by clustering the entire dataset and assign a classifier to classify the samples within each cluster. Experimental results

demonstrate a significant supremacy of the proposed distributed classifier system in comparison with single classifier approaches, especially in the test phase as discussed in section 5. As the future work, distance metric should be selected specifically for each cluster corresponding to its density shape and its statistical properties. For this purpose, a distance learning process can be considered to improve the results.

## References


1. Breiman, L.: Bagging predictors. Journal of Machine Learning 24(2), 123–140 (1996)
2. Schapiro, R.E.: The Strength of Weak Learnability. Journal of Machine Learning 5(2), 197–227 (1990)
3. Wolpert, D.H.: Stacked Generalization. Journal of Neural Networks 5(2), 241–259 (1992)
4. Breiman, L.: Stacked Regression. Journal of Machine Learning 24(1), 49–64 (1996)
5. Smyth, P., Wolpert, D.: Linearly Combining Density Estimators via Stacking. Journal of Machine Learning 36(1), 59–83 (1999)
6. Lazarevic, A., Obradovic, Z.: Boosting Algorithms for Parallel and Distributed Learning. Journal of Distributed and Parallel Databases 11(2), 101–229 (2002)
7. Parimala, M., Lopez, D., Senthilkumar, N.C.: A Survey on Density Based Clustering Algorithms for Mining Large Spatial Databases. International Journal of Advanced Science and Technology 31 (2011)
8. Nagpal, P., Mann, P.: Comparative Study of Density based Clustering Algorithms. International Journal of Computer Applications 27(11), 421–435 (2011)
9. Ester, M., Kriegel, H.P., Sander, J., Xu, X.: A Density-based algorithm for discovering clusters in large spatial databases with noise. KDD 96(34), 226–231 (1996)
10. Ankrest, M., Breunig, M., Kriegel, H., Sander, J.: OPTICS: Ordering Points to Identify the Clustering Structure. In: International Conference on Management of Data, pp. 49–60 (1999)
11. Xiaowei, X., Jägerand, J., Kriegel, H.P.: A fast parallel clustering algorithm - for large spatial databases. Journal of Data Mining and Knowledge Discovery 3, 263–290 (1999)
12. Hinneburg, A., Keim, D.A.: A General Approach to Clustering in Large Databases with Noise. Journal of Knowledge and Information Systems (KAIS) 5(4), 387–415 (2003)
13. Bache, K., Lichman, M.: UCI Machine Learning Repository. University of California, School of Information and Computer Science, Irvine (2013), `http://archive.ics.uci.edu/ml`
14. Cai, D., Zhang, C., He, X.: Unsupervised Feature Selection for Multi-cluster Data. In: 16th ACM SIGKDD Conference on Knowledge Discovery and Data Mining (KDD 2010) (July 2010)
15. Tibshirani, R., Walther, G., Hastie, T.: Estimating the number of clusters in a dataset via the Gap statistic. Journal of the Royal Statistical Society 63(2), 411–423 (2001)
16. Thorndike, R.L.: Who Belongs in the Family? Journal of Psychometrika 18, 267–276 (1953)
17. Rousseeuw, P.J.: Silhouettes: a graphical aid to the interpretation and validation of cluster analysis. Journal of Computational and Applied Mathematics 20(1), 53–65 (1987)
18. Tibshirani, R., Walther, G.: Cluster Validation by Prediction Strength. Journal of Computational and Graphical Statistics 14(3), 511–528 (2005)
19. Entezari-Maleki, R., Rezaei, A., Minaei-Bidgoli, B.: Comparison of Classification Methods Based on the Type of Attributes and Sample Size. Journal of Convergence Information Technology (JCIT) 4(3), 94–102 (2009)
20. Friedman, M.: A correction: The use of ranks to avoid the assumption of normality implicit in the analysis of variance. Journal of the American Statistical Association 32(200), 675–701 (1937)
21. Ting, K., Zhu, L., Wells, J.R.: Local Models—The Key to Boosting Stable Learners Successfully. Journal of Computational Intelligence 29(2), 331–356 (2013)

# Maximum Likelihood Estimation and Integration Algorithm for Modeling Complex Systems

Yoshinao Shiraki

Toho University, Chiba, 274-8510, Japan
shiraki@is.sci.toho-u.ac.jp

**Abstract.** The holonomic gradient descent (HGD) method has been proposed as a means for calculating the maximum likelihood estimate (MLE), and its effectiveness has, in recent years, been reported within the statistics community. The purpose of HGD calculations is to reduce the calculation of the maximum likelihood estimate (MLE) of particular types of functions to calculating the minimum value of the holonomic function. As is well known, the maximum likelihood estimate (MLE) plays an important role in complex systems theory. In the complex systems community, however, little is known about the holonomic gradient descent (HGD) method. In this article, we introduce this method to the complex systems community and review the calculation mechanism of HGD.

**Keywords:** Maximum Likelihood Estimate (MLE), Groebner Basis, Holonomic Gradient Descent (HGD), Integration algorithm.

## 1 Introduction

In order to calculate the maximum likelihood estimate (MLE) it has been proposed to use the holonomic gradient descent (HGD) method, and its effectiveness has, in recent years, been reported within the statistics community ([3,1,12]). The purpose of this method is to reduce the calculation of the maximum likelihood estimate (MLE) of particular types of functions to calculating the minimum value of the holonomic function. As is well known, the maximum likelihood estimate (MLE) plays an important role in optimal control theory (see cf. [5]). In the control community, however, little is known about the holonomic gradient descent (HGD) method. Therefore, in this article, we introduce this method to the complex systems community and review the calculation mechanism of HGD.

The holonomic gradient descent (HGD) method turns an analytical problem into an algebraic one. HGD eases the difficulties of calculating the integrals that appear in likelihood calculations, by utilizing a hlinear algebraic calculationh as follows: First, HGD uses the fact that most probability density functions are holonomic functions[2]. It then reduces the calculation of the definite integral of the probability density function to a hlinear algebraic calculationh on a holonomic function. hThe definite integral in a probability density functionh is the normalization constant, and the hlinear algebraic calculationh is simplified by



A. Sanayei et al. (eds.), *ISCS 2014: Interdisciplinary Symposium on Complex Systems*, Emergence, Complexity and Computation 14, DOI: 10.1007/978-3-319-10759-2_18

hcalculating the Groebner basis[9]". For a differential operator$L$ of rational coefficients, when the equation $L \bullet f = 0$ holds, the function $f$ is called a holonomic function.

Next, let's look back on the likelihood calculation. First, the probability density function $p(x)$ can be written as follows:

$$p(x) = \frac{f(x)}{\int_D f(x)dx}. \tag{1}$$

Here, the definite integral $\int_D f(x)dx$ is the normalization constant and is the central element in the likelihood calculation. It often happens that calculating the normalization constant from the definite integral is difficult. In many cases, the normalization constant cannot be expressed by the simple integral given in equation (1). If $\theta$ represents the dispersion parameters, such as the average, then the definite integral becomes $F(\theta) = \int_D f(\theta, x)dx$. In this case, the conventional likelihood calculation becomes difficult, and it is much better to use the holonomic gradient descent (HGD) method. By taking advantage of the fact that the probability density function is a holonomic function, the difficulties in the calculation can be eased as follows:

1 The normalization constant $F(\theta) = \int_D f(\theta, x)dx$ is also a holonomic function of $\theta$.
2 The use of Groebner basis calculations for the differential equation system becomes applicable.

Fortunately, the fact that hmost probability density functions are holonomic functions h means that a good deal of attention has been focused on the holonomic gradient descent(HGD) method. Of course, rational or polynomial functions are holonomic functions. In addition, holonomic functions have hdesirable propertiesh and are equivalent or superior to trigonometric and polynomial functions. hThe desirable properties of holonomic functionsh are that they are closed under definite integral calculations and sum, difference, and product operations. hThe motivation for thinking about things that have desirable properties such as holonomic functionshis because hpeople want to make concrete things easy to handle algebraicallyh (thought attributed to Mikio Sato) [8].

In Section 2, we review the holonomic gradient descent (HGD) method. In Section 3, we examine the effectiveness of the method, including the effectiveness of using Groebner basis calculations for the algorithm to calculate the minimum value of the holonomic function ([6,7]). Concerning a comparison with the Maximum likelihood method, please refer to [3]. It should be noted that, in this article, we mainly describe the application of the HGD method to maximum likelihood estimates. However, the method is also applicable to other estimation methods, for example, refer to [10] for applications to MAP (Maximum-a-Posteriori (MAP)) estimation, etc..

## 2 Holonomic Gradient Descent (HGD)

In this section, we review the holonomic gradient descent method, focusing on the motivation for its introduction [11].

### 2.1 The Gradient Descent Method and Its Computational Difficulties

The gradient descent method is a powerful tool for determining the maximum or minimum value of a given function $g$, by sequentially updating the solution $z^{(k)}$. When updating the solution, the gradient descent method primarily uses the gradient $\nabla g$ to provide information about increases or decreases in $g$ and also uses the Hessian matrix $H_k$ of the function $g$ as auxiliary information. The solution $z^{(k)}$ is updated according to the following equation:

$$z^{(k+1)} = z^{(k)} + a_k d^{(k)}. \tag{2}$$

Here, $d^{(k)} = -H_k^{-1} \nabla g(z^{(k)})$ is called the search direction and $a_k$ is the updated width. As already mentioned in Section 1, it often occurs that, depending on the given function $g$, we cannot explicitly obtain the Hessian matrix $H_k$ and/or the gradient $\nabla g$. For example, when the normalization constant of the probability density function cannot be obtained analytically, accurate calculations of $H_k$ and $\nabla g$ are difficult.

### 2.2 Holonomic Functions and Their Computational Superiority

On the other hand, when the given function g is a holonomic function, $H_k$ and gradient $\nabla g$ can be easily represented ([12], p.355, Lemma 6.5.1). By calculating the Groebner basis of the differential equation system, it is possible to calculate the $H_k$ and $\nabla g$ sequentially. Fortunately, many functions are holonomic functions. In particular, most probability density functions are holonomic functions. Thus, the maximum likelihood estimate (MLE) is a typical example for which the function is a holonomic function. In MAP (Maximum-a-Posteriori (MAP)) estimation, also, the function is similar to a holonomic function[10].

### 2.3 Holonomic Function and Calculation of the Groebner Basis

As described in Section 1, the holonomic gradient descent (HGD) method turns an analytical problem into an algebraic one. HGD eases the difficulties of calculating the integrals that appear in likelihood calculations, by utilizing a hlinear algebraic calculationh as follows: First, HGD uses the fact that most probability density functions are holonomic functions. It then reduces the calculation of the definite integral of the probability density function to a hlinear algebraic calculationh on a holonomic function. In this subsection, we first describe examples of holonomic functions. Then we describe how the problem of calculating the extreme values of a holonomic function can be reduced to calculating a Groebner basis.

### 2.4 Examples of Holonomic Functions

We show an example of a two-variable holonomic function below. Here, the symbol $\partial_{\theta_i}$ represents a partial derivative; $\frac{\partial}{\partial \theta_i}$. When a two-variable function $f(\theta_1, \theta_2)$ satisfies the following linear differential equation, it is called a two-variable holonomic function:

$$\begin{aligned}(a_p(\theta_1,\theta_2)\partial_{\theta_1}^p + \cdots + a_1(\theta_1,\theta_2)\partial_{\theta_1} + a_0(\theta_1,\theta_2)) \bullet f = 0,\\ (b_p(\theta_1,\theta_2)\partial_{\theta_2}^p + \cdots + b_1(\theta_1,\theta_2)\partial_{\theta_2} + b_0(\theta_1,\theta_2)) \bullet f = 0.\end{aligned} \tag{3}$$

Here, the coefficients $ai; bi$ are polynomial functions of two variables $\theta_1, \theta_2$. For example, function $f$ is a holonomic function because the function $f = \exp(\theta_1\theta_2)$ satisfies the following equation:

$$\begin{aligned}(\partial_{\theta_1} - \theta_2) \bullet f = 0,\\ (\partial_{\theta_2} - \theta_1) \bullet f = 0.\end{aligned} \tag{4}$$

The following functions are examples of holonomic functions.

$$\begin{aligned}&f(x,y,z) = \sin(x) + \sin(y)\cos(z),\\ &f(x,y) = \exp(x+y),\\ &f(x,y) = \textstyle\int_0^{2\pi} \exp(x\cos(t) + y\sin(t))dt,\\ &f(\theta) = \exp(\theta_1\cos(x) + \theta_2\sin(x))/F(\theta), F(\theta) = \textstyle\int_0^{2\pi} \exp(\theta_1\cos(x) + \theta_2\sin(x))dx.\end{aligned} \tag{5}$$

Here, the function $f(\theta)$ is the von Mises distribution([4]). In Section 3, we deal with the calculation of the normalization constant of the von Mises distribution.

### 2.5 Maximum Value of the Holonomic Function and the System of Differential Equations

In order to demonstrate how to find the maximum value of a single variable function $f(x) = \sin(x)$, we shall outline how to use the system of differential equations of the function $f(x)$. Here, $\partial = \frac{\partial}{\partial x}$. First, the function $f(x) = \sin(x)$ satisfies the following equation:

$$(\partial^2 + 1) \bullet \sin(x) = 0. \tag{6}$$

Therefore, the function $f(x) = \sin(x)$ is a holonomic function. By using this fact, the following holds:

$$\begin{pmatrix} \partial \bullet \sin(x) \\ \partial^2 \bullet \sin(x) \end{pmatrix} = \begin{pmatrix} \partial \bullet \sin(x) \\ -\sin(x) \end{pmatrix}. \tag{7}$$

The following equation holds by recursively rewriting the above equation:

$$\partial \bullet \begin{pmatrix} \sin(x) \\ \partial \bullet \sin(x) \end{pmatrix} = \begin{pmatrix} 0 & 1 \\ -1 & 0 \end{pmatrix} \begin{pmatrix} \sin(x) \\ \partial \bullet \sin(x) \end{pmatrix}. \tag{8}$$

Here, we set

$$F(x) = \begin{pmatrix} \sin(x) \\ \partial \bullet \sin(x) \end{pmatrix},$$

then, the following equation holds:

$$\partial \bullet F = \begin{pmatrix} 0 & 1 \\ -1 & 0 \end{pmatrix} F. \tag{9}$$

Using the Taylor expansion formula and equation (9), the following equation holds:

$$F(x+h) = F(x) + h\partial \bullet F(x) + o(h) = F(x) + h \begin{pmatrix} 0 & 1 \\ -1 & 0 \end{pmatrix} F(x) + o(h). \tag{10}$$

Therefore, by using the value of $F(x)$, we obtain an approximate value of $F(x+h)$. Thus, the things we require in order to calculate the maximum value of the function $f(x) = \sin(x)$ are the following: The vector function $F(x)$;

$$F(x) = \begin{pmatrix} \sin(x) \\ \partial \bullet \sin(x) \end{pmatrix},$$

and the system of differential equations of $F(x)$;

$$\partial \bullet F = \begin{pmatrix} 0 & 1 \\ -1 & 0 \end{pmatrix} F.$$

In addition, we need the vector value $F(x_0)$ at a certain point $x_0$ of the function $F(x)$.

[Note 1] In order to reduce the calculation of the maximum value of the function into the calculation of a Groebner basis, it is necessary to convert them into Pfaffian equations. Fortunately, such transforms exist and are configurable (see Chapter 6 in [12]).

## 3 Integration Algorithm

In Section 2, we described the difficulty of calculating the definite integral appearing in the maximum likelihood estimate, and how we could reduce calculation of the definite integral $F(\theta) = \int_D f(\theta, x)dx$ into calculation of a holonomic function. However, that description was only the first part. Now, we describe the calculation for a system of differential equations of the holonomic function $f$. In fact, in order to create a system of differential equations of $F$ from the system of differential equations of $f$, a new algorithm is needed. In this Section, we describe how we reduce the calculation of the holonomic function $F(\theta)$ into calculation of a Groebner basis. The second part is called the integration algorithm in the differential ring. In this Section, we outline one point in [11].

### 3.1 Variable Transformation of the Normalization Constant of a von Mises Distribution

For the maximum likelihood estimate of the von Mises distribution, let us consider the following normalization constant:

$$F(\theta) = \int_0^{2\pi} \exp(\theta_1 \cos(x) + \theta_2 \sin(x))dx. \tag{11}$$

Here, by using the variable transformation $t_1 = \cos(x), t_2 = \sin(x)$, we get the following equation:

$$F(\theta) = \int_0^{2\pi} \exp(\theta_1 t_1 + \theta_2 t_2)dx. \tag{12}$$

By using the calculation for the hyperfunction $h(t) = \delta(t_1^2+t_2^2+1)$ i[11],pp.43-44), we obtain the following equations for $f = \exp(\theta_1 t_1 + \theta_2 t_2)h$:

$$(t_1^2 + t_2^2 - 1)f = 0, \tag{13}$$

$$(t_2(\partial_1 - \theta_1) - t_1(\partial_2 - \theta_2)f = 0, \tag{14}$$

$$(t_i(t_i(\partial_i - \theta_i) + t_j(\partial_j - \theta_j) + 2) - (\partial_i - \theta_i))f = 0, \tag{15}$$

$$(\partial_{\theta_i} - t_i)f = 0. \tag{16}$$

### 3.2 Integration Algorithm for $D$-Modules

Using the four equations from (13) to (16) obtained above, we can calculate a system of differential equations which the function $F(\theta)$ satisfies. When performing this calculation, integration algorithms for $D$-modules are required [6,7]. Here, $D = C < \theta_1, \theta_2, \partial_{\theta_1}, \partial_{\theta_2} >$ represents the differential ring with polynomial coefficients with two-variables $\theta_1, \theta_2$.

[Calculation flow of integration algorithm]
Let us consider the left-ideal $I$ of the differential ring $D$. By using the ideal $I$, we calculate the following integral-ideal:

$$(I + \partial_1 D + \partial_2 D) \cap \mathrm{C} < \theta_1, \theta_2, \partial_{\theta_1}, \partial_{\theta_2} > .$$

Let $I$ represent an element of the integral-ideal. Then, by definition, $I$ can be written in the following form: $l_0 + \partial_1 l_1 + \partial_2 l_2, l_0 \in I, l_1, l_2 \in D$. By modifying equation (14) using equation (16), we have the following:

$$\partial_1 t_2 + \partial_2(-t_2) - \theta_1 t_2 + \theta_2 t_1 \equiv -\theta_1 \partial_{\theta_2} + \theta_2 \partial_{\theta_1} \bmod I + \partial_1 D + \partial_2 D. \tag{17}$$

Therefore, the following is one of the elements of the integral ideal:

$$-\theta_1 \partial_{\theta_2} + \theta_2 \partial_{\theta_1}. \tag{18}$$

By modifying equation (15) using equation (16), we have the following:

$$\partial_1 t_1^2 + \partial_2 t_1 t_2 - t_1 - (\partial_1 - \theta_1) - \theta_1 t_2^2 - \theta_2 t_1 t_2. \tag{19}$$

Here, by using$@t_i^2 = \partial_{\theta_i}^2$ for mod$I + \partial_1 D + \partial_2 D$, the following is one of the elements of the integral ideal:

$$-\partial_{\theta_1} + \theta_1 - \theta_1 \partial_{\theta_1}^2 - \theta_2 t_1 t_2. \tag{20}$$

From equation (13), the following is one of the elements of the integral ideal:

$$\partial_{\theta_1}^2 + \partial_{\theta_2}^2 - 1. \tag{21}$$

Finally, we have the integral ideal: equations (18), (20), and (21).

## 4 Conclusion

In this article, we reviewed the application of the holonomic gradient descent (HGD) method to a calculation of the maximum likelihood estimate (MLE). We also examined the effectiveness of using the Groebner basis of the calculation algorithm for calculating the minimum value of the holonomic function. The main topic described is the application of the holonomic gradient descent (HGD) method to the maximum likelihood estimation method.

## References

1. Hashiguchi, H., Numata, Y., Takayama, N., Takemura, A.: The holonomic gradient method for the distribution function of the largest root of a Wishart matrix. Journal of Multivariate Analysis 117, 296–312 (2013)
2. Hibi, T.: Harmony of Groebner basis and modern industrial society. Sugaku 63(3) (July 2013) (in Japanese)
3. Nakayama, H., Nishiyama, K., Noro, M., Ohara, K., Sei, T., Takayama, N., Takemura, A.: Holonomic Gradient Descent and its Application to the Fisher-Bingham Integral. Advances in Applied Mathematics 47(3), 639–658 (2011)
4. Mardia, K.V., Jupp, P.E.: Directional statistics. Wiley, New York (2000)
5. Milstein, G.N., Nussbaum, M.: Maximum likelihood estimate for nonparametric signal in white noise by optimal control, WIAS-Preprint No. 596, Berlin (2000)
6. Oaku, T.: Algorithms for b-functions, restrictions, and algebraic local cohomology groups of D-modules. Adv. Appl. Math. 19, 61–105 (1997)
7. Oaku, T., Shiraki, Y., Takayama, N.: Algebraic algorithms for D-modules and numerical analysis. In: Li, Z.M., Sit, W. (eds.) Proceedings of the Sixth Asian Symposium on Computer Mathematics, pp. 23–39. World scientific (2003)
8. Sato, M., Kawai, T., Kashiwara, M.: Microfunctions and Pseudo-differential Equations. Lecture Note in Mathematics, vol. 287, pp. 265–529. Springer (1973)
9. Saito, M., Sturmfels, B., Takayama, N.: Gröbner Deformations of Hypergeometric Differential Equations. Springer (2000)
10. Takayama, N.: MAP estimation based on the holonomic gradient method, Harmony of Groebner basis and modern industrial society. Jst Crest (September 8, 2011) (in Japanese)
11. Takayama, N.: Integration algorithm for D-modules and estimation theory. Sugaku Seminar, 41–46 (February 2012) (in Japanese)
12. Edited by JST CREST Hibi team, Gröbner Dojo, Kyoritsu (2011) (in Japanese)

# On Dynamics of an Electromechanical System Supported by Cylindrical Helical Spring Damped by an Impact Damper

Marek Lampart and Jaroslav Zapoměl

Department of Applied Mathematics & IT4Innovations,
VŠB - Technical University of Ostrava, Czech Republic,
Department of Mechanics, VŠB - Technical University of Ostrava, Czech Republic
{marek.lampart,jaroslav.zapomel}@vsb.cz
http://www.vsb.cz

**Abstract.** This paper focuses on vibrations attenuation of an electromechanical system flexibly coupled with a baseplate by cylindrical helical springs and damped by an element that can work either in inertia or impact regime. The model is constructed with three degrees of freedom in the mechanical oscillating part, two translational and one rotational. The system movement is described by three mutually coupled second-order ordinary differential equations. The nonlinearities that significantly influence behavior of the system are impacts if the impact regime is set on. Several important results were obtained by means of computational simulations. Character of the system motion and amplitude of its oscillations strongly depend on the width of clearances between the damping element and the rotor frame. The damping element operating in inertia regime must have precisely chosen mass and reduces efficiently the oscillations amplitude only in a narrow frequency interval. In contrast, the damping device working in impact regime attenuates vibrations of the rotor frame in a wide range of the excitation frequency and the system is showing periodic, quasi periodic and chaotic movements.

**Keywords:** electromechanical system, inertia damper, impact damper, nonlinear stiffness, impacts, vibration attenuation.

## 1 Introduction

One of the most important mechanical phenomena are impacts of solid bodies. The existence of such impacts can be noticed during a large number of natural and technological processes. The impacts are characterized by short duration body collisions, very large impact forces and by near sudden changes of the system state parameters. The experience and theoretical analyses show that the behavior of the impact systems is highly nonlinear, very sensitive to initial conditions and instantaneous excitation effects, leading frequently to irregular vibrations and nearly unpredictable movements. The behavior of each system where the body collisions take place is different, and therefore, each of them must be investigated individually.



A. Sanayei et al. (eds.), *ISCS 2014: Interdisciplinary Symposium on Complex Systems*,
Emergence, Complexity and Computation 14, DOI: 10.1007/978-3-319-10759-2_19

Due to the practical importance, a great deal of attention is focused on analysis of vibro-impact systems, where the vibrations are governed by the momentum transfer and mechanical energy dissipation through the body collisions. This is utilized for impact dampers applied to attenuate high-amplitude oscillations, such as those appearing in subharmonic, self-excited and chaotic vibrations.

Despite the fact that the problem of impacts is very old, the new possibilities of its investigation enabled by efficient computational simulations appeared at the end of the 20th century. The authors in [2] studied the dynamic behavior of an impact damper for vibration attenuation of an externally loaded and self-excited cart that moves in one direction (see also [1]). The damping was produced by impacts of a point body colliding with the cart walls. A number of authors have dealt with the so-called non-ideal problem, which means that the power of the source exciting the oscillator is limited. Into this category belongs the article [10], who extended Chaterjee's model with the cart by attaching a rotor driven by a motor. Application of a non-ideal model to the gear rattling dynamics was done by [7]. Later on, a new mechanical model with clearances for a gear transmission was reported in [6]. Their model has time varying boundaries and impacts between two gears occur at different locations. The horizontal movement of a cart excited by a rotating particle and damped by an impact damper formed by a point body bouncing on the cart walls was investigated by [8]. A chaotic pattern of the oscillations was confirmed by the computational simulations. Thus, the influence of the impact body to the cart mass ratio on its suppression was examined. The non-ideal impact problem completed by flexible stops was analyzed by [12]. The main objective was to study the character of the vibration of the oscillator excited by an unbalanced rotor driven by a motor of limited power. The mutual interaction of a mechanical and electrical system was analyzed by [9]. The investigated unbalanced rotor of an electric motor was attached to a cantilever beam. The amplitude of its bending vibration was limited by a flexible stop. The performed simulations were aimed at studying the character of the induced vibration and at fluctuations of the current in the electric circuit. Vibrations of a rotor supported by bearings with nonlinear stiffness and damping characteristics considering its impacts against the stationary part were investigated by [11]. The shaft was represented by a beam like-body and rotation of the disc was taken into account. The impacts were described both by collisions of rigid bodies utilizing the Newton theory and by impacts with soft stops. Vibration reduction of an electromechanical system by an impact damper having rigid stops was investigated by [3]. Emphasis was put on observing the influence of the inner impacts on the character and reduction of the system vibration dependent on the geometric parameters.

The aim of this paper is an analysis of a system formed by a rotor and its casing flexibly coupled with a baseplate and of an impact body. This impact body is separated from the casing by two gaps, lower and upper ones. The rotor is driven by a motor of limited power and from this point of view the investigated model system can be classified as non-ideal. A new contribution of the presented work consists of investigating the system oscillations as a result of

a combined time variable loading caused by two sources, the rotor unbalance and the baseplate vibrations, and in investigating the interaction between the motor and its feeding electric circuit. Emphasis is put on observing the influence of the inner impacts on the character and reduction of the system vibration dependent on the width of the upper and lower clearances between the rotor frame and the impact body. The investigated system is of great practical importance as it represents a simplified model of a rotating machine, which is excited by a ground vibration and unbalance of the rotating parts and damped by an impact damper. Results of the performed simulations contribute to better understanding of the dynamic behavior of such technological devices and of impact systems with complicated loading, in general.

Behavior of a similar system, where the rotor frame was coupled with the baseplate by plate springs having nonlinear stiffness, was analyzed in [5].

## 2 The Vibrating System

The considered system consists of a rotor (body 1, Figure 1), of its casing (body 2, Figure 1) and of a baseplate (body 3, Figure 1), with which the rotor casing is coupled by a spring and damping element (body 4, Figure 1). The casing and the baseplate can move in a vertical direction and the rotor can rotate and slide together with its casing. Vibration of the baseplate and unbalance of the rotor are the main sources of the casing excitation. To attenuate its oscillation an impact damper was proposed. It consists of a housing fixed to the rotor casing (body 2, Figure 1) and of an impact element (body 4, Figure 1), which is coupled with the housing by a linear spring. The impact body can move only in a vertical direction and is separated from the housing by the lower and upper clearances that limit its vibration amplitude. The rotor is loaded by an external moment produced by a DC motor. Its behavior is described by a moment characteristic, which enables implementation of the influence of the electric parameters of the motor feeding circuit into the mathematical model of the investigated impact system.

The task was to analyze the influence of the upper and lower clearances and the mass of the impact body respectively on attenuation of the rotor frame oscillation and character of its motion.

In the computational model all bodies are considered as absolutely rigid except the contact areas between the impact element and the rotor frame. The cylindrical helical springs coupling the rotor casing and the baseplate have linear characteristic

$$F_K = k_1 \Delta \tag{1}$$

where $F_K$ is the spring force, $k_1$ is the stiffness parameter and $\Delta$ is the spring deformation (compression or extension). The damper between the rotor frame and the baseplate and the spring coupling the impact body with the damper housing are linear. The Hertz theory has been accepted to describe the impacts.

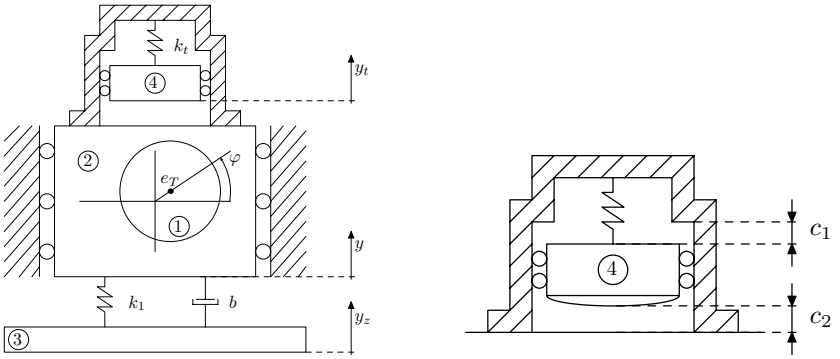


**Fig. 1.** Model of vibrating system

The nonlinear contact stiffness and damping were linearized in the expected range of the contact deformation.

The investigated system has three mechanical degrees of freedom. Its instantaneous position is defined by three generalized coordinates: Y - vertical displacement of the rotor casing, $\mathrm{Y}_t$ - vertical displacement of the impact body and $\Phi$ - angular rotation of the rotor:

$$\begin{aligned}(m+m_R)\ddot{\mathrm{Y}} + m_R e_T \cos(\Phi)\ddot{\Phi} &= m_R e_T \dot{\Phi}^2 \sin(\Phi) - b(\dot{\mathrm{Y}} - \dot{y}_z) - \\ &\quad -k_1(\mathrm{Y} - y_z) - k_t(\mathrm{Y} - \mathrm{Y}_t) - \\ &\quad -(m+m_R)g - F_{I1} - F_{I2}, \\ m_t\ddot{\mathrm{Y}}_t &= F_{I1} + F_{I2} - k_t(\mathrm{Y}_t - \mathrm{Y}) - m_t g, \\ (J_{RT} + m_R e_T^2)\ddot{\Phi} + m_R e_T \cos(\Phi)\ddot{\mathrm{Y}} &= -m_R g e_T \cos(\Phi) + M_Z - k_M\dot{\Phi}\end{aligned} \tag{2}$$

where $\ddot{\mathrm{Y}}$, $\ddot{\mathrm{Y}}_t$ and $\ddot{\Phi}$ denote the second derivative of Y, $\mathrm{Y}_t$ and $\Phi$ respectively, and $\dot{\mathrm{Y}}$ the first derivative of Y with respect to time. Parameters of the system (2) are summarized in Table 1.

It holds for the impact forces $F_{I1}$ and $F_{I2}$

$$F_{I1} = \begin{cases} -k_c(\mathrm{Y}_t - \mathrm{Y} - c_1) - b_c(\dot{\mathrm{Y}}_t - \dot{\mathrm{Y}}) & \text{if condition (4) is satisfied,} \\ 0 & \text{if condition (4) is not satisfied} \end{cases} \tag{3}$$

where condition (4) is defined by

$$\mathrm{Y}_t - \mathrm{Y} - c_1 > 0 \text{ and } -k_c(\mathrm{Y}_t - \mathrm{Y} - c_1) - b_c(\dot{\mathrm{Y}}_t - \dot{\mathrm{Y}}) < 0 \tag{4}$$

and

$$F_{I2} = \begin{cases} -k_c(\mathrm{Y}_t - \mathrm{Y} + c_2) - b_c(\dot{\mathrm{Y}}_t - \dot{\mathrm{Y}}) & \text{if condition (6) is satisfied,} \\ 0 & \text{if condition (6) is not satisfied} \end{cases} \tag{5}$$

where condition (6) is defined by

$$\mathrm{Y}_t - \mathrm{Y} + c_2 < 0 \text{ and } -k_c(\mathrm{Y}_t - \mathrm{Y} + c_2) - b_c(\dot{\mathrm{Y}}_t - \dot{\mathrm{Y}}) > 0 \tag{6}$$

Here $k_c$, $b_c$ denote the contact stiffness and damping and $c_1$, $c_2$ stand for the upper and lower clearances. Conditions (4) and (6) express that the contact forces act only if the impact body and the rotor frame are in contact and that they can be only compressive.

The vibration of the baseplate is defined by the map

$$y_z(t) = A\,(1 - \mathrm{e}^{-\alpha t})\sin(\omega t) \tag{7}$$

where $A$ is the amplitude, $\alpha$ is the constant determining how fast the vibration of the baseplate becomes a steady state and $\omega$ stands for the excitation frequency.

To perform the simulations, the following initial conditions were accepted

$$\dot{\mathrm{Y}}(0) = 0,\ \ \dot{\mathrm{Y}}_t(0) = 0,\ \ \dot{\Phi}(0) = 0,\ \ \Phi(0) = 3/2,$$

$$\mathrm{Y}(0) = -\frac{m + m_R + m_t}{k_1}g,\ \ \mathrm{Y}_t(0) = -\frac{m + m_R + m_t}{k_1}g - \frac{m_t g}{k_t}.$$

This corresponds to the state when in the beginning no moment is applied on the rotor of the electric motor, no contacts between the impact body and the frame occur, the system is in rest, including the baseplate, and takes the stable equilibrium position.

## 3 Main Results

It was shown by [3] that there is a resonance peak for the baseplate excitation frequency of $\omega = 102$ rad s$^{-1}$ for the system parameters summarized in Table 1. Next, parameters $c_1$ and $c_2$ are assumed to be equal for simplicity and together with the mass of the impact element $m_t$ were taken as variables. In the following, the situations are discussed in detail, dependent on clearances between the rotor casing and the impact element, the mass of the impact element and the baseplate excitation frequency.

In the linear system it would always be possible to find the mass of the impact element that would work then as an inertia damper and considerably attenuate the vibration of the rotor frame without any impacts occurring. The amplitude of vibrations of the rotor frame would be considerably attenuated and no impacts would take place. In this cases such a damper can be effective only in a small range of excitation frequencies.

To extend the interval, the mass of the damping element would have to be changed and such manipulation is not easy to accomplish from the technological point of view.

On the contrary it is easy to find a technological solution of the damping device that would make it possible to actively change the clearance width dependent on the excitation frequency to get maximum attenuation of the rotor vibrations. This is suitable especially in the cases when the excitation frequency is not constant but when it can slightly vary in a wider frequency interval.

**Table 1.** Parameters of the system (2)

| value | quantity | format | description |
|---|---|---|---|
| $m$ | 100 | kg | mass of the damping body |
| $m_R$ | 40 | kg | mass of the rotor |
| $m_t$ | 25 | kg | mass of the impact element |
| $k_1$ | $1.42 \times 10^6$ | N m$^{-1}$ | linear stiffness coefficient |
| $J_{RT}$ | 5 | kg m$^2$ | moment of inertia of the rotor |
| $b$ | $1.5 \times 10^3$ | N s m$^{-1}$ | damping coefficient of the suspension |
| $k_t$ | $8 \times 10^4$ | N m$^{-1}$ | coupling stiffness of the impact element |
| $e_T$ | 2 | mm | eccentricity of the rotor center of gravity |
| $\Phi$ | | rad | rotation angle of the rotor |
| $M_Z$ | 100 | N m | starting moment |
| $k_M$ | 8 | N m s rad$^{-1}$ | negative of the motor characteristic slope |
| $\alpha$ | 1 | s$^{-1}$ | parameter of the baseplate excitation |
| $\omega$ | 102 | rad s$^{-1}$ | baseplate excitation frequency |
| $A$ | 1 | mm | amplitude of $y_z$ |
| $k_c$ | $4 \times 10^7$ | N m$^{-1}$ | contact stiffness |
| $b_c$ | $3 \times 10^3$ | N s m$^{-1}$ | coefficient of contact damping |

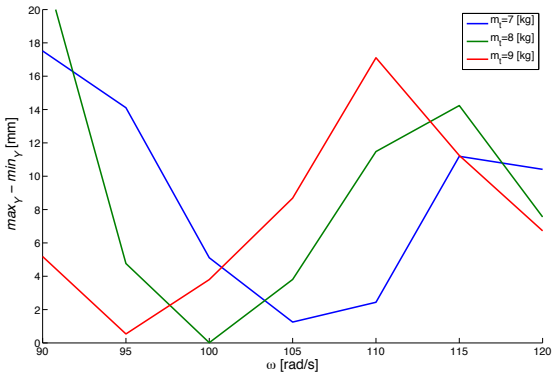


**Fig. 2.** Peak-to-peak vibrations amplitudes of the rotor frame dependent on the excitation frequency for the mass of the impact element $m_t$ from 7 kg to 9 kg. There are no impacts in all these cases.

Figure 3 shows that it is possible to change the clearance width dependent on the excitation frequency intentionally to get maximal attenuation. More precisely, the simulations show (see Figure 2) that for the mass of the impact element $m_t = 8$ kg (corresponding to the resonance peak) the range of the excitation frequency is only (104.5, 108.5) where the attenuation is remarkable (i.e. $\max_Y - \min_Y < 2$ mm.) In this situation the inertia damper works in the range of 6 rad s$^{-1}$. On the other hand, in Figure 3 it is confirmed that for the mass of the impact element $m_t = 25$ kg and the controlled clearance width the range of excitation frequency overlaps 60 rad s$^{-1}$. That is if the damping element is in active control, the clearance is changed dependent on the excitation frequency, attenuation is meaningful for the excitation frequency in the interval (87, 151).

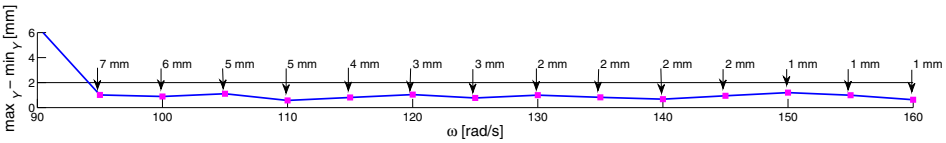


**Fig. 3.** Optimal choice of the clearance $c_1 = c_2$ for the maximal attenuation of vibrations of the rotor body. The attenuation is significant for the range of the excitation frequency $\omega$ from 87 rad s$^{-1}$ to 151 rad s$^{-1}$ and the mass of the impact element $m_t = 25$ kg.

For simulations of the angular frequency $\omega = 100$ rad s$^{-1}$ and the upper and lower clearances between the rotor casing and the impact body $c_1 = c_2 = 6$ mm, $\omega = 110$ rad s$^{-1}$ and $c_1 = c_2 = 5$ mm, $\omega = 150$ rad s$^{-1}$ and $c_1 = c_2 = 1$ mm, respectively the Fourier spectra and phase trajectories show that the movement is formed only by components having the basic, sub and ultra harmonic frequencies as shown on Figures 4 and 5 which corresponds to periodic movements.

Fourier spectrum of the response referred to the excitation frequency $\omega = 110$ rad s$^{-1}$ (Figures 6) shows the side bands around the frequency peaks related to the principal and ultra harmonic components of the motion that is characteristic for quasi-periodic oscillations. The corresponding phase trajectory is depicted in Figure 6.

Finally, Fourier spectrum of the motion excited by the baseplate vibrating with the frequency of $\omega = 185$ rad s$^{-1}$ (Figure 7) has a band character which confirms a chaotic pattern of the system oscillations. The high degree of irregularity of the motion is also evident from the phase trajectory depicted in Figure 7.

The above described situations are also confirmed by the Bifurcation diagram in Figure 8 with respect to the angular frequency $\omega$.

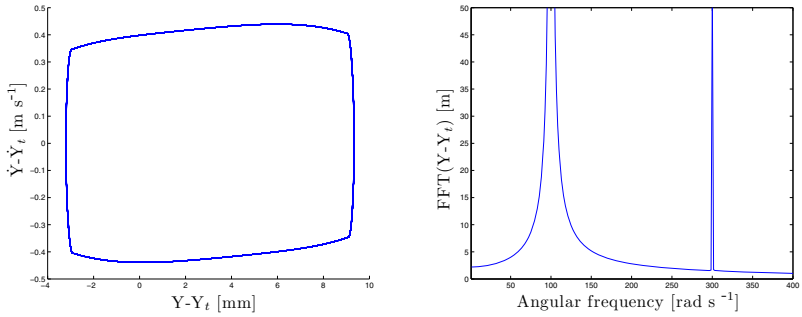


**Fig. 4.** Phase portrait (left), $\mathrm{Y} - \mathrm{Y}_t$ versus $\dot{\mathrm{Y}} - \dot{\mathrm{Y}}_t$ and Fourier spectra (right) for the angular frequency $\omega = 100$ rad s$^{-1}$ and the upper and lower clearances between the rotor casing and the impact body $c_1 = c_2 = 6$ mm

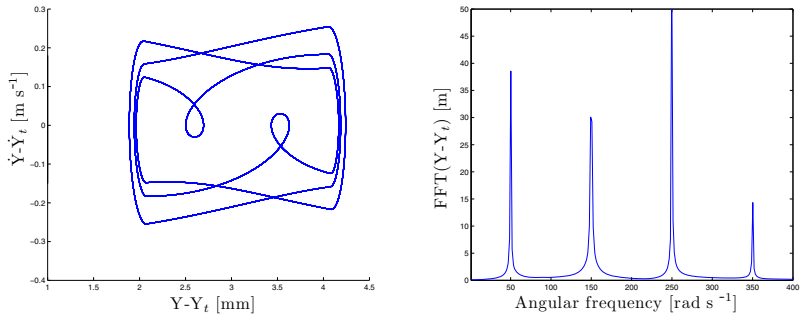


**Fig. 5.** Phase portrait (left), $\mathrm{Y} - \mathrm{Y}_t$ versus $\dot{\mathrm{Y}} - \dot{\mathrm{Y}}_t$ and Fourier spectra (right) for the angular frequency $\omega = 150$ rad s$^{-1}$ and the upper and lower clearances between the rotor casing and the impact body $c_1 = c_2 = 1$ mm

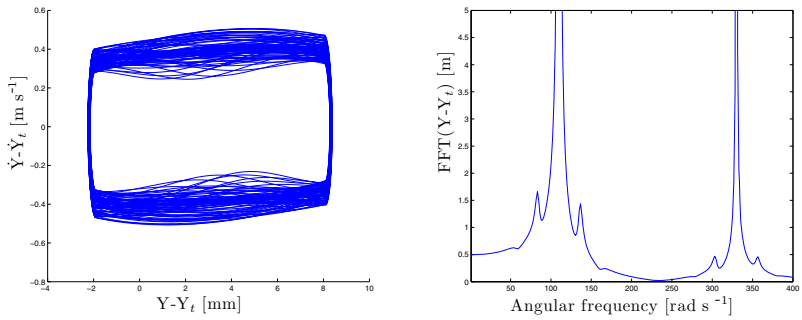


**Fig. 6.** Phase portrait (left), $\mathrm{Y} - \mathrm{Y}_t$ versus $\dot{\mathrm{Y}} - \dot{\mathrm{Y}}_t$ and Fourier spectra (right) for the angular frequency $\omega = 110$ rad s$^{-1}$ and the upper and lower clearances between the rotor casing and the impact body $c_1 = c_2 = 5$ mm

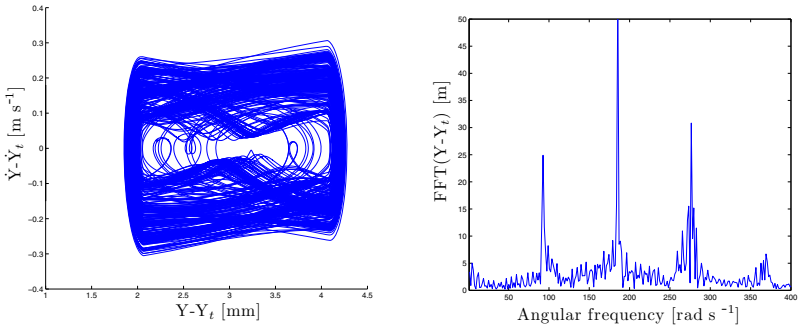


**Fig. 7.** Phase portrait (left), $\mathrm{Y} - \mathrm{Y}_t$ versus $\dot{\mathrm{Y}} - \dot{\mathrm{Y}}_t$ and Fourier spectra (right) for the angular frequency $\omega = 185$ rad s$^{-1}$ and the upper and lower clearances between the rotor casing and the impact body $c_1 = c_2 = 1$ mm

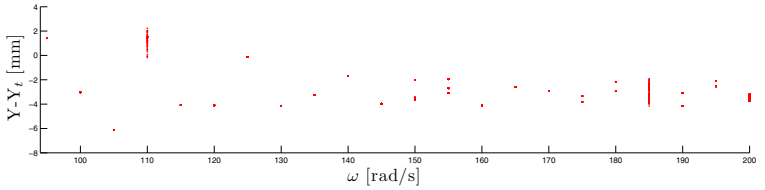


**Fig. 8.** Bifurcation diagram with respect to the angular frequency $\omega$

## 4 Conclusions

In this paper, it was developed and analyzed a new electromechanical system damped by impact element with soft stops dependent on parameters, namely the weight of the impact element, the clearance between the impact body and rotor casing and finally the excitation frequency. This model was inspired by real frequently occurring technological problems when electromechanical rotating machines are excited by a combined loading produced by the rotor unbalance and ground vibrations. The equations of motions were solved numerically by the explicit Runge-Kutta method. The computational simulations showed that the vibration of the baseplate played a key role here and proved that application of the impact body arrived at a significant decrease of vibration amplitude of the rotor frame.

It was observed that for given parameters of the model, the damping element can work as an inertia (there are no impacts) or as an impact damper (impacts occur). Both situations were investigated and commented on. The ranges of parameters for which the attenuation is meaningful were detected. In the case of the inertia damper, the range of the excitation frequency is very narrow. On the other hand, it is quite wider in the case of the impact damping device. Finally, if the damping element is in active control, the clearance is changed dependent on the excitation frequency, attenuation is meaningful in the interval which is ten

times wider then those in the case of the inertia damper. It was also proved by simulations that movements corresponding to the inertia damper show periodic pattern.

**Acknowledgments.** This work was supported by the European Regional Development Fund in the IT4Innovations Centre of Excellence Project (CZ.1.05/1.1.00/02.0070). The work was also supported by the Grant Agency of the Czech Republic, Grant No. P201/10/0887.

## References

1. Chaterjee, A.K., Mallik, A., Ghosh, A.: Impact dampers for controlling self-excited oscillations. Journal of Sound and Vibration 193, 1003–1014 (1995)
2. Chaterjee, A.K., Mallik, A., Ghosh, A.: On impact dampers for non-linear vibration systems. Journal of Sound and Vibration 187, 403–420 (1995)
3. Lampart, M., Zapoměl, J.: Dynamics of the electromechanical system with impact element. Journal of Sound and Vibration 332, 701–713 (2013)
4. Lampart, M., Zapoměl, J.: Dynamical properties of the electromechanical system damped by impact element with soft stops. International Journal of Applied Mechanics 6, 1450016 (2014)
5. Lampart, M., Zapoměl, J.: Dynamics and efficiency of an impact damper. In: Proceedings of the NOSTRADAMUS 2014 Conference (to appear, 2014)
6. Luo, A.C.J., O' Connor, D.: Periodic motions with impacting chatter and stick in a gear transmission system. ASME Journal of Vibration and Acoustics 131 (2009)
7. de Souza, S.L.T., Caldas, I.L., Balthazar, J.M., Brasil, R.M.L.R.F.: Analysis of regular and irregular dynamics of a non ideal gear rattling problem. Journal of Brayilian Society of Mechanical Sciencies 24, 111–114 (2002)
8. de Souza, S.L.T., Caldas, I.L., Viana, R.L., Balthazar, J.M., Brasil, R.M.L.R.F.: Impact dampers for controlling chaos in systems with limited power supply. Journal of Sound and Vibration 279, 955–967 (2005)
9. Půst, L.: Electro-mechanical impact system excited by a source of limited power. Engineering Mechanics 6, 391–400 (2008)
10. Warminski, J., Balthazar, J.M., Brasil, R.M.L.R.F.: Vibrations of a non-ideal parametrically and self-excited model. Journal of Sound and Vibration 245, 363–374 (2001)
11. Zapoměl, J., Fox, C.H.J., Malenovský, E.: Numerical investigation of a rotor system with disc-housing impact. Journal of Sound and Vibration 243, 215–240 (2001)
12. Zukovic, M., Cveticanim, L.: Chaos in non-ideal mechanical system with clearance. Journal of Vibration and Control 8, 1229–1246 (2009)

# Petri Net Models of Purposeful Complex Dynamic Systems

Felipe Lara-Rosano

Centro de Ciencias Aplicadas y Desarrollo Tecnologico
Universidad Nacional Autonoma de Mexico
Mexico-City, Mexico
flararosano@gmail.com

**Abstract.** In this paper a Petri nets modeling approach for purposeful complex dynamic systems is proposed. This approach is based on considering a hierarchy of interrelated systemic goals/functions and emergent outcomes. The system model is a Petri net with two types of elements: goals/functions whose accomplishment is desirable and emergent outcomes that represent systemic properties.

**Keywords:** Purposeful complex dynamic systems, Petri Net Models, Goals and emergent outcomes modeling, Synthetic micro-analysis of purposeful complex systems.

## 1 Introduction

Sources of complexity in the social and behavioral sciences are not only the mechanistic interrelated, asinchronous, non-linearly coupled dynamic elements we find in the human and the social world but the plentiful positive and negative feedback loops (Buckley 1968, *Modern Systems Research for the Behavioral Scientist,* pp xxiv), and a purposeful active behavior of dynamic elements that cannot be captured through common causality (Rosenblueth, Wiener & Bigelow 1943, *Behavior, Purpose and Teleology,* pp 5).

This fact had already been recognized by the economist Ludwig von Mises (1949, *Human Action: A Treatise on Economics* pp 11):

> "Human action is purposeful behavior. Or we may say: Action is will put into operation and transformed into an agency, is aiming at ends and goals, is the ego's meaningful response to stimuli and to the conditions of its environment, is a person's conscious adjustment to the state of the universe that determines his life. Such paraphrases may clarify the definition given and prevent possible misinterpretations. But the definition itself is adequate and does not need complement of commentary."



A. Sanayei et al. (eds.), *ISCS 2014: Interdisciplinary Symposium on Complex Systems*,
Emergence, Complexity and Computation 14, DOI: 10.1007/978-3-319-10759-2_20

According to Rosenblueth, Wiener and Bigelow (1950, *Purposeful and Non.Purposeful Behavior,* pp 32) the analysis of behavior in social and behavioral sciences requires to introduce a teleological method of study:

> It may be mentioned parenthetically that the theory of games is a chapter in the study of two- or more-way purposeful activity …the adoption of a teleological approach simplifies the analysis of goal-directed behavior and enlarges the scope of this analysis. This methodological approach does not imply the philosophical belief in final causes."

Richard Taylor (1950, *Purposeful and Non-Purposeful Behavior: A Rejoinder,* pp 331) discusses the paper by Rosenblueth et al (1943), critizising some of the cybernetic conceptions but stating the conditions to be fulfilled to regard any behavior pattern as purposive:

> "I now suggest the following as necessary and sufficient conditions to be fulfilled, or to be assumed to be fulfilled, in order appropriately to regard any given behavior pattern *as purposive:* There must be, on the part of the behaving entity, i.e., the agent: (a) a desire, whether actually felt or not for some object, event, or state of affairs as yet future; (b) the belief, wether tacit or explicit, that a given behavioral sequence will be efficacious as a means to the realization of that object, event or state of affairs; and c) the behavior pattern in question. Less precisely, this means that to say of a given behavior pattern that is purposeful, is to say that the entity exhibiting that behavior desires some goal, and is behaving in a manner it believes appropriate to the attainment of it.

In 1972 Russell L. Ackoff and Fred Emery, pionners and influential thinkers on the applications of the systems approach to organization diagnostics and planning in his book 1972, *On Purposeful Systems* (pp 4) state:

> In this book we take a holistic view of human behavior and hence necesarily a functional, teleological, or purposeful view. Yet, following Singer (1924, 1959) and Rosenblueth and Wiener (1943, 1950) and Sommerhoff (1950), we try to make all the functional concepts employed as objective, as measurable, as capable of use in experimentation as any structural concepts produced by the mechanistic (so-called behavioristic) view of human behavior.

This book develops the systems theory of purposeful systems as a new foundation for the behavioral sciences:

> This book provides a completely new foundation for the behavioral sciences; a new way of looking at human and social behavior – as a system opf purposefuil (teleological) events. It uses a systems theoretical approach for the study of these phenomena, and thus

> illuminates and extends general system theory. It treats individual purposeful behavior, interactions of purposeful individuals, and purposeful social groups, in a way that is complementary to the traditional mechanistic concept of the world; it makes teleology and mechanism compatible. Only the systems approach, however, can deal with the full richness and complexity of human behavior. (Ackoff and Emery 1972, *On Purposeful Systems* 1972, pp Cover 2)

In his paper *Towards a System of Systems Concepts* (1971, pp 667) Russell L. Ackoff defines a set of systems concepts including the basic definitions for the teleological analysis of complex systems. According to this school of thought the *goal* of a purposeful system in a particular situation is a preferred outcome that can be obtained within a specified time period. The *objective* of a purposeful system in a particular situation is a preferred outcome that cannot be obtained within a specified period but which can be obtained over a longer time period. Pursuit of an objective requires an ability to change goals once a goal has been obtained. This is why such pursuit is possible only for a purposeful system. An *ideal* is an objective which cannot be obtained in any time period but which can be approached without limit. For example, an ideal of scientists is errorless observations. The amount of observer error can be reduced without limit but can never be reduced to zero. Omniscience is another such ideal. Just as goals can be ordered with respect to objectives, objectives can be ordered with respect to ideals.

> Consider a set of possible outcomes ordered along one or more scales (e.g., increasing speeds of travel). Then each outcome is closer to the final one than those which precede it. Each of these outcomes can be a goal in some time period after the 'preceding' goal has been obtained, leading eventually to attainment of the last outcome, the objective. For example, a high-school freshman's goal in his first year is to be promoted to his second (sophomore) year. Passing his second year is a subsequent goal. And so on to graduation, which is his objective.

Then Ackoff defines the different types of teleological systems (Ackoff 1971, pp 666):

> A *goal-seeking system* is one that can respond differently to one or more different external or internal events in one or more different external or internal states and that can respond differently to a particular event in an unchanging environment until it produces a particular state (outcome). Production of this state is its goal. Thus such a system has a *choice* of behavior.
> A *multi-goal-seeking* system is one that is goal-seeking in each of two or more different (initial) external or internal states, and which seeks different goals in at least two different states, the goal being determined by the initial state.
> A purposive system is a multi-goal-seeking system the different goals of which have a common property called the system's purpose. These

> types of system can pursue different goals but they do not select the goal to be pursued. The goal is determined by the initiating event. But such a system does choose the means by which to pursue its goals.
> A purposeful system is one which can change its goals under constant conditions; it selects ends as well as means and thus displays will. Human beings are the most familiar examples of such systems.
> An ideal-seeking system is a purposeful system which, on attainment of any of its goals or objectives, then seeks another goal and objective which more closely approximates its ideal. An ideal-seeking system is thus one which has a concept of 'perfection' or the 'ultimately desirable' and pursues it systematically; that is, in interrelated steps.

The purposeful systems approach of Ackoff has been followed and adopted by the most organizational theorists. According to Marion (1999, *The Edge of Organization: Chaos and Complexity Theories of Formal Social Systems, pp 115*):

> Organizational theorists, and social theorists in general, don't share biology's consternation over conventional teleology. We embrace it for a number of reasons, one of which is because we want to feel in control of our organizations. There are entire models of organization built around the assumption that leaders determine the destiny of their firms and institutions".

This point of view is also shared by social sciences and humanities (Mainzer 2007, *Thinking in Complexity: The Computational Dynamics of Matter, Mind and Mankind,* pp 373):

> In the social sciences and humanities one usually distinguishes strictly between biological evolution and the history of human cultures. The main reason is that the development of nations and cultures is obviously guided by the intentional behavior of humans with their attitudes, emotions, plans, and ideals, while systems in biological evolution are assumed to be driven by unintended self-organization. From a microscopic view, we observe single human individuals with their intentions and desires. Even in biological systems like animal ecologies there are individuals with intentional behavior of some degree.

Finally we must remark that contemporary Social Complexity Science has incorporated purposefulness and intent in the study of social and human dynamics. In fact Beautement & Broenner (2011, *Complexity Demystified: A guide for practitioners* pp 70) ask:

> what is the significance of purpose and intent in relation to dynamic phenomena? Well, it's a simple one it provides a way of disturbing conditions to either move the zone or trigger a phase change such that a new order, and therefore new zones, can arise. Some of the givens and realities that are relevant here include the following:

> A. Purposeful Change Does Not Come by Chance. Complexity science provides a way of identifying the class/type of phenomena one is dealing with and so provides the basis, through purpose and intent, for selecting from a range of options for influencing, shaping and seeding the type of emergence so that what one anticipates is more likely to come about. Hence, putting complexity to work requires a radically different emphasis from reductionist approaches to an emphasis on an awareness of the tensions and drivers of change in real-world phenomena and on having fitness and readiness to adjust to external changes quickly without major internal dislocation. With complexity science having 'explained' the mechanisms by which complex phenomena come about, practitioners can take these insights, add intentionality, and be more aware of how and why they can affect change by getting a better feel of how to tune these properties.
> B. Intentions are Part of the Context. Purpose and intent are considered by complexity science to be modifiers of the properties of the components, or of things that would affect their interactions such as the degree of people's involvement or withdrawal and these will change outcomes. So, part of putting complexity to work, where everything seems different depending on where you stand in relation to the situation, is to be able to appreciate issues from the points-ofview of the other actors who have their own purpose and intent…."
> D. Modelling Intentions needs to be done Appropriately. Though people use models to inform their thinking, another reality is the limited ability of models to accommodate issues related to purpose and intent in practice within the models.

After this short review over the inclusion of teleological methodology in complexity studies in the social, behavioral sciences and humanities in this paper we present a Petri net approach to model purposeful complex dynamic social systems and their interactions with emergent outcomes.

## 2 Synthetic Microanalysis of Purposeful Complex Dynamic Systems

Synthetic Microanalysis is a general theoretical and methodological framework in which concepts describing system elements and composite systems are related to explain the function, structure and behavior of physical, biological, psychological and social complex systems (Auyang 1998) employing, in a complementary way, two consecutive procedures: the systemic decomposition method and the systemic composition method.

The systemic decomposition method begins with a holistic view of the system and its environment, to capture a global view of the system, lowering its complexity. Then it decomposes the system into a hierarchy of successive functional subsystem levels down to find and define the basic components of the system, and detecting all

emergent properties appearing at each level. This operation firstly identifies the supra-system to which the focal system belongs and the functions that this focal system fulfills in the supra-system. Then it identifies from the environment the peer systems belonging to the same supra-system and the interrelations that have with the focal system. The successive application of this method downward the systemic hierarchy allows to reach the basic elements, and explain their interrelationships. In the case of social systems, all these elements may be also social systems except the basic ones, which can be individuals. Once the hierarchy of systems and subsystems is identified, these elements must be analyzed by associating them with the system dynamics through the application of disciplinary and theoretical frameworks to the data.

In order to analyze the system dynamics is necessary to identify the goals that motivate the goal-oriented, purposive and purposeful system components. Firstly identify the highest priority goals/functions of the overall system and the conditions to be fulfilled by its first level subsystems in order to accomplish those goals/functions. These conditions define the goals and/or functions to be accomplished by these first level subsystems (strategy level). Then, for each of these first level goals/functions identify the conditions to be fulfilled by the second level subsystems (tactical level) to accomplish the corresponding first level goal/function. The process is repeated until all the levels up to the basic one are covered. The identified goals/functions at each level must be necessary and sufficient to produce as emergent outcomes the fulfilling of the goals of the next higher level.

The systemic composition method allows then interrelating the component goals/functions at the various levels, starting with the basic level, to find the actions responsible for producing the emergent outcomes at each level up to the overall goals/functions of the whole system whose attainment guarantees the proper system behavior.

In this paper a Petri net approach is proposed to model purposeful complex dynamic systems that can be used to make inferences and to solve problems related to the purposeful complex system dynamics.

## 3 A Petri Net Model for Purposeful Complex Dynamic Systems

In order to model purposeful complex dynamic systems, we give the model the structure of a Petri net (Lara-Rosano 1994 pp126). Formally a Petri net N is a four-tuple, $N = (P,T,I,O)$ where $P = \{p_1, p_2,...,p_n\}$ is a finite set of *places*, $n \geq 0$. $T = \{t_1, t_2,...,t_m\}$ is a finite set of *transitions*, $m \geq 0$. The set of places and the set of transitions are disjoint, $P \cap T = \varnothing$. $I: T \rightarrow P^{\infty}$ is the *input function*, a mapping from transitions to sets of places. $O: T \rightarrow P^{\infty}$ is the *output function*, a mapping from transitions to sets of places. A place $p_i$ is an *input place of a transition* $t_j$ if $p_i \in I(t_j)$; $p_i$ is an *output place of a transition* $t_j$ if $p_i \in O(t_j)$. A Petri net graph is a graphical representation of a Petri net and therefore has two types of nodes: places and transitions. A circle O represents a place and a bar | represents a transition. Some directed arcs connect the places with the transitions and some other directed arcs connect the transitions with the places. There are no arcs connecting places with

places or transitions with transitions, thus the graph representing the system is a bipartite graph.

To model a purposeful complex system as a Petri net we define following structure:

a) There are two kinds of system elements: the system *goals/functions* whose accomplishment define the state of the system and the *emergent outcomes*, that are emergent properties appearing in the system as a result of the synergy of a set of accomplished *goals/functions.* Production of *emergent outcomes* depend from preconditions defined in terms of the state of the system. A precondition is then a logical description of the state of the system that induces an *emergent outcome*. *Emergent outcomes* have also an impact over the accomplishment of one or more *goals/functions*, affecting the state of the system. These changes induced by the *emergent outcomes* are called the postconditions of the *emergent outcome*. Thus between both kind of elements exist causal relationships represented by directed arcs. System *goals/functions* are defined as *places* of the Petri net model (PNM), and represented as circles. *Emergent outcomes* are defined as *transitions* of the PNM and represented as bars. The inputs of a transition are the preconditions of the corresponding *emergent outcome*; the outputs are the postconditions.

b) Because of the bipartite nature of a Petri net, the direct causal antecedents of accomplished *goals/functions* are always *emergent outcomes* of the system or external events provided by the environment. In the same way the direct causal antecedents of *emergent outcomes* are always accomplished *goals/functions* or external inputs provided by the environment.

c) When the accomplishment of the *goal/function* fulfills the precondition of an *emergent outcome*, a *token* is assigned to the *goal/function*. A *marking* $\mu$ is an assignment of tokens to the *goals/functions* of the system. If an accomplished *goal/function* is causal antecedent of several different *emergent outcomes*, with different sets of preconditions, several tokens are assigned to the accomplished *goal/function*, each token with a different color corresponding to every *emergent outcome*.

d) Therefore the holding of a precondition is represented by a token in the place corresponding to the precondition. If all preconditions of an *emergent outcome* have tokens, the *emergent outcome* is enabled and occurs, firing the corresponding transition.

e) The system interacts with the environment through its inputs and outputs. Inputs are considered external events from the environment, with no antecedent, that determine the accomplishment of one or more *goals/functions* inside the model, thus changing the state of the system. These input events constitute the *input layer* of the Petri net. Therefore the input layer represents scenario events or decisions taken by a decision maker. This allows to incorporate policy simulation in the model. Outputs are accomplishment of *goals/functions* or *emergent outcomes* giving the response of the system to the environment.

f) The accomplishment of a *goal/function* is then a product of the synergy of several specific lower level *emergent outcomes* acting together. The directed link $e_{ij}$ from an *emergent outcome i* to a higher level *goal/function* accomplishment *j* indicates that *emergent outcome i* contributes to *goal/function j*.

g) In the same way the production of an *emergent outcome* is then the product of the synergy of specific *goals/functions* acting together. The directed link $e_{ji}$ from a *goal/function j* to an *emergent outcome i* indicates that *goal/function j* contributes to *emergent outcome i*.

h) The firing of an *emergent outcome* is then the result of enabling the corresponding transition through the fulfilling of all its preconditions, that is. when all its precedent *goals/functions* have the corresponding colored token.

i) From the *state vector* and the *emergent outcomes* at time *t*, we may estimate the *state vector* at time $t + \Delta t$, element by element as following:

- The input external events occur or not occur according to problem conditions.
- The *goals/functions* are accomplished or not according to the accomplishment of the required lower level *emergent outcomes* and input *environmental events*.

j) If all preconditions of an *emergent outcome* have the corresponding color tokens, the *emergent outcome* is enabled and occurs, firing the corresponding transition. If the *emergent outcome* occurs, its postconditions modify the *goals/functions* accomplishments, other preconditions may be fulfilled, new tokens may be assigned, new *emergent outcomes* enabled, new transitions fired and so on, until no new *emergent outcomes* are enabled and the execution of the model halts and the accomplishment or not of output *goals/functions* is determined.

One of the advantages of this approach is that different models with different number or kind of elements can be combined in a composed Petri net by introducing new *goals/functions* and/or new *emergent outcomes* and their relationships. This permits to gather knowlege from several experts and/or combine different knowledge domains.

Validation of these purposeful dymanic models are done by simulation of historical situations with the model. The model outcomes are then compared with the available historical evidence and the discrepancies suggest changes in the model elements and its causal connections.

## 4 Conclusions

In this paper a Petri net modeling approach for purposeful complex dynamic systems was proposed. This approach is based on considering a hierarchy of interrelated systemic *goals/functions* and *emergent outcomes*. The system model has *goals/functions* whose accomplishment is desirable and *emergent outcomes* that represent system properties. *Goals/functions* are interpreted as places in a Petri net whose accomplishment may determine the firing of *emergent outcomes* as transitions when the corresponding preconditions at the places are fulfilled. As a simulation tool, the model may combine subjective or intuitive concepts and expert opinions with hard data. The emphasis is placed on finding the significance of structural relations and dynamic behavior, rather than on producing a numerical prediction. Application of this model to real problems and refinement to include thresholds and uncertainty in the causal links are under way.

**Acknowledgement.** This work was supported in part by the project Conacyt 152008.

## References

Ackoff, R.L.: Towards a System of Systems Concepts. Management Science 17(11), 661–671 (1971)

Ackoff, R.L., Emery, F.E.: On Purposeful Systems. Aldine Atherton, Chicago (1972)

Auyang, S.Y.: Foundations of Complex-System Theories in Economics. In: Evolutionary Biology and Statistical Physics. Cambridge University Press, Cambridge (1988)

Beautement, P., Broenner, C.: Complexity Demystified: A Guide for Practitioners. Triarchy Press, Devon (2011)

Buckley, W.: Modern Systems Research for the Behavioral Scientist. Aldine Publishing Co., Chicago (1968)

Churchman, C.W., Ackoff, R.L.: Purposive Behavior and Cybernetics. Social Forces 29(1), 32–39 (1950)

Lara-Rosano, F.: Fuzzy Causal Impact Connectionist Models of Dynamic Systems. In: Lasker, G.E. (ed.) Advances in Systems Studies, vol. II, pp. 22–26. IIAS, Windsor (1995)

Lara-Rosano, F.: Fuzzy Causal Modeling of Complex Systems through Petri Paradigm and Neural Nets. In: Lasker, G.E. (ed.) Advances in Artificial Intelligence and Engineering Cybernetics, vol. III, pp. 125–129. IIAS, Windsor (1994)

Mainzer, K.: Thinking in Complexity: The Computational Dynamics of Matter. Springer, Berlin (1994)

Marion, R.: The Edge of Organization: Chaos and Complexity Theories of Formal Social Systems. Sage Publications, Thousand Oaks (1999)

Peterson, J.L.: Petri Net Theory and the Modeling of Systems. Prentice-Hall, Englewood Cliffs (1981)

Rosenblueth, A., Wiener, N.: Purposeful and Non.Purposeful Behavior. Philosophy of Science 17, 318–326 (1950)

Rosenblueth, A., Wiener, N., Bigelow, J.: Behavior, Purpose and Teleology. Philosophy of Science 10, 18–24 (1943)

Singer, E.A.: Mind as Behavior. R. G. Adams, Columbus (1924)

Singer, E.A.: Experience and Refletion. University of Pennsylvania Press, Philadelphia (1959)

Sommerhof, G.: Analitical Biology, ch. II. Oxford University Press, Oxford (1950)

Taylor, R.: Purposeful and Non-Purposeful Behavior: A Rejoinder. Philosophy of Science 17, 327–332 (1950)

Von Mises, L.: Human Action: A Treatise on Economics. Von Mises Institute, Auburn (1949), Scholar Edition

# Part II

# Evolutionary Computations

# Does Evolutionary Dynamics Need Randomness, Complexity or Determinism?

Ivan Zelinka[1] and Roman Senkerik[2]

[1] VSB-Technical University of Ostrava, 17. listopadu 15 708 33, Ostrava-Poruba, Czech Republic
ivan.zelinka@vsb.cz
[2] Faculty of Applied Informatics, Tomas Bata University in Zlin
senkerik@fai.utb.cz

**Abstract.** Inherent part of evolutionary algorithms that are based on Darwin theory of evolution and Mendel theory of genetic heritage, are random processes. In our as well as another researcher papers is successfully discussed possibility to replace pseudorandom number generators by deterministic chaos generator, generating chaos, and then by $n$ periodical series based on deterministic chaos generators and finally also fully deterministic periodical functions. In all cases was observed that pseudorandom generators can be successfully replaced by chaotic or deterministic generators and thus question whether evolutionary algorithms needs randomness, complexity or determinism and we propose novel way how to understand, analyze and control complex dynamics of evolutionary algorithms.

## 1 Introduction

An important part of evolutionary techniques that are based on Darwin theory of evolution and Mendel theory of genetic heritage, are so called pseudorandom processes. In literature as for example ([1]-[5]), ([9] - [12], [8] and [7]) amongst the others is successfully discussed possibility to replace pseudorandom number generators (PRNG) by deterministic chaos generator (DCHG), generating chaos (thus very complex behavior), and then by $n$ periodical series based on deterministic chaos generators, [6], [19], [20], [21]. Periodic behavior of chaotic systems, in this case of logistic equation (1), is visualized for better imagination in Fig. 1 - 2.

Above mentioned papers papers are discussing use of deterministic chaos inside evolutionary algorithm instead of PRNG investigating relations between chaos and randomness or the latest or using chaos with EAs in applications, amongst the others. Because all those previous experiments were successful or highly comparable with classical evolutionary algorithms powered by classical pseudorandom number generators, another experiments [30] used successfully classical deterministic periodical generator. In all cases was observed that pseudorandom generators can be successfully replaced by chaotic or deterministic



A. Sanayei et al. (eds.), *ISCS 2014: Interdisciplinary Symposium on Complex Systems*, Emergence, Complexity and Computation 14, DOI: 10.1007/978-3-319-10759-2_21

generators and thus question whether evolutionary algorithms needs randomness, complexity or determinism.

For long time various PRNG were used inside evolutionary algorithms. It is well known that an ideal random number generator shall be infinite, aperiodic, uniform, uncorrelated, and computationally efficient. It means that ideal generator produces an endless sequence of numbers without any periodicity, and each number in the sequence has an equal probability of being generated. If seed is not known, then also it is impossible to predict successive terms.

During last few years deterministic chaos systems (DCHG) are used instead of PRNG. As was demonstrated in [1]-[5], very often is performance of EAs using DCHG better or fully comparable with EAs using PRNGs. See for example [1]. Used EAs (we do not discuss here special cases, modified for special experiments) of different kind like for example genetic algorithms [17], differential evolution [14], particle swarm [18], [23], [24], SOMA [13], scatter search [15], evolutionary strategies [16], etc... do not analyze whether used pseudo-random numbers are really random (better to say "well pseudorandom") one and do not use information about its randomness. Pseudorandom numbers are only simply used to select individuals, make mutation, etc. On the other side, as demonstrated in mentioned references, EAs with DCHG gives the same or often better performance. Difference between series from PRNGs and DCHG is that in the case of DCHG one can less-more easily reconstruct/calculate whole series generated by DCHS from arbitrary time series point (of course with very high precision only, otherwise trajectories will diverge soon) or/and reconstruct equations that generate observed chaotic series. Because DCHG can generate periodical series (thanks to final numerical precision - numbers behind decimal point, [6], [19], [20], it is question what will be EAs performance based on classical mathematical periodical functions (CPF) and whether it is comparable with performance of classical EAs with PRNG.

$$x_{n+1} = Ax_n\left(1 - x_n\right) \tag{1}$$

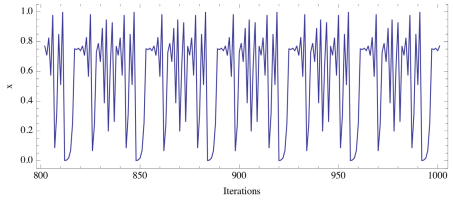


**Fig. 1.** Time series of period 36 (precision = 4) based on Eq. 1 for $A = 4$

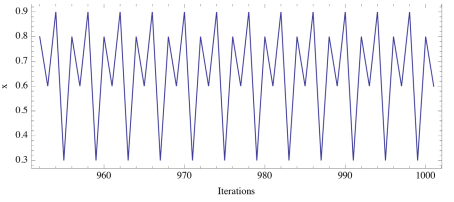


**Fig. 2.** Periodic behavior of logistic equation with numerical precision 1 and $x_{start} = 0.45$

## 2 Existing Experiment Results

Experiments reported above, leading to question whether evolutionary algorithms needs randomness, complexity or determinism were focused on use of periodic series (CPS) generated by CPF instead of series from PRNG. This idea is extension of the [6], [19], where was reported use (DCHG) instead of PRNGs. Idea of use (DCHG) was then modifies so that chaotic systems under given precision generated $n$ periodic series (CHPS), see [6]. Because all experiments has showed that EAs powered by DCHG as well as CHPS shows the same or better performance rather than EAs powered by PRNG, then idea to extend simulations on clearly periodical generators was straightforward. For last experiments reported in [30] was used simple periodic function *sinus*, Eq. (2), and unified into appropriate interval. The $\delta$ parameter was empirically set to 0.3, for explanation see [30]. This trivial "generator" was used to generate real numbers in the interval [0, 1] (for mutations etc.) and integer numbers in interval [1, NP] for parents selection in DE. For SOMA it was not necessary, because parent selection is based on different principles, [13]. For integer numbers has been observed obvious periodicity (see [30] and Fig. 3) with some impact on algorithm performance, that is discussed in the [30].

$$\begin{aligned} &\sin(x) \quad \text{where } x \in [x_{start},\ x_{start}+\delta,\ x_{start}+2\delta,\ ...] \\ &\qquad x_{start} = rnd[0,\ \pi], \quad \delta = 0.3 \end{aligned} \tag{2}$$

The most curious experiments were done in [30] where 2000 evolutionary simulations, based on replacement of PRNGs generators by classical periodical generators (given by (2)) for mutation etc... has been processed and summarized. An example of results is reported in tables 1 - 2 for DE and in tables 3 - 4 for SOMA. In each table is recorded all 5 test functions and its the worst (maximal),

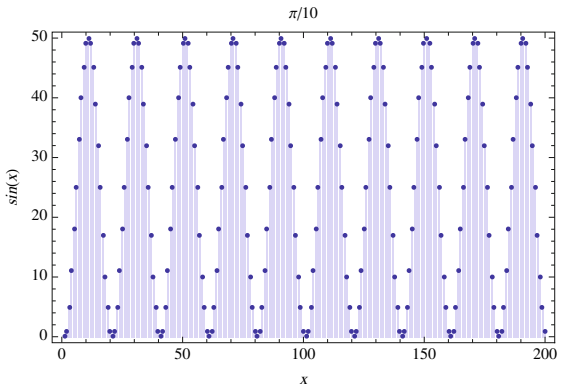


**Fig. 3.** Periodic behavior of Eq. 2 with randomly selected $x_{start}$. The value at the axe $y$ is in fact No. of individual that was selected from population to create an offspring. As visible, for DE such selection caused bad performance because only a few individuals was selected for crossover.

median, average and the best (minimal) values. In each table the result from EAs powered by CPF (2), are bolded if they are the same or better like results from EAs powered by PRNG. Tables are organized according to used algorithms and dimension to made mutual comparison as easy as possible.

**Table 1.** Dimension 5: DE with PRNG

| Function | Max | Median | Average | Min |
|---|---|---|---|---|
| Ackley | 0 | 0 | 0 | 0 |
| Griewangk | 0.00985 | 0.00049 | 0 | 0 |
| Rana | -1872.01 | -1908.92 | -1905.38 | -1961.09 |
| Rastrigin | -1000 | -1000 | -1000 | -1000 |
| Schwefel | -2094.91 | -2094.91 | -2094.91 | -2094.91 |

**Table 2.** Dimension 5: DE with deterministic periodic generator

| Function | Max | Median | Average | Min |
|---|---|---|---|---|
| Ackley | $7.10543 \times 10^{-15}$ | $2.84217 \times 10^{-16}$ | 0 | **0** |
| Griewangk | 0.27834 | 0.18504 | 0.18769 | 0.07529 |
| Rana | -1830.78 | -1904.4 | -1901.9 | **-1972.27** |
| Rastrigin | -926.05 | -982.127 | -994.438 | **-1000** |
| Schwefel | -2094.91 | -2094.91 | -2094.91 | **-2094.91** |

**Table 3.** Dimension 10: SOMA with PRNG

| Function | Max | Median | Average | Min |
|---|---|---|---|---|
| Ackley | 0.00228119 | 0.00132 | 0.00132521 | 0.00062262 |
| Griewangk | 0.0221847 | 0.00475218 | 0.00189315 | 0.0000478522 |
| Rana | -3872.87 | -4005.03 | -3997.3 | -4164.25 |
| Rastrigin | -2000. | -2000. | -2000. | -2000. |
| Schwefel | -4189.83 | -4189.83 | -4189.83 | -4189.83 |

**Table 4.** Dimension 10: SOMA with deterministic periodic generator

| Function | Max | Median | Average | Min |
|---|---|---|---|---|
| Ackley | 5.15986 | 0.103203 | $4.64739 \times 10^{-6}$ | $\mathbf{1.33639 \times 10^{-6}}$ |
| Griewangk | 0.0713621 | 0.0322835 | 0.029518 | $\mathbf{4.29257 \times 10^{-8}}$ |
| Rana | -4108.64 | -4398.14 | -4416.91 | **-4521.97** |
| Rastrigin | -1920.4 | -1980.1 | -1980.1 | **-2000** |
| Schwefel | -4189.83 | -4189.83 | -4189.83 | **-4189.83** |

Algorithms selected for our all previous experiments, reported above, were of different nature like for example differential evolution (DERand1Bin), [14] and SOMA (AllToOne), [13] amongst the others. All experiments has clearly indicated (numerically, no mathematical proof is behind) that randomness (or pseudo randomness in computer applications) is probably not necessary, or better, **randomness is in EAs dynamics aggravating**.

## 3 Evolution as a Feedback Loop Control?

In classical control theory is one of ways how to control dynamical system represented by so called feedback loop, that is depicted at Fig. 4, where $w$ is so called desired value (the aim toward to which we would like to control system), $y$ is output value of controlled system, that is further taken back in feedback loop, subtracted from $w$ and difference $e$ goes to the controller. In controller is $e$ used to calculate the most suitable controller output $u$ so that $y$ will be more close to expected aim of control and future $e = w - y$ will be minimized as much as possible. Whole control process can be influenced by noise $v$, whose existence is not, in control theory, welcome and each control technique try to avoid or eliminate it.

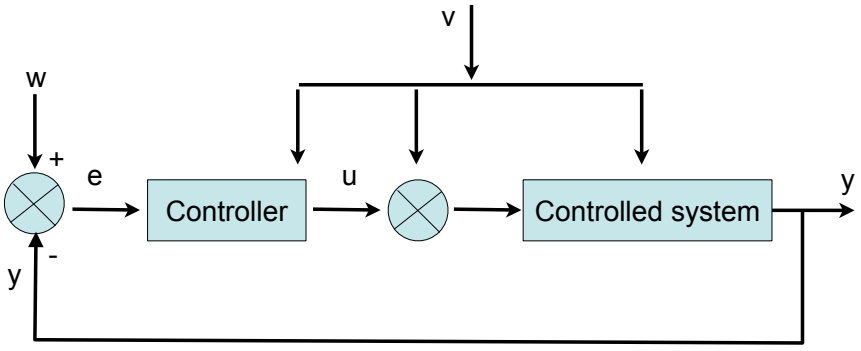


**Fig. 4.** Classical feedback loop control

Between EA dynamics and feedback loop are very tight similarities, that allow us to think about evolutionary algorithm dynamics as if that would be complex feedback loop system. The complexity here is present in evolutionary dynamics in which interact individuals amongst themselves. If EA is considered like a dynamical MIMO system (multiple input - multiple output) then interaction between inputs (parents) is "arbitratrry" driven by PRNGs, DCHS or CPF and output (offsprings) are then result of this interaction. Cost function itself can be very often complex (even without noise) and thanks to feedback loop its complexity **influence dynamics of EA (i.e. controller)**.

In the case of feedback loop interpretation of EAs a very wide spectra of control techniques can be used to control and analyze EAs. Lets take a closer comparison. If EA is considered like feedback loop system, then it can be interpreted so that $w$ is expected (desired) minimal or maximal value of optimization, the $y$ is actual fitness of considered individual(s) (if control is considered like MIMO control), $e$ is difference between individual fitness and aim of optimization. The $e$ is then used by controller, that can be understand like procedures of parents selection and crossover. New individual $u$ is then evaluated by cost function and calculated fitness (controlled system). The role of noise $v$ can be understand like

mutation (input to the controller or addition to $u$) and/or like noise acting on cost function (cost function with noise).

This control theory interpretation of EA dynamics clearly show that randomness is not vital for EA dynamics and is usually **disruptive with negative impact on controlling process**, which is in full coincidence with our previous experimental observations on evolution without PRNGs.

## 4 Conclusion

In this paper we propose novel way how to understand, analyze and control complex dynamics of evolutionary algorithms. The results reported in our previous experiments shows, surprisingly many results from EAs powered by DCHS or CPF are better or the same, and if worst, then in many cases only slightly worst, **which support our ideas, that randomness (i.e. noise) is disruptive with negative impact on evolutionary process**.

The question how much shall be randomness eliminated or used in EAs dynamics from control engineering point of view is further step of pour research.

As an alternative way of EAs dynamics control, reported in [31] is depicted at Fig. 5. Some methods on CML (coupled map lattices) systems control, especially by means of evolutionary algorithms, exist today. The spirit of this idea is to create a closed loop in the following schematic: evolutionary dynamics  complex network  CML system  control CML  control evolutionary dynamics. Reason for this is that this proposed techniques can be used for analysis and control of complex networks exists and if complex network structure would be hidden behind EA dynamics, then it is almost sure, that for example above mentioned

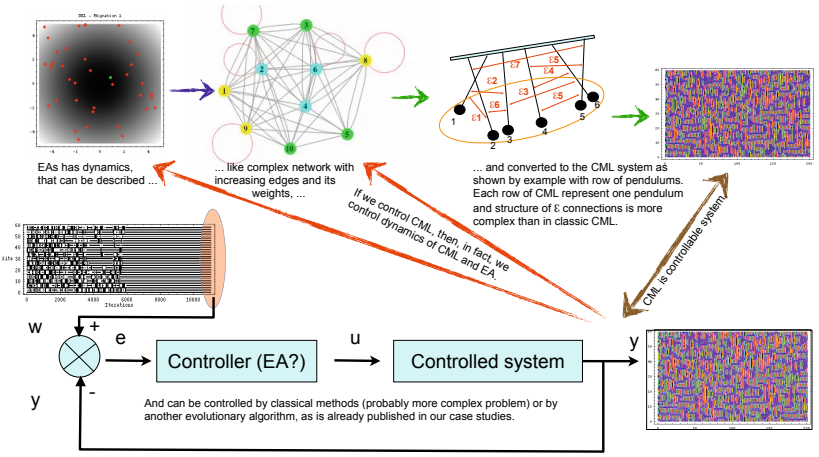


**Fig. 5.** The schematic principle of proposed feedback control EAs and CNS: evolutionary dynamics → complex network → CML system → control CML → control evolutionary (complex network) dynamics

control techniques could be used to improve dynamics of EAs. Complex network is depicted as a set of vertices, mutually joined by single and multiple edges. Each edge can be added or cancelled during the evolution of the network, or importance of an edge can be modified by weights associated to the each edge. Adding or canceling of the edges (or its weights) represents, in fact, dynamics of the algorithm, i.e. network.

Both approaches mentioned here are under intensive investigation and results will be presented soon in another research papers.

**Acknowledgement.** The following two grants are acknowledged for the financial support provided for this research: Grant Agency of the Czech Republic - GACR P103/13/08195S, by the Development of human resources in research and development of latest soft computing methods and their application in practice project, reg. no. CZ.1.07/2.3.00/20.0072 funded by Operational Programme Education for Competitiveness, co-financed by ESF and state budget of the Czech Republic, partially supported by Grant of SGS No. SP2014/159, VŠB - Technical University of Ostrava, Czech Republic, and by European Regional Development Fund under the project CEBIA-Tech No. CZ.1.05/2.1.00/03.0089.

## References

1. Pluhacek, M., Senkerik, R., Davendra, D., Kominkova Oplatkova, Z.: On the Behaviour and Performance of Chaos Driven PSO Algorithm with Inertia Weight. In: Computers and Mathematics with Applications (in print) ISSN 0898-1221
2. Pluhacek, M., Budikova, V., Senkerik, R., Oplatkova, Z., Zelinka, I.: Extended Initial Study on the Performance of Enhanced PSO Algorithm with Lozi Chaotic Map. In: Zelinka, I., Snasel, V., Rössler, O.E., Abraham, A., Corchado, E.S. (eds.) Nostradamus: Mod. Meth. of Prediction, Modeling. AISC, vol. 192, pp. 167–177. Springer, Heidelberg (2013)
3. Pluhacek, M., Senkerik, R., Zelinka, I.: Impact of Various Chaotic Maps on the Performance of Chaos Enhanced PSO Algorithm with Inertia Weight an Initial Study. In: Zelinka, I., Snasel, V., Rössler, O.E., Abraham, A., Corchado, E.S. (eds.) Nostradamus: Mod. Meth. of Prediction, Modeling. AISC, vol. 192, pp. 153–166. Springer, Heidelberg (2013)
4. Pluhacek, M., Senkerik, R., Davendra, D., Zelinka, I.: PID Controller Design For 4th Order system By Means of Enhanced PSO algorithm With Lozi Chaotic Map. In: Proceedings of 18th International Conference on Soft Computing, MENDEL 2012, pp. 35–39 (2012) ISBN 978-80-214-4540-6
5. Pluhacek, M., Budikova, V., Senkerik, R., Oplatkova, Z., Zelinka, I.: On The Performance of Enhanced PSO algorithm With Lozi Chaotic Map An Initial Study. In: Proceedings of 18th International Conference on Soft Computing, MENDEL 2012, pp. 40–45 (2012) ISBN 978-80-214-4540-6
6. Persohn, K.J., Povinelli, R.J.: Analyzing logistic map pseudorandom number generators for periodicity induced by finite precision floating-point representation. Chaos, Solitons and Fractals 45, 238–245 (2012)
7. Davendra, D., Zelinka, I., Senkerik, R.: Chaos driven evolutionary algorithms for the task of PID control. Computers and Mathematics with Applications 60(4), 1088–1104 (2010) ISSN 0898-1221

8. Senkerik, R., Davendra, D., Zelinka, I., Oplatkova, Z., Pluhacek, M.: Optimization of the Batch Reactor by Means of Chaos Driven Differential Evolution. In: Snasel, V., Abraham, A., Corchado, E.S. (eds.) SOCO Models in Industrial & Environmental Appl. AISC, vol. 188, pp. 93–102. Springer, Heidelberg (2013)
9. Lozi, R.: Emergence Of Randomness From Chaos. International Journal of Bifurcation and Chaos 22(2), 1250021 (2012), doi:10.1142/S0218127412500216
10. Wang, X.-Y., Qin, X.: A new pseudo-random number generator based on CML and chaotic iteration. Nonlinear Dynamics An International Journal of Nonlinear Dynamics and Chaos in Engineering Systems, Nonlinear Dyn. 70(2), 1589–1592 (2012), doi:10.1007/s11071-012-0558-0
11. Pareek, N.K., Patidar, V., Sud, K.K.: A Random Bit Generator Using Chaotic Maps. International Journal of Network Security 10(1), 32–38 (2010)
12. Xing-Yuan, W., Lei, Y.: Design of Pseudo-Random Bit Generator Based on Chaotic Maps. International Journal of Modern Physics B 26(32), 1250208, 9 (2012), doi:10.1142/S0217979212502086
13. Zelinka, I.: SOMA – Self Organizing Migrating Algorithm. In: Babu, B.V., Onwubolu, G. (eds.) New Optimization Techniques in Engineering. STUDFUZZ, vol. 141, pp. 167–217. Springer, Heidelberg (2004)
14. Price, K.: An Introduction to Differential Evolution. In: Corne, D., Dorigo, M., Glover, F. (eds.) New Ideas in Optimization, pp. 79–108. McGraw-Hill, London (1999)
15. Glover, F., Laguna, M., Mart, R.: Scatter Search. In: Ghosh, A., Tsutsui, S. (eds.) Advances in Evolutionary Computation: Theory and Applications, pp. 519–537. Springer, New York (2003)
16. Beyer, H.G.: Theory of Evolution Strategies. Springer, New York (2001)
17. Holland, J.H.: Genetic Algorithms. Scientific American, 44–50 (July 1992)
18. Clerc, M.: Particle Swarm Optimization. ISTE Publishing Company (2006) ISBN 1905209045
19. Zelinka, I., Senkerik, R., Pluhacek, M.: Do Evolutionary Algorithms Indeed Require Randomness? In: 2013 IEEE Congress on Evolutionary Computation (CEC), pp. 2283–2289 (2013)
20. Zelinka, I., Chadli, M., Davendra, D., Senkerik, R., Pluhacek, M., Lampinen, J.: Hidden Periodicity - Chaos Dependance on Numerical Precision. In: Zelinka, I., Chen, G., Rössler, O.E., Snasel, V., Abraham, A. (eds.) Nostradamus 2013: Prediction, Model. & Analysis. AISC, vol. 210, pp. 47–59. Springer, Heidelberg (2013)
21. Zelinka, I., Chadli, M., Davendra, D., Senkerik, R., Pluhacek, M., Lampinen, J.: Do Evolutionary Algorithms Indeed Require Random Numbers? Extended Study. In: Zelinka, I., Chen, G., Rössler, O.E., Snasel, V., Abraham, A. (eds.) Nostradamus 2013: Prediction, Model. & Analysis. AISC, vol. 210, pp. 61–75. Springer, Heidelberg (2013)
22. Alatas, B., Akin, E., Ozer, B.A.: Chaos embedded particle swarm optimization algorithms. Chaos, Solitons and Fractals 40(4), 1715–1734 (2009) ISSN 0960-0779
23. Eberhart, R., Kennedy, J.: Swarm Intelligence. The Morgan Kaufmann Series in Artificial Intelligence. Morgan Kaufmann (2001)
24. Dorigo, M., Gambardella, L.M., Birattari, M., Martinoli, A., Poli, R., Stützle, T. (eds.): ANTS 2006. LNCS, vol. 4150. Springer, Heidelberg (2006)
25. Skanderova, L., Zelinka, I., Šaloun, P.: Chaos Powered Selected Evolutionary Algorithms. In: Zelinka, I., Chen, G., Rössler, O.E., Snasel, V., Abraham, A. (eds.) Nostradamus 2013: Prediction, Model. & Analysis. AISC, vol. 210, pp. 111–124. Springer, Heidelberg (2013)

26. Franois, M., Grosges, T., Barchiesi, T., Erra, D., Pseudo-random, R.: number generator based on mixing of three chaotic maps. Commun Nonlinear Sci. Numer. Simulat. 19, 887–895 (2014)
27. Vattulainena, I., Kankaalaa, K., Saarinena, J., Ala-Nissila, T.: A comparative study of some pseudorandom number generators. Computer Physics Communications 86(3), 209–226 (1995)
28. Kanso, A., Smaoui, N.: Logistic chaotic maps for binary numbers generations. Chaos, Solitons and Fractals 40(5), 2557–2568 (2009)
29. Hellekalek, P.: A note on pseudorandom number generators, Simulation Practice and Theory. Simulation Practice and Theory 5(6), p6–p8 (1997)
30. Zelinka, I., Senkerik, R., Pluhacek, M.: Nonrandom Evolutionary Algorithms. In: Proceedings of 20th International Conference on Soft Computing, MENDEL 2014 (2014) ISBN 978-80- 214-4540-6
31. Zelinka, I., Saloun, P., Senkerik, R., Pavlech, M.: Controlling Complexity. In: Zelinka, I., Sanayei, A., Zenil, H., Rossler, O.E. (eds.) How Nature Works. Springer (2014)

# A Brief Survey on the Chaotic Systems as the Pseudo Random Number Generators

Roman Senkerik[1], Michal Pluhacek[1], Ivan Zelinka[2], Donald Davendra[2], and Zuzana Kominkova Oplatkova[1]

[1] Tomas Bata University in Zlin, Faculty of Applied Informatics, Nam T.G. Masaryka 5555, 760 01 Zlin, Czech Republic
{senkerik,pluhacek,oplatkova}@fai.utb.cz
[2] Technical University of Ostrava, Faculty of Electrical Engineering and Computer Science, 17. listopadu 15,708 33 Ostrava-Poruba, Czech Republic
{ivan.zelinka,donald.davendra}@vsb.cz

**Abstract.** This paper briefly investigates the utilization of the both discrete dissipative chaotic system as well as the time-continuous chaotic systems as the chaotic pseudo random number generators. (CPRNGs) Several examples of chaotic systems are simulated, statistically analyzed and compared within this brief survey.

**Keywords:** Chaos, Dissipative systems, Discrete maps, Chaotic flows, Pseudo random number generators.

## 1 Introduction

Generally speaking, the term "chaos" can denote anything that cannot be predicted deterministically. In the case that the word "chaos" is combined with an attribute such as "deterministic", then a specific type of chaotic phenomena is involved, having their specific laws, mathematical apparatus and a physical origin. The deterministic chaos is a phenomenon that - as its name suggests - is not based on the presence of a random or any stochastic effects. It is clear from the structure of the equations (see the section 4), that no mathematical term expressing randomness is present. The seeming randomness in deterministic chaos is related to the extreme sensitivity to the initial conditions [1].

Till now, the chaos has been observed in many of various systems (including evolutionary one). Systems exhibiting deterministic chaos include, for instance, weather, biological systems, many electronic circuits (Chua's circuit), mechanical systems, such as double pendulum, magnetic pendulum, or so called billiard problem.

The idea of using chaotic systems instead of random processes (pseudo-number generators - PRNGs) has been presented in several research fields and in many applications with promising results [2], [3].

Another research joining deterministic chaos and pseudorandom number generator has been done for example in [4]. Possibility of generation of random or pseudorandom



A. Sanayei et al. (eds.), *ISCS 2014: Interdisciplinary Symposium on Complex Systems*, Emergence, Complexity and Computation 14, DOI: 10.1007/978-3-319-10759-2_22

numbers by use of the ultra weak multidimensional coupling of p 1- dimensional dynamical systems is discussed there. Another paper [5] deeply investigate logistic map as a possible pseudorandom number generator and is compared with contemporary pseudorandom number generators. A comparison of logistic map results is made with conventional methods of generating pseudorandom numbers. The approach used to determine the number, delay, and period of the orbits of the logistic map at varying degrees of precision (3 to 23 bits). Another paper [6] proposed an algorithm of generating pseudorandom number generator, which is called (couple map lattice based on discrete chaotic iteration) and combine the couple map lattice and chaotic iteration. Authors also tested this algorithm in NIST 800-22 statistical test suits and for future utilization in image encryption. In [7] authors exploit interesting properties of chaotic systems to design a random bit generator, called CCCBG, in which two chaotic systems are cross-coupled with each other. A new binary stream-cipher algorithm based on dual one-dimensional chaotic maps is proposed in [8] with statistic proprieties showing that the sequence is of high randomness (similar studies in [9], [10], [11]).

## 2 Motivation

Till now the chaos was observed in many of various systems (including evolutionary one) and in the last few years is also used to replace pseudo-number generators (PRGNs) in evolutionary algorithms (EAs).

Recent research in chaos driven heuristics has been fueled with the predisposition that unlike stochastic approaches, a chaotic approach is able to bypass local optima stagnation. This one clause is of deep importance to evolutionary algorithms. A chaotic approach generally uses the chaotic map in the place of a pseudo random number generator [12]. This causes the heuristic to map unique regions, since the chaotic map iterates to new regions. The task is then to select a very good chaotic map as the pseudo random number generator.

The initial concept of embedding chaotic dynamics into the evolutionary algorithms is given in [13]. Later, the initial study [14] was focused on the simple embedding of chaotic systems in the form of chaos pseudo random number generator (CPRNG) for DE and SOMA [15] in the task of optimal PID tuning

Several papers have been recently focused on the connection of heuristic and chaotic dynamics either in the form of hybridizing of DE with chaotic searching algorithm [16] or in the form of chaotic mutation factor and dynamically changing weighting and crossover factor in self-adaptive chaos differential evolution (SACDE) [17]. Also the PSO (Particle Swarm Optimization) algorithm with elements of chaos was introduced as CPSO [18] or CPSO combined with chaotic local search [19].

The focus of our research is the pure embedding of chaotic systems in the form of chaos pseudo random number generator for evolutionary algorithms.

This idea was later extended with the successful experiments with chaos driven DE (ChaosDE) [20], [21] with both and complex simple test functions and in the task of chemical reactor geometry optimization [22].

The concept of Chaos DE has proved itself to be a powerful heuristic also in combinatorial problems domain [23].

At the same time the chaos embedded PSO with inertia weigh strategy was closely investigated [24], followed by the introduction of a PSO strategy driven alternately by two chaotic systems [25] and novel chaotic Multiple Choice PSO strategy (Chaos MC-PSO) [26].

## 3 The Concept of CPRNG

The general idea of CPRNG is to replace the default PRNG with the chaotic system. As the chaotic system is a set of equations with a static start position, we created a random start position, in order to have different start position for different experiments. This random position is initialized with the default PRNG, as a one-off randomizer. Once the start position of the chaotic system has been obtained, the system generates the next sequence using its current position.

The first possible way is to generate and store a long data sequence (approx. 50-500 thousand numbers) during the evolutionary process initialization and keep the pointer to the actual used value in the memory. In case of the using up of the whole sequence, the new one will be generated with the last known value as the new initial one.

The second approach is that the chaotic system is not re-initialized during the experiment and no long data series is stored, thus it is imperative to keep the current state of the chaotic system in memory to obtain the new output values.

As two different types of numbers are required in computer science; real and integers, the modulo operators is used to obtain values between the specified ranges, as given in the following equations (1) and (2):

$$rndreal = \text{mod}\ (\text{abs}\ (rndChaos)\ ,\ 1.0) \tag{1}$$

$$rndint = \text{mod}\ (\text{abs}\ (rndChaos)\ ,\ 1.0) \times Range + 1 \tag{2}$$

Where *abs* refers to the absolute portion of the chaotic map generated number *rndChaos*, and *mod* is the modulo operator. *Range* specifies the value (inclusive) till where the number is to be scaled.

Nevertheless there exist many other approaches as to how to deal with the negative numbers as well as with the scaling of the wide range of the numbers given by the chaotic systems into the typical range 0 – 1:

- Finding of the maximum value of the pre-generated long discrete sequence and dividing of all the values in the sequence with such a maxval number.
- Shifting of all values to the positive numbers (avoiding of ABS command) and scaling.

Utilization of the time-continuous systems (chaotic flows) requires also the investigation on the sampling time. Since the different sampling times gives different final distributions of generated pseudo-random numbers.

## 4 Discrete Chaotic Maps

This section contains the description of discrete dissipative chaotic maps, which was used as the chaotic pseudo random generators. In this research, direct output iterations of the chaotic maps were used for the generation of real numbers scaled into the typical range <0 - 1>. Following chaotic maps were used: Burgers map (3) and Dissipative standard map (4).

The *x*, *y* plots of the chaotic maps are depicted in Fig. 1 - left (Burgers map) and Fig. 3 - left (Dissipative standard map), whereas the right part of aforementioned Figures represents the typical chaotic behavior of the utilized maps given by the examples of direct output iterations.

The illustrative histograms of the distribution of real numbers transferred into the range <0 - 1> generated by means of studied chaotic maps are in Figures 2 and 4.

### 4.1 Burgers Map

The Burgers mapping is a discretization of a pair of coupled differential equations which were used by Burgers [27] to illustrate the relevance of the concept of bifurcation to the study of hydrodynamics flows. The map equations are given in (3) with control parameters $a = 0.75$ and $b = 1.75$ as suggested in [28].

$$\begin{aligned} X_{n+1} &= aX_n - Y_n^2 \\ Y_{n+1} &= bY_n + X_n Y_n \end{aligned} \tag{3}$$

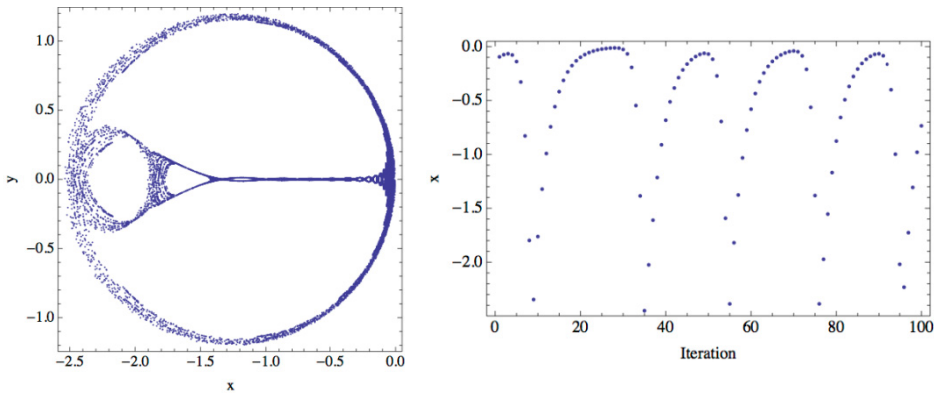


**Fig. 1.** x, *y* plot of the Burgers map (left); Iterations of the Burgers map (variable *x*) (right)

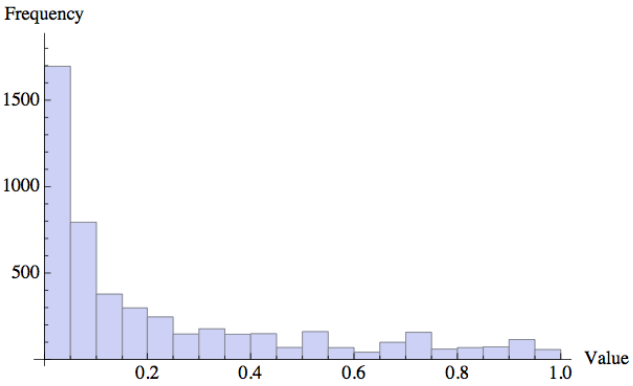


**Fig. 2.** Histogram of the distribution of real numbers transferred into the range <0 - 1> generated by means of the chaotic Burgers map – 5000 samples

### 4.2 Dissipative Standard Map

The Dissipative Standard map is a two-dimensional chaotic map. The parameters used in this work are $b = 0.1$ and $k = 8.8$ as suggested in [28]. For these values, the system exhibits typical chaotic behavior and with this parameter setting it is used in the most research papers and other literature sources. The map equations are given in (4).

$$\begin{aligned} X_{n+1} &= X_n + Y_{n+1} (\mathrm{mod}\, 2\pi) \\ Y_{n+1} &= bY_n + k \sin X_n (\mathrm{mod}\, 2\pi) \end{aligned} \tag{4}$$

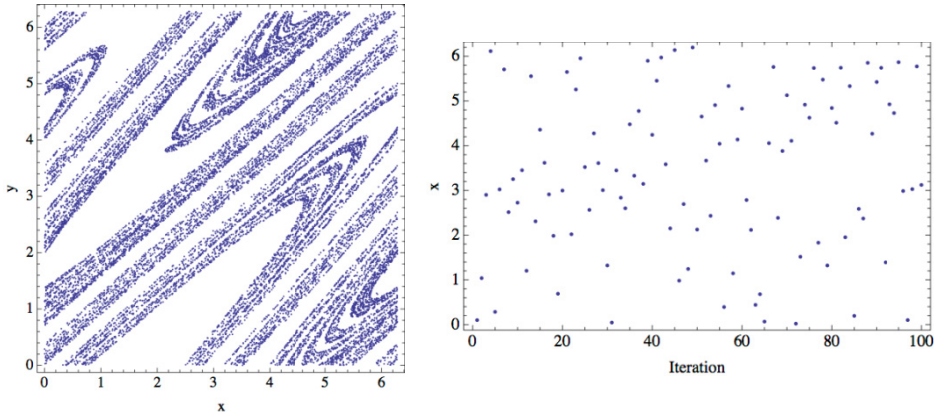


**Fig. 3.** x, *y* plot of the Dissipative standard map (left); Iterations of the Dissipative standard map (variable *x*) (right)

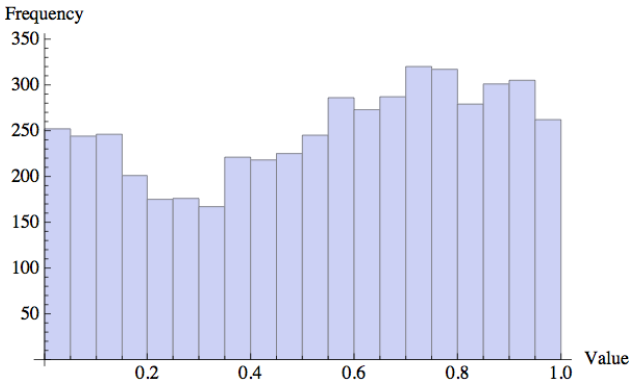


**Fig. 4.** Histogram of the distribution of real numbers transferred into the range <0 - 1> generated by means of the chaotic Dissipative standard map – 5000 samples

## 5 Time-Continuous Chaotic Systems

This section contains the description of time-continuous chaotic system (flows or oscillators), which were used as the chaotic pseudo random generators. Following chaotic systems were tested: unmodified UEDA oscillator (5) and Driven Van der Pol Oscillator (6).

The graphical outputs are organized as in the case of chaotic maps. The left part of the graphic grids (Fig 5 and 7) shows $x$, $y$ parametric plots of the chaotic systems, whereas the right part depicts the typical chaotic behavior of the utilized chaotic systems, represented by the examples of direct output for the variable $x$. Finally the illustrative histograms of the distribution of real numbers transferred into the range <0 - 1> generated by means of studied chaotic systems with the selected sampling rate of 0.5 seconds are in Figures 6 and 8.

### 5.1 UEDA Oscillator

UEDA oscillator is the simple example of driven pendulums, which represent some of the most significant examples of chaos and regularity.

The UEDA system can be simply considered as a special case of intensively studied Duffing oscillator that has both a linear and cubic restoring force. Ueda oscillator represents the both biologically and physically important dynamical model exhibiting chaotic motion. It can be used to explore much physical behavior in biological systems. [29]

The UEDA chaotic system equations are given in (5). The parameters are: $a$ = 1.0 $b$ = 0.05, $c$ = 7.5 and $\omega$ = 1.0 as suggested in [28].

$$\begin{aligned} \frac{dx}{dt} &= y \\ \frac{dy}{dt} &= -ax^3 - by + c\sin \omega t \end{aligned} \tag{5}$$

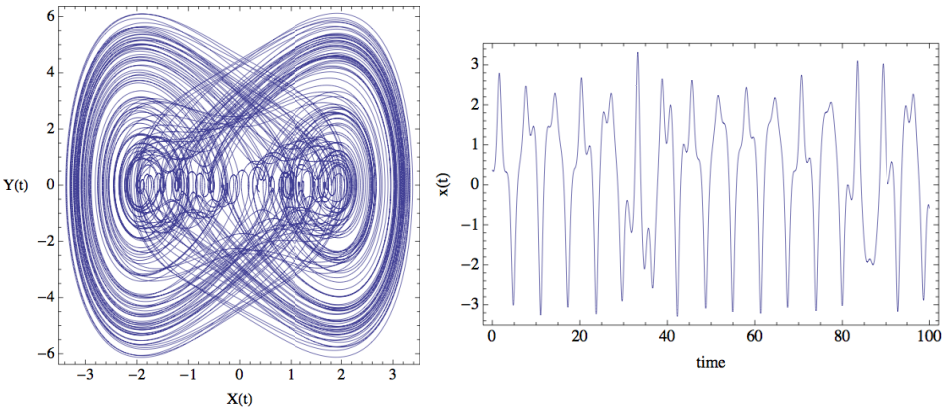


**Fig. 5.** x, *y* parametric plot of the UEDA oscillator (left); Simulation of the UEDA oscillator (variable *x*) (right)

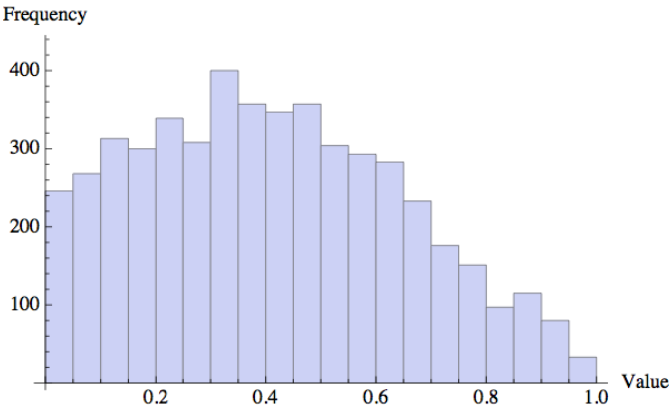


**Fig. 6.** Histogram of the distribution of real numbers transferred into the range <0 - 1> generated by means of the chaotic UEDA oscillator, sampling rate of 0.5 seconds – 5000 samples

### 5.2 Van der Pol Oscillator

Van der Pol oscillator is the simple example of the limit cycles and chaotic behavior in electrical circuits employing vacuum tubes. Similarly to the UEDA oscillator, it can be used to explore physical (unstable) behaviour in biological sciences. [30].

In this paper, the forced, or commonly known as driven, Van der Pol oscillator is investigated. This system consist of the original Van der Pol oscillator definition with the added driving function $a \sin(\omega t)$, thus the differential equations have the form (6). The parameters are: $\mu = 0.2$ $\gamma = 8.0$, $a = 0.35$ and $\omega = 1.02$ as suggested in [28].

$$\frac{dx}{dt} = y$$
$$\frac{dy}{dt} = \mu\left(1 - \gamma x^2\right)y - x^3 + a\sin\omega t \tag{6}$$

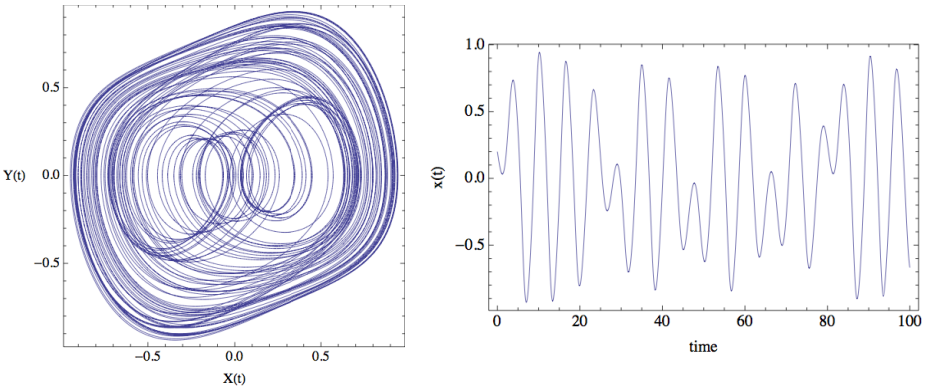


**Fig. 7.** x, *y* parametric plot of the Van der Pol oscillator (left); Simulation of the Van der Pol oscillator (variable *x*) (right)

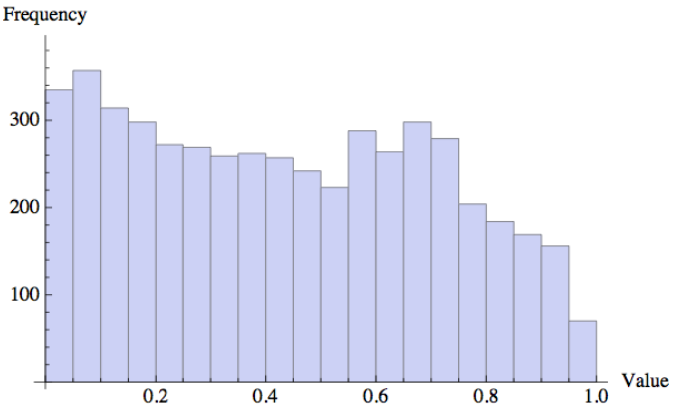


**Fig. 8.** Histogram of the distribution of real numbers transferred into the range <0 - 1> generated by means of the chaotic Van der Pol oscillator, sampling rate of 0.5 seconds – 5000 samples

## 6 Conclusion

This paper was investigating the utilization of the discrete dissipative chaotic system as the chaotic pseudo random number generators. (CPRNGs) Totally four different chaotic systems were simulated, statistically analyzed and compared within this initial research study.

From the graphical comparisons, it follows that through the utilization of different chaotic systems; entirely different statistical characteristics of CPRNGs can be

achieved. Thus the different influence to the system, which utilizes the selected CPRNG, can be chosen through the implementation of particular inner chaotic dynamics given by the particular chaotic system.

Furthermore chaotic systems have additional parameters, which can by tuned. This issue opens up the possibility of examining the impact of these parameters to generation of random numbers, and thus influence on the results obtained by means of either evolutionary techniques or different systems from the softcomputing/ computational intelligence field.

**Acknowledgments.** This work was supported by: Grant Agency of the Czech Republic - GACR P103/13/08195S, is partially supported by Grant of SGS No. SP2014/159 and 170, VŠB - Technical University of Ostrava, Czech Republic, by the Development of human resources in research and development of latest soft computing methods and their application in practice project, reg. no. CZ.1.07/ 2.3.00/20.0072 funded by Operational Programme Education for Competitiveness, co-financed by ESF and state budget of the Czech Republic, further was supported by European Regional Development Fund under the project CEBIA-Tech No. CZ.1.05/2.1.00/03.0089 and by Internal Grant Agency of Tomas Bata University under the project No. IGA/FAI/2014/010.

## References

1. Celikovsky, S., Zelinka, I.: Chaos Theory for Evolutionary Algorithms Researchers. In: Zelinka, I., Celikovsky, S., Richter, H., Chen, G. (eds.) Evolutionary Algorithms and Chaotic Systems. SCI, vol. 267, pp. 89–143. Springer, Heidelberg (2010)
2. Lee, J.S., Chang, K.S.: Applications of chaos and fractals in process systems engineering. Journal of Process Control 6(2-3), 71–87 (1996)
3. Wu, J., Lu, J., Wang, J.: Application of chaos and fractal models to water quality time series prediction. Environmental Modelling & Software 24(5), 632–636 (2009)
4. Lozi, R.: Emergence of Randomness from Chaos. International Journal of Bifurcation and Chaos 22(02), 1250021 (2012)
5. Persohn, K.J., Povinelli, R.J.: Analyzing logistic map pseudorandom number generators for periodicity induced by finite precision floating-point representation. Chaos, Solitons & Fractals 45(3), 238–245 (2012)
6. Wang, X.-Y., Qin, X.: A new pseudo-random number generator based on CML and chaotic iteration. Nonlinear Dyn. 70(2), 1589–1592 (2012)
7. Narendra, K.P., Vinod, P., Krishan, K.S.: A Random Bit Generator Using Chaotic Maps. International Journal of Network Security 10, 32–38 (2010)
8. Yang, L., Wang, X.-Y.: Design of Pseudo-random Bit Generator Based on Chaotic Maps. International Journal of Modern Physics B 26(32), 1250208 (2012)
9. Bucolo, M., Caponetto, R., Fortuna, L., Frasca, M., Rizzo, A.: Does chaos work better than noise? IEEE Circuits and Systems Magazine 2(3), 4–19 (2002)
10. Hu, H., Liu, L., Ding, N.: Pseudorandom sequence generator based on the Chen chaotic system. Computer Physics Communications 184(3), 765–768 (2013)
11. Pluchino, A., Rapisarda, A., Tsallis, C.: Noise, synchrony, and correlations at the edge of chaos. Physical Review E 87(2), 022910 (2013)
12. Aydin, I., Karakose, M., Akin, E.: Chaotic-based hybrid negative selection algorithm and its applications in fault and anomaly detection. Expert Systems with Applications 37(7), 5285–5294 (2010)

13. Caponetto, R., Fortuna, L., Fazzino, S., Xibilia, M.G.: Chaotic sequences to improve the performance of evolutionary algorithms. IEEE Transactions on Evolutionary Computation 7(3), 289–304 (2003)
14. Davendra, D., Zelinka, I., Senkerik, R.: Chaos driven evolutionary algorithms for the task of PID control. Computers & Mathematics with Applications 60(4), 1088–1104 (2010)
15. Zelinka, I.: SOMA — Self-Organizing Migrating Algorithm. In: New Optimization Techniques in Engineering. STUDFUZZ, vol. 141, pp. 167–217. Springer, Heidelberg (2004)
16. Liang, W., Zhang, L., Wang, M.: The chaos differential evolution optimization algorithm and its application to support vector regression machine. Journal of Software 6(7), 1297–1304 (2011)
17. Zhenyu, G., Bo, C., Min, Y., Binggang, C.: Self-Adaptive Chaos Differential Evolution. In: Jiao, L., Wang, L., Gao, X.-b., Liu, J., Wu, F. (eds.) ICNC 2006. LNCS, vol. 4221, pp. 972–975. Springer, Heidelberg (2006)
18. Coelho, L.D.S., Mariani, V.C.: A novel chaotic particle swarm optimization approach using Hénon map and implicit filtering local search for economic load dispatch. Chaos, Solitons & Fractals 39(2), 510–518 (2009)
19. Hong, W.-C.: Chaotic particle swarm optimization algorithm in a support vector regression electric load forecasting model. Energy Conversion and Management 50(1), 105–117 (2009)
20. Senkerik, R., Pluhacek, M., Zelinka, I., Oplatkova, Z.K., Vala, R., Jasek, R.: Performance of chaos driven differential evolution on shifted benchmark functions set. In: Herrero, A., et al. (eds.) International Joint Conference SOCO'13-CISIS'13-ICEUTE'13. AISC, vol. 239, pp. 41–50. Springer, Heidelberg (2014)
21. Senkerik, R., Davendra, D., Zelinka, I., Pluhacek, M., Kominkova Oplatkova, Z.: On the Differential Evolution Drivan by Selected Discrete Chaotic Systems: Extended Study. In: 19th International Conference on Soft Computing, MENDEL 2013, pp. 137–144 (2013)
22. Senkerik, R., Pluhacek, M., Oplatkova, Z.K., Davendra, D., Zelinka, I.: Investigation on the Differential Evolution driven by selected six chaotic systems in the task of reactor geometry optimization. In: 2013 IEEE Congress on Evolutionary Computation (CEC), June 20-23, pp. 3087–3094 (2013)
23. Davendra, D., Bialic-Davendra, M., Senkerik, R.: Scheduling the Lot-Streaming Flowshop scheduling problem with setup time with the chaos-induced Enhanced Differential Evolution. In: 2013 IEEE Symposium on Differential Evolution (SDE), April 16-19, pp. 119–126 (2013)
24. Pluhacek, M., Senkerik, R., Davendra, D., Kominkova Oplatkova, Z., Zelinka, I.: On the behavior and performance of chaos driven PSO algorithm with inertia weight. Computers & Mathematics with Applications 66(2), 122–134 (2013)
25. Pluhacek, M., Senkerik, R., Zelinka, I., Davendra, D.: Chaos PSO algorithm driven alternately by two different chaotic maps - An initial study. In: 2013 IEEE Congress on Evolutionary Computation (CEC), June 20-23, pp. 2444–2449 (2013)
26. Pluhacek, M., Senkerik, R., Zelinka, I.: Multiple Choice Strategy Based PSO Algorithm with Chaotic Decision Making – A Preliminary Study. In: Herrero, Á., et al. (eds.) International Joint Conference SOCO'13-CISIS'13-ICEUTE'13. AISC, vol. 239, pp. 21–30. Springer, Heidelberg (2014)
27. ELabbasy, E., Agiza, H., EL-Metwally, H., Elsadany, A.: Bifurcation Analysis, Chaos and Control in the Burgers Mapping. International Journal of Nonlinear Science 4(3), 171–185 (2007)
28. Sprott, J.C.: Chaos and Time-Series Analysis. Oxford University Press (2003)
29. Bharti, L., Yuasa, M.: Energy Variability and Chaos in Ueda Oscillator, http://www.rist.kindai.ac.jp/no.23/yuasa-EVCUO.pdf
30. Kanamaru, T.: Van der Pol oscillator. Scholarpedia 2(1), 2202 (2007)

# Emergent Behaviors on Coevolutionary Networks of Chaotic Dynamical Systems

A. Anzo and J.G. Barajas-Ramírez*

División de Matemáticas Aplicadas, IPICyT,
Camino a la Presa San José 2055
Col. Lomas 4a Secc. C.P.78216,
San Luis Potosí, S.L.P., México
{andres.anzo,jgbarajas}@ipicyt.edu.mx

**Abstract.** Coevolutionary networks involve two simultaneous dynamical processes: structural evolution and dynamics of nodes. In this context, a current research topic has been the role of coevolution in the emergence of self-organized phenomena. In order to investigate this topic, we propose a network model where each node is a chaotic dynamical system and, simultaneously, the structure of the network evolves according to a local rule. In particular, the local rule updates synchronously the binary state of each link as either "on" or "off". We define the local rule in terms of the state variables of the nodes and the structural features of the network. After iterate the local rule we observe two types of emergent behaviors: the network achieves complete synchronization; and the formation of structural patterns which are displayed in the coupling matrix.

## 1 Introduction

A dynamical network is an ensemble of interconnected dynamical units called nodes which are usually modeled as chaotic dynamical systems. In recent years for such dynamical network significant results have been obtained in regards to the stability of collective behaviors like synchronization [2,3]. These results are based on the assumption that the network structure remains static while nodes change their state variables. However, in many real-life situations the network structure has their own dynamics of change which is driven by processes as the addition or deletion of links.

When structural evolution and dynamics of nodes are considered in a network model, we can observe that they have a causal impact on each other evolution. In other words, the evolution of the structure affects the collective behavior of the nodes, and vice versa [5,4]. Networks with this dynamical attribute are called coevolutionary networks. One of the mayor research questions in this direction can be expressed as follows: what is the role of coevolution in the emergence of self-organized phenomena? In this sense, a methodology to try to elucidate

* We acknowledge financial support from IPICyT and CONACYT.



A. Sanayei et al. (eds.), *ISCS 2014: Interdisciplinary Symposium on Complex Systems*,
Emergence, Complexity and Computation 14, DOI: 10.1007/978-3-319-10759-2_23

a response to this question is to propose models that involve both dynamical processes simultaneously.

There are works in current references that look into modeling coevolutionary networks. For example Sayama and Laramee have proposed a model where, based on the graph grammar formalism, the vicinity of a given node is transformed according to the dynamical state of its neighborhood [6]. On the other hand, Tomita et al. have proposed a generalization of the Cellular Automata (CA) paradigm, where the structural changes are the results of a CA rule operated at each node of the network [7]. An alternative coevolutionary model is the proposed by Smith et al, who have introduced the concept of Network Automata, a network whose structural evolution depends on their own current structural features [8]. With these research works, we can observe that the network exhibit distinct types of structural patterns. However, on these models the state space of each node is discrete, that is, each node takes one state value from a finite set of states. In this context, DeLellis et al. have proposed a coevolution model for networks of chaotic dynamical system [9]. The key idea of this model is to adjust all the connections strengths according to adaptive rules, which are dependent on the state variables of the nodes. DeLellis et al. have shown that with these adaptive rules the network can achieve a synchronous behavior. Nevertheless, in this model the configuration of who is connected with whom remains fixed for all time.

Based on the Cellular Automata framework [10,11], in this contribution we propose a coevolution model for networks of identical chaotic dynamical systems. Our model consists of an iterative local rule describing the logic that establishes whether the binary state of a given link is set to either "on" or "off". In order to define the local rule, we construct two neighborhoods for each possible link in the network: the neighborhood of links and the neighborhood of nodes. In this sense we define the local rule according to dynamical and structural conditions. We change the state "on/off" of the link $(i, j)$ if: I) Dynamical condition.- The binary state of the link is "off" and the dynamical error between the $i$th and $j$th nodes is smaller than that of the neighborhood of nodes ; II) Structural condition.- If the the binary state of the link is "on" and the link betweenness centrality of $(i, j)$ is smaller than that of the neighborhood of links. We implement this local rule synchronously to all possible links at specific points of time. With this local rule we observe two classes of emergent behaviors; on the one hand the network achieves complete synchronization; and on the other hand the formation of structural patterns which are displayed in the coupling matrix.

The remainder of the paper is organized as follows: in section 2 our coevolution model is described with detail. In section 3 we provide some numerical results, and in section 4 we provide some closing remarks.

## 2 Model Description

We consider a network of $N$ identical chaotic dynamical systems coupled by unweighted and bidirectional links which have their own dynamic of change. The state equation of the entire network is described by the following equations:

$$\dot{x}_i(t) = f(x_i(t)) + c\sum_{j=1}^{N} a_{ij}(t)\Gamma(x_j(t) - x_i(t)), \quad i = 1, \ldots, N. \tag{1}$$

where $t$ is the continuous-time scale, $x_i(t) = [x_{i1}(t), x_{i2}(t), \ldots, x_{in}(t)]^T \in \mathbf{R}^n$ is a vector with the state variables of the $i$th node, $f : \mathbf{R}^n \to \mathbf{R}^n$ defines the vector field of the individual chaotic dynamical system of dimension $n$. The coupling of the $i$th node with their neighbors is described via the second term at the right hand of equation (1), where $c$ is the uniform coupling strength between the nodes; $\Gamma \in \mathbf{R}^{n\times n}$ is the inner linking matrix which linking the state variables. We assume that $\Gamma = diag\{r_1, \ldots, r_n\}$ where $r_l = 1$ if two nodes are linked through their $l$-th state variable, and $r_l = 0$ otherwise. The term $A(t) = \{a_{ij}(t)\} \in \mathbf{R}^{N\times N}$ represents a time-varying coupling matrix whose elements are zero or one depending on which nodes are connected or not at a given time instant. This matrix is constructed as follows: if $a_{ij}(t)$ takes the value one at time $t$, then the nodes with labels $i$ and $j$ are connected, otherwise those nodes are not connected. In this context, we say that the binary state of the link $(i, j)$ is "on" at time $t$ if $a_{ij}(t) = 1$; and we say that the binary state of such link is "off" at time $t$ if $a_{ij}(t) = 0$. To complete the construction of the coupling matrix, their diagonal entries are calculated as

$$a_{ii}(t) = -\sum_{\substack{j=1\\ j\neq i}}^{N} a_{ij}(t) = -\sum_{\substack{j=1\\ j\neq i}}^{N} a_{ji}(t), \quad i = 1, 2, \ldots, N, \forall t. \tag{2}$$

We call (2) the diffusive condition. It is worth to remark that each element of the coupling matrix $a_{ij}(t)$, with $i, j = 1, 2, \ldots, N$ and $i \neq j$, is a piecewise-constant and continuous from the right function. We show and example of such functions in Figure 1.

If at a given time instant $t$ the network has not isolated nodes, then from Gerschgoring's circle theorem, the eigenspectrum of the coupling matrix $A(t)$ have the following features: zero is an eigenvalue of multiplicity one; all its non-zero eigenvalues are strictly negative, and they can be ordered as $0 = \lambda_1(t) > \lambda_2(t) \geq \lambda_3(t) \geq \cdots \geq \lambda_N(t)$.

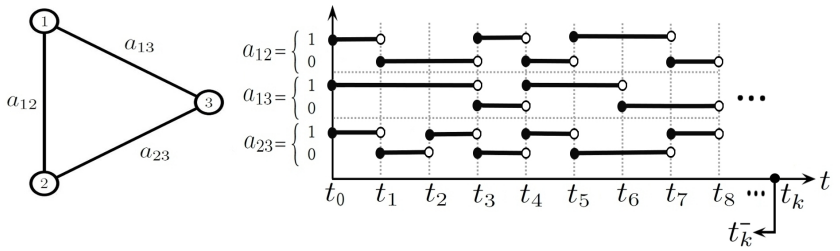


**Fig. 1.** Each element of the the coupling matrix $a_{ij}(t)$, with $i, j = 1, 2, \ldots, N$ and $i \neq j$, is a piecewise-constant and continuous from the right function. We use the notation $t_k^-$ to indicate the instant previous to the $k$-th updating time.

The dynamical network (1) is said to (asymptotically) achieve complete synchronization if the trajectories of every node satisfy

$$\lim_{t\to\infty} \|x_i(t) - x_j(t)\| = 0, \quad \text{for} \quad i,j = 1,2,\ldots,N. \tag{3}$$

Because the diffusive condition (2) the synchronized trajectory of (1) corresponds to that of an isolated node, i.e, $\dot{s}(t) = f(s(t))$; where $s(t) \in \mathbf{R}^n$ is called the synchronized solution [3].

Simultaneously to the dynamics of nodes, we consider that the network structure of (1) evolves driven by a process that updates the binary state "on/off" of all the $N(N-1)/2$ possible links. Furthermore we assume that the update of the binary state of the links occurs instantaneously at specif points of the time scale $t$. We call such points of time the updating times and we denote it as $t_1 < t_2 < \cdots < t_k$, with $k \in \mathbf{Z}^+$. In this contribution we select arbitrarily every updating time; in particular we consider that they are placed over the $t$ scale at regular intervals $T$. Additionally, we use the notation $t_k^-$ to indicate the instant previous to the $k$-th updating time as we illustrate in Figure 1.

In this sense, we model the structural evolution as an operator that at a given updating time $t_k$ alters the elements of the current coupling matrix $A(t_k^-)$ in order to construct the next coupling matrix. For a coevolutionary network, such operator depends both structural and dynamical features of the network at the instant previous to the $k$-th updating time $t_k^-$, that is

$$A(t_k) = \Phi(A(t_k^-), X(t_k^-)), \tag{4}$$

for $k = 1,2,\ldots$ where $X(t_k^-) = [x_1^T(t_k^-), x_2^T(t_k^-), \ldots, x_N^T(t_k^-)]^T \in \mathbf{R}^{Nn}$ is a vector with the $Nn$ state variables of the nodes at time instant $t_k^-$; and $\Phi : \mathbf{R}^{N\times N} \times \mathbf{R}^{Nn} \to \mathbf{R}^{N\times N}$ is the operator that updates the current structure. The action of the operator $\Phi(\cdot)$ consist on visit all the entries of the current coupling matrix $A(t_k^-)$ and update it according to a local rule. Note that this process is analogous to the synchronous update of the cells in the Cellular Automata framework [8,11].

In order to define the local rule we need first to specify the neighborhood for each possible link. In this work we propose to define the neighborhood of each link according to their position within the coupling matrix $A(t)$. In particular we consider the von Neumann neighborhood definition as we illustrate in Figure 2. It is worth remarking that in this neighborhood definition we avoid the diagonal elements of the coupling matrix and we consider a periodic boundary. In this context, if $r$ is the radius of the neighborhood, i.e, the number of neighbors at the right (or left, or up, or down) of the entry $a_{ij}(t_k^-)$, then the neighborhood of links is

$$L_{ij}(t_k^-) = \{a_{i-r,j}(t_k^-), \ldots, a_{i+r,j}(t_k^-), a_{i,j-r}(t_k^-), \ldots, a_{i,j+r}(t_k^-)\}.$$

Additionally, we define the neighborhood of nodes as the set of nodes involved on $L_{ij}(t_k^-)$, i.e.,

$$\mathcal{X}_{ij}(t_k^-) = \{x_{i-r}(t_k^-), \ldots, x_{i+r}(t_k^-), x_{j-r}(t_k^-), \ldots, x_{j+r}(t_k^-)\}.$$

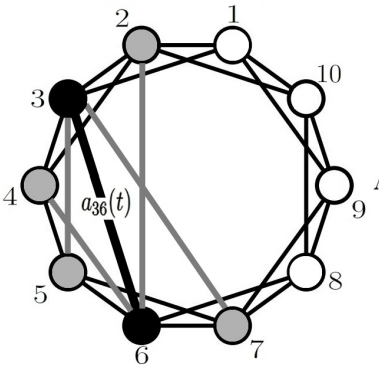


$$A(t)=\begin{pmatrix} a_{11} & a_{12} & a_{13} & a_{14} & a_{15} & a_{16} & a_{17} & a_{18} & a_{19} & a_{110} \\ a_{21} & a_{22} & a_{23} & a_{24} & a_{25} & a_{26} & a_{27} & a_{28} & a_{29} & a_{210} \\ a_{31} & a_{32} & a_{33} & a_{34} & a_{35} & a_{36} & a_{37} & a_{38} & a_{39} & a_{310} \\ a_{41} & a_{42} & a_{43} & a_{44} & a_{45} & a_{46} & a_{47} & a_{48} & a_{49} & a_{410} \\ a_{51} & a_{52} & a_{53} & a_{54} & a_{55} & a_{56} & a_{57} & a_{58} & a_{59} & a_{510} \\ a_{61} & a_{62} & a_{63} & a_{64} & a_{65} & a_{66} & a_{67} & a_{68} & a_{69} & a_{610} \\ a_{71} & a_{72} & a_{73} & a_{74} & a_{75} & a_{76} & a_{77} & a_{78} & a_{79} & a_{710} \\ a_{81} & a_{82} & a_{83} & a_{84} & a_{85} & a_{86} & a_{87} & a_{88} & a_{89} & a_{810} \\ a_{91} & a_{92} & a_{93} & a_{94} & a_{95} & a_{96} & a_{97} & a_{98} & a_{99} & a_{910} \\ a_{101} & a_{102} & a_{103} & a_{104} & a_{105} & a_{106} & a_{107} & a_{108} & a_{109} & a_{1010} \end{pmatrix}$$

$$L_{36}(t) = \{a_{35}(t), a_{37}(t), a_{26}(t), a_{46}(t)\}\,,\ \ \mathcal{X}_{36}(t) = \{x_2(t), x_4(t), x_5(t), x_7(t)\}$$

**Fig. 2.** The construction of the neighborhood for the link $a_{36}(t)$ with $r = 1$. At the left the network structure where gray nodes and gray links indicates the neighborhood of nodes and links for $a_{36}(t)$. At the right the coupling matrix where we highlight the neighborhood of the entry $a_{36}(t)$.

On Figure 2 we show an example of the construction of the two neighborhoods for $r = 1$.

Further, if we consider that all the links are updating with the same local rule, we can rewrite (4) as follows

$$a_{ij}(t_k) = \phi(a_{ij}(t_k^-), L_{ij}(t_k^-), \mathcal{X}_{ij}(t_k^-)), \tag{5}$$

for $i, j = 1, \ldots, N$ with $i \neq j$, where $\phi(\cdot)$ is the local rule which determines the next binary state of the link $a_{ij}$. In order to define the local rule (5) we use the following information: 1) the link $a_{ij}(t_k^-)$ own binary state; 2) the structural features of the links with binary state "on" in $L_{ij}(t_k^-)$; and 3) the dynamical error $e_{pq}(t_k^-) = \left\|x_p(t_k^-) - x_q(t_k^-)\right\|$ between all the pairs of nodes $p, q$ in $\mathcal{X}_{ij}(t_k^-)$.

Concerning to the structural features of the links, in this contribution we consider their betweenness centraliyt $b_{ij}(t_k^-)$, which is defined as the sum of the fraction of all-pairs shortest paths that pass through the link $a_{ij}$ [1]. More precisely, the link betweenness is defined as

$$b_{ij}(t_k^-) = \sum_{\substack{p,q=1 \\ p \neq q}}^{N} \frac{\sigma_{pq}(a_{ij}(t_k^-))}{\sigma_{pq}(t_k^-)} \tag{6}$$

where $\sigma_{pq}(t_k^-)$ is the number of shortest paths connecting $p$ and $q$ at time instant $t_k^-$, while $\sigma_{pq}(a_{ij}(t_k^-))$ is the number of shortest paths connecting $p$ and $q$ and passing through link $a_{ij}(t_k^-)$.

Then, using the information described above, we propose the following local rule

$$a_{ij}(t_k) = \begin{cases} 1 & \text{if} \quad a_{ij}(t_k^-) = 0 \quad \text{and} \quad e_{ij}(t_k^-) \leq \left\langle e_{pq}(t_k^-) \right\rangle_{\mathcal{X}_{ij}} \\ 0 & \text{if} \quad a_{ij}(t_k^-) = 1 \quad \text{and} \quad b_{ij}(t_k^-) \leq \left\langle b_{pq}(t_k^-) \right\rangle_{L_{ij}} \\ a_{ij}(t_k^-) & \text{otherwise} \end{cases} \tag{7}$$

for $i, j = 1, 2, \ldots, N$ with $i \neq j$; $p, q \in \mathcal{X}_{ij}(t_k)$ with $p \neq q$, where $\left\langle \cdot \right\rangle_{X_{ij}}$ and $\left\langle \cdot \right\rangle_{L_{ij}}$ are the average value over the sets $\mathcal{X}_{ij}(t_k^-)$ and $L_{ij}(t_k^-)$ respectively.

On the first part of the local rule (7) we argue that if at the current time the nodes $i$ and $j$ are disconnected, and the dynamical error between their states is smaller than that the average in the neighborhood of nodes, then we create a link between such nodes. On the second part of the rule (7) we argue that if at the current time the nodes $i$ and $j$ are connected, but the link centrality is smaller than that the average in the neighborhood of links, then we remove the link between such links. And on the third part of (7) we argue that the current binary state of the link is preserved if any of these above parts are not satisfied.

We summarize our coevolution model using the following algorithm:

- **Step 1**.- The initial condition for every node is chosen uniformly randomly. Next, the initial network structure ($A_0 = A(t_0)$) is chosen to be a regular graph; and the coupling strength $c$ is selected such that the initial network will not synchronize for the first time instants. On the other hand the updating times are chosen such that $t_{k+1} - t_k = T$, for $k \in \mathbf{Z}^+$, and $T > 0$. For the initial time interval $[0, T)$ the nodes dynamical state are evaluated according to (1) with the fixed network structure $A_0$.
- **Step 2**. At each updating time $t_k$, with $k \in \mathbf{Z}^+$, the local rule (7) is utilized to update all the possible $N(N-1)/2$ links in the network and construct the next structure $A_k = A(t_k)$.
- **Step 3**.- The nodes dynamical state are evaluated according to (1) for $t \in [Tk, T(k+1))$ with the network structure $A_k$.
- **Step 4**.- Repeat Step 2

In the following section, our coevolution model is applied to a network of chaotic dynamical systems.

## 3 Simulation Results

We consider a network described by (1) with $N = 100$ nodes, where each node is a Chua's circuit given by

$$\begin{bmatrix} \dot{x}(t) \\ \dot{y}(t) \\ \dot{z}(t) \end{bmatrix} = \begin{bmatrix} a[-y(t) - NL(x(t))] \\ x(t) - y(t) + z(t) \\ by(t) \end{bmatrix} \tag{8}$$

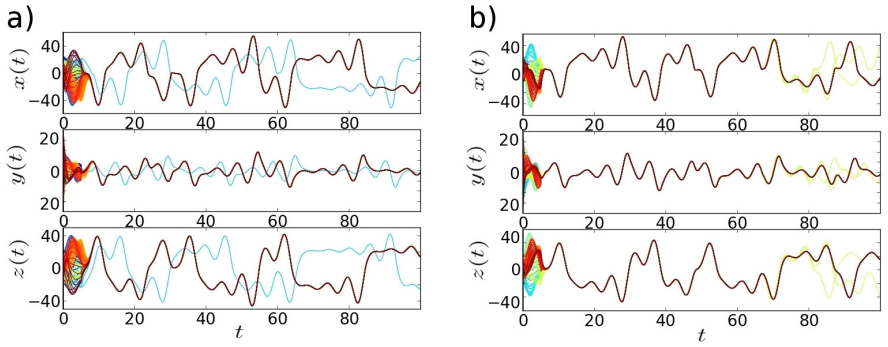


**Fig. 3.** Network of $N = 100$ Chua's circuits, with coupling strength $c = 0.5$ and a) $r = 3$; b) $r = 10$ . Synchronization is achieved after the first updating time $t_1 = 5$.

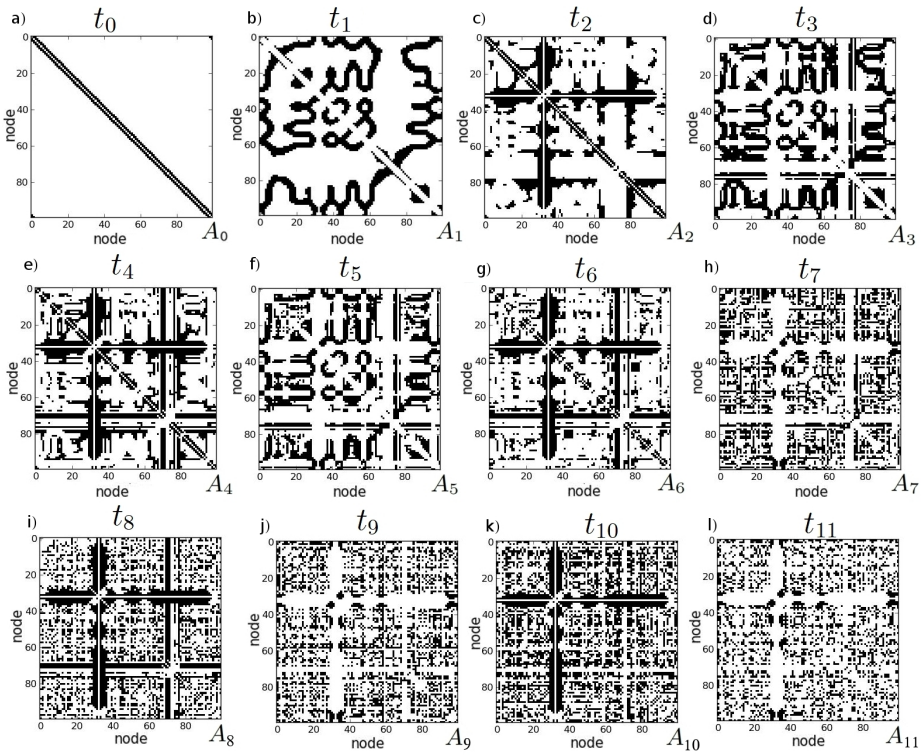


**Fig. 4.** The grid representation of the coupling matrix at different updating times for $N = 100$ nodes, coupling strength $c = 0.5$ and radius $r = 3$

where $NL(x(t)) = m_0x(t) + 0.5(m_1 - m_0)(|x(t) + 1| - |x(t) - 1|)$, with $a = 4.916$, $b = 3.641$, $m_0 = -0.07$ and $m_1 = 1.5$. We select the initial condition for each node randomly from a uniform distribution in the interval $[-20.0, 20.0]$.

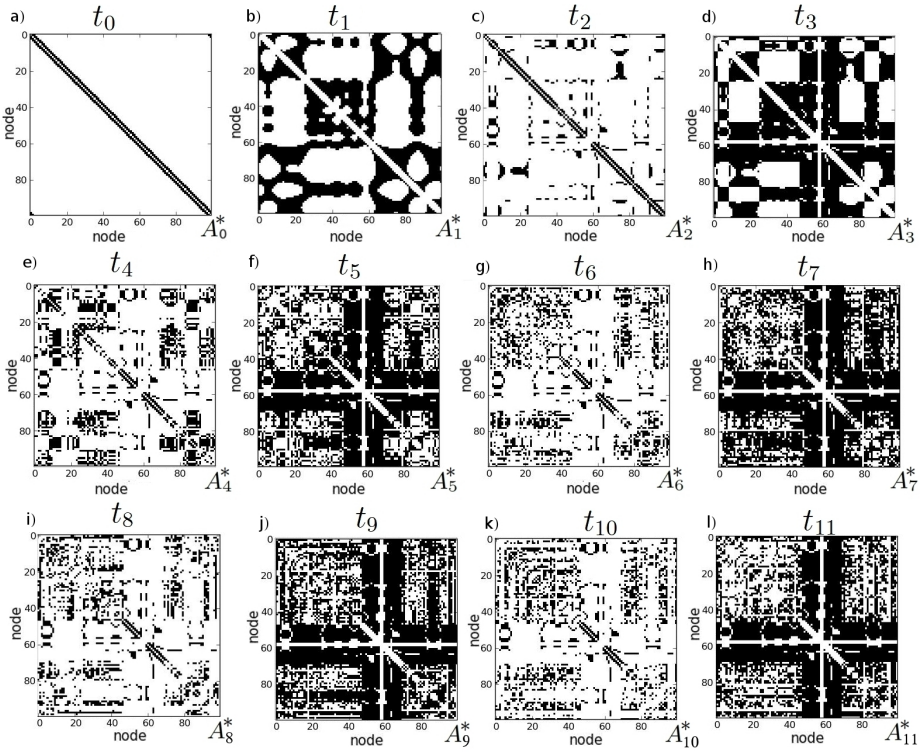


**Fig. 5.** The grid representation of the coupling matrix at different updating times for $N = 100$ nodes, coupling strength $c = 0.5$ and radius $r = 10$

On the other hand, we chose the initial structure $A_0 = A(t_0)$ to be that of a Nearest Neighbors (NN) network where each node is connected with its two forward and two backward neighbors. In Figure 3.a we show the grid representation of the coupling matrix $A_0$, where black squares represent the links with binary state "on"; and white squares represent the links with binary state "off".

To complete the description of (1), we select a uniform coupling strength $c = 0.5$, and we select the inner linking matrix to be the identity matrix $\Gamma = I_n$, where $n = 3$ for the Chua's circuit (7). Using the synchronization criteria shown in [3], we have that our original NN network will not synchronize for the first time instants ($[t_0, t_1)$).

On the other hand, we choose to update synchronously all the possible links at equal time periods, that is, the updating times are selected such that $t_{k+1} - t_k = T = 5$ time steps, with $k \in \mathbf{Z}^+$.

First, we consider that the neighborhood of links is constructed with radius $r = 3$. As a second example we consider $r = 10$. The simulation results for $N = 100$ Chua's circuits are shown in Figs 3. In both examples, synchronization is achieved after the first updating time $t_1$. For the first example, we observe that

**Table 1.** Basic network metrics for the structures in Figure 4; where Avg. is the average value over all the nodes in the network

| | $A_1$ | $A_2$ | $A_3$ | $A_4$ | $A_5$ | $A_6$ | $A_7$ | $A_8$ | $A_9$ | $A_{10}$ | $A_{11}$ |
|---|---|---|---|---|---|---|---|---|---|---|---|
| No. links | 1315 | 1334 | 1801 | 1770 | 1647 | 1609 | 1663 | 1986 | 1520 | 2153 | 1293 |
| No. connected com. | 1 | 2 | 4 | 2 | 4 | 2 | 3 | 2 | 2 | 2 | 2 |
| Avg. node degree | 26.3 | 26.7 | 36.0 | 35.4 | 32.9 | 32.1 | 33.3 | 39.7 | 30.4 | 43.1 | 25.9 |
| Avg. clustering c. | 0.63 | 0.61 | 0.65 | 0.64 | 0.63 | 0.64 | 0.57 | 0.63 | 0.56 | 0.6 | 0.47 |
| Avg. path efficiency | 0.56 | 0.62 | 0.64 | 0.67 | 0.62 | 0.65 | 0.63 | 0.7 | 0.62 | 0.7 | 0.6 |
| Avg. link betweenness | 0.022 | 0.017 | 0.015 | 0.016 | 0.016 | 0.016 | 0.016 | 0.015 | 0.017 | 0.016 | 0.018 |

the trajectory of a single node does not collapse into the synchronized state; and in the second example we observe that all nodes are synchronized after the first updating time $t_1 = 5$, but the trajectory of a single node moves away from the synchronized state after the $t = 75$ time step.

In Figures 4 and 5 we show the grid representation of the coupling matrix at different updating times for the first ($r = 3$) and the second ($r = 10$) example respectively. In both examples we can visually identify various types of structural patterns at each updating time. It is worth to note that in $t_1$, the network structure favors the emergence of a stable synchronized behavior of the nodes. In Tables 1 and 2 we show some basic network metrics for the structures in Figures 3 and 4 respectively. We can observe that the rule (7) favor the formation of groups, and, additionally, imposes a structural evolution that turns off links, to then turn on links as time passes. However the rule tends to decrease the value of the link betweenness centrality.

**Table 2.** Basic network metrics for the structures in Figure 5; where Avg. is the average value over all the nodes in the network

| | $A_1^*$ | $A_2^*$ | $A_3^*$ | $A_4^*$ | $A_5^*$ | $A_6^*$ | $A_7^*$ | $A_8^*$ | $A_9^*$ | $A_{10}^*$ | $A_{11}^*$ |
|---|---|---|---|---|---|---|---|---|---|---|---|
| No. links | 2002 | 533 | 2718 | 1147 | 2961 | 1049 | 3225 | 958 | 3129 | 1062 | 2921 |
| No. connected com. | 1 | 3 | 3 | 3 | 3 | 5 | 3 | 5 | 3 | 3 | 3 |
| Avg. node degree | 40.0 | 10.6 | 54.3 | 22.9 | 59.2 | 21.0 | 64.5 | 19.16 | 62.6 | 21.24 | 58.42 |
| Avg. clustering c. | 0.73 | 0.4 | 0.76 | 0.33 | 0.7 | 0.33 | 0.73 | 0.35 | 0.71 | 0.43 | 0.7 |
| Avg. path efficiency | 0.68 | 0.44 | 0.75 | 0.56 | 0.78 | 0.54 | 0.8 | 0.53 | 0.8 | 0.55 | 0.77 |
| Avg. link betweenness | 0.017 | 0.024 | 0.014 | 0.018 | 0.013 | 0.018 | 0.013 | 0.018 | 0.013 | 0.019 | 0.013 |

## 4 Conclusions

We propose a coevolution model where nodes are chaotic dynamical systems and the network structure changes according to a local rule. In particular, the local rule updates synchronously, at specific points of time, the binary state "on/off" of every possible link. Based on the Cellular Automata framework, we define a local rule that depends on: 1) the binary state of the link; 2) the structural features

of neighboring links; and 3) the dynamical features of neighboring nodes. In this sense we construct the neighborhood for each link according to their position in the coupling matrix, and we consider the von Neumann neighborhood definition. With this model we can observe that, because the interplay between the dynamics of nodes and the structural evolution, the network exhibit two classes of emergent behaviors. On the one hand the structure spontaneously forms various types of structural patterns which are displayed in the coupling matrix. And on the other hand, we observe that the structural features of the network at the first updating time favor the emergence of a stable synchronized behavior on the nodes. Further, we observe that different patterns are former with different radius ($r$) of the neighborhood; additionally, our local rule favors the formation of groups. We believe that our coevolution model provides a scenario for studying the role of coevolution in the emergent behaviors. Other extensions of our model as the insertion of weighted links are currently under study.

## References

1. Newman, M.: Networks: an introduction. Oxford University Press, Inc. (2010)
2. Arenas, A., Daz-Guilera, A., Kurths, J., Moreno, Y., Zhou, C.: Synchronization in complex networks. Physics Reports 469(93), 175–308 (2008)
3. Boccaletti, S., Latora, V., Moreno, Y., Chavez, M., Hwang, D.: Complex networks: Structure and dynamics. Physics Reports 424(4), 175–308 (2006)
4. Mukherjee, A., Choudhury, M., Peruani, F., Ganguly, N., Mitra, B.: Dynamics on and of Complex Networks. Applications to Time-Varying Dynamical Systems, vol. 2. Springer, Heidelberg (2013)
5. Gross, T., Blasius, B.: Adaptive coevolutionary networks: a review. J. R. Soc. Interface 5(20), 259–271 (2010)
6. Sayama, H.: Generative network automata: A generalized framework for modeling dynamical systems with autonomously varying topologies. In: Proceedings of the 2007 IEEE Symposium on Artificial Life, pp. 214–221 (2007)
7. Tomita, K., Kurokawa, H., Murata, S.: Graph-Rewriting Automata as a Natural Extension of Cellular Automata. In: Adaptive Networks: Theory, Models and Applications, ch. 14. Springer, Heidelberg (2009)
8. Smith, D.M.D., Onnela, J.-P., Lee, C.F., Fricker, M., Johnson, N.F.: Network automata and the functional dynamic network framework, arXiv:physics/0701307v3 (physics.soc-ph) (2009)
9. DeLellis, P., Di Bernardo, M., Gorochowski, T.E., Russo, G.: Synchronization and control of complex networks via contraction, adaptation and evolution. Cir. and Sys. Mag. 10(3), 64–82 (2010)
10. Hoekstra, A., Kroc, J., Sloot, P.M.A. (eds.): Simulating Complex Systems by Cellular Automata. Understanding Complex Systems. Springer, Heidelberg (2010)
11. Ilachinski, A.: Cellular Automata: A Discrete Universe. World Scientific, Singapore (2001)

# Chaos Driven PSO – On the Influence of Various CPRNG Implementations – An Initial Study

Michal Pluhacek[1], Roman Senkerik[1], Ivan Zelinka[1], and Donald Davendra[2]

[1] Faculty of Applied Informatics,
Tomas Bata University in Zlin,
T.G. Masaryka 5555, 760 01 Zlin, Czech Republic
{pluhacek,senkerik,zelinka}@fai.utb.cz
[2] Faculty of Electrical Engineering and Computer Science,
VŠB-Technical University of Ostrava,
17. listopadu 15, 708 33 Ostrava-Poruba, Czech Republic
donald.davendra@vsb.cz

**Abstract.** This paper presents deep study of the process of implementation of discrete chaotic maps as chaotic pseudo-random number generators (CPRNGs) for the needs of Particle Swarm Optimization (PSO) algorithm. There are several different ways for the CPRNG creation. This study addresses the main issues (including examples and results comparison) and may serve as a very useful resource for any future researchers.

**Keywords:** Particle swarm optimization, chaos, PSO, Evolutionary algorithm, optimization.

## 1 Introduction

The particle swarm optimization algorithm (PSO) is one of the new and promising swarm intelligence optimization algorithms which are a subset of evolutionary computation techniques (ECTs). The ECTs are a significant class of soft computing optimization methods that is inspired in nature. In past decades various ECTs were used with promising results in many areas of complex optimization [1–8]. Later on, some studies indicated that using chaotic number generators might improve the quality of results, convergence speed or other performance indicators of various ECTs [9 - 16]. Several studies have already dealt with the possibilities of integration of chaotic systems into the PSO algorithm and the performance of such algorithms [11–16]. This paper focuses on the issue of designing chaotic pseudo-random number generator (CPRNG) based on two-dimensional discrete chaotic maps. Several ways of CPRNG design are described and analyzed. Further the different versions of CPRNGs are employed in PSO algorithm and the performance compared on different benchmark functions.

The paper is structured as follows: the second section describes the motivation for this research. In the third section the definition of PSO algorithm is given. Used chaotic maps are described in section four. The process of CPRNG implementation is



A. Sanayei et al. (eds.), *ISCS 2014: Interdisciplinary Symposium on Complex Systems*,
Emergence, Complexity and Computation 14, DOI: 10.1007/978-3-319-10759-2_24

detailed in section five. Used benchmark functions are described in the sixth section and experiment setup is given in the section number seven. Finally the results are presented and discussed in the last two sections.

## 2 Motivation

The interconnection of chaos and ECTs starts to attract increased attention in the past years. In the various researches focused on chaos and ECTs [9-16] the CPRNG based on different two-dimensional discrete chaotic systems is often employed. In the process of CPRNG design there are however some issues that are not usually addressed (typically due to paper length limits etc.). This paper is primarily motivated by experiments with different chaotic systems and their implementation as CPRNGs. It has been found that the way the CPRNG is designed seems to have an impact on the performance of chaos driven ECT (in this case the PSO algorithm). The goal of this study is to investigate this issue, present some ways of CPRNG design and do an in-deep analysis based on experiments with chaos driven PSO algorithm.

## 3 Particle Swarm Optimization

The PSO algorithm is inspired by the natural swarm behavior of animals (such as birds and fish). It was firstly introduced by Eberhart and Kennedy in 1995 [1]. As an alternative to other ECTs, such as Ant Colony Optimization [2], Genetic Algorithms (GA) [4] or Differential Evolution (DE) [5] the PSO became popular method for global optimization. Each particle in the population represents a possible solution of the optimization problem which is defined by the cost function (CF). In each iteration of the algorithm, a new location (combination of CF parameters) of the particle is calculated based on its previous location and velocity vector (velocity vector contains particle velocity for each dimension).

According to the method of selection of the swarm or subswarm for best solution information spreading, the PSO algorithms are noted as global PSO (GPSO) or local PSO (LPSO). Within this research the PSO algorithm with global topology (GPSO) [6] was utilized. The chaotic PRNG is used in the main GPSO formula (1), which determines a new "velocity", thus directly affects the position of each particle in the next iteration.

$$v_{ij}^{t+1} = w \cdot v_{ij}^{t} + c_1 \cdot Rand \cdot (pBest_{ij} - x_{ij}^{t}) + c_2 \cdot Rand \cdot (gBest_j - x_{ij}^{t}) \quad (1)$$

Where:

$v_i^{t+1}$ - New velocity of the *ith* particle in iteration $t$+1.
$w$ – Inertia weight value.
$v_i^{t}$ - Current velocity of the *ith* particle in iteration $t$.
$c_1$, $c_2$ - Priority factors.

$pBest_i$ – Local (personal) best solution found by the *ith* particle.
*gBest* - Best solution found in a population.
$x_{ij}^{t}$ - Current position of the *ith* particle (component *j* of the dimension *D*) in iteration *t*.
*Rand* – Pseudo random number, interval (0, 1). CPRNG is applied only here.

The maximum velocity was limited to 0.2 times the range as it is usual. The new position of each particle is then given by (2), where xit+1 is the new particle position:

$$x_i^{t+1} = x_i^t + v_i^{t+1} \tag{2}$$

Finally the linear decreasing inertia weight [6, 7] is used in the typically referred GPSO design that was used in this study. The dynamic inertia weight is meant to slow the particles over time thus to improve the local search capability in the later phase of the optimization. The inertia weight has two control parameters wstart and wend. A new w for each iteration is given by (3), where t stands for current iteration number and n stands for the total number of iterations. The values used in this study were wstart = 0.9 and wend =0.4.

$$w = w_{start} - \frac{\left(\left(w_{start} - w_{end}\right)\cdot t\right)}{n} \tag{3}$$

## 4 Chaotic Maps

This section contains the description of discrete chaotic maps that were used as the CPRNGs for PSO algorithm in this study. The initial concept of embedding chaotic dynamics into evolutionary algorithms is given in [9].

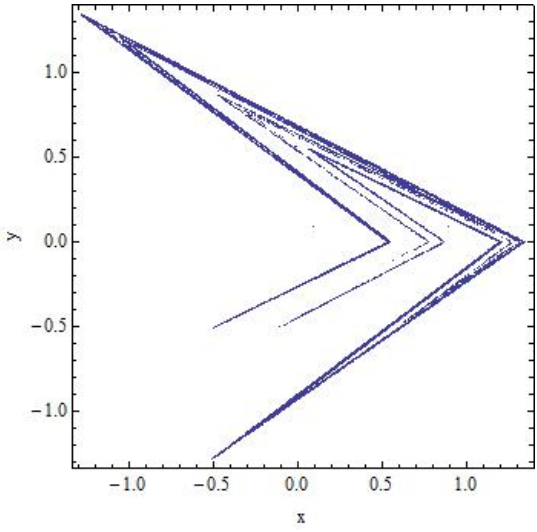


**Fig. 1.** x,y plot of Lozi map

### 4.1 Lozi Map

The Lozi map is a simple discrete two-dimensional chaotic map. The map equations are given in (4). The parameters used in this work are: a = 1.7 and b = 0.5 with respect to [17, 18].

The Lozi map is depicted in Fig. 3.

$$\begin{aligned} X_{n+1} &= 1 - a\left|X_n\right| + bY_n \\ Y_{n+1} &= X_n \end{aligned} \tag{4}$$

### 4.2 Burgers Chaotic Map

The Burgers map (See Fig. 2) is a discretization of a pair of coupled differential equations The map equations are given in (5) with control parameters a = 0.75 and b = 1.75 as suggested in [17].

$$\begin{aligned} X_{n+1} &= aX_n - Y_n^2 \\ Y_{n+1} &= bY_n + X_n Y_n \end{aligned} \tag{5}$$

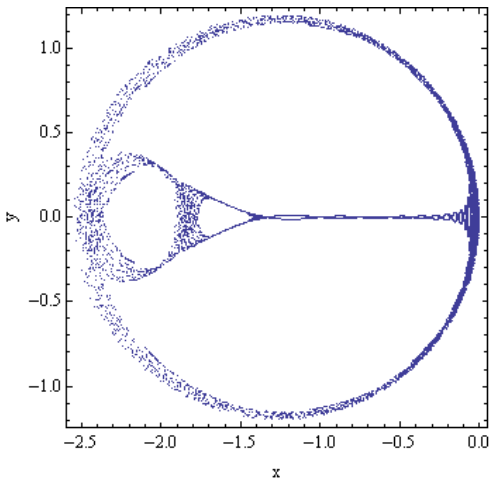


**Fig. 2.** x,y plot of Burgers map

## 5 CPRNG Implementation

For the needs of PSO main formula (1) it is necessary to generate pseudo-random numbers in the interval [0,1] however the majority of chaotic maps does not follow this restriction for the area it covers. It is therefore necessary to transform the output

sequence into the required interval. In the case of two-dimensional discrete chaotic map as output sequence it can be used either the x or y value sequence given by the pair of equations that define the chaotic map (as described in previous section). Fig. 3 gives x value sequence for the first 100 of the Lozi map. Corresponding y value sequence is depicted in Fig. 4. It can be observed that these sequences share certain similarities. However in the case of Burger´s map (Fig. 5 and 6.) the corresponding x and y sequences are significantly more different. Further from this point the PSO versions that use the x value sequence for the CPRNG are noted with "X" and vice versa.

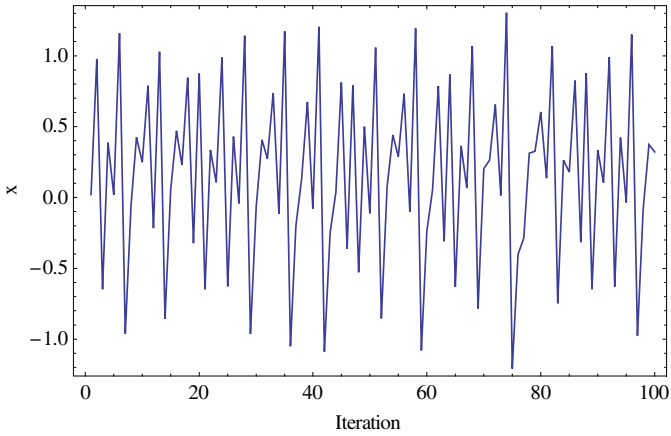


**Fig. 3.** Sample output sequence of the Lozi map (*x* value )

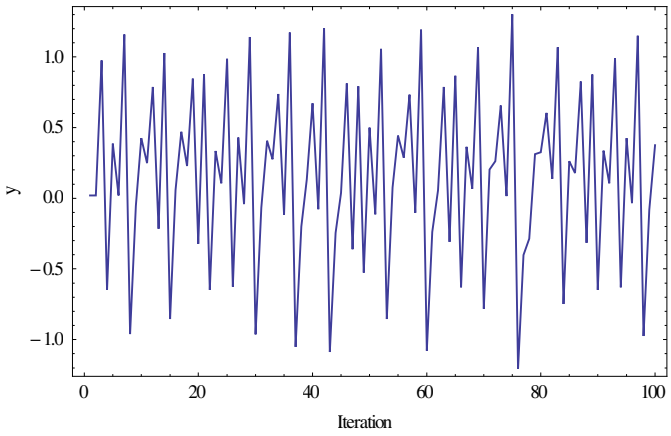


**Fig. 4.** Sample output sequence of the Lozi map (*y* value )

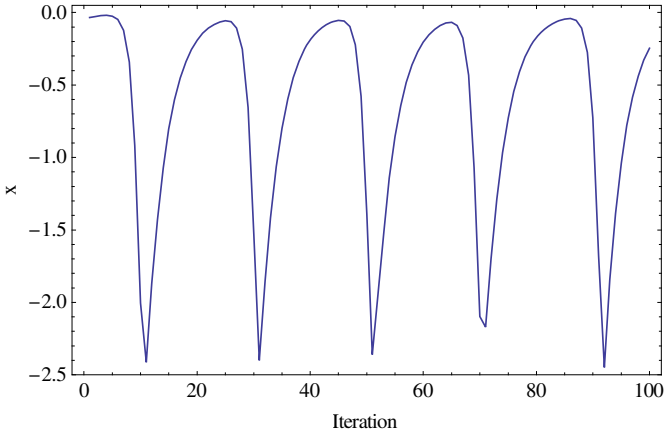


**Fig. 5.** Sample output sequence of the Burger´s map (*x* value )

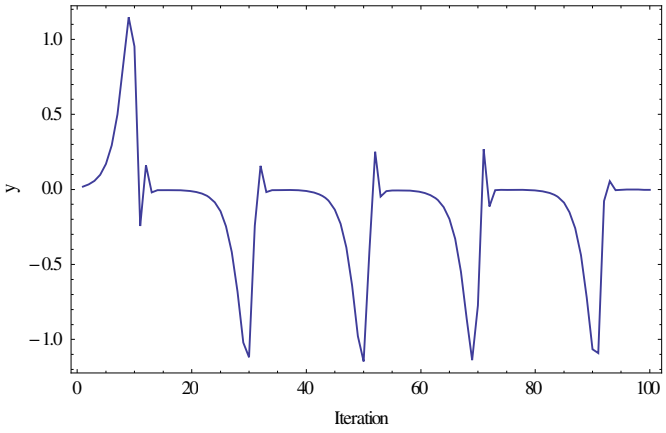


**Fig. 6.** Sample output sequence of the Burger´s map (*y* value )

The performance differences of the "X" and "Y" versions is investigated later in this paper. Furthermore two different approaches for transforming the sequences into the interval [0,1] are utilized in this study. In the first case the absolute value is used to transform negative numbers to positive. All numbers in the sequence are then divided by the maximum value found in the sequence (6). As an example the distribution of CPRNG based on the Lozi map *x* value sequence created this way is given in Fig. 7.

$$X = \left|X^*\right| / Max(X^*) \tag{6}$$

Where:

$X$ – Transformed sequence
$X^*$ – Original sequence
Max(X*) – Maximum number in original sequence

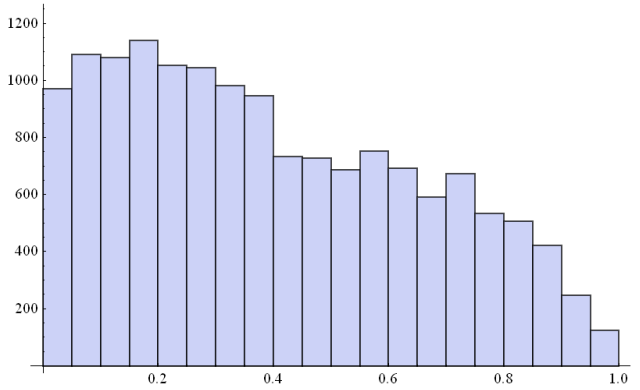


**Fig. 7.** CPRNG based on Lozi map (*x* sequence, absolute value applied) – distribution histogram

Alternatively it is possible to shift the whole sequence to positive numbers and interval [0,1] according to (7). The distribution of CPRNG based on the Lozi map x value sequence created this alternative way is given in Fig. 8. Versions of PSO using this approach are further noted with "s" (as shifted).

$$X = (|Min(X^*)| + X^*)/(|Min(X^*)| + Max(X^*)) \tag{7}$$

Where:

*Min(X*)* – Minimum number in original sequence

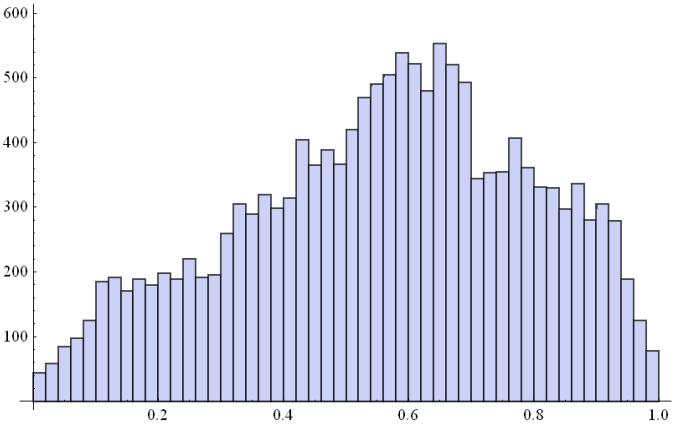


**Fig. 8.** CPRNG based on Lozi map (*x* sequence, shifted) – distribution histogram

# 6 Test Functions

Within this research two well-known and frequently used benchmark functions (given by (8) and (9)) were utilized to demonstrate the difference in performance of various PSO versions. The dimension (D) was set to 30 for all experiments. The global optimum value is 0 for all functions used. The description of used benchmark function follows:

## 6.1 Sphere Function

$$f_1(x) = \sum_{i=1}^{D} x_i^2 \tag{8}$$

Search Range: $[-100,100]^D$
Init. Range: $[-100,50]^D$
Glob. Opt. Pos.: $[0]^D$

## 6.2 Schwefel´s Function

$$f_5(x) = 418.9829 \cdot \mathrm{D} - \sum_{i=1}^{D} -x_i \sin(\sqrt{|x|}) \tag{9}$$

Search Range: $[-500,500]^D$
Init. Range: $[-500,500]^D$
Glob. Opt. Pos.: $[420.96]^D$

# 7 Experiment Setup

The control parameters of PSO algorithm were set following way:
Population size: 40; Iterations: 5000; Runs: 30;

## 7.1 Notation

A several versions of GPSO algorithm were used. The notation follows the pattern described in previous sections. The version is noted according to the chaotic map that was used ("Lozi" or "Burger") + the sequence that was used for CPRNG ("X" or "Y") + "s" if the shifting approach described in section 5 was applied to move the sequence into required interval. Examples:

- GPSO Lozi Y – CPRNG based on the *y* value sequence of Lozi map. Transformed into the interval [0,1] using the absolute value approach.
- GPSO Burger Xs – CPRNG based on the *x* value sequence of Burgers map. Transformed into the interval [0,1] using the shift approach.
- Etc.

As already mentioned in previous sections the CPRNG based on Lozi map or Burger´s map was applied only for the main formula of PSO (1). For other purposes (generating of initial population etc.) default C language built-in pseudorandom number generator was used within all described versions of PSO.

## 8 Results

In this section the results for each test function and version of CPRNG are summarized into a statistical overview (Tables 1 – 4). The best result (Cost function value) and the best mean result are highlighted by bold numbers. Furthermore the mean gBest history for each function and version of CPRNG are depicted in Figs. 9 – 11. The brief results analysis follows in the next section.

**Table 1.** Results - Sphere function – Lozi CPRNGs

| | GPSO Lozi Y | GPSO Lozi X | GPSO Lozi Ys | GPSO Lozi Xs |
|---|---|---|---|---|
| Mean CF Value: | **4.03E-108** | 7.78E-106 | 1.39E-78 | 2.98E-78 |
| Std. Dev.: | 2.18E-107 | 4.26E-105 | 6.78E-78 | 1.39E-77 |
| CF Value Median: | 4.73E-112 | 8.74E-113 | 1.49E-81 | 1.17E-81 |
| Max. CF Value: | 1.20E-106 | 2.33E-104 | 3.72E-77 | 7.57E-77 |
| Min. CF Value: | 2.35E-116 | **3.43E-118** | 1.95E-85 | 7.04E-86 |

**Table 2.** Results – Schwefel´s function – Lozi CPRNGs

| | GPSO Lozi Y | GPSO Lozi X | GPSO Lozi Ys | GPSO Lozi Xs |
|---|---|---|---|---|
| Mean CF Value: | **4.08E+03** | 4.09E+03 | 5.07E+03 | 5.05E+03 |
| Std. Dev.: | 4.46E+02 | 3.26E+02 | 3.93E+02 | 4.77E+02 |
| CF Value Median: | 4.14E+03 | 4.05E+03 | 5.07E+03 | 5.04E+03 |
| Max. CF Value: | 4.78E+03 | 5.07E+03 | 6.02E+03 | 5.98E+03 |
| Min. CF Value: | **3.08E+03** | 3.61E+03 | 4.44E+03 | 4.32E+03 |

**Table 3.** Results - Sphere function – Burger CPRNGs

| | GPSO Burger Y | GPSO Burger X | GPSO Burger Ys | GPSO Burger Xs |
|---|---|---|---|---|
| Mean CF Value: | 1.45E+02 | 3.87E-12 | **2.32E-88** | 2.93E+03 |
| Std. Dev.: | 6.47E+01 | 1.04E-11 | 1.27E-87 | 2.61E+02 |
| CF Value Median: | 1.30E+02 | 1.61E-12 | 2.68E-100 | 3.03E+03 |
| Max. CF Value: | 2.84E+02 | 5.80E-11 | 6.97E-87 | 3.25E+03 |
| Min. CF Value: | 2.96E+01 | 5.25E-14 | **3.11E-111** | 2.29E+03 |

**Table 4.** Results – Schwefel´s function Burger CPRNGs

| | GPSO Burger Y | GPSO Burger X | GPSO Burger Ys | GPSO Burger Xs |
|---|---|---|---|---|
| Mean CF Value: | 3.98E+03 | **2.07E+03** | 4.61E+03 | 8.66E+03 |
| Std. Dev.: | 6.68E+02 | 3.30E+02 | 5.28E+02 | 2.40E+02 |
| CF Value Median: | 3.98E+03 | 2.09E+03 | 4.71E+03 | 8.65E+03 |
| Max. CF Value: | 5.69E+03 | 2.88E+03 | 5.65E+03 | 8.98E+03 |
| Min. CF Value: | 3.07E+03 | **1.54E+03** | 3.57E+03 | 8.01E+03 |

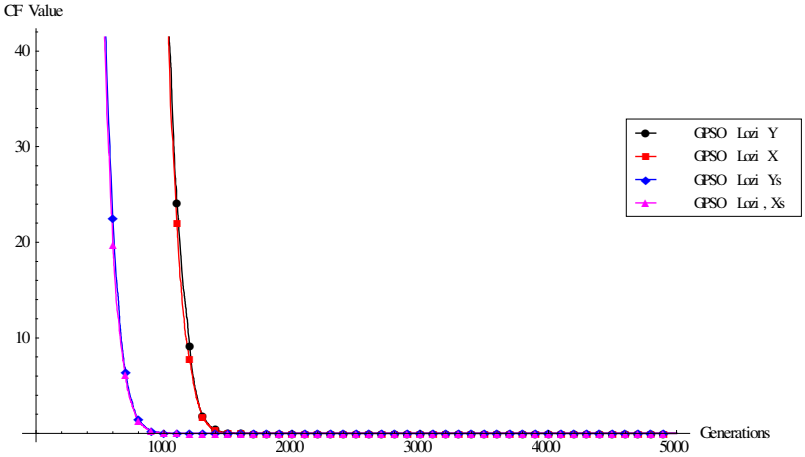


**Fig. 9.** Mean gBest history - sphere function – Lozi CPRNGs

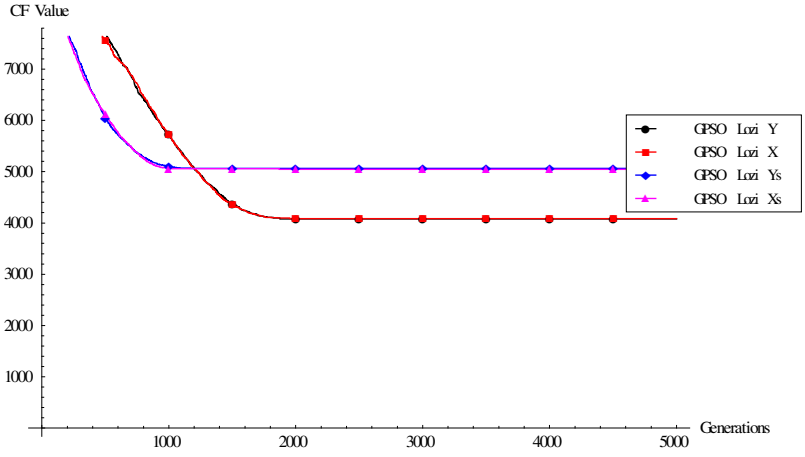


**Fig. 10.** Mean gBest history - Schwefel´s function – Lozi CPRNGs

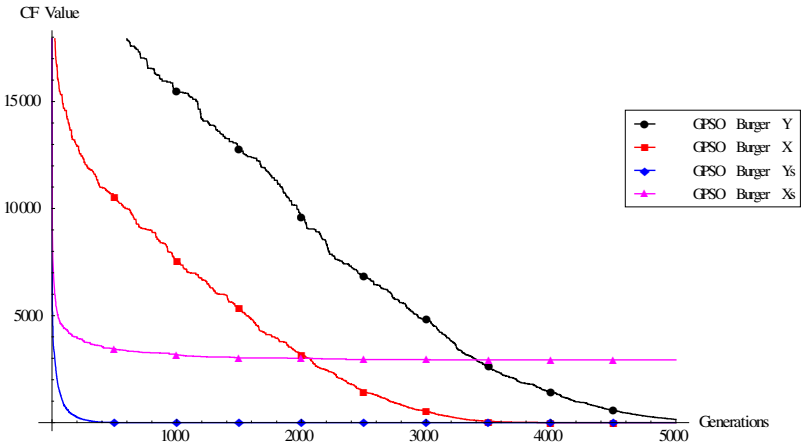


**Fig. 11.** Mean gBest history - sphere function – Burger CPRNGs

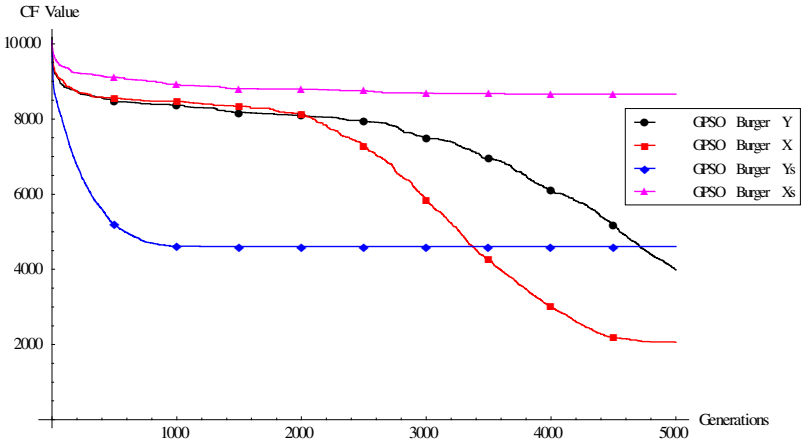


**Fig. 12.** Mean gBest history - Schwefel´s function – Burger CPRNGs

## 9 Brief Analysis of the Results

The results presented in previous section support several claims. Firstly, according to data presented in Tables 1 and 2 and Fig. 9 and 10 the performance of GPSO driven by CPRNG based on Lozi map is not too sensitive to the choice of output sequence (x or y) however it is very sensitive to the way the sequence is transformed to the required [0,1] interval. In the case of used benchmark functions it seems so that it is possible to achieve better mean results when using the "absolute value" approach.

Secondly according to results given in Tables 3 and 4 and the mean gBest history presented in Figs. 11 and 12 its seems that the GPSO driven by CPRNG based on Burger´s map is extremely sensitive to both the output sequence selection and the

method of transformation into the required interval. However different versions of GPSO driven by Burger´s map based CPRNG achieved best mean results on the used benchmark functions.

## 10 Conclusion

In this initial study it was presented the issue of different ways of implementation of discrete two-dimensional chaotic systems as CPRNGs for PSO algorithm. Several different approaches were described and analyzed. According to presented data there are significant differences in performance of PSO algorithm based on the way the CPRNG is designed. Also it seems so that CPRNGs based on different chaotic systems differ significantly in the performance. The goal of this paper was to highlight this issue and in the future serve as a resource for researches in the fast developing area of chaos driven ECTs.

**Acknowledgments.** The following grants are acknowledged for the financial support provided for this research: Grant Agency of the Czech Republic - GACR P103/13/08195S, is partially supported by Grant of SGS No. SP2014/159 and SGS No. SP2014/170 Czech Republic, by the Development of human resources in research and development of latest soft computing methods and their application in practice project, reg. no. CZ.1.07/2.3.00/20.0072 funded by Operational Programme Education for Competitiveness, co-financed by ESF and state budget of the Czech Republic, further was supported by European Regional Development Fund under the project CEBIA-Tech No. CZ.1.05/2.1.00/03.0089 and by Internal Grant Agency of Tomas Bata University under the project No. IGA/FAI/2014/010.

## References

1. Kennedy, J., Eberhart, R.: Particle Swarm Optimization. In: Proceedings of IEEE International Conference on Neural Networks, vol. IV, pp. 1942–1948 (1995)
2. Dorigo, M., Gambardella, L.M., Birattari, M., Martinoli, A., Poli, R., Stützle, T. (eds.): ANTS 2006. LNCS, vol. 4150. Springer, Heidelberg (2006)
3. Eberhart, R., Kennedy, J.: Swarm Intelligence. The Morgan Kaufmann Series in Artificial Intelligence. Morgan Kaufmann (2001)
4. Goldberg, D.E.: Genetic Algorithms in Search Optimization and Machine Learning, p. 41. Addison Wesley (1989) ISBN 0201157675
5. Storn, R., Price, R.: Differential evolution - a simple and efficient heuristic for global optimization over continuous spaces. Journal of Global Optimization 11, 341–359 (1997)
6. Shi, Y.H., Eberhart, R.C.: A modified particle swarm optimizer. In: IEEE International Conference on Evolutionary Computation, Anchorage Alaska, pp. 69–73 (1998)
7. Nickabadi, A., Ebadzadeh, M.M., Safabakhsh, R.: A novel particle swarm optimization algorithm with adaptive inertia weight. Applied Soft Computing 11(4), 3658–3670 (2011) ISSN 1568-4946

8. Zelinka, I.: SOMA - self organizing migrating algorithm. In: Babu, B.V., Onwubolu, G. (eds.) New Optimization Techniques in Engineering, ch. 7, vol. 33. Springer (2004) ISBN: 3-540-20167X
9. Caponetto, R., Fortuna, L., Fazzino, S., Xibilia, M.G.: Chaotic sequences to improve the performance of evolutionary algorithms. IEEE Transactions on Evolutionary Computation 7(3), 289–304 (2003)
10. Davendra, D., Zelinka, I., Senkerik, R.: Chaos driven evolutionary algorithms for the task of PID control. Computers & Mathematics with Applications 60(4), 1088–1104 (2010) ISSN 0898-1221
11. Araujo, E., Coelho, L.: Particle swarm approaches using Lozi map chaotic sequences to fuzzy modelling of an experimental thermal-vacuum system. Applied Soft Computing 8(4), 1354–1364 (2008)
12. Alatas, B., Akin, E., Ozer, B.A.: Chaos embedded particle swarm optimization algorithms. Chaos, Solitons & Fractals 40(4), 1715–1734 (2009) ISSN 0960-0779
13. Pluhacek, M., Senkerik, R., Davendra, D., Kominkova Oplatkova, Z., Zelinka, I.: On the behavior and performance of chaos driven PSO algorithm with inertia weight. Computers and Mathematics with Applications (2013), doi:10.1016/j.camwa.2013.01.016 (Article in press)
14. Pluhacek, M., Budikova, V., Senkerik, R., Oplatkova, Z., Zelinka, I.: On The Performance Of Enhanced PSO Algorithm With Lozi Chaotic Map – An initial Study. In: Proceedings of the 18th International Conference on Soft Computing, MENDEL 2012, pp. 40–45 (2012) ISBN 978-80-214-4540-6
15. Pluhacek, M., Senkerik, R., Zelinka, I., Davendra, I.D.: Chaos PSO algorithm driven alternately by two different chaotic maps - An initial study. In: 2013 IEEE Congress on Evolutionary Computation (CEC), pp. 2444–2449 (2013), doi:10.1109/CEC.2013.6557862, ISBN: 978-1-4799-0451-8
16. Pluhacek, M., Senkerik, R., Zelinka, I., Davendra, D.: New Adaptive Approach for Chaos PSO Algorithm Driven Alternately by Two Different Chaotic Maps – An Initial Study. In: Zelinka, I., Chen, G., Rössler, O.E., Snasel, V., Abraham, A. (eds.) Nostradamus 2013: Prediction, Model. & Analysis. AISC, vol. 210, pp. 77–87. Springer, Heidelberg (2013)
17. Sprott, J.C.: Chaos and Time-Series Analysis. Oxford University Press (2003)
18. Aziz-Alaoui, M.A., Robert, C., Grebogi, C.: Dynamics of a Hénon–Lozi-type map. Chaos, Solitons & Fractals 12(12), 2323–2341 (2001) ISSN 0960-0779

# Evolutionary Based ARIMA Models for Stock Price Forecasting

Tomas Vantuch and Ivan Zelinka

VSB-Technical University of Ostrava, 17. listopadu 15 708 33,
Ostrava-Poruba, Czech Republic
{tomas.vantuch.st,ivan.zelinka}@vsb.cz

**Abstract.** Time series prediction is mostly based on computing future values by the time set past behavior. If the prediction like this is met with a reality, we can say that the time set has a memory, otherwise the new values of time set are not affected by its past values. In the second case we can say, there is no memory in the time set and it is pure randomness. In a faith of "market memory", the stock prices are often studied, analyzed and forecasted by a statistic, an econometric, a computer science... In this article the econometric ARIMA model is taken for previously mentioned purpose and its constructing and estimation is modified by evolution algorithms. The algorithms are genetic algorithm (GA) and particle swarm optimization PSO.

**Keywords:** ARIMA, GA, PSO, AIC, BIC, forecasting.

## 1 Introduction

Nowadays, there is quite often used the econometric ARIMA model [1] proposed by Box and Jenkins for an analysis and a forecast of time series because of its complexity and variability. The main part of the model is the combination of auto-regression (AR) and moving-average (MA) polynomials into one complex polynomial:

$$y_t = \mu + \sum_{i=1}^{p}(\gamma_i y_{t-i}) + \sum_{i=1}^{q}(\theta_i \epsilon_{t-i}) + \epsilon_t \tag{1}$$

This model is based on statistic analysis of a time set. At first, it has to be fulfilled the condition of a stationarity of a time set. A time set is stationary if it does not contain any trends or seasonal behavior and its mean and variance does not change over time. The condition of stationary behavior is crucial for input time set.

The next step in ARIMA modeling is an estimating the model [4–9]. It means to estimate p and q parameters for AR and MA polynomials and the level of differentiation.

An auto-regression is the polynomial that contains variables of the time set moved q-periods back in time and multiplied by AR coefficients $\gamma$. This sum is later increased by model parameter $\mu$ and white noise $\epsilon$.



A. Sanayei et al. (eds.), *ISCS 2014: Interdisciplinary Symposium on Complex Systems*,
Emergence, Complexity and Computation 14, DOI: 10.1007/978-3-319-10759-2_25

$$y_t = \mu + \sum_{i=1}^{p}(\gamma_i y_{t-i}) + \epsilon_t \tag{2}$$

MA polynomial does not contain any variable from a time set and it has nothing to do with familiar known moving-average function. MA contains its own set of MA coefficients multiplied by model residuals and at the end the whole sum is increased by model parameter and white noise.

$$y_t = \mu + \sum_{i=1}^{q}(\theta_i \epsilon_{t-i}) + \epsilon_t \tag{3}$$

The letter "I" in ARIMA model stands for "integrated", which means the level of differentiation of the time set.

The values of p and q parameters for AR and MA part can be obtained from the behavior of auto-correlation (ACF) and partial auto-correlation (PACF) function in the nth level of differentiation [1, 9]. There are alternative methods, that use patterns evaluation by symbols "X" and "O" in a matrix, like SCAN [6], ESACF [7] to determine p and q values.

By all this tasks we can say that the finding of the suitable ARIMA model can be harder and not very solid job and it could be the point of other improvements.

This opportunity is taken in this article. We will try to use an evolution algorithm approach [10] to find the suitable model for the time set. This approach requires to have some clear evaluation function to know if the reproduced model is good enough. The evaluation can be made of AIC [4] and BIC [5] criteria. Both of them are designed like a likelihood penalization criteria

$$[2logL + kp] \tag{4}$$

where $L$ stands for the maximal value of the likelihood function of the model, $p$ is count of model parameters, $k$ has for AIC the value of 2 and for BIC the value is $log(n)$.

The next step it to estimate AR and MA coefficients for our previously obtained model. This coefficients are normally gained from maximum likelihood function [2] that is based on maximization of searched parameters' probability:

$$L(\Theta, x) = f_\Theta(x) = f(x_2|x_1) * f(x_3|x_2) ... * f(x_n|x_{n-1}) \tag{5}$$

This maximum likelihood function can be replaced by other approaches too. For this experiment there is used the particle swarm optimization algorithm [13].

With estimated coefficients we will be able to create forecasting and evaluate it to find out if it is good enough or what can be improved.

## 2 Experiment Design

In this experiment, as it was mentioned before, the main idea was to work with ARIMA model. The first part of the experiment is to create ARIMA(p,d,q)

model by the genetic algorithm [10]. For the GA we will use Java framework ECJ [15], that is known solution for evolutionary based computing methods. The creating of the model by individuals' genotype and its evaluation by AIC and BIC criteria is provided by Matlab econometric toolbox.

This evolved model will have the AR and MA coefficients computed by MLE method, so in the next step we will try to breed the new parameters by PSO algorithm. As an evaluation function for this process will be the quality of the forecasting of the time set evaluated by MSE.

In the end we will compare gained results by forecasting made by classic approach with PSO and we will see whether it is worth.

### 2.1 Data Set

For this experiment historical data of a stock market title as Microsoft(MSFT) were used. This historical data consist of records known as candles, that contains information of some period of time, in this case the period of time was one day. Each candle contains information about the highest price of the period (HIGH), the lowest price of the period (LOW), the first price of the period (OPEN), the last price (CLOSE), the quantity of traded instruments (VOLUME) and of course the time stamp of the period. There are more than ten years of observations but in this experiment, there was not used more than four years of its length, mostly because of longer execution time of all the algorithms. All the historical data were taken from yahoo finance [https://finance.yahoo.com].

## 3 Analysis of Historical Data

As it was said before, at first we analyze our time set for stationarity, autocorrelation and we create the suitable ARIMA model by ACF and PACF approach.

Because we worked with the time set of the stock prices, we can be sure, that this time set will contain up-trends or down-trends, which indicates its non-stationarity. Proceeded Dickey-Fuller test [16] rejected our hypothesis about stationary behavior by resulted value $\gamma* = 0$ as well.

Afterwards, we compute the first differentiation and draw the process of ACF and PACF function. It is expected the "tailing" of the ACF, that will indicate the value of $q$ parameter and "cutting off" of the PACF, that will indicate the value of $p$ parameter.

The chart of ACF shows, that there is no confirmed correlation between time set variables and it indicates stationary behavior of the time set. We check it by new Dickey-Fuller test and the result $\gamma* = 1$ confirms the hypothesis that the differentiated time set is no more non-stationary.

These charts' progresses show some possible combinations of the future ARIMA models. The $p$ and $q$ values will be lower by this method, because there was no present of correlations between variables.

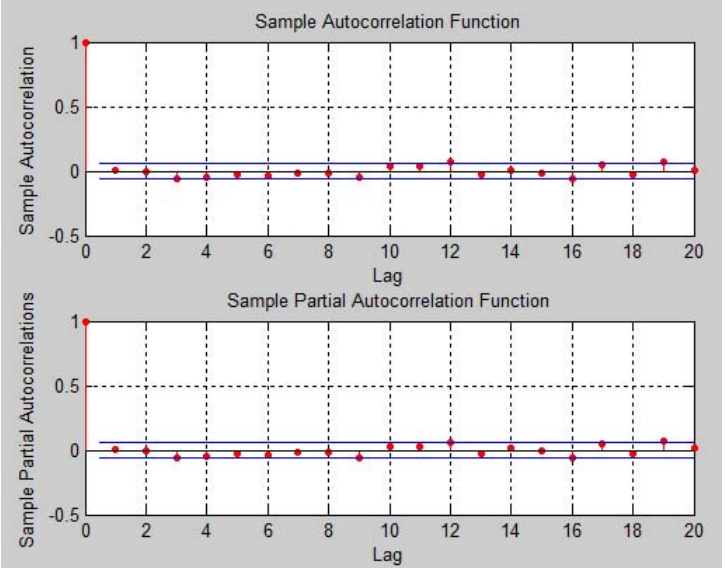


**Fig. 1.** Progress of ACF and PACF function after first differentiation

## 4 Genetic Algorithm Approach for Model Building

The suitable ARIMA model for later testing is evolved by the genetic algorithm. The Genetic algorithm (GA) belongs to evolution algorithms [10]. This set of algorithms works like an imitation of the evolution theory described by Darwin. The GA purpose is to evolve the best combination of variables from the scanning set.

As a first step of the GA there is a population of random individuals. Each of the individuals is represented by the binary vector with the length of 12. The transfer from genotype to phenotype is made by the splitting of whole vector into three parts by four bits and each part belongs to some ARIMA variable like ARIMA(p = 1011,d = 0010,q = 1100).

There is a fitness function for an evaluation of individuals. By the theory of evolution, the fitness function simulates the natural selection. It has a purpose that better individuals according to the fitness will live longer and create the new generation by its crossover. The one-point crossover [12] was used for crossbreeding in this experiment.

The breeded individuals are effected by an added mutation. It means that in the random time, there can be changed one bit of an individual genotype. This process brings to this algorithm some added randomness.

The fitness function of this GA covers the requirement of the minimal value of AIC and BIC and some added advantage for individuals with greater values of $p$ and $q$ parameters. This advantage is added because the longer ARIMA polynomial we will have as result, the more we can optimize by the PSO.

$$fitness = (10^5/AIC + BIC) + p + q \tag{6}$$

The GA runs in this case by this steps:

1. Initialization - creating the first generation from one prototype individual
2. Repeat in limited count of cycles
   (a) Evaluate individuals:
      i. Create the ARIMA model by the binary vector
      ii. Estimate parameters by the default MLE function
      iii. Return AIC and BIC by the minimal likelihood function value
   (b) Proceed crossover on the selected individuals to create new generation
   (c) Add random mutation
3. End of loop
4. Return the best individual

The GA returned in this experiment the ARIMA model with parameters $p = 12, d = 2$ and $q = 8$. This result was compared to the previously chosen models.

**Table 1.** ARIMA models evaluation

| | BIC | AIC |
|---|---|---|
| **ARIMA(12,2,8)** | **485.6266** | **400.4396** |
| ARIMA(1,1,0) | 415.0880 | 403.9767 |
| ARIMA(0,1,1) | 415.0647 | 403.9534 |
| ARIMA(2,1,1) | 423.6821 | 405.1632 |
| ARIMA(1,1,2) | 428.7655 | 406.5429 |
| ARIMA(2,1,3) | 434.0470 | 408.1205 |

The model from the GA has softly greater BIC value but because of lower AIC and much greater count of coefficients, is was chosen as the model for the later PSO optimization and prediction.

## 5 PSO Approach for Parameters Estimation

The evolutionary algorithm used for the breeding of the model coefficients is the particle swarm optimization [13].

The PSO is known, very powerful algorithm inspired by swarm intelligence. Each individual is described by its position, velocity and memory of the latest best position. This algorithm is not divided into generations, because individuals are not dying and creating again, they are just moving during iterations in N-dimensional space. Their moves are affected by its previous best position or the best position in its neighborhood [14]. The quality of the position is evaluated by the objective function, and during every iteration, all the current positions of all individuals are confronted with its best positions.

Obviously the count of dimensions of the searched space influences the count of individuals, which are adjusted. In this case we have 22 dimensional space, We need to breed the AR coefficients, which are the vector of size 12. Than we need to breed MA coefficients, which are the another vector of size 8 and two added variables - one for model constant $\mu$ and another for variance.

In the case of PSO, it was used the item of neighborhood [14] which means that individual is not affected by the best position of all individuals, but only by the best position of smaller amount of closer individuals, its neighbors. The neighborhood is not defined by the distance between individuals, but randomly. The present of the neighborhood brings to this system the opportunity find the best global maximum from more observed local maximums.

The objective function in our case is to decrease the value of MSE of forecasted values to minimum.

The algorithm for parameters breeding:

1. Initialization - place all particles in n-dimensional hyper space and adjust to them the velocity and the neighborhood
2. Repeat in limited count of cycles
   (a) Evaluate the position of individual:
      i. Create the ARIMA model from obtained parameters
      ii. Create the forecasting for next n values
      iii. Compare the forecasting values to real values and compute MSE
   (b) Actualize particles position
   (c) Actualize the previous best position
3. End of the loop
4. Return the particle with the best position

Concretely, each particles' evaluation consists of the creating of the ARIMA model and splitting time set. Time set has to be split into two parts. At first there is the input time set for ARIMA model and the second part will be compared to this ARIMA model prediction. The predicted values are compared to the real values (second part of the time set) and the best fit is saved as the best position.

The best position will do the forecast of next $n$ values and this will be compared to forecast of the same ARIMA model but with coefficients made by the MLE. Arima model has to be estimated and it was provided in Matlab. The same subset from time set was used in case of "estimate" Matlab command and also in the PSO approach.

## 6 Conclusions

This article covers the simple idea of working with ARIMA models by the approach of evolution algorithms. In the section of modeling, there was described very simple kind of obtaining quite suitable ARIMA model without knowledge of stationarity, ACF or PACF. The resulted model had sufficient low values of likelihood penalization criteria like AIC and BIC.

In the second part, there was a task to estimate AR and MA coefficients in "training part" of time set by the PSO algorithm and the best set of coefficients (PSO particle) was used to create prediction compared to classic ARIMA prediction.

There were created two tests for this conclusion. Their difference is the size of time set, adjusted for "training phase". The first has "training phase" of size of ten and the second has this size increased to twenty. The count of particles and iterations was in both test adjusted to same values (particles = 100, iterations = 40).

There are some charts to provide our results.

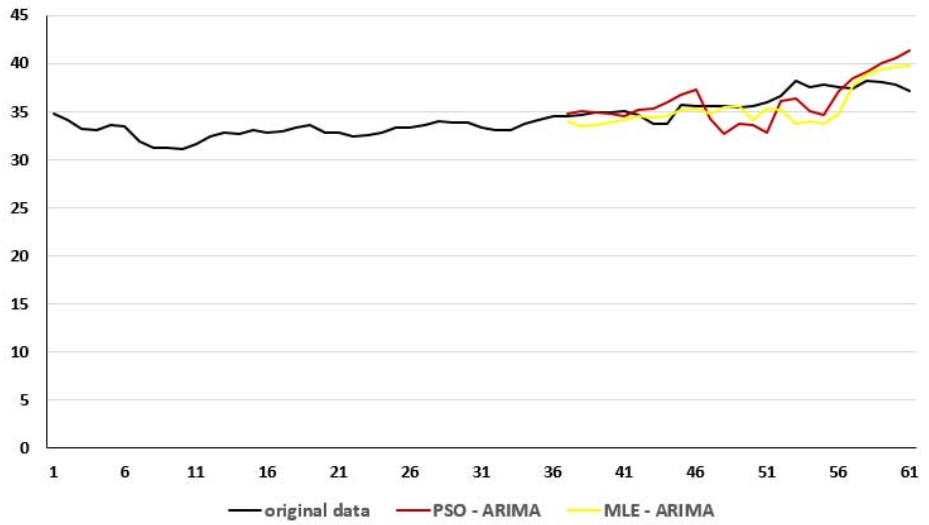


**Fig. 2.** Chart of prediction when size of the "learning phase" was 10

This chart describes the value of MSE between forecasting and real values of time set.

As we can see, these tests do not prove that the estimation of the coefficient by PSO has significantly improved the ARIMA results, but we can say that this combination is at least comparable to standard ARIMA computing.

There are some areas for improvement of this approach. One of the weaknesses of these tests was very low number of PSO iterations. PSO can obtain better results in parallel computing, where it can provide more iterations in a shorter time.

The other improvement can be gained by adjusting bigger time set for learning phase and to work with bigger values of p and q of ARIMA model. Both of these tasks require more computing resources.

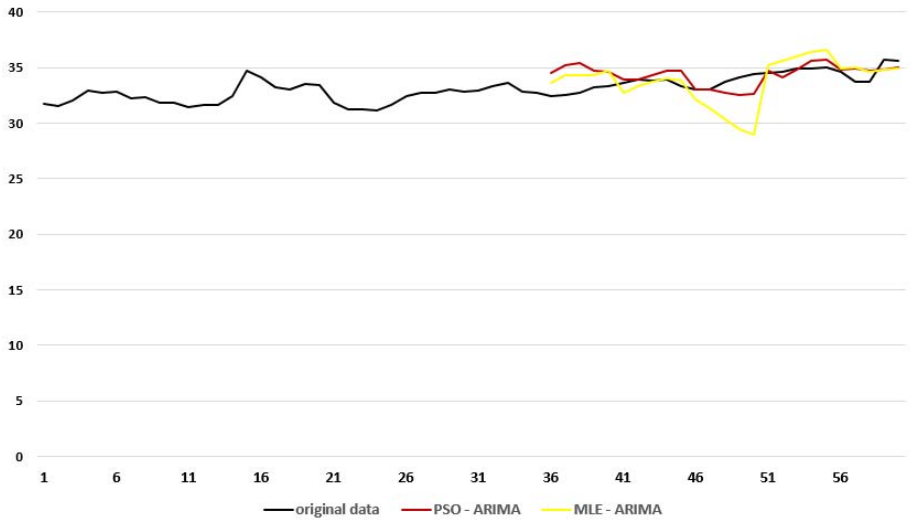


**Fig. 3.** Chart of prediction when size of the "learning phase" was 20

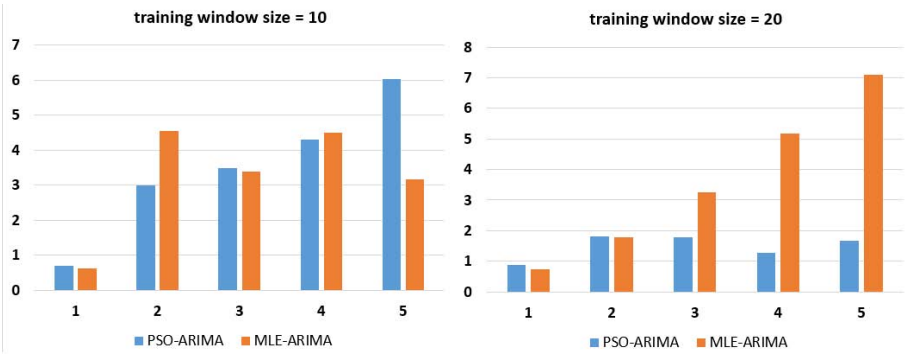


**Fig. 4.** Chart of the MSE on five predicted values during both tests

Finally, there are many other evolutionary algorithms like symbolic regression, differential evolution, neural networks to try to combine them with ARIMA.

**Acknowledgment.** The following grants are acknowledged for the financial support provided for this research: Grant Agency of the Czech Republic - GACR P103/13/08195S, is partially supported by Grant of SGS No. SP2014/159, VB - Technical University of Ostrava, Czech Republic, by the Development of human resources in research and development of latest soft computing methods and their application in practice project, reg. no. CZ.1.07/2.3.00/20.0072 funded by Operational Programme Education for Competitiveness.

## References


1. Box, G.E.P., Jenkins, G.M.: Time Series Analysis: Forecasting and Control. Holden-Day, San Francisco (1976)
2. Ljung, G.M., Box, G.E.P.: The likelihood function of stationary autoregressive-moving average models. Biometrika 66(2), 265–270 (1979)
3. Morf, M., Sidhu, G.S., Kailath, T.: Some new algorithms for recursive estimation on constant linear discrete time systems. IEEE Transactions on Automatic Control 19(4), 315–323 (1974)
4. Akaike, H.: A new look at the statistical model identification. IEEE Transactions on Automatic Control 19(6), 716–723 (1974)
5. Weakliem, D.L.: A Critique of the Bayesian Information Criterion for Model Selection. Sociological Methods and Research 27(3), 359–397 (1999)
6. Tasy, R.S., Tiao, G.C.: Use of canonical analysis in time series model identification. Biometrika 72(2), 299–315 (1985)
7. Tasy, R.S., Tiao, G.C.: Consistent estimates of autoregressive parameters and extended sample autocorrelation function for stationary and nonstationary ARMA model. Journal of the American Statistical Association 79(1), 84–96 (1984)
8. Hannan, E.J., Rissanen, J.: Recursive estimation of mixed autogressive-moving average order. Biometrika 69(1), 81–94 (1982)
9. Hannan, E.J., Quinn, B.G.: The determination of the order of an autoregression. Journal of the Royal Statistical Society B 41(2), 190–195 (1979)
10. Koza, J.R.: Genetic Programming: On the Programming of Computers by Means of Natural Selection. MIT Press, Cambridge (1992)
11. Kinnear Jr., K.E. (ed.): Advances in Genetic Programming. MIT Press, Cambridge (1994)
12. Poli, R., Langdon, W.B.: Genetic Programming with One-Point Crossover
13. Kennedy, J., Eberhart, R.C.: Particle swarm optimization. In: Proc. IEEE Int. Conf. Neural Networks, Perth, Australia, pp. 1942–1948 (November 1995)
14. Kennedy, J.: The particle swarm: Social adaptation of knowledge. In: Proc. 1997 Int. Conf. Evolutionary Computation, Indianapolis, IN, pp. 303–308 (April 1997)
15. White, D.R.: Software review: the ECJ toolkit (March 2012)
16. Dickey, D.G.: Dickey-Fuller Tests. In: International Encyclopedia of Statistical Science, pp. 385–388 (2011)

# On Some False Chaos Indicators When Analyzing Sampled Data

Petra Augustová, Zdeněk Beran, and Sergej Čelikovský

Institute of Information Theory and Automation, v.v.i.,
Academy of Sciences of the Czech Republic, Pod vodárenskou věží 4, P.O. Box 18
182 08 Prague 8, Czech Republic
{augustova,beran,celikovs}@utia.cas.cz

**Abstract.** The main aim of this paper is to demonstrate a possible risk of erroneous conclusions made throughout the process of the sampled data analysis. In particular, it will be shown that the false chaotic behavior of the sampled data may be incorrectly derived from the topological similarity with the already well known chaotic systems like that of Lorenz or from the positivity of the largest Lyapunov exponent. The possible faulty conclusions will be demonstrated using some examples that were recently published in various literature sources.

## 1 Introduction

Analysis and control of complex technological systems as well as of systems arising in physics, natural environment, human society and other important fields has become so complicated that the typical complex system has to be considered as a "black box" and the necessary information concerning it is revealed through a set of data that are conveniently sampled. The interpretation of the data sampled in such a manner thereby appears to be an important task. The importance of the appropriate rigorous interpretation is further strengthened when the nature of the sampled data is chaotic. The main aim of this paper can be briefly summarized as follows. Suppose, in general, that a set of sequences of discretized measurements is given, then the following question naturally arises: Is there an approach to reveal its chaotic behavior once it exists? It is very well known that a proof of the chaotic behavior is a quite peculiar task. In fact, the fundamental question is: What is actually chaos or chaotic behavior of a system represented by a sampled data? The question has not been convincingly answered till now, in particular, due to the large number of existing various chaos definitions, see Preliminaries later on. The definitions differ accordingly to the nature of the systems, e.g., discrete vs. continuous, one-dimensional vs. multidimensional, linear vs. nonlinear, etc. The full exact proof of the chaotic behavior of the one of the first observed chaotically behaving system - the Lorenz system [1] - has been provided actually only quite recently [17],[18],[19]. In other words, the exact proof of the chaotic behavior is a challenge, while quite frequent approach is that if the graphical representation of an analyzed system is topologically similar to



A. Sanayei et al. (eds.), *ISCS 2014: Interdisciplinary Symposium on Complex Systems*,
Emergence, Complexity and Computation 14, DOI: 10.1007/978-3-319-10759-2_26

some well known chaotic attractor, then such a system is considered as chaotic, too. The famous double scroll being the attractor of Lorenz system is quite often addressed in such a way. Another erroneous but generally very often used argument to claim a given system to be chaotic is the positivity of its largest Lyapunov exponent.

The rest of the paper is organized as follows. Some preliminaries are given in the following section. Using convenient examples, Sections 3 and 4 will demonstrate that the above mentioned arguments for the chaos existence may be misleading when interpreting the sampled data. The final section draws some conclusions.

## 2 Preliminaries

First, let us introduce some definitions and connections between them and let us note some wrong interpretations of the chaos widely present in the literature. At the very beginning, one has to distinguish between the chaotic behavior and the stochastic behavior of the system. There are many papers where the authors deal with this problem, see, e.g., [21],[22],[23]. To this end, it is important to underline that the current paper will be devoted to the deterministic chaos only. Considering the linear systems versus non-linear systems, it is very well known that in the case of finite dimension of the phase space the following statement is true. In the case of linear systems and one-/two-dimensional autonomous non-linear systems the chaotic behavior of these systems can not occur due to the Hartman-Grobman theorem, as well as due to the Poincare-Bendixson theorem. Different situation comes up when the linear system is infinite-dimensional. Then, see, e.g., [2], such a system can be chaotic in the Wiggins or Devaney sense, see below. Moreover, it is well known that one-dimensional discrete systems, unlike continuous one, can embody chaotic behavior, see e.g. [6].

In order to present some of the chaos definitions, let us introduce some basic "building stones" first.

**Definition 1.** *A **dynamical system** (se, e.g. [10]), is a tuple $(T, M, \Phi)$ where $T$ is a monoid (a semigroup with a neutral element), written additively, $M$ is a set and $\Phi$ is a function*

$$\Phi : \ U \subset T \times M \to M$$

*with*

$$I(x) = \{t \in T | (t, x) \in U\}$$

$$\Phi(0, x) = x$$

$$\Phi(t_2, \Phi(t_1, x)) = \Phi(t_1 + t_2, x) \quad for \quad t_1, t_2, t_1 + t_2 \in I(x) \ .$$

*The set $M$ is a manifold locally diffeomorphic to a Banach space. If $T$ is an open interval in the real numbers $\mathbf{R}$ the tuple $(T, M, \Phi)$ is a **continuous time dynamical system** of a **flow**. If $T$ are the integers then tuple $(T, M, \Phi)$ is a **discrete-time dynamical system** or a **map** or a **cascade**.*

**Definition 2.** *Let $(M, d)$ be a metric space without isolating points. Then the dynamical system $(T, M, \Phi)$ where $\Phi : U \subset T \times M \to M$, has* ***sensitive dependence on initial conditions****, see, e.g. [6], if there exists a number $\delta > 0$ such that for all $x \in M$ and $\epsilon > 0$ exists some $y \in M$ such that $d(x, y) < \epsilon$ and such that for some $n \geq 0$ it holds $d(\Phi^n x, \Phi^n y) > \delta$ in the case of maps or if there exists a $T > 0$ such that $d(\Phi(t, x), \Phi(t, y)) > \delta \ \ \forall t \geq T$ in the case of flows.*

**Definition 3.** *A dynamical system $(T, M, \Phi)$ where $\Phi : U \subset T \times M \to M$, is* ***topologically transitive****,see, e.g. [6], if for every pair $V, W$ of nonempty open subsets of $M$ there exists some $n \geq 0$ such that $\Phi^n(V) \cap W \neq \emptyset$ in the case of maps or there exists a $T > 0$ such that $\Phi(t, V) \cap W \neq \emptyset \ \ \forall t \geq T$ in the case of flows.*

**Definition 4.** *Let $(X, \mathcal{B}, \mu)$ be a probability space and let a collection of measurable subsets $\zeta = \{C_\alpha \in \mathcal{B} \mid \alpha \in I\}$, where $I$ is a finite or countable set of indices, be a measurable partition. Then the* ***Kolmogorov entropy****, see, e.g. [11], of a measurable partition $\zeta$ is given by*

$$h(\zeta) = \sum_{\mu(C_\alpha)|_{\alpha \in I} \ > 0} \mu(C_\alpha \log(\mu(C_\alpha)) \ \geq \ 0.$$

For a diffeomorphism $F_t : X \to X$, $t \geq 0$, of a compact set $X \subset \mathbf{R}^n$, we assume that there exists an ergodic invariant measure with respect to $F_t$. Let $DF_t(x)$ denote the derivative of $F_t$ at $x$, which is represented by the Jacobian matrix of $F_t$. Then the multiplicative ergodic theorem of Oseledec, see [4], guarantees that at almost every $x \in X$ there exist a decomposition of $\mathbf{R}^n$ into $\mathbf{R}^n = \bigoplus_{i=1}^{r} E_i(x)$ and constants $\lambda_1 < \cdots < \lambda_r$ such that the limits

$$\lambda_i = \lim_{t \to \infty} \frac{1}{t} \log_{10} \parallel DF_t(x) v_i \parallel$$

exist for some nonzero vector $v_i \in E_i(x), \ 1 \leq i \leq r$. Note that $E_i(x)$ is the subspace of $\mathbf{R}^n$ and the symbol $\bigoplus$ denotes the direct sum. The constants $\lambda_i, \ 1 \leq i \leq r$, which depend neither on $v_i$ nor on $x$, are **Lyapunov exponents**. The number $\max_{1 \leq i \leq r} \lambda_i$ is the **largest Lyapunov exponent**.

As already noted, various definitions of chaos are possible, some of them are as follows.

**Definition 5 (Smale).** *The dynamical system is chaotic in the* ***Smale sense****, [3], if its part is topologically conjugated with the Smale horseshoe.*

*Remark 1.* The definition of the Smale horseshoe has a constructive nature and it was first time published in [5].

**Definition 6 (Devaney).** *The dynamical system is chaotic in the* ***Devaney sense****, [6], if it*

1. *has sensitive dependence on initial conditions*
2. *is topologically transitive*

*3. its set of periodic points is dense.*

*Remark 2.* It can be shown that the sensitive dependence on initial conditions can be avoided.

**Definition 7 (Wiggins).** *The dynamical system is chaotic in the* ***Wiggins sense****, [7], if*

1. *has sensitive dependence on initial conditions*
2. *it is topologically transitive.*

**Definition 8 (Gulick).** *The dynamical system is chaotic in the* ***Lyapunov sense****, [8], if it it satisfies at least one of the following conditions*

1. *it has a positive Lyapunov exponent at each point in its domain that is not eventually periodic*
2. *it has sensitive dependence on initial conditions.*

**Definition 9 (Kolmogorov).** *The dynamical system is chaotic in the* ***Kolmogorov sense****, [9], if it has positive Kolmogorov entropy.*

One can often find other chaos definitions in the literature quite often reflecting the wishes and/or needs of the respective authors.

Looking at the definitions above the reader can see that the exact proof of the chaotic behavior of the system that is represented by the sets of sampled data is generally a very tough task. Consequently, people try to use graphical or computational methods instead of the analytical/topological tools to reveal the chaotic behavior. The very well known graphical output is the Lorenz attractor that graphically evokes the double scroll. From time to time that evocation leads some authors to the conclusion that every system that embodies such a pattern has to be chaotic. It will be shown in Section 3 that such conclusion can be wrong. The same situation can occur when the sampled data are concentrated into a small volume where it behaves "strange" - the data is cumulated inside a small phase space where they behave irregularly on the first sight as it will be seen in Example 3 of Section 3.

Applying the Definition 8 to reveal the chaos by analyzing the sampled data seems to make the task much easier. Basically, that definition states that the system is chaotic if the largest Lyapunov exponent is positive. As it will be shown in Section 4, such a statement may be generally misleading when analyzing a priori given sampled data. Nevertheless, it is still frequently mechanically used as an indicator of the chaos - one can encounter usage of such an indicator even in the textbooks like [8] (page 86, Definition 2.3.), repeated for convenience as Definition 8 above. Some other sources where the positivity of the Lyapunov exponent is considered as the only crucial criterion for the chaos existence are as follows:

"Any system containing at least one positive Lyapunov exponent is defined to be chaotic", see [12].

"A positive largest Lyapunov exponent indicates the existence of chaos", see [13].

"A system is chaotic if it has at least one positive Lyapunov exponent", see [14].

"If the system has at least one positive Lyapunov exponent, it indicates the chaos. If the largest Lyapunov exponent is negative then the orbits converge in time and system is insensitive to initial conditions. If it is positive, then the distance between adjacent orbits grows exponentially and system exhibits sensitive dependence on initial conditions, so it is chaotic we say", see [15].

"By definition, any system containing a positive Lyapunov exponent is chaotic", see [16].

Nevertheless, one should note that correct computation of the largest Lyapunov exponent is almost impossible for a priori given data time series produced by some unknown system and sampled at given sampling rate that can not be arbitrarily chosen. Therefore the above statements are often practically misleading. Some examples and analysis are given in the rest of the paper.

## 3 Geometrical Similarity with Lorenz Attractor

First of all, often the famous Lorenz attractor is chosen as an etalon for the chaos indication. Recall that the evolution of the Lyapunov dynamical system is described by a set of the three bi-linear differential equations of the form

$$\begin{aligned} \dot{x} &= \sigma(y - x) \\ \dot{y} &= \rho x - y - xz \\ \dot{z} &= xy - \beta z \end{aligned} \tag{1}$$

where $\sigma = 10,\ \rho = 28,\ \beta = 8/3$. One of the 2D projections of its trajectories in the 3D phase space is shown in Figure 1. The following example shows that some data time series produced in a quite simple way may appear during the analysis as the chaotic one due to geometric resemblance of the Lorenz attractor.

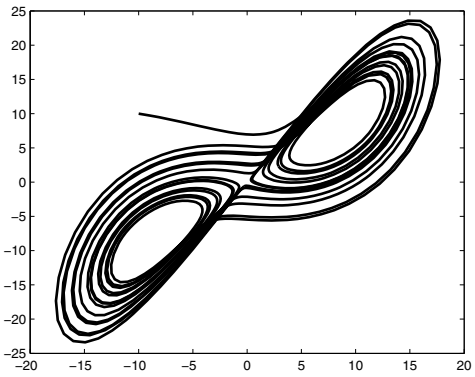


**Fig. 1.** Lorenz attractor

*Example 1.* Consider the following 2D linear dynamical system:

$$\ddot{y} + 2\beta\dot{y} + (\omega^2 + \beta^2)y = 0$$

where $y(t)$ is the scalar state, $\beta = \ln(2)$ is the decay rate, and $\omega = 2\pi$ is the frequency of the damped oscillations. Let $y(t)$ be a solution of the above equation on interval $[0, T]$, $T = 100$ with starting point $y(0) = 1$, $\dot{y}(0) = 10$ solved using the Runge-Kutta ode45 Matlab software. As the solution, a vector $y(i)$ of the size $N = 1333$ has been obtained. A transformation of the solution $y(i)$ gets the following new vector $x(i)$:

$$x(i), \quad i = 1, \cdots, 2N,$$

where

$$x(i) = y(N + 1 - i), \quad i = 1, \cdots, N, \qquad x(i) = 0.5 - y(i), \quad i = N + 1, \cdots, 2N$$

and the sampled data are represented by the above vector $x(i)$, $i = 1, \cdots, 2N$. It is worth to mention that the sampling is irregular due to the varying integration step of the integration procedure represented by the Runge-Kutta integration method as one can see on the figure 3 using hexagonals.

Very often, a high dimensional physical system is only observable through a single scalar variable. The method of time delay embedding, see, e.g. [20], is widely applied to estimate the evolution of the underlying vector field. From a scalar time series $\{x_t\}_{t=1}^{N}$ of $N$ observations one reconstructs a vector time series with evolution topologically equivalent to the original system via the transformation $x_t \to (x_t, x_{t-\tau}, x_{t-2\tau}, \cdots, x_{t-(d_e-1)\tau})$. The quantity $\tau$ is called the ***lag*** or ***time-delay*** and the quantity $d_e$ is called the ***embedding dimension***. Then, the Takens Time-Delay Embedding Theorem, see [20], is used to embed the scalar time series into higher dimensional physical space. Thenceforth one can imagine that the sampled data are represented by the vector $x$ that was acquired as a measurement provided on some "black-box". It is a standard praxis to visualize an one dimensional time series accordingly to the following picture when analyze the time series where the "time"-shift $M$ is the lag. The assessment of the lag value is a serious task as, e.g., the evaluation of the largest Lyapunov exponent or the assessment of the dimension of the trajectory space is heavily dependent

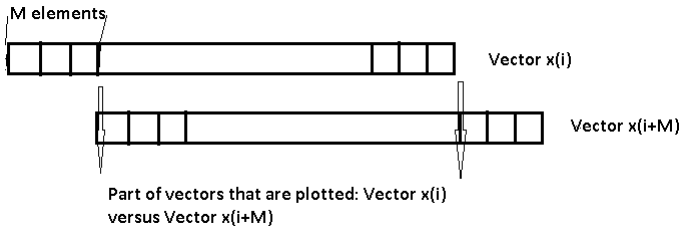


**Fig. 2.** Data visualization using a lag M

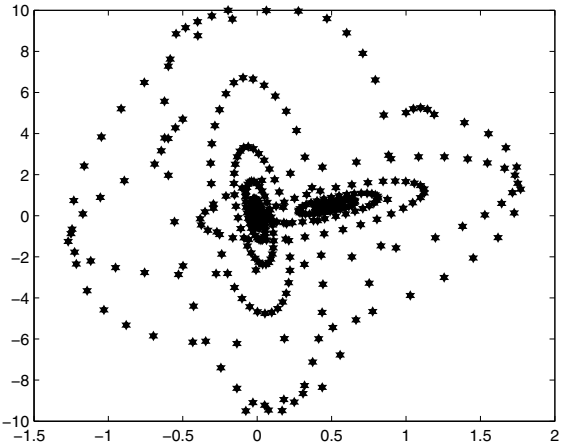


**Fig. 3.** Example 1

on it. The value of $M = 52$ has been chosen. Using the time delay-embedding as a result. Figure 3 has been obtained.

One can see now the similarity of the grafical interpretation of these data to the Lorenz attractor despite this data were created in a rather simple way that can not produce chaotic phenomena.

*Example 2.* In [24] a construction of a new signal comes out from the following function:

$$\psi(t) = \begin{cases} -\frac{1}{2^{-t}+\exp^{10t}} \cos(2\pi t) + 5\exp^{-10t^2} & t < 0 \\ -\frac{1}{2^{-t}+\exp^{10t}} + 5\exp^{-10t^2} & t \geq 0 \end{cases}$$

After some manipulations one gets the following figure, Fig. 4. One can see the similarity with the Lorenz signal Fig. 1 also in this case, though the original data source is apparently no a chaotic one.

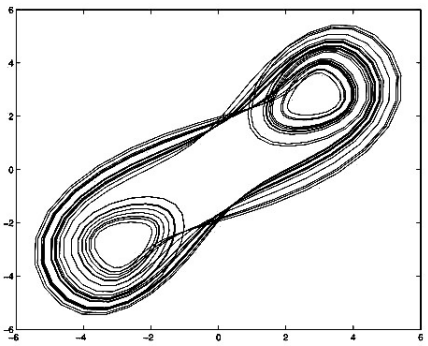


**Fig. 4.** Example 2

The third example shows an irregular behavior of the system although the signal is fully regular.

*Example 3.* In [25] a pulsations of the cepheid models is analyzed. As a reconstructed signal the following one has been used:

$$\begin{aligned} R(t) &= a_1 \cos(\omega_1 t) + a_2 \cos(\omega_2 t) + a_3 \cos(\omega_3 t) \\ &\quad + \frac{1}{2} a_1 a_3 [\cos(\omega_1 + \omega_3)t + \cos(\omega_1 - \omega_3 t)] \\ &\quad + \frac{1}{10} a_2 a_3 [cos(\omega_2 + \omega_3)t + \cos(\omega_2 - \omega_3 t)] \\ &\quad + \frac{1}{10} a_1 a_2 [cos(\omega_1 + \omega_2)t + \cos(\omega_1 - \omega_2 t)] \\ &\quad + \frac{1}{10} a_1^2 \cos(2\omega_1 t) + \frac{1}{10} a_2^2 \cos(2\omega_2 t) \\ V(t) &= \frac{dR(t)}{dt} \end{aligned} \tag{2}$$

where $a_1 = 1,\ a_2 = 0.6,\ a_3 = 0.2,\ \nu_1 = 0.1,\ \nu_2 = 0.048,\ \nu_3 = 0.0252,\ \omega_i = 2\pi\nu_i$. When plotting $R(t)$ versus $V(t)$ one gets the following picture.

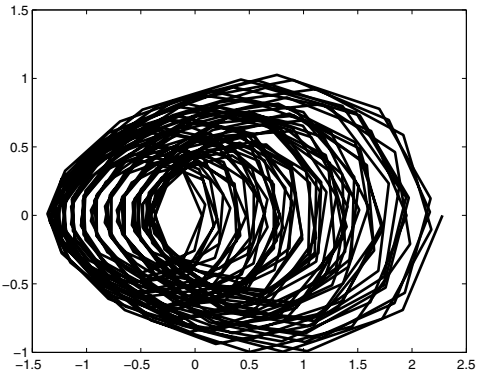


**Fig. 5.** Example 3

The signal is concentrated into a rather small volume and one can see a irregular signal behavior on the first sight though the signal is multi-periodic only.

## 4 Lyapunov Exponent of Sampled Data

Lyapunov exponent serves as a measure that characterizes a regularity of the dynamical system behavior. Very roughly speaking, Lyapunov exponent measures a time evolution of the initially close trajectories in the phase space. The

scenario of the trajectories' distance can be two-folding: either the trajectories can stay close when the time goes to infinity or the trajectories draw apart in an exponential way in the case of positive Lyapunov exponent. There is an indication of possibly chaotic behavior in the second case. But the sign of the largest Lyapunov exponent is not a sufficient one as we will see. Looking at different paper sources it is interesting that in the case of the Lorenz system the maximal Lyapunov exponent can get the values scattered between the values 0.8438 and 1.751. In any case, the positivity of the Lyapunov exponent coincides with the chaotic behavior of the Lorenz system as it has been proven in [17], [18], [19].

On the other side, evaluating the maximal Lyapunov exponent in the case of the above three examples one gets the following values:

| Example # | Largest Lyapunov exponent |
|---|---|
| Example 1 | 0.1389 |
| Example 2 | 0.693 |
| Example 3 | 0.0871 |

Positive values of the largest Lyapunov exponent could indicate chaotic behavior of the corresponding systems. But, as it was shown, the systems are far from being chaotic in the sense of the chaos definitions presented in the preliminary part.

Computations done in section 3 and in section 4 were provided in Matlab software [26]. The Lyapunov exponents were calculated using Matlab's Lyapunov Exponents Toolbox (LET), [27].

## 5 Conclusions

In this paper, the examples of misinterpretations of sampled data to indicate and analyze a possible chaotic behavior were considered. In particular, it was shown that topological resemblance of the graphical representation of scalar data time series plotted in 2-d using suitable time lag to the well-known Lorenz attractor may be present even for simply generated and clearly non-chaotic data. Furthermore, the examples of non-chaotic systems having the numerically computed positive largest Lyapunov exponent were provided as well. In such a way, it was demonstrated that careless analysis of the sampled dynamical systems data may lead to false conclusions which is, moreover, often the case in various published results.

**Acknowledgments.** This work is supported by Czech Science Foundation through the research grant no. 13-20433S.

## References

1. Lorenz, E.N.: Deterministic nonperiodic flow. J. Atmos. Sci. 20, 130–141 (1963)
2. Grosse-Erdmann, G.-K., Manguillot, A.P.: Linear Chaos. Springer (2011)

3. de Almeida, A.M.O.: Hamiltonian Systems: Chaos and quantization. Cambridge University Press, Cambridge (1988)
4. Oseledec, V.I.: A multiplicative ergodic theorem. Lyapunov characteristic numbers for dynamical systems. Trans. Moscow Math. Soc. 19, 197–231 (1968)
5. Smale, S.: Differentiable dynamical systems. NBulletin of the American Mathematical Society 73(6), 747–817 (1967)
6. Devaney, R.: An introduction to chaotic dynamical systems. Addison–Wesley, New York (1989)
7. Wiggins, S.: Chaos transport in dynamical systems. Springer, New York (1992)
8. Gulick, D.: Encounters with chaos. McGraw-Hill, New York (1992)
9. Schuster, H.: Deterministic chaos. VCH, Weinheim (1988)
10. Kotik, K., Lectures, L.: on Dynamical Systems, Structural Stability and their Applications. World Scientific Publishing Co. Pte. Ltd. (1992)
11. Katok, A., Hasselblatt, B.: Introduction to the Modern Theory of Dynamical Systems. Cambridge University Press (1997)
12. Shin, K., Hammond, J.K.: The instantaneous Lyapunov exponent and its application to chaotic dynamical systems. Journal of Sound and Vibration 218(3), 389–403 (1998)
13. Yalamova, R., Qi, L., Wang, L., Chen, Y., Mathews, S., Gong, G.: Detecting Chaos in Financial Time Series. Tech. Print, 1–9 (2006)
14. de Wijn, A.S.: Chaos in systems with many degrees of freedom. PhD thesis, Utrecht University (2004)
15. Özer, A.B., Akin, E.: Tools for detecting chaos. SAÜ Fen Bilimleri Enstitü sü Dergisi 9.Cilt, 1.Sayõ, 60–66 (2005)
16. Lindlay, D.H., Campbell, A.: A chaos approach to bankruptcy prediction. J. of Appl. Business Research 12(4), 1–9 (1996)
17. Mischaikow, K., Mrozek, M.: Chaos in the Lorenz equations: A computer-assisted proof. Bulletin AMS 32(1), 66–72 (1995)
18. Mischaikow, K., Mrozek, M.: Chaos in the Lorenz equations: A computer assisted proof. Part II: Details. Mathematics of Computation 67, 1023–1046 (1998)
19. Mischaikow, K., Mrozek, M., Szymczak, A.: Chaos in the Lorenz equations: A computer assisted proof. Part III: Classical Case Parameter Values. J. of Diff. Equations 169, 17–56 (2001)
20. Robinson, J.C.: Dimensions, Embeddings, and Attractors. Cambrigde University Press (2011)
21. Casdagli, M.: Chaos and Deterministic versus Stochastic Nonlinear Modeling. Santa Fe Institute, SFI Working Paper (July 029, 1991)
22. Puente, C.E., Obren, N., Sivakumar, B.: Chaos and stochasticity in deterministically generated multifractal structures. Fractals 10(1), 91–102 (2002)
23. Neimark, Y.I., Landa, P.S.: Stochastic and chaotic oscillations. Mathematics and Its Applications Soviet Series, vol. 77. Springer, Netherlands (1992)
24. Hirata, Y., Judd, K.: Constructing dynamical systems with specified symbolic dynamics. Chaos: An Interdisciplinary Journal of Nonlinear Science 5(3), 033102-1–033102-6 (2005)
25. Kovács, G., Buchler, J.R.: Regular and irregular nonlinear pulsations in population II cepheid models. The Astrophysical Journal 334, 971–994 (1988)
26. Matlab R2014a release. The MathWorks Inc., Natick (2014)
27. `http://www.mathworks.com/matlabcentral/fileexchange/233-let` (1998)

# Part III

# Complex Biological Systems

# Multifractality in Imaging: Application of Information Entropy for Observation of Inner Dynamics Inside of an Unlabeled Living Cell in Bright-Field Microscopy

Renata Rychtarikova[1], Tomas Nahlik[1], Rebecca Smaha[2], Jan Urban[1], Dalibor Stys Jr.[3], Petr Cisar[1], and Dalibor Stys[1]

[1] Institute of Complex Systems, South Bohemian Research Center of Aquaculture and Biodiversity of Hydrocenoses, FFPW, University of South Bohemia in Ceske Budejovice, Zamek 136, 373 33 Nove Hrady, Czech Republic
{rrychtarikova,stys}@frov.jcu.cz
[2] Department of Chemistry, Princeton University, Princeton, New Jersey 08544, USA
[3] Department of Measurement, Faculty of Electrical Engineering, Czech Technical University in Prague, Technicka 2, 166 27 Prague 6, Czech Republic

**Abstract.** The theoretical background of bright field optical microscopy is not described to the extent that would allow the extraction of as many features of the original object from the image as possible. In this article, we present the determination of image features based on a general assumption that images transmitted by an optical microscope have multifractal character. In order to determine the borders of the determinable point spread function, we derived a Point Divergence Gain ($PDG_{\alpha,x(l),y(l)}$) variable from the Renyi entropy. This variable calculates image points that carry the same information in consequent images captured upon moving the object along the lens' optical axis (z-scan). In this way, we may precisely identify the border of the point spread function of immovable identifiable objects.

**Keywords:** Renyi entropy, multifractality, point spread function, bright-field microscopy.

## 1 Introduction

The goal of microscopy in general is to obtain images of observed objects' positions that exactly copy their actual positions and, if possible, also provide information about the objects' properties at a particular location. In addition, the goal of biological research is to determine the states of elementary units that determine the state of the organism at a particular level: in the case of a cell, the elementary units are organelles and their constituents. The latter limits our ability to manipulate the sample for a microscopy experiment. Instead of technically optimizing an experiment, in most cases we must maximize the information yield from a given image.



A. Sanayei et al. (eds.), *ISCS 2014: Interdisciplinary Symposium on Complex Systems*, Emergence, Complexity and Computation 14, DOI: 10.1007/978-3-319-10759-2_27

In many biological experiments, evaluating the results depends on how the image content is interpreted. This, in practice, means equating the object observed in the dynamic optical image of the cell with the analogous object in the fixed and stained electron microscopic image of a microtome section. The obvious physical limit of this approach is a property of the optical microscope, which is known as the diffraction limit. In this article, we discuss bright field optical microscopy, which is the most commonly used type of microscopy and may be used for unlabeled (or native) specimens. In the discussion section, we take advantage of another of its features, the relative intelligibility of the diffraction pattern formed after transmission of light by the microscope [1].

Instead of examining the imaging model and attempting to reconstruct the positions of elementary diffracting objects in the cell, we have proposed assuming only the multifractal character of the image [2,3]. The origin of multifractality is twofold: it arises from the self-similarity of point spread functions of objects and from the self-organization of observed cells.

Here, we describe an algorithm for determining the spatial extent of point spread functions of stable structures inside living cells. The spatial extent of an image of an individual object is determined by a newly introduced approach: a Point Divergence Gain ($PDG_{\alpha,x(l),y(l)}$) calculation giving the last discriminable intensity level limited by the discretization of the camera chip at each level of the z-series. By this approach, we obtain series of images that depict points in which the information in the image systematically varies, describing the inner dynamics inside the living cell, in this case immovable objects.

## 2 Results and Discussion

### 2.1 Image Processing

In this article we describe an algorithm that uses properties of the point spread function to achieve a more detailed analysis of optical bright-field microscopy images of light-diffracting objects, mainly the static ones. For this purpose, an original z-stack of 12-bit images of a MG-63 osteosarcoma cell, obtained using a versatile sub-microscope (Optax Ltd., CZ) equipped with a Basler ACA2000-340kc color digital camera, is used as an example.

Image processing of the z-stack of the MG-63 cell is shown in Fig. 1. First, columns that serve as internal calibration of the noise in the camera were removed. Then, 92 relevant images corresponding to 100-nm steps of the microscope stage, which is controlled by piezomechanics, were selected from the original 155-image z-stack through consulting the z-position stored in each image's EXIF file (custom adopted). De-mosaicing was performed as published previously [4] by shrinking the number of points in the image to a quarter of the original one: for each four pixels, the red and blue channel levels were adopted to the intensity level captured by the respective chip pixel. The green level was set to the arithmetic average of the two corresponding green levels. By this procedure, we obtained a z-stack of least color map images of a living MG-63 cell. For

further processing, we used individual channels as sources of independent information about the observed signal. The size of the final pixel after de-mosaicing was $68 \times 68$ nm$^2$.

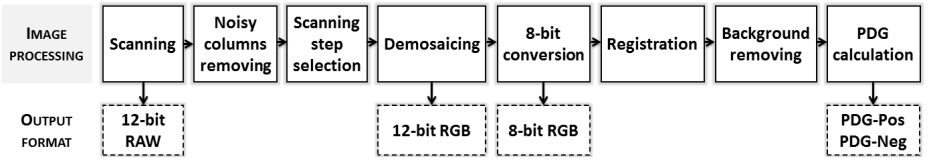


**Fig. 1.** Image processing of a z-stack of images of a MG-63 living cell obtained using bright-field microscopy (Institute of Complex Systems FFPW USB, CZ)

The original 12-bit images were converted to 8-bit resolution by shrinking the original 12-bit signal into an 8-bit signal through re-scaling all occupied intensity levels in the whole image series. This conversion method (least information loss – LIL) allows the data to be viewed in commercial software with minimal loss of information for subsequent image recalculation. The shifted 8-bit images were aligned (registered) and consequently, the single MG-63 cell was cut from the background. This process was performed using the NanoscopeDataProcessing software package (Institute of Complex Systems FFPW USB, CZ).

We analyzed the information content of each image using the Between Entropy Calculator software package [5]. We assumed the most general distribution that can be expected in self-organized objects such as living cells – the multifractal distribution. Here, we introduce a new variable derived from the Renyi entropy – the Point Divergence Gain ($PDG_{\alpha,x(l),y(l)}$) – which quantifies the diversity, uncertainty, and randomness in 3D space:

$$PDG_{\alpha,x,y} = \frac{1}{1-\alpha} \log_2 \frac{\sum_{i=1}^{n} p_i^{\alpha}}{\sum_{i=1}^{n} p_{i,x(l+1),y(l+1)}^{\alpha}} \tag{1}$$

This variable calculates the information change achieved by replacing a particular point at position ($x$,$y$) from an image ($l$) by the point at the same position in the next image ($l$+1). This may result in either increased or decreased information content. The former occurs when the intensity of the point corresponding to a given object in the first image has lower probability of occurrence than the intensity of the same point in the following image, and *vice versa*. As seen in Fig. 2 together, if the information content increases, each pair of consecutive z-stack images at each $\alpha$-coefficient gives rise to two PDG-transformed images – with the loss (the -Neg-1 sub-image) and increase (the -Pos-1 sub-image) of information.

In the formula, the uncertainty and randomness of the described system are connected to the probability of the occurrence of intensity $i$ in the original image ($l$) ($p_{i,x(l),y(l)}$) and to the probability of the given intensity in the same image where the examined point at coordinates ($x$,$y$) was replaced by the point at the same location in the next image ($l$+1) ($p_{i,x(l+1),y(l+1)}$), respectively.

The dimensionless coefficient $\alpha$ is related to the multifractality of the point spread functions. To analyze the cell interior, PDG at $\alpha = 4$ ($PDG_{4,x(l),y(l)}$ in Fig. 2) is the most suitable because it is where the highest number of occupied intensity levels (the highest number of separable groups of different information contribution) were found. This shows the advantage of using the Renyi entropy instead of, for instance, the best known Shannon entropy, which is the limiting value of Renyi entropy as $\alpha \to 1$. In Shannon entropy, numerous image levels would be merged. Nevertheless, even in the case of $\alpha = 4$, we also observed numerous merged intensity levels which separate at different $\alpha$ levels.

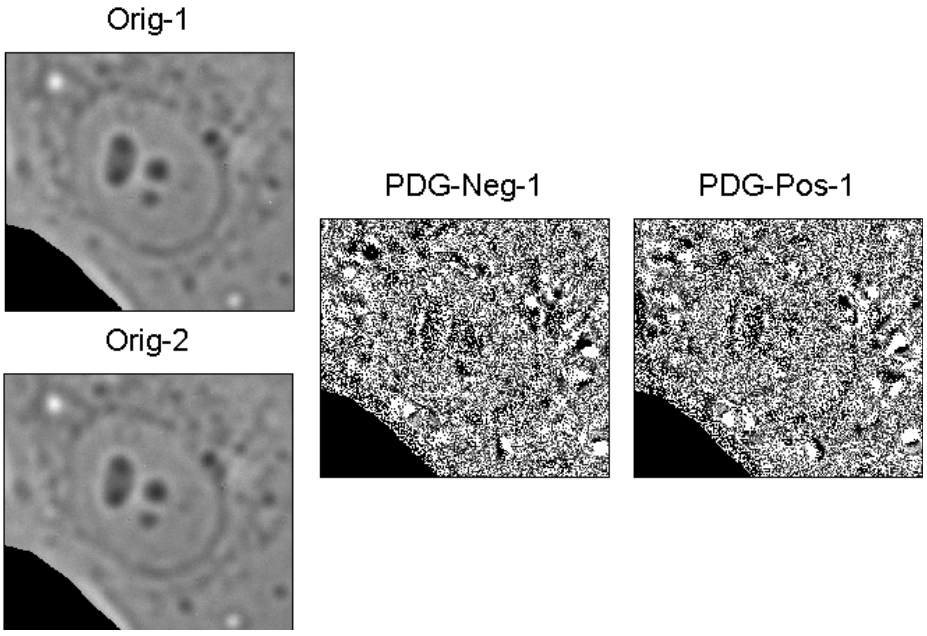


**Fig. 2.** Detail (29.24 × 32.64 $\mu$m$^2$) of the green channel of the original and PDG-transformed z-stack images of a MG-63 living cell around the focus plane (ICS FFPW USB, CZ). Original microscopic images Orig-1 (55th image in the z-stack) and Orig-2 (56th image in the z-stack) produce PDG-Neg-1 (negative information change) and PDG-Pos-1 (positive information change) as a result of exchanging pixels at the same position in the original images.

### 2.2 Analysis of Zero Digital Levels of PDG-Transformed Images

The image is composed of contributions from different image levels. The $PDG_{\alpha,x(l),y(l)}$ calculation helps to indicate where the image of a certain observed object is located and serves to highlight the object borders, even those which are not evident in the original data sets. Thus, the change in an image

series through a z-scan is the result of either an object's appearance or disappearance from the image or changes in the point spread function of the object with the distance from its ideal focal plane.

In this article, we limit ourselves to the detection and analysis of point spread functions of static large homogenous diffracting organelles (Fig. 3), which are projected in the green channel of the original microscopic images. Their PDG-transformed sub-images are shown in Fig. 2.

Fig. 3a depicts four $PDG_{4,x(l),y(l)} = 0$ sub-images. PDG-Neg-1 and PDG-Pos-1 were extracted from the PDG-transformed sub-images shown in Fig. 2; analogously, PDG-Neg-2 and PDG-Pos-2 were thresholded in the green channel of PDG-sub-images calculated from Orig-2 and Orig-3 images (i.e. the 56th and 57th z-stack images, respectively). Rounding during re-scaling of the $PDG_{4,x(l),y(l)}$-values from double-precision floating point format to 8-bit unsigned integer number format resulted in a depiction of points different from 0. The points that correspond to 0 are found through the intersection of $PDG_{4,x(l),y(l)} = 0$ digital levels of each pair of PDG-sub-images (Fig. 3b). By this procedure, we identified the points in the point spread function for which the image is homogeneous within the precision of the 8-bit intensity section and the distance along the z-axis spanning two consequent physical levels. In fact, points that truly do not change between two consequent images in a z-scan are very rare and their quantity obviously depends on the step size chosen for the z-scan as well as the digital camera's discretization.

Consequently, the intersection of 0 points of two consecutive PDG-1 and PDG-2 images (Fig. 3c) gives us static objects and other intensities that did not change in two consecutive original images. This complementarity is the result of calculating PDG-values from two consecutive original z-stack images (Fig. 2). We can find two types of objects in Fig. 3c: those for which we may also detect parts of the point spread function corresponding to a second diffraction ring, and those for which only the part of the point spread function that contains the core of the diffracting object itself was observed. The former objects behave exactly as expected by the Abbe model [6]. For the behavior of objects not showing secondary interference, another model is needed. We expect that other extant objects not showing secondary interference are composed from a relatively dilute solution of small diffracting objects of a size reported to be observable by video-enhanced microscopy [7]. It should be noted that objects detectable by video-enhancement are usually detected without any secondary diffraction rings. With regard to their observability, the extent of the effective point spread function of these objects under a given technical set-up must be smaller than that proposed by the Abbe [6] or Nijboer-Zernike [1,8,9] models. Since there is no real reason why there should be two models describing the imaging of relatively small and large objects, this finding requires additional examination.

This method of image processing connects to the complementarity of zero levels in PDG-transformed images, emphasizes variability in structure details, and is mathematically distinguishable by semantic measurement. It can thus potentially be used for segmentation and 3D reconstruction of organelles.

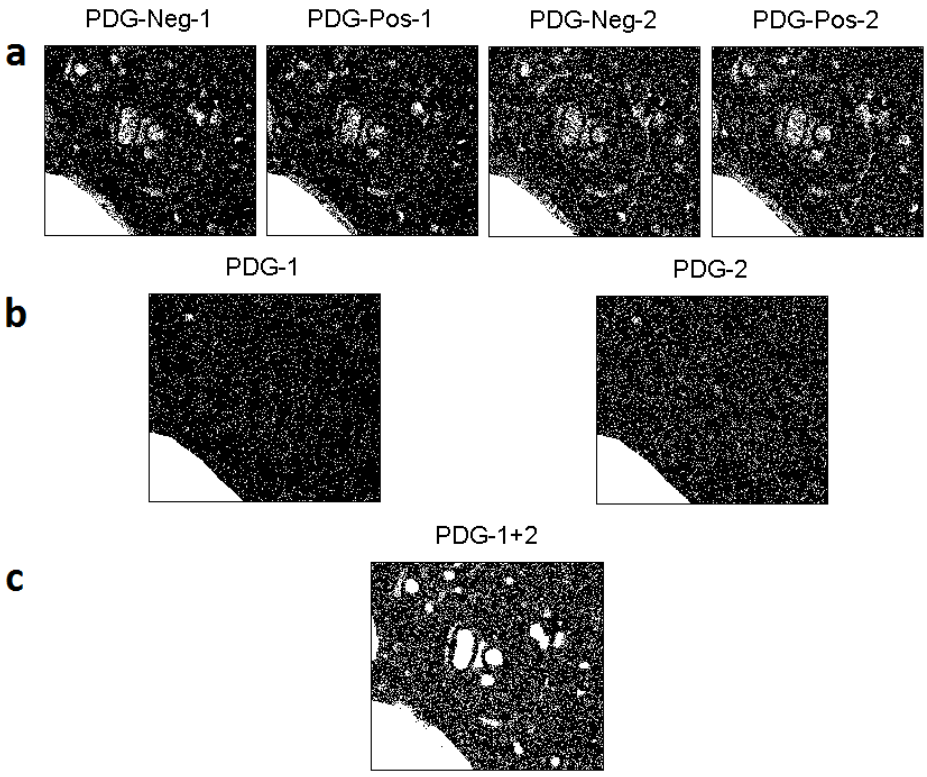


**Fig. 3.** Analysis of immovable organelles in a z-stack of 29.24 × 32.64 $\mu$m$^2$ images of a MG-63 living cell at $PDG_{4,x(l),y(l)} = 0$ levels of the green channels. **(a)** $PDG_{4,x(l),y(l)} = 0$ intensities thresholded in PDG-sub-images shown in Fig. 2; these points were formed by re-scaling PDG-values from double-precision to unsigned integers. **(b)** Intersection of PDG-Neg-1 and PDG-Pos-1 sub-images (PDG-1) and PDG-Neg-2 and PDG-Pos-2 sub-images (PDG-2); these points show intensities that did not change between two consecutive images (Orig-1 → Orig-2, Orig-2 → Orig-3) of the z-stack and correspond to diffracting objects of the size down to 68 × 68 × 100 nm$^3$. **(c)** $PDG_{4,x(l),y(l)} = 0$ points calculated as the intersection of PDG-1 and PDG-2 images. It depicts large homogeneous static objects and other unchanged intensities between two consecutive images in a z-stack.

**Acknowledgment.** This work was partly supported and co-financed by the South Bohemian Research Center of Aquaculture and Biodiversity of Hydrocenoses (CZ.1.05/2.1.00/01.0024), LO1205 from MEYS CR (NPU I program), and Postdok JU (CZ.1.07/2.3.00/30.0006).

## References

1. Braat, J.J.M., Dirksen, P., Janssen, A.J.E.M.: Assessment of an Extended Nijboer-Zernike Approach for the Computation of Optical Point-Spread Functions. J. Opt. Soc. Am. A 19, 858–870 (2002)
2. Stys, D., Urban, J., Vanek, J., Cisar, P.: Analysis of Biological Time-Lapse Microscopic Experiment from the Point of View of the Information Theory. Micron 42, 360–365 (2011)
3. Štys, D., Jizba, P., Papáček, Š., Náhlík, T., Císař, P.: On Measurement of Internal Variables of Complex Self-Organized Systems and Their Relation to Multifractal Spectra. In: Kuipers, F.A., Heegaard, P.E. (eds.) IWSOS 2012. LNCS, vol. 7166, pp. 36–47. Springer, Heidelberg (2012)
4. Tkacik, G., Garrigan, P., Ratliff, C., Milcinski, G., Klein, J.M., Seyfarth, L.H., Sterling, P., Brainard, D.H., Balasubramanian, V.: Natural Images from the Birthplace of the Human Eye. PLoS One 6(6), e20409 (2011)
5. `http://www.expertomica.eu/software.php`
6. Abbe, E.: Beiträge zur Theorie des Mikroskops und der mikroskopischen Wahrnehmung. Archiv für Mikroskopische Anatomie 9(1), 469–480 (1874)
7. Lichtscheidel, I.K., Foissner, I.: Video Microscopy of Dynamic Plant Cell Organelles: Principles of the Technique and Practical Application. J. Microsc.-Oxford 181, 117–128 (1996)
8. Zernike, F.: The Concept of Degree of Coherence and Its Application to Optical Problems. Physica 5, 785–795 (1938)
9. Nijboer, B.R.A.: The Diffraction Theory of Aberrations. Ph.D. dissertation, University of Groningen, Groningen, The Netherlands (1942)

# Trajectory Tracking for Genetic Networks Using Control Theory

Natalja Strelkowa

Boehringer Ingelheim Pharma GmbH and Co. KG
Rhineland-Palatinate, Germany
natalja.strelkowa@gmail.com

**Abstract.** Synthetic biology has impressively progressed during the last decades making it possible to rationally design and implement genetic networks with new functionalities in living microorganisms. With these new technologies the expression of genes can be observed using fluorescent markers and influenced using light flashes and photo-active expression inducers. In this contribution, we suggest the implementation of external feedback control for dynamic trajectory tracking of a synthetic genetic network. The feedback control can be implemented in living microorganisms using fluorescent markers for system readout and photo-active gene expression inducers for external control signals. In particular we show that hierarchical or sequential design for synthetic gene networks makes controlled trajectory tracking possible using the readout and control actions on few instead of all genes. Optimised trajectory tracking opens the possibility to interact and influence genetic networks in a very precise manner in terms of time and location with minimal cell burden.

**Keywords:** synthetic gene networks, feedback control, generalised repressilator, trajectory tracking.

Control theoretical concepts have proved useful for the understanding of several biological mechanisms [1]. These concepts have also been used to design optimised intervention strategies with natural systems. In particular, feedback control based on the input-output relationships seems promising many applications in Life Sciences. In Epidemiology for instance sequential non-pharmaceutical interventions as first response to a pandemic threats can be formulated as control theoretical problems [2]. In Medicine optimised drug treatment of HIV-infected patients can be found using control theoretical framework [3]. Also in Neuroscience, control theoretical concepts have been widely applied, see for example [4], where the well-known Kalman filter was used for estimation of the system state and parameters in neural cortex model.

Synthetic biology is another quickly advancing scientific branch where the applications of control theory can be promising [5, 6]. Recent progress in this field shows that the two necessary pieces for the implementation of external feedback control namely targeted interference for control signal implementation



A. Sanayei et al. (eds.), *ISCS 2014: Interdisciplinary Symposium on Complex Systems*, Emergence, Complexity and Computation 14, DOI: 10.1007/978-3-319-10759-2_28

and dynamic gene state tracing for system state readout. Fluorescent markers can for example be used for quantitative *in vivo* estimates of gene expression states [7, 8] and monochromatic light can be used for implementation of targeted gene expression induction [9, 10].

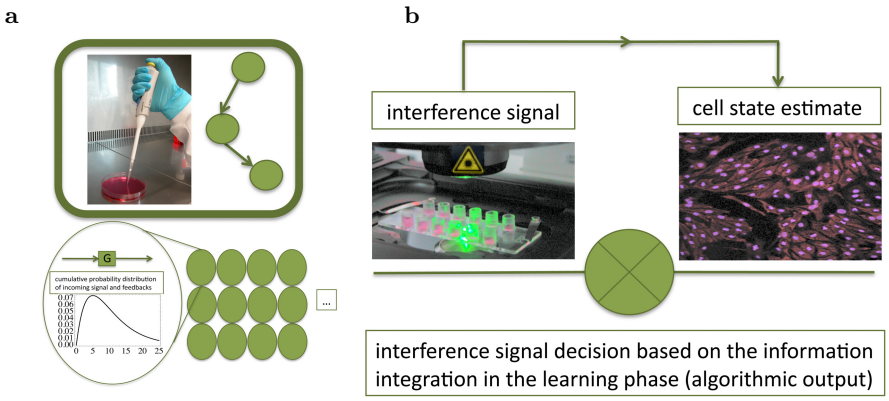


**Fig. 1. Adaptation of control-theoretical approach to genetic networks. a)** In the training phase the dynamics of the system are studied and time traces of key variables, for instance protein concentrations, are collected. The approach can be applied to experimentally measured time traces as well as for simulated time traces. **b)** Based on the integrated information in the training set, a state dependent feedback control strategy is induced in order to conduct a genetic network to a desired state or track a dynamic trajectory.

The definition of a control problem also requires a specification of the optimisation criterion. In many classical applications of the nonlinear control theory it is the minimal energy [11]. For Synthetic Biology we rather suggest the minimisation of metabolic cell burden due to high number of heterologous proteins. So the gene network functionality as well as controlled tracking of predefined trajectories or control towards a particular state should be achieved with the usage of as few heterologous proteins as possible.

For the induction of optimised tracking policies we use the reinforcement learning framework as described in Ref. [12]. This algorithm uses time traces to induce a multi-dimensional function $Q(\mathbf{n}, \mathbf{u})$, which is the score of a control action $\mathbf{u} \in U$ for a system state $\mathbf{n} \in \mathbb{N}^s$. The optimised intervention strategy for direction of the network to a desired state is obtained by taking the maximum of this score function at each state $\mathbf{n}$: $\max_{\mathbf{u}\in U} Q(\mathbf{n}, \mathbf{u})$.

In this contribution we demonstrate how a genetic network inspired by synthetic biology can be used for controlled trajectory tracking. Recently we investigated the generalised repressilator model - genes ordered in a ring structure and sequentially repressing the following gene (see Fig. 2) - and found that even numbered gene rings possess unstable limit cycles showing long lasting transient oscillations [16, 17]. Here, we apply trajectory tracking control in order to

keep even numbered rings in this oscillating state. The control strategy for this tracking problem is induced via reinforcement learning [12].

In the previous publication we have induced a control strategy for toggling a genetic switch [13]. The aim of the control policy in the previous publication was to lead a genetic network to a desired system state. Here, we expand the application of the control theory in synthetic biology to tracking pre-defined trajectories and use the even numbered gene ring model as an example.

## Methods Description: The Reinforcement Learning Approach

Reinforcement learning approaches have been proved to be useful for a wide range of applications, where only few information on the underlying process is available [12, 14]. The major requirement on the underlying process is that it is first order Markovian, which means that the following state is fully determined by the information on the current state. In particular classical mass-action kinetics underpinning gene expression processes can be formulated as first order Markovian processes using either Master equation or differential equations [15].

Reinforcement learning can be used to find optimised control strategies for problems, which can be approximated as general first order Markov processes. Using otherwise notation as in Ref. [15] Markov property for successive times (i. e. $t_0 < (t_0 + \delta t) < \cdots < t$) and control signals $\mathbf{u} \in U$ can be formulated as:

$$\begin{aligned} &Pr(\mathbf{n}(t), \mathbf{u}(t), t | \mathbf{n}_0, \mathbf{u}_0, t_0; \ldots; \mathbf{n}(t-\delta t), \mathbf{u}(t-\delta t), (t-\delta t)) \\ &= Pr(\mathbf{n}(t), \mathbf{u}(t), t | \mathbf{n}(t-\delta t), \mathbf{u}(t-\delta t), (t-\delta t)) \end{aligned} \tag{1}$$

That means a process is first order Markovian if the state transition probability $Pr(\mathbf{n}(t), \mathbf{u}(t)|\cdot)$ at the time $t$ only depends on the state of the system at the time $t - \delta t$ and is not dependent or affected by other previous states.

Master equation formulation for gene expression networks dynamics fullfils this requirement since the time evolution of the probability $P$ on discrete set of states $\mathbf{n} \in \mathbb{N}^s$ is a PDE

$$\frac{dP(\mathbf{n}, t)}{dt} = \sum_{\mathbf{n}'} W(\mathbf{n}|\mathbf{n}', \mathbf{u}) P(\mathbf{n}', t) - W(\mathbf{n}'|\mathbf{n}, \mathbf{u}) P(\mathbf{n}, t)$$

where $W(\cdot|\cdot)$ are transition probabilities per unit time, which are now also dependent on the external control signals $\mathbf{u} \in U$.

Approximate dynamics of the Master equation can be formulated as a stochastic differential equation (SDE) or as an ordinary differential equation (ODE) $d_t x = f(x)$ (see [15] for connections between the formalisms via $\Omega$-expansion). The deterministic approximation $x = \phi(x_0, t - t_0)$ is a special case for a Markov process with a $\delta$-peak transition probability $\delta(x - \phi(x_0, t - t_0))$. Similarly an SDE is a Markov process, where the transition probabilities are modulated by Gaussian noise.

Processes described by Master equations, stochastic or ordinary differential equations are first order Markovian and can be expanded in order to include

external input signals. In principle the system dynamics, i.e. state transitions upon applied external control signals, can also be obtained directly from the experiment as time traces taken at small enough intervals.

At each state transition a control signal $\mathbf{u}(t)$ can be applied to the system. What we would like to know is: if the system is in a state $\mathbf{n}$, what is the best action on the long term to be applied? This question is answered by a control strategy $\mu(\cdot) : \mathbb{N}^s \rightarrow U$, which is the mapping from the state space into the action space.

The framework set up for a specific system usually starts with the definition of desired and forbidden/undesired states and actions. We use the function $r(\mathbf{n}(t), \mathbf{u}(t))$ in order to associate an instantaneous reward to each state transition. This function must be bounded. The reward for the transition to desired target states is defined as high, for the undesired or forbidden states as low and neutral for all other states. The induced scores for the transitions from each state $\mathbf{n} \in \mathbb{N}^s$ if the control action $\mathbf{u}$ is applied. The action with the highest score will identify the optimised control strategy $\mu$.

Score functions for strategies $\mu$ will be denoted as $J^{\mu}_{\infty}$, i.e. the expected score obtained over an infinite time horizon when the system is controlled using the control policy $\mu$: $\mathbf{u}(t) = \mu(\mathbf{n}(t)), \forall t$. For a given initial condition $\mathbf{n}_0$, $J^{\mu}_{\infty}$ is given by:

$$J^{\mu}_{\infty}(\mathbf{n}) = E\left[\int_{t=0}^{\infty} \gamma^t r(\mathbf{n}, \mu(\mathbf{n}(t)))dt \,\middle|\, \mathbf{n}_0 = \mathbf{n}\right] \tag{2}$$

where $\gamma$ is a discount factor ($0 \leq \gamma < 1$) that weights short-term rewards more than long-term ones, and where the conditional expectation is taken over all trajectories starting with the initial condition $\mathbf{n}_0$. We target to find an approximation of the optimal policy $\mu^*$, which maximizes the expectation $J^{\mu}_{\infty}$ for all system states in the considered hypercube $\mathbf{n} \in \mathbb{N}^s$.

## Controlling Even-Number Gene Rings around Unstable Periodic Orbits

We have introduced a design for a genetic oscillator some years ago where the application of the control theory can help to find optimal sequence of external interference signals, i.e. an optimised control policy [16, 17].

The suggested design of a genetic network consists of genes ordered in a ring structure where each gene represses its follower in the network (see Fig. 2). The steady state system dynamics without the external control actions are such that a ring with an even number of genes acts as a switch in the stable degenerated solution. Either the first gene and all odd numbered genes are expressed and the second gene and all even numbered genes are repressed or vice versa (see Ref. [16, 17]).

This system also has an oscillating transient solution which can last for a long time for some initial conditions. This transient solution is explained by an unstable limit cycle due to the first Hopf bifurcation in even numbered rings [17].

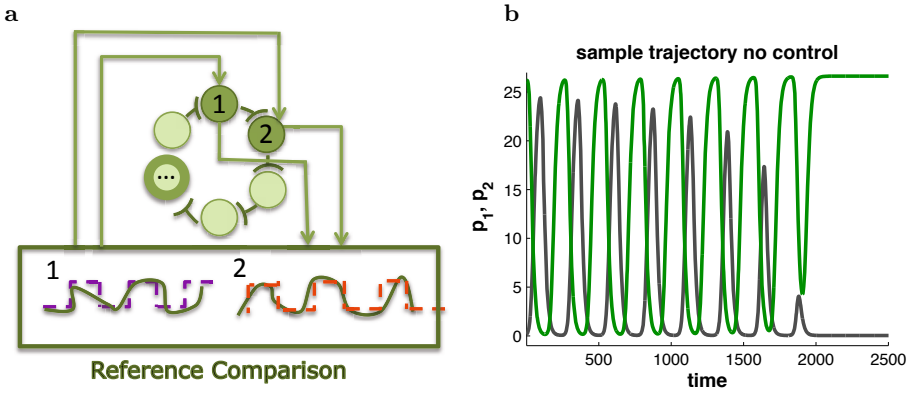


**Fig. 2. The generalized repressilator model. a)** Network scheme of the generalised repressilator with readout and control action points. The gene repression is marked with the symbol $\perp$. **b)** Dynamics of even-numbered rings without the control actions. Simulated time traces of two sequential genes in the repression ring are shown. Starting in oscillating dynamical state the ring converges to the globally stable fixed point solution [16, 17]. The oscillations are non-sustainable transient without.

Using external control signals on two consecutive genes in the ring the system can be kicked between the oscillating regime and the stable steady state and also kept in the oscillating state [16].

In this article we will induce an optimised control policy in order to keep the ring in the oscillating state. The control problem is defined as trajectory tracking of the oscillating pattern.

### Definition of the Trajectory Control

The even gene ring system is described by the following set of ODEs:

$$\begin{aligned} \dot{m}_j &= \frac{c_1}{1+p_{j-1}^2} - c_2 m_j + \delta_{j1} u_1 q_{s_1} + \delta_{j2} u_2 q_{s_2} \\ \dot{p}_j &= c_3 m_j - c_4 p_j \end{aligned} \tag{3}$$

with the usual definition for $\delta_{ij}$ as Kronecker symbol [15] and using otherwise the same set of constants as in Ref. [16].

The control signals $\mathbf{u} \in \{u_1, u_2, 0\}$ are applied on the transcriptional level to the first and the second genes in this scenario. The strength of the light signals on the mRNA production is denoted by $q_{s_i}$.

Using the kick signals the ring can be brought to the stable steady state and back to the oscillating state [16]. We start the trajectory tracking control from the oscillating state, i.e. close nearby to the trajectory which we want to track. Then the goal of the control policy will be to induce a control policy which should keep the ring in the oscillating state.

The reference trajectory is a nonlinear curve, which can be obtained either experimentally shortly after the ring has been put in an oscillating state or from the unstable limit cycle of model simulations.

Finally, the instantaneous reward function needs to be defined for the trajectory tracking system. We use a distance function between the observed state $\mathbf{p(t)} = (p_1(t), p_2(t))$ and the reference trajectory $\mathbf{p}_0(t)$:

$$r(\mathbf{p}, \mathbf{u}, t) = \exp(-|\mathbf{p}(t) - \mathbf{p_0}(t)|) \tag{4}$$

Due to the inherent circular symmetry of the system the read-out and control interface contain only the states and control interactions points of the first two genes, other variables describing transcriptional level and the expression of other genes are not part of this control scheme.

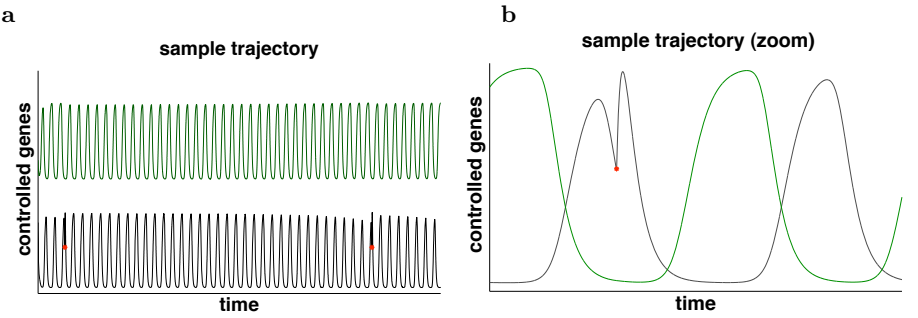


**Fig. 3. Optimised tracking of an unstable periodic trajectory in the generalized repressilator model. a)** A sample trajectory starting at the limit cycle for two observed and controlled genes. The aim of the control policy is to keep the ring in the oscillating state around the unstable periodic limit cycle. As the oscillation starts to flatten off (noticeable by continuously decreasing oscillation amplitude), control actions marked with red stars are applied preventing the ring from approaching the stable non-oscillating state. **b)** zoom into the trajectory shown in a) around the second control signal.

## Discussion

We applied the concept of trajectory tracking to a model of a synthetic genetic network in an unstable, but long lasting oscillation state. The objective of the formulated feedback control was to track the oscillation trajectory avoiding the over-expression of controlled genes and reducing the burdening of the cells by sparse usage of heterologous proteins. Therefore we have formulated the tracking optimisation problem inducing the expression of the controlled genes by just enough to keep the genetic network in the oscillating state.

In our test network we readout and influence only two genes out of 10 genes, and it is sufficient to keep the ring in the oscillating state. This has of course to do with the circular symmetry of the network and with the fact that sequential

genes are dynamically dependent on the controlled genes. It means that synthetic genetic networks with a hierarchical or sequential organisation can be controlled using partial and not full system observability. Indeed natural and also designed

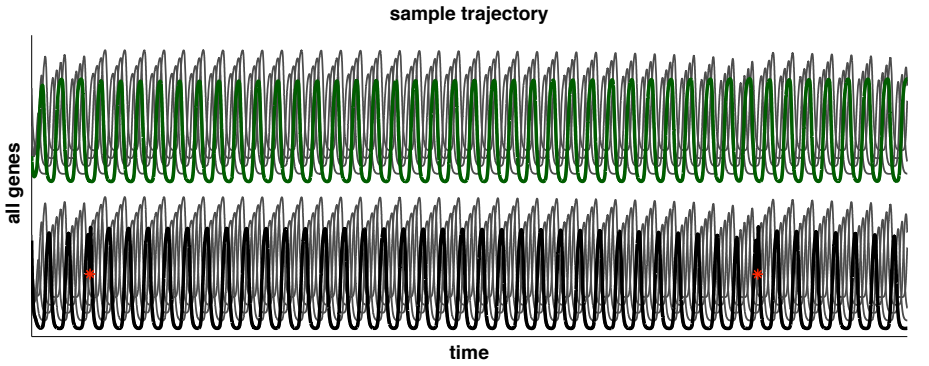


**Fig. 4. Control of 2 genes keeps a 10 gene-ring in the oscillating state around an unstable periodic orbit.** The control procedure has been designed for a gene ring with 10 genes, but we have used only the time traces of the first 2 genes for the policy induction. The genes which time evolution has been used for readout and control signal interference are shown in full colours, the time traces of the dependent genes are shown in gray.

networks are often organised as cascades of genes or as feedback loops containing several genes [18]. If we want to control these networks towards desired states or towards pre-specified dynamic trajectories then we need to find few interaction points, i.e. key genes for readout and control interactions.

Designed synthetic networks should be organised in a hierarchical manner so that the infeasible complete observability of the genetic network including readout of all components is not necessary for the implementation of the external feedback control. Such key genes for dynamic control can be found based on the connectivity matrix of the genetic network and this would be an interesting direction towards advancing Synthetic Biology field.

For engineered networks we usually will have a quantitative model for the genetic network. The control deduction technique applied in this contribution does not use this information, mainly due to the fact that the models are still not precise enough for a quantitative estimate of the expected system state. A further development of this framework could be to expand the approach so that it would take the model prediction into account while learning, as is done for instance for the Kalman filter.

## References

[1] Csete, M.E., Doyle, J.C.: Reverse engineering of biological complexity. Science 295, 1664–1669 (2002)
[2] Lin, F., Muthuraman, K., Lawley, M.: An optimal control theory approach to non-pharmaceutical interventions. BMC Infectious Diseases 10, 32 (2010)
[3] Stan, G.B., Belmudes, F., Fonteneau, R., Zeggwagh, F., Lefebvre, M.A., et al.: Modelling the influence of activation-induced apoptosis of cd4[sup + ] and cd8[sup + ] t-cells on the immune system response of a hiv-infected patient. IET Systems Biology 2, 94–102 (2008)
[4] Schiff, S.J., Sauer, T.: Kalman filter control of a model of spatiotemporal cortical dynamics. J. Neural Eng. 5, 1–8 (2008)
[5] Khalil, A.S., Collins, J.J.: Synthetic biology: applications come of age. Nat. Rev. Genet. 11, 367–379 (2010)
[6] Cameron, D.E., Bashor, C.J., Collins, J.J.: A brief history of synthetic biology. Nat. Rev. Micro. 12, 381–390 (2014)
[7] Cai, L., Friedman, N., Xie, X.S.: Stochastic protein expression in individual cells at the single molecule level. Nature 440, 358–362 (2006)
[8] Bennett, M.R., Hasty, J.: Microfluidic devices for measuring gene network dynamics in single cells. Nat. Rev. Genet. 10, 628–638 (2009)
[9] Shimizu-Sato, S., Huq, E., Tepperman, J.M., Quail, P.H.: A light-switchable gene promoter system. Nat. Biotech. 20, 1041–1044 (2002)
[10] Levskaya, A., Weiner, O.D., Lim, W.A., Voigt, C.A.: Spatiotemporal control of cell signalling using a light-switchable protein interaction. Nature 461, 997–1001 (2009)
[11] Slotine, J.J.E., Li, W.: Applied nonlinear control. Prentice-Hall, New Jersey (1991)
[12] Ernst, D., Geurts, P., Wehenkel, L.: Tree-based batch mode reinforcement learning. Journal of Machine Learning Research 6, 503–556 (2005)
[13] Strelkowa, N.: Inference of Optimized Control Strategies for Genetic Networks. In: ISCS 2013: Interdisciplinary Symposium on Complex Systems. Emergence, Complexity and Computation, vol. 8, pp. 265–270. Springer, Heidelberg (2014)
[14] Bertsekas, D.: Dynamic Programming and Optimal Control, 2nd edn., vol. I. Athena Scientific, Belmont (2000)
[15] van Kampen, N.G.: Stochastic Processes in Physics and Chemistry, 3rd edn. Elsevier, Amsterdam (2007)
[16] Strelkowa, N., Barahona, M.: Switchable genetic oscillator operating in quasi-stable mode. Journal of the Royal Society Interface (2010)
[17] Strelkowa, N., Barahona, M.: Transient dynamics around unstable periodic orbits in the generalized repressilator model. Chaos: An Interdisciplinary Journal of Nonlinear Science 21, 023104 (2011)
[18] El-Samad, H., Khammash, M.: Modelling and analysis of gene regulatory networks using feedback control theory. International Journal of Systems Science 41, 17–33 (2010)

# Modeling and Optimization of Microalgae Growth in Photobioreactors: A Multidisciplinary Problem

Štěpán Papáček[1], Jiří Jablonský[1], Karel Petera[2], Branislav Rehák[3], and Ctirad Matonoha[4]

[1] University of South Bohemia in Ceske Budejovice, FFPW USB, CENAKVA, Institute of Complex Systems, Zámek 136, 373 33 Nové Hrady, Czech Republic
spapacek@frov.jcu.cz, jiri.jablonsky@gmail.com
[2] Czech Technical University in Prague, Faculty of Mechanical Engineering, Technicka 4, 166 07 Prague 6, Czech Republic
Karel.Petera@fs.cvut.cz
[3] Institute of Information Theory and Automation, Academy of Sciences of the Czech Republic, 182 09 Prague, Czech Republic
rehakb@utia.cas.cz
[4] Institute of Computer Science, Academy of Sciences of the Czech Republic, Pod Vodarenskou vezi 2, 182 07 Prague 8, Czech Republic
matonoha@cs.cas.cz

**Abstract.** Microalgae have the potential to be a major biofuel source in the future. Computational biology plays a key role in understanding biological processes within microalgae and optimizing biofuel production. Here, we present a multidisciplinary, multi-timescale modeling approach of microalgae growth in photobioreactors. Our modeling framework bridges biology (cell growth), physics (hydrodynamics and light distribution), and optimization together. This framework consists of (i) the state system (mass balance equations in form of advection-diffusion-reaction PDEs), (ii) the fluid flow equations (the Navier-Stokes equations), and (iii) the optimization problem formulation. The modeling and optimization of microalgae growth in a Couette-Taylor reactor is presented to demonstrate this method. We show how the flashing light effect can be an intrinsic part of the model. Finally, we discuss further methodological integration with the metabolomic-transcriptomic kinetic model, which explains cellular concentrations of key metabolites in connection with cell growth.

**Keywords:** Microalgae, photobioreactor, optimization, multiscale modeling, flashing light effect.

## 1 Introduction

Microalgae are re-gaining more attention in biotechnology due to its new potential as a biofuel source, such as modification for high lipid content. However,



A. Sanayei et al. (eds.), *ISCS 2014: Interdisciplinary Symposium on Complex Systems*, Emergence, Complexity and Computation 14, DOI: 10.1007/978-3-319-10759-2_29

reliable methods with predictive power for *in silico* simulation of microalgal growth in production systems, such as photobioreactors (PBR), are missing.

The modeling of microalgal behavior and growth is a very complex problem, that involves three-dimensional multiphase (gas-liquid-solid) flow dynamics, description of properties within PBR, e.g., irradiance distribution, and multi-dimensional functionality of cellular processes. Moreover, all these parts interact across different timescales. Thus, one has to solve theoretical (e.g., how to cope with multi-timescale phenomena, to prove the existence and regularity of optimal solutions, etc.) and practical (enormous computational requirement) issues. As a consequence, one or more interacting parts of the system are implemented either in over-simplified or even inadequate way.

While most studies on PBR focus on specific problems without clear connection to the whole production process, in this communication we formulate the unified framework for modeling of microalgae growth in a PBR. We provide a simple case study of microalgae growth in the Couette-Taylor reactor, a device where the so-called Taylor vortices can induce high frequency light-dark cycles regime.

## 2 State and Fluid-Dynamic Models

The material (mass) balance equations for the state variables of interest (e.g., microbial species, nutrients, $CO_2$, $O_2$, etc.) have to be solved simultaneously with the fluid dynamics (momentum balances, continuity equations). Nevertheless, according to [1], the stationary flow field inside the production system (e.g., photobioreactor, open pond or raceway) is not affected by mass transfer and reaction for many biotechnological processes with Newtonian flow behavior. This assumption permits the separation of both models and consequently the reduction of the computational effort due to the fact that each model can be solved with different numerical method and with different spatial-temporal discretization (on different numerical grids). The separation can be total (for the stationary flow field in a continuous system) or stepwise, e.g., reflecting some sequence of quasi-steady states in a production system operated in batch mode.

Moreover, we would ideally model the transport of material (including photons) to and from the surface of microbial cells and the corresponding biological reactions (cell metabolism). The model parameters would be independent of the PBR size, operational mode, etc. However, there are two reasons why this approach (*microkinetics*) is rather theoretical:

- To model all the transport phenomena influencing the microenvironment is still almost numerically prohibitive. E.g., the length scales over which it is necessary to resolve the mass transport could be smaller than the fluid-flow scales, especially in the turbulent flow regime. Special approaches must be used in such cases, which results in a very large number of mesh cells substantially limiting consequent optimization calculations.
- Due to the inhomogeneity of cell population there could be morphological differentiation of cells caused by shifted cell cycle and overall changes in gene expression that are almost impossible to observe.

Thus being able to measure only averaged behavior over a large number of cells in different states, we opt for the integral description called the *macrokinetics* and the respective model parameters have to be tuned dynamically.

### 2.1 State Model

The material balance equations for the state variables of interest describe the transport and reaction of the reacting species or components:

$$\frac{\partial c_i}{\partial t} + \nabla \cdot (vc_i) - \nabla \cdot (D_e \nabla c_i) = R(c_i) + S(c_i), \quad x \in \Omega \subset R^3, \quad t \in [t_0, T], \quad (1)$$

with the initial condition $c_{i_0} = c_i(x, t_0),\ x \in \Omega \subset R^3$, and the boundary condition (impermeability of the domain boundary): $\nabla c_i(x,t) = 0,\ x \in \partial\Omega,\ t \in [t_0, T]$, where $c_i = c_i(x,t),\ i = 1, ..., m$, are conservative quantities, e.g. a concentration or cell density of the $i^{th}$ component, $v$ is the velocity flow field, and $x$ stands for a position vector in a coordinate system. $D_e(x)$ is the dispersion coefficient, which corresponds to the diffusion coefficient in microstructure description and becomes a mere empirical parameter that suitably describes mixing in the system. It is influenced by the molecular diffusion and velocity profile. $R(c_i)$ and $S(c_i)$ are the reaction and source (inlets/outlets) terms, respectively.

The source term $S(c_i)$, e.g. the load of nutrients, is usually modeled as a corresponding boundary condition. However, in order to further simplify the analytical study of the existence of an optimal solution, cf. [2], and respecting that the location of discharge of some material could be inside the domain $\Omega$, we prefer the above form (1).

The reaction term $R(c_i)$ in the transport equation (1) is usually provided by a "specialist" not being familiar with the complications residing in the fact that the relevant transport and reaction phenomena are multi-scale. If we realize that the characteristic times of microalgae growth and turbulent diffusion are of the order of hours and seconds, respectively, then after adopting whatever growth kinetic model, only two alternatives exist: either (i) to neglect the details concerning mixing phenomena, e.g. by accepting the hypothesis that the entire cell culture dispersed in medium was homogenized at each calculation step (cf. [3], where the time step $\Delta t$ was set to 3600 s), or (ii) to observe the changes due to the hydrodynamic mixing and neglect those of biochemical reaction. Both alternatives lose the coupling between transport and reaction phenomena, which qualifies the corresponding modeling framework as unsatisfactory. Our proposition of how to solve the above mentioned difficulties is based on the multi-timescale approach, practically shown in Section 3.

### 2.2 Fluid-Dynamic Model

If we model only the incompressible liquid phase (suspension of water, nutrients and microalgae), then the classical system of Navier-Stokes equations and the continuity equation are used as a fluid-dynamic model

$$\rho\frac{\partial v}{\partial t} + \rho(v\cdot\nabla)v = f - \nabla p + \mu\nabla^2 v, \quad \nabla\cdot v = 0, \tag{2}$$

in $(t_0, T)\times\Omega$ with suitable boundary conditions on $(t_0, T)\times\partial\Omega$ and initial conditions in $\Omega$. Here $v, p, f, \rho$, and $\mu$ denote the fluid velocity, the pressure, the volumetric forces, fluid density, and dynamic viscosity, respectively.

### 2.3 Numerical Aspects of the Solution of PDEs (1-2)

Using a suitable numerical method, the partial differential equations (1-2) can be transformed into a system of linear algebraic equations. In the fluid flow problems, the finite volume approach (FVM) is more popular in obtaining the discretized form of equations than other approaches like finite element (FEM) or finite differences (FDM) method, especially with unstructured grids. The system of discretized equations is usually solved iteratively to find the values of velocities and other scalar quantities like concentrations in all grid points.

When the number of grid points is large, the solution domain can be split into several regions (partitions), solving each of them in parallel to decrease the computational time. One of such methods is the Lattice Boltzmann method (LBM), cf. [4], which provides a superior parallel performance. A good parallel performance of this method can be advantageously employed in GPU computations, cf. [5].

### 2.4 Process Control and Optimization of Design and Operational Variables

Our approach is entirely model-based and rather than on a real-time control is focused on the optimal PBR design and control, which could answer the questions about the optimal PBR performance in the preliminary stage of the PBR design *in silico*. Further we formulate the optimal control & design problem, denoted by $(\mathcal{P})$, with the following elements:

- **Design variables:** Let us suppose the PBR structure is parameterized, i.e. the PBR geometry is determined by $p$ time independent design variables $d = (d_1, ..., d_p)$. These variables must be nonnegative and bounded by a certain maximal admissible value or they must lie in an admissible set: $d \in \mathcal{U}^d_{ad}$.
- **Operational variables (Controls):** Let us suppose the PBR is controlled by means of the operational (generally time dependent) control variables $g(t)$. E.g. for the batch operation mode: incident irradiance $I_0(t)$, a quantity $\omega(t)$ corresponding to the pumping or mixing, the inflow rate of nutrients $S(c_j)$, $j = 1, ..., n$, the initial microbial concentration $c_x(t_0)$ and the total time of cultivation $T$. For the continuous mode: the steady-state microbial concentration $c_x$ and the dilution rate $D$. For technological reasons, some constraints are applied (e.g. nonnegativity and boundedness): $g \in \mathcal{U}^c_{ad}$.
- **State variables:** The state variables $c(x,t) = c_i(x,t)$, $i = 1, ..., m$, are concentrations of some conservative quantities or cell densities. There could be some thresholds or constraints specified by the relation $c \in \mathcal{U}^s_{ad}$.

- **Model parameters:** Although many authors disregard this issue, we have to be aware that not only the optimization but also the parameter estimation and model verification might be unfeasible with increasing model complexity. For instance, the reader is referred to our work [6].
- **Objective function:** Let us suppose, we have only one objective to optimize. For example, we are interested in maximizing biomass production, so we maximize the (averaged) volumetric productivity setting the cost functional $J(d, g)$ as follows:

$$J(d,g) = \frac{1}{\mathrm{meas}(\Omega)\ T} \int_0^T \int_\Omega \mu(x,t)\ c_x(t)\ \mathrm{d}x\mathrm{d}t\ , \tag{3}$$

  where $\mu(x,t)$ is the specific growth rate of the algal biomass, which mainly depends on the irradiance distribution, defined as $\mu := \frac{1}{c_x}\frac{\mathrm{d}c_x}{\mathrm{d}t}$.

Finally, we formulate the optimal control & design problem $(\mathcal{P})$ describing the optimal PBR performance:

$$\max J(d,g) \quad \text{such that} \quad d \in \mathcal{U}_{ad}^d,\ g \in \mathcal{U}_{ad}^c,\ c \in \mathcal{U}_{ad}^s \quad \text{verifies (1-2).} \tag{$\mathcal{P}$}$$

To demonstrate that the problem $(\mathcal{P})$ admits, at least, a solution, and to derive optimality conditions is out of the scope of this paper. For a similar problem see e.g. [2].

## 3 Case Study – Microalgae Growth in CTBR

We present a model of microalgae growth in the Couette-Taylor photobioreactor (CTBR) in this section. CTBR is a special device basically composed from two coaxial rotating cylinders: the inner is rotating and the outer is homogeneously illuminated. The flow regime inside the Couette-Taylor device belongs to the intensively studied topics of mathematical physics since 1923, cf. [7]. Our main interest concerns the Taylor vortex flow, when the so-called Taylor vortices can induce high frequency light-dark cycles regime. We show the positive impact of this hydrodynamically induced light fluctuation on performance index, i.e. we demonstrate that the flashing light effect forms an intrinsic part of the model. Assuming that the whole geometrical design and irradiance distribution are axisymmetrical, we care only about the flow description in the radial direction, i.e. in direction of light gradient. Moreover, if the inner cylinder rotation $\omega$, which induces the flow, is constant, the convective flow in the radial direction can be described by the effective dispersion coefficient $D_{eff}$, and the state system (1) actually changes into the stationary 1D diffusion(dispersion)-reaction PDE, cf. [8]. The reaction model is described in the following subsection.

### 3.1 Model of Photosynthetic Factory – PSF Model

The light inside PBR is the main limiting factor in biotechnological applications. We therefore focus on the case in which microbiological photosynthesis is

light limited only, i.e., $CO_2$ and nutrients abundant environment. Thus we were looking for a model which is able to describe three basic phenomena occurring simultaneously in three largely separated time-scales: (i) cell growth, (ii) photoinhibition, and (iii) photosynthetic light and dark reactions. Therefore, the reaction model has to be "dynamic" and cope with the following experimental observations: (i) the steady-state kinetics (so-called *P–I curve*) is of *Haldane* type or *Substrate inhibition kinetics*; (ii) the "slow" dynamics of the photoinhibition can not be depreciated (it is observable as the so-called afternoon depression on the open ponds, cf. [9]), (iii) the microalgal culture in suspension has the so-called *light integration* property; i.e. as the light/dark cycle frequency is growing, production rate (measuring e.g. *via* oxygen evolution rate) goes to a certain limit value, which depends on the average irradiance only, cf. [10],[11]. All these features are comprised of the **model of photosynthetic factory – PSF** described in detail below.

The state vector $y$ of the PSF model is three dimensional, namely, $y = (y_R, y_A, y_B)^\top$, where $y_R$ represents the probability that PSF is in the resting state $R$, $y_A$ the probability that PSF is in the activated state $A$, and $y_B$ the probability that PSF is in the inhibited state $B$. The possible transitions between states are of zeroth or first order respective to the irradiance $I(t)$:

$$\begin{bmatrix} \dot{y_R} \\ \dot{y_A} \\ \dot{y_B} \end{bmatrix} = \begin{bmatrix} 0 & \gamma & \delta \\ 0 & -\gamma & 0 \\ 0 & 0 & -\delta \end{bmatrix} \begin{bmatrix} y_R \\ y_A \\ y_B \end{bmatrix} + I(t) \begin{bmatrix} -\alpha & 0 & 0 \\ \alpha & -\beta & 0 \\ 0 & \beta & 0 \end{bmatrix} \begin{bmatrix} y_R \\ y_A \\ y_B \end{bmatrix}. \tag{4}$$

For given values of the model parameters $\alpha$, $\beta$, $\gamma$, $\delta$ and the input variable, i.e. the irradiance $I(t)$, the ODE system (4) can be solved either by numerical methods or by asymptotic methods. For the special case of the periodic piecewise constant input, the state trajectories were calculated explicitly in [12].

The PSF model is completed by an equation connecting the hypothetical states of the PSF model with the specific growth rate $\mu$. According to [9],[13], the rate of photosynthetic production is proportional (there is a dimensionless constant $\kappa$) to the number of transitions from the activated to the resting state: $\frac{\mathrm{d}}{\mathrm{d}t} c_x = (\kappa\ \gamma\ y_A(t) - Me)\ c_x$ , where the maintenance term $Me$ corresponds to the energetic requirements for internal metabolism and allows the negative growth (i.e. the decay of cell concentration) rate in light condition below the compensation point. Considering that the value of $\kappa \cdot \gamma$ is of order $10^{-4}$, cf. [13], and $y_A(t)$ is periodic with period $h$ (a quasi steady-state is reached), cf. [12] for more details, we have the following relation for the specific growth rate $\mu$: $\mu = \frac{\kappa\gamma}{h} \int_0^h y_A(t)\mathrm{d}t - Me$ .

The above equation reveals why PSF model can successfully simulate the microalgae growth in high-frequency fluctuating light conditions: the growth is described through the "fast" state $y_A$, hence we reach the sensitivity to high-frequency inputs, see e.g. flashing light experiments [11]. As we know, this highly required sensitivity is not achieved by any other model describing the microalgae growth in PBR.

Now we explain how to introduce the reaction term into the transport equation (1). Let us evaluate the PSF model states as relative concentrations (molar fractions) of microbial cells in each state ($R$, $A$, or $B$). Define the variables $c_i$ as the concentrations of cells in respective states of PSF model, and $c_x$ as an overall microbial cell concentration. The concentrations are generally varying in time and space, so $c_i = c_i(x,t),\ i \in \{R, A, B\}$. Nevertheless it holds that $c_x = c_R + c_A + c_B$. Consequently, we re-define the state vector of PSF model as follows: $y = (y_R, y_A, y_B)^\top := \frac{1}{c_x}\ (c_R, c_A, c_B)^\top$. Furthermore, after dividing (1) by $c$, we can substitute the right hand side of the PSF model equation (4) with the reaction term on the right hand side (where $\mathcal{A}$ and $\mathcal{B}$ stand for the corresponding matrices in (4)) of the following equation:

$$\frac{\partial y}{\partial t} + \nabla \cdot (vy) - \nabla \cdot (D_e \nabla y) = \big[\mathcal{A} + I(x,t)\mathcal{B}\big] y. \tag{5}$$

Equation (5) with suitable initial and boundary conditions represents the PDE based model for describing multi-scale transport and reaction phenomena not only in CTBR but also in a general PBR. To evaluate the spatio-temporal average of specific growth rate in PBR, we use [13] to get

$$\mu = \frac{\kappa\gamma}{\mathrm{meas}(\Omega)\ T} \int_0^T \int_\Omega (y_A(x,t) - Me)\ \mathrm{d}x\mathrm{d}t, \tag{6}$$

which is used for evaluation of the objective function $J$, cf. (3).

### 3.2 Simulation Results and Discussion

For a laboratory bioreactor based on Couette-Taylor flow, and for the long term cultivation of the microalgae culture in continuous mode (we supposed the quasi-steady state is reached), we solve the stationary form of PDEs (1-2). We apply the multi-timescale PSF model to the domain with heterogeneously distributed relevant parameters, being the irradiance $I(x)$, distributed according to the exponential Lambert-Beer law, and hydrodynamic dispersion $D_{eff}(x)$. For the parameter values and more details see [8].

We solve the following boundary value problem with homogeneous Neumann boundary conditions and inhomogeneous right-hand side:

$$-\frac{1}{x}\left[xp(x)y_A'\right]' + Da_{II}\left(\frac{I(x)}{q_1} + q_2\right) y_A = Da_{II}\left(\frac{I(x)}{q_1} + q_2\right) y_{A_{ss}},$$

$$x \in (r_0/R, 1), \quad y_A'(r_0/R) = 0, \quad y_A'(1) = 0, \tag{7}$$

where $r_0$ and $R$ are the inner and outer cylinder radii, respectively, $p(x) := \frac{D_{eff}}{D_0}$, $D_0$ is some characteristic value, units $\left[m^2 s^{-1}\right]$, and $Da_{II} := \frac{q_4\ R^2}{D_0}$ is the so-called *Damköhler number* of second type, which characterizes the ratio of reaction rate and mixing rate (due to the hydrodynamic dispersion). As $Da_{II} > 0$, and the transformed model parameters $q_i > 0,\ i \in \{1, 2, 4\}$, the problem (7) has a

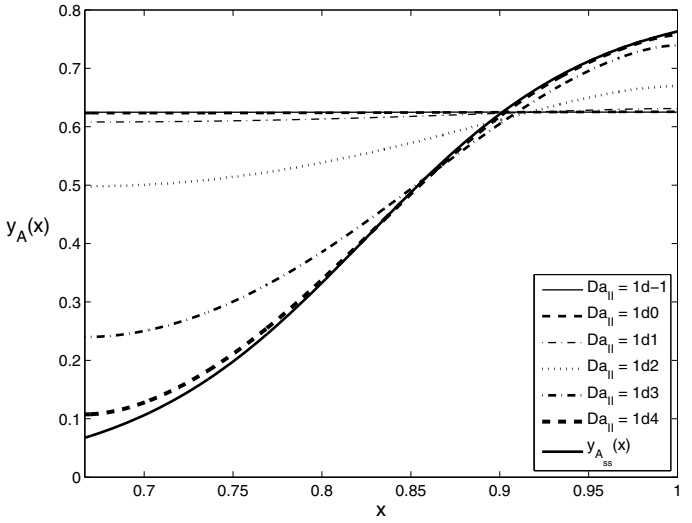


**Fig. 1.** Dependence of the solution of (7) on the radial position in CTBR for different mixing rates (inversely proportional to $Da_{II}$). For the low $Da_{II}$, i.e. high mixing rate, the effect of the heterogeneous light distribution is suppressed.

unique solution. It was solved numerically using the finite difference scheme. Fig. 1 shows the dependence of the solution $y_A(x)$ on the *Damköhler number* $Da_{II}$. We can see that the solution becomes flatter for decreasing $Da_{II}$ and for $Da_{II} = 0.1$ it is nearly constant. It holds that $y_A(x) \to 0.625$ for $Da_{II} \to 0$. Notice also that the value $y_A = 0.625$ corresponds to the value $y_{A_{ss}}(I_{opt})$, cf. [8]. This means that the ODE system (7) performs the "averaging" of $I(x)$ for the case $Da_{II} \to 0$ because the incident irradiance (the irradiance on the outer surface of CTBR) was chosen in such a manner that the average irradiance inside CTBR equals the optimal irradiance $I_{av} = I_{opt}$.

From practical point of view, in order to maximize the specific growth rate, it is important to evaluate the integral average of the activated state $y_A(x)$, being proportional to the performance index $J$. Fig. 2 shows the dependence of $J$ on $Da_{II}$. The maximum value arises for $Da_{II} \to 0$ and its value is again $J = 0.625$. Practically it means to set the mixing rate on its upper bound.[1]

Our results reflect well the dependence of microalgae growth on the *Damköhler number* $Da_{II}$, i.e. on hydrodynamic dispersion permitting the announcement of our statement about light integration property of PSF model for CTBR as well. The resulting photosynthetic production rate in a photo-bioreactor goes (with growing mixing rate) to a certain limit value, which depends on the average irradiance only.

[1] Obviously, there is a known phenomenon called *hydrodynamical shear stress* making the higher mixing or pumping rates prohibitive. By incorporating this effect, e.g. on the $Me$ term, cf. (6), our result would be more realistic.

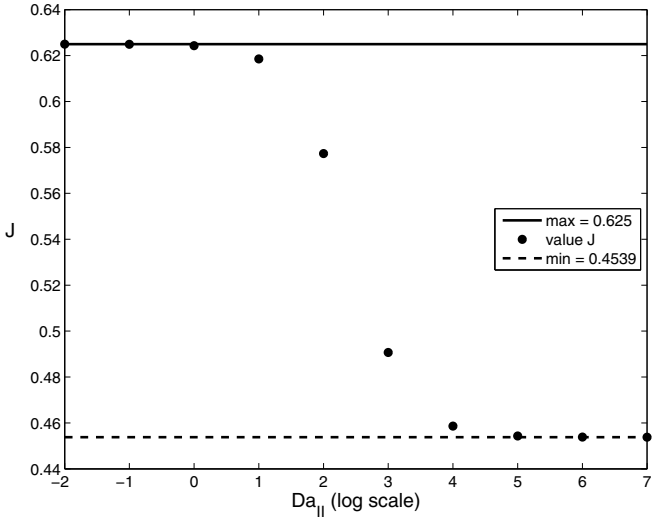


**Fig. 2.** Performance index $J$, cf. (3), vs. $Da_{II}$. The average irradiance in the culture is set to the optimal value $I_{opt}$. Indeed, for $Da_{II} \to 0$ it holds $J \to y_{A_{ss}}(I_{opt}) = 0.625$.

## 4 Conclusions and Future Prospects

The model of photosynthetic factory, introduced in the previous section, is a first approximation how to model a microalgae cell in PBR. It considers a growth rate, i.e., biomass production, but it cannot tell us anything about a particular metabolite, e.g. lipid, which could be interesting as a biofuel. Moreover, it neglects possible subpopulations or complex cellular functions such as metabolic regulation. It is therefore desirable to employ a complex cellular model which could analyze different subpopulations scenarios in the PBR but also provide an answer about how to boost or reduce certain metabolic pathways. There are three ways of incorporating the cellular functions into kinetic model of PBR: reduced model of light photosynthetic reactions, reduced model of carbon metabolism, and model of whole cell. The first two options work with a simplified view of the cell and consider parts of those cellular functions which can be easily measured. There are chlorophyll fluorescence and oxygen evolution in the case of light reactions, both phenomena can be modeled within a single but complex model.

We are developing a multi-scale kinetic model for photosynthetic cyanobacteria, combining various omic data sets (metabolic, transcriptomics, etc.) from different steady and transient states. Such models can explain metabolic regulation such as isozymes, cf. [14], or even predict the cellular concentration of metabolites. Combining the results from the reduced model of algae and advanced model of cyanobacterial cell should allow the development of a complex multi-level kinetic model of algae, integrated into the model of PBR.

**Acknowledgement.** This work was supported by the CENAKVA CZ.1.05/2.1.00/01.0024, by the CENAKVA II (project LO1205 with a financial support from the MEYS under the NPU I program), by the Postdok JU (CZ.1.07/2.3.00/30.0006), by the grant MŠMT MSM 600 766 58 08 of the Ministry of Education, Youth and Sports of the Czech Republic, and by the long-term strategic development financing of the Institute of Computer Science (RVO:67985807).

## References

1. Schugerl, K., Bellgardt, K.: Bioreaction Engineering, Modeling and Control. Springer, Heidelberg (2000)
2. Alvarez-Vázquez, L., Fernández, F.: Optimal control of bioreactor. Applied Mathematics and Computation 216, 2559–2575 (2010)
3. Muller-Feuga, A., Guédes, R.L., Pruvost, J.: Benefits and limitations of modeling for optimization of *Porphyridium cruentum* cultures in an annular photobioreactor. Journal of Biotechnology 103, 153–163 (2003)
4. Succi, S.: The Lattice Boltzmann equation. Oxford University Press (2001)
5. Štumbauer, V., Petera, K., Štys, D.: The lattice Boltzmann method in bioreactor design and simulation. Mathematical and Computer Modelling 57, 1913–1918 (2013)
6. Rehák, B., Čelikovský, S., Papáček, Š.: Model for photosynthesis and photoinhibition: Parameter identification based on the harmonic irradiation $O_2$ response measurement. Joint Special Issue of TAC IEEE and TCAS IEEE, 101–108 (2008)
7. Taylor, G.I.: Stability of a viscous liquid containing between two rotating cylinders. Phil. Trans. Royal Society 223, 289–343 (1923)
8. Papáček, Š., Štumbauer, V., Štys, D., Petera, K., Matonoha, C.: Growth impact of hydrodynamic dispersion in a couette-taylor bioreactor. Mathematical and Computer Modelling 54, 1791–1795 (2011)
9. Eilers, P., Peeters, J.: Dynamic behaviour of a model for photosynthesis and photoinhibition. Ecological Modelling 69, 113–133 (1993)
10. Terry, K.L.: Photosynthesis in modulated light: Quantitative dependence of photosynthetic enhancement on flashing rate. Biotechnology and Bioengineering 28, 988–995 (1986)
11. Nedbal, L., Tichý, V., Xiong, F., Grobbelaar, J.: Microscopic green algae and cyanobacteria in high-frequency intermittent light. J. Appl. Phycol. 8, 325–333 (1996)
12. Papáček, Š., Čelikovský, S., Štys, D., Ruiz-León, J.: Bilinear system as modelling framework for analysis of microalgal growth. Kybernetika 43, 1–20 (2007)
13. Wu, X., Merchuk, J.: A model integrating fluid dynamics in photosynthesis and photoinhibition processes. Chemical Engineering Science 56, 3527–3538 (2001)
14. Jablonský, J., Hagemann, M., Schwarz, D., Wolkenhauer, O.: Phosphoglycerate mutases function as reverse regulated isoenzymes in synechococcus elongatus pcc 7942. PLOS One 8, e58281 (2013)

# Digital Processing of *Toxoplasma gondii* Cysts in Meat Samples for Human Consumption in Colombia

Quiñones Armando and Juez-C Graciela

Research group BIOAXIS, Bioengineering Program, El Bosque University, Bogotá, Colombia
{quinonesarmando,juezgraciela}@unbosque.edu.co

**Abstract.** *Toxoplasma gondii* is an important pathogen of humans and other warm-blooded vertebrate animals. This parasite is clinically important due to the diseases that it may cause on the fetus, namely chorioretinitis, microcephaly, hydrocephaly, mental retardation and hepatosplenomegaly, among others. The parasite affects also immunocompromised patients that suffer from any type of cancer, organ transplantations and HIV, reactivating the infection. Zoonosis in Colombia is an issue of high epidemiological importance due to the transmission of pathogens. A deeper study on toxoplasmosis requires the analysis of the developmental stages of the parasite, including the cyst, which allows it to evade the immune system and to get established in the host organism permanently. The goal of this work was to develop a digital image processing algorithm based on texture recognition to allow automatic detection of the cysts associated to pathogen *T. gondii* from isolated Colombian native strains from meat samples for human consumption, using computational software Matlab 2013, specifically through the Image Processing Toolbox.

**Keywords:** *Toxoplasma gondii*, Eccentricity, Co-ocurrence.

## 1 Introduction

Toxoplasma gondii is an intracellular parasite member of the phylum Apicomplexa. It is an important pathogen in a variety of animals including humans. Infection in intermediate hosts, including humans, occurs through different ways; namely transmission from mother to fetus through the placenta, transmission of tachyzoites in organ transplantation, ingestion of bradyzoites or tachyzoites directly present in undercooked meat [1], and ingestion of oocysts present in water for human consumption [2].

This parasite is of widespread clinical importance due to the diseases caused on the fetus. A number of clinical studies suggest there are different clinical manifestations that may occur in individuals with congenital toxoplasmosis, including chorioretinitis, microcephaly, hydrocephalus, encephalitis, mental retardation, hepatosplenomegaly, eritroblastocis, among others [3]. Furthermore, this pathogen may generate opportunistic infection in immunocompromised patients with any type of cancer [4] or



A. Sanayei et al. (eds.), *ISCS 2014: Interdisciplinary Symposium on Complex Systems*,
Emergence, Complexity and Computation 14, DOI: 10.1007/978-3-319-10759-2_30

organ transplantation [3]; additionally, people with HIV are extremely vulnerable to the development of toxoplasmic encephalitis [5]. Consequently, about 30 to 50% of people with HIV who have had chronic infection with *T. gondii* have developed toxoplasmic encephalitis; also, during pregnancy, there is some probability that acute infections with *T. gondii* lead to congenital diseases [6]. Moreover, seropositivity of *T.* gondii has been associated with the manifestation of other chronic infections such as chronic hepatitis B, diabetes mellitus, neoplasms, schizophrenia and arthritis [7]. *T. gondii* strongly predominates because of its powerful interconversion features, which endow it with the ability to resist the immune system effectively. This parasite has a very complex life cycle that includes sexual and asexual stages that depend on its biological development. The sexual cycle occurs only in the intestine of cats that are the definitive hosts [8].

Unlike the sexual cycle, the asexual cycle can occur in most types of the intermediate hosts [9]. When the host develops immunity, the amount of free tachyzoites decreases and their intracellular multiplication slows down. Within a few weeks, by interconversion, the tachyzoites (i.e. proliferative phase or acute phase of the parasite) become bradyzoites (i.e. move into their chronic phase), which ultimately forms the actual tissue cysts. These cysts grow in some tissues, especially in the brain, protecting the parasites against the immune response of the host cell [8].

Undoubtedly, one of the most complex survival strategies of this parasite is its ability to take advantage of immunosuppressed hosts and reactivate the infection, causing potentially fatal encephalitis [9]. The increased interest on the consequences of immunodeficiency has led several researchers to focus on the recrudescence of toxoplasmosis; for example, in immunocompromised individuals infected with HIV, the bradyzoites found in tissues may differentiate into tachyzoites, which generates abscesses in the brain, leading to fatal problems for patients [5]. This cyst stage of *T. gondii* has not been exhaustively characterized, which encourages researchers to continue studying the mechanisms that allow the parasite to stay in the host cell for months, years, and even lifetime [10].

Studying such mechanisms represents an important contribution in the knowledge of Toxoplasma-associated infections and will surely provide a better understanding of each of the events involved in the pathogenesis of toxoplasmosis. The goal of this work was to develop a digital image processing algorithm based on texture recognition to allow automatic detection of cysts of *T. gondii,* which have been isolated from Colombian native strains, obtained from mouse brain tissue, which were previously inoculated with samples of heart and tongue of porks for human consumption. The mathematical algorithm was developed using specific stages computational software Matlab 2013, specifically through the Image Processing Toolbox, which allowed segmenting these images, highlighting typical features of the cysts and calculating its eccentricity as a circularity criterion.

## 2 Materials and Methods

The development of *T. gondii* cysts was studied on mouse brain tissue infected with avirulent strain JUEZ1. The samples were isolated cuts of pork for human consumption ready to eat by Colombian population. To detect cysts of the parasite, heart tissue and tongue of pork were isolated, these samples were processed and then inoculated into mice for to allow development the parasite. Then the mice were sacrificed by isolating the brain tissue in which molecular processes and histochemical staining were carried out, that allowed the visualization of *T. gondii* cysts, obtaining images and subsequent detection by the mathematical algorithm.

The histochemical analysis were performed with Periodic-Acid-Schiff (PAS) and Giemsa reagents. Visualization was performed at different scales using a Carl Zeiss 37081 AX10sKop 40 microscope, obtaining images directly from a Nikon Carl Zeiss SONY DSC-S85 (4.1 Mega pixels CCD 6x zoom) camera. Histological procedures were conducted in the laboratories of BBMP (Parasite Biochemistry and Molecular Biology) at Universidad de Los Andes, Bogotá, Col.

### Algorithm

To carry out the analysis of *T. gondii* cysts, images were processed using specific stages (Fig. 1) of a computational software tool (Matlab 2013), specifically through an Image Processing Toolbox that allowed segmenting the images as well as highlighting typical features of the cysts and calculating their eccentricity according to a circularity criterion. Qualitative image analysis was performed using uniform distribution histograms (Fig. 2) and conversion to grayscale histogram equalization. A segmentation process allowed information removal using a threshold area as a parameter. Features such as circularity and eccentricity were extracted of cyst images (Fig. 3). Finally, through a co-occurrence matrix (Formulas 1, 2), texture analysis was carried out using the homogeneity index (Formula 3) as a fundamental parameter that provides information of the local regularity of the texture (Fig. 5), also detecting the cyst itself (Fig. 4 A, B, C).

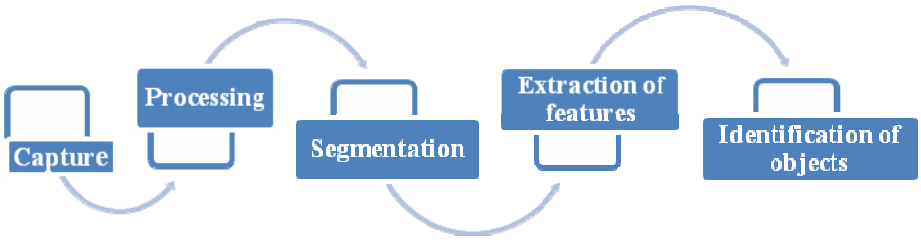


**Fig. 1.** Flowchart of the stages of cyst image processing

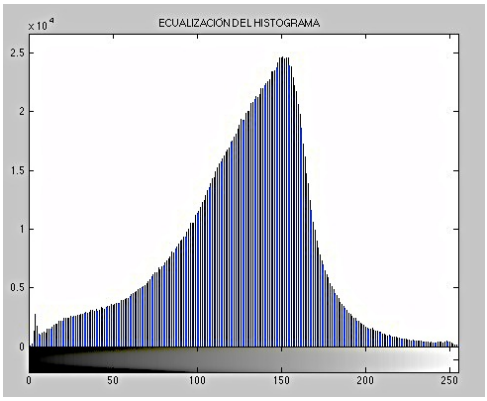


**Fig. 2.** Preprocessing of cyst images. Matlab 2013.

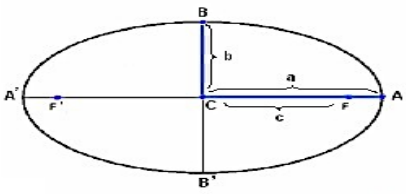


Elementos de una elipse: Semieje mayor $\overline{CA} = a$, semieje menor $\overline{CB} = b$ y la distancia focal $\overline{CF} = c$.

$$e = \frac{c}{a}$$

- $a \geq c$ y por lo tanto el valor de $e$ oscila entre 0 - 1.
- Cuando la e = 0, tenemos el caso de a = b y por lo tanto es un circunferencia (*figura 6.3.2*).
- Si e = 1, semieje mayor coincide con la distancia focal y el semieje menor es igual a 0. Será el caso de un segmento de recta (*figura 6.3.3*).

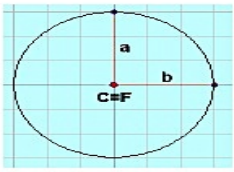


Circunferencia a=b y C=F.

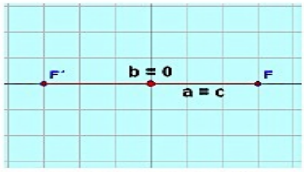


Segmento de Recta a=c y b=0.

**Fig. 3.** Segmentation process. Circularity and Eccentricity. Matlab 2013.

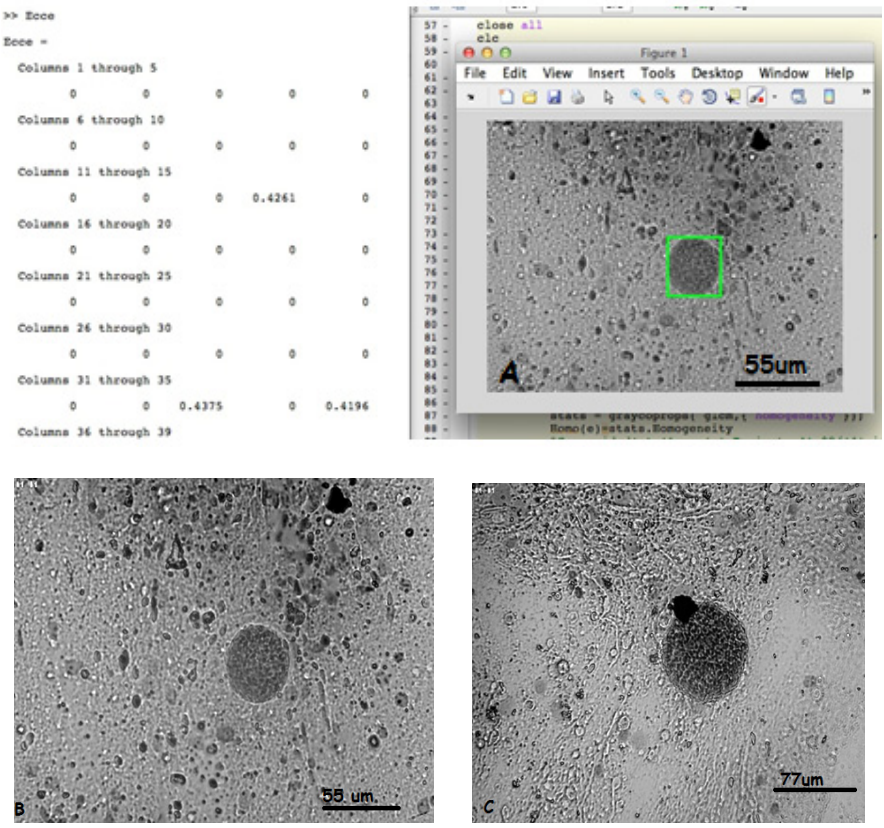


**Fig. 4.** Texture and Homogeneity of image. Matlab 2013. Cysts of *Toxoplasma gondii.* Colombian native Strain JUEZ1. Giemsa staining, mouse brain tissue with eight-month infection. Cyst of 55um in diameter, 100x (A,B). Cyst of 77um in diameter, 100x (C). Carl Zeiss 37081 AX10sKop 40 Microscope.

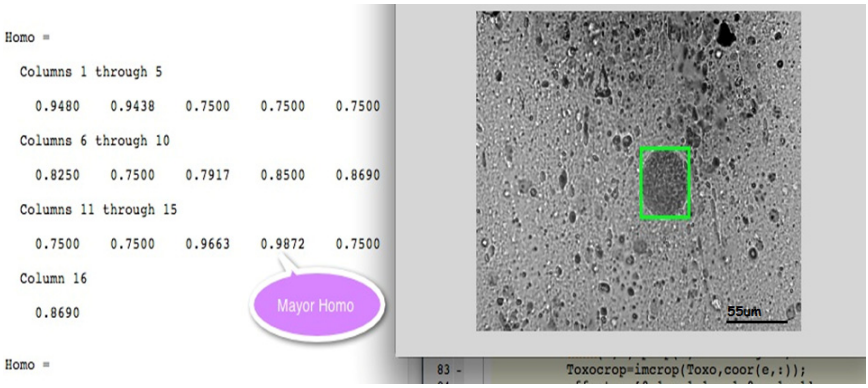


**Fig. 5.** Parameters of homogeneity of cyst image. Matlab 2013.

**Co-occurrence Matrix**

$$C(l,m|\Delta i,\Delta j) = \text{ocurrencia}\ \{I(i,j)=l \text{ and } I(i+\Delta i,j+\Delta j)=m\} + \text{ocurrencia}\ \{I(i,j)=l \text{ and } I(i-\Delta i,j-\Delta j)=m\} \quad (1)$$

$$N_d[i,j] = \frac{C_d[i,j]}{\sum_i \sum +jC_d[i,j]} \quad (2)$$

**Homogeneity**

$$Homogeneity = \sum_i \sum_f = \frac{C_{if}}{1+(i+j)^2} \quad (3)$$

**The Performance Indices of the Algorithm Are as Follows:**

$$\text{Classification accuracy} = \frac{Number\ of\ events\ correctly\ classifield}{Total\ number\ of\ events} = \frac{60}{60} = 1 \quad (4)$$

$$\text{Sensitivity} = \frac{True\ positives}{True\ positives + False\ negatives} = \frac{40}{40+0} = 1 \quad (5)$$

$$\text{Specificity} = \frac{True\ negatives}{True\ negatives + False\ positives} = \frac{20}{20+0} = 1 \quad (6)$$

$$Error = \frac{Falsenegatives + Falsepositives}{Truenegatives + Trupositives} = \frac{0}{60} = 0 \quad (7)$$

## 3 Results

For the detection of *T. gondii* (Fig. 6 A, B, C, D) in cysts images, the algorithm of automatic detection is mainly based on two metrics: namely an index of circularity, which initially allowed the differentiation of forms or organelles present in the image, and a texture analysis, whose parameter was homogeneity (understood as the way local regularity of the intensity of pixels in the area of the detected circle is distributed). The circularity index makes use of a threshold, considering the images that exist within various cellular structures that are similar to those of circular-shapeed cysts. This indicates that the threshold rule allowed discrimination of all those circular shapes that had a circular area below the threshold. Applying this digital image processing algorithm to microscopic optical images of the avirulent Colombian native JUEZ1 strain cysts of *T. gondii*, automatic detection was achieved (Figs. 6 A, B, C, D). Thus it can be stated that the algorithm proved highly sensitive and reliable as a computational tool, also capable of accelerating the detection and counting processes of cysts of *T. gondii* in biological samples.

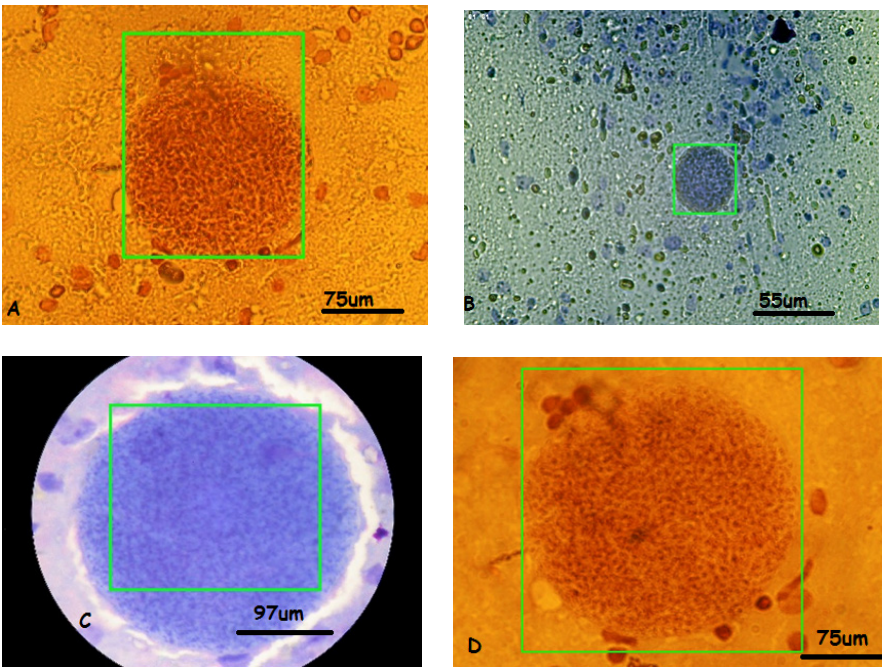


**Fig. 6.** Image processing with Matlab 2013. Cysts of *Toxoplasma gondii of* Colombian native Strain JUEZ1. Giemsa staining, mouse brain tissue with eight-month infection. Cyst of 75um in diameter, 1000x (A). Cyst of 55um in diameter, 100x (B). Cyst of 97um in diameter, 1000x (C). Cyst of 75um in diameter, 1000x (D). Carl Zeiss 37081 AX10sKop 40 Microscope.

## 4 Conclusions

The algorithm was tested with 60 images with the presence of cysts of *Toxoplasma gondii*, already identified. The results show high sensitivity and specificity (i.e. small error) as shown in formula 7. Applying this digital image processing algorithm to microscopic optical images of the avirulent Colombian native JUEZ1 strain, cysts of *T. gondii* were automatically detected, thus it can be stated that the algorithm proved highly sensitive and reliable as a computational tool, also capable of accelerating the detection and counting processes of cysts of *T. gondii* in a biological sample.

This work provides a computational tool to deepen the study on toxoplasmosis in Colombia through the automation, unbiased detection and quantification of *T. gondii* cysts in biological samples. Future work shoukd continue with the analysis of a wide range of images in order to validate the efficiency of the algorithm.

**Acknowledgment.** Barbara H. Zimmermann, Head of BBMP research group at Universidad de Los Andes. Juan Miguel Escobar, Head of the Bioengineering program at Universidad El Bosque.

## References

1. Tenter, A.M., Heckeroth, A.R., Weiss, L.M.: Toxoplasma gondii: from animals to humans. Int. J. Parasitol. 31(2), 217–220 (2001)
2. Aubert, D., Villena, I.: Detection of Toxoplasma gondiioocysts in water: proposition of a strategy and evaluation in Champagne-Ardenne Region, France. Mem. Inst. Oswaldo Cruz 104(2), 290–295 (2009)
3. Derouin, F., Pelloux, H.: Prevention of toxoplasmosis in transplants patients. Clin. Microbiol. Infect. 14(12), 1089–1101 (2008)
4. Yuan, Z., Gao, S., Liu, Q., Xia, X., Liu, X., Liu, B., Hu, R.: Toxoplasma gondii antibodies in cáncer patients. Cancer Lett. 254(1), 71–74 (2007)
5. Israelski, D.M., Remington, J.S.: Toxoplasmic encephalitis in AIDS. Clin. Infect. Dis. 15(2), 211–222 (1992)
6. Sibley, L.D., Boothroyd, J.C.: Virulent strains of Toxoplasma gondiicomprise a single clonal lineage. Nature 359(6390), 82–85 (1992)
7. Shin, D.W., Cha, D.Y., Hua, Q.J., Cha, G.H., Lee, Y.H.: Seroprevalence of Toxoplasma gondii infection and characteristics of seropositive patients in general hospitals in Daejeon, Korea. Korean J. Parasitol. 47(2), 125–130 (2009)
8. Dubey, J.P., Lindsay, D.S., Speer, C.A.: Structures of Toxoplasma gondii Tachyzoites, Bradyzoites, and Sporozoites and Biology and Development of Tissue Cysts. Clinical Microbiology Reviews 11, 267–299 (1998)
9. Manger, I.D., Hehl, A., Parmley, S., Sibley, L.D., Marra, M., Hillier, L., Waterston, R., Boothroyd, J.C.: Expressed sequence tag analysis of the bradyzoite stage of Toxoplasma gondii: identification of developmentally regulate genes. Infect. Immun. 66(4), 1632–1637 (1998)
10. Weiss, L.M., Kim, K.: The development and biology of bradyzoites of Toxoplasma gondii. Front Biosci. 1(5), 391–405 (2000)

# Modeling of Tumour Growth Induced by Circadian Rhythm Disruption in Epithelial Tissue

Dmitry Bratsun[1], Andrey Zakharov[1], and Len Pismen[2]

[1] Theoretical Physics Department, Perm State Humanitarian Pedagogical University, 614990, Perm, Russia
dmitribratsun@rambler.ru, az1211@mail.ru
[2] Department of Chemical Engineering, Technion - Israel Institute of Technology, 32000, Haifa, Israel
pismen@technion.ac.il

**Abstract.** We propose a multiscale model of cancer tumour growth in a quasi epithelial tissue. Basic model of the epithelium growth describes the appearance of intensive movement and growth of tissue via mechanisms of division and intercalation of cells. It is assumed that the movement of cells is caused by the wave of mitogen-activated protein kinase (MAPK), which in turn activated by the chemo-mechanical signal propagating along tissue due to its local damage. It is assumed also that cancer cells can arise from local failure of a spatial synchronization of circadian rhythms. We hope that the subsequent study of the dynamic properties of the model could determine the relationship between the occurrence of the cancer cells and development of the entire tissue coordinating its evolution through the exchange of chemical and mechanical signals.

**Keywords:** cancer modeling, circadian rhythms, gene regulation, signaling, time-delay, complexity in biology.

## 1 Introduction

Cancer modeling has, over the years, grown immensely as one of the challenging topics involving applied mathematicians, physicists working with researchers active in the biological sciences. The natural motivation is not only scientific as the cancer has now become the most common cause of death [1] .

One of the main problems of mathematical modeling of cancer (as, indeed, any biological system) is the multiscale nature of this phenomenon [2]. The characterization of the system suggests the identification of three natural scales which are also connected to different stages of the disease: processes on the cellular scale are triggered by signals stemming from the sub-cellular level and have an impact on the macroscopic scale, i.e. on the organism, when tumours grow and spread. Let us consider some of the approaches to modeling. At the cellular scale a system of coupled ODEs can be used to model large systems of cell populations, where each variable corresponds to a well-defined biological



A. Sanayei et al. (eds.), *ISCS 2014: Interdisciplinary Symposium on Complex Systems*, Emergence, Complexity and Computation 14, DOI: 10.1007/978-3-319-10759-2_31

property characteristic of all cells of the same population. The paper [3] seems to be first to initiate a systematic development of population dynamics models focused on cancer. This approach has been developed by various authors toward accounting for more fine effects (see, for example, survey [4]). The advantage of the above approach is that models are easily tractable, allowing a relatively rapid identification of the parameters, but it omits potentially important phenomena, such as spatial aspects, and heterogeneity among cells. Another type of modeling, when in addition to population dynamics enter certain variables determining the average structure of a population of cancer cells (for example, age of cells) can be attributed to semi-phenomenological models with internal structure [5].

A large body of literature has been devoted to models which link the cellular scale to the macroscopic tissue scale [2]. In this way, models can address how changes in cell-cell interactions affect the macroscopic properties of the tumour. The most common approach here - the tumour is considered as a continuous medium. As a rule, the PDEs system include the mass balance equation for the cellular medium and of reaction-diffusion equations, which describes the field of chemical signals exchanged between cells. Such models can be attributed to the phenomenological ones with all the evident disadvantages that inherent to them. For example, in [6], the tumour is considered as a solid matrix of the porous medium, which interacts with saturating its cellular liquid of normal cells. Thus, the authors can describe some spatial features of real tumours.

A more effective trend seems to be discrete simulations. Unlike continuum models, discrete models have the ability to track the behaviour of single cells. Due to advances in biotechnologies, there is an increasing amount of experimental data available at a single cell level which merit inclusion in mathematical models. Here one can find models based on cellular automata [7] or random walk cells [8]. In addition, hybrid models began to appear, which include continuous medium approach and the discrete nature of the tumour. There is a large group of models dealing with the interaction at the sub-cellular and cellular level [2]. It is motivated by the fact that the whole system is driven, to some extent, by genetic mutations. For example, the paper [9] addresses the issue as too strong expression of certain genes can lead to malfunction of the cells, i.e. make it a cancer cell. Here one can use a popular approach of the stochastic description of the processes of gene regulation [10]. The weak point of this simulation is that the process of formation of the tumour remains outside the model.

Since the cancer is multiscale phenomenon, the most realistic approach to modeling requires consideration in the model processes at all levels of description. Due to the difficulties of this approach, there are not so many attempts to do it. One of the first attempt to implement it is commonly referred to [11]. Authors have applied a hybrid approach, including calculation of cellular automata whose state is determined by a continuous distribution of oxygen around the blood vessel near the origin of the tumour. In another remarkable work [12] the authors examined the spherically growing tumour, which included lattice-model of discrete cells. The system of the ODEs describing the processes of a gene

regulation have been used separately for each cell in the population. Cells can mechanically interact with each other through the lattice gas.

Thus, we can conclude that any realistic modeling of tumour growth involves the development of a dynamic model of interaction of a large number of cells [13]. This model must take into account the physical properties of individual cells in the ensemble: to describe a dynamically changing volume and surface of cells, its elasticity with respect to external mechanical impacts, the ability to move, divide, etc. These processes must be influenced by the exchange between the cells of various signals. The signals should be generated at the sub-cellular level (transcription/translations) or macroscopic level (collective behaviour). Therefore, the model should be a combination of a discrete system with individual cell dynamics and continuous medium chemical fields that are common to the whole ensemble. The development of such models of complex systems is not trivial. But the progress in this area over the last ten years and the simultaneous breakthrough in the computer technology currently brought researchers to the possibility of full realistic simulation of functioning of a living tissue.

In this paper we use the model of the growing epithelium, we have proposed previously [14,15]. This model meets all the above criteria: it includes the cellular level (division, proliferation and shape change of each cell under external pressure of a whole ensemble), the level of the gene (the molecular dynamics of MAPK), as well as the macroscopic level of the ensemble of cells (the collective behaviour via polarization mechanism). This model seems to be the most realistic model of a cellular tissue reported in the literature. Although the epithelium is a quasi-2D medium, the model can be easily generalized to the case of 3D tissue. In numerical calculations [15], the number of cells reached several thousands. But the calculation of larger systems is limited only by the power of the computer.

The main idea of this work is that a tumour occurrence driven by the circadian rhythm disruption in the epithelial tissue. It has been recognized in recent years that core circadian genes seem to be important in tissue homeostasis and tumorigenesis. Many studies have shown that circadian clock gene deregulation is implicated in the development of cancer and other diseases [16,17]. Circadian rhythms are biological rhythms that are common to almost all living organisms. Timing of circadian clocks is established in a cell-autonomous manner by a self-sustaining molecular oscillator that consists of intertwined negative and positive transcription/translation-based feedback loops. We have supplemented the epithelium model [15] by sub-cellular dynamic model of circadian rhythms proposed in our previous paper [18], where the time-delay effect of protein synthesis reactions in the transcription and translation processes of genes is the key element of oscillations mechanism. In addition, we have developed the simple phenomenological model of the cell differentiation.

## 2 Cellular Model of Epithelial Tissue

Epithelial tissue is a layer of cells covering the surface of an organ or body. Thus, one may use only quasi-two-dimensional system in modeling the epithelium behaviour, that makes the calculations easier. The model suggested in [15]

includes the calculation of separate cells dynamics, which are presented in the form of polygons. The initial configuration is a regular hexagonal lattice. In the course of spreading, it becomes distorted and incorporates also polygons with a different number of vertices due to cell division and proliferation. Generally, the system has been dimensioned in such a way, as hexagonal cell is the most probable form of a cell. The cells are closely located to each other forming solid two-dimensional epithelial surface (Fig.1).

The model has a set of properties, which are suitable to simulate the real features of the epithelium:

- possibility to change the cell's size in the process of tissue evolution and to change the local mechanical properties of environment;
- possibility for the total number of cells to spread by their division;
- possibility for the cells to move by the mechanism of intercalation;
- the calculation of the dynamics of concentration, which participate in the regulation of tissues activities;
- exchange of chemical signals between the neighbouring cells through common border (Fig.1);
- effect of cells polarization, which occurs under the external conditions.

To describe the model in more detail, we define the elastic potential energy $E$ of the tissue by summing up the contributions of the perimeter $L$ and the area $A$ of each cell:

$$E = \frac{1}{2} \sum_{cells} \left( \mu L^2 + \eta (A - A_0)^2 \right), \tag{1}$$

where $\mu$ is attributed to the action of active contractile forces within the cell cortex, $\eta$ is an elastic constant that reflects resistance to stretching or compressing the cell vertically when its area decreases or increases at conserved volume, and $A_0$ is the reference cell area.

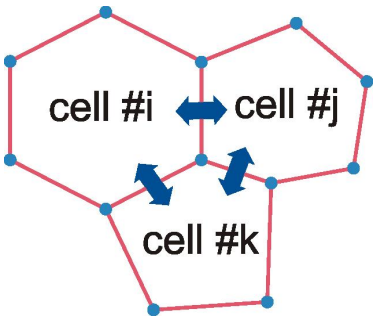


**Fig. 1.** Elements of the chemo-mechanical model of an epithelial tissue

The tissue is evolved by moving the cell nodes (Fig.1). The mechanical force acting on any $j$th node is defined as the derivative of the potential energy with respect to the node position $\mathbf{R}_j$ :

$$\mathbf{F}^j_{mech} = -\frac{\partial E}{\partial \mathbf{R}_j}. \tag{2}$$

The crucial ingredient of the model is the active force [15]. For any $j$th cell, the active force is directed along the polarization vector $\mathbf{P}_j$ and is dependent on the local MAPK concentration $M_j$. We assume that the cells polarize under the influence of the active force exerted by adjacent cells, which reflects cell

interaction through adherens junctions and ensures coherence of motion. Accordingly, the active force is computed as the average over adjacent cells:

$$\mathbf{F}^j_{act} = \langle M_k \mathbf{P}_k \rangle_{k \in adj(j)} . \tag{3}$$

Then we write the dynamic equation of the polarization vector as

$$\frac{d\mathbf{P}_j}{dt} = D_p \left( \kappa \mathbf{F}^j_{act} + \mathbf{F}_{st} \right) - \beta_p \mathbf{P}_j, \tag{4}$$

where $D_p$ is the polarization mobility coefficient, $\kappa$ is the polarization diffusivity, $\beta_p$ is the linear polarization decay and $\mathbf{F}_{st}$ is an uncorrelated zero mean stochastic input. Since the motion is strongly overdamped, the appropriate equation governing the displacement velocities $\mathbf{V}_i$ should be based on Aristotelean rather than Newtonian dynamics, having the form similar to the Darcy law with the mobility coefficient $K$. We also introduce a threshold force $F_0$ below which the node remains immobile:

$$\mathbf{V}_i = \frac{d\mathbf{R}_i}{dt} = KH \left( |\mathbf{F}^i_{mech} + \mathbf{F}^i_{act}| - F_0 \right) (\mathbf{F}^i_{mech} + \mathbf{F}^i_{act}), \tag{5}$$

where $H$ is the Heaviside step function. Although the mobility should be generally anisotropic in a polarizable medium, we assume $K$ to be scalar, both for simplicity and due to the lack of data. Generally, the equations (1-2,4-5) define the dynamics of the tissue on the cellular level. The active force (3) links the cellular scale to the macroscopic tissue scale.

Let us discuss now the gene level. MAPK activation, caused by either chemical or mechanical signaling, plays a crucial role in cell spreading, as indicated by suppression of spreading by MAPK inhibition [19]. Although the mechanism of MAPK action remains so far unclear, it is reasonable to assume that it enables active traction, as implied in Eq. (3). The experiment suggests that MAPK can be activated both chemically and mechanically. We assume that the MAPK level is driven by both the injury signal $C$ and strain $\sigma = A - A_0$, defined as the change of the cell area relative to the reference value $A_0$. The dynamic equation of the activated MAPK concentration in a $i$th cell is written as

$$\tau_0 \frac{dM_i}{dt} = C_i + \frac{aH(\sigma_i)\sigma_i}{1 + b\sigma_i} - \beta_m M_i, \tag{6}$$

where the MAPK activation is assumed to be linear in the signal concentration, $\beta_m$ is the linear decay coefficient and $\tau_0$ is the capacity constant. The mechanically induced activation is supposed to occur under extension only.

It is assumed that the signaling species is transported diffusively from one cell to the other, whereas its flux does not depend on the distance between the two cells $i$ and $j$ but is proportional to the boundary length $L_{ij}$. This implies that the transport is limited by the transfer though cell membranes. Allowing for a linear decay with the coefficient $\beta_c$, we write the equation for the signal concentration in a $j$th cell as

$$\frac{dC_j}{dt} = \sum_{i \in adj(j)} \alpha L_{ij} (C_i - C_j) - \beta_c C_j, \tag{7}$$

where $\alpha$ is the transfer coefficient. The link between sub-cellular and macroscopic scales is established through the Eq. (7), since the field of the activator $C$ is global for the whole tissue.

## 3 Submodel of Circadian Rhythms

To describe the circadian rhythms in cells we use the dynamic model proposed in [18]. The model is rather general by nature, although it was originally suggested to describe the circadian rhythms of the organism *Neurospora crassa*. The time-delay effect of protein synthesis reactions in the transcription and translation processes of genes is the key element of oscillations mechanism (Fig.2). In fact, the time delay in the processes of transcription/translation is, perhaps, the easiest source of oscillations in the genetic systems [20]. These processes are both very slow and consist of multistage biochemical reactions involving the sequential assembly of long molecules. Thus, these processes are long in time and particularly time-delayed. It is evident that the delay prevents the system from achieving equilibrium, and results instead in the familiar limit cycle oscillations.

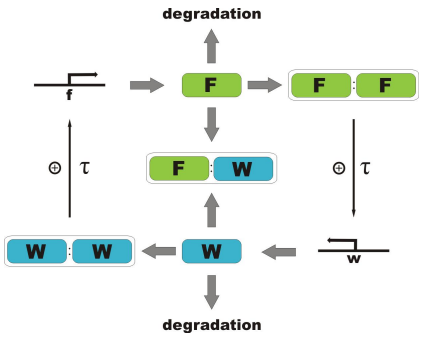


**Fig. 2.** Network architecture of the circadian rhythm molecular components [18]

We have shown in [13,18] that the primary set of biochemical reactions reflecting the molecular components of bioclocks can be reduced to the following two-variable discrete reaction-diffusion system for $i$th cell:

$$\frac{dF_i}{dt} = \frac{1}{(1+4K_1^F F_i)}\left(k_F \frac{K_1^W K_2^F W_i^2(t-\tau)}{1+K_1^W K_2^F W_i^2(t-\tau)} - B_F F_i - kF_i W_i\right) + \\ + \sum_{j\in adj(i)} \alpha L_{ij}(F_j - F_i), \tag{8}$$

$$\frac{dW_i}{dt} = \frac{1}{(1+4K_1^W W_i)}\left(k_W \frac{K_1^F K_2^W F_i^2(t-\tau)}{1+K_1^F K_2^W F_i^2(t-\tau)} - B_W W_i - kF_i W_i\right), \tag{9}$$

where $F$ and $W$ stand for number of isolated monomers of two proteins responsible for the circadian rhythms [18]. The core of the model describing the temporal behavior of the system is based on the interplay between two dynamical variables, concentrations of the $F$ and $W$ proteins, where the synthesis of both proteins is delayed in time. For the sake of simplicity we have not introduced a separate type of protein transporting the circadian signal outside the cell. This means that the synthesis of the transport protein occurs relatively quickly compared with the characteristic period of the circadian rhythm. This assumption

is justified, since the transcription of circadian genes usually a lengthy process. In the suggested model the transportation function is performed by the same protein $F$ (8). Its partner, protein $W$, may move only inside the cell space. The term responsible for the cell-to-cell signaling in Eq.8 is written similarly as it was in (7). Notice that after the division of a cell, the daughter cells inherit the phase of the circadian rhythm of the parent cell.

Spatio-temporal dynamics of the system (8-9) has been studied in [13,18]. We found the effect of clustering of cells [13] and different wave patterns [18].

## 4 Submodel of Differentiation of Cells

As already mentioned above, core circadian genes seem to be important in tissue homeostasis and tumorigenesis. Molecular mechanisms of generation of circadian rhythms organize a biochemical network in suprachiasmatic nucleus and peripheral tissues, building cell autonomous clock pacemakers. Rhythmicity is observed in transcriptional expression of a wide range of clock-controlled genes that regulate a variety of normal cell functions, such as cell division and proliferation. Desynchrony of this rhythmicity seems to be implicated in several pathologic conditions, including tumorigenesis and progression of cancer. There is more and more increasing evidence that links dysfunction of the clockwork with the pathogenesis of cancer [16,17].

Since the exact mechanism linking the circadian oscillations and cancer is unknown, we propose a simple phenomenological model. The basic idea of the mechanism of differentiation is a local oscillation phase failure in the common field of spatial synchronized circadian rhythms in the epithelial tissue.

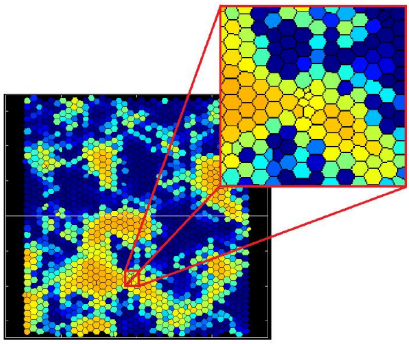

**Fig. 3.** Clustering of circadian rhythms: oscillations of the $F$ protein in the epithelium

The preliminary numerical simulations have shown that in the case of a large amount of cells a complete synchronization, meaning total alignment of the oscillation phases in all cells cannot be achieved. Instead here the macroscopic effect of clustering is revealed: the cells develop two approximately equal communities, which collectively oscillate in anti-phase (Fig.3). These two groups are separated by a thin layer of cells oscillating with the intermediate values of phase. Let us introduce the local value of the phase difference of the circadian rhythm of $j$th cell with respect to the adjacent cells:

$$\Phi_j = \langle |\phi_j - \phi_k| \rangle_{k \in adj(j)} , \tag{10}$$

where $\phi$ is the oscillation phase. If the cell is in a fully synchronized field, the value of $\Phi$, obviously, will be zero, since the cell oscillation phase will not differ

from the oscillation phase of neighbors. On the other hand, the dephasing (10) grows near the boundary of the clusters (Fig.3). The maximum value of the dephasing would occur in case of an isolated cell inside the phase cluster (there are several such cells in Fig.3). According to our hypothesis, this cell is most at risk to differentiate into cancerous state. Then, the dynamic equation for the state of $j$th cell can be written as

$$\frac{dX_i}{dt} = -\lambda X_i(1 - X_i)(A - X_i) + \Phi_i \xi_i(t), \tag{11}$$

where $X$ is the state function, $\lambda$ is the damping parameter, $\xi(t)$ is a noise term with the amplitude depending on the dephase value. Without the noise Eq.(11) has two stable stationary solutions: $X = 0$ stands for the normal state of the cell, $X = 1$ is responsible for the cancer state. The parameters of the model are calibrated so that the differentiation would occur under the influence of noise, but only at a high value of the dephasing (Fig.4), and the reverse transition of already differentiated cell is not possible in principle.

As it known, while the normal cells stop division in the presence of genetic damage, the cancer cells continue to divide. The results of this are daughter cells that contain abnormal DNA. Continued cell division leads to the formation of a tumour. In order to model this transition, the set of parameters that determine the physical and chemo-mechanical properties ($\eta$, $A_0$) and parameters of cell functioning (for example, a rate of cell division) of cancer cells has been changed after the differentiation. Thus, it is formed a separate species of cells that constitute their own medium (tumour).

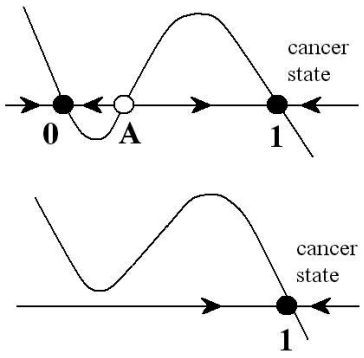


**Fig. 4.** Phase portrait of the system (11) without the noise (top) and under non-zero stochastic input (bottom)

## 5 Numerical Simulations

The model equations contain a large number of parameters; their values are mostly not known from independent measurements but only their relative values are essential. In our computations, we adopt the values in the ranges making the simulation results qualitatively compatible with the experimental observations (where it is possible). The typical values of the parameters are given in Table 1.

The typical result of numerical simulation is presented in Fig.5. One can see that the size and shape of the cells differentiated into the cancerous state differ from the normal members of the community. Cancer cells are approximately twice as large and irregular in a shape. The normal healthy cells that border on the cancer cells are experiencing the significant stress: they are squeezed and

**Table 1.** List of principal parameters

Mechanical Properties and Polarization

| $\mu$ | $\eta$ | $K$ | $F_0$ | $A_0$(norm.) | $D$ | $\beta_p$ | $\kappa$ | $A_0$(cancer) |
|---|---|---|---|---|---|---|---|---|
| 1.0 | 1.0 | 1.0 | 0.02 | $3\sqrt{3}/2$ | 0.4 | 1.0 | 0.1 | $9\sqrt{3}/4$ |

Signal and MAPK

| $\tau_0$ | $a$ | $b$ | $\beta_m$ | $\beta_c$ | $\alpha$ |
|---|---|---|---|---|---|
| 0.1 | 500 | 70 | 1.0 | 0.1 | 0.1 |

Circadian rhythms and Differentiation

| $\tau$ | $k$ | $k_F$ | $k_W$ | $K_1^F$ | $K_2^F$ | $K_1^W$ | $K_2^W$ | $B_F$ | $B_W$ | $\lambda$ | $A$ |
|---|---|---|---|---|---|---|---|---|---|---|---|
| 6.0 | 30 | 8.0 | 4.0 | 5.0 | 5.0 | 5.0 | 5.0 | 0.3 | 0.4 | 10 | 0.15 |

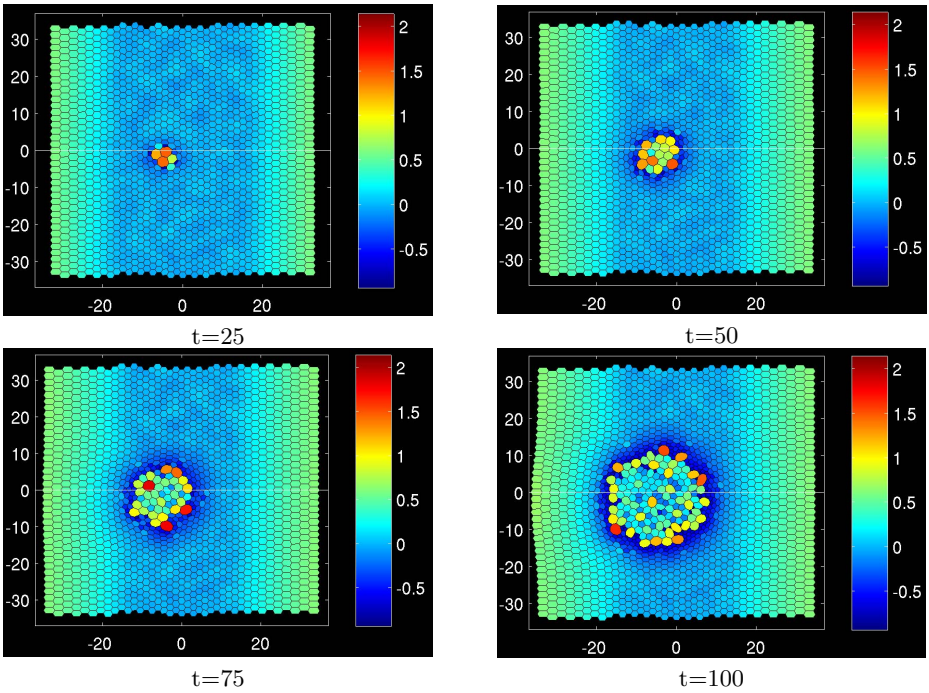


**Fig. 5.** Evolution of the cancer tumour in epithelial tissue in time. Scaling corresponds to changes in cell size relative to the average size of a normal cell.

stretched. Since the period of the division of cancer cells is shorter, the tumour evolves rapidly increasing the occupied area.

## 6 Discussion and Conclusions

The cancer is certainly the complex biological system. Therefore the cancer modeling dealt with in this paper needs a miltiscale mathematical approach. We propose a minimal multiscale model which includes three natural scales connected to different stages of the disease: processes on the cellular scale are triggered by circadian rhythm signals stemming from sub-cellular level and have an impact on the macroscopic scale characterized by a long-range coordination of dynamics of multiple cells in epithelium. The basic medium, where tumour grows and spreads, is constructed to take into account chemo-mechanical interactions including a chemical effect of strain, chemically induced polarization and active traction, and interaction between polarized cells. Many details of this model need experimental verification, as direct identification of the mechanisms involved in this feedback loop is not yet available.

Nonetheless, research across the last three decades has revolutionized our understanding of cancer. In large part, this success was made possible by the development and application of the techniques of molecular biology, techniques that enabled researchers to probe and describe features of individual cells in ways unimaginable not so long ago. Today, we know that cancer is a disease of molecules and genes, and we even know some of them involved.

To our opinion, a new type of simulation should be able to include experimentally discovered new molecular mechanisms. Our model is designed so that it can easily be modified to take account of any new feedbacks arising between chemo-mechanical behavior of cells and the gene regulation processes. In this version of the model we have considered only two of these molecular mechanisms that have been studied experimentally: the excitation of the wave of mitogen-activated protein kinase responsible for the movement of cells and circadian rhythms generation responsible for the synchronization of cell activity in a tissue. But other mechanisms can be easily added. Moreover, since the present model includes individual behavior of each cell with its own gene regulation dynamics, it can be used to simulate the targeted therapeutic interventions for various types of cancer. As it is known, many proteins possess interacting faces with unique recognition patterns that allow them to selectively recognize and bind to proteins to form homo- and hetero-complexes, thus activating biological pathways. Therefore, targeting protein-protein interactions has the potential to produce highly selective drugs. Computational approaches can assist in the identification and optimization of ligands at all stages of the drug discovery process, and computer-aided rational design is a particularly powerful tool for studying the interaction of agents at protein-protein interfaces. In the model presented here an important role has been played by the hetero-dimer complex $FW$ which ensures the generation of the circadian rhythm in each cell (see Eqs. 8-9). Particularly intriguing result of the work is also the possibility of modeling the impact of the intracellular processes on the dynamics of a whole organ and vice versa.

We anticipate that this work will encourage further quantitative studies and will, in its turn, be adjusted and modified as more data become available.

**Acknowledgements.** The research has been supported by the Ministry of Education of Perm Region (grant C-26/244), Program of Strategic Development of Perm State Humanitarian Pedagogical University (project 031-F) and grant of Russian Fund for Basic Research (14-01-96022r_ural_a).

## References

1. Weber, G.F.: Molecular Mechanisms of Cancer. Springer (2007)
2. Bellomo, N., Li, N.K., Maini, P.K.: On the foundations of cancer modelling: selected topics, speculations, and perspectives. Mathematical Models and Methods in Applied Sciences 18, 593–646 (2008)
3. Gyllenberg, M., Webb, G.: A nonlinear structured population model of tumour growth with quiescence. J. Math. Biol. 28, 671–684 (1990)
4. Kimmel, M., Lachowicz, M., Świerniak, A.: Cancer growth and progression, mathematical problems and computer simulations. Int. J. Appl. Math. Comput. Sci. 13, 279–429 (2003)
5. Dyson, J., Villella-Bressan, R., Webb, G.: The steady state of a maturity structured tumor cord cell population. Discr. Cont. Dyn. Syst. B 4, 115–134 (2004)
6. Ambrosi, D., Preziosi, L.: On the closure of mass balance models for tumour growth. Math. Mod. Meth. Appl. Sci. 12, 737–754 (2002)
7. Smolle, J., Stettner, H.: Computer simulation of tumour cell invasion by a stochastic growth model. J. Math. Biol. 160, 63–72 (1993)
8. Anderson, A.: A hybrid mathematical model of solid tumour invasion: The importance of cell adhesion. Math. Med. Biol. 22, 163–186 (2005)
9. Vogelstein, B., Kinzler, K.W.: Cancer genes and the pathways they control. Nature Med. 10, 789–799 (2004)
10. Komarova, N.: Stochastic modeling of loss- and gain-of-function mutation in cancer. Math. Mod. Meth. Appl. Sci. 17, 1647–1674 (2007)
11. Alarcon, T.: A cellular automaton model for tumour growth in inhomogenous environment. J. Theor. Biol. 225, 257–274 (2003)
12. Kim, Y., Stolarska, M.A., Othmer, H.G.: A hybrid model for tumour spheroid growth in vitro I: Theoretical development and early results. Math. Mod. Meth. Appl. Sci. 17, 1773–1798 (2007)
13. Zakharov, A., Bratsun, D.: Synchronization of Circadian Rhythms at Scale of Gene, Cell and Whole Organism. In: Sanayei, A., Zelinka, I., Rossler, O.E. (eds.) ISCS 2013. Emergence, Complexity and Computation, vol. 8, pp. 345–355. Springer, Heidelberg (2014)
14. Viktorinová, I., Pismen, L.M., Aigouy, B., Dahmann, C.: Modelling planar polarity of epithelia: The role of signal relay in collective cell polarization. J. R. Soc. Interface 8, 1059–1063 (2011)
15. Salm, M., Pismen, L.M.: Chemical and mechanical signaling in epithelial spreading. Phys. Biol. 9, 026009–026023 (2012)
16. Greene, M.W.: Circadian rhythms and tumor growth. Cancer Letters 318, 115–123 (2012)
17. Rossetti, S., Esposito, J., Corlazzoli, F., Gregorski, A., Sacchi, N.: Entrainment of breast (cancer) epithelial cells detects distinct circadian oscillation patterns for clock and hormone receptor genes. Cell Cycle 11, 350–360 (2012)

18. Bratsun, D., Zakharov, A.: Deterministic modeling spatio-temporal dynamics of delay-induced circadian oscillations in Neurospora crassa. In: Sanayei, A., Zelinka, I., Rossler, O.E. (eds.) ISCS 2013. Emergence, Complexity and Computation, vol. 8, pp. 179–189. Springer, Heidelberg (2014)
19. Nikolic, D.L., Boettiger, A.N., Bar-Sagi, D., Carbeck, J.D., Shvartsman, S.Y.: Role of boundary conditions in an experimental model of epithelial wound healing. Am. J. Physiol. Cell Physiol. 291, 68–75 (2006)
20. Bratsun, D., Volfson, D., Hasty, J., Tsimring, L.S.: Delay-induced stochastic oscillations in gene regulation. Proc. Natl. Acad. Sci. U.S.A. 102, 14593–14598 (2005)

# Part IV

# Complex Networks

# Comparing Overlapping Properties of Real Bipartite Networks

Fabien Tarissan

Sorbonne Universités, UPMC Université Paris 6 and CNRS, UMR 7606, LIP6, Paris

**Abstract.** Many real-world networks lend themselves to the use of graphs for analysing and modelling their structure. But such a simple representation has proven to miss some important and non trivial properties hidden in the bipartite structure of the networks. Recent papers have shown that overlapping properties seem to be present in bipartite networks and that it could explain better the properties observed in simple graphs. This work intends to investigate this question by studying two proposed metrics to account for overlapping structures in bipartite networks. The study, conducted on four dataset stemming from very different contexts (computer science, juridical science and social science), shows that the most popular metrics, the clustering coefficient, turns out to be less relevant that the recent redundancy coefficient to analyse intricate overlapping properties of real networks.

**Keywords:** Complex networks, Bipartite graphs, Social networks, Overlapping.

## 1 Introduction

Many complex networks lend themselves to the use of graphs for analysing and modelling their structure. Usually, vertices of the graph stand for the nodes of the network and the edges between vertices stand for (possible) interactions between nodes of the network. This approach have proven to be useful to identify non trivial properties of the structure of networks in very different contexts, ranging from computer science (the Internet, peer-to-peer networks, the web), to biology (protein-protein interaction networks, gene regulation networks), social science (friendship networks, collaboration networks), linguistics, economy, etc. [17,4,12,2,6,13,1,14].

Although useful, such a simple representation is not particularly close to the real structure of most of real networks. If one considers for instance actor networks which link actors performing in the same movies [17,11] or co-authoring networks which link authors publishing together [11,12], one would rather relate actors to the movies they performed in and authors to their papers. This observation led the community to use *bipartite graphs* instead, i.e. graphs in which nodes can be divided into two disjoint sets, $\top$ (e.g. movies) and $\bot$ (e.g. actors), such that every link connects a node in $\top$ to one in $\bot$. Bipartite graphs are a



A. Sanayei et al. (eds.), *ISCS 2014: Interdisciplinary Symposium on Complex Systems*, Emergence, Complexity and Computation 14, DOI: 10.1007/978-3-319-10759-2_32

fundamental object which has proven to be very efficient for both the analysis [5,16,1,14] and the modelling [3,15] of complex networks as it is able to reveal patterns that could not have been detected on simple graphs.

In a recent work [15], this framework has been investigated in an attempt to propose, for the first time, a bipartite model of the Internet topology. It relies on recent developments in topology discovery [8,7] that allows for revealing two layers in the Internet structure. The model remains simple: it only takes as input the node degree sequence for both layers and randomly generates a bipartite graph respecting those distributions. The paper showed that, despite the simplicity of the model, realistic network properties, such as high local density and non trivial correlations among properties of the nodes of the lower layer, emerge naturally. But it also showed that the model fails in reproducing the overlapping observed in the two-layer structure.

The present paper extends the analysis of overlapping structures to a wide variety of networks and tries to identify how bipartite metrics can account for those complex properties. In particular, it investigates whether two recently proposed metrics, namely the *bipartite clustering coefficient* and *bipartite redundancy coefficient*, are relevant for explaining the observed overlaps.

The remaining of the paper is organised as follow: Section 2 will review the technical background necessary for going throughout the paper; Section 3 will present the main obtained results and finally Section 4 will conclude the paper and open on new perspectives.

## 2 Background

In this section, we introduce the required background for the remainder of the paper. First, we focus on the different dataset (Section 2.1) we used in this study. Then, we recall the necessary definitions of the bipartite graph framework and its related metrics (Section 2.2).

### 2.1 Dataset

As stated in the introduction, many real networks exhibit a complex structure that involves several layers. In order to be as general as possible in the present study, we used a wide variety of networks presenting a two-level structure. We chose to focus on an infrastructure network (Internet), a juridical network (International Criminal Court decisions network) and two social networks (a co-publication network and a network composed of YouTube users). Here below we describe the four dataset and precise, for each one, the meaning of the upper layer ($\top$ nodes) and the lower layer ($\bot$ nodes):

**Internet [15,8]:** In this network, $\bot$ nodes stands for Internet routers and $\top$ nodes indicates the presence of Ethernet switches whose purpose is to induce indirect connections among routers. The dataset used in this study corresponds to a measurement campaign conducted in September 2006.

**ICC [14]:** This dataset describes the juridical decisions taken by the International Criminal Court (ICC) in the Lubanga case. Here, $\perp$ nodes stands for the juridical decisions made by the judges and $\top$ nodes for the articles of the Rome Statute they invoked. The dataset was extracted from a public server in March of 2013.

**Publications [10]:** This network describes the scientific collaboration among researchers through co-published papers. It is based on preprints posted to the *Condensed Matter* section of arXiv E-Print Archive between 1995 and 1999. In this network, $\perp$ nodes stands for authors and $\top$ nodes for articles.

**YouTube [9]:** This dataset describes some characteristics of YouTube users. It has been collected in 2007 and show the relation between users ($\perp$) and their membership ($\top$).

As we will see further (see Section 3.1 in particular), although the nature of those networks are very different, their two-level structure share some particular and non trivial properties, among which the classical heterogeneous distribution of the degree of the nodes. Note that the size of the networks varies from thousands of nodes to hundred of thousand of nodes. For this reason, all the distributions that we will study further will be normalised by the size of the networks in order to ease the comparisons.

### 2.2 Bipartite Graphs

*Bipartite graphs* – also referred to sometime by two-mode networks – are triplets $G_b = (\top, \perp, E_b)$, where $\top$ is the set of *top* nodes (the papers in the Publication dataset for instance), $\perp$ the set of *bottom* nodes (the authors), and $E_b \subseteq \top \times \perp$ the set of links between $\top$ and $\perp$ (that relate the papers to their authors in our example). We denote by $n_\top$ (resp. $n_\perp$) the number of top nodes (resp. bottom nodes) and by $m_{bip}$ the number of links.

Compared to standard graphs, nodes in a bipartite graph are separated in two disjoint sets, and the links are always between a node in one set and a node in the other set. Note that from a given bipartite graph, one can always induce a corresponding simple graph by a $\perp$-projection. In the case of the Publication network, it would generate a simple graph in which nodes are authors and a link relates two authors if they have published a joint paper. This would allow to reuse all the metrics defined for standard graphs.

But we can also compute specific metrics for bipartite graphs, such as $k_\top$ (resp. $k_\perp$) the average degree of top nodes (resp. bottom nodes), $d^+_\top$ (resp. $d^+_\perp$) the maximal degree observed in top nodes (resp. bottom nodes) and $\delta_\mathfrak{b} = \frac{m_\mathfrak{b}}{n_\top . n_\perp}$ the density of the bipartite graph.

Those are natural extensions of standard metrics defined for simple graphs. But for more intricate properties, it can be tedious to propose a "natural" definition. This is the case for the local density in the graph (more or less the density around a node) which is usually captured by the clustering coefficient.

The reason for the difficulty in defining such an extension is that it relies on the presence of triangles which does not exist in bipartite graphs. As suggested in [5], one can however rely on the following coefficient that tends to capture the overlapping between the neighbourhood of two nodes of $\top$. Let $N_\top(u)$ for $u \in \top$ denote the set of neighbours (i.e. bottom nodes $u$ is linked to) and $N_\bot(u)$ the dual definition for $\bot$ nodes. Then we define:

$$\texttt{cc}_\top(u,v) = \frac{|N_\top(u) \cap N_\top(v)|}{|N_\top(u) \cup N_\top(v)|}. \tag{1}$$

This coefficient is interesting as it captures the relative overlap between neighbourhoods of top nodes, i.e. $\texttt{cc}_\top(u,v)$ is equal to 1 if the neighbourhood of $u$ and $v$ intersects exactly, to 0 if they do not share any neighbour. From this coefficient, it becomes natural to define the clustering coefficient related to a specific $\top$ node $v$. This is given by:

$$\texttt{cc}_\top(v) = \frac{\sum_{u \in N_\bot N_\top(v)} \texttt{cc}_\top(u,v)}{|N_\bot N_\top(v)|}. \tag{2}$$

This coefficient enables in particular to study the distribution of this property over the top nodes as well as its correlation with the degree or other properties. Then one can naturally compute the *bipartite top clustering coefficient* $\texttt{cc}_{\texttt{bip}}$ of $G_b$ as the average value of $\texttt{cc}_\top(v)$ over all the nodes $v$ of $\top$. More formally:

$$\texttt{cc}_{\texttt{bip}}(G_b) = \frac{1}{|\top|} \sum_{v \in \top} \texttt{cc}_\top(v). \tag{3}$$

However it has been shown in [5] that this coefficient might miss some important properties of the overlapping between $\top$ nodes in the bipartite structures. This is why the authors suggested to use the *redundancy coefficient* $\texttt{rd}_\top(v)$ of a node $v$ which focuses on the impact of removing $v$ as regard the $\bot$-projection. Intuitively, a high value of the coefficient indicates that two $\bot$ nodes $v$ relates are likely to be related by another $\top$ node. Formally, the coefficient is given by:

$$\texttt{rd}_\top(v) = \frac{|\{\{u,w\} \in N_\top(v)^2 \text{ s.t. } \exists v' \neq v, (v',u) \in E_b \text{ and } (v',w) \in E_b\}|}{\frac{|N_\top(v)|(|N_\top(v)|-1)}{2}}. \tag{4}$$

Following this definition, we can derive naturally the redundancy coefficient $\texttt{rd}_{\texttt{bip}}$ of the bipartite graph $G_b$, defined as the average value of the former coefficient over all $\top$ nodes. More formally:

$$\texttt{rd}_{\texttt{bip}}(G_b) = \frac{1}{|\top|} \sum_{v \in \top} \texttt{rd}_\top(v). \tag{5}$$

## 3 Analysis of the Bipartite Structure

The purpose of this section is to analyse the overlapping observed in the bipartite structure of the four dataset presented in Section 2.1. We will focus in particular

**Table 1.** Global properties of the bipartite structure of the dataset

| | **Internet** | **ICC** | **Publication** | **YouTube** |
|---|---|---|---|---|
| $n_\top$ | 10 224 | 713 | 22 015 | 30 087 |
| $n_\bot$ | 9 758 | 1 360 | 16 726 | 94 238 |
| $m_\mathtt{b}$ | 25 422 | 6 670 | 58 595 | 293 360 |
| $\delta_\mathtt{b}(*10^{-3})$ | 0.26 | 6.88 | 0.16 | 0.10 |
| $k_\top$ | 2.5 | 9.4 | 2.7 | 9.8 |
| $k_\bot$ | 2.6 | 4.9 | 3.5 | 3.1 |
| $d^+_\top$ | 58 | 250 | 18 | 7 591 |
| $d^+_\bot$ | 41 | 81 | 116 | 1 035 |

**Table 2.** Value of the overlapping coefficients of the bipartite structures

| | **Internet** | **ICC** | **Publication** | **YouTube** |
|---|---|---|---|---|
| $\mathtt{cc}_\mathtt{bip}$ | 0.32 | 0.15 | 0.39 | 0.16 |
| $\mathtt{rd}_\mathtt{bip}$ | 0.11 | 0.69 | 0.63 | 0.33 |

to the two metrics that have been proposed to account for such a topological property, namely the bipartite clustering coefficients and the bipartite redundancy coefficients (referred to further simply as clustering and redundancy). First, we start by looking at some global and standard statistics defined for bipartite graphs (Section 3.1). Then we turn to the overlapping properties and study distributions and correlations among the different metrics (Section 3.2).

### 3.1 A Global Perspective

The first statistics we focus on concern some basic properties observed in most real-world networks, formally presented in the previous section. Table 1 presents the results for the four dataset of Section 2.1. As expected, all usual observations made on real-world networks stand also for the networks under study. In particular the graph is sparse (on the order of magnitude of $10^{-4}$) and the maximal degree is several orders of magnitude higher that the average degree, which indicates usually some heterogeneity in the degree of the nodes.

This is confirmed by the inverse cumulative distribution of the degree of the nodes (both $\top$ and $\bot$) presented in Figure 1. It clearly shows a heavy-tail distribution for all the four dataset and the nodes of the two layers.

### 3.2 Analysis of the Overlapping Structure

We focus now more precisely to the core of the analysis related to the overlapping in the bipartite structure. First, Table 2 presents the global values of the two coefficients computed for all the dataset. It shows that, although the two

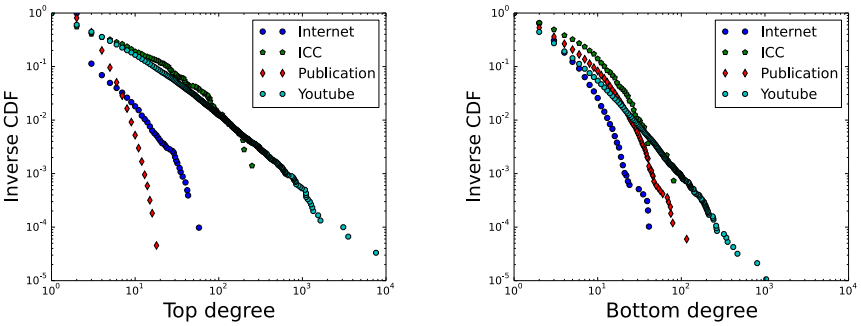


(a) Top nodes (b) Bottom nodes

**Fig. 1.** Inverse CDF of the node degree distribution

coefficients intend to capture the same property (overlapping patterns), they strongly differ on each dataset. The most obvious case is the ICC since the clustering coefficient is quite low (0.15) but the redundancy is very high (0.69). For the other dataset the gap is less important but we can notice that the higher coefficient depends on the dataset thus showing that no general behaviour can be drown here.

Those global average metrics do not allow for a detailed comprehension of the coefficients. Fortunately, we can compute them for each of the $\top$ nodes in the networks. This allows to study several properties related to it such as the distribution of the coefficients. Figure 2 presents the inverse cumulative distribution of the clustering (Figure 2(a)) and the redundancy (Figure 2(a)). We can observe that the distributions of the two coefficients are very different. For the clustering, the plot shows that the decrease of the value is very sharp and for low values. The majority of $\top$ nodes have indeed a small clustering coefficient. This indicates that the overlapping, according to this metrics, is not particularly important in the networks.

For the redundancy, the behaviour is different. Except for the Internet case, for which one can observe a sharp decrease, the value is uniformly distributed among the nodes. As opposed to the clustering, this seems to indicate on the contrary that some overlaps are present in three over four dataset. Note for instance that the fraction of $\top$ nodes having a redundancy of 1 is non negligible: 9% in Internet, 13% in the YouTube case, 46% in the ICC network and 52% in the Publication network. Taking this last case as an example it means that, for more than half of the articles of the Publication network, every authors have also published together at least one other article. This indicates a strong overlapping in the network which, in the case of co-publication networks, is not surprising but is not captured by the clustering coefficient.

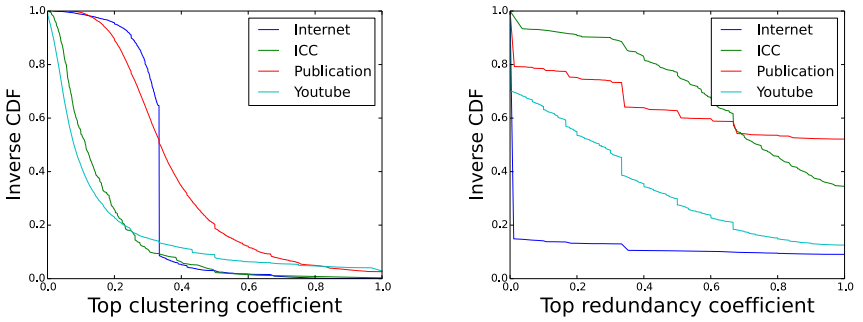


(a) Clustering (b) Redundancy

**Fig. 2.** Inverse CDF of the clustering and redundancy coefficients

The distribution shown above is interesting but it does not help to understand why some coefficients are high and other low. In order to understand better the situation, we show Figure 3 the correlation between the degree of a $\top$ node and the value of its clustering (Figure 3(a)) or its redundancy (Figure 3(b)). More precisely, a $(x, y)$ dot in the plots means that the average value of the coefficient for nodes having degree $x$ is $y$. Figure 3(a) shows a very interesting fact: the value of the clustering seems to be completely governed by the degree of the corresponding node. The higher the degree, the lower the clustering. Such a correlation makes the interest of the coefficient weak since it seems derivable from the degree of the nodes. On the contrary, Figure 3(b) does not present such a correlation, except for the PUBLICATION network for which one observe a similar behaviour. The notion engulfed in the redundancy coefficient seems then, to that regard, contain more information than simpler local properties.

## 4 Conclusion

In this paper, we studied the overlapping properties observed in the bipartite structure of different networks exhibiting a two-level structure. The main concern of the study was to discriminate between two recently proposed metrics to account for such properties, namely the clustering coefficient and the redundancy coefficient.

By analysing the structure of 4 networks stemming from very different contexts, we showed that the notion captured by the clustering coefficient turns out to be quite poor as it is closely related to the simple degree of the node. On the contrary, the behaviour of the redundancy coefficient is totally unpredictable regarding local properties such as the degree. The value of the coefficient is not related to simple local properties of the nodes, at least in 3 of the 4 dataset of the study.

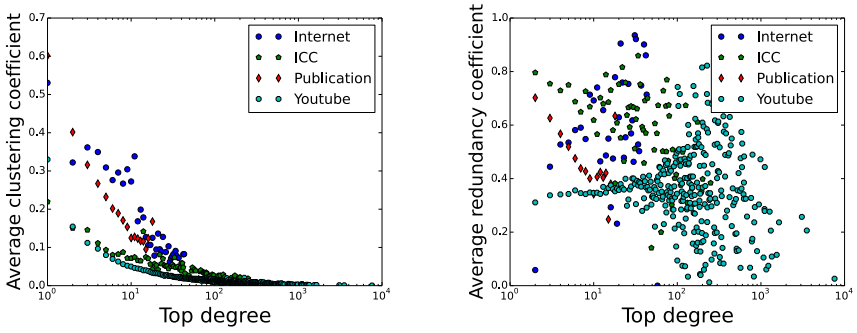


(a) Clustering (b) Redundancy

**Fig. 3.** Correlation between the degree and the overlapping coefficients

Understanding the characteristics of the bipartite structure of real networks are fundamental for several reasons. First, as shown in several studies, such structures help understanding non trivial properties of simple networks (see [15] for instance). But more importantly it has been shown to be a better support for models, enabling in particular to generate random structures closer to real ones than most of classical models [15].

To that regard, the present work opens the way to several improvements in recently proposed models. It shows in particular that one could improve bipartite models by integrating such a property in the model, which has not been done so far. One way to achieve this goal would be to *encode* the redundancy in an artificial third level and control the coefficient by randomly permuting links in such a tripartite structure. We let such an investigation as a further work.

**Acknowledgement.** This work is partly funded by the National Center for Scientific Research (CNRS) through the PEPS Project "DoRé".

## References

1. Ahn, Y.-Y., Ahnert, S.E., Bagrow, J.P., Barabási, A.-L.: Flavor network and the principles of food pairing. Scientific Reports 1 (2011)
2. Battiston, S., Catanzaro, M.: Statistical properties of corporate board and director networks. The European Physical Journal B-Condensed Matter and Complex Systems 38(2), 345–352 (2004)
3. Guillaume, J.-L., Latapy, M.: Bipartite graphs as models of complex networks. Physica A: Statistical Mechanics and its Applications 371(2), 795–813 (2006)
4. i Cancho, R.F., Solé, R.V.: The small world of human language. Proceedings of the Royal Society of London. Series B: Biological Sciences 268(1482), 2261–2265 (2001)

5. Latapy, M., Magnien, C., Del Vecchio, N.: Basic notions for the analysis of large two-mode networks. Social Networks 30(1), 31–48 (2008)
6. Le Fessant, F., Handurukande, S.B., Kermarrec, A.-M., Massoulié, L.: Clustering in peer-to-peer file sharing workloads. In: Voelker, G.M., Shenker, S. (eds.) IPTPS 2004. LNCS, vol. 3279, pp. 217–226. Springer, Heidelberg (2005)
7. Mérindol, P., Donnet, B., Bonaventure, O., Pansiot, J.-J.: On the impact of layer-2 on node degree distribution. In: Proc. ACM/USENIX Internet Measurement Conference (IMC) (November 2010)
8. Mérindol, P., Van den Schriek, V., Donnet, B., Bonaventure, O., Pansiot, J.-J.: Quantifying ASes multiconnectivity using multicast information. In: Proc. ACM/USENIX Internet Measurement Conference (IMC) (November 2009)
9. Mislove, A., Marcon, M., Gummadi, K.P., Druschel, P., Bhattacharjee, B.: Measurement and Analysis of Online Social Networks. In: Proceedings of the 5th ACM/Usenix Internet Measurement Conference (IMC 2007), San Diego, CA (October 2007)
10. Newman, M.E.J.: The structure of scientific collaboration networks. Proceedings of the National Academy of Sciences of the United States of America 98(2), 404–409 (2001)
11. Newman, M.E., Strogatz, S.H., Watts, D.J.: Random graphs with arbitrary degree distributions. Physics Reviews E, 64 (2001)
12. Newman, M.E., Watts, D.J., Strogatz, S.H.: Random graph models of social networks. Proceedings of the National Academy of Sciences of the United States of America 99(suppl. 1), 2566–2572 (2002)
13. Prieur, C., Cardon, D., Beuscart, J.-S., Pissard, N., Pons, P.: The stength of weak cooperation: A case study on flickr. arXiv preprint arXiv:0802.2317 (2008)
14. Tarissan, F., Nollez-Goldbach, R.: The network of the international criminal court decisions as a complex system. In: Sanayei, A., Zelinka, I., Rossler, O.E. (eds.) ISCS 2013: Interdisciplinary Symposium on Complex Systems. Emergence, Complexity and Computation, vol. 8, pp. 225–264. Springer (2013)
15. Tarissan, F., Quoitin, B., Mérindol, P., Donnet, B., Pansiot, J.-J., Latapy, M.: Towards a bipartite graph modeling of the internet topology. Computer Networks 57(11), 2331–2347 (2013)
16. Tumminello, M., Miccichè, S., Lillo, F., Piilo, J., Mantegna, R.N.: Statistically validated networks in bipartite complex systems. PloS One 6(3), e17994 (2011)
17. Watts, D.J., Strogatz, S.H.: Collective dynamics of 'small-world' networks. Nature 393(6684), 440–442 (1998)

# Risk Perception and Epidemic Spreading in Multiplex Networks

Franco Bagnoli[1] and Emanuele Massaro[2]

[1] Dept. Physics and Astronomy and CSDC, University of Florence, Via G. Sansone, 1 50019 Sesto Fiorentino (FI) Italy Also INFN, Sez. Firenze
franco.bagnoli@unifi.it
[2] Risk and Decision Science Team, US Army Engineer Research and Development Center, 696 Virginia Rd., COncord, MA 01742, and Department of Civil and Environmental Engineering, Carnegie Mellon University, 5000 Forbes Ave, Pittsburgh, PA 15213
emassaro@andrew.cmu.edu

**Abstract.** In this paper we study the interplay between epidemic spreading and risk perception on multiplex networks. The basic idea is that the effective infection probability is affected by the perception of the risk of being infected, which we assume to be related to the number of infected neighbours. We re-derive previous results using a self-organized method, that automatically gives the percolation threshold in just one simulation. We then extend the model to multiplex networks considering that people get infected by contacts in real life but often gather information from an information networks, that may be quite different from the real ones. The similarity between the real and information networks determine the possibility of stopping the infection for a sufficiently high precaution level: if the networks are too different there is no mean of avoiding the epidemics.

## 1 Introduction

Recently, the Health magazine reported "Although H1N1 influenza killed more than 4,000 people in the United States in 2009-2010, this outbreak was relatively mild compared to some flu pandemics" [1].

Indeed, the twentieth century was characterized by a series of more serious events. During the 1918-19 the world assisted to the so-called *Spanish Flu*. Starting from three different places: Brest (France), Boston (Massachusetts) and Freetown (Sierra Leone), the disease spread worldwide, killing 25 million people in 6 months (about 17 million in India, 500,000 in the United States and 200,000 in the United Kingdom).

In 1957, another pandemic originated in China and spread rapidly in Southeast Asia, taking hence the name of *Asian*. The virus responsible was identified in the subtype H2N2, new to humans, resulting from a previous human H1N1 virus that was remixed with a duck virus from which it received the genes encoding the H2 and N2. This pandemic took eight months to travel worldwide and caused one to two million victims.



A. Sanayei et al. (eds.), *ISCS 2014: Interdisciplinary Symposium on Complex Systems*, Emergence, Complexity and Computation 14, DOI: 10.1007/978-3-319-10759-2_33

The 1968 pandemic was the mildest of the twentieth century and started once again in China. From there it spread to Hong Kong, where more than half a million people fell ill, and in the same year reached the United States and the rest of the world.

Given these facts (and the whole records of pandemics in history [2]), it is not surprising that the public health organizations are concerned about the appearance of a new deadly pandemics.

However, in recent decades there have been many cases of false or exaggerated information about epidemics. One example if the *Swine flu* of 1976, or the *Avian flu* in 1997 where a United Nations health official warned that the virus could kill up to 150 million worldwide [1] or the more recent 2009 *H1N1 flu*, during whose outbreak the U.K. Department of Health warned about 65000 possible deaths as reported by the Daily Mail in 2010 [3]. Fortunately these fears did not realize.

These catastrophic scenarios and the extent of their impacts on the economic and social contexts induce a reflection on the method used to forecast the evolution of a disease in real world. It is well known that in deeply connected networks (and in particular in scale-free ones without strong compartmentalization) the epidemic threshold of standard epidemic modeling is vanishing [4,5,6,7,8]. However, the last deadly pandemics of pest in Europe happened in 1820 [2], and worldwide in Vietnam in the 60's; the last pandemic influenza, Hong Kong flu, in 1968-1969. In other words, the last rapid deadly pandemics happened well before the appearance of highly-connected human networks.

Clearly, the public health systems put a lot of efforts in trying to make people aware of the dangers connected to hygiene, dangerous sexual habits and so on. Indeed, the current worldwide diffusion of large-scale diseases (HIV, seasonal influenza, cold, papilloma virus, herpes virus, viral hepatitis among others) is deeply related to their silent (and slow) progression or to the assumption (possibly erroneous) or their harmlessness. However, it is well known that the direct experience (contact with actual ill people) is much more influential than public exhortations.

Therefore, in order to accurately modeling the spreading of a disease in human societies, we need to take into account the perception of its impacts and the consequent precautions that people take when they become aware of an epidemic. These precautions may consist in changes in personal habits, vaccination or modifications of the contact network.

We are here interested in diseases for which no vaccination is possible, so that the only way of avoiding a pandemic is by means of an appropriate level of precautions, in order to lower the infection rate below the epidemic threshold. We also assume that there is no acquired immunity from the disease and that its consequences are sufficiently mild not to induce a radical change in social contacts.

In a previous work [9], some of us investigated the influence of the risk perception in epidemic spreading. We assumed that the knowledge about the diffusion of the disease among neighbors (without knowing who is actually infected)

effectively lowers the probability of transmission (the effective infectiousness). We studied the worst case of an infection on a scale-free network with exponent $\gamma = 2$ and we showed that in this case no degree of prevention is able to stop the infection and one has to take additional precaution for hubs (such as public officers and physicians).

We extend here the investigation to different network structures, on order to obtain a complete reference frame. For regular, random, Watts-Strogatz small-world and non-assortative scale-free networks with exponent $\gamma > 3$ there is always a finite level of precaution parameter for which the epidemics go extinct. For scale-free networks with $\gamma < 3$ the precaution level depends on the cutoff of the power-law, which at least depends on the finite number of the network.

We consider then an important factor of modern society: the fact that most of information comes no more from physical contacts nor from broadcasting media, but rather from the "virtual" social contact networks [10,11,12]. A recent study, *State of the news media* for the United States [13], highlights this phenomena. It shows the extent of the influence of social networks, for what concerns subscribers who can read news published by newspapers. The 9% of the population claims to inquire "very often" through Facebook and Twitter and seven out of ten members are addressed to articles (from newspapers and other sources) by friends and family members.

We are therefore confronted with news coming mainly from an information network. On the other hand, the real network of contacts is the environment where actual infections occur. We extend our model to the case in which the source of information (mixed real and virtual contacts) does not coincide with the actual source of infection (the real contacts).

This system is well represented as a multiplex network [14,15,16,17,18], *i.e.*, a graph composed by several layers in which the same set of $N$ nodes can be connected to each other by means of links belonging to different layers, which represents a specific case of interdependent network [19,20]. Recently, Granell et al. [21] have pointed out the attention to an interesting scenario where the multiplex corresponds to a two-layers network, one where the dynamics of the awareness about the disease (the information dynamics) evolves and another where the epidemic process spreads.

The first layer represents the information network where people become aware of the epidemic thanks to news coming from virtual and real contacts in various proportions. The second layer represents the real contact network where the epidemic spreading takes place.

In this paper we want to model the effect of the virtual information for simulating the awareness of the agents in the real-world network contacts. We study how the percolation threshold of a susceptible-infected-susceptible (SIS) dynamics depends on the perception of the risk (that affects the infectivity probability) when this information comes from the same contact network of the disease or from a different network. In other words, we study the interplay between risk perception and disease spreading on multiplex networks.

We are interested in the epidemic threshold, which is a quantity that it is not easy to obtain automatically (for different values of the parameters) using numerical simulations. We extend a self-organized formulation of percolation phenomena [22] that allows to obtain this threshold in just one simulation (for a sufficiently large system).

## 2 The Network Model

In this section we show our method for generating multiplex networks. First of all we describe the mechanisms for generating *regular*, *random* and *scale-free* networks.

Let us denote by $a_{ij} = 0, 1$ the adjacency matrix of our network, $a_{ij} = 1$ if there is a link from $j$ to $i$ and zero otherwise. We shall denote by $k_i = \sum_j a_{ij}$ the connectivity of site $i$ and by $j_1^{(i)}, j_2^{(i)}, \ldots, j_{k_i}^{(i)}$ its neighbourhood ($a_{i,j_n^{(i)}} = 1$). We shall consider only symmetric networks. We generate networks with $N$ nodes and $2mN$ links, so that the average connectivity is $\langle k \rangle = 2m$.

- Regular 1D: Nodea are arranged on a ring (periodic boundary condition). Any given node establishes a link with the $m$ closest nodes at its right. For instance for $m = 2$, node 1 establishes a link with nodes 2 and 3, node 2 with nodes 3 and 4, and so on until nodes $N - 2$ and $N - 1$ establish a link with node 1.
- Random: Any node establishes $m$ links with randomly chosen nodes, avoiding self-loops and multiple links. The probability distribution of random networks is Possonian, $P(k) = \frac{z^k e^{-z}}{k!}$, where $z = \langle k \rangle$.
- Scale-Free: we use a configurational model fixing also a cutoff $K$. First, at each node $i$ out of $N$ is assigned a connectivity $k_i$ draft from a power-law distribution $P(k) = Ak^{-\gamma}$, $m \leq k \leq K$, with $A = (\gamma - 1)/(m^{1-\gamma} - K^{1-\gamma})$. Then links are connected at random aviding self-loops and multiple links, and finally the total number of link is pruned in order to adjust the total number of links. This mechanism allow us to generate scale-free networks with a given exponent $\gamma$. We generally use $\gamma = 2.1$.

In order to generate multiplex networks composed by two sub-networks that we call *Real* ($R$) and *Information* ($I$). We generate freely the real network by choosing one from regular, random or scale-free. Then we generate a *Virtual* network ($V$) also chosen from the three benchmark networks, with same average connectivity $\langle k \rangle = 2m$. In order to construct the information network we overlap the real and the virtual ones and then, for each node, we prune its "real" links with probability $q$ and its "virtual" ones with probability $1 - q$. The overlap between the real and the information networks is thus $1 - q$. The information network is not symmetric.

This procedure allow us to study the effects of the difference between the $R$, where the epidemic spreading takes place, and $V$ which is the information network where actors become aware of the disease (*i.e.*, over which they evaluate the perception of the risk of being infected).

## 3 Infection Model and Mean-Field Approximation

Following Ref. [9], we assume that the probability that a site $i$ is infected by a neighbour $j$ is given by

$$u(s,k) = \tau \exp\left(-J\frac{s}{k_i}\right),$$

where $\tau$ is the "bare" infection probability and $s$ is the number of infected neighbours. The idea is that the perception of the risk, modeled as the percentage of infected neighbours and modulated by the factor $J$ effectively lowers the infection probability (for instance because people takes more precautions). In the case of information networks, the perception is computed on the mixed real-virtual neighbourhood, while the actual infection process takes places on the real network.

It is possible to derive a simple mean-field approximation for the fixed-$k$ case. Denoting by $c$ the fraction of infected individuals at time $t$ and by $c'$ those at time $t+1$, we have, considering a random network,

$$c' = \sum_{s=0}^{k} \binom{k}{s} c^s (1-c)^{k-s} p(s,k) \tag{1}$$

where $p(s,k)$ is the probability of being infected if there are $s$ out of $k$ infected neighbours. The probability $p$ depends on $u$ as $p(s,k) = 1-\big[1-u(s,k)\big]^s$, since the infection processes are independent (although the infection probabilities are coupled by the "perception"-dependent infection probability $q$, Eq. (11). Near the threshold, the probability $u$ is small, and therefore we can approximate

$$p(s,k) \simeq s u(s,k) = s\tau \exp\left(-J\frac{s}{k}\right).$$

Replacing into Eq. 1, we get

$$c' = \sum_{s=0}^{k} \binom{k}{s} c^s (1-c)^{k-s} s\tau \exp\left(-J\frac{s}{k}\right),$$

and setting $a = \exp\left(-J\frac{s}{k}\right)$,

$$c' = \tau \sum_{s=0}^{k} \binom{k}{s} c^s (1-c)^{k-s} s a^s,$$

which gives

$$c' = \tau a k (ca + 1 - c)^{k-1}.$$

The critical threshold $J_c$ corresponds to the stationary state $c' = c$ in the limit $c \to 0$, *i.e.*,

$$\tau = \frac{1}{k} \exp\left(\frac{J_c}{k}\right); \qquad J_c = k \ln(k\tau). \tag{2}$$

This prediction is quite accurate: in Fig. 2 the comparison between Eq. (2) and actual simulations in reported for different values of $\langle k\rangle$ using random networks.

The analysis can be extended to non-homogeneous networks with connectivity distribution $P(k)$ like the scale-free ones. We can start analysing a node with connectivity $k$

$$c'_k = \sum_{s_1,s_2,\ldots,s_k=0}^{1} \sum_{j_1,j_2,\ldots,j_k=0}^{\infty} \prod_{i=1}^{k} C(j_i,k) I(s_i,j_i) T(k|s_i),$$

where we denote with $i = 1,\ldots,k$ the neighbours, $s_i = 0, 1$ is their state (healthy, infected) and $j_i$ their connectivity. $C(j,k)$ is the probability that a node with connectivity $j$ is attached to node with connectivity $k$, $I(s_i,j_i)$ is the probability that the neighbour $i$ is infected, and $T(k|s_i)$ is the probability that it transmits the infection to the node under investigation.

Clearly, $\sum_j C(j,k) = 1$. We use symmetric networks, so $jC(j,k)P(j) = kC(k,j)P_k$ (detailed balance). For non-assortative networks, $C(j,k)$ does not depend on $k$, and summing over the detailed balance condition, $C(j,k) = jP(j)/\langle k\rangle$. The quantity $I(s_i,j_i)$ is simply $c_{j_i}^{s_i}(1-c_{j_i})^{1-s_i}$ and $T(k|s_i) = 1-(1-\tau\exp(-Js/k))^s$, where $s = \sum_i s_i$ (risk perception). Near the extinction, $\tau\exp(-Js/k)$ is small and we can approximate $T(k|s_i) = s\tau\exp(-Js/k)$,

Summing up, we have

$$\begin{aligned} c'_k &= \sum_{s_1,s_2,\ldots,s_k=0}^{1} \sum_{j_1,j_2,\ldots,j_k=0}^{\infty} \prod_{i=1}^{k} \frac{j_i P(j_i)}{\langle k\rangle} c_{j_i}^{s_i}(1-c_{j_i})^{1-s_i} s\tau \exp\left(-J\frac{s}{k}\right), \\ &= \sum_{s_1,s_2,\ldots,s_k=0}^{1} s\tau\exp\left(-J\frac{s}{k}\right) \prod_{i=1}^{k}\sum_{j_i=0}^{\infty} \frac{j_i P(j_i)}{\langle k\rangle} c_{j_i}^{s_i}(1-c_{j_i})^{1-s_i}. \end{aligned}$$

Since $s_i = 0, 1$, $c_{j_i}^{s_i}(1-c_{j_i})^{1-s_i}$ is either $s_i$ or $1-s_i$. Let us define $\tilde{c} = \sum_j jc_j/\langle k\rangle$, and we get

$$\begin{aligned} c'_k &= \sum_{s_1,s_2,\ldots,s_k=0}^{1} s\tau\exp\left(-J\frac{s}{k}\right) \prod_{i=1}^{k} \tilde{c}^{s_i}(1-\tilde{c})^{1-s_i} = \sum_{s=0}^{k} \binom{k}{s} s\tau\exp\left(-J\frac{s}{k}\right) \tilde{c}^s(1-\tilde{c})^{k-s} \\ &= \tilde{c}k\tau\exp\left(\frac{-Js}{k}\right)\left(\tilde{c}\exp\left(-\frac{J}{k}\right)+1-\tilde{c}\right). \end{aligned}$$

Near the epidemic threshold $\tilde{c}\to 0$, and

$$\tilde{c}' = \frac{1}{\langle k\rangle}\sum_k kc'_k P(k) = \frac{\tau\tilde{c}}{\langle k\rangle}\sum_k k^2 P(k)\exp\left(-\frac{J}{k}\right).$$

The correspondence between $\tau_c$ and $J_c$ is therefore

$$\tau_c(J_c) = \frac{\langle k\rangle}{\sum_k k^2 P(k)\exp\left(-\frac{J_c}{k}\right)}, \tag{3}$$

which, for $J_c = 0$, gives $\tau_c = \langle k \rangle / \langle k^2 \rangle$, that for a sharply peaked $P(k)$ corresponds to Eq. (2).

By using a continuous approximation, it is possible to make explicit the relationship between $\tau$ and $J_c$ in the scale-free case. Eq. (3) becomes

$$\tau_c(J_c) = \frac{\langle k \rangle}{\int_m^K k^2 P(k) \exp\left(-\frac{J_c}{k}\right) \, \mathrm{d}k}, \tag{4}$$

Substituting, for the scale free case, $P(k) = Ak^{-\gamma}$, where $A$ is the normalization constant so that $\int_m^K P(k) = 1$

$$A = \frac{\gamma - 1}{m^{1-\gamma} - K^{1-\gamma}} \simeq (\gamma - 1) m^{\gamma - 1},$$

if $K \gg m$ (and $\gamma < 3$). We get

$$\langle k \rangle = \frac{\gamma - 1}{\gamma - 2} \cdot \frac{m^{2-\gamma} - K^{2-\gamma}}{m^{1-\gamma} - K^{1-\gamma}} \simeq \frac{\gamma - 1}{\gamma - 2} m$$

for $K \gg m$, and

$$\tau_c(J_c) = J_c^{3-\gamma} \left[ \Gamma\left(\gamma - 3, \frac{J_c}{K}\right) - \Gamma\left(\gamma - 3, \frac{J_c}{m}\right) \right], \tag{5}$$

where $\Gamma(a, x)$ is the incomplete gamma function. Eq. (5) diverges for $K \to \infty$ and thus for infinite networks $J_c = 0 \; \forall \tau$. However, real networks always have a cut-off (at least due to the finite number of nodes) [23]. For $J_c = 0$ we recover the standard threshold

$$\tau_c(0) = \frac{\gamma - 3}{\gamma - 2} \cdot \frac{m^{2-\gamma} - K^{2-\gamma}}{m^{3-\gamma} - K^{3-\gamma}} \simeq \frac{3 - \gamma}{\gamma - 2} \cdot \frac{m^{2-\gamma}}{K^{3-\gamma}} \tag{6}$$

The problem of epidemic threshold in finite-size scale-free networks was studied in Ref. [24]. The conclusions there is that even in finite-size networks the epidemics is hard to stop. Indeed, we find numerically that the epidemics always stops in finite scale-free networks although the required critical value of $J_c$ may be quite large.

In Fig. 3 the comparison between the mean-field prediction, Eq. (3), and actual simulations is shown, for three instances of a scale-free network generated with the same parameters. The theoretical prediction coincides with the simulations only for $J_c = 0$. Moreover, although the simulation results seems to be sufficiently independent on the details of the generated networks, the theoretical prediction is quite sensible to them. The continuous approximation, Eq. (6) gives, for $m = 2$, $K = 300$ and $\gamma = 2.4$, a value $\tau(0) \simeq 0.037$, quite different from the computed one $\tau(0) \simeq 0.08$.

## 4 The Self-organized Percolation Method

Here we show a self-organized percolation method that allow to obtain the critical value of the percolation parameter in a single run, for a given network. We

consider a parallel SIS process, which is equivalent to a directed percolation problem where the directed direction is time.

Let us denote by $x_i(t) = 0, 1$ (0 =healthy, 1 =infected), the percolating variable and by $p$ the control parameter (percolation probability).

Let us start considering the problem of directed percolation (simple infection). Considering $p$ is fixed, the stochastic evolution process for the network is defined as

$$x_i(t+1) = \bigvee_{j=j_1^{(i)},\ldots,j_{k_i}^{(i)}} [p > r_{ij}(t)] x_j(t) \tag{7}$$

where $\bigvee$ represents the OR operator and the multiplication represents the AND. The square bracket represents the the truth function, $[\cdot] = 1$ if "$\cdot$" is true, and zero otherwise. The quantity $r_{ij}(t)$ is a random number between 0 and 1 that varies with $i$, $j$ and $t$. We want to derive an equation for $p_i(t)$, which is the minimum value of $p$ for which $x_i(t)$ is infected. We can replace $x_i(t)$ by $[p > p_i(t)]$. Eq. 7 becomes:

$$[p > p_i(t+1)] = \bigvee_{j=j_1^{(i)},\ldots,j_{k_i}^{(i)}} [p > r_{ij}(t)][p > p_j(t)]. \tag{8}$$

Now $[p > a][p > b]$ is equal to $[p > \max(a, b)]$ and $[p > a] \vee [p > b]$ is equal to $[p > \min(a, b)]$, therefore Eq. 8 becomes:

$$[p > p_i(t+1)] = \left[ p > \left( \operatorname*{MIN}_{j=j_1^{(i)},\ldots,j_{k_i}^{(i)}} \max\big(r_{ij}(t), p_j(t)\big) \right) \right], \tag{9}$$

and therefore we get the equations for the $p_i$'s

$$p_i(t+1) = \operatorname*{MIN}_{j=j_1^{(i)},\ldots,j_{k_i}^{(i)}} \max\big(r_{ij}(t), p_j(t)\big). \tag{10}$$

Let assume that at time $t = 0$ all sites are infected, so that $x_i(0) = 1\ \forall p$. We can alternatively write $p_i(0) = 0$ (since the minimum value of $p$ for which $x_i(0) = 1$ is one for sure. We can therefore iterate Eq. 10 and get the asymptotic distribution of $p_i$. The minimum of this distribution gives the critical value $p_c$ for which there is at least one percolating cluster with at least one "infected" site at large times. As usual, $t$ cannot be infinitely large for finite $N$ otherwise there will be surely a fluctuation that will bring the system into the absorbing (healthy $x_i = 0$) configuration.

We shall now consider the problem of firect percolation with risk perception. Now, let us apply the method to a more difficult problem, for which the percolation probability depends on the fraction of infected sites in the neighborhood (risk perception). As above, we define the infection probability $u$ as

$$u(s, k) = \tau \exp\left(-J \cdot \frac{s}{k}\right) \tag{11}$$

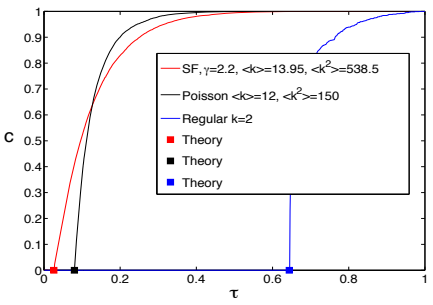


**Fig. 1.** Asymptotic number of infected individuals $c$ versus the bare infectiousness probability $\tau$ for the SIS dynamics for different networks, $N = 10000$.

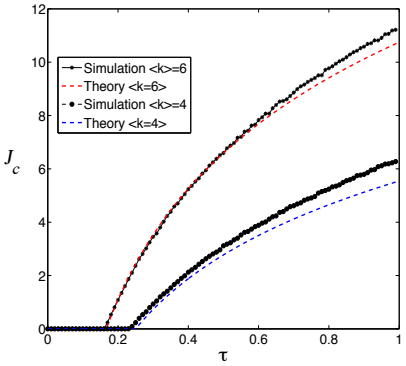


**Fig. 2.** Comparison between mean field approximation and simulations for random networks with different values of $\langle k \rangle$.

where $\tau$ is the bare infection probability, $s$ is the number of infected neighbors and $k$ is the node connectivity. In this case we want to find the minimum value of the parameter $J$ for which there is no spreading of the infection at large times. The quantity $[u > r] = [\tau \exp(-Js/k) > r]$ is equivalent to $[J < -(k/s)\ln(r/\tau)]$. Therefore Eq. (8) is replaced by

$$[J < J_i(t+1)] = \bigvee_{j=j_1^{(i)},\ldots,j_{k_i}^{(i)}} \left[ J < -\frac{k_i}{s_i} \ln\left(\frac{r_{ij}(t)}{\tau}\right)\right] [J < J_j(t)] \qquad (12)$$

where

$$s_i \equiv s_i(J) = \sum_{j=j_1^{(i)},\ldots,j_{k_i}^{(i)}} x_j = \sum_{j=j_1^{(i)},\ldots,j_{k_i}^{(i)}} [J_j(t) \geq J]. \qquad (13)$$

So

$$[J < J_i(t+1)] = \bigvee_{j=j_1^{(i)},\ldots,j_{k_i}^{(i)}} \left[ J < -\frac{k_i}{s_i(J_j(t))} \ln\left(\frac{r_{ij}(t)}{\tau}\right)\right] [J < J_j(t)] \qquad (14)$$

and therefore

$$J_i(t+1) = \underset{j=j_1^{(i)},\ldots,j_{k_i}^{(i)}}{\mathrm{MAX}} \min\left( -\frac{k_i}{s_i(J_j(t))} \ln\left(\frac{r_{ij}(t)}{\tau}\right), J_j(t)\right). \qquad (15)$$

Analogously to the previous case, the critical value of $J_c$ is obtained by taking the maximum value of the $J_i(t)$ for some large (but finite) value of $t$.

We can now turn to the problem of computing the critical value $J_c$ if the perception is computed on the information network that is partially different from that of the real infection. Here the perception of the importance of the

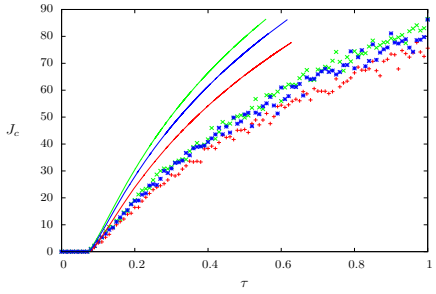


**Fig. 3.** Comparison between the results of the mean field approximation and simulations for three instances of scale-free networks with $\gamma = 2.4$, $N = 10000$, $m = 2$ and $K = 300$. Although the simulations give similar results, the mean-field computations (that coincide with the simulation only for $J_c = 0$) are very dependent on the details of the network.

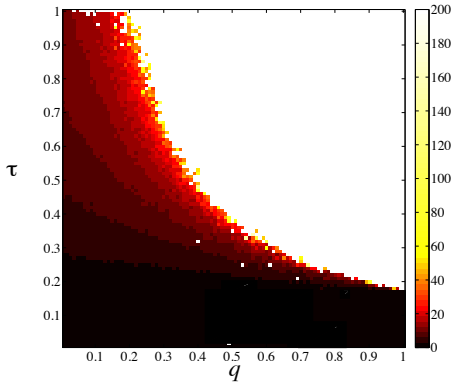


**Fig. 4.** Critical precaution threshold $J_c$ (color code) as a function of the bare infectiousness $\tau$ and of the difference between the real and the information network $q$. Here the real and virtual networks are Poissonian (random) with $\langle k \rangle = 6$ and $N = 1000$. In the darker region there is always a value of $J_c$ able to stop the epidemics, while in the lighter region the epidemics cannot be stopped. The separation boundary is the stoppability frontier.

infection, $\overline{s}_i$, is computed on the neighbours $\overline{j}^{(i)}$ on the information network. The perceived number of infected neighbours depends on how many of them, in the information network, have a value $J_{\overline{j}}$ larger than that computed in the real network, i.e.,

$$J_i(t+1) = \underset{j=j_1^{(i)},\ldots,j_{k_i}^{(i)}}{\text{MAX}} \min\left(-\frac{k_i}{\overline{s}_i(J_j)} \ln\left(\frac{r_{ij}(t)}{\tau}\right), J_j(t)\right), \tag{16}$$

where

$$\overline{s}_i(J) = \sum_{\overline{j}=\overline{j}_1^{(i)},\ldots,\overline{j}_{k_i}^{(i)}} [J_{\overline{j}} \geq J]. \tag{17}$$

In other words: for any value of $J$ in the real neighbourhood one computes how many neighbours $\overline{j}$ in the *information* network have $J_{\overline{j}} \geq J$. This is the perceived value of the risk.

## 5 Results

In this section we show the results of the self-organized percolation method in both single-layered and multiplex networks (with and without risk perception).

For our experiments we fixed the size of the networks $N = 1000$ and the *percolation time* $T = 10000$.

We investigated the SIS dynamics over regular, Poisson and scale-free networks as shown in Fig. 1: in particular we evaluated the critical epidemic threshold values $p_c \equiv \tau_c$ for which there is at least one percolating clusters with at least one infected nodes.

Considering a regular lattice with connectivity degree $k = 2$, we found $\tau_c \simeq 0.6447$ which is compatible with the results of the bond percolation transition in the Domany-Kinzel model [25].

In the case of random networks with Poisson degree distributions the critical epidemic threshold $\tau_c = \langle k \rangle / \langle k^2 \rangle \simeq \langle k \rangle^{-1}$ if the distribution is sharp [5]. Indeed, for Poisson network with $\langle k \rangle = 12$ the self-organized percolation method gives $\tau_c \simeq 0.08 \simeq 1/12$.

For a scale-free network with $\langle k \rangle = 13.95$ and $\langle k^2 \rangle = 538.5$ we get from simulations $\tau_c \simeq 0.026$, in agreement with the expected value.

We then investigated the effects of risk perception in a simple model of epidemic spreading. Here we show the results of the direct percolation method comparing the simulations with the theoretical formulation derived in Section 3.

Results are quite interesting if compared with the simple SIS dynamics (Fig. 1) here we are able to stop the epidemic increasing the bare infection $\tau$ until $\tau = 1$. Considering for instance the case of random networks with $\langle k \rangle = 6$ in which we found a critical value of $\tau_c = 0.165$ (Fig. 1) while in Fig we observe that after that value of $\tau_c$ we need to adopt a precaution level $J > 0$ in order to stop the spreading of the disease. The same consideration can be done also for the other scenarios.

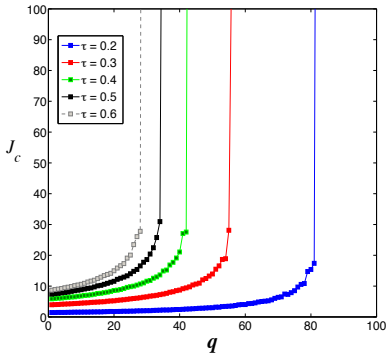


**Fig. 5.** Critical precaution threshold $J_c$ versus the difference between the real and the information network $q$ for some values of the bare infectiousness $\tau$ (from right to left: $\tau = 0.2, 0.3, \ldots, 0.6$). Random real and virtual networks, both with $\langle k \rangle = 6$ and $N = 10000$.

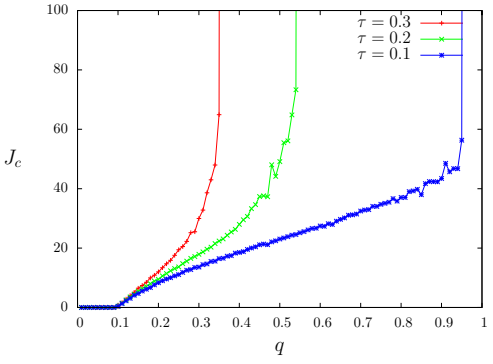


**Fig. 6.** Critical precaution threshold $J_c$ versus the difference between the real and the information network $q$ for some values of the bare infectiousness $\tau$(from right to left $\tau = 0.1, 0.2, 0.3$). Random real network and scale-free virtual network, both with $\langle k \rangle = 6$, $N = 10000$.

### 5.1 Multiplex Risk Perception

Finally, we illustrate our results for risk perception in multiplex networks. The phase diagram for the risk-perception in modelling SIS dynamics in multiplex networks is reported in Fig. 4. The general shape of this phase diagram can be understood considering the continuous approximation, Eq. (4). A given node of connectivity $k$ is connected, in the information network, to a $(1-q)k$ real neighbours, and to $qk$ virtual ones. At the threshold, the global fraction of infected sites is small. For the spreading of the epidemics, the important sites are those that have a infected real neighbour. It might be assumed that the virtual neighbours, being uncorrelated with the real ones, do not contribute at all to the risk perception. Among the real neighbours, the fraction $kq$ replaced by virtual ones has become invisible, and so the perception decreases by a factor $q$. Replacing $J_c$ with $qJ_c$ in Eq. (4) for the scale-free case one gets $\tau q^{3-\gamma} = \text{const}$, and indeed the shape of the stoppability frontier of Fig. 4 resembles that of a generalized hyperbola.

The general trend is that, increasing the difference $q$ between the information network and the real one it becomes harder to stop an epidemics. It is interesting to investigate this transition. As we can see in Fig. 6, this transition is quite sharp, especially for low values of $\tau$. A similar scenario holds for a mixture of random real and random ghost networks, as shown in Fig. 5.

## 6 Conclusions

We investigated the interplay between epidemic spreading and risk perception on multiplex networks, exploiting mean-field approximations and a self-organized method, that automatically gives the percolation threshold in just one simulation. We focused on multiplex networks, considering that people get infected by contacts in real life but often gather information from an information networks, that may be quite different from the real ones. The main conclusion is that the similarity between the real and information networks determine the possibility of stopping the infection for a sufficiently high precaution level: if the networks are too different there is no mean of avoiding the epidemics. Moreover, especially for low values of the bare infectiousness probability, this transition occurs sharply without evident forerunners. This last observation remarks that, although the virtual world has indeed the advantage of allowing a fast diffusion of information, real epidemics still propagate in the real world. This is of particular importance for "neglected" diseases, possibly diffused in marginalized parts of the population that have little access to Internet (and that in any case are not part of the "neighbourhood" of "real neighbors" belonging to other social classes).

**Acknowledgements.** FB acknowledges partial financial support from the EU projects 288021 (EINS – Network of Excellence in Internet Science) and 611299 (FP7 Programme on Collective-Awareness Platforms SciCafe2.0). The authors are grateful to Dr. Nicola Perra for helpful discussions.

## References


1. Pandemic Scares Throughout History. Health Magazine (2013)
2. Wikipedia (2013), http://en.wikipedia.org/wiki/Pandemic
3. The "false" pandemic: Drug firms cashed in on scare over swine flu, claims Euro health chief. Daily Mail (2010)
4. Moore, C., Newman, M.E.J.: Epidemics and percolation in small-world networks. Phys. Rev. E 61, 5678–5682 (2000)
5. Pastor-Satorras, R., Vespignani, A.: Epidemic spreading in scale-free networks. Phys. Rev. Lett. 86, 3200–3203 (2001)
6. Newman, M.E.J.: Exact solutions of epidemic models on networks. Working Papers 01-12-073, Santa Fe Institute (December 2001)
7. May, R.M., Lloyd, A.L.: Infection dynamics on scale-free networks. Phys. Rev. E 64, 066112 (2001)
8. Pastor-Satorras, R., Vespignani, A.: Immunization of complex networks. Phys. Rev. E 65, 036104 (2002)
9. Bagnoli, F., Liò, P., Sguanci, L.: Risk perception in epidemic modeling. Phys. Rev. E 76, 061904 (2007)
10. Ginsberg, J., Mohebbi, M., Patel, R., Brammer, L., Smolinski, M., Brilliant, L.: Detecting influenza epidemics using search engine query data. Nature 457, 1012–1014 (2009)
11. Scanfeld, D., Scanfeld, V., Larson, E.L.: Dissemination of health information through social networks: Twitter and antibiotics. American Journal of Infection Control 38(3), 182–188 (2010)
12. Chew, C., Eysenbach, G.: Pandemics in the age of twitter: Content analysis of tweets during the 2009 h1n1 outbreak. PLoS One 5(11), 014118 (2010)
13. The State of the News Media. The Pew Research Center's project for Excellence in Journalism (2010)
14. Kurant, M., Thiran, P.: Layered complex networks. Phys. Rev. Lett. 96, 138701 (2006)
15. Mucha, P.J., Richardson, T., Macon, K., Porter, M.A., Onnela, J.-P.: Community structure in time-dependent, multiscale, and multiplex networks. Science 328(5980), 876–878 (2010)
16. Szell, M., Lambiotte, R., Thurner, S.: Multirelational Organization of Large-scale Social Networks in an Online World (2010)
17. Arenas, A., Lozano, S., Rodriguez, X.-P.: Evolution of cooperation in multiplex networks. Scientific Reports 2 (2012)
18. Bianconi, G.: Statistical mechanics of multiplex networks: Entropy and overlap. Phys. Rev. E 87, 062806 (2013)
19. Buldyrev, S.V., Parshani, R., Paul, G., Stanley, H.E., Havlin, S.: Catastrophic cascade of failures in interdependent networks. Nature 464(7291), 1025–1028 (2010)
20. Gao, J., Buldyrev, S.V., Stanley, H.E., Havlin, S.: Networks formed from interdependent networks. Nat. Phys. 8(1), 40–48 (2012)
21. Granell, C., Gómez, S., Arenas, A.: Dynamical interplay between awareness and epidemic spreading in multiplex networks. Phys. Rev. Lett. 111, 128701 (2013)

22. Bagnoli, F., Palmerini, P., Rechtman, R.: Algorithmic mapping from criticality to self-organized criticality. Phys. Rev. E 55, 3970–3976 (1997)
23. Dorogovtsev, S.N., Mendes, J.F.F.: Evolution of networks. Advances in Physics 51, 1079–1187 (2002)
24. Pastor-Satorras, R., Vespignani, A.: Epidemic dynamics in finite size scale-free networks. Physical Review E 65(035108) (2002)
25. Domany, E., Kinzel, W.: Equivalence of cellular automata to ising models and directed percolation. Phys. Rev. Lett. 53, 311–314 (1984)

# Applications of Multifractal Diffusion Entropy Analysis to Daily and Intraday Financial Time Series

Petr Jizba[1,2] and Jan Korbel[1,3]

[1] Faculty of Nuclear Sciences and Physical Engineering,
Czech Technical University in Prague, Břehová 7, 115 19, Prague, Czech Republic
[2] Institute for Theoretical Physics, Freie Universität Berlin,
Arnimallee 14, 14195, Berlin, Germany
[3] Max-Planck-Institute for the History of Science,
Boltzmannstr. 22, 14195 Berlin, Germany
{petr.jizba,korbeja2}@fjfi.cvut.cz

**Abstract.** Scaling properties and fractal structure are one of the most important aspects of real systems that point to their complexity. These properties are closely related to the theory of multifractal systems and theory of entropy. Estimation of scaling (or multifractal) exponents belongs to the essential techniques that can reveal complexity and inner structure of the system. To successful techniques belongs Multifractal diffusion entropy analysis, based on estimation of Rényi entropy of the system. In the recent article [1], we have discussed one possible method of estimation Rényi entropy from proper estimation of underlying probability histograms. In Ref. [2], we have applied the method to daily and intraday financial data in order to test the stability of the system. This article summarizes existing progress in this field and shows the robustness of the method on high-frequency financial data.

**Keywords:** Financial time series, Rényi entropy, Multifractal analysis.

## 1 Introduction

Complex systems are currently in a viewfinder of many scientists across the fields. This is because complexity and emergent behavior is observed on a large number of various dynamical systems as for example dynamical [3], physical [4], climatic [5], biological [6], social [7] and financial [8]. Classical models exhibit lack of power to capture the complexity of such systems and there is necessary to come with some new concepts, as e.g. *Multifractal analysis*, introduced e.g., in [9–11]. Particular methods, as e.g., *Detrended Fluctuation Analysis* [12], *Wavelet Analysis* [13], *Generalized Hurst Exponent* [14], have celebrated a great success in order to reveal scaling exponents. In the recent paper [1], we investigated yet another approach, i.e. *Diffusion Entropy Analysis* [15, 16], which is based on estimation of Rényi entropies, that are closely related to scaling exponents [17]. We have shown that it is necessary to estimate the bin-with of



A. Sanayei et al. (eds.), *ISCS 2014: Interdisciplinary Symposium on Complex Systems*,
Emergence, Complexity and Computation 14, DOI: 10.1007/978-3-319-10759-2_34

probability histograms properly. Moreover, in [2] we have applied the MFDEA approach to several types of financial time series in order to test the robustness of the method and its limitations. We have also used high-frequency data to compare the spectra with analysis on daily data.

This paper is organized as follows: after an introduction to multifractal analysis in Sect. 2, the main method of the paper, i.e., Multifractal Detrended Fluctuation Analysis, is briefly introduced in Sect. 3. Sect. 4 is devoted to the overview of theoretical aspects of the method, while Sect. 5 presents the application of the method on some particular examples of financial time series.

## 2 Multifractal Analysis

In this section we briefly introduce some basics of multifractal analysis [9,11,18, 19]. Let us have a discrete time series $\{x_i\}_{i=1}^{N}$, with a characteristic time lag $s$. All obtained values are divided into separate regions $K_j$ and empirical probabilities $p_j$ in each region are calculated as $p_j = N_j/N$, where $N_j$ is a number of elements that falls into region $K_j$. Let us assume that these probabilities scale with $s$ as $p_j(s) \propto s^{\alpha_j}$, where $\alpha_j$ is a typical exponent for the region $K_j$. We assume that probability of regions scaling with an exponent $\alpha$ depends smoothly on $\alpha$ so

$$\rho(s,\alpha)\mathrm{d}\alpha \;=\; c(\alpha)s^{-f(\alpha)}\mathrm{d}\alpha\,. \tag{1}$$

Here $f(\alpha)$ is called *multifractal spectrum*, which is nothing else than a scaling exponent of $\rho(s,\alpha)$. Usually, we also define an alternative multifractal measure called *partition function* $Z(q,s) = \sum_j p_j^q(s)$. In this case, partition function scales as

$$Z(q,s) \;=\; \sum_j p_j^q(s) \propto s^{\tau(q)}\,. \tag{2}$$

It can be easily shown, that $\tau(q) = \max_\alpha(q\alpha - f(\alpha))$ [11]. This is nothing else than Legendre transform from $(\alpha, f(\alpha))$ to $(q, \tau(q))$.

Exponent $\tau(q)$ is closely related to Rényi entropy $H_q(s) = \frac{1}{1-q}\ln Z(q,s)$. For $\lim_{q\to 1} H_q$, be become the well-known Shanon entropy. Scaling exponents of Rényi entropy $D_q$, obtained from relation $H_q(s) \sim s^{D_q}$, are connected to scaling exponents $\tau(q)$ by a relation $D_q \;=\; \frac{\tau(q)}{q-1}$.

Scaling exponents $D_q$ are also known as *generalized dimensions* [11,17]. For particular values generalized dimensions coincide with other familiar fractal dimensions as informational dimension or correlation dimension. The important implication from the above relations is that it is possible to estimate any of the scaling exponents ($f(\alpha)$, $\tau(q)$ and $D_q$) and then to transform them to the others.

## 3 Multifractal Detrended Fluctuation Analysis

The Multifractal Detrended Fluctuation Analysis is based on estimation of (continuous) Rényi entropy,

$$H_q(t) \;=\; \frac{1}{1-q}\ln\int p^q(x,t)\mathrm{d}x\;, \tag{3}$$

from which we get the scaling exponents via the relation

$$H_q(t) \;=\; \delta(q)\ln t + B(q) \tag{4}$$

In case of complex processes (e.g., Multifractal Random Walk [20], Multifractal Model of asset Returns [21] and also models discussed in Refs. [1, 17]), the $\delta(q)$ is actually $q$-dependent function and is closely related to $D_q$.

The estimation of the exponents consists of two steps: firstly, we have to to estimate the probability distribution $p(x,t)$ for different times; secondly, from estimated distributions we can calculate Rényi entropies and subsequently $\delta(q)$-spectrum from the linear regression. In case of stationary time series, we use the so-called *Fluctuation collection algorithm* (FCA). We sum up all noise-like values of the series into partial sums. These sums of fluctuations $\xi^k(s) = \sum_{t=1}^{n-s} x_{t+k}(s)$ can be therefore exploited to probability estimation; when we divide the space into boxes $K_i$ of length $h$ (also called bin-width), the *histogram* $\hat{p}_j(s)$ that approximates theoretical probability distribution is defined as

$$\hat{p}_j(s) \;\equiv\; \frac{\#\{k \mid \xi^k(s) \in K_j\}}{N-s+1}\,, \tag{5}$$

where symbol # denotes the number of elements. The whole algorithm is depicted in Fig. 1. Of course, the important role in histogram estimation plays the choice of bin-width $h$. In extreme cases, i.e., when number of boxes $K_i$ is too large or too small, we get a degenerate histogram that for too few boxes looses too much information about the distribution shape (shown in Fig. 2), in case of too many boxes, the histogram disintegrates into counting function of particular values. This affects also the precision of spectrum estimation (Fig. 3). The next section discusses the problem optimal histogram bin-width in case of MFDEA method.

## 4 Optimal Bin-Width of Histograms in MFDEA Approach

In theory of statistics we have to usually create an approximation $\hat{p}(x)$ of probability distribution $p(x)$ from input data $\{x_i\}_{i=1}^N$. The histogram is in one-dimensional case defined as

$$\hat{p}(x) \;=\; \frac{1}{Nh}\sum_{j=1}^{n_B}\nu_j\chi_j(x)\,, \tag{6}$$

where $n_B$ is number of boxes $K_j$, $\nu_j$ is the absolute occurrence frequency of $K_j$ and $\chi_j(x)$ is a characteristic function of interval $\mathcal{K}_j = [x_0 + (j-1)h, x_0 + jh]$. The optimal bin-width $h^*$, for which the histogram is most proper approximation of $p(x)$, can be obtained by several different approaches, from classical *Sturges rule* [22], that simply estimates the optimal number of bins as $n_B = 1+\log_2 N$, to the approaches based on asymptotic mean squared integrated

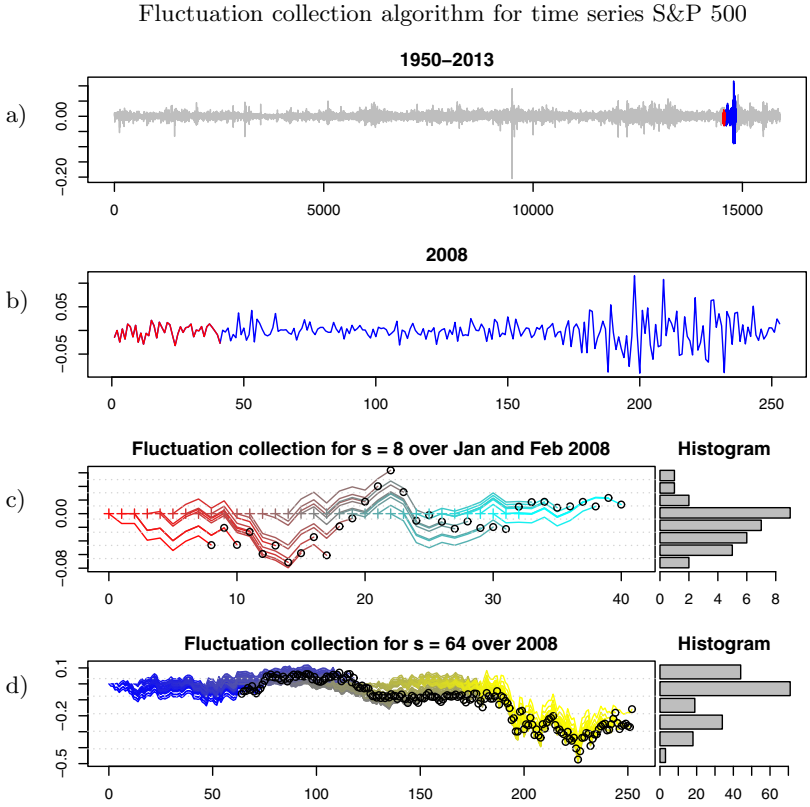


**Fig. 1.** Illustration of *fluctuation collection algorithm*. From above: a) Time series of financial index S&P500 from January 1950 to March 2013, containing approx. 16000 entries. b) A subset of S&P500 for the year 2008 alone. c) Fluctuation collection algorithm for the first two months of 2008 and $s = 8$ days. Series are partially integrated, i.e., fluctuation sums are collected into the histogram on the right-hand side. d) Fluctuation collection algorithm for the whole year 2008 for $s = 64$. Bin-widths of both histograms were estimated separately for both histograms.

error, as i.e., *Scott rule* [23], which estimates the bin-width as $\hat{h}^{Sc} = 3.5\hat{\sigma}N^{-1/3}$, respectively *Freedman-Diaconis rule* [24], which estimates the bin-width as $\hat{h}^{FD} = 2(\widehat{IQR})N^{-1/3}$, where $\hat{\sigma}$ is empirical variance and $\widehat{IQR}$ is *interquantile range*.

In case of MFDEA approach, we need not only approximations of $p(x)$, but also its powers $p^q(x)$ (in most cases, the estimation restricts only for $q > 0$, because of instability for negative coefficients [17]). We show that it is also necessary to choose different bin-widths for every $q$. The natural measure of discrepancy between histogram and theoretical distribution is the *expected Rényi divergence*

$$\mathbb{E}_{\mathcal{H}}[D_q(p||\hat{p})] \;=\; \frac{1}{q-1}\mathbb{E}_{\mathcal{H}}\left[\ln \int_{\mathbb{R}} \hat{p}^{1-q}(x)p^q(x)\mathrm{d}x\right], \qquad (7)$$

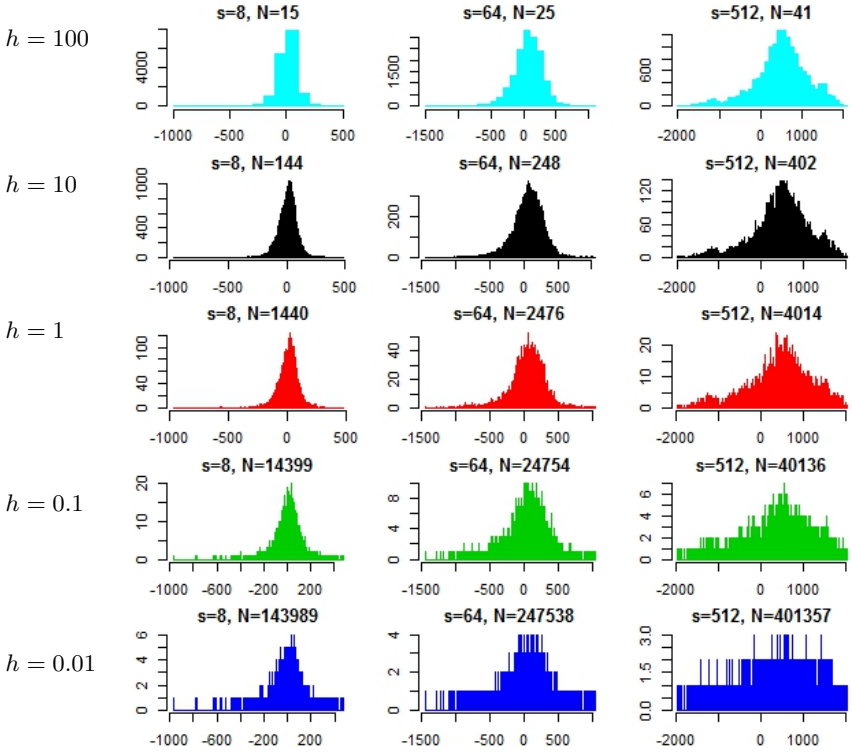


**Fig. 2.** Un-normalized (or frequency-based) histograms of the fluctuation sums $\sigma_s$, with $s = 8$, 64 and 512 and with bin-widths $h = 100, 10, 1, 0.1$ and 0.01, measured in units $u = 3 \times 10^{-4}$ for better visualization. We can see that for not optimal bin-widths, the shape of histogram is not appropriately approximating the theoretical probability distribution, i.e., we observe under-fitted or over-fitted histograms.

where $\mathbb{E}_{\mathcal{H}}$ denotes the average over all possible histograms. Unfortunately, dealing with the divergence is technically difficult, so we rather use similar approach based on mean-squared integrated error between $q$-th powers of $p(x)$ and $\hat{p}(x)$ [1]

$$\mathbb{E}_{\mathcal{H}} \|p^q - \hat{p}^q\|_{L_2}^2 = \mathbb{E}_{\mathcal{H}} \int_{\mathbb{R}} (p^q(x) - \hat{p}^q(x))^2 \mathrm{d}x \,. \tag{8}$$

The main advantage lies in the fact that when minimizing the error, we can interchange the integral and expectation value, so we get

$$\min_{h>0} \mathbb{E}_{\mathcal{H}} \|p^q - \hat{p}^q\|_{L_2}^2 = \min_{h>0} \sum_{j=1}^{n_B} \int_{\mathcal{K}_j} \mathbb{E}_{\nu_j} \left[ \left( p^q(x) - \frac{\nu_j^q}{N^q h^q} \right)^2 \right] \mathrm{d}x \,. \tag{9}$$

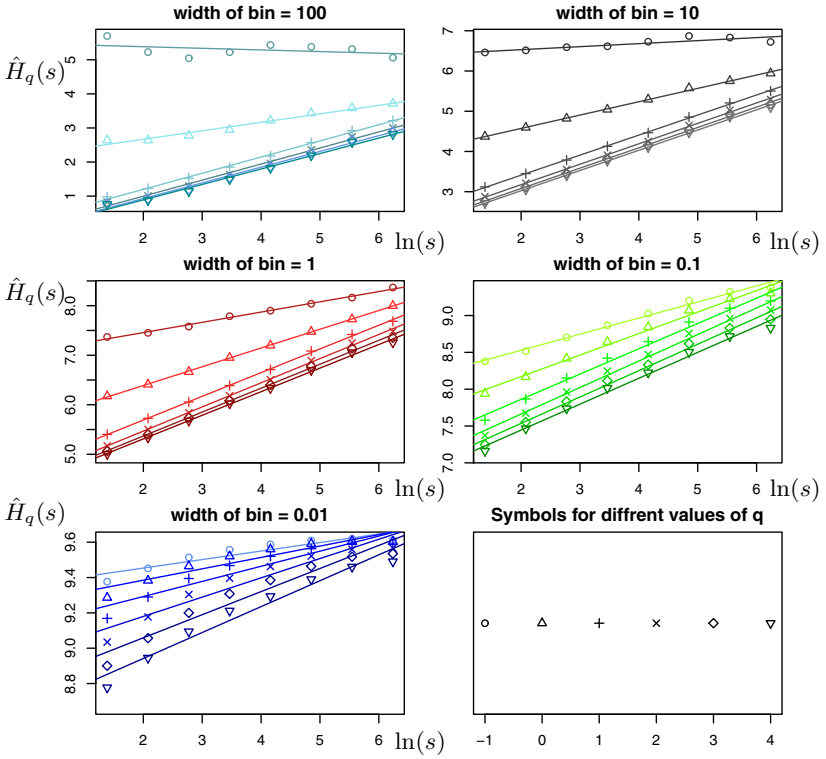


**Fig. 3.** Linear fits of estimated Rényi entropy vs. logarithm of $s$ with $h = 100, 10, 1, 0.1, 0.01$, measured in the same units as in Fig. 2, i.e., in units $u = 3 \times 10^{-4}$. Note, in particular, that the error is also non-trivially reflected in the defining linear regression for the scaling exponents (also dependent on $q$). This means that choice of a single $h^*$ valid for all $q$'s leads to incorrect results and one has to resort to $h_q^*$ that is $q$-dependent.

Here, the expected value is calculated only locally, i.e. as mean of multinomial variable $\nu_j \in \{1, \ldots, n\}$. Calculating of the optimal value in the leading order $\mathcal{O}(N^{-2} + hN^{-1})$ [25], gives us the optimal value $h_q^*$ equal to [1]

$$h_q^* = \sqrt[3]{\frac{6q^2}{N} \frac{\int_{\mathbb{R}} p^{2q-1}(x)\mathrm{d}x}{\int_{\mathbb{R}} (\mathrm{d}p^q(x)/\mathrm{d}x)^2 \mathrm{d}x}}\,. \tag{10}$$

Assuming that the normality of $p(x)$, we get

$$h_q^* = \sigma N^{-1/3} \sqrt[3]{24\sqrt{\pi}} \frac{q^{1/2}}{\sqrt[6]{2q-1}} = h_1^* \rho_q\,, \tag{11}$$

where the $h_1^*$ corresponds to the classic result obtained by Scott [23]. The estimation rule is then defined as $h_q^{Sc} = 3.5\hat{\sigma}N^{-1/3}\rho_q$, and similarly is estimated the Freedman-Diaconis rule as $h_q^{FD} = 2.6(\widehat{IQR})N^{-1/3}\rho_q$. For estimation of $\delta(q)$-spectrum, we need to have exponents on several time scales. In this case, the most

appropriate way is to estimate all histograms at the same bin-width, otherwise one would need to keep in mind the necessity of recalculation of histograms.

The optimal bin-width for several simultaneously estimated histograms can be obtained by minimization of the *Total mean squared error*, which is nothing else than sum of mean squared errors for particular histograms listed in Eq. (8). Having several time scales $\{s_1, \ldots, s_m\}$, we get that the optimal bin-width that minimizes total mean squared error under an assumption of normal underlying distribution is equal to [1]

$$h_q^* = (24\sqrt{\pi})^{1/3} \rho_q \sqrt[3]{\frac{\sum_{i=1}^{m} \sigma_{s_i}^{2(1-q)} / N_{s_i}}{\sum_{i=1}^{m} \sigma_{s_i}^{-(1+2q)}}}, \tag{12}$$

where $\sigma_{s_i}$ and $N_{s_i}$ are standard deviation of probability distribution in time $s_i$ and $N_{s_i} = N - s_i + 1$ is the number of fluctuations collected at time $s_i$. After inserting the empirical variance and the multiple of interquartile range, one obtains analog bin-width rules to the case, when $i = 1$, i.e. when we have to optimize only one histogram.

## 5 Numerical Estimation of Scaling Exponents of Financial Time Series

The numerical analysis is divided into two parts. Firstly, in [1], we have estimated the optimal win-width $h_q$ and the $\delta(q)$-spectrum for the time series of daily returns of financial index S&P500. In Fig. 4, optimal bin-width and $\delta(q)$-spectrum are depicted for both Scott and Freedman-Diaconis method. We observe that for values $q < 1/2$, the bin-width diverges and the spectrum collapses. That is caused by leading-order expansion and normality assumption. This problem could be patched by estimation of bounded model, which would not allow only values larger than some given threshold. Nevertheless, theoretical estimation of such threshold is almost improbable and the improper estimation of the maximal value could affect the whole spectrum estimation. This is one of the limitations of the method.

In the second part of the analysis [2], we have used the MFDEA to investigate scaling exponents of financial time series. We have investigated several kinds of data, from share prices, indices, currency ratios to volatility. We have used two types of time series, i.e., daily data and minute data. We try to estimate the spectrum with help of MFDEA method to see the differences between the nature of time series and to test the robustness of the method. We can observe a distinct difference between the spectrum of volatility compared to other spectra, which is given by its nature and memory effects observed usually in the volatility series [8]. We can observe that especially in case of intraday data, the spectrum is not smooth, or there are present some outliers in the spectrum. That can be caused by the fact that for short periods, financial data exhibit heavy-tailed persistent behavior, which should be modeled by power-law models rather than Gaussian distributions.

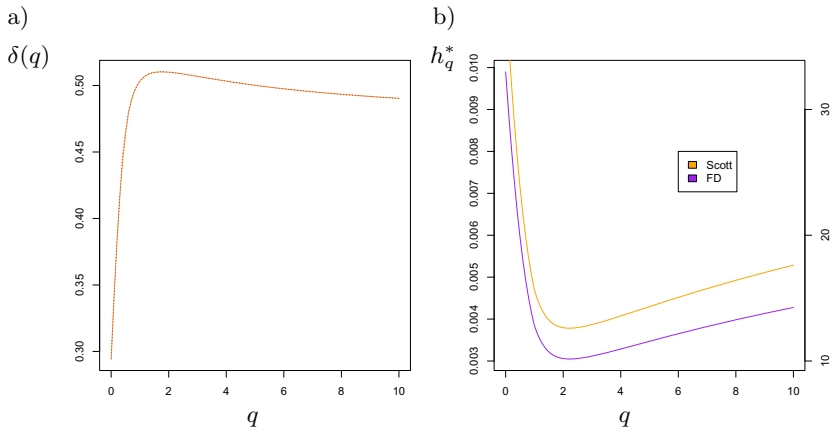


| method | optimal bin-width for $q = 1$ |
|---|---|
| Scott | 0.00470 |
| Freedman–Diaconis | 0.00384 |

**Fig. 4.** From left: a) $\delta(q)$ spectrum for bin-widths estimated by different methods. Spectra for both methods almost everywhere coincide. b) Optimal bin-widths $\hat{h}_q^*$ for both methods. Under figures: Table with optimal values of $h_1^*$ for different methods.

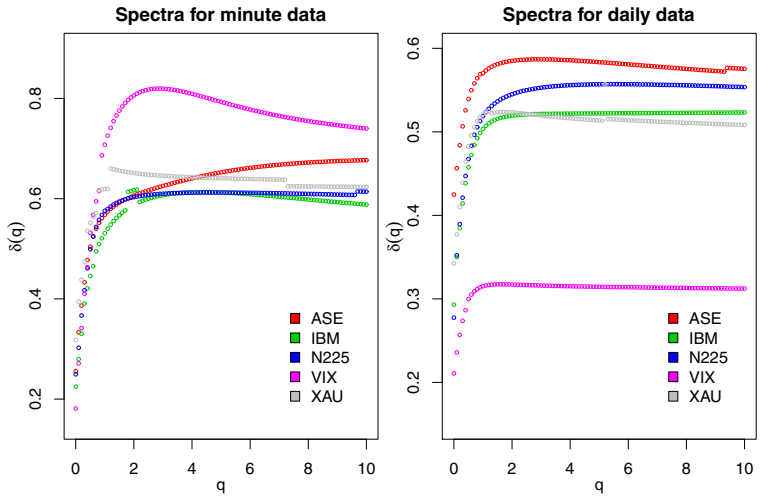


**Fig. 5.** $\delta(q)$-spectrum of various financial time series. Spectra are estimated for five different series (Athens stock index, IBM stock price, Nikkei 225 stock index, Volatility index of S&P 500 and gold price) and two different time scales (minute data and daily data). Minute time series are from year 2013 and have approximately $10^5$ entries, daily data are from the last ten to twenty years (depending on the particular series) and have 5000 to 10000 records.

## 6 Conclusions and Perspectives

In this paper we have used the Multifractal Diffusion Entropy Analysis to estimate $\delta$-spectrum of several financial time series. In a theoretical part of the paper we have discussed some aspects of multifractal analysis and stressed the recent progress in the MFDEA method, including optimal bin-width estimation [1]. The optimal bin-width was obtained by minimization of mean squared integrated error. In the latter part of the paper, the $\delta$-spectrum was estimated for financial time series on two different time scales [2]. The estimation showed us the necessity of a proper bin-width estimation. The limitations in case of heavy-tailed models were also discussed and authors believe that future research will bring some more results that would include also power-law distributions.

**Acknowledgments.** We want to thank to Xaver Sailer of Nomura, Ltd., who provided us with financial data. This work was supported by the Grant Agency of the Czech Republic, grant No. GCP402/12/J077, and the Grant Agency of the CTU in Prague, grant No. SGS13/217/OHK4/3T/14.

## References

1. Jizba, P., Korbel, J.: Multifractal diffusion entropy analysis: Optimal bin-width of probability histograms. Physica A 413, 438–458 (2014)
2. Jizba, P., Korbel, J.: Multifractal diffusion entropy analysis: Applications to financial time series. In: Proceedings ITISE 2014, International Work-Conference on Time Series (2014)
3. Bar-Yam, Y.: Dynamics of complex systems, vol. 213. Addison-Wesley, Reading (1997)
4. Kleinert, H.: Path Integrals in Quantum Mechanics, Statistics, Polymer Physics and Financial Markets, 4th edn. World Scientific (2009)
5. Lovejoy, S., Schertzer, D.: The weather and Climate: emergent laws and multifractal cascades. Cambridge University Press (2013)
6. Jensen, H.J.: Self-organized criticality: emergent complex behavior in physical and biological systems, vol. 10. Cambridge University Press (1998)
7. Luhmann, N.: Social systems. Stanford University Press (1995)
8. Mantegna, R., Stanley, H.E.: An introduction to econphysics: cirrelations and complexity in finance. Cambridge University Press (2000)
9. Harte, D.: Multifractals: Theory and Application. Chapmann & Hall/CRC (2001)
10. Mandelbrot, B.: Self-affine fractals and fractal dimension. Physica Scripta 32, 257–260 (1985)
11. Hentschel, H., Procaccia, I.: The infinite number of generalized dimensions of fractals and strange attractors. Physica D 8(3), 435–444 (1983)
12. Kantelhardt, W., Zschiegner, S., Koscielny-Bunde, E., Havlin, S., Bunde, A., Stanley, H.E.: Multifractal detrended fluctuation analysis of nonstationary time series. Physica A 316, 87 (2002)
13. Muzy, J.F., Bacry, E., Arneodo, A.: Multifractal formalism for fractal signals: The structure-function approach versus the wavelet-transform modulus-maxima method. Phys. Rev. E 47(2), 875 (1993)

14. Morales, R., Matteo, T.D., Gramatica, R., Aste, T.: Dynamical generalized hurst exponent as a tool to monitor unstable periods in financial time series. Physica A 391(11), 3180 (2012)
15. Scafetta, N., Grigolini, P.: Scaling detection in time series: diffusion entropy analysis. Phys. Rev. E 66(3), 036130 (2002)
16. Huang, J., et al.: Multifractal diffusion entropy analysis on stock volatility in financial markets. Physica A 391(22), 5739 (2012)
17. Jizba, P., Arimitsu, T.: The world according to Rényi: thermodynamics of multifractal systems. Annals of Physics 312(1), 17 (2004)
18. Mandelbrot, B.: Multifractals and 1/f Noise: Wild Self-Affinity in Physics (1963-1976). Springer (1999)
19. Stanley, H.E., Meakin, P.: Multifractal phenomena in physics and chemistry. Nature 335(29), 405 (1988)
20. Bacry, E., Delour, J., Muzy, J.F.: A multifractal random walk. Phys. Rev. E 64, 200–201 (2000)
21. Mandelbrot, B., Calvet, L., Fisher, A.: A multifractal model of asset returns. Cowles Foundation Discussion Papers (1164)
22. Sturges, H.: The choice of a class-interval. J. Amer. Statist. Assoc. 21, 65 (1926)
23. Scott, D.W.: Multivariate density estimation: Theory, practice and visualisation. John Willey and Sons, Inc. (1992)
24. Freedman, D., Diaconis, P.: On the histogram as a density estimator. Zeitschrift für Wahrscheinlichkeitstheorie und Verwandte Gebiete 57(4), 453 (1981)
25. Scott, D.W.: Feasibility of multivariate density estimates. Biometrika 78(1), 197 (1991)

# An Economic Approach to the Evolution of an Ecology

Doug McLeod

Charles Sturt University, Bathurst Australia

**Abstract.** We construct a simple economic model for a biological system using Markov chains with variable coefficients, in order to investigate how a biological system organizes itself and whether any measure of progress can be defined. We show that if exchange of resources between creatures is based on relative scarcity, we get a similar outcome to a market economy even though such exchanges are not reciprocal. The biological economy promotes the development of specialization and interdependence - an ecology. Within the framework of this simple model, the number of creatures increases over time which may be construed as a large scale trend.

**Keywords:** complexity, economic biology, Lesley matrix, evolutionary biology, large scale trend.

## 1 Introduction

Nowadays biologists prefer to speak in terms of 'large scale trends' rather than 'progress' in evolution. McShea [1] identifies eight evolutionary trends: entropy, energy intensiveness, evolutionary versatility, developmental depth, structural depth, adaptedness, size of creature and complexity. What is interesting about McShea's list is the omission of two dimensions which to an economist would seem most obvious:

- efficiency of resource usage
- amount of total biomass

We model the evolution of an ecosystem by employing the following concepts from economics. Our agents are referred to as creatures rather than firms or consumers.

- *Resources* We focus on resources rather than on predation which is more typical of biological models. Economics investigates the allocation of scarce resources so we assume that one resource is fixed in amount. In Malthusian fashion we take it that this sets an upper limit on the population of creatures.
- *Exchange* Here we do not have a monetary economy but one based on the donation of resources by one creature to another without reciprocal compensation. As we shall see, this does not make as much difference to behaviour or the final outcome as one might expect, because there is a pattern of resource flows within the community.



A. Sanayei et al. (eds.), *ISCS 2014: Interdisciplinary Symposium on Complex Systems*,
Emergence, Complexity and Computation 14, DOI: 10.1007/978-3-319-10759-2_35

- *Behaviour* is habitual. Creatures have fixed probabilities of doing various things in particular situations so their behaviour can be represented by a Markov chain. This is not the normal assumption is economics, which is based on optimisation (but from an empirical point of view, habitual behaviour is probably closer to the truth even in economic contexts).
- *Mutation* alters the behaviour of creatures, this is represented by a change of the coefficients in the Markov matrices. Mutation combined with natural selection leads to the same result as conscious optimisation.

We investigate the development of interrelationships and complexity in the system. The conclusions are that efficiency in resource usage will increase over time, and the number (or biomass) of individuals will increase as a result. The model is biological in a broad conceptual sense but it is a question whether enough biological detail has been incorporated to make our conclusions compelling to a practicing biologist.

## 2 The Model

There are two resources which a creature needs to sustain itself, and the amount of each resource changes in each period according to production, consumption and trade. When the creature is born, state B, it has the amount $\left(X^{1B}, X^{2B}\right)$ of resources 1, 2. If the amount of *either* resource falls to 0 then the creature dies, state D, and disappears. If the amount of *both* resources increases to the life state L or better, $\left(X^{1L}, X^{2L}\right)$, then the creature reproduces, creating $S$ new creatures which commence their life back at the B state.

*Production*: In the case of Resource 1 (r1), production increases the amount of r1 by one if it occurs. There is a fixed amount of resource in each period $L$ available to be allocated amongst $N$ creatures, and this affects the probability $p^{1P}$ of any one creature producing in the period.

$$N\ p^{P1} = L \tag{1}$$

In the case of Resource 2 (r2), production proceeds by the creature converting its stocks of r1 into r2. The amount of r1 decreases by 1 and the amount of r2 increases by 1.

*Consumption*: There are three subcategories:

- Metabolic. There is a fixed probability of metabolic consumption of each resource. The amount decreases by one.
- Reproduction. When a creature has the resources required for production $\left(X^{1L}, X^{2L}\right)$ or more and the reproduction transition is chosen, S new creatures are created at the birth state $B$.

$$\begin{bmatrix} X^{1L} \\ X^{1L} \end{bmatrix} = S \cdot \begin{bmatrix} X^{1B} \\ X^{2B} \end{bmatrix} \tag{2}$$

If the creature has more resources than the minimum required for reproduction, there will be a reduction of net resources. This is a type of wastage referred to as L (life) wastage.

- Death. If consumption or production causes a creature to run out of either resource then it dies and is transferred to the death state D. There is no transition from the death state. The resource which has been consumed will decrease by 1 as usual, but some amount of the other resource will be lost also - this type of wastage is referred to as D (death) wastage.

*Trade*: We assume that creatures move around their environment and they meet randomly. Where one creature has a resource and meets another creature, there is some chance that a unit of resource will be transferred to the other creature. The resource flow can go either way, but there is no reciprocity in a given transaction. Nor of course is there any expectation of reciprocity in the future, although it may work out that way. Such trade is symbiotic, each creature produces resources which the other creature can use. In practice most symbiotic relationships in biology occur at the cellular level, where different kinds of bacteria have various chemical roles to play; bacteria are the chemical processing plants of the living world. Symbiotic relationships can be distinguished from parasitic relationships, where the flow of resources can only go one way. The chains of predation which we tend to associate with biology fit into this class.

We assume trading relationships which reflect relative abundance (and scarcity), and this is what gives rise to the economic character of the trading. Trade is divided into:

- Trade in. Resources are received by the creature
- Trade out. Resources are lost by the creature

*Sitting*: This means that the creature stays in its current state and nothing changes. It has residual probability remaining after other processes have been accounted for.

*The transition matrix*: We represent state transitions by a transition matrix $\mathbf{M}_{M*M}$. Each element $m_{ij}$ of **M** gives the probabilities of transition from state *j* in this period to state *i* in the next period, i.e. we read down the columns to see what happens to state *j*. The creature may remain in the same state between one period and the next, this is represented by a probability at the diagonal element $m_{jj}$. Each possible combination of resource amounts $\left(X^1, X^2\right)$ corresponds to a state, so the dimension *M* of the matrix **M** is equal to the number of distinct resource states, i.e.

$$M = \left(X^{1MAX} + 1\right) \cdot \left(X^{2MAX} + 1\right) \tag{3}$$

D states like $\left(X^1,0\right)$ and $\left(0,X^2\right)$ which contain 0 of one resource are included to allow resource tracking but as they represent death they are never occupied and their columns contain only zeros. L states contain some probabilities which are multiplied by the number of descendants *S*. The elements in a column do not always sum to unity as probabilities are expected to, so the matrix **M** is not exactly a Markov chain matrix but rather a Lesley matrix, after biologist Patrick Lesley who introduced such matrices in the 1940s. In the biological literature the states in Lesley matrices usually represent different ages or developmental states, but here states represent resource amounts.

*The steady state.* The distribution of the population of the creature is denoted by $\boldsymbol{\pi}_{M*1}$ and the elements of $\boldsymbol{\pi}$ sum to unity. The Perron-Frobenius theorem states that for an irreducible non-negative real matrix there is a unique positive real and maximal eigenvalue, and a corresponding unique real positive eigenvector. As it is possible within transition matrix **M** to move from any states other than the D states to adjacent resource states (i.e. neighbouring states on the resource grid) and subsequently to any other state, **M** is irreducible save for the D states. We ignore the D states and their corresponding rows and columns in matrix **M**, and apply the Perron-Frobenius theorem to the remainder of **M**. We then apply the results to **M** by adding a zero to the eigenvectors for the D state.

So
$$\mathbf{M}\boldsymbol{\pi} = \lambda\,\boldsymbol{\pi} \tag{4}$$

where $\boldsymbol{\pi}_{M*1}$ represents the steady state distribution of population,
$\lambda_{1*1}$ is the rate of increase of the population per period

Also
$$\mathbf{v}\mathbf{M} = \lambda\mathbf{v} \tag{5}$$

where $\mathbf{v}_{1*M}$ represents the fitness coefficients (within the biological literature, the reproduction coefficients) of a population. Each element of fitness vector $\mathbf{v}$ represents the expected number of descendants that creatures in that state will have, measured relative to other states. Elements in the D state are zero. Here we scale eigenvector **v** so that

$$\mathbf{v}\,\boldsymbol{\pi} = 1 \tag{6}$$

*Resources*. We introduce the resource vector $\mathbf{X}_{K*M}$ which gives the amount of each of K resources for each state in **M**. Here $K = 2$. The expected amount of resource held per creature $\mathbf{R}_{K*1}$ is given by:

$$\mathbf{R} = \mathbf{X}\boldsymbol{\pi} \tag{7}$$

Resource matrix $\mathbf{R}$ is non-negative. The change in resource per creature per period is denoted $\Delta\mathbf{R}_{K*1}$.

RESULT 1: RESOURCE THEOREM. A population is stable if and only if the expected amount of resource per creature is stable.

$$\mathbf{X}(\mathbf{M}-\mathbf{I})\boldsymbol{\pi} = \mathbf{0}_{K*1} \tag{8}$$

PROOF: *Expected change in resource per creature by state* $= \mathbf{X}^{final} - \mathbf{X}^{initial}$ (9)

$$= \mathbf{XM} - \mathbf{X} = \mathbf{X}(\mathbf{M}-\mathbf{I}) \tag{10}$$

so $$\Delta\mathbf{R} = \mathbf{X}(\mathbf{M}-\mathbf{I})\boldsymbol{\pi} = (\lambda - 1)\mathbf{X}\boldsymbol{\pi} = (\lambda - 1)\mathbf{R} = 0 \quad \text{if } \lambda = 1 \tag{11}$$

#

*Creatures:* We introduce different types of creature, denoted c1 and c2 and indicated by subscripts on the variables. We assume that the creatures share same set of resource requirements and states although their transition matrices might differ in certain respects. This may appear to fly in the face of the obvious differences between different creatures, but the biochemical differences between creatures are surprisingly small on a cellular level, with similar or identical chemical processes being employed. What we observe are largely differences in scale and adaptation. Here we are interested in speciation - development of different species from one original - and the branching species will be identical in the first instance.

*Stability methodology*: We assume that changes in evolutionary time are relatively slow compared to the flow of generations, so only the steady state eigenvectors need to be considered and not transitory population dynamics.

## 3 Modelling Evolution

By representing creatures and their processes with a Markov chain we have a natural entry point for imposing mutation on the production function, namely changing the elements in the transition matrix. Two distinct types of mutation can be implemented in this model:

- incremental shifts, where a transition matrix parameter is perturbed incrementally.
- deletions, where the creature loses the ability to do something. Deletions are not incremental but involve setting parameters to zero. It is relatively easy for a creature to lose the ability to do something, since doing it requires everything to be functioning correctly.

The following result applies to incremental shifts:

RESULT 2: FITNESS THEOREM. The impact on the growth rate $d\lambda$ of an incremental mutation in the transition matrix **M** is given by:

$$d\lambda = \mathbf{v}\,d\mathbf{M}\,\boldsymbol{\pi} \tag{12}$$

PROOF: Differentiate (12) to get

$$d\mathbf{M}\boldsymbol{\pi} + \mathbf{M}d\boldsymbol{\pi} = d\lambda\,\boldsymbol{\pi} + \lambda\,d\boldsymbol{\pi} \tag{13}$$

$$\mathbf{v}\,d\mathbf{M}\boldsymbol{\pi} + \mathbf{v}\,\mathbf{M}d\boldsymbol{\pi} = \mathbf{v}\,d\lambda\,\boldsymbol{\pi} + \mathbf{v}\,\lambda\,d\boldsymbol{\pi} \qquad \text{times } \mathbf{v} \text{ on LHS} \tag{14}$$

$$\mathbf{v}\,d\mathbf{M}\boldsymbol{\pi} + \lambda\,\mathbf{v}\,d\boldsymbol{\pi} = d\lambda\cdot 1 + \mathbf{v}\,\lambda\,d\boldsymbol{\pi} \qquad \text{by (5), (6)} \tag{15}$$

#

This result (which curiously I have not found within the biological literature) gives a simple test of the fitness of a mutation representable by the elements of the transition matrix **M**. We do not have to consider the change in the transition matrix $d\mathbf{M}$ in the context of changes to the population vector $d\boldsymbol{\pi}$ or the fitness vector $d\mathbf{v}$ - which may not be known - but can evaluate $d\mathbf{M}$ using the existing population and fitness vectors $\boldsymbol{\pi}$ and **v**.

As we will show, deletion mutations may have considerable evolutionary importance as they cause the creature to specialize. We state a variant form of the Fitness Theorem which applies to these discrete jumps in matrix coefficients.

RESULT 3: DISCRETE FITNESS THEOREM. Suppose a population is stable ($\lambda = 1$) and a coefficient in the transition matrix **M** is set to zero and the diagonal element in that column altered to compensate (i.e. $m_{ij}^{new} = 0$ and $m_{jj}^{new} = m_{jj}^{0} + m_{ij}^{0}$).

If $$\mathbf{v}\Delta\mathbf{M}\boldsymbol{\pi} > 0 \tag{16}$$

then $$\lambda^{new} = \mathbf{v}^{new}\mathbf{M}^{new}\boldsymbol{\pi}^{new} > 1 \tag{17}$$

where $\Delta\mathbf{M}$ is not infinitesimal, and $\mathbf{M}^{new} = \mathbf{M}^{0} + \Delta\mathbf{M}$

PROOF: Straightforward and available from the author on request.

If this criterion is satisfied by every column of the transition matrix **M** then the deletion of the capability will enhance fitness.

## 4 Modelling the Processes

We now show how production, consumption and trade are represented in transition matrix **M**. Define:

$\boldsymbol{\gamma}_{M*M}$ : the gamma matrix for a process consists of the coefficients for the process in transition matrix **M** together with an offsetting entry in the diagonal element. There is a gamma matrix for each different process and resource. For the reproduction process (one of the consumption processes), the offset entry in the diagonal element is $-p^{REPROD}$ not $-S\cdot p^{REPROD}$. In this way we can break up the **M** matrix into components:

$$\mathbf{M} = \mathbf{I} + \sum_{K=1,2} \boldsymbol{\gamma}^{KP} + \boldsymbol{\gamma}^{KC} + \boldsymbol{\gamma}^{KT} + \boldsymbol{\gamma}^{KD} + \boldsymbol{\gamma}^{KL} \qquad \text{sum over both resources r1 and r2} \tag{18}$$

i.e. $$\mathbf{M}-\mathbf{I}=\sum_{K=1,2}\boldsymbol{\gamma}^{KP}+\boldsymbol{\gamma}^{KC}+\boldsymbol{\gamma}^{KT}+\boldsymbol{\gamma}^{KD}+\boldsymbol{\gamma}^{KL} \tag{19}$$

where superscript P denotes production, C metabolic consumption, T trade, D death wastage and L life wastage (i.e. reproduction consumption).

$\boldsymbol{\Gamma}_{M*M}$: Signature matrix. Some processes (production, consumption and trade) use signature matrices, which factor out the probability of the event and leave the elements which define the process, i.e.

$$\boldsymbol{\gamma}_{M*M}=p_{1*1}\boldsymbol{\Gamma}_{M*M} \tag{20}$$

Usually the signature matrix $\Gamma$ consists of unity elements and $p$, a scalar, is the probability of the process, which can vary. For trading out, the signature matrix takes a different form.

$a_{scalar}^{TYPE}$: This is the expected amount of resource generated per creature per period for the given process shown by the superscript.

$$a^{TYPE}=\mathbf{X}\boldsymbol{\gamma}^{TYPE}\boldsymbol{\pi} \quad =p\mathbf{X}\boldsymbol{\Gamma}^{TYPE}\boldsymbol{\pi} \qquad \text{using (20)} \tag{21}$$

Total resource amount for all processes is zero at equilibrium, as required by the Resource Theorem:

$$\mathbf{X}\left(\mathbf{M}-\mathbf{I}\right)\boldsymbol{\pi}=\mathbf{0}_{K*1} \qquad \text{by (8)} \tag{22}$$

$$\mathbf{X}^{K}\left(\boldsymbol{\gamma}^{KP}+\boldsymbol{\gamma}^{KC}+\boldsymbol{\gamma}^{KT}+\boldsymbol{\gamma}^{KD}+\boldsymbol{\gamma}^{KL}\right)\boldsymbol{\pi}=\mathbf{0}_{1*1} \qquad \text{by (19), one resource only} \tag{23}$$

so $$a^{KP}+a^{KC}+a^{KT}+a^{KD}+a^{KL}=0 \qquad \text{by (21)} \tag{24}$$

Two creatures may differ in their production characteristics but at equilibrium the total amount each produces must sum to zero. Consumption $a^{KC}$ is defined to be the same for each creature, so the corresponding adjustments occur in production, trade and wastage.

We now consider the detail of each process.

*Production r1*: Gamma for r1, $\boldsymbol{\gamma}^{1P}$, transfers to a state one unit higher in r1.

i.e. $$\boldsymbol{\gamma}^{1P}=\begin{bmatrix}-p^{1P} & & & \\ p^{1P} & -p^{1P} & & \\ & p^{1P} & -p^{1P} & \\ & & p^{1P} & 0\end{bmatrix}=p^{1P}\begin{bmatrix}-1 & & & \\ 1 & -1 & & \\ & 1 & -1 & \\ & & 1 & 0\end{bmatrix}=p^{1P}\boldsymbol{\Gamma}^{1P} \tag{25}$$

In the maximal state there is a zero, but it is assumed there is no chance of actually reaching that state.

so
$$a^{1P} = p^{1P}\begin{bmatrix}0 & 1 & 2 & 3\\ 2 & 2 & 2 & 2\end{bmatrix}\begin{bmatrix}0 & & & \\ & -1 & & \\ & 1 & -1 & \\ & & 1 & 0\end{bmatrix}\boldsymbol{\pi} = p^{1P}\begin{bmatrix}\boldsymbol{\iota}\\ \mathbf{0}\end{bmatrix}\boldsymbol{\pi} = \begin{bmatrix}p^{1P}\\ 0\end{bmatrix} \tag{26}$$

where $\boldsymbol{\iota}_{1*M}$ contains 1s in active states A.

*Production r2*: r2 increases by one unit and r1 is reduced by one unit.

$$a^{2P} = p^{2P}\mathbf{X}\,\boldsymbol{\Gamma}\,\boldsymbol{\pi} \tag{27}$$

$$= p^{2P}\begin{bmatrix}5 & 4 & 3 & \\ 1 & 2 & 3 & \end{bmatrix}\begin{bmatrix}-1 & & & \\ 1 & -1 & & \\ & 1 & -1 & \\ & & & 1\end{bmatrix}\boldsymbol{\pi} \tag{28}$$

$$= p^{2P}\begin{bmatrix}-1 & -1 & -1 & \\ 1 & 1 & 1 & \end{bmatrix}\boldsymbol{\pi} \tag{29}$$

$$= p^{2P}\begin{bmatrix}-1\\ 1\end{bmatrix} \tag{30}$$

i.e. expression $\mathbf{X}\,\boldsymbol{\Gamma}\,\boldsymbol{\pi}$ reduces to a production vector. This can be used to apply linear production theory to this model to specify what production vectors are viable given the consumption vector.

*Metabolic consumption:* Gamma $\boldsymbol{\gamma}^{KC}$ subtracts one from the resource.

$$\boldsymbol{\gamma}^{KC} = \begin{bmatrix}0 & p^{KC} & & & \\ & -p^{KC} & p^{KC} & & \\ & & -p^{KC} & p^{KC} & \\ & & & -p^{KC}\end{bmatrix} = p^{KC}\begin{bmatrix}0 & 1 & & \\ & -1 & 1 & \\ & & -1 & 1\\ & & & -1\end{bmatrix} = p^{KC}\boldsymbol{\Gamma}^{KC} \tag{31}$$

In the D states there are zeros, but there is no probability of being in these states.

$$a^{1C} = p^{1C}\begin{bmatrix}0 & 1 & 2 & 3\\ 2 & 2 & 2 & 2\end{bmatrix}\begin{bmatrix}0 & 1 & & \\ & -1 & 1 & \\ & & -1 & 1\\ & & & -1\end{bmatrix}\boldsymbol{\pi} = -p^{1C}\begin{bmatrix}\boldsymbol{\iota}\\ 0_{K*1}\end{bmatrix}\boldsymbol{\pi} = -\begin{bmatrix}p^{1C}\\ 0\end{bmatrix} \tag{32}$$

*Reproduction consumption*: The signature matrix transfers the creature from the L state to the B state.

*D wastage and L wastage*: These are not constant but vary according to the state in the matrix. Both of these amounts are non-positive for every state.

*Net trade*: It is possible to choose signature matrices for trade such that the expected amount of net trade is given by:

$$a_1^{KT} = a_1^{KTI} + a_1^{KTO} \tag{33}$$

$$= c^K x_2^K N_2 - c^K x_1^K N_2 = N_2 c^K \left( x_2^K - x_1^K \right) \tag{34}$$

The author will provide details on request. We see trade is proportional to the difference in means between the populations. Note that intra-species trade will net out to zero as there is no difference in population mean between a population and itself.

## 5 Building Blocks

*Positive, neutral and negative production*: We define gross production in resource *K* per creature per period, $a^{KG}$, as the net of production, consumption and D wastage. It does not include trade or L wastage.

$$a^{KG} = a^{KP} + a^{KC} + a^{KD} \tag{35}$$

We define net production in resource *K* per creature per period, $a^{KN}$, as gross production plus net trade. L wastage is still excluded.

$$a^{KN} = a^{KP} + a^{KC} + a^{KD} + a^{KT} \tag{36}$$

If production sums to zero we refer to the process as being neutral. If production is positive (negative) we say the process is positive (negative). This applies to both gross and net measures.

*Standard results from classical ruin theory*: If a point starts at *t* in a grid running between 0 and *T*, and in each move moves up one space with probability *p* and down one space with probability *q*, then

- If *p* is somewhat greater than *q*, then the probability of reaching *T* is close to unity, and the duration of the game is a first order function of *t* (proportional to *t*).
- If $p = q$ then the probability of reaching *T* is proportional to *t*, and the duration of the game is a second order function of *t* (proportional to $t^2$).

We use this to make the heuristic assumptions (which are simplifications of the reality) that:

- If a creature's net resource process is positive, the creature has no chance of running out of that resource, and the creature will reach the amount of that resource required for reproduction, $\mathbf{X}^L$, quickly.
- If a creature's net resource process is neutral then the creature may run out of the resource, and it will take a long time for the creature to reach the amount of that resource required for reproduction.

*Building block results*: The following rules govern resource production and trading:

RESULT 4: NO NEGATIVE PROCESS. A creature cannot be net negative in a resource.

RESULT 5: AT LEAST ONE NEUTRAL PROCESS. The creature cannot have positive net production in every process at equilibrium; net production in at least one process must be neutral.

RESULT 6: HABITAT THEOREM. If a creature is net neutral in resource *K*,

$$x^K = \mathbf{X}^{KB} \tag{37}$$

Of course particular creatures can have amounts of K which differ from $\mathbf{X}^{KB}$, it is the average over all creatures which equals $\mathbf{X}^{KB}$. A positive resource reaches its requirement for positive resource *J*, $\mathbf{X}^{JL}$ an order of magnitude sooner than neutral resource *K* but has to 'wait for it' there until the creature has a full quota of all resources and can reproduce.

RESULT 7: NET TRADE. If one creature c1 is net positive and another c2 is net neutral then trade is given by:

$$a_1^{KT} = N_2 c^K \left( \mathbf{X}^{KB} - x_1^K \right) \tag{38}$$

$$a_2^{KT} = N_1 c^K \left( x_1^K - \mathbf{X}^{KB} \right) \tag{39}$$

Result follows immediately from (34) and Result 6 Habitat theorem.

The following results work the other way around, inferring production strength from trading.

RESULT 8: POSITIVE FOR TRADE OUT. If a creature trades out resource *K* then it is net positive and gross positive in *K*.

RESULT 9: COMPARATIVE PRODUCTION. If a creature's gross production exceeds another's in a resource, i.e.

$$a_1^{KG} > a_2^{KG} \tag{40}$$

then the creature is net positive in that resource.

RESULT 10: TWO POSITIVE PROCESSES. If two different creatures are both gross positive in a resource, the creatures will be net positive in that resource as well.

*Proofs*: The proofs are sketched out below:

PROOF 4: If a creature were net negative, i.e. $a^{KN} < 0$, then

$$a^{K\,TOTAL} = a^{KN} + a^{KL} < 0 + 0, \qquad \text{contrary to (8).} \tag{41}$$

#

PROOF 5: Suppose all resources have net positive processes. Consider the resource *K* which increases at the slowest rate. Then since the creature reproduces as soon as resource K increases up to $\mathbf{X}^{KL}$, there is no life wastage $a^{KL}$ of that resource. So total production $a^{KT} = a^{KN} + a^{KL}$ is greater than 0, contrary to Resource Theorem (8) #

PROOF 6: By Result 5, creature must be net neutral in at least one resource, *J* say. By definition of a neutral resource, the expected rate of increase per period is zero so the average amount does not change from the original endowment $\mathbf{X}^{KB}$ #

PROOF 8: If c1 is net neutral in resource *K* then it will not trade out, by (39). So c1 is net positive in *K*. By premise c1 trades out the resource, so its gross production must be even greater #

PROOF 9: Assume not, then the creature c1 is net neutral in resource K. Then by (39) it must be gaining resource K in trade and creature c2 must be losing it. So by (40), c2 must be net negative in K, contrary to Result 1 Resource Theorem. #

PROOF 10: Suppose c1 trades out to c2 in resource *K*. By Result 8, c1 must be net positive in *K*. c2 is gross positive and receives more *K* from trade so is net positive in *K* also. #

## 6 System Results

*One creature*: Assume that production of r2 exceeds the need for it, so r2 is a gross positive process. It follows by Result 5 that r1 is a neutral process, so $a^{1D} = 0, a^{1L} = 0$.

The system is given below. Each row represents a resource, denoted by superscript 1,2. There are three equations in three unknowns $N, x_2^1, a^{1P}$. Processes $a^{2P}, a^{1C}, a^{2C}$ are constant with respect to amount *N* but production $a^{1P}$ varies with amount *N*.

$$\begin{bmatrix} a^{1P} & -a^{2P} & a^{1C} & \\ & a^{2P} & a^{2C} & a^{2W} \end{bmatrix} = \begin{bmatrix} 0 \\ 0 \end{bmatrix} \tag{42}$$

$$Na^{1P} = L \tag{43}$$

RESULT 11: SINGLE SPECIES EQUILIBRIUM. Total population is given by

$$N = -\frac{L}{a^{1C} + a^{2C} + a^{2W}} \qquad \text{(note this is positive)} \tag{44}$$

PROOF: Add (42)A and (42)B to get:

$$a^{1P} + a^{1C} + a^{2C} + a^{2W} = 0 \tag{45}$$

$$\frac{L}{N} + a^{1C} + a^{2C} + a^{2W} = 0 \qquad \text{sub } a^{1P} \text{ (43). Rearrange for result.} \tag{46}$$

#

*Two creatures, incremental mutation case:* Introduce a creature with an incremental mutation, so there are now two types of creature, one with the original transition matrix $\mathbf{M}$ and the other with new transition matrix $\mathbf{M}_1 = \mathbf{M} + d\mathbf{M}$.

RESULT 12: INCREMENTAL MUTATION. If the mutation affects a neutral process, only one type of creature can survive in equilibrium.

PROOF: Denote original creature c1 and suppose r1 is its neutral process. Suppose firstly that the mutation is positive so new creature c2 is more efficient in producing r1 than c1. Process r2 is unaffected so is gross positive for both creatures.

Assume c1 and c2 both survive in equilibrium.
By Result 9, c2 is net positive in r1.
By Result 10, c2 is net positive in r2.
By Result 5, c2 is not net positive in both processes. CONTRA.
Similarly if the mutation is negative #

To see what happens in practice we employ a dynamic argument. Assess the fitness of the new creature c2 using the Result 2 Incremental Fitness Theorem. If criterion $\mathbf{v}d\mathbf{M}\boldsymbol{\pi} < 0$, rate of increase $d\lambda < 0$ and c2 will go extinct immediately. If $\mathbf{v}d\mathbf{M}\boldsymbol{\pi} > 0$ then $d\lambda > 0$ and c2 will increase. As the total number of creatures $N$ increases, the probability of production of r1, $p^{P1}$, will decrease pursuant to resource constraint (43) and this impacts on both creatures. For c2, the decrease in $p^{P1}$ will reduce $\mathbf{v}d\mathbf{M}\boldsymbol{\pi}$ and rate of increase $d\lambda$ but c2 will remain viable. For c1, decrease in $p^{P1}$ leads to $\mathbf{v}d\mathbf{M}\boldsymbol{\pi} < 0$ and $d\lambda < 0$. c1 will reduce until it is extinct. The population size $N$ will have been increased.

*Two creatures, deletion mutation case:* Given the excess of r2, Result 3 Discrete Fitness Theorem suggests that a mutation whereby the creature no longer produces r2 will be viable. Assume such a creature, c2, arises. If c2 is going to be viable then the results in the previous section imply the following:

- By Result 4 No negative process, process c2r2 is gross negative so c2 must trade in and make the process net neutral.

- By Result 8 Positive for trade out, process c1r2 must remain net positive to sustain trade.
- By Result 5 At least one neutral process, process c1r1 must be a neutral process.
- By Result 9 Comparative production, process c2r1 must be a positive process as it is more productive than process c1r1, which has an additional subtraction of amount $a^{P2}$.

In writing the system, we omit creature subscripts where the process is the same for both creatures. There are five equations in five unknowns $N_1, N_2, x_1^2, x_2^1, a^{1P}$. Processes $a^{2P}, a^{1C}, a^{2C}$ are constant with respect to amounts $N_1, N_2$ and means $x_1^2, x_2^1$. We look at the change in resources which the introduction of c2 in amount $N_2$ creates.

c1: $$N_1\begin{bmatrix} a^{1P} & -a^{2P} & +a^{1C} & & +N_2a^{1T} \\ & a^{2P} & +a^{2C} & +a_1^{2W} & -N_2a^{2T} \end{bmatrix}=\begin{bmatrix}0\\0\end{bmatrix} \tag{47}$$

c2: $$N_2\begin{bmatrix} a^{1P} & & +a^{1C} & +a_2^{1W} & -N_1a^{1T} \\ & & +a^{2C} & & +N_1a^{2T} \end{bmatrix}=\begin{bmatrix}0\\0\end{bmatrix} \tag{48}$$

$$N_1a^{1P}+N_2a^{1P}=L \qquad a^{1P}=p^{1P} \text{ by (26) and ignoring 0 element} \tag{49}$$

The trade amounts are given by:

$$a^{1T}=c^1\left(x_2^1-X^{1B}\right) \tag{50}$$

$$a^{2T}=c^2\left(x_1^2-X^{2B}\right) \tag{51}$$

RESULT 13: SYSTEM EQUILIBRIUM. If c2 is viable, i.e. c2 is able to procure sufficient resources by trade to cover consumption of r2:

$$a^{2C}+N_1a^{2T}>0 \qquad \text{evaluated at } N_1=N^{ONE\ CREATURE}, N_2=0 \tag{52}$$

then $$N_2>0 \tag{53}$$

and $$\Delta N>0 \qquad \text{where } N=N_1+N_2 \tag{54}$$

PROOF: Add equations (47)A, (47)B, (48)A, (48)B to get:

$$Na^{1P}+Na^{1C}+Na^{2C}+\left(N_1a_1^{2W}+N_2a_2^{1W}\right)=0 \tag{55}$$

We want to compare waste with one creature case. Restate that case and subtract:

$$Na^{1P\ ORIG}+Na^{1C}+Na^{2C}+Na^{2W\ ORIG}=0 \qquad (45)^*N,\ a^{1C}, a^{2C} \text{ constant} \tag{56}$$

$$\left(Na^{1P}-Na^{1P\ ORIG}\right)+\left(N_1a_1^{2W}+N_2a_2^{1W}\right)-Na^{2W\ ORIG}=0 \qquad (55) \text{ less } (56) \tag{57}$$

Find the $\left(Na^{1P} - Na^{1P\,ORIG}\right)$ term using the c1r1 process equations and eliminate:

$$\left(Na^{1P} - Na^{1P\,ORIG}\right) + N \cdot N_2 a^{1T} = 0 \qquad (47)^*N \text{ less } (42)^* N \qquad (58)$$

$$\left(N_1 a_1^{2W} + N_2 a_2^{1W}\right) - \left(Na^{2W\,ORIG} + N \cdot N_2 a^{1T}\right) = 0 \qquad (57) \text{ less } (58) \qquad (59)$$

Derive expression for $N$ here and compare with the one creature case:

$$L + Na^{1C} + Na^{2C} + \left(Na_1^{2W\,ORIG} + N \cdot N_2 a^{1T}\right) = 0 \qquad (55) \text{ with } (49),(59) \qquad (60)$$

$$N = -\frac{L}{a^{1C} + a^{2C} + a_1^{2W\,ORIG} + N_2 a^{1T}} \qquad \text{rearranging} \qquad (61)$$

$$N^{ONE\ CREATURE} = -\frac{L}{a^{1C} + a^{2C} + a_1^{2W\,ORIG}} \qquad \text{restating (44)} \qquad (62)$$

$$N > N^{ONE\ CREATURE} \quad \text{i.e. } dN > 0 \qquad \text{if } N_2 a^{1T} > 0 \text{, i.e. if } N_2 > 0 \qquad (63)$$

We now evaluate $N_2$ using differentials. The initial position for evaluating differential expressions is:

$$N_2 = 0 \qquad (64)$$

$$da^{1P} = \frac{-a^{1P} dN}{N} \qquad \text{differentiating (49)} \qquad (65)$$

$$da^{1P} + dN_2 a^{1T} + N_2 da^{1T} = 0 \qquad \text{differentiating (47)A} \qquad (66)$$

$$\frac{-a^{1P} dN}{N} + dN_2 a^{1T} = 0 \qquad \text{by (65), (66) and (64)} \qquad (67)$$

$$\text{so} \quad dN_2 = \frac{dN}{N} \cdot \frac{a^{1P}}{a^{1T}} > 0 \qquad \text{if } dN > 0 \qquad (68)$$

We see by (63), (68) that a consistent positive solution exists for both variables. #

The amount of wastage of resource 1 in the one creature case is reduced here by the amount of resource 1 which creature 1 gains by trade, $N_2 a^{1T}$, and this is what drives the increase in amount $N$. We see that the expansion of the ecosystem to two creatures leads to a more efficient utilization of the available resources, and consequently an expansion in the total number of creatures. We also see that a deletion mutation is compatible with the existence of both creatures, unlike incremental mutations. This suggests that deletion mutations are the cause of the specialization we see in nature, and indeed in human economies.

*Two creatures, two deletion mutations (parasite) case:* Could a new creature trade in both resources and survive? In this model, one of the original creature's processes would be a neutral process (Result 5 At least one neutral process) and not make resources available for trade (Result 8 Positive for trade out), so the new creature would not be able to trade in that resource and survive. To model parasitism requires that a creature can trade in resources more aggressively than in the normal case.

## 7 Conclusion

We have shown that speciation will lead to an increase in the number of creatures which a given amount of resource *L* will support, because it allows a resource to be produced in proportion to its requirements even if the naturally available production function for the resource results in an oversupply. This conclusion holds within a system where the two creatures are identical in other respects. We can imagine that as the creatures begin to pursue different types of production, they will acquire further characteristics which fit them more nearly to their chosen role - in other words, they adapt and become more efficient. We see the interesting result that an ecology is likely to derive from deletion mutations rather than incremental mutations because deletion mutations lead to interdependence of species, rather than replacement of one species by a more efficient one. Finally, we have shown that the economic concepts of efficiency and quantity may also define long term trends in biology, and deserve to be considered alongside more obvious measures of complexity.

## Reference

1. McShea, D.W.: Possible largest-scale trends in organismal evolution: eight live hypotheses. Annual Review of Ecology and Systematics 29, 293–318 (1998)

# Foraging Multi-Agent System Simulation Based on Attachment Theory

Carlos Alberto Riveros Varela[1], Ferney Beltrán Velandia[1], Miguel Alberto Melgarejo Rey[1], Nadya González Romero[2], and Nelson Obregón Neira[2]

[1] Universidad Distrital "Francisco José de Caldas", Bogotá, Colombia
carlosriverosv@gmail.com, {kilmfer,mmelgarejo}@ieee.org
[2] Pontificia Universidad Javeriana, Bogotá, Colombia
ngonzale328@gmail.com, nobregon@javeriana.edu.co

**Abstract.** A multi-agent system is developed to simulate the emergency of collective behavioral patterns in a foraging model based on the Ant Foraging Model made in NetLogo®. Two kind of agents are implemented, secure and selfish, and they are modeled considering the attachment theory, which describes the dynamics of long-term relationships between humans and establishes specific behavioral patterns. 100 simulations are developed varying the amount of selfish and secure agents, the results show that secure agents are more collaborative than selfish ones and the steps of simulation substantially decrease when secure agents are most than selfish agents.

**Keywords:** Multi-Agent System, Attachment Theory, Foraging Model, Human Behavioral Patterns.

## 1 Introduction

Human beings tend to explore the environment to find out information which let them self-regulate and protect their integrity [1]. Through the behavioral system, one person can respond in different ways to different stimulations and exhibit some behaviors for specific situations. The behavioral system is composed by 4 sub-systems: exploration, alert, membership and attachment, and the attachment theory is developed based on the last one; it describes the dynamics of long-term relationships between humans and establishes specific behavioral patterns. The correct development of those patterns is strongly influenced by the childhood relationship between people and their attachment figure.

Complexity has been recognized as a discipline which try to explain those natural phenomena hard to understand beginning with the individual behavior of their components. Complexity has been defined from different kind of disciplines but there is not an agreement among these yet [2]. However, Bar Yam has given his definition of a complex system as a system formed out of many components whose behavior is emergent, that is, the behavior of the system cannot be simply inferred from the behavior of its components [3]. When the complex



A. Sanayei et al. (eds.), *ISCS 2014: Interdisciplinary Symposium on Complex Systems*, Emergence, Complexity and Computation 14, DOI: 10.1007/978-3-319-10759-2_36

system components, often called agents, can adapt or learn as the interact, it is referred as a Complex Adaptive Systems (CAS) [4]. According to the Holland definition [4]:

> *"A CAS is a complex, self-similar collectivity of interacting adaptive agents".*

Multi-agent systems (MAS) are used to model and simulate CAS where multiple agents interact within a specific environment. An agent has a set of rules and properties which governs their behavior and their making decision capability. MAS have some common properties involving autonomous/self-driven agents, local interactions, variable connections, collective behaviors, distributed regions and communicating neighbors [5]. The aim of MAS is to achieve global emergence behaviors merging from a specific model with a particular purpose where a set of local behavior rules is defined among agents and their environment [6].

NetLogo® is an agent-based programming language and integrate modeling environment to simulate MAS [7], An Ant Foraging Model developed by Uri Wilensky in 1997 [8] and simulated in NetLogo® is create a Foraging MAS simulation of two types of human behavior (secure and selfish agents) based on the attachment theory.

## 2 Methods

### 2.1 Ants Foraging NetLogo® Model

This project called Ants Foraging was developed in NetLogo® by Uri Wilensky and it shows an ants colony forages for food where each ant has a set of simple rules that let it to interact with its environment and other ants. When an ant finds a piece of food, it carries the food back to the nest while drops a chemical as it moves. When other ants "sniff" the chemical, they follow the chemical toward the food. The more ants carry food to the nest the more they reinforce the chemical trail. The environment has a shape of 71x71 patches, 3 food placements and 1 nest.

### 2.2 Attachment Theory and Agents

Taking into account the attachment theory, two types of agents are developed: selfish and secure people. Selfish agent represent people who are not collaborative trying to do all by themselves, they do not tend to communicate with other people, they prefer to work lonely as fast as they can. The secure agents tend to be more collaborative and communicate with people, they could not be faster than selfish people when they do something, but they are better working in a team. For simulation, selfish agents are faster than secure ones, but their chemical (called communication trail for humans) is smaller than the chemical trail of secure agents.

### 2.3 Agent Behavior

The state diagram of a single agent is shown in Fig. 1; firstly, the agent is born and pass to the state "look for food". If it perceives a communication trail, it means that other agent which is carrying food was near there and the first ant will change its orientation toward the strongest perception, and turn back to "look for food" state; if it does not perceive a communication trail, it will move randomly and continue in the "look for food" state; if the agent finds food, it will pick food up and change its state to "look for the nest". Until the agent does not find the nest, it will drop a communication trail as it moves. When the agent finds the Nest, it drops food and come back to state "look for food".

### 2.4 Simulations

The proposal of this work is related to the emergence of collective behavior from ant foraging model where two kind of agents interact (selfish and secure people) based on behavioral patterns of people describe in [1], the environment is the same to the "Ant Foraging" model from NetLogo®. Table 1 shows some static characteristics for the environment, selfish and secure agents. 100 simulations are developed varying the amount of selfish and secure agents in this order: 10 experiments for 0 selfish agents and 100 secure agents at first, then 10 experiments for 10 selfish and 90 secure agents, until the last 10 experiments with 100 selfish and 0 secure agents. The amount of food collected for each kind of agent and the steps of simulation are the measures of the system.

## 3 Results

Table 2 shows the percentage of total food collected by secure and selfish agents as well as its standard deviation and the minimum, maximum and the mean value of steps (time of simulation) until all food were collected. 10 simulations were performed keeping 100 agents by each group varying the amount of secure and selfish ones in 10. When 90 % of agents have a secure behavioral pattern and only 10 % of them are of selfish the total amount of food collected by secure ones is 17.48 % versus 5.45 % of food collected when 90 % of them are selfish and only 10 % are secure. This would prove the emergency of a collaborative behavior from secure agents to the selfish ones, which does not happen otherwise. In Fig. 2 is shown the communication trail formed by secure agents and Fig. 3 shows the same for selfish agents. Figure 2 shows a vast amount of trail is formed, which helps selfish agents to increase their amount of food collected as can be seen in the slope of Fig. 4. Otherwise when selfish agents are most, their communication trail does not help secure agents to collect food. In Table 2 the mean of simulation steps increases as more selfish agents exist and this increment affects negatively the population time spend to collect all food.

**Table 1.** Principal Characteristics of Multi-agent system

| | Speed | Communication Trail | Shape | Movement | population | food |
|---|---|---|---|---|---|---|
| Secure Agents | 0.8 | 200 | Big | random $\pm 40^\circ$ | 100-0 | |
| Selfish Agents | 1 | 10 | Small | random $\pm 10^\circ$ | 0-100 | |
| Environment | | | 71x71 | | 100 | 3 |

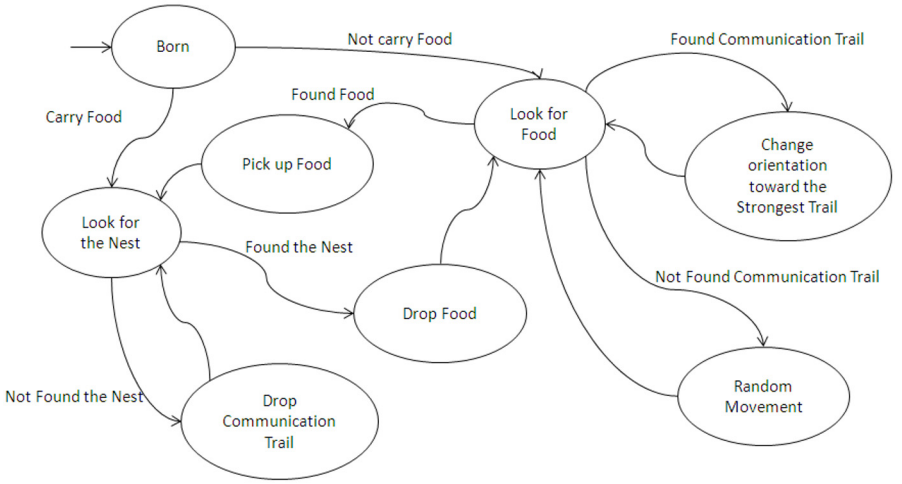


**Fig. 1.** Agent state diagram

**Table 2.** Total food collected by selfish and secure agents for foraging simulations

| Secure Agents | Selfish Agents | Total food of secure Agents | | Total food of selfish agents | | Steps of Simulation | | |
|---|---|---|---|---|---|---|---|---|
| | | Mean() | Std dev | Mean() | Std dev | Mean(step) | Minimum | Maximum |
| 100 | 0 | 100 | 0 | 0 | 0 | 1379 | 1066 | 1784 |
| **90** | **10** | **82.51** | **2.68** | **17.49** | **2.68** | **1461.6** | **1022** | **2240** |
| 80 | 20 | 67.91 | 3.10 | 32.09 | 3.10 | 1677.6 | 950 | 2910 |
| 70 | 30 | 52.74 | 2.82 | 47.26 | 2.82 | 2327.4 | 1464 | 4310 |
| 60 | 40 | 44.21 | 2.42 | 55.79 | 2.42 | 2365.3 | 928 | 3420 |
| 50 | 50 | 33.70 | 3.44 | 66.30 | 3.44 | 2577.7 | 1294 | 3670 |
| 40 | 60 | 24.46 | 2.33 | 75.54 | 2.33 | 3109.7 | 1637 | 3770 |
| 30 | 70 | 17.57 | 1.76 | 82.42 | 1.76 | 3298 | 2940 | 4180 |
| 20 | 80 | 10.74 | 1.72 | 89.26 | 1.72 | 3617.8 | 3027 | 4216 |
| **10** | **90** | **5.46** | **1.05** | **94.54** | **1.04** | **3372.1** | **3056** | **3822** |
| 0 | 100 | 0 | 0 | 100 | 0 | 3401 | 3050 | 3800 |

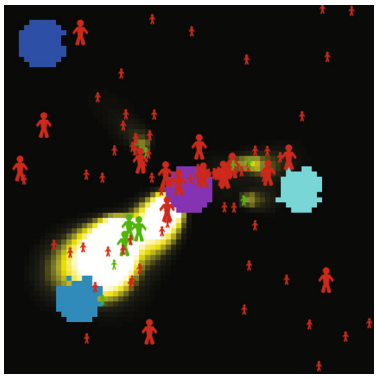

**Fig. 2.** Communication trail formed by a group of secure agents

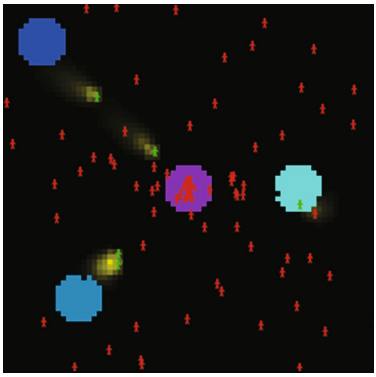

**Fig. 3.** Communication trail formed by a group of selfish agents

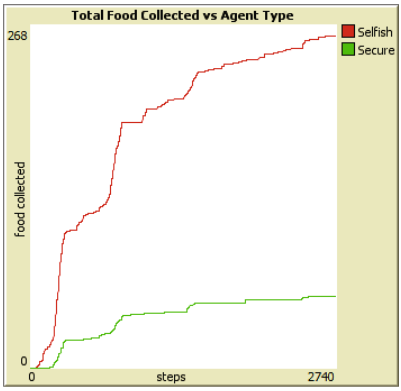


**Fig. 4.** Total food collected in a simulation where selfish agents are most than secure ones

## 4 Conclusions

- There is a significant difference on simulation time between population with more secure agents and population with more selfish agents. The mean of steps for 100 selfish agents is twice as long as for 100 secure agents. It could happen because selfish agents tend to be less communicative and collaborative with other agents.
- Collaborative behavior from secure agents to selfish agents is evidenced when they were searching for food and a trail between food place and the nest was created. It is observed that 17.48 % of food was collected by selfish agents when there were 90 % of secure agents on simulation, whereas only 5.45 % of food was collected by secure agents when there were 90 % of selfish ones.

## References

1. Gonzalez, N.: Modelo Generativo para la visualización de emergencias sociales futuras (2013), http://prezi.com/fdv9_bh5f1r3/apego/?utm_source=website&utm_medium=prezi_landing_related_solr&utm_campaign=prezi_landing_related_owner
2. Maldonado, C.E., Alfonso, N.: El Mundo de las Ciencias de la Complejidad. Editorial Universidad del Rosario (2010)
3. Bar-Yam, Y.: The emergence of complexity. Addison-Wesley (2004)
4. Holland, J.H.: Studying complex adaptive systems. Journal of Systems Science and Complexity 19, 1–8 (2006)
5. Lu, J., Chen, G., Yu, X.: Modelling, analysis and control of multi-agent systems: A brief overview. In: 2011 IEEE International Symposium of Circuits and Systems (ISCAS), pp. 2103–2106 (2011)
6. Macal, C.M., North, M.J.: Tutorial on Agent-Based Modeling and Simulation PART 2: How to Model with Agents. In: Proceedings of the Winter Simulation Conference, WSC 2006, pp. 73, 83, 3–6 (2006)
7. Wilensky, U.: NetLogo Ants model (1997), http://ccl.northwestern.edu/netlogo/models/Ants
8. Zhang, C., Jia, S., Wei, F.: Artificial ant colony foraging simulation and emergent property analysis. In: IEEE Congress on Evolutionary Computation, CEC 2008, pp. 1907, 1912, 1–6 (2008)

# A Spatial Model for Infrastructure Network Generation and Evolution

Gaihua Fu*, Sean Wilkinson, and Richard Dawson

School of Civil Engineering and Geosciences, Newcastle University,
Newcastle upon Tyne, U.K.
{Gaihua.Fu,Sean.Wilkinson,Richard.Dawson}@ncl.ac.uk

**Abstract.** Infrastructure systems are vitally important to our society as they deliver the goods and services that communities require to function. This reliance on infrastructure systems makes any disruption to their functioning liable to result in disproportionate consequences to communities. In this paper we investigate key parameters that exist in real world networks in an attempt to uncover the driving forces of network generation and evolution. We then present a network model that can reproduce networks with several non-trivial properties that are the key signature of real infrastructure networks. By changing the drivers that control evolution of our synthetic networks, the model can potentially help us to better predict what a future infrastructure network may look like, and how resilience it will be to future hazards.

**Keywords:** complex system, infrastructure network, network evolution.

## 1 Introduction

Of the various physical components that form our society, infrastructure networks are one of the most vital parts. Infrastructure systems, such as electrical distribution, water and transport networks, deliver goods and services to our communities as well as promoting social well-being and supporting economic growth. Our reliance on these systems is now so great that we are acutely exposed to disturbances to these systems and disruption to their functioning can lead to disproportionate consequences to the communities that rely on them [1-3]. Hence the ability to understand the key features of resilient networks and their capability to adapt to future changes are vitally important.

Among other techniques employed to study the properties of infrastructure systems, network modelling approaches [4, 5] have been employed to understand how an infrastructure system behaves itself in network disruption and to predict how it might grow and evolve over time [6-10]. As discussed in [11], as these networks serve populations, they too must evolve in response to evolving populations and demographic shifts. This evolution is believed to be governed by a few simple rules, that optimise their ability to provide services to the populations that rely on them [11-

* Corresponding author.



A. Sanayei et al. (eds.), *ISCS 2014: Interdisciplinary Symposium on Complex Systems*,
Emergence, Complexity and Computation 14, DOI: 10.1007/978-3-319-10759-2_37

13] and result in emergent behaviour and network structures possessing particular architectures [14, 15].

Based on existing studies on spatial network generation [10, 16, 17], in this paper we propose a spatial network model in an attempt to reproduce networks that exhibit structure and properties as observed in real infrastructure networks. We consider that three factors, network service demand, network efficiency, and network cost, are the main elements that drive the evolution of an infrastructure network. We show how this model can be used to generate various network structures in response to different drivers. Our preliminary experimental results show that the proposed model generates networks that present several non-trivial properties that are the key signature of real infrastructure networks. The model can also potentially help us to better predict what a future infrastructure network may evolve into, the likely benefits it will impart on the communities it supports and how vulnerable it will be to hazard and help to support interventions that may achieve these aims.

## 2 Empirical Analysis of Real Infrastructure Networks

We have studied the properties of a few real world infrastructure networks, in an attempt to uncover the driving force of network evolution. We first investigated how infrastructure facilities are distributed in space and found that many of them have a clustered node distribution. The scale of this nodal clustering varies from one system to another. For example, we have observed very tight nodal clusters in railway networks and power distribution networks; whereas nodes in telecom and water distribution systems form very loose clusters resulting in a more dispersed nodal distribution. We observed that the clustering of infrastructure facilities is correlated with population density and we believe that this is a proxy for infrastructure service demand. This *correlation* between demand and infrastructure facilities has been proven by our research and is summarised in Figure 1, which shows spatial distribution of population (an indication of service demand) and the distribution of a sample of infrastructure in England and Wales.

We went on to examine how infrastructure facilities are connected or linked to each other. We believe that infrastructure network linkages are formed by balancing network cost and efficiency. If one is interested in minimising the network construction and operation cost, then an optimal network is the one with many short range links. We made a rather simplified assumption here that the cost of a network is only dependent on the physical length of its links. Conversely if one is interested in efficient network service transportation, then an optimal network is the one with short average path length (APL [18]).

To prove this, we studied the cost and efficiency of a few infrastructure networks, and uncover the relationship between two. We found that an efficient network is usually not economic. For example, an Air traffic or Internet network has a small APL and it only takes 2 or 3 steps (APL) to travel from one node to another, but it has long edge length and therefore costs more to build or operate. On the other hand, an economic network such as road and railway network has many short links, but it is

usually less efficient and it takes many hops (having a large APL) in order to travel from one place to another. This supports the intuitive conclusions that cost and efficiency are two competing variables in the formation of networks. Depending on the purpose of networks, an infrastructure network may be designed to bias towards one variable or may consider both variables.

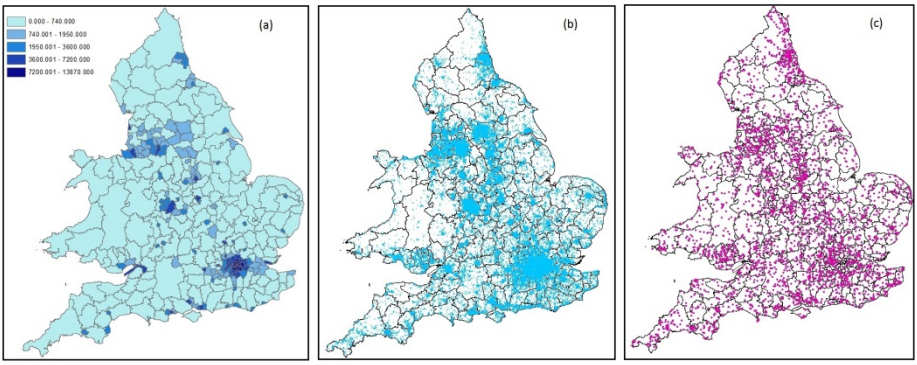


**Fig. 1.** Distribution of population and infrastructure facilities in the area of England and Wales (a) population density in km$^2$ obtained from 2011 Census data [19] (b) spatial distribution of electricity substations (c) spatial distribution of telecom masts

## 3 A Spatial Network Model

We have developed a spatial network model in an attempt to reproduce networks that exhibit structure and properties as observed in real infrastructure networks. To generate a network in a predefined geographical space S, we consider that three factors, network demand, network efficiency, and network cost, are the main elements that drive the evolution of an infrastructure network. The demand for a network service in our model influences how a network node $i$ is distributed in S, and nodes of different spatial distributions can be generated depending on the scale of their correlation to population/ demand density.

Once a network node $i$ is introduced into an area $a$ in S, it connects to existing network nodes. Our research suggests that most nodes choose to connect to nodes that are in its proximity. This reduces the network construction cost. To reduce the number of *hops* for a network service to be delivered to another network place, a node often chooses to connect to a high degree/capacity node. This improves network efficiency. As such we have two variables that regulate network linkages. One aims to reducing the cost of network construction, and one aims to improving network efficiency.

We use $d_{ij}$ to denote the geographical distance between node $i$ and node $j$, and $k_j$ denotes the degree of node $j$. The probability of building an edge $< i, j >$

between a newly introduced node $i$ and an existing node $j$ is jointly determined by $k_j$ and $d_{ij}$, and it is proportional to $k_j$ and is inversely proportional to $d_{ij}$. The larger is $k_j$, or smaller is $d_{ij}$, the more likely that $i$ is connected to $j$. To be able to generate a range of networks, scaling parameters are used to 1) govern the preference for connecting to proximate nodes and 2) govern the preference of connecting to high degree nodes.

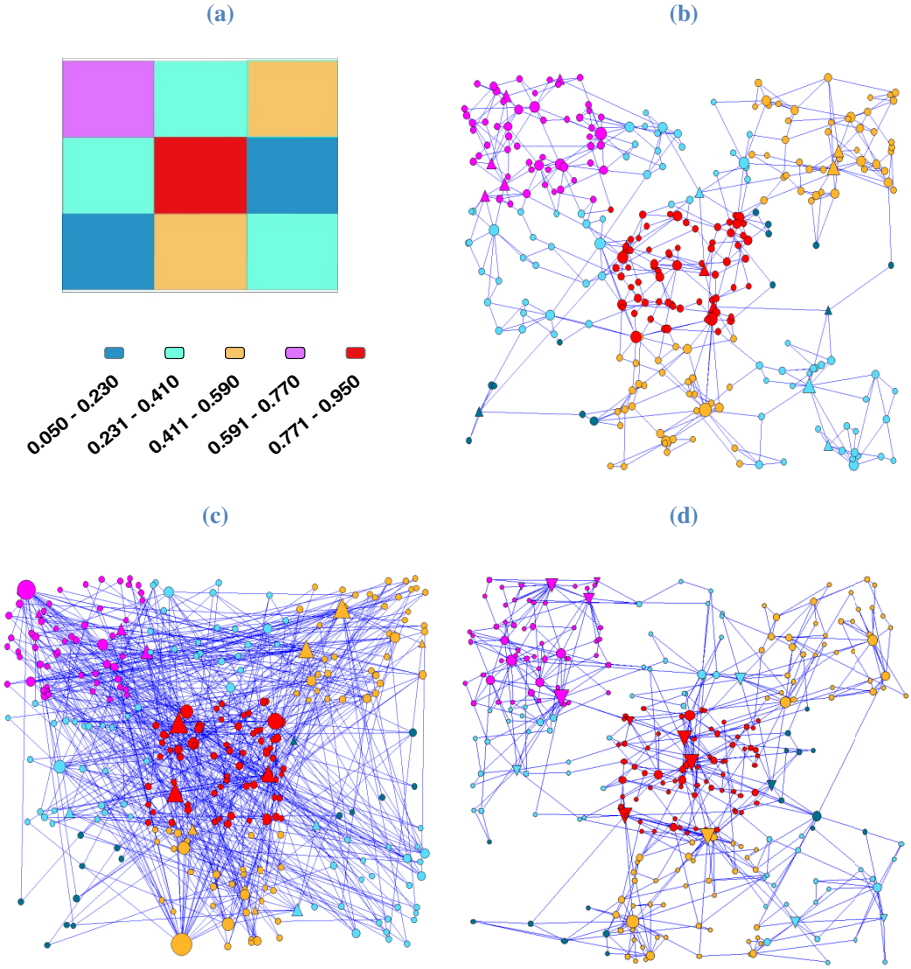


**Fig. 2.** Networks generated with our model (a) demand distribution (b) a network which emphases low cost and the resultant network exhibits short links and spatial clusters (c) a network which emphases efficiency and hub nodes emerge in the resultant network (d) a network which puts emphasis on both low cost and efficiency, and the resultant network exhibits spatial clusters with local hub nodes.

The proposed model is powerful and able to generate a range of networks. Figure 2 shows a few example networks generated with our model. We assume the availability of demand distribution as presented in Figure 2(a). For demonstration purpose, nodes are plotted in the same color with its demand area , and the size of a node is plotted proportionally to its degree. For networks with little preference for attaching to high degree nodes, increasing the preference for short links will encourage a linage to a proximate node and spatial clusters start to emerge. An example network of this type is presented in Figure 2(b). These types of networks cost less to build but are not efficient, exhibiting spatial and topological properties demonstrated by electricity or road networks. For networks with little preference for attaching to a proximate node, increasing the preference for a high degree node results in the emergence of network hubs. An example network is shown in Figure 2(c). This type of networks is efficient but costs more to build, bearing properties that are similar to that of Internet or airway traffic networks. By setting the preference for a node that is both in proximate and of high degree, we generate a network that exhibits spatial clusters as well as hub nodes, which makes the network both economic and efficient. An example network of this type is shown in Figure 2(d).

## 4 Simulation and Validation

We validated the proposed network model by trying to re-generated networks that share properties of real infrastructure networks, and we use the 2011 UK Census statistics [19] as a demand input to our model. For demonstration purpose, we present simulation results for the railway network of England and Wales, where a network node is a train station, and there is an edge between two nodes if they are connected by a rail line. There are total 3547 network nodes, and the average node degree of the network is 2.92. The nodes are spatially clustered and a strong correlation to the demand is identified. Our analysis shows that the network has a rather uniform node degree distribution, with 2- and 3-degree nodes accounting for 64% of all nodes, and the highest node degree is 8. Hence no preference is given for connection to high degree nodes. The network shows a clear bias towards short range edges, with the longest edge of the network spans only about 4% of the diameter of its embedding space.

Calibrating a set of parameters, we have simulated the railway network of England and Wales. The results were obtained by averaging over 100 realisations. Figure 3 shows the distribution of network nodes for the network, and results are compared against that of the real network. The good match between two were obtained.

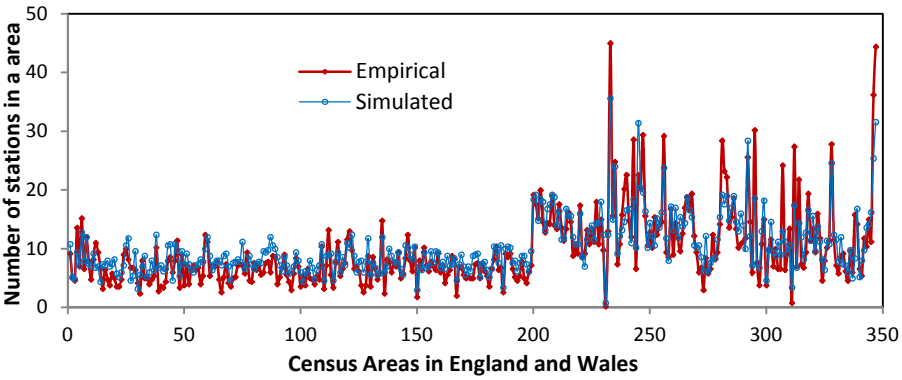


**Fig. 3.** Distribution of the network nodes

Figure 4 compares the edge length distribution of simulated networks and real network. Again, good agreement is observed between simulated networks and real network. Similar results were obtained for other networks investigated in this research, and a reader is referred to [20] for our further experimental results on this.

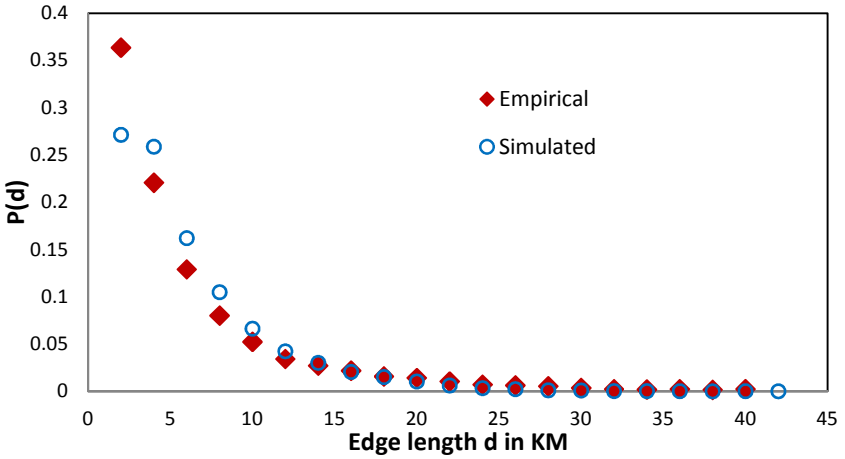


**Fig. 4.** Distribution of edge length

## 5 Conclusions

This paper presents observed relationships between population density, infrastructure density and connectivity in infrastructure networks. These are then used to develop a spatial network model which forms network facilities and connecting linkages by balancing three driving factors namely; infrastructure service demand, network efficiency, and network cost. Through empirical study and computer simulation, we show that proposed network model is capable of reproducing networks that exhibit

structure and properties observed in real infrastructure networks. The model may be useful in testing scenarios of infrastructure development by changing the relative importance of the driving factors and observing the resulting network and its associated properties.

## References


1. Wilkinson, S.M., Alarcon, J.E., Mulyani, R., Whittle, J., Chian, S.C.: Observations of damage to buildings from M w 7.6 Padang earthquake of 30 September 2009. Nat. Hazards 63, 521–547 (2012)
2. Fu, G., Dawson, D., Khoury, M., Bullock, S.: Interdependent networks: Vulnerability analysis and strategies to limit cascading failure. Eur. Phys. J. B 87, 148 (2014)
3. Dunn, S., Fu, G., Wilkinson, S., Dawson, D.: Network Theory for Infrastructure Systems Modelling. Proceedings of the ICE - Engineering Sustainability 166, 281–292 (2013)
4. Newman, M., Barabasi, A., Watts, D.: The Structure and Dynamics of Networks. Princeton University Press, USA (2006)
5. Albert, R., Barabasi, A.: Statistical mechanics of complex networks. Rev. Mod. Phys. 74, 47–97 (2002)
6. Rosas-Casals, M., Valverde, S., Sole, R.V.: Topological vulnerability of the European power grid under errors and attacks. Int. J. Bifurcat. Chaos 17, 2465–2475 (2007)
7. Albert, R., Albert, I., Nakarado, G.: Structural vulnerability of the North American power grid. Phys. Rev. E 69, 025103 (2004)
8. Ten, C., Liu, C., Manimaran, G.: Vulnerability Assessment of Cybersecurity for SCADA Systems. IEEE T. Power Syst. 23, 1836–1846 (2008)
9. Cohen, R., Erez, K., Ben-Avraham, D., Havlin, S.: Breakdown of the Internet under intentional attack. Phys. Rev. Lett. 86, 3682–3685 (2001)
10. Yook, S.H., Jeong, H.W., Barabasi, A.L.: Modeling the Internet's large-scale topology. P. Natl. Acad. Sci. USA 99, 13382–13386 (2002)
11. Gastner, M.T., Newman, M.E.J.: Optimal design of spatial distribution networks. Phys. Rev. E 74 (2006)
12. Wilkinson, S., Dunn, S., Ma, S.: The vulnerability of the European air traffic network to spatial hazards. Nat. Hazards 60, 1027–1036 (2012)
13. Bettencourt, L.M.A., Lobo, J., Helbing, D., Kuehnert, C., West, G.B.: Growth, innovation, scaling, and the pace of life in cities. P. Natl. Acad. Sci. USA 104, 7301–7306 (2007)
14. Crucitti, P., Latora, V., Marchiori, M.: A topological analysis of the Italian electric power grid. Physica. A 338, 92–97 (2004)
15. Carvalho, R., Buzna, L., Bono, F., Gutierrez, E., Just, W., Arrowsmith, D.: Robustness of trans-European gas networks. Phys. Rev. E 80, 016106 (2009)
16. Cao, X.B., Du, W.B., Hu, M.B., Rong, Z.H., Sun, P., Chen, C.L.: Topology Property and Dynamic Behavior of a Growing Spatial Network. Int. J. Mod. Phys. C 22, 333–345 (2011)
17. Barthelemy, M.: Spatial Networks. Phys. Rep. 499, 1–101 (2011)
18. Gross, J.L., Yellen, J.: Handbook of Graph Theory. CRC Press (2004)
19. Office for National Statistics, `http://www.ons.gov.uk/ons/rel/census/2011-census/population-and-household-estimates-for-england-and-wales—unrounded-figures-for-the-data-published-16-july-2012/index.html`
20. Fu, G., Wilkinson, S., Dawson, D.: A Network Model for Infrastructure Network Evolution and Resilience Study. Newcastle University (2014)

# Author Index